

DISSERTATION

FLUORINATED MATERIALS SYNTHESIS AND CHARACTERIZATION FOR ENERGY
STORAGE AND ENERGY CONVERSION APPLICATIONS

Submitted by

Eric V. Bukovsky

Department of Chemistry

In partial fulfillment of the requirements

For the Degree of Doctor of Philosophy

Colorado State University

Fort Collins, Colorado

Fall 2015

Doctoral Committee:

Advisor: Steven H. Strauss

Christopher Ackerson

Debbie Crans

B. George Barisas

Sally Sutton

Copyright by Eric Vannest Bukovsky 2015
All Rights Reserved

ABSTRACT

FLUORINATED MATERIALS SYNTHESIS AND CHARACTERIZATION FOR ENERGY STORAGE AND ENERGY CONVERSION APPLICATIONS

The synthesis and characterization of multiple fluorinated, *p*-block, cage, and organic compounds will be presented. The research effort is split up in to main topics, (i) fluorinated superweak anions based on B₁₂ cages, and (ii) perfluoroalkylation of polycyclic aromatic hydrocarbon (PAH) and fullerene compounds. In the first three chapters, superweak anion research is presented; a new purification method for the synthetic intermediate K₂B₁₂F₁₂, synthesis and thermal and physical characterization of highly purified (H₃O)₂B₁₂F₁₂·*n*H₂O, Li₂B₁₂F₁₂ and Na₂B₁₂F₁₂ (synthesized from K₂B₁₂F₁₂), and an HF-free, improved synthesis method and characterization of KB₁₂F₁₁NH₃. Furthermore, the unanticipated, rapid fluorination of KB₁₂H₁₁NH₃ in the presence of HF, contrary to, previously observed, slowed fluorination of K₂B₁₂H₁₂ in the presence of HF, will also be described.

Single crystal X-ray structures of three new isomers of C₆₀(CF₃)₁₀ are discussed, and one putative isomer of C₆₀(CF₃)₁₀ is confirmed along with comparisons of their crystal packing properties compared to 1,9-C₆₀(*cyclo*-CF₂(2-C₆F₄)), and industry-standard fullerene acceptor phenyl-C₆₁-butyric acid methyl ester (PCBM). Discussion of how the structural and electrochemical data of the new C₆₀(CF₃)₁₀ isomers and 1,9-C₆₀(*cyclo*-CF₂(2-C₆F₄)) agree with currently accepted literature will also be discussed.

A new metal reactor design for the radical reactions of CF₃I and polycyclic aromatic hydrocarbons (PAH) and fullerenes, and initial results will be discussed and compared to

previous reaction methods. Single crystal X-ray structures of four separate compounds believed to be "trapped intermediates" formed from the radical substitution reaction isolated from radical reactions with CF_3I using different PAHs and different reactions conditions will be discussed as well as the implications these trapped intermediates have on the proposed mechanism of $\text{CF}_3\cdot$ radical substitution reactions. Crystal packing and nearest molecule analysis of five $\text{PAH}(\text{CF}_3)_n$ will be compared to a single crystal X-ray structure of triphenylene with a C_4F_4 substitution. Insights into the structural effects of CF_3 substitutions compared to the flat C_4F_4 substitutions, and, how those effects would translate into electronic communication in the solid state will be discussed.

Finally, wet milling of metallurgical grade silicon in an attritor mill, under anaerobic and aerobic conditions with and without surface passivating additives to study the affects oxygen and additives can have on milled particle properties such as, crystallinity by powder X-ray diffraction, surface bonds by X-ray photoelectronspectroscopy, dynamic light scattering particle size, N_2 gas uptake BET surface area and reactivity towards oxygen will be discussed. Under anaerobic conditions silicon was found to form Si-C bonds in the presence of dry- air-free heptane. Additionally, the extensive effect oxygen has on the comminution of silicon and the surprising result that, even in aerobic conditions, formation of Si-C bonds is observed.

All of the research described in this dissertation has applications in one or multiple energy storage or energy conversion devices. The superweak anion salts as electrolyte salts in battery or fuel cell, $\text{C}_{60}(\text{CF}_3)_{10}$ and 1,9- $\text{C}_{60}(\text{cyclo-CF}_2(2-\text{C}_6\text{F}_4))$, as electron acceptor materials in organic photovoltaic devices, and multiple $\text{PAH}(\text{CF}_3)_n$ compounds as OLED active layer materials.

ACKNOWLEDGMENTS

First and foremost, I want to thank my wonderful wife Desirée Bukovsky for supporting me in everything I have done, for making me do something fun to take my mind off graduate school from time to time, pouring me a glass of whisk(e)y when I had a particularly bad day, or generally being her wonderful self to make me smile. It's been said many times that behind every great man is a great woman, only time will tell how great Eric "Buck", V. Bukovsky becomes, but I already know my wife, Desirée B. Bukovsky PT, DPT (Doctor of Physical Therapy) *is great*. Des, I sure do love you, and after this dissertation is complete I won't be late coming home because I am "roto-vaping", nor will I have to come in late at night and "top off the traps." I would like to thank my hound dogs, Jaxon and Daisy Mae for always being fun, a little crazy, stealing my space heater when I would write in the basement, and putting me to sleep with their rhythmic breathing when they slept.

I would like to thank my advisor Prof. Steven H. Strauss Ph.D., I know we disagreed on a good number of things but I learned an awful lot from you, likely through our disagreements. I learned not only random chemistry facts or how to perform good/meaningful research, or how to design the perfect experiment (which doesn't exist), but also how to generally be a good scientist, how to perform quality research, that disagreement with others in science usually means you're working on something interesting and you're asking the right questions, and most important of all be sure not to fool yourself, and you are the easiest person to fool! Also, I would like to thank Steve for being a stickler on grammar, spelling, punctuation, and formatting; while these things were merely just a nuisance to me before, somewhere along the way I realized, with Steve's patient help, communicating your research and ideas accurately, is at least, if not more important,

than the research itself. I would like to thank my co-advisor Dr. Olga V. Boltalina for always being there when I needed help, being an additional scientist and friend I could discuss my ideas and problems with, not being afraid to ask the tough questions during group meeting, and every now and then surprising the group with delicious baked goods and cakes; there is nothing better than an "Olga cake" at group meeting when you have just spent 9 h in the lab on an experiment that didn't work. I would like to thank my research group (all of the various iterations) for training me to be more flexible and versatile (usually without intending to) and for being good friends throughout the ordeal that is chemistry graduate school. I would especially like to thank Long K. San and Ty T. Clikeman who started in the Strauss research group with me, for keeping each other honest, focused and motivated, Karlee P. Castro for being a great scientist, dog sitter, and overall great person to ask for sound advice of any kind, James B Whitaker for teaching CHEM 462 with me multiple times, Bryon W. Larson for always being helpful (when he was around) and Dr. Igor V. Kuvychko for listening, helping and for being a great roommate for a short time, Amanda M. Pluntze for working with and continuing the boron research, and Nicholas J. Deweerd for working on and taking over the metal reactor experiments and helping to put that experimental reactor through its paces. Finally, I would like to thank the CSU chemistry faculty overall (obviously including the accountants, office assistants and secretaries, without whom I would have missed every deadline imaginable) for always having open doors and time to discuss ideas, I know not all chemistry faculties are this overall helpful to their graduate students and I think this is one area that sets CSU chemistry department apart.

I would also like to thank my friends Derek W. Thompson PE, Brandon E. Pioreschi MD, and Michael T. Dixon for being great friends, offering support, guidance, and wisdom, (sometimes even the lack of wisdom) and even though we are all on different paths, we all

started out as "Hellva Engineers". I would also like to thank some of the great friends and family here in Fort Collins, Rod and Patricia Wright for letting a poor grad student with his wife and hound dogs come and have a nice meal, for helping with the house and in countless other ways, Temple and Amanda Abney for fun games and lots of laughter, and Robert and Kerry Hodgens, for great meals, great stories and great times, yes I am doing the dance, you all know which one.

Finally, I would like to thank my father, John M. Bukovsky, mother, Amy M. Silver and stepmother, Peggy A. Meservey for always supporting me in my endeavors; whether it was playing hockey without ever having done it before, rebuilding an engine for my car, going to college, or moving halfway across the country for a job. I especially want to thank my father for fostering my desire to learn, explore, and understand the world around me; and for showing me that patience and persistence along with inventiveness to attack a problem in many ways will solve most problems. I would also like to thank my father for helping me understand that it's better to "do" and "build" everything right the first time. Most of all, for believing in me growing up which gave me the confidence to propose, do, and try things other people are afraid to do or won't even try, because, those ideas that raise doubt are sometimes the ideas that will solve the tough problems.

TABLE OF CONTENTS

| | |
|---|-----------|
| ABSTRACT..... | ii |
| ACKNOWLEDGMENTS | iv |
| TABLE OF CONTENTS..... | vii |
| LIST OF TABLES | xiii |
| LIST OF FIGURES | xiv |
| LIST OF ACRONYMES AND ABBREVIATIONS..... | xx |
| Chapter 1. Introduction and Justification of Research..... | 1 |
| 1.2 Radical Substitution and Addition Synthesis with Perfluoroalkyl and Perfluoroaryl Groups, Single Crystal X-ray Structural Characterization and Mechanistic Insight..... | 7 |
| 1.3 Preparation and Characterization of Silicon Nanoparticles by Anaerobic Wet Milling..... | 9 |
| Chapter 1 References | 12 |
| Chapter 2. Improved Synthesis and Purification the of Superweak Anion Salts | |
| Li₂B₁₂F₁₂, Na₂B₁₂F₁₂, and K₂B₁₂F₁₂..... | 17 |
| 2.1 Introduction and Justification..... | 17 |
| 2.1.1 Published Synthesis and Purification Methods of K ₂ B ₁₂ F ₁₂ and Li ₂ B ₁₂ F ₁₂ ·nH ₂ O..... | 21 |
| 2.1.2 Safety Concerns Regarding the use of H ₂ O ₂ to Purify Crude K ₂ B ₁₂ F ₁₂ | 24 |
| 2.2 Results | 28 |
| 2.2.1 Separating and Identifying the Colored Yellow impurity Produced During K ₂ B ₁₂ F ₁₂ Synthesis | 28 |
| 2.2.2 Hypotheses and Control Experiments to Identify Yellow Impurity..... | 29 |
| 2.2.3 Attempts to Remove Yellow Impurity Produced During K ₂ B ₁₂ F ₁₂ Synthesis By Oxidation | 31 |
| 2.2.4 Attempts to Remove Yellow Impurity Produced During K ₂ B ₁₂ F ₁₂ Synthesis By Reduction..... | 32 |
| 2.2.5 Improved Purification Method of K ₂ B ₁₂ F ₁₂ without H ₂ O ₂ | 33 |
| 2.2.6 Synthesis of High-Purity Li ₂ B ₁₂ F ₁₂ ·nH ₂ O and Na ₂ B ₁₂ F ₁₂ ·nH ₂ O with Cation-Exchange Starting from K ₂ B ₁₂ F ₁₂ | 34 |
| 2.2.7 Determination of Optimal Drying Conditions for Li ₂ B ₁₂ F ₁₂ ·nH ₂ O and Na ₂ B ₁₂ F ₁₂ ·nH ₂ O to Make Anhydrous Li ₂ B ₁₂ F ₁₂ and Na ₂ B ₁₂ F ₁₂ | 34 |
| 2.3 Dissusion | 35 |
| 2.3.1 Possible Causes of Violent Reaction..... | 35 |
| 2.3.2 Identification of the Yellow Impurity in K ₂ B ₁₂ F ₁₂ Crude Product | 37 |
| 2.3.3 New Purification Method of K ₂ B ₁₂ F ₁₂ Crude Product | 40 |
| 2.3.4 Synthesis of High-Purity Li ₂ B ₁₂ F ₁₂ ·nH ₂ O and Na ₂ B ₁₂ F ₁₂ ·nH ₂ O with Cation-Exchange from K ₂ B ₁₂ F ₁₂ and Dehydration to Li ₂ B ₁₂ F ₁₂ and Na ₂ B ₁₂ F ₁₂ | 41 |
| 2.4 Summary and Conclusions..... | 42 |
| 2.5 Experimental | 43 |

| | |
|---|-----------|
| 2.5.1 Reagents and Solvents | 43 |
| 2.5.2 Instrumentation | 44 |
| 2.5.3 Modified Purification of Crude $K_2B_{12}F_{12}$ | 45 |
| 2.5.4 Synthesis of $Li_2B_{12}F_{12}$ and $Na_2B_{12}F_{12}$ from $K_2B_{12}F_{12}$ | 46 |
| Chapter 2 References | 66 |
| Chapter 3. Synthesis and Properties of Anhydrous and Hydrated Hydronium Salts of | |
| $B_{12}F_{12}^{2-} (H_3O)_2B_{12}F_{12} \cdot n(H_2O)$ ($n = 6, 4, 2, 0$): In Search of $H_2B_{12}F_{12}$ | 68 |
| 3.1 Introduction and Justification | 68 |
| 3.2 Possible Synthetic Routes to $H_2B_{12}F_{12}$, Literature Methods for Making | |
| $H_2B_{12}F_{12}$ and Related Superacids | 71 |
| 3.2.1 Chosen Synthetic Method for $H_2B_{12}F_{12}$ | 75 |
| 3.3 Results | 75 |
| 3.3.1 Synthesis of $(H_3O)_2B_{12}F_{12} \cdot nH_2O$ by Strong Acid Cation Exchange | 75 |
| 3.3.2 Crystal Structure of $(H_3O)_2B_{12}F_{12} \cdot nH_2O$ ($n = 6, 4$) | 77 |
| 3.3.3 Purity Analysis by 1H , ^{19}F [^{11}B], and ^{11}B [^{19}F] NMR Spectroscopy, and ICP-AES | 81 |
| 3.3.4 DSC analysis of $(H_3O)_2B_{12}F_{12} \cdot 6H_2O$ | 82 |
| 3.3.5 Raman and FT-IR of $(H_3O)_2B_{12}F_{12} \cdot 6H_2O$ and $(H_3O)_2B_{12}F_{12}$ | 82 |
| 3.3.6 Synthesis of Metal Salts Using $(H_3O)_2B_{12}F_{12} \cdot nH_2O$ as a reagent: | |
| $ZnB_{12}F_{12} \cdot 6H_2O$ Proof of Concept | 83 |
| 3.3.7 Hydration/Dehydration of $(H_3O)_2B_{12}F_{12} \cdot nH_2O$ by TGA | 84 |
| 3.3.8 DFT Structure Calculations of $(H_3O)_2B_{12}F_{12}$ and $H_2B_{12}F_{12}$ | 85 |
| 3.3.9 Thermal Stability of $(H_3O)_2B_{12}F_{12} \cdot nH_2O$, and attempted dehydration to | |
| $H_2B_{12}F_{12}$ | 85 |
| 3.3.10 Thermal Behavior of $(NH_4)_2B_{12}F_{12} \cdot 4H_2O$, and stable hydrates | 87 |
| 3.3.11 Crystal Structure of $(NH_4)_2B_{12}F_{12} \cdot 4H_2O$, Alternative Hypothesis for | |
| Two Discrete Mass Losses in $(NH_4)_2B_{12}F_{12} \cdot nH_2O$ TGA | 88 |
| 3.4 Discussions | 90 |
| 3.4.1 Synthesis of $(H_3O)_2B_{12}F_{12} \cdot nH_2O$ by Strong-Acid Cation-Exchange Resin | 90 |
| 3.4.2 Hydration/Dehydration of $(H_3O)_2B_{12}F_{12} \cdot nH_2O$ by TGA | 90 |
| 3.4.3 DFT Structure Calculations of $(H_3O)_2B_{12}F_{12}$ and $H_2B_{12}F_{12}$ | 92 |
| 3.4.4 Comparison of Hydrogen Bonded Networks in $(H_3O)_2B_{12}F_{12} \cdot 4H_2O$ and | |
| $(NH_4)_2B_{12}F_{12} \cdot 4H_2O$ Crystal Structures | 92 |
| 3.4.5 Apparent Volume of Water Molecules in K^+ , NH_4^+ , and H_3O^+ Hydrated salts | |
| of $B_{12}F_{12}^{2-}$ | 93 |
| 3.4.6 Attempted Synthesis of $H_2B_{12}F_{12}$ by Thermal Removal of H_2O or NH_3 and | |
| Thermal Stability of $(H_3O)_2B_{12}F_{12} \cdot nH_2O$ and $(NH_4)_2B_{12}F_{12} \cdot nH_2O$ | 94 |
| 3.5 Summary and Conclusions | 97 |
| 3.6 Future Work | 98 |
| 3.7 Experimental | 99 |
| 3.7.1 Reagents and Solvents | 99 |

| | |
|---|------------|
| 3.7.2 Instrumentation | 100 |
| 3.7.3 Synthesis of $(\text{H}_3\text{O})_2\text{B}_{12}\text{F}_{12}\cdot n\text{H}_2\text{O}$ from Strong Acid Cation Exchange | 103 |
| 3.7.4 Purity Analysis by ^1H , ^{19}F [^{11}B], and ^{11}B [^{19}F] NMR Spectroscopy and ICP-AES | 104 |
| 3.7.5 Synthesis of Metal Salts Through $(\text{H}_3\text{O})_2\text{B}_{12}\text{F}_{12}\cdot n\text{H}_2\text{O}$: $\text{ZnB}_{12}\text{F}_{12}\cdot 6\text{H}_2\text{O}$ Proof of Concept | 105 |
| 3.7.6 Synthesis of $(\text{NH}_4)_2\text{B}_{12}\text{F}_{12}\cdot n\text{H}_2\text{O}$ from Neutralization of $(\text{H}_3\text{O})_2\text{B}_{12}\text{F}_{12}\cdot n\text{H}_2\text{O}$ | 105 |
| Chapter 3 References | 149 |
| Chapter 4. New or Improved Syntheses of the $\text{B}_{12}\text{H}_{11}(\text{NH}_3)^-$ and $\text{B}_{12}\text{F}_{11}(\text{NH}_3)^-$ Anions and the 1,2-, 1,7-, and 1,12- Isomers of $\text{B}_{12}\text{H}_{10}(\text{NH}_3)_2$ and $\text{B}_{12}\text{F}_{10}(\text{NH}_3)_2$ and Their Spectroscopic and Structural Characterization..... | 153 |
| 4.1 Introduction and Justification | 153 |
| 4.2 Results and Discussion | 155 |
| 4.2.1 Improved and Efficient Fluorination of $\text{B}_{12}\text{H}_{11}(\text{NH}_3)^-$ | 156 |
| 4.2.2 Efficient per- <i>B</i> -fluorination of $\text{B}_{12}\text{H}_{11}(\text{NH}_3)^-$ with F_2/N_2 in MeCN | 158 |
| 4.2.3 Single Crystal X-ray Structure of $\text{Na}(\text{H}_2\text{O})_4\text{B}_{12}\text{F}_{11}(\text{NH}_3)$: Evidence for $\text{NH}\cdots\text{F}$ Hydrogen Bonding | 164 |
| 4.2.4 Why Does HF protect $\text{B}_{12}\text{F}_{11}(\text{NH}_3)^-$ From Decomposition in the Presence of F_2 ? | 166 |
| 4.2.5 Why Does the Presence of HF Accelerate the F_2 Fluorination of $\text{B}_{12}\text{H}_{11}(\text{NH}_3)^-$? ... | 169 |
| 4.2.6 Improved Synthesis, Purification, and Spectroscopic Characterization of the Isomers of $\text{B}_{12}\text{H}_{10}(\text{NH}_3)_2$ and $\text{B}_{12}\text{F}_{10}(\text{NH}_3)_2$ | 171 |
| 4.2.7 NMR characterization | 172 |
| 4.2.8 Fluorination of $\text{B}_{12}\text{H}_{10}(\text{NH}_3)_2$ Isomers | 173 |
| 4.2.9 The X-ray Structures of 1,2-, 1,7- and 1,12- $(\text{NH}_3)_2\text{B}_{12}\text{H}_{10}$ and 1,7- and 1,12- $(\text{NH}_3)_2\text{B}_{12}\text{F}_{10}$ | 174 |
| 4.3 Summary and Conclusions | 174 |
| 4.4 Future Work | 176 |
| 4.5 Experimental | 177 |
| 4.5.1 Reagents and Solvents | 177 |
| 4.5.2 Instrumentation | 178 |
| 4.5.3 Synthesis of $\text{KB}_{12}\text{H}_{11}\text{NH}_3$ | 180 |
| 4.5.4 Synthesis of $\text{KB}_{12}\text{F}_{11}\text{NH}_3$ in anhydrous MeCN | 181 |
| 4.5.5 Synthesis of $\text{KB}_{12}\text{F}_{11}\text{NH}_3$ with ca. 2.0% HF in anhydrous MeCN | 182 |
| 4.5.6 Separation of 1,2-, 1,7-, and 1,12- $(\text{NH}_3)_2\text{B}_{12}\text{X}_{10}$ ($\text{X} = \text{H}, \text{F}$) | 182 |
| 4.5.7 Synthesis of 1,2-, 1,7-, and 1,12- $(\text{NH}_3)_2\text{B}_{12}\text{F}_{10}$ | 183 |
| Chapter 4 References | 210 |
| Chapter 5. Single-Crystal X-ray Structural Characterization of C_{60} Derivatives with Perfluoroalkyl and Related Perfluorinated Substituents: Seven Isomers of $\text{C}_{60}(\text{CF}_3)_{10}$ and 1,9-$\text{C}_{60}(\text{cyclo-CF}_2(2-\text{C}_6\text{F}_4))$, a Faux Hawk Fullerene with PCBM-like Properties | 212 |
| 5.1 Introduction and Justification | 212 |

| | |
|--|------------|
| 5.2 Results..... | 216 |
| 5.2.1 Three new isomers of C ₆₀ (CF ₃) ₁₀ | 216 |
| 5.2.2 Molecular Structure of 1,9-C ₆₀ (<i>cyclo</i> -CF ₂ (2-C ₆ F ₄)). | 218 |
| 5.3 Discussion | 218 |
| 5.3.1 Fullerene Cage C–C Distances, Distinction Between Single and Double Bonds | 218 |
| 5.3.2 The Electronic Consequences of Non-Terminal Double Bonds in Pentagons. | 219 |
| 5.3.3 Solid-State Packing of C ₆₀ (CF ₃) ₁₀ Isomers. | 222 |
| 5.3.4 Solid-State Packing of 1,9-C ₆₀ (<i>cyclo</i> -CF ₂ (2-C ₆ F ₄)) and Comparison with Single-Crystal X-ray Structures of PCBM and PCBM-like Molecules | 225 |
| 5.4 Experimental Section | 228 |
| 5.4.1 Reagents and Solvents/Instrumentation | 228 |
| 5.5 Experimental Section | 228 |
| Chapter 5 References | 260 |
| Chapter 6. Versatile Robust Metal Reactor for High Temperature Trifluoromethylation of PAHs and Fullerenes; X-ray Structural Characterization of PAH(CF₃)_n and Related Compounds and Insights into the Mechanism of Radical Substitution..... | 263 |
| 6.1 Introduction and Justification | 263 |
| 6.2 Synthesis of PAH(CF ₃) _n in Sealed Glass Ampoules | 267 |
| 6.2.1 Problems Associated with Glass Ampoule Reactor Based Reaction Set-up | 269 |
| 6.2.2 Design Requirements For New Reactor | 271 |
| 6.3 Structural Evidence for the Free Radical Substitution Mechanism on PAHs by CF ₃ • Radicals | 273 |
| 6.4 Structural and Packing Analysis of PAH(CF ₃) _n 's and Related Compounds | 277 |
| 6.5 Results..... | 278 |
| 6.5.1 Metal Reactor for High Pressure, High Temperature Reactions of CF ₃ I and PAH..... | 278 |
| 6.5.2 Testing the High Pressure and Temperature Metal Reactor | 279 |
| 6.5.3 Crystal Structure of Intermediate Compounds as Evidence of Proposed Radical Substitution Mechanism | 283 |
| 6.5.4 Structural Analysis of PAH(CF ₃) _n 's and Related Compounds..... | 285 |
| 6.6 Discussions | 290 |
| 6.6.1 Metal Reactor for High Pressure, High Temperature Reactions of CF ₃ I with Either PAH or Fullerene Based Reactants | 290 |
| 6.6.2 Structural Evidence of Intermediate Compounds in Support of a Proposed Radical Substitution Mechanism | 296 |
| 6.6.3 Structural Analysis of PAH(CF ₃) _n 's and Related Structures..... | 297 |
| 6.7 Summary and Conclusions | 299 |
| 6.8 Future Work | 300 |
| 6.9 Experimental..... | 301 |
| 6.9.1 Reagents and Solvents | 301 |

| | |
|---|------------|
| 6.9.2 Instrumentation | 302 |
| 6.9.3 Synthesis with Anthracene and CF ₃ I in Metal Reactor | 303 |
| 6.9.4 Synthesis of H ₂ -CORO(CF ₃) ₇ -1 and H ₂ -CORO(CF ₃) ₈ -1 in Metal Reactor..... | 304 |
| 6.9.5 Synthesis with C ₆₀ and CF ₃ I in Metal Reactor..... | 304 |
| 6.9.6 Synthesis with C ₇₀ and CF ₃ I in Metal Reactor..... | 305 |
| Chapter 6 References | 351 |
| Chapter 7. Preparation and Characterization of Silicon Nanoparticles by Anaerobic Wet Milling..... | 353 |
| 7.1 Introduction and Justification | 353 |
| 7.2 Results..... | 358 |
| 7.2.1 Anaerobic Powder XRD Method..... | 359 |
| 7.2.2 Anaerobic Milling of Metallurgical Grade Silicon in Heptane. | 360 |
| 7.2.3 Anaerobic Milling of Metallurgical Grade Silicon in Mesitylene with Pyrene Additive | 363 |
| 7.2.4 Aerobic Milling of Metallurgical Grade Silicon in Heptane | 365 |
| 7.2.5 Aerobic Milling of Metallurgical Grade Silicon in Mesitylene with Pyrene Additive..... | 365 |
| 7.2.6 DLS Particle Size Analysis of Milled Metallurgical Grade Silicon Samples..... | 366 |
| 7.3 Discussion..... | 366 |
| 7.3.1 Anaerobic vs. Aerobic Milling of Metallurgical Grade Silicon Without Surface Passivating Additives..... | 367 |
| 7.3.2 Anaerobic Milling of Metallurgical Grade Silicon With and Without Surface Passivating Additives..... | 371 |
| 7.3.3 Milling Time for Anaerobic Milling of Metallurgical Grade Silicon Without Surface Passivating Additives Compared to Anaerobic With Surface Passivating Additives..... | 371 |
| 7.3.4 Anaerobic vs. Aerobic Milling of Metallurgical Grade Silicon with Surface Passivating Additives..... | 373 |
| 7.3.5 DLS Experiments Do Not Appear To Correlate With BET Surface Area Measurements of Metallurgical Grade Silicon Nanoparticles. | 374 |
| 7.4 Summary and Conclusion | 376 |
| 7.5 Future Work | 377 |
| 7.6 Experimental..... | 378 |
| 7.6.1 Necessary Design Parameters, Requirements for Mill and Rotary Evaporator and Requirements for Anaerobic, Moisture Free Atmospheric Conditions | 378 |
| 7.6.2 Reagents and Solvents | 387 |
| 7.6.3 Instrumentation and Material Analysis Techniques. | 387 |
| 7.6.4 Anaerobic Milling in Heptane | 391 |
| 7.6.5 Anaerobic Milling in Mesitylene with Pyrene Additive..... | 393 |

| | |
|---|------------|
| 7.6.6 Aerobic Milling of Silicon in Heptane..... | 393 |
| 7.6.7 Aerobic Milling of Silicon in Mesitylene with Pyrene Additive | 394 |
| Chapter 7 References | 430 |
| Chapter 8. Summary and Future Work | 433 |

LIST OF TABLES

| | |
|--|-----|
| Table 3-1. Selected interatomic distances and angles for $(\text{H}_3\text{O})_2\text{B}_{12}\text{F}_{12}\cdot 6\text{H}_2\text{O}$ | 139 |
| Table 3-2. Crystallographic data and refinement parameters for $(\text{H}_3\text{O})_2\text{B}_{12}\text{F}_{12}\cdot 6\text{H}_2\text{O}$, $(\text{H}_3\text{O})_2\text{B}_{12}\text{F}_{12}\cdot 4\text{H}_2\text{O}$, $(\text{NH}_4)_2\text{B}_{12}\text{F}_{12}\cdot 6\text{H}_2\text{O}$ | 140 |
| Table 3-3. Centroid-centroid distances of nearest neighbor centroids for $(\text{H}_3\text{O})_2\text{B}_{12}\text{F}_{12}\cdot 6\text{H}_2\text{O}$, $(\text{H}_3\text{O})_2\text{B}_{12}\text{F}_{12}\cdot 4\text{H}_2\text{O}$, $(\text{NH}_4)_2\text{B}_{12}\text{F}_{12}\cdot 6\text{H}_2\text{O}$ | 141 |
| Table 3-4. Crystallographic oxygen-oxygen distances involving H_3O^+ ions | 142 |
| Table 3-5. Mass changes for hydration/dehydration of $(\text{H}_3\text{O})_2\text{B}_{12}\text{F}_{12}\cdot 6\text{H}_2\text{O}$ phases | 143 |
| Table 3-6. Selected interatomic distances for the PBE0 DFT-predicted structures. | 144 |
| Table 3-7. PBE0 DFT-optimized coordinates for $\text{B}_{12}\text{F}_{12}^{2-}$ | 145 |
| Table 3-8. PBE0 DFT-optimized coordinates for $(\text{H}_3\text{O})_2\text{B}_{12}\text{F}_{12}$ | 146 |
| Table 3-9. PBE0 DFT-optimized coordinates for $\text{H}_2\text{B}_{12}\text{F}_{12}$ | 147 |
| Table 3-10. Mass changes for loss of $\text{H}_2\text{O}/\text{NH}_3$ from $(\text{NH}_4)_2\text{B}_{12}\text{F}_{12}\cdot 2\text{H}_2\text{O}$ to $\text{H}_2\text{B}_{12}\text{F}_{12}$ | 148 |
| Table 4-1. Crystallographic data and refinement parameters for $\text{NaB}_{12}\text{F}_{11}\text{NH}_3\cdot 4\text{H}_2\text{O}$ 1 | 206 |
| Table 4-2. Selected interatomic distances and angles for $\text{NaB}_{12}\text{F}_{11}\text{NH}_3\cdot 4\text{H}_2\text{O}^a$ | 207 |
| Table 4-3. NMR chemical shifts and coupling constants of $\text{B}_{12}\text{H}_{10}(\text{NH}_3)_2$ and for $\text{B}_{12}\text{F}_{10}(\text{NH}_3)_2$ isomers. | 208 |
| Table 4-4. Important Crystallographic data for 1,2-, 1,7-, and 1,12- $\text{B}_{12}\text{H}_{10}(\text{NH}_3)_2$ and for 1,7- and 1,12- $\text{B}_{12}\text{F}_{10}(\text{NH}_3)_2$ | 209 |
| Table 5-1. Previously known and new $\text{C}_{60}(\text{CF}_3)_{10}$ compounds. | 255 |
| Table 5-2. Crystal data, structure refinement parameters; faux hawk fullerene, 60-10-1 | 256 |
| Table 5-3. Crystal data, structure refinement parameters; new $\text{C}_{60}(\text{CF}_3)_{10}$ isomers | 257 |
| Table 5-4. Electrochemical properties of $\text{C}_{60}(\text{CF}_3)_{10}$ isomers | 258 |
| Table 5-5. Interatomic distances and angles for 1,9- $\text{C}_{60}(\text{cyclo-CF}_2(2-\text{C}_6\text{F}_4))$ | 259 |
| Table 6-1. PAHs discussed in Chapter 5 | 343 |
| Table 6-2. Reactions for making $\text{PAH}(\text{R}_F)_n$ and TMF | 345 |
| Table 6-3. Crystallographic data and refinement parameters for structures with sp^3 carbon atoms | 346 |
| Table 6-4. Bond lengths and angles of sp^3 carbons | 347 |
| Table 6-5. Crystallographic data for ACRD-4-1, ANTH-6-1, AZUL-4-1, and NAPH-4-1 | 348 |
| Table 6-6. Important crystallographic data for, and PHNZ-4-1, and TRPH(C_4F_4) | 349 |
| Table 6-7. Nearest crystallographic neighbors | 350 |
| Table 7-1. Summary of milling experimental details | 427 |
| Table 7-2. Amounts of various elements in all samples studied by XPS | 428 |
| Table 7-3. Dynamic light scattering estimated particle size | 429 |

LIST OF FIGURES

| | |
|--|-----|
| Figure 2-1. Typical batch of crude $K_2B_{12}F_{12}$ | 48 |
| Figure 2-2. Yellow $K_2B_{12}F_{12}$ solution after the 2 nd fluorination..... | 49 |
| Figure 2-3. Intensity of colored impurities after $K_2B_{12}F_{12}$ fluorination..... | 50 |
| Figure 2-4. Filtered $K_2B_{12}F_{12}$ post 6% aqueous H_2O_2 treatment..... | 51 |
| Figure 2-5. Molecular packing of structure $K_2(H_2O_2)_{1.5}(H_2O)_{0.5}B_{12}F_{12}$ | 52 |
| Figure 2-6. Proton NMR spectrum of crude $K_2B_{12}F_{12}$.after Al_2O_3 column separation..... | 53 |
| Figure 2-7. Fluorine-19 NMR of crude $K_2B_{12}F_{12}$ after Al_2O_3 column separation | 54 |
| Figure 2-8. Electrochemical oxidation of 0.064 M solution of $B_{12}F_{12}^{2-}$ to $B_{12}F_{12}^-$ | 55 |
| Figure 2-9. UV-Vis spectrum of the $B_{12}F_{12}^-$ species | 56 |
| Figure 2-10. Fluorine-19 NMR spectrum of MeCN treated with $F_2(g)$ | 57 |
| Figure 2-11. Solution of MeCN during fluorination of $K_2B_{12}H_{12}$ with $F_2(g)$ at 0 °C..... | 58 |
| Figure 2-12. Crude aqueous $K_2B_{12}F_{12}$, with Zn solid, and with conc HCL..... | 59 |
| Figure 2-13. Fluorine-19 NMR spectra of aqueous and organic layers after extraction | 60 |
| Figure 2-14. Proton NMR spectrum of $K_2B_{12}F_{12}$ purified by aqueous $KHCO_3$ | 61 |
| Figure 2-15. Boron-11 [¹⁹ F] NMR spectrum of $K_2B_{12}F_{12}$ purified by aqueous $KHCO_3$ | 62 |
| Figure 2-16. Fluorine-19 [¹¹ B] NMR spectrum of $K_2B_{12}F_{12}$ | 63 |
| Figure 2-17. Thermogravimetric analysis of $Li_2B_{12}F_{12} \cdot nH_2O$ | 64 |
| Figure 2-18. Thermogravimetric analysis of $Na_2B_{12}F_{12} \cdot nH_2O$ | 65 |
| Figure 3-1. Hydrogen fluoroborate acid electrolytes preliminary longevity in fuel cells | 106 |
| Figure 3-2. Synthesized $(H_3O)_2B_{12}F_{12} \cdot nH_2O$ proton NMR spectra..... | 107 |
| Figure 3-3. Proton NMR impurities spectrum from Amberlyst 15 resin into D_2O | 108 |
| Figure 3-4. Portion of the $(H_3O)_2B_{12}F_{12} \cdot 6H_2O$ structure | 109 |
| Figure 3-5. Segment of $(H_3O)_2B_{12}F_{12} \cdot 6H_2O$ showing the orientation of a $B_{12}F_{12}^{2-}$ anion..... | 110 |
| Figure 3-6. Segment of the $[H_3O^+/3H_2O]_n$ network..... | 111 |
| Figure 3-7. Drawing of the unit cell $(H_3O)_2B_{12}F_{12} \cdot 6H_2O$ | 112 |
| Figure 3-8. The O–H···O and O–H···F hydrogen bonds in $(H_3O)_2B_{12}F_{12} \cdot 6H_2O$ | 113 |
| Figure 3-9. Another view of the H_3O^+/H_2O layers in $(H_3O)_2B_{12}F_{12} \cdot 6H_2O$ | 114 |
| Figure 3-10. Plot of B–B and B–F distances in $(H_3O)_2B_{12}F_{12} \cdot 6H_2O$ | 115 |
| Figure 3-11. Dimensional views of the $(H_3O)_2B_{12}F_{12} \cdot 4H_2O$ crystal structure | 116 |
| Figure 3-12. Pronounced corrugation of $(H_3O)_2B_{12}F_{12} \cdot 4H_2O$ | 117 |
| Figure 3-13. Comparison of B_{12} centroid closest neighbors in $(H_3O)_2B_{12}F_{12} \cdot 4H_2O$,..... | 118 |
| Figure 3-14. Centroids of O–H···O hydrogen bonded hexagons | 119 |
| Figure 3-15. Positioning of $B_{12}F_{12}^{2-}$ anion relative to the layer $[H_3O^+/2H_2O]_n$ | 120 |
| Figure 3-16. Proton, ¹¹ B[¹⁹ F], and ¹⁹ F[¹¹ B] NMR spectra of $(H_3O)_2B_{12}F_{12} \cdot nH_2O$ in D_2O | 121 |

| | |
|--|-----|
| Figure 3-17. Thermogram of $(\text{H}_3\text{O})_2\text{B}_{12}\text{F}_{12}\cdot 6\text{H}_2\text{O}$ in aluminum pan..... | 122 |
| Figure 3-18. Crystal structure of $\text{ZnB}_{12}\text{F}_{12}\cdot 6\text{H}_2\text{O}$ synthesized from Zn metal | 123 |
| Figure 3-19. Decomposition when attempting to thermally dry $\text{M}(\text{B}_{12}\text{F}_{12})\cdot 6\text{H}_2\text{O}$ salts..... | 124 |
| Figure 3-20. Thermogravimetric analysis of $(\text{H}_3\text{O})_2\text{B}_{12}\text{F}_{12}\cdot 6\text{H}_2\text{O}$ | 125 |
| Figure 3-21. Theoretical structures of $(\text{H}_3\text{O})_2\text{B}_{12}\text{F}_{12}$ | 126 |
| Figure 3-22. Thermogravimetric analysis of $(\text{H}_3\text{O})_2\text{B}_{12}\text{F}_{12}\cdot 6\text{H}_2\text{O}$ | 127 |
| Figure 3-23. $(\text{H}_3\text{O})_2\text{B}_{12}\text{F}_{12}\cdot n\text{H}_2\text{O}$ Fluorene-19 NMR spectra in CD_3CN | 128 |
| Figure 3-24. ESI-MS analysis of $(\text{H}_3\text{O})_2\text{B}_{12}\text{F}_{12}\cdot 0\text{H}_2\text{O}$ after heated to 300 °C | 129 |
| Figure 3-25. Fluorine-19 NMR spectrum of $(\text{H}_3\text{O})_2\text{B}_{12}\text{F}_{12}\cdot n\text{H}_2\text{O}$ after held isothermally at 200 °C under vacuum for 24 h..... | 130 |
| Figure 3-26. Thermogravimetric analysis of $(\text{NH}_4)_2\text{B}_{12}\text{F}_{12}\cdot n\text{H}_2\text{O}$ | 131 |
| Figure 3-27. Boron-11, and ^{19}F NMR spectroscopy analysis of $(\text{NH}_4)_2\text{B}_{12}\text{F}_{12}\cdot n\text{H}_2\text{O}$ | 132 |
| Figure 3-28. Proton NMR spectrum of a sample of $(\text{NH}_4)_2\text{B}_{12}\text{F}_{12}\cdot n\text{H}_2\text{O}$ | 133 |
| Figure 3-29. Thermogravimetric analysis of $(\text{NH}_4)_2\text{B}_{12}\text{F}_{12}\cdot 2\text{H}_2\text{O}$ | 134 |
| Figure 3-30. Ribbon of hydrogen bonded NH_4^+ and H_2O molecules with $\text{B}_{12}\text{F}_{12}^{2-}$ anions | 135 |
| Figure 3-31. The $\text{B}_{12}\text{F}_{12}^{2-}$ anions in cubic close packed array | 136 |
| Figure 3-32. Hydrogen bonded network of $[\text{NH}_4^+/2\text{H}_2\text{O}]_n$ | 137 |
| Figure 3-33. Predicted and hypothetical structures of $(\text{H}_3\text{O})_2\text{B}_{12}\text{F}_{12}$ and $(\text{NH}_4)_2\text{B}_{12}\text{F}_{12}$ | 138 |
| Figure 4-1. IUPAC numbering scheme for icosahedral B_{12} clusters | 184 |
| Figure 4-2. Rate of fluorination of $\text{K}_2\text{B}_{12}\text{H}_{12}$ with and without HF..... | 185 |
| Figure 4-3. Isotopologue patterns for mass spectra of $\text{B}_{12}\text{F}_{11}(\text{NH}_3)^-$ | 186 |
| Figure 4-4. Rate of fluorination of $\text{KB}_{12}\text{H}_{11}\text{NH}_3$ with and without KF monitored by NI-ESI mass spectra..... | 187 |
| Figure 4-5. Comparison of $\text{B}_{12}\text{HF}_{10}(\text{NH}_3)^-$ and $\text{B}_{12}\text{F}_{11}(\text{NH}_3)^-$ in fluorination of $\text{KB}_{12}\text{H}_{11}\text{NH}_3$ with KF | 188 |
| Figure 4-6. Number of F atoms per average $\text{B}_{12}\text{H}_{11-n}\text{F}_n(\text{NH}_3)^-$ anion during F_2 fluorination of $\text{KB}_{12}\text{H}_{11}\text{NH}_3$ with and without KF..... | 189 |
| Figure 4-7. Rate of fluorination of $\text{KB}_{12}\text{H}_{11}\text{NH}_3$ with and without HF monitored by NI-ESI mass spectra..... | 190 |
| Figure 4-8. Rate of fluorination of $\text{KB}_{12}\text{H}_{11}\text{NH}_3$ with HF with and without $\text{F}_2(\text{g})$ monitored by NI-ESI mass spectra | 191 |
| Figure 4-9. F Number of F atoms per average $\text{B}_{12}\text{H}_{11-n}\text{F}_n(\text{NH}_3)^-$ anion during F_2 fluorination of $\text{KB}_{12}\text{H}_{11}\text{NH}_3$ with and without HF..... | 192 |
| Figure 4-10. Thermal ellipsoid plot of the $\text{B}_{12}\text{F}_{11}(\text{NH}_3)^-$ | 193 |
| Figure 4-11. Plots of the B–B distances in $\text{KB}_{12}\text{F}_{11}(\text{NH}_3)$, and $(\text{H}_3\text{O})_2\text{B}_{12}\text{F}_{12}\cdot 6\text{H}_2\text{O}$ | 194 |
| Figure 4-12. One-dimensional hydrogen bonding network in $\text{Na}(\text{H}_2\text{O})_4\text{B}_{12}\text{F}_{11}(\text{NH}_3)$ | 195 |
| Figure 4-13. Location of $\text{B}_{12}\text{F}_{11}\text{NH}_3^-$ anion in $\text{NaB}_{12}\text{F}_{11}\text{NH}_3\cdot 4\text{H}_2\text{O}$ hydrogen bonded network..... | 196 |
| Figure 4-14. Planes of $(\text{H}_2\text{O})_4$ tetramer in $\text{NaB}_{12}\text{F}_{11}\text{NH}_3\cdot 4\text{H}_2\text{O}$ | 197 |
| Figure 4-15. NaF_4O_2 coordination spheres in $\text{Na}(\text{H}_2\text{O})_4\text{B}_{12}\text{F}_{11}(\text{NH}_3)$ | 198 |
| Figure 4-16. Comparison of Na^+ coordination sphere in $\text{Na}(\text{H}_2\text{O})_4\text{B}_{12}\text{F}_{11}(\text{NH}_3)$ $\text{Na}_2(\text{H}_2\text{O})_4\text{B}_{12}\text{F}_{12}$ crystal structures | 199 |

| | |
|--|-----|
| Figure 4-17. Na ⁺ and NH ₃ coordination between two B ₁₂ F ₁₁ (NH ₃) ⁻ | 200 |
| Figure 4-18. Reaction of B ₁₂ H ₁₂ ²⁻ on the surface of F ₂ bubble | 201 |
| Figure 4-19. Boron-11 NMR spectra of organic and aqueous soluble B ₁₂ cages after separation of B ₁₂ H ₁₁ NH ₃ ⁻ from crude reaction mixture | 202 |
| Figure 4-20. NH region of ¹ H- ¹⁵ N HSQC NMR spectrum of CD ₃ CN solution | 203 |
| Figure 4-21. NH region of ¹ H- ¹⁵ N HSQC NMR spectra of purified samples of 1,2-, 1,7-, and 1,12-B ₁₂ H ₁₀ (CH ₃) ₂ | 204 |
| Figure 4-22. Thermal ellipsoid plots of three isomers of B ₁₂ H ₁₀ (NH ₃) ₂ borate cage compounds | 205 |
| Figure 5-1. The structure of and Schlegel diagrams for C ₆₀ (CF ₃) ₁₀₋₃ | 230 |
| Figure 5-2. Schlegel diagrams for the previously known isomers of C ₆₀ (CF ₃) ₁₀ | 231 |
| Figure 5-3. Schlegel diagrams for the new isomers of C ₆₀ (CF ₃) ₁₀ | 232 |
| Figure 5-4. Schlegel diagrams to compare CF ₃ addition patterns for isomers of C ₆₀ (CF ₃) ₁₀ | 233 |
| Figure 5-5. Thermal ellipsoid plots of the two unique C ₆₀ (CF ₃) ₁₀₋₁ molecules | 234 |
| Figure 5-6. Thermal ellipsoid plots of the six new isomers of C ₆₀ (CF ₃) ₁₀ | 235 |
| Figure 5-7. A portion of the X-ray structure of 60-10-12 showing CF ₃ close contacts | 236 |
| Figure 5-8. Comparison of underivatized C ₆₀ and the fullerene cage of C ₆₀ (CF ₃) ₁₀₋₁₂ | 237 |
| Figure 5-9. Thermal ellipsoid plot of 1,9-C ₆₀ (<i>cyclo</i> -CF ₂ (2-C ₆ F ₄)) | 238 |
| Figure 5-10. X-ray vs. DFT-optimized cage C–C distances of C ₆₀ (CF ₃) ₁₀₋₁ and C ₆₀ (CF ₃) ₁₀₋₉ | 239 |
| Figure 5-11. X-ray determined cage C–C bond distances in C ₆₀ Pt(OEP)·2C ₆ H ₆ compared to C ₆₀ (CF ₃) ₁₀₋₃ molecule | 240 |
| Figure 5.12. Experimental first reduction potentials of many C ₆₀ (CF ₃) _n compounds | 241 |
| Figure 5.13. Schlegel and LUMO diagrams showing the <i>nt</i> -DBIPs in C ₆₀ (CF ₃) ₁₀₋₁ , C ₆₀ (CF ₃) ₁₀₋₂ , and C ₆₀ (CF ₃) ₁₀₋₃ | 242 |
| Figure 5-14. Comparison of the DFT-predicted LUMOs of C ₆₀ (CF ₃) ₁₀₋₈ , C ₆₀ (CF ₃) ₁₀₋₆ , and C ₆₀ (CF ₃) ₁₀₋₁ with C ₆₀ (CF ₃) ₁₀₋₁₂ , C ₆₀ (CF ₃) ₁₀₋₃ , and C ₆₀ (CF ₃) ₁₀₋₁₀ | 243 |
| Figure 5-15. DFT-predicted LUMO and LUMO+1 C ₆₀ (CF ₃) ₁₀₋₁₁ | 244 |
| Figure 5-16. Molecular packing in X-ray structures of C ₆₀ (CF ₃) ₁₀₋₉ , C ₆₀ (CF ₃) ₁₀₋₁₀ , C ₆₀ (CF ₃) ₁₀₋₁₁ ·CDCl ₃ , and C ₆₀ (CF ₃) ₁₀₋₁₂ | 245 |
| Figure 5-17. Molecular packing pattern for the X-ray structure of C ₆₀ (CF ₃) ₁₀₋₈ ·CHCl ₃ | 246 |
| Figure 5-18. Graph showing linear correlation of solvent free crystal density and centroid to centroid distances | 247 |
| Figure 5-19. Molecular packing in the X-ray structure of C ₆₀ (CF ₃) ₁₀₋₁₃ | 248 |
| Figure 5-20. Packing of molecules in X-ray structures of C ₆₀ (CF ₃) ₁₀₋₁₃ and C ₆₀ (CF ₃) ₁₀₋₉ | 249 |
| Figure 5-21. Comparison of the molecular structures of the faux hawk fullerene with PCBM | 250 |

| | |
|---|-----|
| Figure 5-22. Comparison of nearest-neighbor centroid packing patterns of PCBM experimental single crystal density at 100 K and powder XRD experimental single crystal density at 300 K..... | 251 |
| Figure 5-23. Molecular packing of faux hawk from single-crystal X-ray structure..... | 252 |
| Figure 5-24. Molecular packing of PCBM from single-crystal X-ray structure..... | 253 |
| Figure 5-25. Unit cell packing pattern of C ₆₀ cage centroids in faux hawk fullerene..... | 254 |
| Figure 6-1. Diagram of reaction set-up of PAH and gaseous CF ₃ I, sealed glass ampoule..... | 306 |
| Figure 6-2. Thermal ellipsoid plots of PAH(CF ₃) _n products produced in sealed glass ampoules..... | 307 |
| Figure 6-3. Two reactions of PAH with CF ₃ I, one with Cu powder and one without..... | 308 |
| Figure 6-4. High temperature valve and reactor..... | 309 |
| Figure 6-5. High temperature valve and large reactor..... | 310 |
| Figure 6-6. Proton NMR spectra of purified ANTH-6-1, compared to crude reaction mixture from ANTH with CF ₃ I in metal reactor..... | 311 |
| Figure 6-7. Proton NMR spectra of purified ANTH-6-1, compared to crude reaction mixture from ANTH with CF ₃ I in metal reactor..... | 312 |
| Figure 6-8. Analytical HPLC trace of the CORO with 34.3 equiv CF ₃ I reaction in metal reactor crude reaction mixture..... | 313 |
| Figure 6-9. Proton NMR spectrum of CORO with 34.3 equiv CF ₃ I crude reaction mixture..... | 314 |
| Figure 6-10. Fluorine-19 NMR spectrum of CORO with 34.3 equiv CF ₃ I crude reaction mixture..... | 315 |
| Figure 6-11. Crystal structure of H ₂ CORO(CF ₃) ₇₋₁ and H ₂ CORO(CF ₃) ₈₋₁ | 316 |
| Figure 6-12. Analytical HPLC trace of the CORO with 7 equiv CF ₃ I reaction in metal reactor crude reaction mixture..... | 317 |
| Figure 6-13. Proton NMR spectrum of crude mixture of CORO and 7 equiv of CF ₃ I..... | 318 |
| Figure 6-14. Fluorine-19 NMR spectrum of crude mixture CORO and 7 equiv of CF ₃ I..... | 319 |
| Figure 6-15. Analytical HPLC of crude mixture produced by C ₆₀ and 40.4 equiv of CF ₃ I..... | 320 |
| Figure 6-16. Fluorine-19 NMR of crude mixture produced by C ₆₀ and 40.4 equiv of CF ₃ I..... | 321 |
| Figure 6-17. Fluorine-19 NMR spectrum of C ₆₀ (CF ₃) ₁₂ -S ₆ | 322 |
| Figure 6-18. Analytical HPLC of C ₇₀ and 20 equiv of CF ₃ I..... | 323 |
| Figure 6-19. Fluorine-19 NMR of crude mixture produced by C ₇₀ and 20 equiv of CF ₃ I..... | 324 |
| Figure 6-20. NI-ESI mass spectrum of crude mixture produced by C ₇₀ and 20 equiv of CF ₃ I..... | 325 |
| Figure 6-21. Single crystal XRD structure of H ₂ TETR-8-1 with 2 sp ³ carbon atoms..... | 326 |
| Figure 6-22. Single crystal XRD structure H ₂ ANTH ₂ (Bn _F) ₂ dimer, 2 sp ³ carbon atoms..... | 327 |

| | |
|--|-----|
| Figure 6-23. Disordered CF ₃ groups on <i>ortho</i> sp ³ carbon atoms in H ₂ CORO structures..... | 328 |
| Figure 6-24. Proton NMR of isolated H ₂ CORO(CF ₃) ₈ -1 in CDCl ₃ | 329 |
| Figure 6-25. Thermal ellipsoid plot and ACRD-4-1 disorder..... | 330 |
| Figure 6-26. Layers of ACRD-4-1 top down and side view..... | 331 |
| Figure 6-27. Preliminary crystal structure of ANTH-6-1 | 332 |
| Figure 6-28. ANTH-6-1 packing | 333 |
| Figure 6-29. Thermal ellipsoid plot and AZUL-4-1 disorder..... | 334 |
| Figure 6-30. AZUL-4-1 top down and side view. | 335 |
| Figure 6-31. Thermal ellipsoid plot of staggered layer of NAPH-4-1 molecules | 336 |
| Figure 6-32. NAPH-4-1 structure top down and side view | 337 |
| Figure 6-33. Thermal ellipsoid plot PHNZ-4-1 and orientation in layers | 338 |
| Figure 6-34. Pseudo-hexagonal array of PHZN-4-1 layers, top down, and side view | 339 |
| Figure 6-35. Thermal ellipsoid plot of TRPH(C ₄ F ₄) and 4 layers of TRPH(C ₄ F ₄) | 340 |
| Figure 6-36. Pseudo-hexagonal array of TRPH(C ₄ F ₄) molecules | 341 |
| Figure 6-37. Aromatic overlap of TRPH(C ₄ F ₄) crystal structure..... | 342 |
| Figure 7-1. Different regions of surface potential of a particle suspended in a solution..... | 395 |
| Figure 7-2. Schematic of Netzsch MiniCer Laboratory mill..... | 396 |
| Figure 7-3. SEM images of A-H/M-5.5h aerobic milled MGS particles | 397 |
| Figure 7-4. TEM images of A-H/M-5.5h aerobically milled MGS | 398 |
| Figure 7-5. Comparison of effect of Apiezon Type N grease on two silicon powder samples analyzed by powder XRD. | 399 |
| Figure 7-6. Powder XRD pattern of AA-H-1h in Apiezon Type N grease before and after 52 days | 400 |
| Figure 7-7. Anaerobic powder XRD of AA-H-1 through 5h..... | 401 |
| Figure 7-8. TEM images of AA-H-1h, crystalline regions of 10–50 nm in length..... | 402 |
| Figure 7-9. TEM images of AA-H-5h, crystalline regions of 5–12 nm in length..... | 403 |
| Figure 7-10. X-ray photoelectron spectroscopy of A-H-1h, A-H-3h, and A-H-5h..... | 404 |
| Figure 7-11. X-ray photoelectron spectroscopy of A-H-3h as made and sputtered..... | 405 |
| Figure 7-12. Rate of O ₂ uptake post treatment of anaerobic milled MGS | 406 |
| Figure 7-13. Anaerobic powder XRD of MGS, milled in mesitylene with pyrene additive | 407 |
| Figure 7-14. Rate of O ₂ post treatment of Anaerobic milled MGS with pyrene additive..... | 408 |
| Figure 7-15. X-ray photoelectron spectroscopy of A-M/P-5h and AA-M/P-5h..... | 409 |
| Figure 7-16. Dynamic light scattering analysis of 5 samples compared | 410 |
| Figure 7-17. X-ray photoelectron spectroscopy of A-H-5h and AA-H-5h..... | 411 |
| Figure 7-18. Powder XRD of all MGS sampled milled for 5 or 5.5 h..... | 412 |
| Figure 7-19. Double-wide, double-deep Vacuum Atmospheres HE-453-4 glovebox..... | 413 |
| Figure 7-20. Components and required connections of the Netzsch Minicer mill | 414 |
| Figure 7-21. Original electrical connection diagram of Netzsch Minicer mill..... | 415 |

| | |
|---|-----|
| Figure 7-22. Original cooling water, seal fluid, and inert gas connection diagram of Netzsch Minicer mill..... | 416 |
| Figure 7-23. Jefferson 0.25 kVA buck-boost transformer, and multi-meter | 417 |
| Figure 7-24. Specifications for the Pave Technology electrical bulkhead connector..... | 418 |
| Figure 7-25. Final version of Al roof panel for glovebox..... | 419 |
| Figure 7-26. Receptacle and plug for main power mounted inside of the Al roof panel..... | 420 |
| Figure 7-27. The Netzsch main electronic control unit | 421 |
| Figure 7-28. Bulkhead fittings for glovebox..... | 422 |
| Figure 7-29. The Netzsch mill and seal-fluid unit | 423 |
| Figure 7-30. Final mill and axillary parts in glovebox | 424 |
| Figure 7-31. Threaded pressure sensors on seal fluid tank..... | 425 |
| Figure 7-32. Unistrut® rack inside glovebox to suspend sonicator and other parts..... | 426 |

LIST OF ACRYONYMS AND ABBREVIATIONS

| | |
|---------------------|--|
| ⊙ | Centroid of a B ₁₂ cage, fullerene or polycyclic aromatic hydrocarbon |
| aHF | Anhydrous HF |
| anhyd | Anhydrous |
| conc | Concentration |
| dd-H ₂ O | Distilled Deionized Water |
| DFT | Density Functional Theory |
| DLS | Dynamic Light Scattering |
| DSC | Differential Scanning Calorimetry |
| equiv | Equivalence |
| esd | Estimated Standard Deviation (standard error) in SC-XRD derived results |
| FT-IR | Fourier Transform Infrared Spectroscopy |
| ICP-AES | Inductively Coupled Plasma Atomic Emission Spectroscopy |
| aHF | Anhydrous hydrogen fluoride |
| Li-ion | Lithium ion (typically in reference to lithium ion batteries) |
| LSP | Least squares plane |
| MeCN | Acetonitrile |
| NI-ESI-MS | Negative Ion Electrospray Mass Spectrometry |
| NMR | Nuclear Magnetic Resonance |
| OCDB | <i>Ortho</i> -dichlorobenzene |
| OFET | Organic Field Effect Transistor |
| OLED | Organic Light Emitting Diode |
| OPV | Organic Photovoltaic |
| OSC | Organic Semiconductor |
| PAH | Polycyclic Aromatic Hydrocarbon |
| PXRD | Powder X-ray Diffraction |
| RT | Room Temperature |
| SC-XRD | Single Crystal X-ray Diffraction |
| TGA | Thermogravimetric Analysis |
| TOC | Total organic carbon |
| UV-vis | Ultraviolet-visible Spectroscopy |
| XPS | X-ray Photoelectron Spectroscopy |

Chapter 1.

Introduction and Justification for Research

1.1 Synthesis of Superweak Anion Salts of $B_{12}F_{12}^{2-}$, $B_{12}F_{11}NH_3^-$ and Neutral Species 1,2-, 1,7-, and 1,12- $B_{12}F_{10}(NH_3)_2$.

The Strauss research group at Colorado State University has a longstanding interest in the synthesis and application of highly-fluorinated superweak anions (i.e., extremely weakly coordinating anions^{1,2}), including the polyhedral carborane and borane anions 1-R- $CB_{11}F_{11}^-$,³ $B_{12}F_{12}^{2-}$,^{4,5} and $B_{12}F_{11}(NH_3)^-$.⁶ The primary use of superweak anions (the term superweak anion, conceptually the conjugate base of an actual or hypothetical superacid, was introduced by Strauss at an ACS National Meeting symposium on weakly coordinating anions organized by Strauss and C. A. Reed in 1998.^{7,8}) is to generate, isolate, and characterize reactive cationic species that are not stable in the presence of traditional weakly-coordinating anions, such as ClO_4^- , PF_6^- , $CF_3SO_3^-$, etc.⁹⁻²³ Practical applications that justify superweak-anion research include highly conductive electrolytes,²⁴⁻³² reversible gas absorbents,³³ and metallocenium catalyzed olefin polymerization.³⁴⁻³⁷ Some of the most effective superweak anions are $CB_{11}H_{12-n}X_n^-$ ($X = F, Cl, Br, CH_3, CF_3$) and $B_{12}X_{12}^{2-}$ ($X = F, Cl$), and some of the extremely reactive cations or cation-like species isolated with these anions include $H_9O_4^+$,³⁸ H_3O^+ ,³⁹ $C_6H_7^+$,^{40,41} $Cu(CO)_4^+$,²⁰ $Ag(CH_2Cl_2)^+$,⁴² and $Al(CH_3)_2^+$.⁴³ The first two chapters of this dissertation describe the author's research of salts of the $B_{12}F_{12}^{2-}$ anion and methods to make the $K_2B_{12}F_{12}$ salt, and salts derived from $K_2B_{12}F_{12}$ in high purity. The salt $K_2B_{12}F_{12}$ was first prepared in 38% yield by Solntsev et al. in 1992.⁴⁴ An improved preparation (72% yield) was reported by the Strauss research group in 2003,⁴⁵ and a scaled-up synthesis (ca. 18 g, 74% yield) was reported by the Strauss-Boltalina

group in 2009.⁴⁶ Important superweak anion properties exhibited by $B_{12}F_{12}^{2-}$ are oxidative stability (4.9 V vs $Li^{+/0}$),⁴⁵ weakly-basic periphery (i.e., B–F bonds instead of B–O or B–Cl bonds), large size (antipodal $F\cdots F$ distance ca. 9.2 Å), charge delocalization, low (if any) polarizability, and symmetric charge distribution.

The Strauss group has been studying the structures and physicochemical properties of a variety of metal and nonmetal salts of the icosahedral superweak anion $B_{12}F_{12}^{2-}$.⁴⁵⁻⁵⁰ The guiding hypothesis in this research is that the unique combination of size, shape, high symmetry, thermal stability, and extremely weak Brønsted and Lewis basicity of this anion will lead to unanticipated structures and properties (i.e., unanticipated relative to salts of $B_{12}H_{12}^{2-}$,⁵¹⁻⁵⁴ $B_{12}Cl_{12}^{2-}$,⁵⁵⁻⁵⁷ $B_{12}(OH)_{12}^{2-}$,^{58,59} and $B_{12}(CH_3)_{12}^{2-}$,⁶⁰ and of salts of typical fluoroanions such as BF_4^- , PF_6^- , SbF_6^- , $Sb_2F_{11}^-$, SiF_6^{2-} , MnF_6^{2-} , etc.). For example, $K_2B_{12}H_{12}$ exhibits the common antiferite structure,⁵¹ but $K_2B_{12}F_{12}$ exhibits the intermetallic Ni_2In structure⁴⁷ (the B_{12} centroids occupy the idealized HCP positions of the In atoms⁶¹), which is likely the first and only example structure of an ionic compound with a polyatomic anion that was observed at ordinary temperatures and pressures. Interesting one and two dimensional hydrogen bonded networks involving H_3O^+ , NH_4^+ , and H_2O in the single crystal X-ray structurally characterized compounds $(H_3O)_2B_{12}F_{12}\cdot 6H_2O$, $(H_3O)_2B_{12}F_{12}\cdot 4H_2O$, $(NH_4)_2B_{12}F_{12}\cdot 4H_2O$, and $NaB_{12}F_{11}NH_3\cdot 4H_2O$ will be discussed adding to the unanticipated structures manifested from the superweak properties of $B_{12}F_{12}^{2-}$ and $B_{12}F_{11}NH_3^-$.

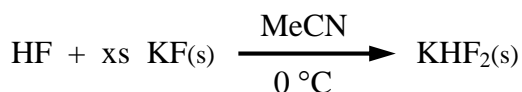
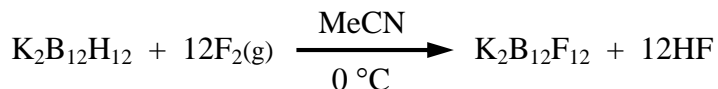
Superweak anions are also of interest to the chemistry community because of their ability to form superacids, i.e.; acids that are stronger than 100% sulfuric acid.⁶² While acids of other $B_{12}X_{12}^{2-}$ ($X = Cl, Br$) anions⁶³ have been synthesized and characterized, the putative $H_2B_{12}F_{12}$ has yet to be synthesized. Based on the strength of the B–F bond, low polarizability, and weak

Lewis base interactions of fluorine it is conceivable that $\text{H}_2\text{B}_{12}\text{F}_{12}$ would be a stronger acid than previously isolated dodecaborate superacids $\text{H}_2\text{B}_{12}\text{X}_{12}$ ($\text{X} = \text{Cl}, \text{Br}$). The $\text{H}_2\text{B}_{12}\text{Cl}_{12}$ acid is strong enough to protonate benzene to form the benzenium cation and is theorized to have a Hammett acidity of greater than -17 .⁶³ Continuing this research, new synthetic routes to make the putative super acid $\text{H}_2\text{B}_{12}\text{F}_{12}$ will also be discussed. Besides simply making the strongest possible acid, strong acids with stable anions have the ability to easily make stable hydronium (H_3O^+) salts. The nature of hydronium ions (i) in bulk aqueous solutions,⁶⁴⁻⁶⁶ (ii) on the surface of aqueous solutions (i.e., at the air/water interface, where H_3O^+ ions may be concentrated relative to the bulk solution),^{67,68} and (iii) as free H_3O^+ ions⁶⁹ or as $[(\text{H}_3\text{O})_n(\text{H}_2\text{O})_m]^{n+}$ clusters⁷⁰⁻⁷² within the confines of solid-state structures, are of longstanding interest as well as of current interest to many chemists. Furthermore, the acid salts $(\text{H}_3\text{O})_2\text{B}_{12}\text{Cl}_{12} \cdot n\text{H}_2\text{O}$ ⁷³ and $(\text{H}_3\text{O})_2\text{B}_{12}\text{F}_{12} \cdot n\text{H}_2\text{O}$ ⁷⁴ have been considered as practical, more chemically inert alternatives to H_3PO_4 proton conducting electrolytes for acid fuel cells^{24,74}, but have yet to be structurally characterized. As mentioned above four possible structures involving extensive hydrogen bonded networks which have the potential to be solid proton conductors will be discussed.

Superweak anion salts, specifically of the form $\text{M}_2\text{B}_{12}\text{F}_{12}$ ($\text{M} = \text{Li}, \text{Na}$) are being researched as highly conductive thermally stable electrolytes for electrochemical devices to improve the lifetime and safety for large electrochemical cells.^{24-28,30-32,75-77} Superweak anions are desirable as electrolyte salts because they are weak Brønsted and Lewis bases, electrochemically and thermally stable, and are not plagued with the thermal equilibrium and hygroscopicity problems of legacy electrolyte salt LiPF_6 .⁷⁸ The purity of all materials in an electrochemical cell is extremely important. Any impurities can have adverse, non-reversible reactions under the oxidative and reductive conditions during charge and discharge cycles. To further the research

and development of these important superweak anion electrolyte salts, the precursor material, $\text{K}_2\text{B}_{12}\text{F}_{12}$ needs to be made in high purity. From highly purified $\text{K}_2\text{B}_{12}\text{F}_{12}$, the $\text{Li}_2\text{B}_{12}\text{F}_{12}$ and $\text{Na}_2\text{B}_{12}\text{F}_{12}$ salts can also be made in high purity.

The recently scaled-up synthetic method for making $\text{K}_2\text{B}_{12}\text{F}_{12}$ (ca. 18 g, 74% yield) was reported by Peryshkov and Strauss et al. in 2009 using a glass reactor, MeCN solvent and $\text{F}_2/\text{N}_2(\text{g})$ bubbled through the MeCN solution.⁴⁶ The synthetic methodology developed by Peryshkov et al. for easier, scalable synthesis of $\text{K}_2\text{B}_{12}\text{F}_{12}$, shown in the equations below, had four advantages compared to the Monel reactor method: (i) scaled reaction to 10 g of $\text{K}_2\text{B}_{12}\text{H}_{12}$ starting material; (ii) shortened reaction time to from 7 days to 2 days; (iii) efficient use of $\text{F}_2(\text{g})$; and (iv) replaced liquid anhydrous HF with a less reactive, less volatile solvent.^{42,46} The reaction of $\text{K}_2\text{B}_{12}\text{H}_{12}$ with $\text{F}_2(\text{g})$ (20% $\text{F}_2(\text{g})/\text{N}_2(\text{g})$) in MeCN is shown below.



This shorter, simpler synthetic method in MeCN allowed for a rapid and scaled-up synthesis of $\text{K}_2\text{B}_{12}\text{F}_{12}$, which is the precursor for all $\text{B}_{12}\text{F}_{12}^{2-}$ salts produced in the Strauss-Boltalina research group. One drawback to this synthetic method for making $\text{K}_2\text{B}_{12}\text{F}_{12}$ from $\text{K}_2\text{B}_{12}\text{H}_{12}$ in MeCN with $\text{F}_2(\text{g})$ is that it resulted in a yellow/yellow-orange impurity in the crude $\text{K}_2\text{B}_{12}\text{F}_{12}$ reaction product. The originally published method for the removal of the colored impurity was

heating in 6% aqueous H₂O₂; while this can be a common purification method in academic and laboratory settings, scaling such a process would be nearly impossible due to safety concerns.

In order to make K₂B₁₂F₁₂ and salts produced from it, namely (H₃O)₂B₁₂F₁₂, Li₂B₁₂F₁₂ and Na₂B₁₂F₁₂, even more commercially viable and to further the research of these materials as electrolyte salts for secondary Li-ion batteries, and as proton conducting salts for hydrogen fuel cell applications, a more reproducible purification method for K₂B₁₂F₁₂ is required. The identity of the yellow colored impurity was investigated and a modified purification method to remove the colored impurities was developed eliminating the need for H₂O₂. Finally, a new method to make (H₃O)₂B₁₂F₁₂, Li₂B₁₂F₁₂ and Na₂B₁₂F₁₂ in high purity from K₂B₁₂F₁₂ was also necessary (and will be presented) to demonstrate that these salts can be made in high purity, and to send collaborators samples of (H₃O)₂B₁₂F₁₂, Li₂B₁₂F₁₂, and Na₂B₁₂F₁₂ for further study as electrolytes for fuel cell and secondary battery research, respectively.

Besides electrochemical conducting mediums, there are other potential uses for molecules or molecular ions containing a high weight% of naturally-occurring boron (and therefore a relatively high weight% of ¹⁰B) that have nothing to do with reactive cations.⁷⁹ Three of the most important uses are boron neutron capture therapy (BNCT),⁸⁰⁻⁸³ thermal neutron detectors (TNDs) for homeland security applications,⁸⁴ and extractants for nuclear waste.⁸⁵ For applications such as these, derivatization of the borane cluster is desirable (i.e., derivatization other than per-*B*-fluorination). Instead of only one site of substitution in 1-R-CB₁₁F₁₁⁻ (i.e., the C atom), the monoammonio anions B₁₂H₁₁(NH₃)⁻,⁸⁶ B₁₂F₁₁(NH₃)⁻,⁶ and B₁₂Cl₁₁(NH₃)⁻⁸⁷ have three sites of substitution (i.e., the three N-H bonds) and the diammonio compounds 1,2-, 1,7-, and 1,12-B₁₂H₁₀(NH₃)₂ have six sites of substitution. A non-nuclear application of these fluorinated anions and neutral species is the preparation of anions for ionic liquids^{88,89}, or a neutral borane "metal-

organic framework" like material by polymerizing the diammonio $B_{12}H_{10}(NH_3)_2$ or $B_{12}F_{10}(NH_3)_2$ isomers. Another non-nuclear application is as starting materials for the preparation of non-linear optical materials.^{90,91} These applications may or may not benefit from per-*B*-fluorination depending on the nature of the other components with which they are mixed or to which they are attached (e.g., peptides and other biomolecules for BNCT and the scintillators and polymers used for TNDs, etc.). A final non-nuclear application, a new project in the Strauss-Boltalina group, is the use of polymerizable derivatives of the per-*B*-fluorinated mono- and diammonio clusters (i.e., derivatives with polymerizable hydrocarbyl substituents on the N atoms) to form protective polymeric coatings on anodes for secondary lithium-ion batteries while at the same time allowing high lithium-ion mobility through the coating.

The direct fluorination of $CsB_{12}H_{11}(NH_3)$ in anhydrous HF (LAHF) with 20/80 F_2/N_2 , reported by Strauss and co-workers in 2003,⁶ is not very efficient. The reaction was carried out in a Monel reactor in a batch process and had a modest yield of 41%. Moreover, only ca. 0.8 g of $CsB_{12}H_{11}(NH_3)$ could be fluorinated per batch, because the use of elevated pressures of F_2/N_2 resulted in cluster degradation and even lower yields. Related to the synthesis of $B_{12}F_{11}NH_3^-$, some goals of the work reported in chapter 4 were (i) to scale up the fluorination reaction to 2 g of $KB_{12}H_{11}(NH_3)$ using MeCN in a glass round-bottom flask instead of LAHF in a Monel reactor, and to do so without sacrificing the yield or purity of the final product, $KB_{12}F_{11}(NH_3)$, and (ii) to obtain a precise single-crystal X-ray structure of a salt of the $B_{12}F_{11}(NH_3)^-$ monoanion.

Chapters 2, 3, and 4 describe the fluorination of B_{12} clusters ($B_{12}H_{12}^{2-}$, $B_{12}H_{11}NH_3^-$, and isomers of $B_{12}H_{10}(NH_3)_2$) in MeCN, and the compounds, salts and characterization of those compounds. Parts or all of this work have also been published with the author of this dissertation

as the main author of *Euro. J. Inorg. Chem.* **2012**, and co-author of *Polyhedron* **2013** and a book chapter from "Efficient Preparation of Fluorine Compounds" edited by Herbert Roesky, 2012, as well as the main author of a paper yet to be submitted regarding the fluorination of $\text{KB}_{12}\text{H}_{11}\text{NH}_3$ in MeCN with 20/80 $\text{F}_2/\text{N}_2(\text{g})$.

1.2 Radical Substitution and Addition Synthesis, with Perfluoroalkyl and Perfluoroaryl groups, Single Crystal X-ray Structural Characterization, and Mechanistic Insight.

Replacement of legacy silicon and metal based electronic components in common electronic devices such as semiconductors, field effect transistors, light emitting diodes, and photovoltaics with rationally designed, tuned organic materials or hybrids promises many added benefits. Novel, sustainable, earth-abundant organic electronic materials will lead to lower-cost, lower-weight, flexible electronic devices. Besides being comprised of mostly being earth-abundant elements such as carbon, nitrogen, oxygen, and hydrogen, organic electronic materials can be, and already are in some cases, solution processed rather than requiring energy intensive purification, growth of large single crystals, and further etching and processing or chemical vapor deposition.⁹² Furthermore, organic electronic materials hold the promise of functioning in ways metal and semi-metal based semiconductors cannot, especially when considering the possible 3D architectures of self-assembled organic electronic materials.⁹³

Good electron-accepting fullerenes, required for fullerene based organic photovoltaic devices (OPV), were structurally compared. All of the fullerene packing and crystal structures discussed, with the exception of 1,9- $\text{C}_{60}(\text{cyclo-CF}_2(2-\text{C}_6\text{F}_4))$, are trifluoromethylfullerenes (TMF), an important class of fullerenes with many structurally and electrochemically characterized isomers of $\text{C}_{60}(\text{CF}_3)_{10}$. The group of $\text{C}_{60}(\text{CF}_3)_{10}$ isomers is the largest group of isomers of any fullerene with any addends. The first reduction potential ($E_{1/2}(0/-)$) of these spans nearly 0.5 eV, and this

class of fullerene isomers has led to many important discoveries in how the electronic properties of the C₆₀ cage are affected by the addition pattern, as well as how changes in $E_{1/2}(0/-)$ affect the C₆₀(CF₃)₁₀ compounds properties in OPV devices. Further, single crystal X-ray structural analysis of many of the C₆₀(CF₃)₁₀ isomers as well as 1,9-C₆₀(*cyclo*-CF₂(2-C₆F₄)) regarding nearest neighboring molecules, and cage surface cage surface distances will be compared to the current industry-standard electron accepting fullerene in OPV devices, phenyl-C₆₁-butyric acid methyl ester (PCBM) in Chapter 5. Parts or all of this work have been presented by the author at 2014 Electrochemical Society Conference, Orlando FL, will be the subject of a book chapter to be completed by October of this year with Dr. Olga Boltalina as the editor, and in *Chem. Sci.* **2015** with the author as a co-author of that work.

New organic electronic materials need to be electronically, thermally, chemically, and photo-stable for use in devices. Currently, one of the areas with the greatest need for new materials is air-, or more accurately oxygen-, stable *n*-type organic semiconductors.⁹⁴⁻¹⁰⁰ A synthetic target for air-stable *n*-type organic materials has been hypothesized by Chang et al. based on comparing experimental air stability of materials in organic field effect transistors (OFET), to their DFT-predicted gas-phase electron affinities.⁹⁴ This hypothetical gas-phase electron affinity limit for air-stable *n*-type organic electronic materials of 2.8 eV has been used in the literature as a good starting point for making air-stable organic *n*-type semiconductor materials. In an effort to make such compounds, so their physical and electrochemical properties can be studied, and further develop the field of *n*-type organic semiconductor materials, a new reactor was designed to improve the previous method of making polycyclic aromatic hydrocarbons (PAH) with multiple perfluoroalkyl and perfluoroaryl (R_F) substitutions in the Strauss-Boltalina research group developed by Post-doctoral researcher Igor V. Kuvychko.^{95-97,101,102} Substituting R_F groups in

place of H atoms on stable PAHs has been shown to increase the measured gas-phase electron affinities of many PAHs and these molecules are of interest to the organic electronic community.⁹⁵ The single crystal X-ray structures of some of these PAH(R_F)_n compounds will be presented, looking particularly at the effect different R_F groups have on the proximity of nearest neighboring molecules in the solid state structures, an important property when looking at the overall functionality of organic conducting and semiconducting materials which requires electronic communication between molecules.

The mechanism of radical substitution of R_F groups on PAHs starting from R_FI will also be analyzed. Multiple previous works have discussed multiple reaction pathways and important intermediate transition states, however no single consensus regarding the reaction mechanism has been accepted.^{95,97,103-106} Single crystal X-ray structures of multiple, new, trapped intermediate compounds, using multiple synthetic methods, and various PAH and R_FI reagents, with structurally similar sp³ carbons gives insight into the radical substitution mechanism. Further understanding of this mechanism and the intermediates would allow for more selective radical reactions starting from R_FI reagents. The new synthesis reactor, structural characterization, and mechanistic insights are described in Chapter 6. Parts or all of this work have also been published with the author of this dissertation as a co-author in *Chem. Comm.* **2014**, and *Chem. Euro. J.* **2014**, a recently submitted article in *Angew. Chem. Int. Ed.* **2015**.

1.3 Preparation and Characterization of Silicon Nanoparticles by Anaerobic Wet Milling.

Comminution by mechanical attrition (grinding) is a routine method to reduce particle size which is beneficial for: increasing surface area and reactivity of a material, increasing solubility, maximizing solids loading, thickening and stabilizing slurries/suspensions, intimate homogenization of powdered materials, homogenizing particle size and morphology, and top

down manufacture of nanoparticles.¹⁰⁷⁻¹¹⁶ The desirability of nanoparticles for a host of reasons makes them attractive synthetic targets; however, commonly employed bottom-up synthesis, while well-established, is sensitive to many variables and requires exceptional control over solvent, reagents and any possible contaminants (known or otherwise), temperatures, reaction time, pH, surfactants, and other additives for reproducibility.¹¹⁷⁻¹¹⁹ Top-down grinding of materials to form nanoparticles is attractive from the standpoint of cost and, in certain materials; the usage of the nanoparticles will tolerate irregular morphology and larger size distribution of milled nanoparticles.^{111-113,115,116} The properties that make nanoparticles attractive (rapid solubility, increased suspension properties, rapid reaction rates, high surface areas) also make them difficult to synthesize in high purity. Whether via solution based, bottom-up synthesis or top-down grinding based methods; in both cases any and all compounds that can interact with the nascent surface have the possibility of reacting and contaminating the particle surface. Simple, top-down grinding methods with precise control over all reagents and contaminants are required to make further strides in this field.

The grinding method most discussed in literature, which is easily adapted to anaerobic conditions, is a ball mill either inside an inert atmosphere glovebox, or charging a ball mill jar in an inert atmosphere and then sealing with an inert gas. While it is simple to adapt a ball mill to a glovebox, presumably without even opening the glovebox face, ball mills themselves are ill-suited for efficient production of high purity nanoparticles.^{107-109,120} First, ball mills are known to have poor efficiency when grinding a material below ca. 1 μm , this is due to simple statistics. Second, a ball mill relies on high-energy impact to fracture particles, in the process, damaging the milling media, and milling jar over time and is known to contaminate the sample.¹⁰⁷⁻¹⁰⁹

A mill design well suited to efficiently grinding materials to fine particulate size, 10–1 μm size and easily into the nm range, is a stirred media mill, sometimes called an attritor mill or stirred ball mill.^{107,120,121} The attritor mill imparts energy to fine milling media in a stationary vessel through a rotating mixer, maximizing the mechanical energy imparted to the milling media and material.^{107,109} It has been claimed that a stirred media mill can grind a material up to 10 times faster compared to a conventional ball mill.^{109,122} A stirred media mill can operate with a sample suspended in a solvent or a dry sample allowing fine control over what contacts the freshly exposed reactive material during the grinding process. Experiments involving milling of metallurgical grade silicon in an attritor mill and studying the resulting surface chemistry, crystallinity, and bulk surface properties as a function of, aerobic/anaerobic conditions and reactive milling solvent or additives are presented in Chapter 7. This work has not yet been published, but there is a manuscript in progress.

Chapter 1 References

- (1) Strauss, S. H. *Chem. Rev.* **1993**, *93*, 927.
- (2) Krossing, I.; Raabe, I. *Angew. Chem.* **2004**, 2066.
- (3) Ivanov, S. V.; Rockwell, J. J.; Polyakov, O. G.; Gaudinski, C. M.; Anderson, O. P.; Solntsev, K. A.; Strauss, S. H. *J. Am. Chem. Soc.* **1998**, *120*, 4224.
- (4) Ivanov, S. V.; Miller, S. M.; Anderson, O. P.; Solntsev, K. A.; Strauss, S. H. *J. Am. Chem. Soc.* **2003**, *125*, 4694.
- (5) Peryshkov, D. V.; Popov, A. A.; Strauss, S. H. *J. Am. Chem. Soc.* **2009**, *131*, 18393.
- (6) Ivanov, S. V.; Davis, J. A.; Miller, S. M.; Anderson, O. P.; Strauss, S. H. *Inorg. Chem.* **2003**, *42*, 4489.
- (7) *Chem. Eng. News*, March 31.
- (8) Lupinetti, A. J.; Strauss, S. H. *Chemtracts–Inorg. Chem.* **1998**, *11*, 565.
- (9) Rosenthal, M. R. *Journal of Chemical Education* **1973**, *50*, 331.
- (10) Beck, W.; Suenkel, K. *Chem Rev* **1988**, *88*, 1405.
- (11) Newbound, T. D.; Colman, M. R.; Miller, M. M.; Wulfsberg, G. P.; Anderson, O. P.; Strauss, S. H. *J Am Chem Soc* **1989**, *111*, 3762.
- (12) Strauss, S. H. *Chem Rev* **1993**, *93*, 927.
- (13) Strauss, S. H. *Chemtracts-Inorganic Chemistry* **1994**, *6*, 1.
- (14) Lupinetti, A. J.; Strauss, S. H. *Chemtracts-Inorganic Chemistry* **1998**, *11*, 565.
- (15) Reed, C. A. *Accounts of Chemical Research* **1998**, *31*, 133.
- (16) Krossing, I.; Raabe, I. *Angewandte Chemie International Edition* **2004**, *43*, 2066.
- (17) Krossing, I.; Reisinger, A. *Coordination Chemistry Reviews* **2006**, *250*, 2721.
- (18) Reed, C. A. *Accounts of Chemical Research* **2009**, *43*, 121.
- (19) Nava, M. J.; Reed, C. A. *Inorg Chem* **2010**, *49*, 4726.
- (20) Ivanov, S. V.; Miller, S. M.; Anderson, O. P.; Strauss, S. H. *Crystal Growth & Design* **2004**, *4*, 249.
- (21) Ivanova, S. M.; Ivanov, S. V.; Miller, S. M.; Anderson, O. P.; Solntsev, K. A.; Strauss, S. H. *Inorg Chem* **1999**, *38*, 3756.
- (22) King, B. T.; Noll, B. C.; McKinley, A. J.; Michl, J. *J Am Chem Soc* **1996**, *118*, 10902.
- (23) Zharov, I.; Weng, T.-C.; Orendt, A. M.; Barich, D. H.; Penner-Hahn, J.; Grant, D. M.; Havlas, Z.; Michl, J. *J Am Chem Soc* **2004**, *126*, 12033.
- (24) Rupich, M. W.; Foos, J. S.; Brummer, S. B. *Journal of The Electrochemical Society* **1985**, *132*, 119.
- (25) Koczorowski, Z.; Zagórska, I. *J Appl Electrochem* **1980**, *10*, 75.
- (26) Arai, J.; Matsuo, A.; Fujisaki, T.; Ozawa, K. *Journal of Power Sources* **2009**, *193*, 851.
- (27) GirishKumar, G.; Bailey, W. H.; Peterson, B. K.; Casteel, W. J. *Journal of The Electrochemical Society* **2011**, *158*, A146.
- (28) Ionica-Bousquet, C. M.; Casteel Jr, W. J.; Pearlstein, R. M.; GirishKumar, G.; Pez, G. P.; Gómez-Romero, P.; Palacín, M. R.; Muñoz-Rojas, D. *Electrochemistry Communications* **2010**, *12*, 636.
- (29) Ivanov, S. V.; Casteel, W. J.; Pez, G. P.; Google Patents: 2009.

- (30) Pez, G.; Ivanov, S.; Dantsin, G.; Casteel, W.; Lehmann, J. In *Google Patents*; Pez Guido P, Ivanov Sergei V, Gennady Dantsin, Casteel William J Jr, Lehmann John F, AIR PRODUCTS AND CHEMICALS, INC., PENNSYLVANIA: 2007.
- (31) Ivanov, S. V.; Casteel, W. J.; Bailey, W. H. In *Google Patents*; Air Products And Chemicals, Inc.: 2011.
- (32) Vaughey, J.; Jansen, A. N.; Dees, D. W. In *Google Patents*; Uchicago Argonne, Llc: 2010.
- (33) Polyakov, O. G.; Strauss, S. H.; Kuvychko, I. V. In *Google Patents*; Synkera Technologies, Inc.: 2008.
- (34) Chen, E. Y.-X.; Marks, T. J. *Chem Rev* **2000**, *100*, 1391.
- (35) Mariott, W. R.; Gustafson, L. O.; Chen, E. Y. X. *Organometallics* **2006**, *25*, 3721.
- (36) Bochmann, M. *Journal of Organometallic Chemistry* **2004**, *689*, 3982.
- (37) Bochmann, M. *Organometallics* **2010**, *29*, 4711.
- (38) Xie, Z. W.; Bau, R.; Reed, C. A. *Inorg Chem* **1995**, *34*, 5403.
- (39) Bukovsky, E. V.; Fiedler, S. R.; Peryshkov, D. V.; Popov, A. A.; Strauss, S. H. *European Journal of Inorganic Chemistry* **2012**, 208.
- (40) Reed, C. A.; Fackler, N. L. P.; Kim, K.-C.; Stasko, D.; Evans, D. R.; Boyd, P. D. W.; Rickard, C. E. F. *J Am Chem Soc* **1999**, *121*, 6314.
- (41) Reed, C. A.; Kim, K.-C.; Stoyanov, E. S.; Stasko, D.; Tham, F. S.; Mueller, L. J.; Boyd, P. D. W. *J Am Chem Soc* **2003**, *125*, 1796.
- (42) Peryshkov, D. V. Dissertation, Colorado State University, 2011.
- (43) Ivanov, S. V.; Peryshkov, D. V.; Miller, S. M.; Anderson, O. P.; Rappe, A. K.; Strauss, S. H. *Journal of Fluorine Chemistry* **2012**, *143*, 99.
- (44) Solnstev, K. A.; Mebel, A. M.; Votnova, N. A.; Kuznetsov, N. T.; Charkin, O. P. *Koord. Khim.* **1992**, *18*, 340.
- (45) Ivanov, S. V.; Miller, S. M.; Anderson, O. P.; Solntsev, K. A.; Strauss, S. H. *J Am Chem Soc* **2003**, *125*, 4694.
- (46) Peryshkov, D. V.; Popov, A. A.; Strauss, S. H. *J Am Chem Soc* **2009**, *131*, 18393.
- (47) Peryshkov, D. V.; Strauss, S. H. *Journal of Fluorine Chemistry* **2010**, *131*, 1252.
- (48) Peryshkov, D. V.; Popov, A. A.; Strauss, S. H. *J Am Chem Soc* **2010**, *132*, 13902.
- (49) Peryshkov, D. V.; Goresnik, E.; Mazej, Z.; Strauss, S. H. *Journal of Fluorine Chemistry* **2010**, *131*, 1225.
- (50) Shackelford, S. A.; Belletire, J. L.; Boatz, J. A.; Schneider, S.; Wheaton, A. K.; Wight, B. A.; Ammon, H. L.; Peryshkov, D. V.; Strauss, S. H. *Org Lett* **2010**, *12*, 2714.
- (51) Tiritiris, I.; Schleid, T. *Zeitschrift für anorganische und allgemeine Chemie* **2003**, *629*, 1390.
- (52) Tiritiris, I.; Schleid, T.; Müller, K.; Preetz, W. *Zeitschrift für anorganische und allgemeine Chemie* **2000**, *626*, 323.
- (53) Wunderlich, J. A.; Lipscomb, W. N. *J Am Chem Soc* **1960**, *82*, 4427.
- (54) Her, J.-H.; Yousufuddin, M.; Zhou, W.; Jalisatgi, S. S.; Kulleck, J. G.; Zan, J. A.; Hwang, S.-J.; Bowman, R. C.; Udovic, T. J. *Inorg Chem* **2008**, *47*, 9757.
- (55) Derendorf, J.; Ke, Knapp, C.; Ruhle, M.; Schulz, C. *Dalton Transactions* **2010**, *39*, 8671.
- (56) Geis, V.; Gutsche, K.; Knapp, C.; Scherer, H.; Uzun, R. *Dalton Transactions* **2009**, 2687.
- (57) Tiritiris, I.; Schleid, T. *Zeitschrift für anorganische und allgemeine Chemie* **2004**, *630*, 1555.

- (58) Stasko, D. J.; Perzynski, K. J.; Wasil, M. A.; Brodbeck, J. K.; Kirschbaum, K.; Kim, Y. W.; Lind, C. *Inorg Chem* **2004**, *43*, 3786.
- (59) Peymann, T.; Herzog, A.; Knobler, C. B.; Hawthorne, M. F. *Angewandte Chemie International Edition* **1999**, *38*, 1061.
- (60) Peymann, T.; Knobler, C. B.; Hawthorne, M. F. *J Am Chem Soc* **1999**, *121*, 5601.
- (61) A. Szytula, J. L. *Handbook of Crystal Structures and Magnetic Properties of Rare Earth Intermetallics*; CRC Press: Boca Raton, 1994.
- (62) McNaught, A. D. W., A.; Nic, M. J., J.; Kosata, B.; Updates by Jenkins, A. In *IUPAC. Compendium of Chemical Terminology, 2nd ed. (the "Gold Book")*; 2nd ed.; Blackwell Scientific Publications: Oxford, 2006.
- (63) Avelar, A.; Tham, F. S.; Reed, C. A. *Angewandte Chemie International Edition* **2009**, *48*, 3491.
- (64) Stoyanov, E. S.; Stoyanova, I. V.; Reed, C. A. *J Am Chem Soc* **2010**, *132*, 1484.
- (65) Stoyanov, E. S.; Stoyanova, I. V.; Reed, C. A. *Chemical Science* **2011**, *2*, 462.
- (66) Xu, J.; Izvekov, S.; Voth, G. A. *The Journal of Physical Chemistry B* **2010**, *114*, 9555.
- (67) Jagoda-Cwiklik, B.; Cwiklik, L.; Jungwirth, P. *The Journal of Physical Chemistry A* **2011**, *115*, 5881.
- (68) Takahashi, H.; Maruyama, K.; Karino, Y.; Morita, A.; Nakano, M.; Jungwirth, P.; Matubayasi, N. *The Journal of Physical Chemistry B* **2011**, *115*, 4745.
- (69) Stoyanov, E. S.; Kim, K. C.; Reed, C. A. *J Am Chem Soc* **2006**, *128*, 1948.
- (70) Bernal, I. *Comptes Rendus Chimie* **2006**, *9*, 1454.
- (71) Bernal, I. *Comptes Rendus Chimie* **2008**, *11*, 942.
- (72) Yang, Z.; Hua, S.; Hua, W.; Li, S. *The Journal of Physical Chemistry B* **2011**, *115*, 8249.
- (73) Knoth, W. H.; Miller, H. C.; Sauer, J. C.; Balthis, J. H.; Chia, Y. T.; Muetterties, E. L. *Inorg Chem* **1964**, *3*, 159.
- (74) Casteel William J Jr, I. S. V., Pez Guido P; H01B1/12 ed.; office, U. P., Ed.; Casteel William J Jr, Ivanov Sergei V, Pez Guido P: United States of America, 2006.
- (75) Ivanov, S. V.; Casteel, W. J., Jr.; Pez, G. P.; Air Products and Chemicals, Inc.: European Patent Application, 2006.
- (76) Chen, Z.; Ren, Y.; Jansen, A. N.; Lin, C.-k.; Weng, W.; Amine, K. *Nat Commun* **2013**, *4*, 1513.
- (77) Hayamizu, K.; Matsuo, A.; Arai, J. *Journal of The Electrochemical Society* **2009**, *156*, A744.
- (78) Goodenough, J. B.; Kim, Y. *Chemistry of Materials* **2010**, *22*, 587.
- (79) Sivaev, I. B.; Bregadze, V. I.; Sjöberg, S. *Collect. Czech. Chem. Commun.* **2002**, *67*, 679.
- (80) Hawthorne, M. F. *Pure Appl. Chem.* **1991**, *63*.
- (81) Sivaev, I. B.; Bruskin, A. B.; Nesterov, V. V.; Antipin, M. Y.; Bregadze, V. I.; Sjöberg, S. *Inorg. Chem.* **1999**, *38*, 5887.
- (82) Genady, A. R. *Acta Chim. Slov.* **2012**, *59*, 89.
- (83) El-Zaria, M. E.; Genady, A. R.; Nakamura, H. *New J. Chem.* **2010**, *34*, 1612.
- (84) Bertrand, G. H. V.; Hamel, M.; Sguerra, F. *Chem. Eur. J.* **2014**, *20*, 15660.
- (85) Bernard, R.; Cornu, D.; Gruner, B.; Dozol, J. F.; Miele, P.; Bonnetot, B. *J. Organomet. Chem.* **2002**, *657*, 83.
- (86) Hertler, W. R.; Raasch, M. S. *J. Am. Chem. Soc.* **1964**, *86*, 3661.
- (87) Bolli, C.; Derendorf, J.; Jenne, C.; Scherer, H.; Sindlinger, C. P.; Wegener, B. *Chem. Eur. J.* **2014**, *20*, 13783.

- (88) Justus, E.; Voge, A.; Gabel, D. *Eur. J. Inorg. Chem.* **2008**, 5245.
- (89) Justus, E.; Rischka, M.; Wishart, J. F.; Werner, K.; Gabel, D. *Chem. Eur. J.* **2008**, *14*, 1918.
- (90) Bernard, R.; Cornu, D.; Baldeck, P. L.; Daslavsky, J.; Letoffe, J. M.; Scharff, J. P.; Miele, P. *Dalton Trans.* **2005**, 3065.
- (91) Bernard, R.; Cornu, D.; Scharff, J. P.; Chiriach, R.; Miele, P. *Inorg. Chem.* **2006**, *45*, 8743.
- (92) Forrest, S. R. *Nature* **2004**, *428*, 911.
- (93) Zhang, X.; Bauerle, P.; Aida, T.; Skabara, P.; Kagan, C. *Organic Electronics for a Better Tomorrow: Innovation, Accessibility, Sustainability*, Chemical Sciences and Society Summit (CS3), 2012.
- (94) Chang, Y.-C.; Kuo, M.-Y.; Chen, C.-P.; Lu, H.-F.; Chao, I. *The Journal of Physical Chemistry C* **2010**, *114*, 11595.
- (95) Kuvychko, I. V.; Castro, K. P.; Deng, S. H. M.; Wang, X.-B.; Strauss, S. H.; Boltalina, O. V. *Angewandte Chemie International Edition* **2013**, *52*, 4871.
- (96) Kuvychko, I. V.; Dubceac, C.; Deng, S. H. M.; Wang, X.-B.; Granovsky, A. A.; Popov, A. A.; Petrukhina, M. A.; Strauss, S. H.; Boltalina, O. V. *Angewandte Chemie International Edition* **2013**, *52*, 7505.
- (97) Kuvychko, I. V.; Spisak, S. N.; Chen, Y.-S.; Popov, A. A.; Petrukhina, M. A.; Strauss, S. H.; Boltalina, O. V. *Angewandte Chemie International Edition* **2012**, *51*, 4939.
- (98) Mottishaw, J. D.; Sun, H. *The Journal of Physical Chemistry A* **2013**, *117*, 7970.
- (99) Sun, H.; Putta, A.; Billion, M. *The Journal of Physical Chemistry A* **2012**, *116*, 8015.
- (100) Sun, H.; Tottempudi, U. K.; Mottishaw, J. D.; Basa, P. N.; Putta, A.; Sykes, A. G. *Crystal Growth & Design* **2012**, *12*, 5655.
- (101) Clikeman, T. T.; Bukovsky, E. V.; Kuvychko, I. V.; San, L. K.; Deng, S. H. M.; Wang, X.-B.; Chen, Y.-S.; Strauss, S. H.; Boltalina, O. V. *Chemical Communications* **2014**, *50*, 6263.
- (102) San, L. K.; Bukovsky, E. V.; Kuvychko, I. V.; Popov, A. A.; Strauss, S. H.; Boltalina, O. V. *Chemistry – A European Journal* **2014**, *20*, 4373.
- (103) Studer, A. *Angewandte Chemie International Edition* **2012**, *51*, 8950.
- (104) Chamberlain, G. A.; Whittle, E. *Transactions of the Faraday Society* **1971**, *67*, 2077.
- (105) Charles, S. W.; Pearson, J. T.; Whittle, E. *Transactions of the Faraday Society* **1961**, *57*, 1356.
- (106) Charles, S. W.; Whittle, E. *Transactions of the Faraday Society* **1960**, *56*, 794.
- (107) Balaz, P. In *Mechanochemistry in Nanoscience and Minerals Engineering*; Springer-Verlag Berlin Heidelberg: 2008, p 413.
- (108) Balaz, P.; Achimovicova, M.; Balaz, M.; Billik, P.; Cherkezova-Zheleva, Z.; Criado, J. M.; Delogu, F.; Dutkova, E.; Gaffet, E.; Gotor, F. J.; Kumar, R.; Mitov, I.; Rojac, T.; Senna, M.; Streletskii, A.; Wiczorek-Ciurawa, K. *Chemical Society reviews* **2013**, *42*, 7571.
- (109) Castro, C. L., Mitchell, B. S. In *Synthesis, Functionallization and Surface Treatment of Nanoparticles*; Baraton, M. I., Ed.; American Scientific Publishers: 2002, p 450.
- (110) McMahan, B. W.; Perez, J. P. L.; Yu, J.; Boatz, J. A.; Anderson, S. L. *ACS Applied Materials & Interfaces* **2014**, *6*, 19579.
- (111) Xing, T.; Sunarso, J.; Yang, W.; Yin, Y.; Glushenkov, A. M.; Li, L. H.; Howlett, P. C.; Chen, Y. *Nanoscale* **2013**, *5*, 7970.
- (112) Kim, H. S.; Hong, S. J. *Current Nanoscience* **2014**, *10*, 118.
- (113) Akdogan, N. G.; Hadjipanayis, G. C.; Sellmyer, D. J. *Journal of Applied Physics* **2009**, *105*, 07A710.

- (114) Monteiro, A.; Afolabi, A.; Bilgili, E. *Drug Development and Industrial Pharmacy* **2013**, *39*, 266.
- (115) Wang, W.; Datta, M. K.; Kumta, P. N. *J. Mater. Chem.* **2007**, *17*, 3229.
- (116) Wang, W.; Kumta, P. N. *J. Power Sources* **2007**, *172*, 650.
- (117) Kwon, S. G.; Hyeon, T. *Small* **2011**, *7*, 2685.
- (118) Ghorpade, U.; Suryawanshi, M.; Shin, S. W.; Gurav, K.; Patil, P.; Pawar, S.; Hong, C. W.; Kim, J. H.; Kolekar, S. *Chemical Communications* **2014**, *50*, 11258.
- (119) Williams, J. V.; Kotov, N. A.; Savage, P. E. *Industrial & Engineering Chemistry Research* **2009**, *48*, 4316.
- (120) Jankovic, A. *Minerals Engineering* **2003**, *16*, 337.
- (121) Stenger, F.; Mende, S.; Schwedes, J.; Peukert, W. *Chemical Engineering Science* **2005**, *60*, 4557.
- (122) Suryanarayana, C. *Progress in Materials Science* **2001**, *46*, 1.

Chapter 2.

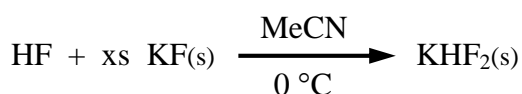
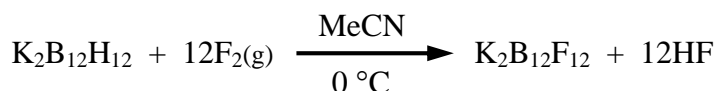
Improved Synthesis and Purification the of Superweak Anion Salts $\text{Li}_2\text{B}_{12}\text{F}_{12}$, $\text{Na}_2\text{B}_{12}\text{F}_{12}$, and $\text{K}_2\text{B}_{12}\text{F}_{12}$

2.1 Introduction and Justification

Superweak anion salts, specifically of the form $\text{M}_2\text{B}_{12}\text{F}_{12}$ ($\text{M} = \text{Li}, \text{Na}$) are being researched as highly conductive thermally stable electrolytes for electrochemical devices to improve the lifetime and safety for large electrochemical cells.¹⁻¹¹ Superweak anions are desirable as electrolyte salts because they are; weak Bronsted and Lewis bases, electrochemically and thermally stable, and are not plagued with the thermal equilibrium and hygroscopicity problems of legacy electrolyte salt LiPF_6 .¹² The purity of all materials in an electrochemical cell is extremely important. Any impurities can have adverse, non-reversible reactions under the oxidative and reductive conditions during charge and discharge cycles. To further research and development of these important superweak anion electrolyte salts, the precursor material, $\text{K}_2\text{B}_{12}\text{F}_{12}$ had to be made in high purity. From highly purified $\text{K}_2\text{B}_{12}\text{F}_{12}$, the $\text{Li}_2\text{B}_{12}\text{F}_{12}$ and $\text{Na}_2\text{B}_{12}\text{F}_{12}$ salts could be made in high purity.

The precursor to the desired electrolyte salts is $\text{K}_2\text{B}_{12}\text{F}_{12}$ which is made from $\text{K}_2\text{B}_{12}\text{H}_{12}$ and $\text{F}_2(\text{g})$.¹³ Besides scaling and improving the $\text{K}_2\text{B}_{12}\text{F}_{12}$ synthesis for electrolyte research, development of a simple and efficient synthesis of $\text{K}_2\text{B}_{12}\text{F}_{12}$ allowed rapid progress in the knowledge and understanding of the superweak anion $\text{B}_{12}\text{F}_{12}^{2-}$.¹³⁻²⁰ The $\text{K}_2\text{B}_{12}\text{F}_{12}$ salt was first prepared in 38% yield by heating $\text{K}_2\text{B}_{12}\text{H}_{12}$ in supercritical HF by Solntsev et al. in 1992.¹⁴ An improved preparation (ca. 1.5 g 72% yield) was reported by the Strauss-Boltalina group in 2003 using LAHF solvent and a mixture of $\text{F}_2/\text{N}_2(\text{g})$ at high pressure in a Monel reactor.¹⁶ Recently, a

scaled-up synthesis of $\text{K}_2\text{B}_{12}\text{F}_{12}$ (ca. 18 g, 74% yield) was reported by Peryshkov and Strauss-Boltalina et al. in 2009 that used a glass reactor, MeCN solvent and $\text{F}_2/\text{N}_2(\text{g})$ bubbled through the MeCN solution.¹⁹ The synthetic methodology developed by Peryshkov et al. for easier, scalable synthesis of $\text{K}_2\text{B}_{12}\text{F}_{12}$, shown in the equations below, had four advantages compared to the Monel reactor method: (i) scaled reaction to 10 g of $\text{K}_2\text{B}_{12}\text{H}_{12}$ starting material; (ii) shortened reaction time to from 7 days to 2 days; (iii) efficient use of $\text{F}_2(\text{g})$; and (iv) replaced liquid anhydrous HF with a less reactive, less volatile solvent.^{13,19} The reaction of $\text{K}_2\text{B}_{12}\text{H}_{12}$ with $\text{F}_2(\text{g})$ (20% $\text{F}_2(\text{g})/\text{N}_2(\text{g})$) in MeCN at 0 °C was still not fully fluorinated after ca. 28 equiv of F_2 in the



absence of added KF. It was found that the buildup of HF in the reaction mixture slowed the rate of fluorination over time. If the reaction went to completion in the 500 mL reaction mixture as described in the literature, the concentration of HF would be 0.53 M.¹⁹ To stop the buildup of HF during the fluorination reaction, Peryshkov et al. added finely-ground $\text{KF}(\text{s})$ to the reaction mixture to irreversibly react with HF forming insoluble $\text{KHF}_2(\text{s})$, effectively removing it from the reaction mixture, allowing the fluorination to go to completion in less time using only 13–14 equiv F_2

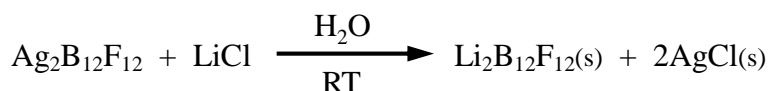
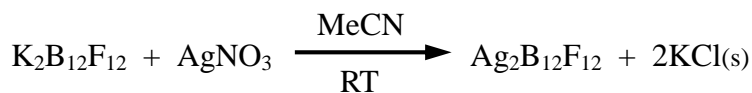
This shorter and simpler synthetic method in MeCN allowed for a rapid and scaled-up synthesis of $\text{K}_2\text{B}_{12}\text{F}_{12}$, which is the precursor for all $\text{B}_{12}\text{F}_{12}^{2-}$ salts produced in the Strauss-Boltalina research group. One drawback to this synthetic method for making $\text{K}_2\text{B}_{12}\text{F}_{12}$ from $\text{K}_2\text{B}_{12}\text{H}_{12}$ in MeCN with $\text{F}_2(\text{g})$ is that it resulted in a yellow/yellow-orange impurity in the crude

$\text{K}_2\text{B}_{12}\text{F}_{12}$ reaction product (hereinafter, the term *crude product* refers to the solid $\text{K}_2\text{B}_{12}\text{F}_{12}$ reaction product isolated immediately after F_2/N_2 fluorination, filtration, and removal of MeCN by rotary evaporation, and the term *yellow impurity* refers to one or more yellow/yellow-orange impurities). A photograph of the yellow $\text{K}_2\text{B}_{12}\text{F}_{12}$ crude product prepared by the author of this dissertation using the literature procedure just described is shown in Figure 2-1. In the author's hands, the yellow impurity proved very difficult to remove, as described in a later section.

This chapter describes this author's improved (safer and more reliable) $\text{K}_2\text{B}_{12}\text{F}_{12}$ purification method for the $\text{K}_2\text{B}_{12}\text{F}_{12}$ crude product. The author found that the fluorination of $\text{K}_2\text{B}_{12}\text{H}_{12}$ described by Peryshkov et al. in 2009 was straightforward. However, the 2009 procedure for the purification of the yellow $\text{K}_2\text{B}_{12}\text{F}_{12}$ crude product was not reproducible and required an extensive investigation into the chemical and physical properties of the yellow impurity. In the end, a new purification method was developed and is described in this chapter.

In addition to the new purification method of $\text{K}_2\text{B}_{12}\text{F}_{12}$ a new synthesis method to produce high purity $\text{Li}_2\text{B}_{12}\text{F}_{12}$ and $\text{Na}_2\text{B}_{12}\text{F}_{12}$ will be discussed. Recent, academic, as well as commercial interest in both $\text{Li}_2\text{B}_{12}\text{F}_{12}$ and $\text{Na}_2\text{B}_{12}\text{F}_{12}$ as Li^+ or Na^+ conducting electrolytes has led this author to research novel, scalable, methods to produce highly purified $\text{Li}_2\text{B}_{12}\text{F}_{12}$ and $\text{Na}_2\text{B}_{12}\text{F}_{12}$.^{3-5,10,21,22} Additionally, commercial sponsors sought out the expertise of the Strauss-Boltalina research group to make 15 g each of the $\text{Li}_2\text{B}_{12}\text{F}_{12}$ and $\text{Na}_2\text{B}_{12}\text{F}_{12}$ salts for electrolyte research. Since a known method to make the precursor $\text{K}_2\text{B}_{12}\text{F}_{12}$ has already been developed^{13,19}, a high purity metathesis method converting from the K^+ to either the Li^+ or Na^+ was necessary. The previous metathesis method to make new metal salts of $\text{B}_{12}\text{F}_{12}^{2-}$ employed by the Strauss-Boltalina group worked well for initial characterization experiments. However, the synthetic method did not take

into account the high purity requirement for $B_{12}F_{12}^{2-}$ salts when they are used for electrochemical research.



The downside of using the $Ag_2B_{12}F_{12}$ salt as a convenient intermediate to make highly purified metal salts of $B_{12}F_{12}^{2-}$ (previously demonstrated by the Strauss-Boltalina Group) is that $Ag_2B_{12}F_{12}$ forms many solvated states with acetonitrile.¹³ The $Ag_2B_{12}F_{12}$ salt has three known solvate phases with MeCN $Ag_2(CH_3CN)_x B_{12}F_{12}$ where $x = 2, 4,$ and 5 have been characterized by SC-XRD. There are likely other solvated phases yet uncharacterized, that makes stoichiometric addition of $Ag_2(CH_3CN)_x B_{12}F_{12}$ difficult. Also, typical of most Ag^+ salts, $Ag_2B_{12}F_{12}$ is photosensitive, which complicates preparation of highly purified $Ag_2B_{12}F_{12}$, which, in turn, would decrease the purity of the resulting $M_2B_{12}F_{12}$ ($M = Li^+, Na^+$) salts.

A method to prepare very pure $(H_3O)_2B_{12}F_{12} \cdot nH_2O$ using high-quality cation-exchange resin, published by the author of this dissertation in *Eur. J. Inorg. Chem.* in 2012,²³ and described in Chapter 3, was adapted to prepare very pure $Li_2B_{12}F_{12}$ and $Na_2B_{12}F_{12}$ from $K_2B_{12}F_{12}$ (the degree of purity will be discussed below). A known problem with using strong-acid cation-exchange resin to exchange monovalent metal cations occurs when the cations are not sufficiently different in size or charge, resulting in poor exchange efficiency and hence lower purity, an undesirable consequence when the salt is to be an electrolyte for electrochemical research and/or devices. A

second challenge is that the product from the cation-exchange resin would be aqueous and would have to be dried to make it anhydrous for electrochemical research. Starting from $\text{K}_2\text{B}_{12}\text{F}_{12}$ and converting to the desired products $\text{Li}_2\text{B}_{12}\text{F}_{12}$ or $\text{Na}_2\text{B}_{12}\text{F}_{12}$ the exchange efficiency needed to be investigated. Furthermore, TGA experiments needed to be performed to determine if $\text{Li}_2\text{B}_{12}\text{F}_{12} \cdot n\text{H}_2\text{O}$ or $\text{Na}_2\text{B}_{12}\text{F}_{12} \cdot n\text{H}_2\text{O}$ could be completely dehydrated without decomposition.

2.1.1 Published Synthesis and Purification Methods of $\text{K}_2\text{B}_{12}\text{F}_{12}$ and $\text{Li}_2\text{B}_{12}\text{F}_{12} \cdot n\text{H}_2\text{O}$.

The synthetic procedure of Peryshkov et al. in their 2009 *J. Am. Chem. Soc.* paper is as follows:¹⁹

"The compound $\text{K}_2\text{B}_{12}\text{H}_{12}$ (KatChem, 10.1 g, 45.9 mmol, used as received) was dissolved in a mixture of MeCN (490 mL, used as received) and [deionized distilled] H_2O (12 mL) in a three-neck 1-L Pyrex round-bottom flask to give a colorless solution. Finely ground KF (22.7 g, 390 mmol) was added, most of which did not dissolve. A 20/80 F_2/N_2 mixture was bubbled through the reaction mixture at the rate of 115–125 mL min^{-1} for 6 h with vigorous stirring (this procedure constitutes Step 1 of the fluorination). *CAUTION: F_2/N_2 mixtures are extremely hazardous and should only be handled by trained personnel.* The reaction mixture became pale yellow after 3 h of fluorination. The gas flow was stopped after 6 h, and the reaction mixture was bubbled with N_2 for 30 min to remove traces of F_2 . The mixture was filtered and the filtrate evaporated to dryness under vacuum. The solid residue was dissolved in 500 mL of anhydrous MeCN [method of drying/purifying MeCN described below] and filtered. Finely ground KF (27.3 g, 470 mmol) was added to the filtrate. The 20/80 F_2/N_2 mixture

was bubbled through the reaction mixture with vigorous stirring for 7 h but at a slightly lower rate, 100-110 mL min⁻¹, than in Step 1."

In the Peryshkov et al. 2009 *J. Am. Chem. Soc.* paper the anhydrous/purified MeCN used in the second fluorination step was produced as follows: MeCN (Aldrich, ACS grade) (i) the as-received solvent was refluxed over anhydrous AlCl₃ for 1 h and then distilled; (ii) the distillate was refluxed over KMnO₄ and K₂CO₃ for 15 min and then distilled again; (iii) the second distillate was refluxed over KHSO₄ for 1 h and then distilled a third time; (iv) the third distillate was refluxed over CaH₂ for 4–6 h, was then distilled for the fourth and last time and stored under nitrogen.²⁴

The purification procedure for crude K₂B₁₂F₁₂ described in the 2009 *J. Am. Chem. Soc.* paper is as follows:¹⁹

"After the fluorination reaction was determined to be complete by NI-ESI-MS, the reaction mixture was purged with N₂ and filtered. The filtrate was neutralized to pH 7 or greater with aqueous KHCO₃. All volatiles were removed under vacuum. The pale-yellow solid residue was mixed with 100 mL of untreated MeCN and filtered. The filtrate was evaporated to dryness under vacuum. The resulting yellow solid was dissolved in 6% [wt/wt, ca. 2 M] aqueous hydrogen peroxide (50 mL) and heated to 80 °C for 2 h, during which the solution became colorless. In order to isolate K₂B₁₂F₁₂, the colorless solution was evaporated to dryness, and the white solid residue was recrystallized from MeCN and dried at 60 °C under vacuum."

A photograph of the resulting K₂B₁₂F₁₂ crude product produced by the author of this dissertation after the N₂ purge, filtration, neutralization, drying, MeCN dissolve, filter and drying

steps is shown in Figure 2-1. Also in this author's hands the amount of the yellow impurity or intensity did not appear to change whether dry acetonitrile was used in the second fluorination step or not. It should be noted that this author never tried the multi-step purification of MeCN, the anhydrous MeCN used for this author's experiments was prepared by drying with > 20 vol% 3 Å molecular sieves 48 h with agitation, distill under 99.999% N_{2(g)}, bubble room temperature solvent with 99.999% N_{2(g)} 30 min to deoxygenate. With as received or with dry MeCN, at the end of the second fluorination step, the solution was bright yellow as shown in Figure 2-2 (top). However, upon neutralization with aqueous KHCO₃ as prescribed, the solution turned orange as shown in Figure 2-2 (bottom) and would further darken upon concentration as shown in Figure 2-3. In the 20+ attempts by this author to synthesize and purify K₂B₁₂F₁₂ following the literature methods, the aqueous hydrogen peroxide treatment never resulted in a colorless solution. On at least one occasion, drying the crude K₂B₁₂F₁₂ mixture after the 6% aqueous hydrogen peroxide heating treatment resulted in an apparently friction-sensitive dry solid that exhibited a violent reaction when scrapped with a metal spatula. Compounds that exhibit violent reactions are typically described as shock-sensitive.

Many materials that exhibit a violent release of energy are said to be shock-sensitive. However, the adjective *shock-sensitive* is ambiguous because it does not indicate whether the material is impact-, friction-, heat-, electrostatic-sensitive, (or other) and these are very different properties. Furthermore, the word *shock* implies a shock wave, which is a propagating disturbance that travels faster than the speed of sound through the material (whether it be a solid, liquid, or gas) and that causes plastic deformation by an abrupt, nearly discontinuous change in pressure, temperature, and density of the medium.²⁵ In other words, a material should be described as shock-sensitive if and only if a shock wave initiates the violent reaction. Note that a

shock-sensitive material can *also* be impact-, friction-, heat-, or electrostatic-sensitive, but the proper test for shock sensitivity is beyond the capabilities of most chemistry laboratories, and in general the term should not be used unless the proper test has been done.

The compound $\text{Li}_2\text{B}_{12}\text{F}_{12}$ has been synthesized previously and published, Ivanov et al. 2003 *J. Am. Chem. Soc.* starting from aqueous $\text{K}_2\text{B}_{12}\text{F}_{12}$. First the acid salt, $(\text{H}_3\text{O})_2\text{B}_{12}\text{F}_{12}\cdot n\text{H}_2\text{O}$ was produced with Amberlist 15 strong-acid cation-exchange resin.¹⁶ The aqueous acid was then neutralized to $\text{pH} = 7$ with aqueous LiOH solution, then all volatiles were removed by vacuum. The solid was then dried at $180\text{ }^\circ\text{C}$ for 16 h to produce dry $\text{Li}_2\text{B}_{12}\text{F}_{12}$. From the paper, the only analysis performed was FT-IR to determine that the product was anhydrous.¹⁶ The compositional purity of $\text{B}_{12}\text{F}_{12}^{2-}$ was demonstrated by ^{11}B and ^{19}F NMR spectroscopy and by NI-ESI-MS, however, there is no discussing on cation purity.

2.1.2 Safety Concerns Regarding the use of H_2O_2 to Purify Crude $\text{K}_2\text{B}_{12}\text{F}_{12}$.

The original method to remove the yellow impurity (described above) was never completely successful in the hands of this author, always resulting in pale yellow $\text{K}_2\text{B}_{12}\text{F}_{12}$ crystals, even after recrystallization from MeCN or H_2O as shown in Figure 2-4. On multiple occasions the concentration of H_2O_2 was increased (up to 10% wt/wt in some experiments) in an attempt to remove all of the color from crude $\text{K}_2\text{B}_{12}\text{F}_{12}$. On at least one occasion there was a significant amount of H_2O_2 or some other reactive compound remaining in the aqueous solution and when dried under vacuum, a sensitive material was produced that exhibited a large and violent reaction when scrapped with a metal spatula. The ensuing explosion of the ca. 15 g sample caused the 250 mL round bottom flask to fracture into many pieces with such force that it caused lacerations to this author's hands, arms, face, chest and abdomen, even while wearing proper lab attire, (a thick cotton lab coat, nitrile gloves and safety glasses). While this author sustained no

permanent, debilitating, injuries from this accident, there are many scars to remind this author of the result. To get an idea of the energy generated from this reaction, there were pieces of glass found in the authors' hands and wrists that had to be surgically removed 6 months after the explosion. Pieces of glass from the violent reaction were found, that had penetrated through two sides of an empty cardboard box and then buried into ca. 1.0 cm of drywall. Additionally, the bench top, where the flask was sitting on a cork ring, was pitted from glass fragment impacts and the heating water bath of a nearby rotary evaporator sustained damage to the external case and internal components rendering it unrepairable.

The identity of the sensitive material(s) is still in question, it could have been highly concentrated H_2O_2 with residual MeCN, or it could have been something similar to the known salt, $\text{K}_2(\text{H}_2\text{O}_2)_{1.5}(\text{H}_2\text{O})_{0.5}\text{B}_{12}\text{F}_{12}$ shown in Figure 2-5, that has been studied by single crystal X-ray crystallography, or a combination of the two.^{13,26} A similar compound, $\text{Rb}_2(\text{H}_2\text{O}_2)_2\text{B}_{12}(\text{OH})_{12}$ was also published with the following warning,

"Caution! Please be aware of the danger, the synthesis of the title compounds $[\text{Rb}_2(\text{H}_2\text{O}_2)_2\text{B}_{12}(\text{OH})_{12}$ and $\text{Rb}_2(\text{H}_2\text{O})_2\text{B}_{12}(\text{OH})_{12}$] is associated with. Especially $\text{Rb}_2(\text{H}_2\text{O}_2)_2\text{B}_{12}(\text{OH})_{12}$ has to be prepared and handled with extreme caution. It is very sensitive to heat and friction and can explode by the lightest touch! Even milligram portions will explode with a loud blast and a greenish fireball. Departure from the published procedure is not recommended. Ensure the identity and purity of all reagents and use an adequate shielding to contain possible explosions"²⁷

Furthermore It is known that 40% and greater concentrated solutions of H_2O_2 and organic solvents are explosive, having energy typical of common organic, "CHNO" explosives, but much

more sensitive.²⁸ Additionally, it is likely that $B_{12}F_{12}^{2-}$ would also react rapidly and violently with strong oxidizing agents forming the more energetically favorable B–O bonds and breaking B–F bonds. Empirical evidence of $K_2B_{12}F_{12}$ reactivity with strong oxidizing agents has been given by an experiment by Prof. Steven Strauss-Boltalina and collaborators at Jožef Stefan Institute, Ljubljana, Slovenia. The experiment, in an argon filled glovebox, consisted of $K_2B_{12}F_{12}(s)$ powder combined with solid $XeF_2(s)$ powder resulting in a rapid vigorous burning reaction. Further evidence of this reactivity of $K_2B_{12}F_{12}$ with oxidizing agents was given by a control experiment comprised of a small amount of purified $K_2B_{12}F_{12}$, and 30% wt/wt aqueous H_2O_2 . The two compounds were mixed on an anvil and allowed to dry to a white solid; then the solid was struck with a hammer (impact sensitivity test) resulting in a loud sharp crack, indicating an energetic reaction. The implications (even if this experiment was not an exact replica of the accident) are that $K_2B_{12}F_{12}$ and solid $H_2O_2 \cdot nH_2O(s)$ (or whatever solid did form) are an energetic mixture and will react upon impact. Finally, it should be pointed out that H_2O_2 does not form an azeotrope with H_2O , and, heating H_2O_2 in H_2O for prolonged periods of time does not appreciably decompose H_2O_2 .²⁸ Therefore, water can be removed from aqueous solutions of H_2O_2 concentrating the H_2O_2 to solutions greater than 90% H_2O_2 wt/wt.²⁸

A hypothetical mechanism or understanding of the role of H_2O_2 in discoloring the crude $K_2B_{12}F_{12}$ was never researched prior to this incident. It was found after this incident that the aqueous 6% H_2O_2 solution with $K_2B_{12}F_{12}$ crude product (made from $K_2B_{12}H_{12}$ supplied by Air Products and Chemical Inc.) had residual H_2O_2 after the 2 h heating at 80 °C. The presence of H_2O_2 was determined by addition of $MnO_2(s)$ to the aqueous solution with the observation of vigorous bubbling; $MnO_2(s)$ is known to catalyze $H_2O_2(aq)$ into $O_2(g)$ and $H_2O(l)$.²⁸

It does not make sense to this author why an impurity, which was created in a strongly oxidizing solution, would be removed by another strongly oxidizing solution such as 6% wt/wt aqueous H_2O_2 . This author acknowledges that increasing the concentration of aqueous H_2O_2 during the purification was likely unsafe (a lesson not soon to be forgotten). However, there is something amiss that would insinuate all previous purifications of crude $\text{K}_2\text{B}_{12}\text{F}_{12}$ should have been equally as reactive since they would have ca. 3.33 g of H_2O_2 per purification of $\text{K}_2\text{B}_{12}\text{F}_{12}$ crude product. If all of the H_2O_2 had remained after the heating at 80 °C for 2 h, then at least one other time some violent reaction should have occurred (this reaction has been performed about 50 times by this author and other group members). Interestingly, all previous batches of $\text{K}_2\text{B}_{12}\text{F}_{12}$ prior to the violent reaction were made from $\text{K}_2\text{B}_{12}\text{H}_{12}$ supplied by KatChem spol. s r. o. Czech Republic, as well as all batches of $\text{K}_2\text{B}_{12}\text{F}_{12}$ made by former Strauss-Boltalina group member Dr. Peryshkov. The batch that reacted violently was made with $\text{K}_2\text{B}_{12}\text{H}_{12}$ supplied by Air Products and Chemical Inc., intended for electrolyte research, indicating it was of very high purity. Assuming no H_2O_2 decomposition occurred in the 2 h heating of the 6% wt/wt aqueous hydrogen peroxide solution, then the H_2O_2 concentration for the remaining solid sample would be very high. If nothing in the $\text{K}_2\text{B}_{12}\text{F}_{12}$ crude product was reacting with the H_2O_2 causing a color change, and nothing else was reacting with the H_2O_2 to decompose it (as evidenced by the $\text{MnO}_2(\text{s})$ reaction) then it is possible the H_2O_2 simply stayed intact during the purification step. The only way for the sensitive material to not have been made previously is if the H_2O_2 was being decomposed by some unknown impurity either in the crude $\text{K}_2\text{B}_{12}\text{F}_{12}$, on the glassware or from an unknown source. Otherwise this incident seems to have been inevitable (regardless of the H_2O_2 conc.). After the incident, an investigation was undertaken by this author to determine the yellow impurity produced during fluorination of $\text{K}_2\text{B}_{12}\text{H}_{12}$ with $\text{F}_2(\text{g})$ in MeCN, and to better

understand the properties of the yellow impurity with the aim to develop a safer, more reliable purification of $\text{K}_2\text{B}_{12}\text{F}_{12}$ crude product.

2.2 Results

2.2.1 Separating and Identifying the Colored Yellow impurity Produced During $\text{K}_2\text{B}_{12}\text{F}_{12}$ Synthesis.

Many attempts were made to separate with the intent to identify the yellow impurity produced in the fluorination of $\text{K}_2\text{B}_{12}\text{H}_{12}$ in 0 °C MeCN with $\text{F}_2(\text{g})$ and excess $\text{KF}(\text{s})$. The colorant(s) appeared to have similar solubility as $\text{K}_2\text{B}_{12}\text{F}_{12}$ in all solvents tested (methanol, ethanol, 1-propanol, 2-propanol, 1-butanol, 2-butanol, acetonitrile diethyl ether, ethyl acetate, dichloromethane, 1,2-dichloroethane, chloroform, carbon tetrachloride, and perfluoroheptane). The yellow impurity did not easily separate with organic solvents and H_2O via liquid-liquid extraction nor was the color completely removed upon recrystallization of $\text{K}_2\text{B}_{12}\text{F}_{12}$ from dd- H_2O or MeCN (see Figure 2-4). However, it was found that the yellow impurity could be mostly separated and concentrated from crude $\text{K}_2\text{B}_{12}\text{F}_{12}$ with an Al_2O_3 column using 95:5 v:v of acetonitrile:water that eluted the $\text{K}_2\text{B}_{12}\text{F}_{12}$. The orange oil that was retained on the column was eluted with H_2O , collected, and concentrated. The orange/brown viscous oil that was collected in this manner was analyzed by ^1H , $^{19}\text{F}[^{11}\text{B}]$ NMR (see Figures 2-6 and 2-7). Proton and $^{19}\text{F}[^{11}\text{B}]$ NMR of the orange oil collected after Al_2O_3 column separation of $\text{K}_2\text{B}_{12}\text{F}_{12}$ crude product did not yield any identifiable impurities, except F^- , singlet, $\delta -75.5$, similar to that reported by Christe et al. for F^- in MeCN²⁹, and HF_2^- , doublet $\delta -124.5$ and -125 with $J_{\text{HF}} = 54.0$ Hz. Christe et al. explain that the HF_2^- chemical shift has a strong dependence on the solvent system and the relative concentrations of F^- and HF_2^- .^{29,30}

2.2.2 Hypotheses and Control Experiments to Identify Yellow Impurity.

Hypotheses for the cause of the color that have been explored include: reaction of MeCN with $F_2(g)$ or F^- to form a colored species, decomposition/reaction of an impurity in the MeCN with $F_2(g)$ or F^- , the partial decomposition of B_{12} cages to a quasi-stable colored intermediate, or oxidation of $B_{12}F_{12}^{2-}$ to $B_{12}F_{12}^-$ at a potential of 4.6–4.9 V vs. Li^{+0} .¹⁶ The oxidation of $B_{12}F_{12}^{2-}$ to $B_{12}F_{12}^-$ was first demonstrated by the Strauss-Boltalina research group, a CV from that experiment is shown in Figure 2-8. The radical anion $B_{12}F_{12}^-$, was later demonstrated to be a yellow colored radical using in-situ UV-vis cyclic voltammetry⁴, the UV-vis spectra of $B_{12}F_{12}^{2-}$ and $B_{12}F_{12}^-$ and a photograph of the $B_{12}F_{12}^-$ in solution is shown in Figure 2-9.

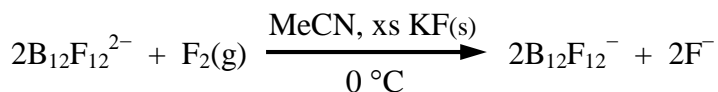
Inherent to the industrial synthesis and handling of MeCN as a byproduct from the synthesis of acrylonitrile, there are many possible contaminants in commercial MeCN that could be reacting to form the colored yellow impurity. Those contaminants include acrylonitrile, acetic acid, ammonia, ammonium acetate, propionitrile and allyl alcohol, all of which are reactive and could have adverse effects in the fluorination reaction. Typical reagent grade (or better) MeCN purchased for laboratory use is purified to remove these known contaminants, since documentation cannot be found on acceptable concentrations of these contaminants they were still be considered as possible causes of the observed yellow impurity in $K_{12}B_{12}F_{12}$ crude product. Determination of an impurity in MeCN that would react with $F_2(g)$, $KF(s)$, $K_2B_{12}H_{12}(solv)$, $HF(solv)$, or any other possible intermediate or combination of species and intermediates in the fluorination of $K_2B_{12}H_{12}$ with $F_2(g)$ would be difficult. However, to simplify this control experiment fresh $K_2B_{12}H_{12}$ was fluorinated with recycled MeCN, that is, MeCN that had already been exposed to $F_2(g)$ (i.e. recycled from a previous fluorination reaction). If there was an impurity in the MeCN that did react with $F_2(g)$ or any other compound/intermediate

during the reaction, then it would have already reacted and been removed from the recycled MeCN. The MeCN was removed from the reaction mixture by rotary-evaporation, and was collected and recycled for a new fluorination. This control experiment with MeCN previously treated with $F_2(g)$ produced $K_2B_{12}F_{12}$ crude product that was just as colored as previous batches indicating there was not an impurity in the MeCN that could be removed by this method. A further control experiment was performed where a sample of as received MeCN was treated with $F_2(g)$ for 2 h, after which the solution was purged with $N_2(g)$ and analyzed by ^{19}F NMR spectroscopy run on the neat MeCN unlocked. The MeCN was not discolored after the 2 h treatment with $F_2(g)$, however, it was acidic. The ^{19}F NMR spectrum in Figure 2-10 shows a large number of fluorine environments in the MeCN. This experiment is not comparable to an actual reaction since the $B_{12}H_{12}^{2-}$ and $B_{12}H_{12-x}F_x^{2-}$ species consume the $F_2(g)$ but does demonstrate that MeCN will react with $F_2(g)$.

It is known that during the fluorination, a measurable amount of the B_{12} cages decompose and ultimately result in BF_4^- . The final yield described in the literature based on starting $K_2B_{12}H_{12}$ is 74.2%.¹⁹ However, some of the partially decomposed cages could result in the yellow impurity, or be a reactive intermediate facilitating the formation of the yellow impurity. If this were the case the orange oil separated by an Al_2O_3 column would exhibit some broad ^{19}F peaks due to coupling to the quadrupolar nuclei ^{10}B or ^{11}B , but this was not observed (see Figure 2-7).

Finally, it has been demonstrated that $B_{12}F_{12}^{2-}$ can be oxidized to produce the stable radical $B_{12}F_{12}^{-4,16}$, and that this radical species is yellow in color as shown in Figure 2-9. The quasi-reversible oxidation, $B_{12}F_{12}^{-/2-}$ has an $E_{1/2}$ value of 4.9 V relative to $Li^{+/0}$ as shown in Figure 2-8.¹⁶ It should be noted that the reduction potential of $F_2(g)$ is 5.92 V relative to $Li^{+/0}$ ³¹, indicating

that $F_2(g)$ is a sufficiently strong oxidizing agent to oxidize $B_{12}F_{12}^{2-}$. During the fluorination of $K_2B_{12}H_{12}$ the reaction mixture starts colorless and only slightly turns yellow after the first 8–10 h, then slowly begins to transition to a bright yellow color as shown in Figure 2-11. Whether the solution is bright yellow or darker, upon work up (purging with $N_2(g)$, filtered, filtrate neutralized with excess $KHCO_3$, filtrate dried to a solid) the final crude $K_2B_{12}F_{12}$ is always a dark color as shown in Figure 2-1. Since $F_2(g)$ is a strong enough oxidizing agent to oxidize $B_{12}F_{12}^{2-}$, as the reaction nears the end, and not all $F_2(g)$ is consumed towards the end of the reaction, it should oxidize $B_{12}F_{12}^{2-}$ to $B_{12}F_{12}^-$ as shown in the reaction scheme below, causing the initial color change from colorless to bright yellow.



2.2.3 Attempts to Remove Yellow Impurity Produced During $K_2B_{12}F_{12}$ Synthesis By Oxidation.

Presuming that the yellow impurity was being removed by heating in 6% aqueous H_2O_2 , other methods of oxidation were attempted. Oxidation methods included treatment of $K_2B_{12}F_{12}$ crude product with; (i) multiple cycles of heating in 80 °C in 6% aqueous H_2O_2 for 2 h with each cycle followed by decomposing the H_2O_2 with solid MnO_2 , (ii) treatment with 6% aqueous H_2O_2 and UV light for 5–10 h, and (iii) treatment with $O_3(g)$ for 5 min. None of those methods of oxidation made the $K_2B_{12}F_{12}$ crude product color lighten significantly or disappear. A final control experiment to see if only the water had an effect was performed. A sample of $K_2B_{12}F_{12}$ crude product in dd- H_2O was heated to 80 °C for 2 h and exhibited nearly the same degree of lightening of color as observed with 6% wt/wt aqueous H_2O_2 . Because of the results of these

control experiments, and the fact that the yellow impurity is likely produced by oxidation, further methods to remove the yellow impurity by oxidation were not explored.

2.2.4 Attempts to Remove Yellow Impurity Produced During $K_2B_{12}F_{12}$ Synthesis By Reduction.

Presuming the yellow impurity is an oxidized species, various reduction methods were attempted to see if the color would fade or disappear upon reduction. Reduction methods included treatment of $K_2B_{12}F_{12}$ crude product with; (i) Zn(s) and HCl(aq) at RT, (ii) NaBH₄ in MeCN at RT for multiple hours, (iii) N₂H₄·H₂O in MeCN at RT for multiple hours, (iv) Mg(s) (surface cleaned) in H₂O at RT for multiple hours, (v) (NH₄)₂Ce(NO₃)₆ in H₂O at RT for multiple hours, (vi) Na(s) in MeCN at RT for multiple hours, (vii) Ag(s) (surface cleaned) in MeCN at RT for multiple hours, and (viii) bulk electrolysis/electrochemical reduction for 12 h in anhydrous MeCN at RT. Out of all of the aforementioned methods to reduce/discolor the yellow impurity, the only method that exhibited a rapid and complete color change was reduction with Zn(s) and HCl(aq). First, an unknown concentration of crude $K_2B_{12}F_{12}$ yielding a yellow solution in H₂O was mixed with Zn(s). No observable color change occurred after 15 min with only Zn(s). Next, a few drops of conc. HCl was added to the solution and it was mixed and rapidly turned colorless. The photographs of the color of an aqueous solution of $K_2B_{12}F_{12}$ crude product, change upon addition of Zn(s) and color change upon addition of HCl(aq) to the $K_2B_{12}F_{12}$ crude product aqueous solution with Zn(s) are shown in Figure 2-12. While the color rapidly disappeared upon treatment with Zn(s) and aq. HCl, upon separation and work of the mixture, the result was light yellow crystals. Furthermore, this purification method would likely produce a mixed cation salt comprised of Zn²⁺ and K⁺ cations that would have to be further purified to produce the desired $K_2B_{12}F_{12}$. As a control experiment a fresh sample of $K_2B_{12}F_{12}$ crude product was treated with

acid or base to see if the color of the yellow impurity changed at different pH, no visible differences were observed at low or high pH.

2.2.5 Improved Purification Method of $\text{K}_2\text{B}_{12}\text{F}_{12}$ without H_2O_2 .

After purging the 500 mL acetonitrile reaction mixture (still containing solid KF, KHF_2 and dissolved $\text{K}_2\text{B}_{12}\text{F}_{12}$) with $\text{N}_2(\text{g})$, to sweep out any unreacted F_2 gas, ca. 200 mL of dd- H_2O was added. Solid KHCO_3 (ca. 50 g) was added with stirring until two discrete layers formed. The bicarbonate salt (i) raises the ionic strength of the aqueous layer creating two layers, and (ii) neutralizes any remaining HF. The less-dense, dark orange-brown acetonitrile layer contained most of the desired product $\text{K}_2\text{B}_{12}\text{F}_{12}$ along with the undesirable yellow impurity. The more-dense aqueous layer contained KF, KBF_4 , KHCO_3 , K_2CO_3 , and a small amount of $\text{K}_2\text{B}_{12}\text{F}_{12}$. The two layers are separated and the aqueous layer was washed four times with 40–50 mL of MeCN to remove residual $\text{K}_2\text{B}_{12}\text{F}_{12}$, the washings were combined with the main orange colored organic layer. The $^{19}\text{F}[^{11}\text{B}]$ NMR spectrum of the aqueous and organic layers, shown in in Figure 2-13, demonstrates the efficiency of this primary separation. The acetonitrile solution was evaporated to dryness and further dried on a Schlenk vacuum line overnight. The resulting yellow solid (ca. 18 g) was dissolved in ca. 100 mL of 1 M aqueous KOH. Liquid-liquid extraction with four 30 mL portions of ethyl acetate removes most of the $\text{K}_2\text{B}_{12}\text{F}_{12}$. The combined ethyl acetate layers were evaporated to dryness, and the light yellow solid was dissolved in 1 M KOH. This liquid-liquid extraction procedure with 1 M KOH and ethyl acetate was repeated two more times to yield, after evaporation to dryness, 14.6 g of a faint yellow solid $\text{K}_2\text{B}_{12}\text{F}_{12}$ (yield 73% based on $\text{K}_2\text{B}_{12}\text{H}_{12}$). The purity of the $\text{K}_2\text{B}_{12}\text{F}_{12}$ is exhibited by ^1H , $^{19}\text{F}[^{11}\text{B}]$, and $^{11}\text{B}[^{19}\text{F}]$ NMR spectra shown in Figures 2-14–2-16. Final colorless $\text{K}_2\text{B}_{12}\text{F}_{12}$ is produced by either eluting an acetonitrile solution of the light-yellow $\text{K}_2\text{B}_{12}\text{F}_{12}$ through a neutral alumina

column (ca. 200 g, ca. 20 cm height, 2.4 cm diameter) with 95:5 v:v acetonitrile:water with an overall product yield of ca. 70% (depending on column efficiency), or, recrystallization from dd-H₂O with an overall product yield of ca. 60% based on K₂B₁₂F₁₂.

2.2.6 Synthesis of High-Purity Li₂B₁₂F₁₂·nH₂O and Na₂B₁₂F₁₂·nH₂O with Cation-Exchange Starting from K₂B₁₂F₁₂.

The high purity of the starting K₂B₁₂F₁₂ material made recrystallization of the resulting Li₂B₁₂F₁₂·nH₂O and Na₂B₁₂F₁₂·nH₂O unnecessary, for both salts, white crystalline solids were obtained after removing H₂O by rotary evaporation. After a single pass through a Li⁺ saturated cation exchange column, Li₂B₁₂F₁₂·nH₂O contained 0.06 mol% K⁺, 0.27 mol% Na⁺, 99.57 mol% Li⁺ and small amounts of Cu²⁺ (0.02 mol%) and Mg²⁺ (0.05 mol%) measured by ICP-AES. After a single pass through a Na⁺ saturated cation exchange column, Na₂B₁₂F₁₂·nH₂O contained 0.043 mol% K⁺, 0.071 mol% Li⁺, 99.87 mol% Na⁺ and small amounts of Ca²⁺ (0.010 mol%) and Mg²⁺ (0.004 mol%) measured by ICP-AES. All other metal ions measured by ICP-AES in the Li₂B₁₂F₁₂·nH₂O and Na₂B₁₂F₁₂·nH₂O samples were less than 0.01 mol%. Aqueous solutions of the Li₂B₁₂F₁₂ and Na₂B₁₂F₁₂ were passed a second time through a freshly prepared Li⁺ or Na⁺ ion-exchange column to reduce the amount of K⁺ and other metal ions to less than 0.01 mol%. The anion B₁₂F₁₂²⁻ had a purity of 99.5+ mol% with no detectable BF₄⁻ or other contaminants as determined by ¹H, ¹¹B[¹⁹F], and ¹⁹F[¹¹B] NMR.

2.2.7 Determination of Optimal Drying Conditions for Li₂B₁₂F₁₂·nH₂O and Na₂B₁₂F₁₂·nH₂O to Make Anhydrous Li₂B₁₂F₁₂ and Na₂B₁₂F₁₂.

In order for the Li₂B₁₂F₁₂·nH₂O and Na₂B₁₂F₁₂·nH₂O salts to be used in electrolyte research the salts need to be anhydrous. Water in the electrolyte can affect chemical and electrochemical

stability of the electrolyte and other components, ion mobility, salt solubility in the electrolyte solvent and augment the potential window of the electrolyte causing other adverse problems with the cell. It was previously determined by SC-XRD that $\text{Li}_2\text{B}_{12}\text{F}_{12}$ and $\text{Na}_2\text{B}_{12}\text{F}_{12}$ both exist as the tetrahydrate phases when crystallized from H_2O .¹³ Using TGA, it was found that $\text{Li}_2\text{B}_{12}\text{F}_{12}\cdot 4\text{H}_2\text{O}$ could be thermally dehydrated without decomposition at 175 °C and $P(\text{H}_2\text{O}) = 0$ Torr as demonstrated in Figure 2-17. Furthermore, it was found that the $\text{Li}_2\text{B}_{12}\text{F}_{12}\cdot 4\text{H}_2\text{O}$ phase is stable at 35 °C and $P(\text{H}_2\text{O}) = 13$ Torr. The $\text{Li}_2\text{B}_{12}\text{F}_{12}\cdot n\text{H}_2\text{O}$ was ca. $n = 3.5$ after drying to a solid by rotary evaporation. The $\text{Na}_2\text{B}_{12}\text{F}_{12}\cdot n\text{H}_2\text{O}$ salt was found to thermally dehydrate without decomposition at 150 °C and $P(\text{H}_2\text{O}) = 0$ Torr as demonstrated in Figure 2-18. The $\text{Na}_2\text{B}_{12}\text{F}_{12}\cdot n\text{H}_2\text{O}$ was ca. $n = 2$ after drying to a solid by rotary evaporation.

2.3 Dissusion.

2.3.1 Possible Causes of Violent Reaction.

There are two logical possibilities for what could have caused the violent reaction experienced by the author of this dissertation based on the empirical information collected before and after the incident. First, the use of a higher than prescribed concentration of H_2O_2 ; or second, changing to a new source of $\text{K}_2\text{B}_{12}\text{F}_{12}$ starting material. The mass of H_2O_2 in the 50 mL of 6% wt/wt aqueous hydrogen peroxide solution equates to 3.33 g of H_2O_2 , assuming ca. 15 g of $\text{K}_2\text{B}_{12}\text{F}_{12}$ the H_2O_2 would be ca. 18% of the total solid sample mass, or 2.85 equiv of H_2O_2 per $\text{K}_2\text{B}_{12}\text{F}_{12}$. Similarly, the 10% wt/wt aqueous hydrogen peroxide solution equates to 5.55 g of H_2O_2 which would be ca. 27% of the total solid sample mass, or 4.74 equiv of H_2O_2 per $\text{K}_2\text{B}_{12}\text{F}_{12}$. It was shown with Air Products and Chemicals Inc. sourced $\text{K}_2\text{B}_{12}\text{F}_{12}$ that significant amounts of H_2O_2 remained after the 2 h heating purification of $\text{K}_2\text{B}_{12}\text{F}_{12}$ crude product. If

$K_2(H_2O_2)_{1.5}(H_2O)_{0.5}B_{12}F_{12}$ (or something similar) was the compound responsible for the violent reaction, then if only a fraction of the H_2O_2 remained in either concentration of H_2O_2 , both would have formed at least some if not all of the known peroxide compound when dried. Similarly, if the friction and impact sensitive energetic species is a mixture of $K_2B_{12}F_{12}$ and concentrated H_2O_2 , then again, either of the above mixtures would have produced some energetic material. If any energetic material had been produced in the 50+ reactions that had been performed with H_2O_2 , then it is reasonable to assume, at least one other dried purification mixture would have been energetic, resulting in a similar violent reaction. However, no previous violent reaction has been observed. This leads to two possible conclusions: (i) $K_2B_{12}F_{12}$ and solid and highly concentrated H_2O_2 do not form an energetic mixture, sensitive to friction and impact; or (ii) some unknown impurity in the $K_2B_{12}H_{12}$ sourced from KatChem was reacting with H_2O_2 rendering it safe in all previous reactions using KatChem $K_2B_{12}H_{12}$ material. It should be doubly noted that a separate experiment with $K_2B_{12}F_{12}$ and dried H_2O_2 did form an impact sensitive mixture as described previously.

Conversely, if it was the case that the original source of $K_2B_{12}H_{12}$ (KatChem spol. s r. o. Czech Republic) had an impurity of almost any transition metal oxide, than the H_2O_2 would have been decomposed during the aqueous H_2O_2 purification step rendering the dried $K_2B_{12}F_{12}$ free of H_2O_2 .²⁸ Once this author switched to the new $K_2B_{12}H_{12}$ sourced from Air Products and Chemicals Inc. intended to be used for synthesis of electrolyte grade materials, then during the aqueous H_2O_2 purification the H_2O_2 would not have reacted or decomposed. When dried, the H_2O_2 would merely concentrate forming a friction and impact sensitive mixed material. It is this author's conclusion that switching to the more highly purified $K_2B_{12}H_{12}$ did not decompose the H_2O_2 resulting in the accident. Unfortunately all of the KatChem $K_2B_{12}H_{12}$ has been used and so

metals analysis of it cannot be performed to give more evidence to this hypothesis. Either way, because of this incident, the H_2O_2 heating purification procedure has never been performed again without using $\text{MnO}_2(\text{s})$ (or some other transition metal oxide) to decompose remaining $\text{H}_2\text{O}_2(\text{aq})$ prior to drying to a solid.

2.3.2 Identification of the Yellow Impurity in $\text{K}_2\text{B}_{12}\text{F}_{12}$ Crude Product.

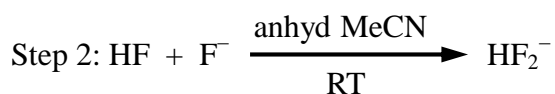
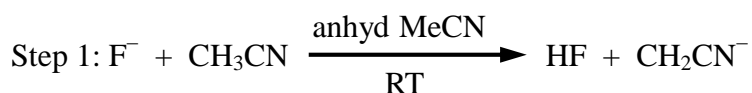
After multiple attempts to separate, collect and analyze the yellow impurity formed during the fluorination of $\text{K}_2\text{B}_{12}\text{H}_{12}$ with $\text{F}_2(\text{g})$, in MeCN, a few important properties of the yellow impurity have been determined. First, the yellow impurity did discolor upon treatment with $\text{Zn}(\text{s})$ and $\text{HCl}(\text{aq})$, but did not discolor with any other attempted reduction method. Zinc metal and $\text{HCl}(\text{aq})$ is a commonly used but complex reducing agent because it is not exactly known what is the true reducing agent in the reaction. It is known that $\text{H}_2(\text{g})$ is formed as a product, which has a oxidation potential of 3.05 V vs $\text{Li}^{+/0}$ and $\text{Zn}(\text{s})$, also in the mixture, has a oxidation potential of 2.29 V vs $\text{Li}^{+/0}$. However, when the reduction was attempted with $\text{Na}(\text{s})$ in dry MeCN, no color change was observed, and the oxidation potential of $\text{Na}(\text{s})$ is 0.34 V vs $\text{Li}^{+/0}$, meaning it is a stronger reducing agent than $\text{H}_2(\text{g})$ or $\text{Zn}(\text{s})$ and did not result in a noticeable color change. This could be due to the colored yellow impurity persist until a salt is formed Zn^{2+} forming a colorless complex.

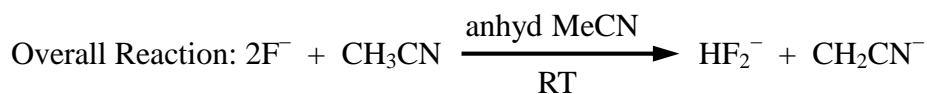
Next the yellow impurity could be mostly separated by retaining on an Al_2O_3 column, collecting the yellow $\text{K}_2\text{B}_{12}\text{F}_{12}$ by elution with 95:5 v:v acetonitrile:water. The yellow impurity would elute from the column with H_2O and when collected and concentrated formed an orange oil. This indicates the yellow impurity is highly charged, and there apparently is more than one impurity as the $\text{K}_2\text{B}_{12}\text{F}_{12}$ that eluted from the column was still a faint yellow, and even elution through longer or multiple columns did not remove the faint color. The yellow impurity collected

from the Al_2O_3 and condensed to an orange oil had many types of fluorine environments according the ^{19}F NMR, but no boron, so it was not a partial B_{12} cluster.

The yellow impurity also does not appear to be caused by a contaminant in commercial MeCN. Fluorination reaction using MeCN previously exposed to $\text{F}_2(\text{g})$ exhibited the same degree of coloration as fluorination reactions using MeCN from the bottle. Rigorously dry MeCN used in the second fluorination step also did not appear to make a difference in the final color of the crude material. However, when treated with $\text{F}_2(\text{g})$, as received MeCN exhibited many fluorine environments. It is unknown at this time if those all of those signals are due to various $\text{F}_2(\text{g})$ MeCN reactions, or if they are caused by MeCN and other contaminants in MeCN reacting with $\text{F}_2(\text{g})$.

It is known from multiple references regarding the purification of MeCN for electrochemical and HPLC purposes that MeCN can be oxidized when refluxed with P_2O_5 to yield (eventually, in unpredictable quantities) an orange gel that is hard to separate from the MeCN.^{24,32-34} Furthermore, Christe et al.³⁰ hypothesized that F^- (originating from $[\text{N}(\text{CH}_3)_4]\text{F}$) is a base sufficiently strong enough, in anhydrous MeCN (Christe et al. purified MeCN by refluxing over P_2O_5 and distilling into flamed out glassware on a vacuum line bringing H_2O content to ≤ 4 ppm³⁰) to react in the following possible mechanism in the scheme below producing CH_2CN^- .³⁰





Additionally, Christe et al. state in that text "In addition to an increase in the intensity of the HF_2^- the originally colorless MeCN solutions also developed a yellow color on standing".

The work by Christe et al. demonstrate that MeCN will react with F^- over time, however, for that reaction to proceed it has to be anhydrous MeCN, otherwise F^- would preferentially react with H_2O forming HF and OH^- . In the fluorination of $\text{K}_2\text{B}_{12}\text{H}_{12}$ with $\text{F}_2(\text{g})$ the addition of excess $\text{KF}(\text{s})$ is necessary to remove HF that has been shown to hinder the reaction.^{13,19} However, that $\text{KF}(\text{s})$, being a hygroscopic salt, likely removes the small amount of water contamination from the MeCN during the reaction, thereby making the MeCN anhydrous or very nearly anhydrous, allowing the reaction discussed by Christe et al. to proceed.

An alternative strongly oxidizing species, HOF, stabilized by MeCN, and researched by Shlomo Rozen, spanning more than two decades, is formed in solutions of 10% H_2O in MeCN treated with $\text{F}_2(\text{g})$.³⁵⁻³⁷ The putative HOF species is such a strong oxidizing agent Rozen et al. has shown that epoxidation of sterically hindered tetrasubstituted alkenes are easily epoxidated with 90% yield in minutes.³⁶ This is quite a powerful oxidizing agent when comparing the same substrate with typical oxidizing agents such as H_2O_2 , metachloroperoxybenzoic acid (MCPBA) and dimethyldioxane that produced 25% or less yield in 24 or more hours.³⁶ Since the HOF species is known to exist in reaction conditions similar to that used to make $\text{K}_2\text{B}_{12}\text{F}_{12}$ it could also be the case that the yellow impurity is due to oxidation of MeCN by MeCN:HOF as described in other texts. However, it should be noted that the water contaminant in the MeCN used in the fluorination of $\text{K}_2\text{B}_{12}\text{H}_{12}$ is $\leq 0.01\%$ wt/wt, not 10% H_2O as described by Rozen et al. Furthermore, the water contaminant of the MeCN used in fluorination of $\text{K}_2\text{B}_{12}\text{H}_{12}$ is likely

further reduced by the addition of excess KF(s) that can act as a good water absorbent. So while the HOF species is plausible, it is this author's conclusion that it would be in negligible concentration during the first and second fluorination steps.

The oxidation of $B_{12}F_{12}^{2-}$ forming a colored species is a plausible cause of the observed color. The oxidized species $B_{12}F_{12}^-$ could also be the strong oxidizing agent causing the color change, possibly through reaction with MeCN or other species in the reaction mixture. Based on the work of Christie et al. and other published literature, the chemical oxidation of MeCN with strong oxidizing agents resulted in an orange colorant. Reaction of $B_{12}F_{12}^-$ with MeCN could be the source of the color. However, remembering that the $E_{1/2}$ of $B_{12}F_{12}^{-/2-}$ is 4.9 V vs Li^{+0} ,¹⁶ and that the reduction potential of $F_2(g)$ is 5.92 V vs. Li^{+0} ³¹ it is likely that $F_2(g)$ is the initiation source causing the color change since MeCN can be oxidized at ca. 5.54 V vs Li^{+0} ,³⁸. Conversely, the $B_{12}F_{12}^-$ radical would only oxidize at potentials at or below 4.9 V vs. Li^{+0} , leading to the conclusion that while $B_{12}F_{12}^-$ may be the source of the initial bright yellow color change, it cannot oxidize MeCN. Additionally, since the recovered final product is not yellow, and by no other indication is final product $B_{12}F_{12}^-$, this also indicates that $B_{12}F_{12}^-$ must be getting reduced back to $B_{12}F_{12}^{2-}$ and in the process oxidizing something else, which is possibly colored, upon final work up and purification. Along this line of reasoning, if an easily separable electron donating additive could be found that would irreversibly reduce with $B_{12}F_{12}^-$, then the reaction mixture may not require as much purification.

2.3.3 New Purification Method of $K_2B_{12}F_{12}$ Crude Product.

The purification method developed by this author of $K_2B_{12}F_{12}$ crude product has other advantages besides not using aqueous H_2O_2 . First, it is more consistent and with enough ethyl acetate/1 M KOH extraction cycles has reproducibly produced nearly colorless $K_2B_{12}F_{12}$.

Second, the primary separation step with water and KHCO_3 is more efficient at separating KBF_4 than the previously published method.¹⁹ The KBF_4 impurity does have a low solubility in MeCN but some can be carried through with the $\text{K}_2\text{B}_{12}\text{F}_{12}$ product. The KBF_4 contaminate becomes an important problem when using cation exchange resin and converting to a different cation. Case in point, if a mixture of $\text{K}_2\text{B}_{12}\text{F}_{12}$ and KBF_4 is converted to $\text{Na}_2\text{B}_{12}\text{F}_{12}$ and NaBF_4 , then the solubilities of the two salts are too similar and there is no simple way to separate the desired $\text{B}_{12}\text{F}_{12}^{2-}$ product from the BF_4^- impurity without converting back to the potassium salts of the respective anions.

2.3.4 Synthesis of High-Purity $\text{Li}_2\text{B}_{12}\text{F}_{12}\cdot n\text{H}_2\text{O}$ and $\text{Na}_2\text{B}_{12}\text{F}_{12}\cdot n\text{H}_2\text{O}$ with Cation-Exchange from $\text{K}_2\text{B}_{12}\text{F}_{12}$ and Dehydration to $\text{Li}_2\text{B}_{12}\text{F}_{12}$ and $\text{Na}_2\text{B}_{12}\text{F}_{12}$.

The cation exchange method, developed in this work, producing highly purified $\text{Li}_2\text{B}_{12}\text{F}_{12}$ and $\text{Na}_2\text{B}_{12}\text{F}_{12}$ starting from highly purified $\text{K}_2\text{B}_{12}\text{F}_{12}$ performed sufficiently well, is convenient and inexpensive. The previously reported methods going through the $\text{Ag}_2\text{B}_{12}\text{F}_{12}\cdot n\text{CH}_3\text{CN}$ ¹³ or using strong-acid cation-exchange resin to make the acid form of $\text{B}_{12}\text{F}_{12}^{2-}$ and then neutralize that with the desired hydroxide salt¹⁶ created too many possibilities for unwanted contamination. Interestingly, the Purolite UCW 9126 resin used to convert from the K^+ to either the Li^+ or Na^+ salts exhibited excellent exchange efficiencies of greater than 99+ mol% cation exchange on a single pass through the columns. A second pass through a fresh column was determined necessary to bring the K^+ concentration below 0.01 mol%. Also, it was found that both $\text{Li}_2\text{B}_{12}\text{F}_{12}\cdot n\text{H}_2\text{O}$ and $\text{Na}_2\text{B}_{12}\text{F}_{12}\cdot n\text{H}_2\text{O}$ could be thermally dehydrated at 175 °C and 150 °C under vacuum, allowing complete drying of the salts for possible use as electrolyte salts.

2.4 Summary and Conclusions

While it is still unknown at this time what compound(s) were friction sensitive resulting in a violent reaction, multiple questionable conditions and hypothesis have been explored. This author concludes that transition to a new source of $K_2B_{12}H_{12}$ was most likely the cause of the accident compared to all other alternative hypothesis. It is possible some other unknown change in the 6% wt/wt aqueous H_2O_2 purification step could have resulted in the violent reaction. However, it is likely not the case that the change in H_2O_2 concentration was the cause since a control experiment showed that H_2O_2 was still present after the 2 h heating of crude $K_2B_{12}F_{12}$ in 6% wt/wt aqueous H_2O_2 .

The definitive identity of the yellow impurity has not been determined, however, it is likely created by a reactive species oxidizing MeCN initiating the formation of MeCN oligomers that eventually colors the reaction mixture a range of colors from yellow to orange or brown depending on concentration. Based on published literature and the aforementioned findings presented in this chapter it is this author's conclusion that the yellow impurity is comprised of various sized acetonitrile oligomers. The oxidation of MeCN forming an orange colorant has been previously observed experimentally by multiple researchers in the literature. The oxidizing species in this work could be $F_2(g)$, F^- in dry MeCN, or HOF stabilized by the MeCN solution. The oligomerization process initiates slowly at 0 °C (since color is not observed right away) by one or all of the aforementioned strongly oxidizing species. Once the active oligomers are formed they continue to react with more MeCN as the fluorination reaction continues forming larger, more highly colored oligomers. Because the oligomers are different sizes they act differently when eluted through an Al_2O_3 column, most get stuck to the column, but shorter

oligomers make it through the column with the $\text{K}_2\text{B}_{12}\text{F}_{12}$ as evidenced by the light yellow $\text{K}_2\text{B}_{12}\text{F}_{12}$ eluted through an Al_2O_3 column under certain solvent conditions.

A new purification method has been developed that is safer and more reliable for purification of $\text{K}_2\text{B}_{12}\text{F}_{12}$ crude product allowing future research of the important superweak anion $\text{B}_{12}\text{F}_{12}^{2-}$. The new purification method also has the advantage of separating reaction byproducts KBF_4 and other undesirable salts with a primary liquid:liquid extraction resulting in higher purity $\text{K}_2\text{B}_{12}\text{F}_{12}$ after that step.

Finally, highly purified $\text{K}_2\text{B}_{12}\text{F}_{12}$ has been successfully converted to either $\text{Li}_2\text{B}_{12}\text{F}_{12}\cdot n\text{H}_2\text{O}$ or $\text{Na}_2\text{B}_{12}\text{F}_{12}\cdot n\text{H}_2\text{O}$ while maintaining the the cation purity using a high purity cation-exchange resin. The strong-acid cation-exchange resin Purolite UCW 9126 exhibited a high exchange efficiency when converting from the K^+ to the Li^+ or Na^+ salts, however, a second pass through a freshly prepared cation exchange resin was deemed necessary to reduce the K^+ to ≤ 0.01 mol%. The $\text{Li}_2\text{B}_{12}\text{F}_{12}\cdot n\text{H}_2\text{O}$ or $\text{Na}_2\text{B}_{12}\text{F}_{12}\cdot n\text{H}_2\text{O}$ hydrates have been shown to thermally dehydrate to the desired $\text{Li}_2\text{B}_{12}\text{F}_{12}$ and $\text{Na}_2\text{B}_{12}\text{F}_{12}$ salts without thermal decomposition. Using the cation-exchange resin and thermal drying of the resulting $\text{Li}_2\text{B}_{12}\text{F}_{12}\cdot n\text{H}_2\text{O}$ or $\text{Na}_2\text{B}_{12}\text{F}_{12}\cdot n\text{H}_2\text{O}$ hydrates produces a highly purified salt suitable for electrolyte reasearch with methods that are suitable for scaling to larger quantities.

2.5 Experimental

2.5.1 Reagents and Solvents.

The strong-acid cation-exchange resin used was Purolite UCW9126 (The Purolite Company) and was treated per manufacture guidelines prior to use, loaded in dd- H_2O and flushed with 20–30 BV of dd- H_2O . The two sources of $\text{K}_2\text{B}_{12}\text{H}_{12}$ used were Katchem spol. sr. o. (used as

received) and Air Products and Chemicals Inc. (dissolved in water and dried by rotary evaporation twice to remove methanol impurity). The MeCN was Fisher, ACS grade with < 0.01% water, used as received. The F₂/N₂ gas mixture (20/80 ± 5%, Matheson Tri-gas) was used as received. The K₂B₁₂F₁₂ was prepared using previously established procedures and checked for purity by ¹¹B[¹⁹F], ¹⁹F[¹¹B] and ¹H, NMR and by NI-ES-MS.¹⁹ The LiCl (Mallinckrodt Chemicals, ACS grade, minimum 99% LiCl) and NaCl (Fisher, ACS grade, minimum 99% NaCl) for charging the cation exchange column were used as received. The deuterated NMR solvents/standards D₂O (Cambridge Isotopes Laboratories, Inc., 99.8% D), CD₃CN (Cambridge Isotopes Laboratories, Inc., 99.8% D, distilled from activated 3 Å molecular sieves and stored over activated 3 Å). Distilled deionized water was prepared by passing distilled water with through a Barnstead Nanopure deionization system producing water with a final resistance of at least 18 MΩcm.

2.5.2 Instrumentation.

TGA Analysis: Thermogravimetric analysis was performed with a TA Instruments Model 2950 TGA with Airgas UHP grade He(g) or liquid boil off N₂(g) (passed through H₂O and O₂ absorbent columns before instrument) at a flow rate of 55–60 ml min⁻¹. Data were analyzed with TA Universal Analysis Version 4.5A.

Negative Ion Electrospray Mass Spectroscopy: Mass spectra were recorded using a 2000 Finnigan LCQ-DUO mass-spectrometer with MeCN as the carrier solvent. The instrument parameters were tuned to maximize the KB₁₂F₁₂⁻ signal in a sample of K₂B₁₂F₁₂ dissolved in MeCN. Samples were on the order of 10–50 μM concentration in as received MeCN or 3:1 dd-H₂O:MeCN.

NMR Spectroscopy: NMR spectra were taken on a 400 MHz automatic tune, Inova Varian instrument or a 300 MHz manual tune Inova Varian instrument in 5 mm NMR spectroscopy grade glass tubes. Nuclei observed for $(\text{H}_3\text{O})_2\text{B}_{12}\text{F}_{12} \cdot n\text{H}_2\text{O}$ was $^{11}\text{B}[^{19}\text{F}]$, (^{11}B frequency was 128.24 MHz and ^{19}F was 376.01 MHz on the 400 MHz instrument, ^{11}B pulse angle = 90° , pulse time = 13.5×10^{-6} s acquisition time = 0.200 s, and relaxation delay was = 0.900 s, spectral width 20491.8 Hz), and $^{19}\text{F}[^{11}\text{B}]$ (^{19}F was 376.01 MHz and ^{11}B frequency was 128.24 MHz on the 400 MHz instrument, ^{19}F pulse angle = 30° , pulse time = 4.63×10^{-6} s, acquisition time = 0.865 s, relation delay = 1.000 s, spectral width = 37878.8 Hz), and ^1H (399.7 MHz on the 400 MHz instrument).

ICP-AES: Metals analysis was performed by Bryan Brittan using a Perkin-Elmer Model 7300 DV ICP-OES, ICP-AES instrument. Elements analyzed for each sample were Ag, Al, As, Au, B, Ba, Be, Ca, Cd, Ce, Co, Cr, Cu, Fe, K, Li, Mg, Mn, Mo, Na, Ni, P, Pb, Pd, Pt, S, Sb, Se, Si, Sn, Sr, Te, Ti, Tl, U, V, W, Zn, and Zr. Samples were diluted in a mixture of metals free acids (1% v:v hydrochloric acid and 5% v:v nitric acid) to a known concentration and were an average of 3 replicates. Ytterbium was used as an internal standard and 15 interelement correction standards were used to correct for easily ionizable elements

2.5.3 Modified Purification of Crude $\text{K}_2\text{B}_{12}\text{F}_{12}$.

After purging the 500 mL acetonitrile reaction mixture (still containing solid KF, KHF_2 and dissolved $\text{K}_2\text{B}_{12}\text{F}_{12}$) with N_2 (g), to sweep out any unreacted F_2 gas, ca. 200 mL of dd- H_2O was added. Solid KHCO_3 (ca. 50 g) was added with stirring until two discrete layers formed. The bicarbonate salt (i) raises the ionic strength of the aqueous layer separating the layers, and (ii) neutralized any remaining HF. The less-dense, dark orange-brown acetonitrile layer contained

most of the desired product $\text{K}_2\text{B}_{12}\text{F}_{12}$ along with one or more undesirable colored impurities. The more-dense aqueous layer contained KF , KBF_4 , KHCO_3 , K_2CO_3 , and a small amount of $\text{K}_2\text{B}_{12}\text{F}_{12}$. The two layers are separated and the aqueous layer was washed four times with 40–50 mL of acetonitrile to remove residual $\text{K}_2\text{B}_{12}\text{F}_{12}$, the washings were combined with the main orange colored organic layer. The $^{19}\text{F}[^{11}\text{B}]$ NMR (Figure 2-13) of the aqueous and organic layers demonstrates the efficiency of this primary separation. The acetonitrile solution was evaporated to dryness and the yellow solid (ca. 18 g) was dissolved in 100 mL of ca. 1 M aqueous KOH . Extraction with four 30 mL portions of ethyl acetate removes most of the $\text{K}_2\text{B}_{12}\text{F}_{12}$. The combined ethyl acetate layers were evaporated to dryness, and the solid was dissolved in 1 M KOH . This liquid-liquid extraction procedure with 1 M KOH and ethyl acetate was repeated two more times to yield, after evaporation to dryness, 14.6 g of a faint yellow solid $\text{K}_2\text{B}_{12}\text{F}_{12}$ (yield 73% based on $\text{K}_2\text{B}_{12}\text{H}_{12}$). The purity of the $\text{K}_2\text{B}_{12}\text{F}_{12}$ is exhibited by ^1H , $^{19}\text{F}[^{11}\text{B}]$, and $^{11}\text{B}[^{19}\text{F}]$ NMR (Figures 2-14–2-16). Final colorless $\text{K}_2\text{B}_{12}\text{F}_{12}$ can be produced by either; acetonitrile solution of the light-yellow $\text{K}_2\text{B}_{12}\text{F}_{12}$ eluted through a neutral alumina column (ca. 200 g, ca. 20 cm height, 2.4 cm diameter) with 95:5 v:v acetonitrile:water with an overall product yield of ca. 70% (depending on column efficiency), or, recrystallization from dd- H_2O with an overall product yield of ca. 60% based on $\text{K}_2\text{B}_{12}\text{H}_{12}$.

2.5.4 Synthesis of $\text{Li}_2\text{B}_{12}\text{F}_{12}$ and $\text{Na}_2\text{B}_{12}\text{F}_{12}$ from $\text{K}_2\text{B}_{12}\text{F}_{12}$.

Two Purolite UCW 9126 strong-acid ion-exchange columns of ca. 2.0 cm inner diameter and 100 cm in length were rinsed with copious amounts of dd- H_2O . The columns (received in the H^+ form) were then treated with 24 bed volumes of ca. 10% LiCl or NaCl (depending on the desired salt) solution at a flow rate of 4–8 BV/h to exhaustively convert the resin to the Li^+ or Na^+ form. The resin was then rinsed with 10 BV of dd- H_2O to remove excess treatment solution. The

column size and resin volume were such that $< 10\%$ of the column capacity was utilized per synthesis.

The $\text{Li}_2\text{B}_{12}\text{F}_{12}$ and $\text{Na}_2\text{B}_{12}\text{F}_{12}$ salts were synthesized by passing an aqueous solution of 99.5+ mol% $\text{K}_2\text{B}_{12}\text{F}_{12}$, (ca. 5–10 g in 150 ml dd- H_2O) through the first charged column (Li^+ or Na^+) at a flow rate of ca. 1–5 BV/h followed by 10 BV of dd- H_2O . The collected solution was condensed to ca. 100 ml by rotary-evaporation and then passed through the second freshly charged ion-exchange column following the aforementioned procedure. The resulting colorless $\text{Li}_2\text{B}_{12}\text{F}_{12}$ or $\text{Na}_2\text{B}_{12}\text{F}_{12}$ salts were dried to a white to off white solid by rotary-evaporation and then further dried by heating to 150–175 °C under dynamic vacuum for a minimum of 24 h.

2.5.5 Thermogravimetric Analysis of $\text{M}_2\text{B}_{12}\text{F}_{12} \cdot n\text{H}_2\text{O}$ ($\text{M} = \text{Na}^+$ or Li^+) to Determine Sufficient Drying Conditions.

Samples were from dried $\text{Li}_2\text{B}_{12}\text{F}_{12} \cdot n\text{H}_2\text{O}$ or $\text{Na}_2\text{B}_{12}\text{F}_{12} \cdot n\text{H}_2\text{O}$ on the order of 15–20 mg in mass and were contained in an open platinum pan. Experiments were performed with a purge of dry $\text{He}(\text{g})$ or $\text{N}_2(\text{g})$, or with gas wet with a known $P(\text{H}_2\text{O})$. A $P(\text{H}_2\text{O}) = 6(1)$ Torr generated by bubbling dry gas through a saturated aqueous solution of MgCl_2 at 20 °C. The partial pressure of water under these conditions was found in literature and verified by previous tensimetric experiments.^{33,39} The $P(\text{H}_2\text{O}) = 13(1)$ Torr was generated by passing dry $\text{He}(\text{g})$ or $\text{N}_2(\text{g})$, through a water bubbler that was held at 15 °C. Both $\text{Li}_2\text{B}_{12}\text{F}_{12} \cdot n\text{H}_2\text{O}$ and $\text{Na}_2\text{B}_{12}\text{F}_{12} \cdot n\text{H}_2\text{O}$ samples were started with unknown equivalents of H_2O , and were dehydrated to a constant mass.

2.7 Figures



Figure 2-1. A typical batch of crude $K_2B_{12}F_{12}$ made by this author collected and dried to a solid after bubbling with $N_2(g)$ to remove any remaining $F_2(g)$, filtered, then the filtrate was neutralizing with aqueous $KHCO_3$ and dried to a solid.



Figure 2-2. Top, Yellow $\text{K}_2\text{B}_{12}\text{F}_{12}$ solution after the 2nd fluorination reaction step in dry MeCN. The solution has not yet been neutralized with aqueous KHCO_3 . Bottom, The same solution treated with aqueous KHCO_3 solution until neutral. The solution changed from yellow to orange over time. The solution was allowed to settle so the intensity of the orange color could be observed without the white solid artificially lightening the color.



Figure 2-3. Intensity of colored impurities after $\text{K}_2\text{B}_{12}\text{F}_{12}$ fluorination in dry MeCN. Solution was bubbled with $\text{N}_2(\text{g})$ to remove any trace $\text{F}_2(\text{g})$, and filtered to remove $\text{KF}(\text{s})$ and $\text{KHF}_2(\text{s})$, and neutralized with aqueous KHCO_3 . The solution was condensed by rotary evaporation without alteration from the pictures in Figure 2-2

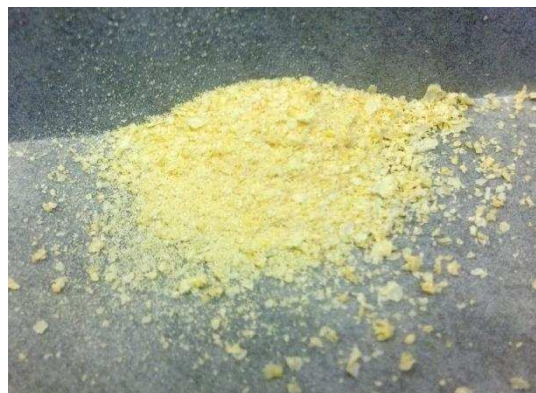


Figure 2-4. Filtered $\text{K}_2\text{B}_{12}\text{F}_{12}$ post 6% aqueous H_2O_2 treatment and crystallized from H_2O and washed with cold H_2O . The large crystals exhibit a yellow color even after washing, and are a yellow powder when ground.

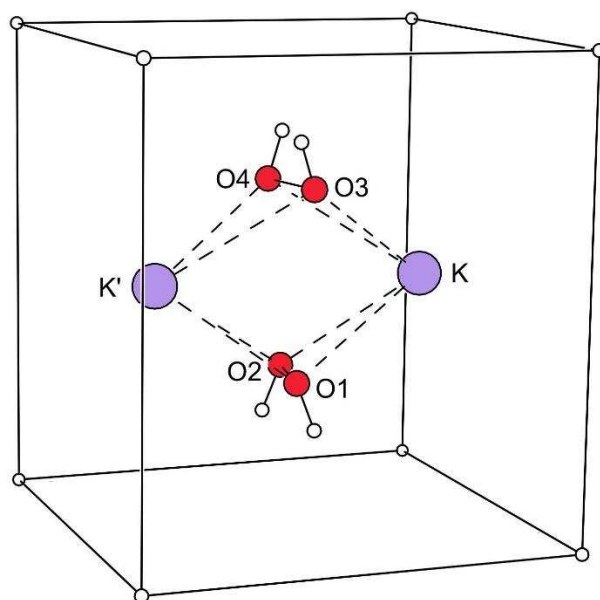


Figure 2-5. The packing of cations, anions, and H_2O_2 molecules in the structure of $\text{K}_2(\text{H}_2\text{O}_2)_{1.5}(\text{H}_2\text{O})_{0.5}\text{B}_{12}\text{F}_{12}$.²⁶ The B_{12} centroids, depicted as small spheres, form a tetragonal array around the $\text{K}_2(\mu\text{-H}_2\text{O}_2)_2^{2+}$ moieties. The partial occupancy of the H_2O_2 sites by H_2O molecules is not shown. This structure was determined by Dmitry Peryshkov.

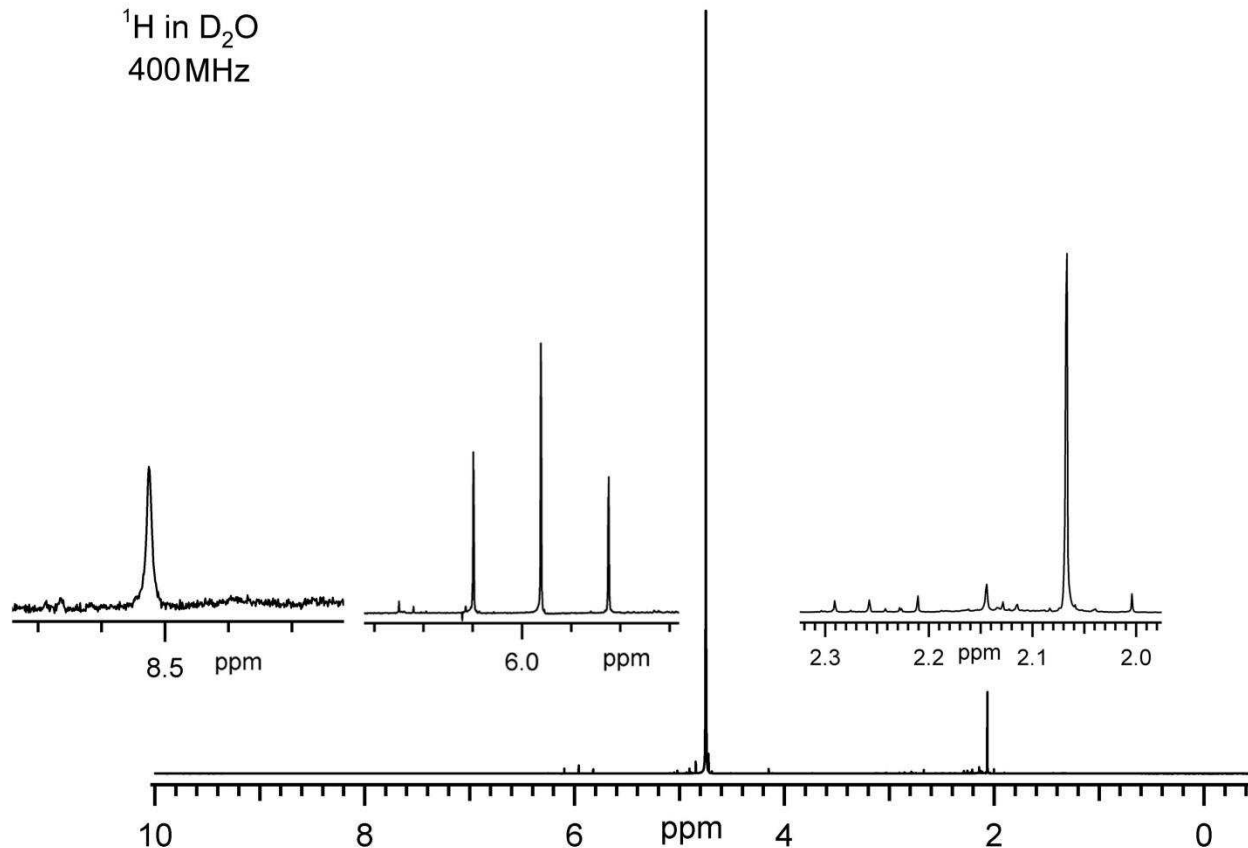


Figure 2-6. Proton NMR spectrum of the orange oil collected after Al₂O₃ column separation of crude K₂B₁₂F₁₂. The chemical shift was referenced to the residual solvent peak of D₂O δ 4.75. The apparent triplet at δ 5.96 and has asymmetric coupling constants of $J = 54.8$ Hz (left) and $J = 55.2$ Hz (right) and has a 1:1.85:1 integration ratio. The peak at δ 2.07 is MeCN in D₂O. The other peaks have not been identified.

$^{19}\text{F}\{^{11}\text{B}\}$ in D_2O
379 MHz

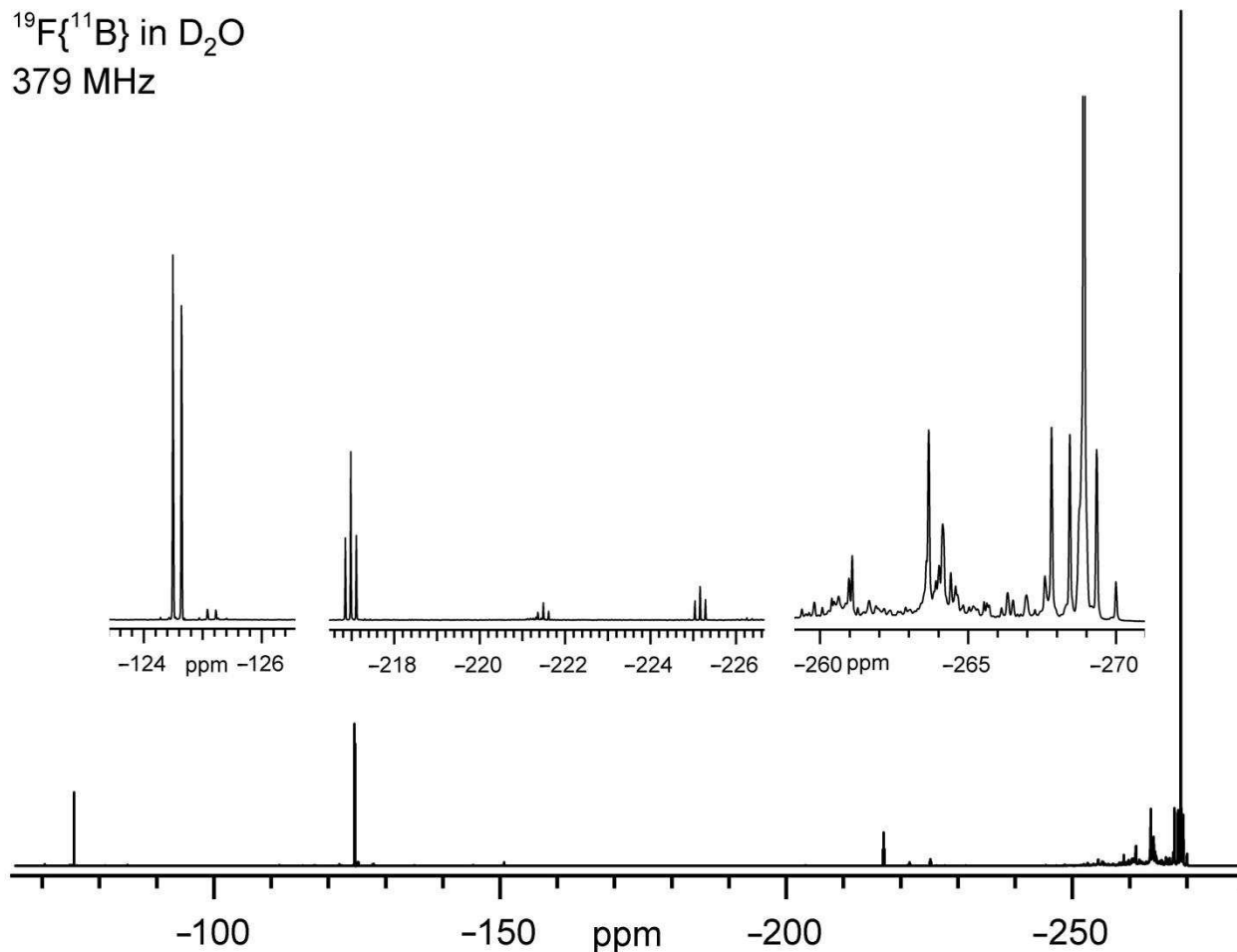


Figure 2-7. Fluorene-19 [^{11}B] decoupled NMR of the orange oil collected after Al_2O_3 column separation of crude $\text{K}_2\text{B}_{12}\text{F}_{12}$. This spectrum is referenced to $\text{B}_{12}\text{F}_{12}^{2-}$ δ -269 ($\text{B}_{12}\text{F}_{12}^{2-}$ δ -269 relative C_6F_6). The singlet at δ -75.5 is F^- , the two doublets at δ -124.5 and 125 , both with $J = 54.0$ Hz are likely HF_2^- . The triplet peaks at δ -217.0 , 221.5 and 225.2 each have symmetric coupling constants of $J = 47.7$, 47.7 , and 44.5 Hz.

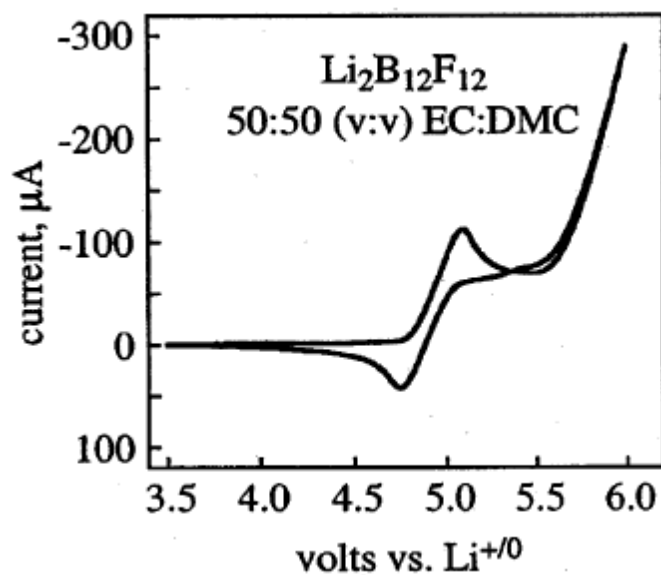


Figure 2-8. Electrochemical oxidation of 0.064 M solution of $\text{B}_{12}\text{F}_{12}^{2-}$ to $\text{B}_{12}\text{F}_{12}^{-}$ in 50:50 (v:v) mixture of ethylene carbonate:dimethyl carbonate. The quasi-reversible $\text{B}_{12}\text{F}_{12}^{-/2-}$ $E_{1/2}$ value is 4.9 V relative to $\text{Li}^{+/0}$ with Pt working and counter electrodes and Li foil reference electrode. There was no supporting electrolyte. This figure is taken from reference 16.

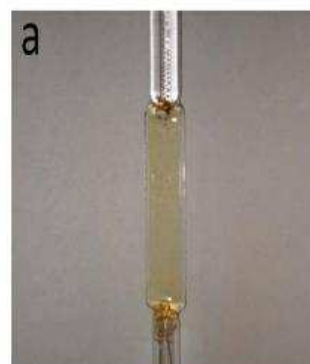
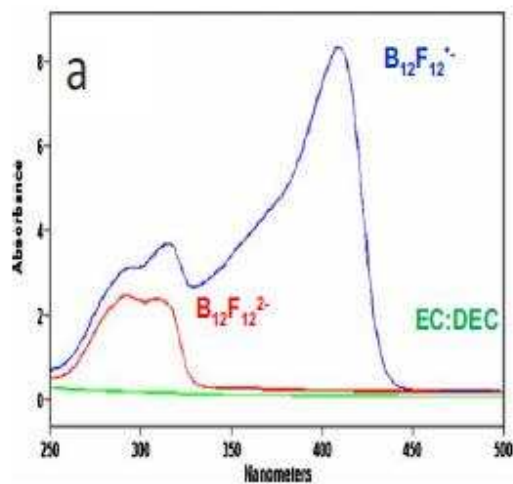


Figure 2-9. Left, UV-Vis spectrum of the $B_{12}F_{12}^-$ species compared to $B_{12}F_{12}^{2-}$ in a mixture of ethylene carbonate (EC):diethylene carbonate (DEC). Right, image of $B_{12}F_{12}^-$ in a mixture of EC:DEC in a UV-vis spectroelectrochemistry experiment where $Li_2B_{12}F_{12}$ was oxidized electrochemically then a UV-vis spectra of the oxidized species was collected. Both images are taken from reference 4.

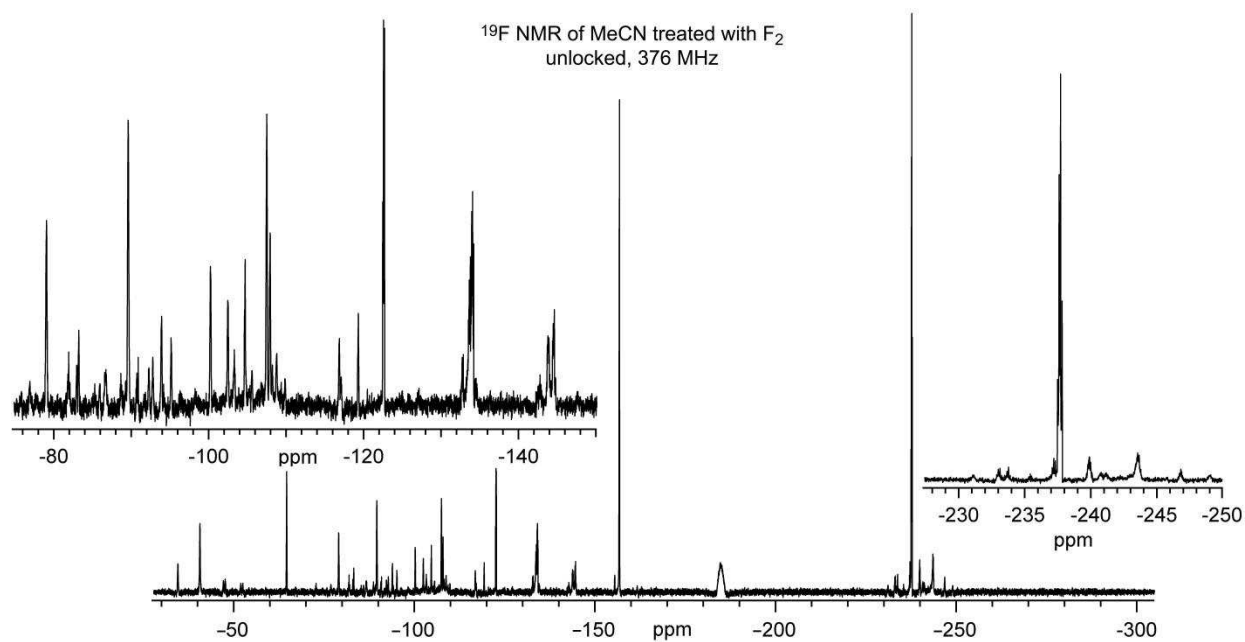


Figure 2-10. Fluorine-19 NMR spectrum of MeCN treated with F₂(g) for 2 h, then purged with N₂(g). The NMR sample was performed unlocked on a sample of the treated MeCN. Notice the significant amount of fluorine environments after the residual F₂(g) had been purged from the solution. All of these environments are either from F₂(g) reaction with MeCN or from with F₂(g) reacting with impurities in MeCN.

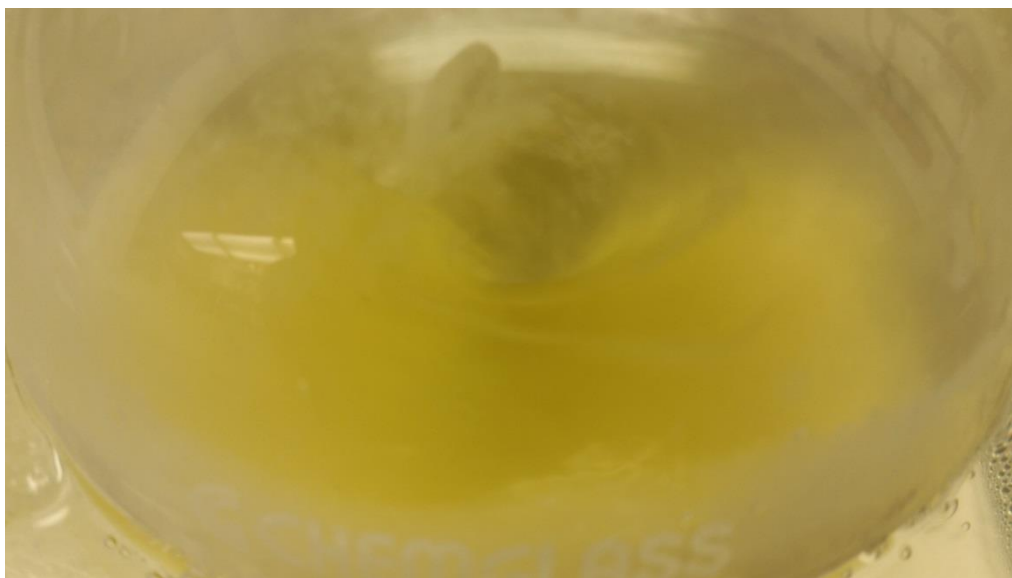


Figure 2-11. Bright yellow solution of MeCN during fluorination of $\text{K}_2\text{B}_{12}\text{H}_{12}$ with $\text{F}_2(\text{g})$ at $0\text{ }^\circ\text{C}$. This color is believed to be the oxidation of $\text{B}_{12}\text{F}_{12}^{2-}$ to $\text{B}_{12}\text{F}_{12}^-$ by $\text{F}_2(\text{g})$. Once the $\text{F}_2(\text{g})$ has stopped bubbling through the solution and the solution sits for ca. 3–5 h the color of the solution will change from bright yellow to a dark orange.

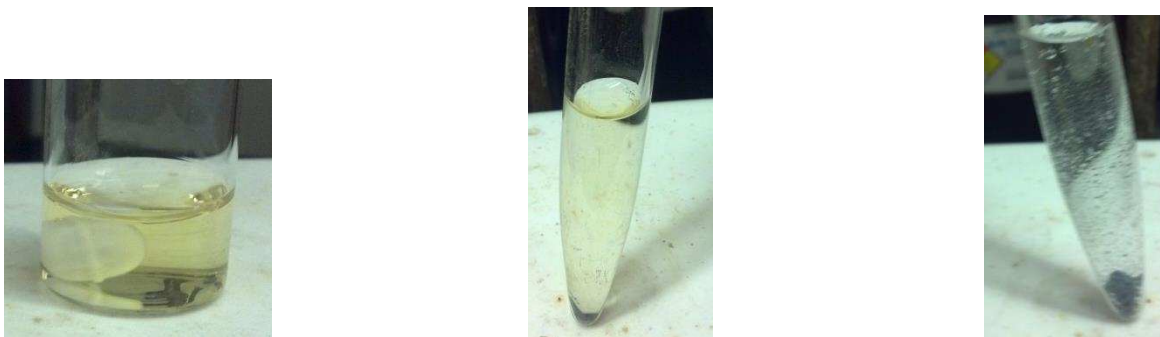


Figure 2-12. (Left) Crude aqueous $K_2B_{12}F_{12}$. (Middle) Crude aqueous $K_2B_{12}F_{12}$ after mixing for 15 minutes with $Zn(s)$. The sample was then centrifuged to make the solution and the yellow color clearer and more visible for the picture. (Right) Crude aqueous $K_2B_{12}F_{12}$ with $Zn(s)$ after the addition of 3–4 drops of concentrate HCl , mixing for 15 min then centrifuging to settle the unreacted $Zn(s)$ for a clear picture. The mixture with $Zn(s)$ and $HCl(aq)$ immediately exhibited a color change once conc. HCl was added.

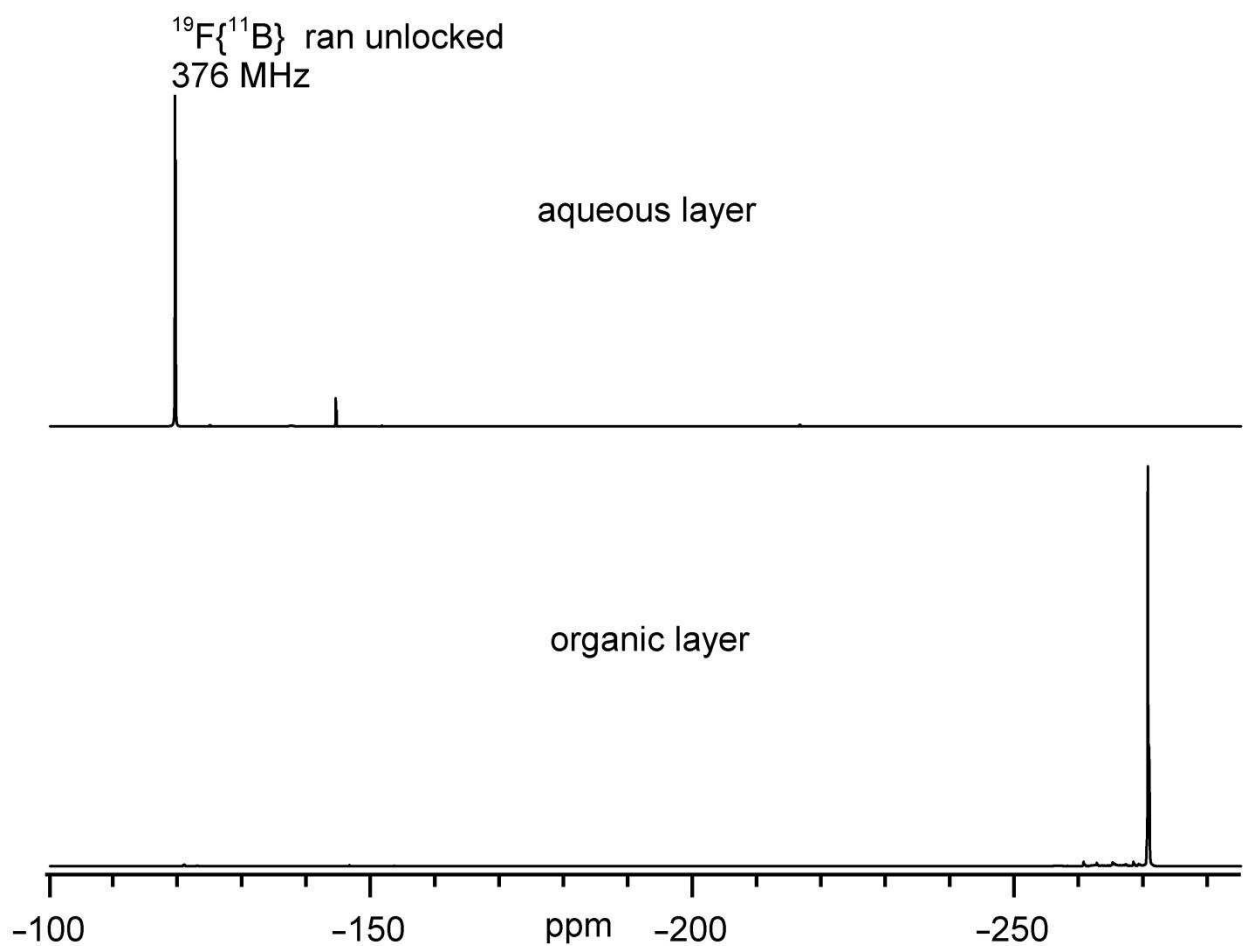


Figure 2-13. Fluorine-19 [^{11}B] NMR spectra of the aqueous and organic layers after liquid:liquid extraction with aqueous KHCO_3 and acetonitrile. Top spectrum is the aqueous layer, note very little signal for $\text{B}_{12}\text{F}_{12}^{2-}$ at $\delta -269$ is exhibited indicating good removal of the $\text{K}_2\text{B}_{12}\text{F}_{12}$ from the aqueous layer. The aqueous layer contains F^- and BF_4^- , $\delta -127$ and BF_4^- $\delta -152$ respectively. Additionally in the organic layer little if any BF_4^- is observed making this separation more efficient in terms of separation of $\text{B}_{12}\text{F}_{12}^{2-}$ from BF_4^- , a known contaminate that is also difficult to remove by selective solubility from $\text{B}_{12}\text{F}_{12}^{2-}$ depending on the counter ion.

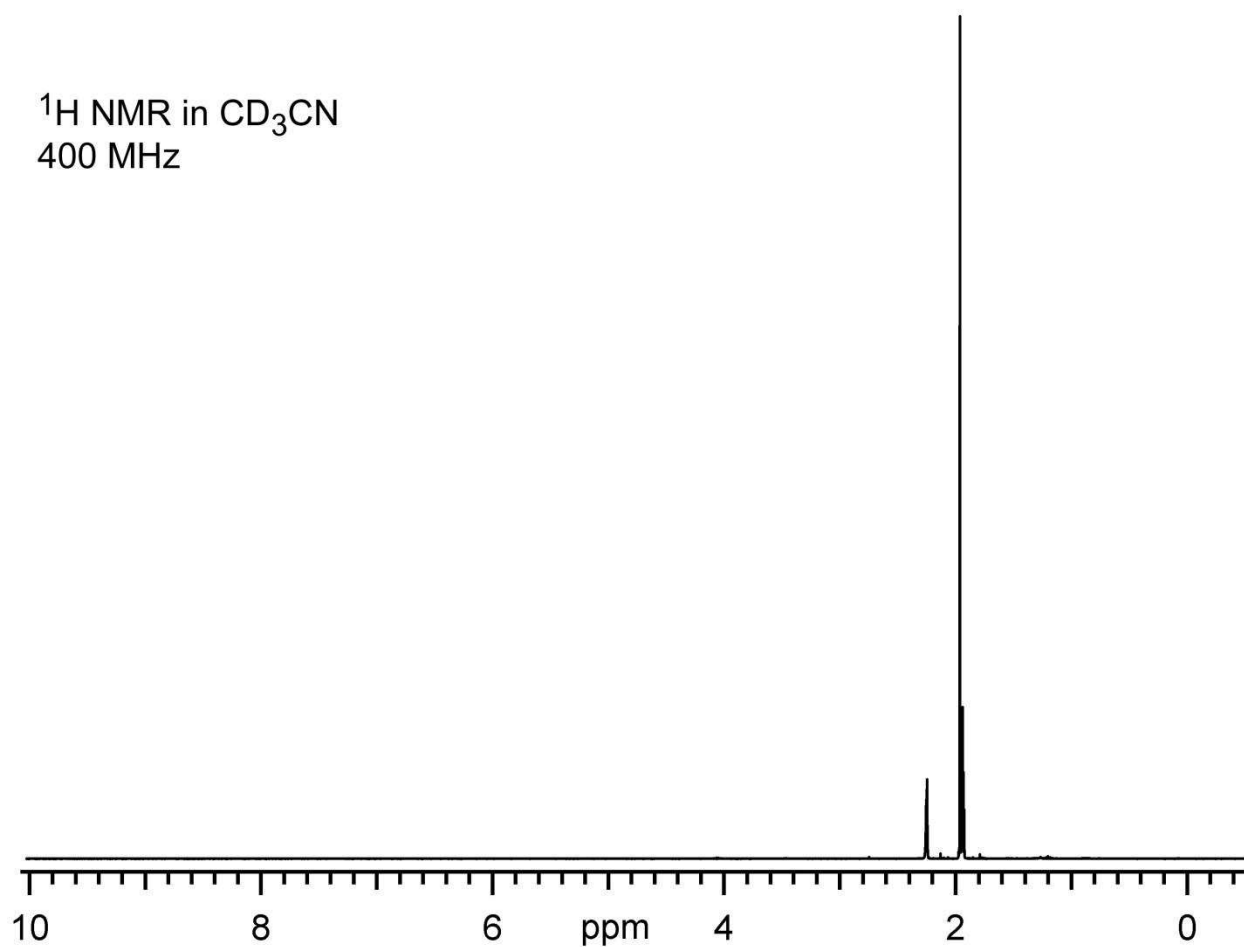


Figure 2-14. Proton NMR spectrum of $\text{K}_2\text{B}_{12}\text{F}_{12}$ purified by aqueous KHCO_3 :acetonitrile liquid:liquid extraction then 1 M KOH :ethyl acetate liquid:liquid extraction, Al_2O_3 column chromatography and recrystallization from water. The tallest peak at δ 1.96 is CH_3CN . The peak at δ 2.26 is from water. The spectrum was referenced based on the residual proton solvent peak of CHD_2CN at δ 1.94.

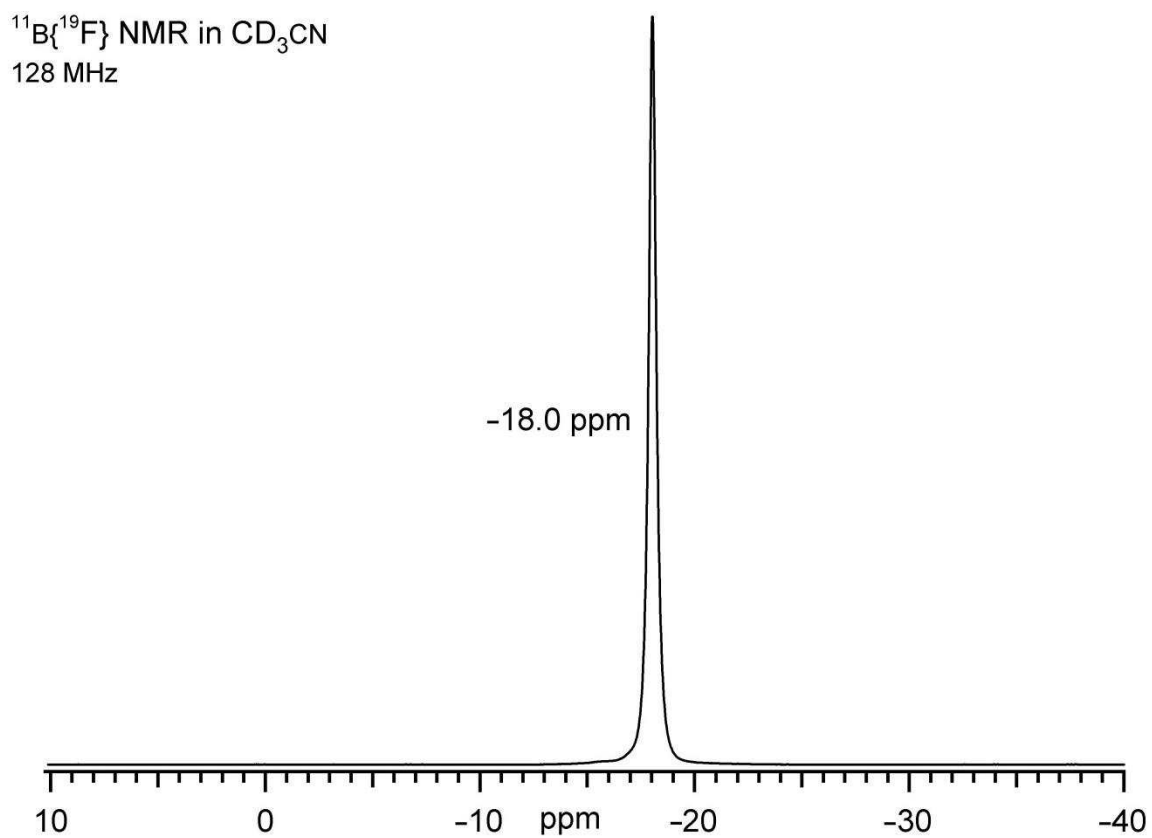


Figure 2-15. Boron-11 [^{19}F] NMR spectrum of $\text{K}_2\text{B}_{12}\text{F}_{12}$ purified by aqueous KHCO_3 :acetonitrile liquid:liquid extraction then 1 M KOH :ethyl acetate liquid:liquid extraction, Al_2O_3 column chromatography and recrystallization from water. The only observed peak at δ -18 is typical for $\text{B}_{12}\text{F}_{12}^{2-}$.

$^{19}\text{F}\{^{11}\text{B}\}$ NMR in CD_3CN
376 MHz

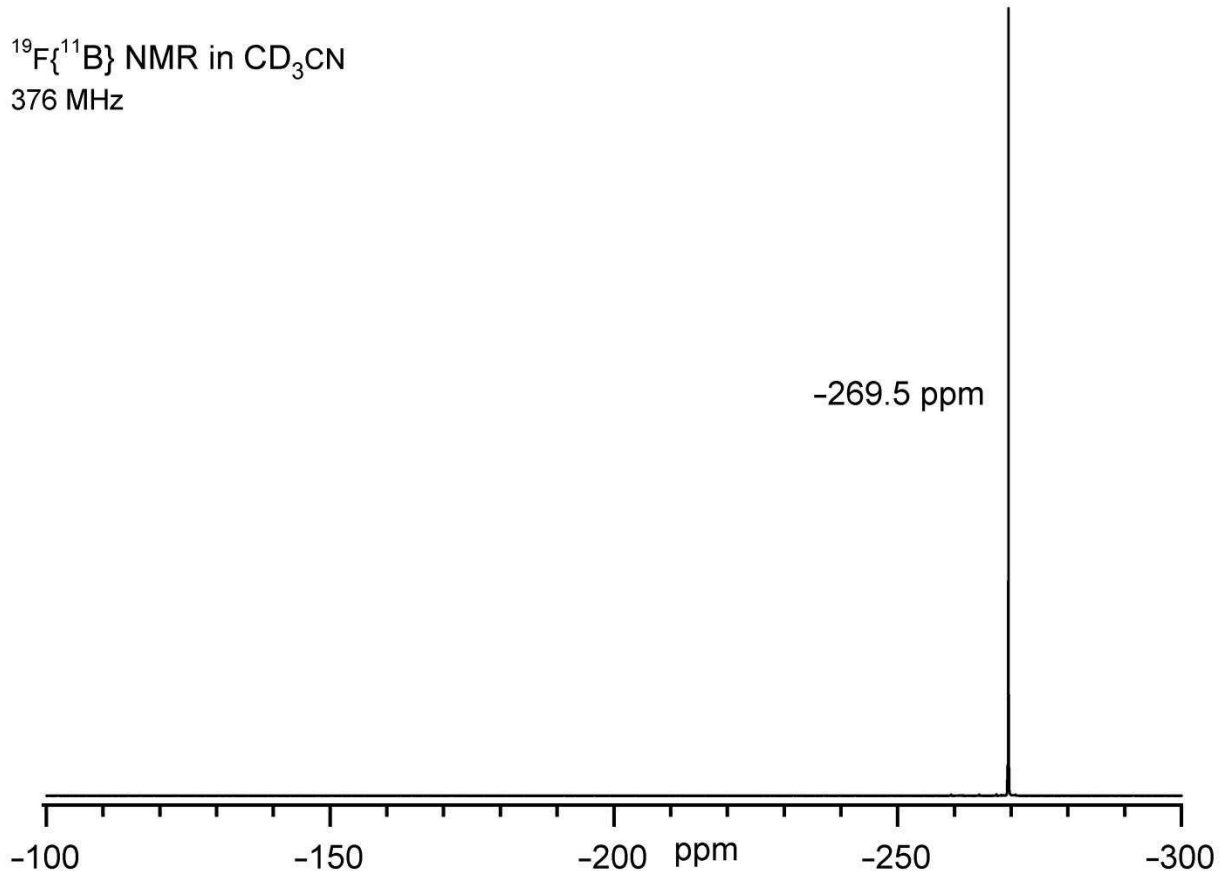


Figure 2-16. Fluorine-19 [^{11}B] NMR spectrum of $\text{K}_2\text{B}_{12}\text{F}_{12}$ purified by aqueous KHCO_3 :acetonitrile liquid:liquid extraction then 1 M KOH :ethyl acetate liquid:liquid extraction, Al_2O_3 column chromatography and recrystallization from water. The only observed peak at δ -269.5 is typical for $\text{B}_{12}\text{F}_{12}^{2-}$.

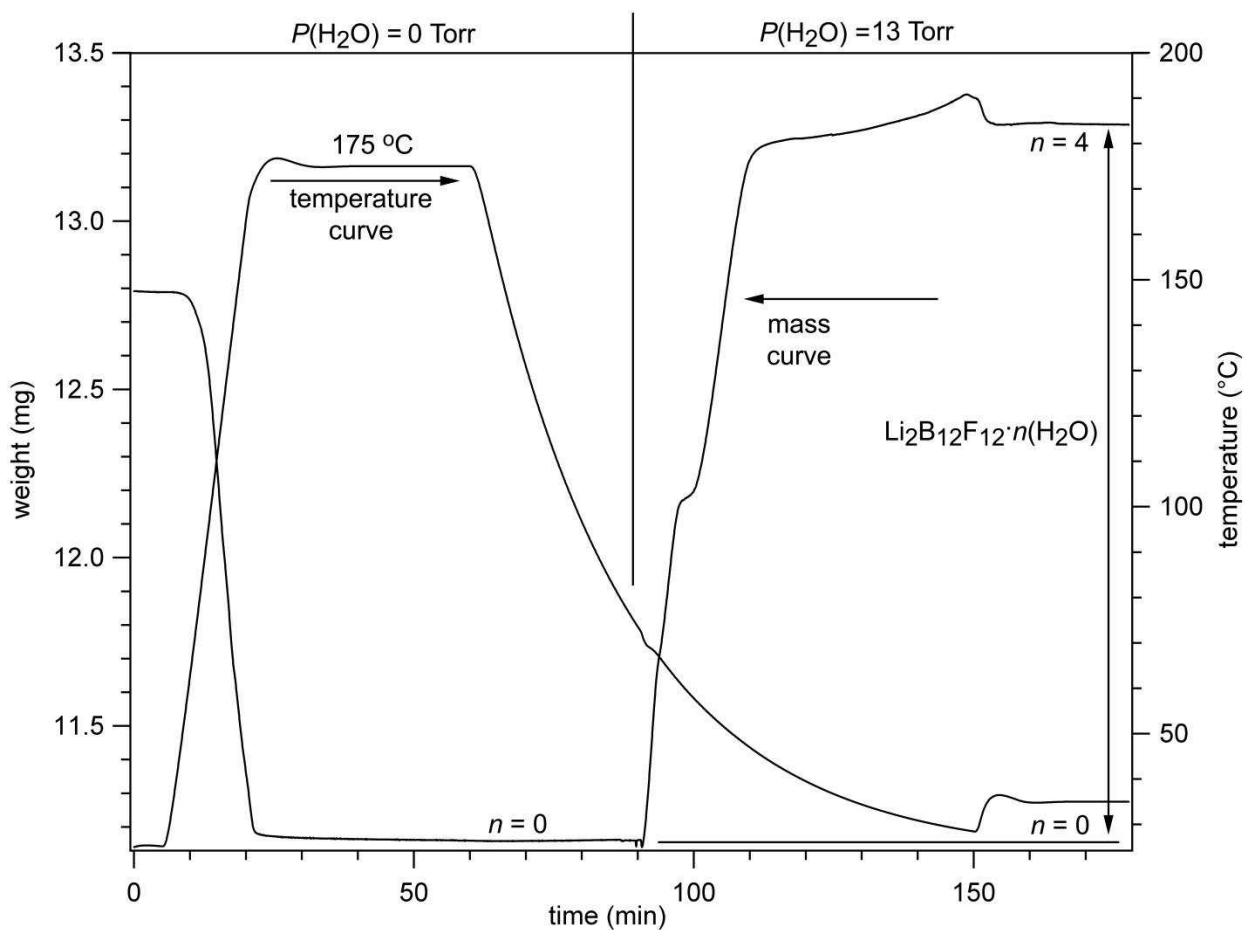


Figure 2-17. Thermogravimetric analysis of $\text{Li}_2\text{B}_{12}\text{F}_{12} \cdot n\text{H}_2\text{O}$ determining suitable drying conditions. The sample was initially dried at $175\text{ }^\circ\text{C}$ until a constant mass was reached. Then the temperature was cooled and the purge gas was switched to $P(\text{H}_2\text{O}) = 13\text{ Torr}$, (dry $\text{He}(\text{g})$ bubbled through H_2O at $15\text{ }^\circ\text{C}$). The sample rapidly rehydrated and was hydrating past 4 equiv H_2O when cooled to $25\text{ }^\circ\text{C}$. When the temp was raised to $35\text{ }^\circ\text{C}$, the $\text{Li}_2\text{B}_{12}\text{F}_{12} \cdot 4\text{H}_2\text{O}$ was stable. Based on this TGA experiment the $\text{Li}_2\text{B}_{12}\text{F}_{12}$ produced after drying by rotary-evaporation had ca. $n = 3.5\text{H}_2\text{O}$ and could be dried fully by heating to $175\text{ }^\circ\text{C}$ for an extended period of time.

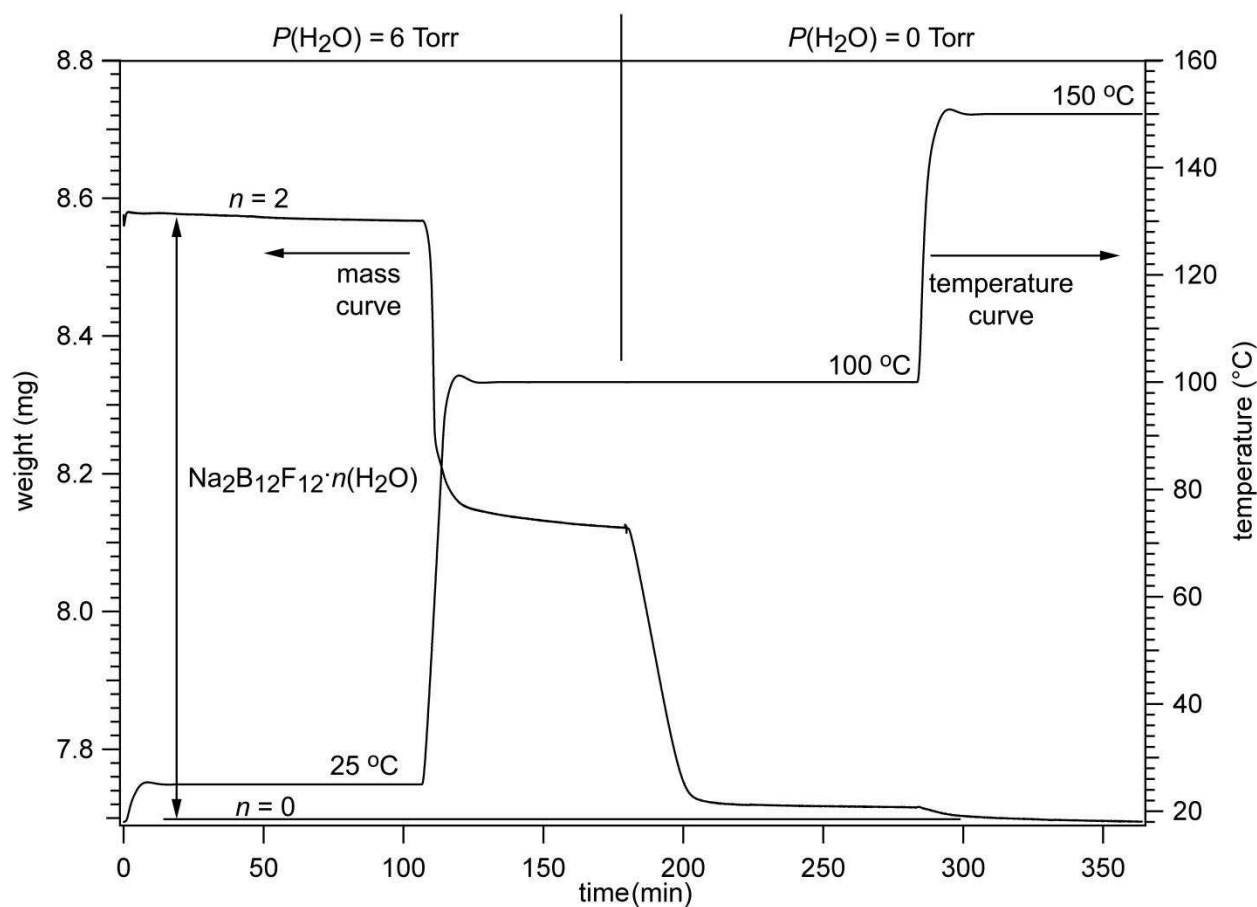


Figure 2-18. Thermogravimetric analysis of $\text{Na}_2\text{B}_{12}\text{F}_{12} \cdot n\text{H}_2\text{O}$ determining suitable drying conditions. The sample was initially dried equilibrated at 25 °C and $P(\text{H}_2\text{O}) = 6 \text{ Torr}$ until a nearly constant mass was reached. Then the temperature was increased to 100 °C losing 1 equiv H_2O . Then the $P(\text{H}_2\text{O})$ was changed to 0 Torr and little mass change was observed. Finally the sample was heated to 150 °C with $P(\text{H}_2\text{O}) = 6 \text{ Torr}$ and the mass lowered equating to 1equiv H_2O Based on this TGA experiment the $\text{Na}_2\text{B}_{12}\text{F}_{12}$ produced after drying by rotary-evaporation had ca. $n = 2\text{H}_2\text{O}$ and could be dried fully by heating to 150 °C for an extended period of time.

Chapter 2 References

- (1) Rupich, M. W.; Foos, J. S.; Brummer, S. B. *Journal of The Electrochemical Society* **1985**, *132*, 119.
- (2) Koczorowski, Z.; Zagórska, I. *J Appl Electrochem* **1980**, *10*, 75.
- (3) Arai, J.; Matsuo, A.; Fujisaki, T.; Ozawa, K. *Journal of Power Sources* **2009**, *193*, 851.
- (4) GirishKumar, G.; Bailey, W. H.; Peterson, B. K.; Casteel, W. J. *Journal of The Electrochemical Society* **2011**, *158*, A146.
- (5) Ionica-Bousquet, C. M.; Casteel Jr, W. J.; Pearlstein, R. M.; GirishKumar, G.; Pez, G. P.; Gómez-Romero, P.; Palacín, M. R.; Muñoz-Rojas, D. *Electrochemistry Communications* **2010**, *12*, 636.
- (6) Ivanov, S. V.; Casteel, W. J.; Bailey, W. H. In *Google Patents*; Air Products And Chemicals, Inc.: 2011.
- (7) Ivanov, S. V.; Casteel, W. J., Jr.; Pez, G. P.; Air Products and Chemicals, Inc.: European Patent Application, 2006.
- (8) Pez, G.; Ivanov, S.; Dantsin, G.; Casteel, W.; Lehmann, J. In *Google Patents*; Pez Guido P, Ivanov Sergei V, Gennady Dantsin, Casteel William J Jr, Lehmann John F, AIR PRODUCTS AND CHEMICALS, INC., PENNSYLVANIA: 2007.
- (9) Vaughey, J.; Jansen, A. N.; Dees, D. W. In *Google Patents*; Uchicago Argonne, Llc: 2010.
- (10) Chen, Z.; Ren, Y.; Jansen, A. N.; Lin, C.-k.; Weng, W.; Amine, K. *Nat Commun* **2013**, *4*, 1513.
- (11) Hayamizu, K.; Matsuo, A.; Arai, J. *Journal of The Electrochemical Society* **2009**, *156*, A744.
- (12) Goodenough, J. B.; Kim, Y. *Chemistry of Materials* **2010**, *22*, 587.
- (13) Peryshkov, D. V. Dissertation, Colorado State University, 2011.
- (14) Solntsev, K. A.; Ivanov, S. V.; Sakharov, S. G.; Katsner, S. B.; Chernayavskii, A. S.; Votnova, N. A.; Klyuchishche, E. A.; Kuznetsov, N. T. *Russ. J. Coord. Chem.* **1997**, *23*, 369.
- (15) Solntsev, K. A.; Mebel, A. M.; Votnova, N. A.; Kuznetsov, N. T.; Charkin, O. P. *Koord. Khim.* **1992**, *18*, 340.
- (16) Ivanov, S. V.; Miller, S. M.; Anderson, O. P.; Solntsev, K. A.; Strauss-Boltalina, S. H. *J Am Chem Soc* **2003**, *125*, 4694.
- (17) Peryshkov, D. V.; Bukovsky, E. V.; Folsom, T. C.; Strauss-Boltalina, S. H. *Polyhedron* **2013**, *58*, 197.
- (18) Peryshkov, D. V.; Goreschnik, E.; Mazej, Z.; Strauss-Boltalina, S. H. *Journal of Fluorine Chemistry* **2010**, *131*, 1225.
- (19) Peryshkov, D. V.; Popov, A. A.; Strauss-Boltalina, S. H. *J Am Chem Soc* **2009**, *131*, 18393.
- (20) Peryshkov, D. V.; Popov, A. A.; Strauss-Boltalina, S. H. *J Am Chem Soc* **2010**, *132*, 13902.
- (21) Casteel William J Jr, I. S. V., Pez Guido P; H01B1/12 ed.; office, U. P., Ed.; Casteel William J Jr, Ivanov Sergei V, Pez Guido P: United States of America, 2006.
- (22) Ivanov, S. V.; Casteel, W. J.; Pez, G. P.; Google Patents: 2009.

- (23) Bukovsky, E. V.; Fiedler, S. R.; Peryshkov, D. V.; Popov, A. A.; Strauss-Boltalina, S. H. *European Journal of Inorganic Chemistry* **2012**, 208.
- (24) Walter, M.; Ramaley, L. *Analytical Chemistry* **1973**, 45, 165.
- (25) Anderson, J. D. J. *Fundamentals of Aerodynamics 3rd Ed.*; 3rd ed.; McGraw-Hill Science/Engineering/Math, 1984.
- (26) Peryshkov, D. V.; Bukovsky, E. V.; Folsom, T. C.; Strauss-Boltalina, S. H. *Polyhedron* **2013**, 58, 197.
- (27) Schölkopf, T.; Van, N.-D.; Schleid, T. *Inorganica Chimica Acta* **2011**, 374, 181.
- (28) Jones, C., W. *Applications of Hydrogen Peroxide and Derivatives*; Royal Society of Chemistry: Cambridge, United Kingdom, 1999.
- (29) Christe, K. O.; Wilson, W. W. *Journal of Fluorine Chemistry* **1990**, 46, 339.
- (30) Christe, K. O.; Wilson, W. W. *Journal of Fluorine Chemistry* **1990**, 47, 117.
- (31) Brown, T., L.; LeMay, H. E., Jr.; Bursten, B. E.; Burdge, J., R. *Chemistry The Central Science*; 8th ed.; Prentice Hall, NJ, 2000.
- (32) Coetzee, J. F. *Purification of Acetonitrile and Test for Impurities; A Report Prepared for The International Union of Pure and Applied Chemistry by The Commission on Electroanalytical Chemistry*, University of Pittsburgh.
- (33) Coetzee, J. F.; Cunningham, G. P.; McGuire, D. K.; Padmanabhan, G. R. *Analytical Chemistry* **1962**, 34, 1139.
- (34) Forcier, G. A.; Olver, J. W. *Analytical Chemistry* **1965**, 37, 1447.
- (35) Rozen, S.; Brand, M. *Angewandte Chemie International Edition in English* **1986**, 25, 554.
- (36) Rozen, S.; Golan, E. *European Journal of Organic Chemistry* **2003**, 2003, 1915.
- (37) Rozen, S. *Eur. J. Org. Chem.* **2005**, 2433.
- (38) Bard, A. J.; Faulkner, L. R. *Electrochemical methods: fundamentals and applications*; 2nd ed.; John Wiley and Sons: United States of America, 2001.
- (39) Kou, Y.; Schmidt, S. J. *Food Chemistry* **1999**, 66, 253.

Chapter 3.

Synthesis and Properties of Anhydrous and Hydrated Hydronium Salts of $B_{12}F_{12}^{2-}$

$(H_3O)_2B_{12}F_{12} \cdot n(H_2O)$ ($n = 6, 4, 2, 0$): In Search of $H_2B_{12}F_{12}$

3.1 Introduction and Justification

Superweak anions (in this text a superweak anion is defined as the conjugate base of a real or hypothetical superacid) are frequently exploited to generate, isolate, and characterize reactive cationic species that are not stable in the presence of traditional weakly-coordinating anions, such as ClO_4^- , PF_6^- , $CF_3SO_3^-$, etc.¹⁻¹⁵ Practical applications that justify superweak-anion research include highly conductive electrolytes,¹⁶⁻²⁴ reversible gas absorbents,²⁵ and metallocenium catalyzed olefin polymerization.²⁶⁻²⁹ Some of the most effective superweak anions are $CB_{11}H_{12-n}X_n^-$ ($X = F, Cl, Br, CH_3, CF_3$) and $B_{12}X_{12}^{2-}$ ($X = F, Cl$), and some of the extremely reactive cations or cation-like species isolated with these anions include $H_9O_4^+$,³⁰ H_3O^{+31} , $C_6H_7^+$,^{32,33} $Cu(CO)_4^+$,¹² $Ag(CH_2Cl_2)^+$,³⁴ and $Al(CH_3)_2^+$.³⁵ My research involves the $B_{12}F_{12}^{2-}$ anion. It was first prepared in 38% yield by Solntsev et al. in 1992.³⁶ An improved preparation (72% yield) was reported by the Strauss-Boltalina research group in 2003,³⁷ and a scaled-up synthesis (ca. 18 g, 74% yield) was reported by the Strauss-Boltalina group in 2009.³⁸ Important properties of superweak anions that are exhibited by $B_{12}F_{12}^{2-}$ are oxidative stability (4.9 V vs $Li^{+/0}$),³⁷ weakly-basic periphery (i.e., B–F bonds instead of B–O or B–Cl bonds), large size (antipodal F...F distance ca. 9.2 Å), charge delocalization, and symmetric charge distribution.

The Strauss-Boltalina group has been studying the structures and physicochemical properties of a variety of metal and nonmetal salts of the icosahedral superweak anion $B_{12}F_{12}^{2-}$.³⁷⁻⁴² The

guiding hypothesis in this research is that the unique combination of size, shape, high symmetry, thermal stability, and extremely weak Brønsted and Lewis basicity of this anion will lead to unanticipated structures and properties (i.e., unanticipated relative to salts of $B_{12}H_{12}^{2-}$,⁴³⁻⁴⁶ $B_{12}Cl_{12}^{2-}$,⁴⁷⁻⁴⁹ $B_{12}(OH)_{12}^{2-}$,^{50,51} and $B_{12}(CH_3)_{12}^{2-}$,⁵² and of salts of typical fluoroanions such as BF_4^- , PF_6^- , SbF_6^- , $Sb_2F_{11}^-$, SiF_6^{2-} , MnF_6^{2-} , etc.). For example, $K_2B_{12}H_{12}$ exhibits the common antifluorite structure,⁴³ but $K_2B_{12}F_{12}$ exhibits the intermetallic Ni_2In structure³⁹ (the B_{12} centroids occupy the idealized HCP positions of the In atoms⁵³), which is likely the first and only example structure of an ionic compound with a polyatomic anion that was observed at ordinary temperatures and pressures.

Superweak anions are also of interest to the chemistry community because of their ability to form superacids, i.e.; acids that are stronger than 100% sulfuric acid.⁵⁴ While acids of other $B_{12}X_{12}^{2-}$ ($X = Cl, Br$) anions⁵⁵ have been synthesized and characterized, the putative $H_2B_{12}F_{12}$ has yet to be synthesized. Based on the strength of the B–F bond, low polarizability, and weak Lewis base interactions of fluorine it is conceivable that $H_2B_{12}F_{12}$ would be a stronger acid than previously isolated dodecaborate superacids $H_2B_{12}X_{12}$ ($X = Cl, Br$). The $H_2B_{12}Cl_{12}$ acid is strong enough to protonate benzene to form the benzenium cation and is theorized to have a Hammett acidity of greater than -17 .⁵⁵ Besides simply making the strongest possible acid, strong acids with stable anions have the ability to easily make stable hydronium (H_3O^+) salts. The nature of hydronium ions (i) in bulk aqueous solutions,⁵⁶⁻⁵⁸ (ii) on the surface of aqueous solutions (i.e., at the air/water interface, where H_3O^+ ions may be concentrated relative to the bulk solution),^{59,60} and (iii) as free H_3O^+ ions⁶¹ or as $[(H_3O)_n(H_2O)_m]^{n+}$ clusters⁶²⁻⁶⁴ within the confines of solid-state structures, are of longstanding interest as well as of current interest to many chemists. Furthermore, the acid salts $(H_3O)_2B_{12}Cl_{12} \cdot nH_2O$ ⁶⁵ and $(H_3O)_2B_{12}F_{12} \cdot nH_2O$ ⁶⁶ have been

considered as practical, more chemically inert alternatives to H_3PO_4 electrolytes for acid fuel cells^{16,66}, but have yet to be structurally characterized.

Besides the purely academic aspect of this research regarding superweak anions, superacids, and their respective solvated salts described in the paragraphs above, my research also involved a practical synthesis of 15 g of $(\text{H}_3\text{O})_2\text{B}_{12}\text{F}_{12}\cdot n\text{H}_2\text{O}$ for its use as a hydrogen fuel cell proton conducting electrolyte, the work supported by UTC power, an industrial sponsor. The current electrolyte for such fuel cells, concentrated H_3PO_4 , is highly corrosive, and is known to have adverse irreversible effects shortening the usable life of the Pt catalyst in the cathode. It was discovered that the phosphate cation competes for active sites on the Pt catalyst drastically reducing the rate of the oxygen reduction reaction and the overall efficiency of the fuel cell stack over a 2–3 year period.⁶⁷ The proposal with UTC power, Clemson University, Colorado State University and National Renewable Energy Laboratory was intended to solve the phosphate poisoning problem by replacing the currently used electrolytes with novel electrolytes based on fluoroborate or fluoroheteroborate acid structures comprising the formula $\text{H}_a\text{M}_b\text{Q}\cdot n\text{H}_2\text{O}$, where H is a proton, M is a different cation (if necessary), and Q is the fluoroborate or fluoroheteroborate anion.

In hydrogen fuel cell systems the purity of the electrolyte is critical for long term stability. Preliminary investigations by UTC Power with fluoroborate acid electrolytes of various purities already benchmarked what purity of fluoroborate anion was necessary for long term device performance (Figure 3-1)⁶⁷. It was discovered that even as little as 0.7% H_3BO_3 drastically reduced the cell life indicated by a decrease in cell voltage. Salts of $\text{B}_{12}\text{F}_{12}^{2-}$ can have anion contamination due to incomplete fluorination ($\text{B}_{12}\text{F}_{12-n}\text{H}_n^{2-}$ where $n \neq 0$), or cation contaminations requiring cation purity to also be investigated. No previous work concerning the

purity assessment of salts of $B_{12}F_{12}^{2-}$ has been done. Therefore, new synthetic methods that take into account cation and anion purity had to be designed, and analytical techniques needed to be developed by the author to quantify their respective purity in order to meet the strict purity requirements for fuel cell electrolyte.

This chapter describes the author's efforts to synthesize the putative superacid $H_2B_{12}F_{12}$ through the $(H_3O)_2B_{12}F_{12} \cdot nH_2O$ or other non-metal salts of $B_{12}F_{12}^{2-}$, synthesis of gram scale quantities of highly purified $(H_3O)_2B_{12}F_{12} \cdot nH_2O$, characterize the crystal structures of discrete isolated hydrate phases of $(H_3O)_2B_{12}F_{12} \cdot nH_2O$ and other non-metal salts, investigate hydration/dehydration rates and conditions of $(H_3O)_2B_{12}F_{12} \cdot nH_2O$ and develop a new method to make other metal salts of $B_{12}F_{12}^{2-}$ starting from $(H_3O)_2B_{12}F_{12} \cdot nH_2O$. In order to complete these tasks the author had to develop and validate synthetic methods for $(H_3O)_2B_{12}F_{12} \cdot nH_2O$ and corresponding analytical techniques to study and verify its purity.

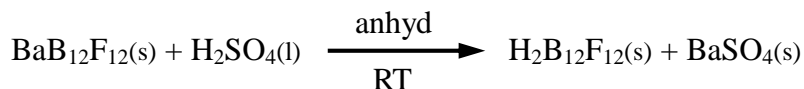
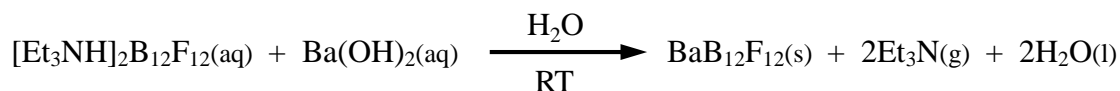
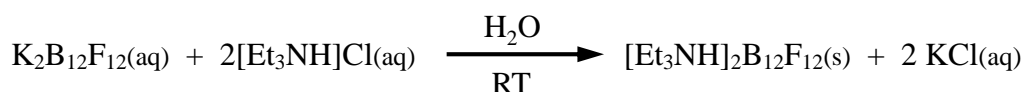
3.2 Possible Synthetic Routes to $H_2B_{12}F_{12}$, Literature Methods for Making $H_2B_{12}F_{12}$ and Related Superacids.

In this section two existing procedures, several potentially applicable methods from the literature and original ideas by this author for synthesis of $(H_3O)_2B_{12}F_{12} \cdot nH_2O$ and $H_2B_{12}F_{12}$ will be discussed. It should be pointed out that synthesis of superacids using typically synthetic techniques requires extremely anhydrous and conditions. If glass is used it must be rigorously dried to ensure no moisture is present that would react forming H_3O^+ instead of the desired H^+ .

The synthesis and characterization of the putative conjugate acid of $B_{12}F_{12}^{2-}$ has previously been reported in a patent by Ivanov et al.²¹ Two synthetic routes to synthesize $H_2B_{12}F_{12}$ described by this patent are described as examples 1 and 2. Patent example 1 from Ivanov et al. involves direct fluorination of $H_2B_{12}F_{12} \cdot nH_2O$ in liquid anhydrous HF (LAHF) with a 20/80

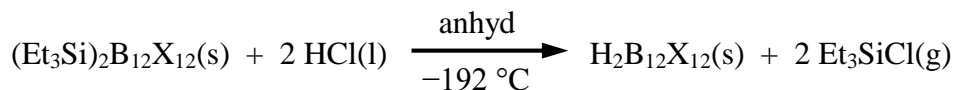
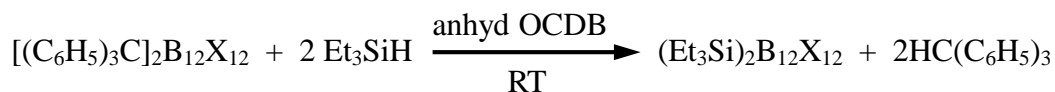
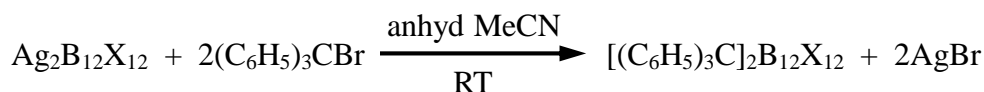
ratio of F₂/N₂ gas resulting in ca. 90 mol% H₂B₁₂F₁₂·nH₂O, also producing the undesirable anions B₂₄F₂₂⁴⁻, B₁₂F₁₁(OH)²⁻, and BF₄⁻ in 0.01, 0.05 and 0.36 mol% respectively. This approach requires the use of toxic LAHF in the process, and produces unwanted anionic products that would be difficult to separate from the desired B₁₂F₁₂²⁻ anion, likely requiring multiple separation steps decreasing the overall yield.

Patent example 2 describes making pure K₂B₁₂F₁₂, then through a series of metathesis steps shown in the scheme below forming H₂B₁₂F₁₂.



This method has the benefit of being able to make highly purified BaB₁₂F₁₂(s) which forms hydrated phases that are easily removed with mild heating. However, this method also requires, anhydrous H₂SO₄ to make H₂B₁₂F₁₂ directly which is very difficult if not impossible to make and keep. Or, aqueous H₂SO₄ could be used forming (H₃O)₂B₁₂F₁₂·nH₂O, however, the water content of the BaB₁₂F₁₂ and H₂SO₄ would need to be accurately known in order to avoid contamination of the product with SO₄²⁻ or residual BaB₁₂F₁₂ forming a mixture of salts. If accurate titration were achieved the hydrates would still need to be thermally or chemically removed to end up with H₂B₁₂F₁₂. Multiple experimentally unavoidable errors inherent in this method make it undesirable, especially for moderate scale (15 g) and high purity.

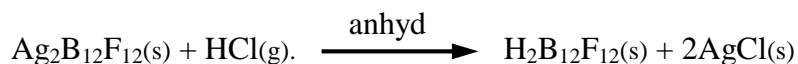
Methods similar to those employed by Reed et al., whose research involves synthesis and characterization of similar carborane superweak anions $\text{CB}_{11}\text{H}_{12-n}\text{X}_n^-$ ($\text{X} = \text{F}, \text{Cl}, \text{Br}, \text{CH}_3, \text{CF}_3$ and combinations of these X groups)^{7,68-70}, as well as $\text{H}_2\text{B}_{12}\text{X}_{12}$ ($\text{X} = \text{Cl}, \text{Br}$)^{48,55} superacids researched by Reed et al. and Knapp et al. are also applicable to $\text{H}_2\text{B}_{12}\text{F}_{12}$ and were considered. A synthetic route used to great success for making $\text{H}_2\text{B}_{12}\text{Cl}_{12}$, $\text{H}_2\text{B}_{12}\text{Br}_{12}$ and similar carborane based superacids could be employed for making $\text{H}_2\text{B}_{12}\text{F}_{12}$.^{55,71} This generalized method also utilizes multiple metathesis steps shown in the reaction scheme below.



This multi-step metathesis works well because by design the byproducts formed in the metathesis are easily separated from the desired compounds. However, this method requires rigorously anhydrous, oxygen free techniques at every metathesis step. Also, it is known from work by previous Strauss-Boltalina group member, Dmitry Peryshkov that $\text{Ag}_2\text{B}_{12}\text{F}_{12}$ forms many solvated states with acetonitrile.³⁴ The $\text{Ag}_2\text{B}_{12}\text{F}_{12}$ salt has three known solvate phases with CH_3CN ($\text{Ag}_2(\text{CH}_3\text{CN})_x\text{B}_{12}\text{F}_{12}$ where $x = 2, 4, \text{ and } 5$ have been characterized by single crystal X-ray crystallography) and likely other solvated phases yet uncharacterized, that makes stoichiometric addition of $\text{Ag}_2(\text{CH}_3\text{CN})_x\text{B}_{12}\text{F}_{12}$ difficult. Also, typical of most Ag^+ salts,

$\text{Ag}_2\text{B}_{12}\text{F}_{12}$ is photo-sensitive, making it difficult to end up with highly purified $\text{Ag}_2\text{B}_{12}\text{F}_{12}$ which will decrease the purity of the resulting $\text{H}_2\text{B}_{12}\text{F}_{12}$.

Metathesis through the $\text{Ag}_2\text{B}_{12}\text{F}_{12}$ salt, used extensively by former group member Dmitry Peryshkov to synthesize and characterize Li^+ through Cs^+ , Mg^{2+} through Ba^{2+} , Ni^{2+} , Cu^{2+} , and Zn^{2+} salts of $\text{B}_{12}\text{F}_{12}^{2-}$ could also be employed. The corresponding synthetic route hypothesized by this author for making the $\text{H}_2\text{B}_{12}\text{F}_{12}$ is to take pure $\text{K}_2\text{B}_{12}\text{F}_{12}$ and gravimetrically convert that to the $\text{Ag}_2\text{B}_{12}\text{F}_{12}$ salt with AgNO_3 in dry CH_3CN precipitating KNO_3 .³⁴ After recovering $\text{Ag}_2\text{B}_{12}\text{F}_{12}$ gravimetrically convert it to $\text{H}_2\text{B}_{12}\text{F}_{12}$ with 2 equivalents of anhydrous $\text{HCl}(\text{g})$ as shown in the reaction scheme below. If it turns out that $\text{H}_2\text{B}_{12}\text{F}_{12}(\text{s})$ sublimates at low temperature then it could be separated from $\text{AgCl}(\text{s})$ by a simple sublimation under vacuum.



However, the same problems plaguing the purity of $\text{Ag}_2\text{B}_{12}\text{F}_{12}$ would be an issue following this method.

More recently, a method to make $(\text{H}_3\text{O})_2\text{B}_{12}\text{F}_{12} \cdot n\text{H}_2\text{O}$ using highly purified cation exchange resin (published by this author 2012, *Eur. J. Inorg. Chem.*³¹) is a clean method to make the $(\text{H}_3\text{O})_2\text{B}_{12}\text{F}_{12} \cdot n\text{H}_2\text{O}$ salt. The $(\text{H}_3\text{O})_2\text{B}_{12}\text{F}_{12} \cdot n\text{H}_2\text{O}$ could then be carefully dried (thermal or chemical) of the hydrate to form $\text{H}_2\text{B}_{12}\text{F}_{12}$. The cation exchange method was discussed in the Ivanov et al. patent, but was dismissed as too time consuming, see quote below.

“The above described acid ($\text{H}_2\text{B}_{12}\text{F}_{12}$) also can be produced by the common method for the preparation of acids with polyhedral borate anions, which includes eluting a salt of the anion via an ion-exchange column in H^+ form and removing

water under reduced pressure. However, in contrast to the procedure of this example, that method maybe time consuming and may require evaporation of large amounts of water. It may also result in contamination of the product acids with organic impurities.”²¹

Similar to careful drying of $(\text{H}_3\text{O})_2\text{B}_{12}\text{F}_{12}\cdot n\text{H}_2\text{O}$, a method going through the NR_3H^+ (R = H or other) salt and then thermally removing NR_3 will also be discussed as a method to cleanly synthesize $\text{H}_2\text{B}_{12}\text{F}_{12}$.

3.2.1 Chosen Synthetic Method for $\text{H}_2\text{B}_{12}\text{F}_{12}$.

After examination of the synthetic procedures described above and comparing their advantages and shortcomings the method based on cation-exchange of $\text{K}_2\text{B}_{12}\text{F}_{12}$ was chosen. It was concluded that it will enable the highest possible cation and anion purity, and can be readily scaled to multi-gram synthesis. Starting from highly purified $\text{K}_2\text{B}_{12}\text{F}_{12}$ and using ultra high purity cation exchange resin, the resulting $(\text{H}_3\text{O})_2\text{B}_{12}\text{F}_{12}\cdot n\text{H}_2\text{O}$ will be of high purity, with the added ability to produce large quantities as well as scalable should the $(\text{H}_3\text{O})_2\text{B}_{12}\text{F}_{12}\cdot n\text{H}_2\text{O}$ become industrially useful.

3.3 Results

3.3.1 Synthesis of $(\text{H}_3\text{O})_2\text{B}_{12}\text{F}_{12}\cdot n\text{H}_2\text{O}$ by Strong Acid Cation Exchange.

After examination of the synthetic procedures described in Patent examples 1 and 2, cation-exchange of $\text{K}_2\text{B}_{12}\text{F}_{12}$ (the purity of $\text{K}_2\text{B}_{12}\text{F}_{12}$ was discussed in a separate chapter) was suggested to yield products of the highest purity and easy scale up of the reaction. The $(\text{H}_3\text{O})_2\text{B}_{12}\text{F}_{12}\cdot n\text{H}_2\text{O}$

salt was synthesized via ion-exchange using two different strong acid cation-exchange resins (Purolite UCW9126 and Amberlyst 15) that have the same $-\text{C}_6\text{H}_4\text{SO}_3^-$ exchange functionality. Recovered $(\text{H}_3\text{O})_2\text{B}_{12}\text{F}_{12}\cdot n\text{H}_2\text{O}$ product from the Amberlyst 15 resin appeared to have a darker color upon drying to a solid; indicating greater amounts of impurity as well as a detectable amount of unidentifiable contaminants by ^1H NMR (see Figures 3-2 & 3-3). The impurities in the $(\text{H}_3\text{O})_2\text{B}_{12}\text{F}_{12}\cdot n\text{H}_2\text{O}$ product from Amberlyst 15 resin appeared to be low in concentration by ^1H NMR. In a separate experiment with the goal of identifying those impurities leeching from the column, several liters of H_2O were flushed through a column of fresh Amberlyst 15 resin and dried to a dark brown oil; the oil was then diluted with ca. 0.5 mL of D_2O for NMR analysis (Figure 3-3). Even in this case when higher impurity concentration produced a highly colored solution, the ^1H NMR exhibited a low signal to noise ratio due to a low concentration of multiple possible impurities. The product obtained from the Purolite resin was much lighter in color and had no observable impurities by ^1H NMR (Figure 3-2) indicating a lower degree of contamination with the colored impurity(ies), therefore the Purolite resin was chosen for subsequent $(\text{H}_3\text{O})_2\text{B}_{12}\text{F}_{12}\cdot n\text{H}_2\text{O}$ syntheses. The Purolite resin is commonly used for treatment of water for semiconductor processing and is specified to leach < 20 ppb Δ TOC after 60 bed volumes (BV) of dd- H_2O at a flow rate of 30 BV/h. Leach levels of TOC for the Amberlyst 15 resin could not be found.

Recrystallized $(\text{H}_3\text{O})_2\text{B}_{12}\text{F}_{12}\cdot n\text{H}_2\text{O}$ (slow recrystallization from dd- H_2O) produced clear colorless solid; however, final yields of recrystallized $(\text{H}_3\text{O})_2\text{B}_{12}\text{F}_{12}\cdot n\text{H}_2\text{O}$ varied from 20 to 50% due to the high solubility of $(\text{H}_3\text{O})_2\text{B}_{12}\text{F}_{12}\cdot n\text{H}_2\text{O}$ in H_2O and washing with minimal cold water dissolved significant quantities of the product. The low recrystallization yield was initially unacceptable for producing multi-gram quantities of the material. The products for collaborators

were taken from the Purolite UCW9126 ion-exchange resin and dried to a solid with no further purification. However, after obtaining a crystal structure of $(\text{H}_3\text{O})_2\text{B}_{12}\text{F}_{12}\cdot 6\text{H}_2\text{O}$ (section 3.3.2) and determining that the hexahydrate is the stable phase at 25 °C in a vapor pressure of water of 6 Torr (section 3.3.7) purification of $(\text{H}_3\text{O})_2\text{B}_{12}\text{F}_{12}\cdot 6\text{H}_2\text{O}$ by crystallization at the appropriate conditions (25 °C, $P(\text{H}_2\text{O}) = 6$ Torr) is possible and can be scaled.

3.3.2 Crystal Structure of $(\text{H}_3\text{O})_2\text{B}_{12}\text{F}_{12}\cdot n\text{H}_2\text{O}$ ($n = 6, 4$).

Crystals of $(\text{H}_3\text{O})_2\text{B}_{12}\text{F}_{12}\cdot 6\text{H}_2\text{O}$ suitable for single crystal XRD were grown by this author by slow evaporation of dd- H_2O . Drawings of the structure of $(\text{H}_3\text{O})_2\text{B}_{12}\text{F}_{12}\cdot 6\text{H}_2\text{O}$ are shown in Figures 3-4–3-9. Selected interatomic distances and angles are listed in Table 3-1, pertinent crystallographic data is listed in Table 3-2. The structure of the $\text{B}_{12}\text{F}_{12}^{2-}$ anion in this compound is normal^{39,42,72-74} (it is also the most precise structure of any molecular B_{12} species, with B–F and B–B esd's of 0.0008–0.0014 Å; see Figure 3-10). The anions are packed in a CCP-like array, with a network of H_3O^+ ions and H_2O molecules intercalated between parallel planes of anions (Figure 3-4). The B_{12} centroid (\odot) in each of those parallel close-packed-like planes are rigorously coplanar. The $\odot\cdots\odot$ distances are 8.411 and 8.521 Å within the close-packed planes and, because of the presence of the "layers of aqueous acid," are 8.703 and 8.914 between the close-packed planes (close packed distances listed in Table 3-3). The shortest interionic F...F distances are 2.686(1) and 2.780(1) Å (cf. the sum of van der Waals radii, ca. 3 Å).⁷⁵

The $[\text{H}_3\text{O}^+/\text{3H}_2\text{O}]_n$ network consists of O–H...O connected O_6 rings, with each O atom hydrogen-bonded to three other O atoms, as shown in Figure 3-5. The network "layer" can be denoted L6(6) using the nomenclature developed for H_2O networks.⁷⁶⁻⁷⁸ The O...O distances clearly show that the H_3O^+ ions (O1) and H_2O molecules (O2, O3) are ordered: O1...O2 and

O1...O3 are 2.590(1) and 2.5739(8) Å, respectively, and O2...O3 and O3...O3' are 2.8920(8) and 2.911(1) Å, respectively. The three H₃O⁺ H atoms and one H atom from each of the two types of H₂O molecules are also ordered. The second H atoms on O2 and O3 are disordered over two and three positions, respectively. The H₃O⁺ H atoms and the disordered H atoms on O2 and O3 are involved in hydrogen bonding within the L6(6) layers; the ordered H atoms on O2 and O3 each interact, in bifurcated fashion, with two F atoms as shown in Figure 3-8.

There are three types of O₆ rings, two of which are relatively planar and one of which is in a chair configuration. There is an (H₂O)₆ hexagon (two O2 and four O3 atoms, avg. displacement ±0.114 Å from the least-squares O₆ plane), the centroid for which is labelled X2 in Figure 3-5. There is also a [(H₃O)₂(H₂O)₄]²⁺ (or H₁₄O₆²⁺) hexagon (two O1, two O2, and two O3 atoms, avg. displacement ± 0.031 Å), which is similar in structure to the discrete H₁₄O₆²⁺ dihydronium hexagon found in the structure of (H₁₄O₆)₂(FeCl₄)₂Cl₂·C₃₆H₃₆N₂₄O₁₂·3H₂O^{79,80} and predicted to be stable as isolated H₁₄O₆²⁺ O₆ hexagons in the gas phase.⁸¹ The centroids of the O₆ hexagons are labelled X1 and X1' in Figure 3-5. The X1 and X1' O₆ hexagons are tilted 53.2° to one another and 59.0° to the X2 hexagon. Note that the ⊙...X1 and ⊙...X2 vectors, shown as dashed lines in Figure 3-5, are nearly coincident with B–F bonds such that the B₁₂F₁₂²⁻ anions are located in the triple-hexagon valleys, nearly centered over half of the O2 atoms in each network layer, as shown in Figure 3-6 (the other half of the O2 atoms are at triple-hexagon peaks and have B₁₂F₁₂²⁻ anions "beneath" them).

There are 10 B₁₂F₁₂²⁻ anions associated with a single unit cell, 8 at the corners and 2 on opposite faces, for a total of 2 complete anions as shown in Figure 3-7. The two B₁₂F₁₂²⁻ anions on opposite faces of the unit cell sit above and below the triple-hexagon valleys giving rise to the corrugated appearance of the [H₃O⁺/3H₂O]_n L6(6) network layers. There are 20 O atoms

associated with a single unit cell, 8 on faces, and 12 that are completely in the cell (including 4 H_3O^+ cations (O1)). Therefore, there are 4 H_3O^+ cations, 2 complete $\text{B}_{12}\text{F}_{12}^{2-}$ anions, and 12 complete H_2O molecules per unit cell.

The chair-configuration $[(\text{H}_3\text{O})_2(\text{H}_2\text{O})_4]^{2+}$ O_6 rings have two O1 atoms and four rigorously-coplanar O3 atoms. These rings combine with the triple-hexagon peaks and valleys to form the $[\text{H}_3\text{O}^+/3\text{H}_2\text{O}]_n$ L6(6) network layers in $(\text{H}_3\text{O})_2\text{B}_{12}\text{F}_{12}\cdot 6\text{H}_2\text{O}$. Although L6(6) layers involving only H_2O molecules are known, there is, as far as this author could find, only one other example of a structure that may contain an L6(6) layer formed by H_2O molecules and H_3O^+ ions (refcode BIKVIA10).⁸² However, the author of that study left open the possibility that none of the H_2O molecules in the L6(6) layer were protonated, which would be consistent with the observation that all of the O...O distances in the L6(6) layer were 2.77 Å or longer, and the three O...O distances involving the putative H_3O^+ ions were 2.83, 2.90, and 3.08 Å. Table 3-4 lists O...O distances for structures with unambiguous H_3O^+ ions hydrogen bonded to two or three H_2O molecules. All of those distances are ≤ 2.69 Å, and in every case at least one O...O distance per H_3O^+ ion is ≤ 2.58 Å including the $(\text{H}_3\text{O})_2\text{B}_{12}\text{F}_{12}\cdot 6\text{H}_2\text{O}$ presented in this work.

The tetrahydrate of the hydronium salt $(\text{H}_3\text{O})_2\text{B}_{12}\text{F}_{12}\cdot 4\text{H}_2\text{O}$ was synthesized and structurally characterized by collaborators Konrad Seppelt and his graduate student, Moritz Malischewski at Freie Universität Berlin, using $\text{K}_2\text{B}_{12}\text{F}_{12}$ synthesized and purified by the author of this dissertation. The Figures 3-11–3-15 result from the analysis of the $(\text{H}_3\text{O})_2\text{B}_{12}\text{F}_{12}\cdot 4\text{H}_2\text{O}$ structure by the author. The structural analysis focuses on the comparison to the $(\text{H}_3\text{O})_2\text{B}_{12}\text{F}_{12}\cdot 6\text{H}_2\text{O}$ structure, especially highlighting the differences in the hydrogen bonded O–H...O networks. The unit cell consists of 8 H_3O^+ cations, 4 $\text{B}_{12}\text{F}_{12}^{2-}$ anions (2 complete B_{12} cages and 4 others on faces of the cell), and 16 H_2O molecules, some H_2O molecules are entirely within the unit cell

and some are shared on faces. Following the same nomenclature used to describe the 2-dimensional hydrogen bonded $[\text{H}_3\text{O}^+/3\text{H}_2\text{O}]_n$ interconnected network in $(\text{H}_3\text{O})_2\text{B}_{12}\text{F}_{12}\cdot 6\text{H}_2\text{O}$ this structure can be described as L6(4)18(8). The $(\text{H}_3\text{O})_2\text{B}_{12}\text{F}_{12}\cdot 4\text{H}_2\text{O}$ has $[\text{H}_3\text{O}^+/2\text{H}_2\text{O}]_n$ interconnected networks with O...O distances between H_3O^+ ions and H_2O molecules of 2.463, 2.588, and 2.690 Å, and O...O distances between adjacent H_2O molecules ranging from 2.846, and 2.905 Å. There are two different H_3O^+ environments, one with 3 O...O interactions with adjacent H_2O molecules and the other environment has 2 O...O interactions with adjacent H_2O molecules and one O...F interaction (2.75 Å) with a $\text{B}_{12}\text{F}_{12}^{2-}$ anion. In the $(\text{H}_3\text{O})_2\text{B}_{12}\text{F}_{12}\cdot 4\text{H}_2\text{O}$ the $[\text{H}_3\text{O}^+/2\text{H}_2\text{O}]_n$ interconnected networks have a more pronounced corrugation compared to the $(\text{H}_3\text{O})_2\text{B}_{12}\text{F}_{12}\cdot 6\text{H}_2\text{O}$ structure (see Figures 3-11 and 3-12) wherein the B_{12} cages also oscillate up and down mimicking the corrugated pattern of the $[\text{H}_3\text{O}^+/2\text{H}_2\text{O}]_n$ layers and are not planar as observed in the $(\text{H}_3\text{O})_2\text{B}_{12}\text{F}_{12}\cdot 6\text{H}_2\text{O}$ structure. The B_{12} cages sit on opposite sides of the ring comprised of 18 oxygen atoms from H_3O^+ cations and H_2O . This shift in the B_{12} cage position has an interesting manifestation in the B_{12} cage nearest neighbors. Besides oscillating within a layer, the B_{12} cage centroids still occupy a distorted hexagonal close packed arrangement, however, the hexagonal close packed arrangement is not parallel with the $[\text{H}_3\text{O}^+/2\text{H}_2\text{O}]_n$ layers (Figure 3-13) like it was in the $(\text{H}_3\text{O})_2\text{B}_{12}\text{F}_{12}\cdot 6\text{H}_2\text{O}$ structure. Instead the close packed arrangement is at an angle of 34.2° with the B_{12} centroids. The hexagons comprised of 2 H_3O^+ cations antipodal to one another in the hexagon and 4 H_2O molecules are on opposite sides of a column of $\text{B}_{12}\text{F}_{12}^{2-}$ anions and are planar with a LSP of 0.028Å. The hexagons on the same side of a column of $\text{B}_{12}\text{F}_{12}^{2-}$ anions are rigorously parallel and are 69.8° from the hexagons on the other side of the column of $\text{B}_{12}\text{F}_{12}^{2-}$ anions (see Figure 3-12). The rings of 18 hydrogen bonded O...O waters and hydronium cations have 4 hexagons bordering them, two of the hexagons are

parallel to each other and are 69.8° from the other two hexagons. Centroids of the hydrogen bonded hexagons form a diamond in the unit cell with two of the centroids on the diagonal opposite edges of the unit cell and the other two centroids are on the faces perpendicular to the edge centroids of the unit cell (see Figure 3-14) forming a (011) plane in the unit cell. The centroid of each hexagon has a fluorine atom from 2 opposing $B_{12}F_{12}^{2-}$ anions, one on either side, pointing nearly perpendicular to the centroid with a distance of 1.315 \AA from the centroid. The nearest neighbor $\odot \cdots \odot$ distances in the $(H_3O)_2B_{12}F_{12} \cdot 4H_2O$ structure are on average smaller by 0.04 \AA , but have a range of $7.576\text{--}10.105$ compared with the range of $\odot \cdots \odot$ distances for $(H_3O)_2B_{12}F_{12} \cdot 6H_2O$ structure of $8.411\text{--}8.914 \text{ \AA}$. A table of all $\odot \cdots \odot$ distances, cell volume, Z and single crystal density for both the $(H_3O)_2B_{12}F_{12} \cdot 6H_2O$ structure and $(H_3O)_2B_{12}F_{12} \cdot 4H_2O$ structure are shown in Table 3-3.

3.3.3 Purity Analysis by 1H , $^{19}F[^{11}B]$, and $^{11}B[^{19}F]$ NMR Spectroscopy, and ICP-AES.

The product $(H_3O)_2B_{12}F_{12} \cdot nH_2O$ was 99.6+ mol% conversion of $K_2B_{12}F_{12}$ to $(H_3O)_2B_{12}F_{12} \cdot nH_2O$ after a single pass through an H^+ charged ion-exchange resin. Major metal contaminants were residual K^+ and Na^+ at concentrations of 180 ppm (0.22 mol%) and 77 ppm (0.16 mol%) respectively, measured by Bryon Britten by ICP-AES. All other ions measured by ICP-AES were less than 0.01 mol%. Further removal of K^+ and Na^+ required a second pass through a fresh H^+ charged ion-exchange resin column. The anion $B_{12}F_{12}^{2-}$ had a purity of 99.5+ mol% with no detectable BF_4^- as determined by $^{11}B[^{19}F]$ and $^{19}F[^{11}B]$ NMR spectra are shown in Figure 16. Molar equivalence of water for $(H_3O)_2B_{12}F_{12} \cdot nH_2O$ was initially determined to be $n = 4$ using an internal NMR standard. The standard should be such that a known ratio of F to H allowing ratios of the specific ^{19}F and 1H peaks to be correlated for relative F to H quantification.

The compound 1,4-bis(trifluoromethyl)benzene (PTFMB) was chosen as the standard as it yields only singlet ^{19}F and ^1H signals and has chemical shifts that do not overlap with the ^{19}F and ^1H signals of interest in the $(\text{H}_3\text{O})_2\text{B}_{12}\text{F}_{12}\cdot n\text{H}_2\text{O}$ analyte.

3.3.4 DSC analysis of $(\text{H}_3\text{O})_2\text{B}_{12}\text{F}_{12}\cdot 6\text{H}_2\text{O}$.

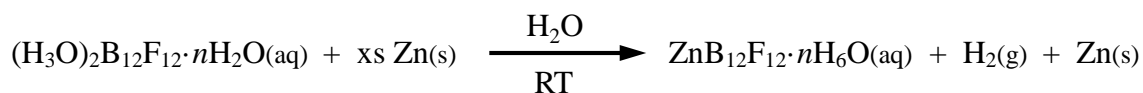
A DSC thermogram of $(\text{H}_3\text{O})_2\text{B}_{12}\text{F}_{12}\cdot 6\text{H}_2\text{O}$ exhibited a sharp endotherm indicative of a melting event with a peak maximum temperature (T_{max}) of $67.7\text{ }^\circ\text{C}$ and a broad exothermic event with a $T_{max} = 110.8\text{ }^\circ\text{C}$ (see Figure 3-17). Knowing the hygroscopicity of $(\text{H}_3\text{O})_2\text{B}_{12}\text{F}_{12}\cdot 6\text{H}_2\text{O}$ (deliquesces at $25\text{ }^\circ\text{C}$ if $P(\text{H}_2\text{O}) > 6(1)\text{ Torr}$, section 3.3.7) it can be deduced that $(\text{H}_3\text{O})_2\text{B}_{12}\text{F}_{12}\cdot 6\text{H}_2\text{O}$ (equivocally written as $\text{H}_2\text{B}_{12}\text{F}_{12}\cdot 8\text{H}_2\text{O}$) is essentially melting/dissolving at elevated temperatures. The gradual decrease in heat flow during the initial heating of the sample is likely due to loss of water from the sample preceding the melting event. The broad exothermic event observed at $T_{max} = 110.8\text{ }^\circ\text{C}$ is likely a slow reaction of the acid, $(\text{H}_3\text{O})_2\text{B}_{12}\text{F}_{12}\cdot n\text{H}_2\text{O}$, with the Al pan (note: Al will react with 1 M HCl; by unit cell volume, solid $(\text{H}_3\text{O})_2\text{B}_{12}\text{F}_{12}\cdot 6\text{H}_2\text{O}$ has a $[\text{H}_3\text{O}^+] = 7.29\text{ M}$). Finally a broad unknown endothermic event occurred at $194.6\text{ }^\circ\text{C}$, no other thermal events were observed up to $357\text{ }^\circ\text{C}$.

3.3.5 Raman and FT-IR of $(\text{H}_3\text{O})_2\text{B}_{12}\text{F}_{12}\cdot 6\text{H}_2\text{O}$ and $(\text{H}_3\text{O})_2\text{B}_{12}\text{F}_{12}$.

The IR and Raman spectra of $(\text{H}_3\text{O})_2\text{B}_{12}\text{F}_{12}\cdot 6\text{H}_2\text{O}$ and $(\text{H}_3\text{O})_2\text{B}_{12}\text{F}_{12}$ (IR exhibited B–F stretching and broad, non-descriptive O–H stretching, Raman exhibited B–B stretching) were not very diagnostic, and it was not possible to determine whether $(\text{H}_3\text{O})_2\text{B}_{12}\text{F}_{12}$ is molecular (i.e., the H_3O^+ ions do not bridge $\text{B}_{12}\text{F}_{12}^{2-}$ anions) or has $\text{B}_{12}\text{F}_{12}^{2-}$ anions bridged by H_3O^+ ions.

3.3.6 Synthesis of Metal Salts Using $(\text{H}_3\text{O})_2\text{B}_{12}\text{F}_{12}\cdot n\text{H}_2\text{O}$ as a reagent: $\text{ZnB}_{12}\text{F}_{12}\cdot 6\text{H}_2\text{O}$ Proof of Concept.

Because of the ability to easily purify the $(\text{H}_3\text{O})_2\text{B}_{12}\text{F}_{12}\cdot n\text{H}_2\text{O}$ and make a specific hydration state under the right temperature and humidity conditions, the $(\text{H}_3\text{O})_2\text{B}_{12}\text{F}_{12}\cdot n\text{H}_2\text{O}$ salt is ideal as a starting material for making other metal salts. Due to the acidity of the $(\text{H}_3\text{O})_2\text{B}_{12}\text{F}_{12}\cdot n\text{H}_2\text{O}$ salt it was used to oxidize a more reactive neutral metal Zn^0 forming the hydrated metal salt of $\text{B}_{12}\text{F}_{12}^{2-}$. As a proof of concept $\text{ZnB}_{12}\text{F}_{12}\cdot 6\text{H}_2\text{O}$ was synthesized by the author of this dissertation in the following reaction scheme shown below and crystallized.



By using the neutral metal it was easy to make the salt cleanly with excess Zn metal, then filtering unreacted solid once the reaction was complete. This way the desired salt is formed with no impurities and the hydration state of the $(\text{H}_3\text{O})_2\text{B}_{12}\text{F}_{12}\cdot n\text{H}_2\text{O}$ salt does not have to be precisely known since the acid Zn^0 reaction will go to completion. The crystals of $\text{ZnB}_{12}\text{F}_{12}\cdot 6\text{H}_2\text{O}$ grown from water by this author and the crystal structure obtained by Brian Newell is shown in Figure 3-18. Other metal salts could be synthesized from the $(\text{H}_3\text{O})_2\text{B}_{12}\text{F}_{12}\cdot n\text{H}_2\text{O}$ salt using $\text{M}(\text{OH})_x$, M_2O_x , or $\text{M}_2(\text{CO}_3)_x$ by starting with a known concentration solution of $(\text{H}_3\text{O})_2\text{B}_{12}\text{F}_{12}\cdot n\text{H}_2\text{O}$ (determined by common acid base titration) and reacting with the proper equivalence of $\text{M}(\text{OH})_x$, M_2O_x , or $\text{M}_2(\text{CO}_3)_x$. All of the above methods will initially make $\text{M}_2(\text{B}_{12}\text{F}_{12})_x \cdot 6\text{H}_2\text{O}$ salts, similar to $\text{ZnB}_{12}\text{F}_{12}\cdot 6\text{H}_2\text{O}$, however, if rigorously anhydrous salts are required the H_2O ligands can be exchanged for a different ligand by recrystallization from a solution of the desired ligand. For example $\text{ZnB}_{12}\text{F}_{12}\cdot 6\text{H}_2\text{O}$ can be converted to $\text{ZnB}_{12}\text{F}_{12}\cdot n\text{CH}_3\text{CN}$ by dissolving

ZnB₁₂F₁₂·6H₂O in CH₃CN and recrystallizing the compound. It is known from previous work by Dmitry Peryshkov that attempting to thermally dehydrate M(B₁₂F₁₂)·6H₂O salts (where M = Co²⁺, Mg²⁺, Ni²⁺, Zn²⁺) in the TGA led to decomposition, see Figure 3-19.

3.3.7 Hydration/Dehydration of (H₃O)₂B₁₂F₁₂·nH₂O by TGA.

Thermogravimetric measurements (see Figure 3-20) demonstrate that (H₃O)₂B₁₂F₁₂·6H₂O undergoes rapid dehydration in three discrete stages to (H₃O)₂B₁₂F₁₂·4H₂O, (H₃O)₂B₁₂F₁₂·2H₂O, and (H₃O)₂B₁₂F₁₂, depending on the temperature and the pressure of water vapor present. The crystalline phase (H₃O)₂B₁₂F₁₂·6H₂O is stable at 25 °C when $P(\text{H}_2\text{O}) = 6$ Torr (i.e., in the presence of dry He that has been bubbled through a saturated aqueous solution of MgCl₂ at 20 °C) but is deliquescent at 25 °C when $P(\text{H}_2\text{O}) > 6$ Torr. The phase (H₃O)₂B₁₂F₁₂·4H₂O is stable at 55 °C when $P(\text{H}_2\text{O}) = 6$ Torr taking 11.7 min for the dehydration to take place from the hexahydrate. The phase (H₃O)₂B₁₂F₁₂·2H₂O is stable at 120 °C when $P(\text{H}_2\text{O}) = 6$ Torr requiring 7.4 min for dehydration to take place from the tetrahydrate. In the absence of water vapor at 150 °C, the mass of the sample corresponds to (H₃O)₂B₁₂F₁₂ requiring 72.7 min to dehydrate from (H₃O)₂B₁₂F₁₂·2H₂O. Rehydration to the hexahydrate from (H₃O)₂B₁₂F₁₂ (taking up 6 eq. of H₂O) was the slowest process taking 105.6 min. The mass of these hydrate phases corresponds well to the theoretical mass percent starting from the (H₃O)₂B₁₂F₁₂·6H₂O hydrate phases and then losing 2 waters per phase change (see Table 3-5). A second experiment to determine the rate of rehydration from the (H₃O)₂B₁₂F₁₂·2H₂O gaining 2 eq. of H₂O to form (H₃O)₂B₁₂F₁₂·4H₂O (the temperature at which (H₃O)₂B₁₂F₁₂·4H₂O is stable) showed that (H₃O)₂B₁₂F₁₂·2H₂O at 55 °C and

$P(\text{H}_2\text{O}) = 6$ Torr (the temperature and humidity conditions at which $(\text{H}_3\text{O})_2\text{B}_{12}\text{F}_{12}\cdot 4\text{H}_2\text{O}$ is stable) did not gain mass after 15 min. The $(\text{H}_3\text{O})_2\text{B}_{12}\text{F}_{12}\cdot 2\text{H}_2\text{O}$ hydrate phase only began to take up H_2O once the sample was cooled to 35 °C. At 35 °C and $P(\text{H}_2\text{O}) = 6$ Torr the hydration rate of $(\text{H}_3\text{O})_2\text{B}_{12}\text{F}_{12}\cdot 2\text{H}_2\text{O}$ was $0.043 \text{ mg min}^{-1}$ and while cooled to 25 °C from 35 °C the hydration rate slowed to $0.033 \text{ mg min}^{-1}$.

3.3.8 DFT Structure Calculations of $(\text{H}_3\text{O})_2\text{B}_{12}\text{F}_{12}$ and $\text{H}_2\text{B}_{12}\text{F}_{12}$.

Tentatively assuming molecularity, the PBE0 DFT-predicted molecular structures of $(\text{H}_3\text{O})_2\text{B}_{12}\text{F}_{12}$ and the putative superacid $\text{H}_2\text{B}_{12}\text{F}_{12}$ are shown in Figure 3-21 and relevant interatomic distances are listed in Table 3-6, the PBE0 DFT-optimized coordinates for $\text{B}_{12}\text{F}_{12}^{2-}$, $(\text{H}_3\text{O})_2\text{B}_{12}\text{F}_{12}$, and $\text{H}_2\text{B}_{12}\text{F}_{12}$ are listed in Tables 3-7, 3-8, and 3-9 respectively, DFT calculations performed by collaborator Dr. Alexey A. Popov at IFW Leibniz Institute for Solid State and Materials Research Dresden Germany.

3.3.9 Thermal Stability of $(\text{H}_3\text{O})_2\text{B}_{12}\text{F}_{12}\cdot n\text{H}_2\text{O}$, and attempted dehydration to $\text{H}_2\text{B}_{12}\text{F}_{12}$.

Thermal stability of $(\text{H}_3\text{O})_2\text{B}_{12}\text{F}_{12}\cdot n\text{H}_2\text{O}$ was investigated by TGA and long duration heating in a tube furnace. A TGA experiment of $(\text{H}_3\text{O})_2\text{B}_{12}\text{F}_{12}\cdot n\text{H}_2\text{O}$ exhibited mass loss greater than that expected to form the hypothetical $\text{H}_2\text{B}_{12}\text{F}_{12}$ compound, indicating decomposition, thermogram shown in Figure 3-22. From multiple TGA experiments it is known that $(\text{H}_3\text{O})_2\text{B}_{12}\text{F}_{12}\cdot 0\text{H}_2\text{O}$ is the stable hydrate at 150 °C and $P(\text{H}_2\text{O}) = 0$ Torr. A correction of the adjusted final mass percent of $\text{H}_2\text{B}_{12}\text{F}_{12}$ in the experiment in Figure 3-22 was ca. 72.76%; if the $\text{H}_2\text{B}_{12}\text{F}_{12}$ phase was stable at 300 °C and $P(\text{H}_2\text{O}) = 0$ Torr the mass should have remained constant after reaching 72.76%. At 300 °C the sample continued to lose mass below 72.76% to

ca. 72.63%, a difference of 0.13% from the theoretical mass of $\text{H}_2\text{B}_{12}\text{F}_{12}$. Previous TGA experiments indicated that each $(\text{H}_3\text{O})_2\text{B}_{12}\text{F}_{12} \cdot n\text{H}_2\text{O}$ phase was stable under certain conditions for 30 min and had excellent agreement with the theoretical masses shown in Table 3-5, however in this experiment the experimental mass was trending down over the 30 min time period and the final mass after 30 min was not in good agreement with the theoretical mass. The 300 °C TGA sample cooled to room temp in the TGA inert atmosphere and was collected and analyzed by ^{19}F NMR spectroscopy in CD_3CN shown in Figure 3-23 exhibiting a multiplet of at least 6 peaks rather than the typical doublet peak at ca. -270 ppm. Mass spectrometry via NI-ESI-MS shown in Figure 3-24 revealed anions consistent with $\text{B}_{12}\text{F}_{11}\text{OH}^{2-}$ ($m/z = 357.1$ for $\text{B}_{12}\text{F}_{11}\text{OH}_2^-$ vs. $m/z = 359.7$ for $\text{B}_{12}\text{F}_{12}^-$) indicating that rapid thermal drying of $(\text{H}_3\text{O})_2\text{B}_{12}\text{F}_{12} \cdot n\text{H}_2\text{O}$ to $\text{H}_2\text{B}_{12}\text{F}_{12}$ is not a reversible process and it likely involves the process of substitution of F groups for OH groups on the B_{12} cage as the last water is removed. This result is not surprising since the first reported synthesis of $\text{B}_{12}\text{F}_{12}^{2-}$ in 1962 actually resulted in producing $\text{B}_{12}\text{F}_{11}\text{OH}^{2-}$.⁸³

A longer thermal stability test was performed on $(\text{H}_3\text{O})_2\text{B}_{12}\text{F}_{12} \cdot n\text{H}_2\text{O}$ to assess if hydroxyl substitution would occur at a lower temperature over an extended period of time. A recrystallized $(\text{H}_3\text{O})_2\text{B}_{12}\text{F}_{12} \cdot n\text{H}_2\text{O}$ sample was placed in a long glass ampoule with an air-free Teflon® valve whereby the sample was put under dynamic vacuum, slowly heated to 200 °C, and held isothermally at ca. 200 ± 2 °C for 24 h. After 24 h the sample was collected for NMR analysis following common inert atmosphere techniques. The resulting ^{19}F NMR spectrum shown in Figure 3-25 indicated that at 200 °C, for 24 h, no observable decomposition had occurred.

The $(\text{H}_3\text{O})_2\text{B}_{12}\text{F}_{12} \cdot n\text{H}_2\text{O}$ was shown to decompose in the rapidly heated TGA experiment when heated to 300 °C, thus the desired synthetic target $\text{H}_2\text{B}_{12}\text{F}_{12}$ was not isolated. However, at 200 °C for 24 h under dynamic vacuum a $(\text{H}_3\text{O})_2\text{B}_{12}\text{F}_{12}$ material survived and did not exhibit any

changes in the $^{11}\text{B}[^{19}\text{F}]$ or $^{19}\text{F}[^{11}\text{B}]$ NMR spectra. This indicates that the compound is stable at this temperature, but did not indicate what hydrate phase was present. Based on previous experience with hydration/dehydration states of $(\text{H}_3\text{O})_2\text{B}_{12}\text{F}_{12}\cdot n\text{H}_2\text{O}$, it is believed under dynamic vacuum at 200 °C the sample should have been in the $(\text{H}_3\text{O})_2\text{B}_{12}\text{F}_{12}\cdot 0\text{H}_2\text{O}$ hydrate phase.

3.3.10 Thermal behavior of $(\text{NH}_4)_2\text{B}_{12}\text{F}_{12}\cdot n\text{H}_2\text{O}$ and Stable Hydrates.

Since the desired $\text{H}_2\text{B}_{12}\text{F}_{12}$ could not be formed by thermal dehydration of $(\text{H}_3\text{O})_2\text{B}_{12}\text{F}_{12}\cdot n\text{H}_2\text{O}$, then a new synthetic route was proposed. It was hypothesized from a previous thermal stability experiment of $(\text{NH}_4)_2\text{B}_{12}\text{F}_{12}\cdot n\text{H}_2\text{O}$ (work by Dmitry Peryshkov) that it might be possible to thermally dehydrate $(\text{NH}_4)_2\text{B}_{12}\text{F}_{12}\cdot n\text{H}_2\text{O}$ to $(\text{NH}_4)_2\text{B}_{12}\text{F}_{12}$ then in the last step thermally remove 2 eq. of NH_3 leaving behind the super acid $\text{H}_2\text{B}_{12}\text{F}_{12}$, the thermogram is shown in Figure 3-26. At the time the only known hydrate phase of $(\text{NH}_4)_2\text{B}_{12}\text{F}_{12}\cdot n\text{H}_2\text{O}$ was $n = 2$ shown by a crystal structure of $(\text{NH}_4)_2\text{B}_{12}\text{F}_{12}\cdot 2\text{H}_2\text{O}$ by Dmitry Peryshkov.³⁴ To test the thermal removal of 2 eq. $\text{NH}_3(\text{g})$ a TGA experiment was performed with $(\text{NH}_4)_2\text{B}_{12}\text{F}_{12}\cdot n\text{H}_2\text{O}$ made by neutralizing $(\text{H}_3\text{O})_2\text{B}_{12}\text{F}_{12}\cdot n\text{H}_2\text{O}(\text{aq})$ with $\text{NH}_4\text{OH}(\text{aq})$ and recrystallized from water, performed by W. Matt Jones. Prior to attempting to make $\text{H}_2\text{B}_{12}\text{F}_{12}$ from $(\text{NH}_4)_2\text{B}_{12}\text{F}_{12}\cdot n\text{H}_2\text{O}$ a TGA experiment was performed to determine a stable hydrate phase as so a known hydrate phase and starting composition could be used for the experiment. It was found that $(\text{NH}_4)_2\text{B}_{12}\text{F}_{12}\cdot 2\text{H}_2\text{O}$ is stable with $P(\text{H}_2\text{O}) = 6$ Torr or $P(\text{H}_2\text{O}) = 0$ Torr water vapor over the sample at 25 °C. Also it was found that the $(\text{NH}_4)_2\text{B}_{12}\text{F}_{12}\cdot n\text{H}_2\text{O}$ loses 2 eq. H_2O slowly at 35–50 °C and $P(\text{H}_2\text{O}) = 0$ Torr. Next, a long-term thermal stability experiment on $(\text{NH}_4)_2\text{B}_{12}\text{F}_{12}\cdot n\text{H}_2\text{O}$ performed by W. Matt Jones indicated the increased thermal stability over $(\text{H}_3\text{O})_2\text{B}_{12}\text{F}_{12}\cdot n\text{H}_2\text{O}$ by slow thermal dehydration under dynamic vacuum. In this experiment a sample of

$(\text{NH}_4)_2\text{B}_{12}\text{F}_{12}\cdot n\text{H}_2\text{O}$ was heated at a rate of $2.0\text{ }^\circ\text{C min}^{-1}$ to $200\text{ }^\circ\text{C}$ held isothermal for 24 h under dynamic vacuum in a long glass ampoule with an air-free Teflon® valve. After 24 h the temperature was increased at a rate of $2.0\text{ }^\circ\text{C min}^{-1}$ to $300\text{ }^\circ\text{C}$ and the sample was again held isothermally at $300\text{ }^\circ\text{C}$ for 24 h under dynamic vacuum. The sample, once dried, was treated rigorously anhydrous and the entire sealed ampoule was pumped into a glovebox. The sample appeared brown/grey in color, a sample of this material was analyzed by $^{11}\text{B}[^{19}\text{F}]$, and $^{19}\text{F}[^{11}\text{B}]$ NMR in dry CD_3CN is shown in Figure 3-27, and ^1H NMR in dry CD_3CN is shown in Figure 3-28.

Finally, a TGA experiment was performed to make $\text{H}_2\text{B}_{12}\text{F}_{12}$ from the more thermally stable $(\text{NH}_4)_2\text{B}_{12}\text{F}_{12}\cdot n\text{H}_2\text{O}$ by the thermal loss of 2 eq. NH_3 . A sample of $(\text{NH}_4)_2\text{B}_{12}\text{F}_{12}\cdot 2\text{H}_2\text{O}$ was equilibrated in the TGA then the temperature was slowly increased observing mass loss (see Figure 3-29). The theoretical mass of the $(\text{NH}_4)_2\text{B}_{12}\text{F}_{12}\cdot n\text{H}_2\text{O}$ and its hydrate phases is shown in Table 3-10. From Figure 3-29 the first mass loss equated to 2 eq. of H_2O and occurred slowly (ca. 57 min to lose 2 eq. H_2O) at a temperature range of ca. $35\text{--}50\text{ }^\circ\text{C}$. The $(\text{NH}_4)_2\text{B}_{12}\text{F}_{12}$ salt was stable at $50\text{ }^\circ\text{C}$ and up to ca. $450\text{ }^\circ\text{C}$. After the temperature was increased past $450\text{ }^\circ\text{C}$ the sample began to lose mass, but the observed mass loss continued past the theoretical mass corresponding to $\text{H}_2\text{B}_{12}\text{F}_{12}$.

3.3.11 Crystal Structure of $(\text{NH}_4)_2\text{B}_{12}\text{F}_{12}\cdot 4\text{H}_2\text{O}$, Alternative Hypothesis for Two Discrete Mass Losses in $(\text{NH}_4)_2\text{B}_{12}\text{F}_{12}\cdot n\text{H}_2\text{O}$ TGA.

In the process of preparing a purified sample of $(\text{NH}_4)_2\text{B}_{12}\text{F}_{12}\cdot n\text{H}_2\text{O}$ for the TGA experiment to thermally make $\text{H}_2\text{B}_{12}\text{F}_{12}$ by loss of $n\text{H}_2\text{O}$ and 2 eq. NH_3 , W. Matt Jones crystallized a sample of $(\text{NH}_4)_2\text{B}_{12}\text{F}_{12}\cdot n\text{H}_2\text{O}$ that had a different unit cell than previously observed by Dmitry Peryshkov.³⁴ The SC-XRD was collected, the structure was solved and refined by this author and

determined to be $(\text{NH}_4)_2\text{B}_{12}\text{F}_{12}\cdot 4\text{H}_2\text{O}$, shown in Figures 3-30–3-32. The $(\text{NH}_4)_2\text{B}_{12}\text{F}_{12}\cdot 4\text{H}_2\text{O}$ hydrate phase was not stable in air and would lose 2 eq. of H_2O to form the $(\text{NH}_4)_2\text{B}_{12}\text{F}_{12}\cdot 2\text{H}_2\text{O}$ at ambient temperature and humidity conditions. The $(\text{NH}_4)_2\text{B}_{12}\text{F}_{12}\cdot 4\text{H}_2\text{O}$ single crystal data collection was performed at $-40\text{ }^\circ\text{C}$ since temperatures lower than $-40\text{ }^\circ\text{C}$ cracked the crystal, likely due to a phase change.

The $(\text{NH}_4)_2\text{B}_{12}\text{F}_{12}\cdot 4\text{H}_2\text{O}$ does have a significant hydrogen network with one disordered water molecule about a special position, (see Figures 3-30 and 3-31) however, this network is continuous in only 1 dimension instead of two dimensions as observed in the $(\text{H}_3\text{O})_2\text{B}_{12}\text{F}_{12}\cdot 6\text{H}_2\text{O}$ and $(\text{H}_3\text{O})_2\text{B}_{12}\text{F}_{12}\cdot 4\text{H}_2\text{O}$ structures. The $(\text{NH}_4)_2\text{B}_{12}\text{F}_{12}\cdot 4\text{H}_2\text{O}$ hydrogen bonded structure would be considered a T4(2)6(2) following the literature nomenclature.^{77,78} The hydrogen bonded network of $[\text{NH}_4^+/\text{2H}_2\text{O}]_n$ in the $(\text{NH}_4)_2\text{B}_{12}\text{F}_{12}\cdot 4\text{H}_2\text{O}$ structure has $\text{N}\cdots\text{O}$ distances of 2.794 and 2.913 Å for $\text{N1}\cdots\text{O1}$ and $\text{N1}\cdots\text{O1}'$ respectively, and $\text{N1}\cdots\text{O3}$, $\text{N1}\cdots\text{O3}'$ distances of 2.861 and 2.950 Å respectively, and $\text{O1}\cdots\text{O2}$ distances of 2.850 Å (see Figure 3-32). The 6 membered rings are made up of 2 NH_4^+ cations, 4 water molecules, one of which is disordered and the ring is not planar and deviates from the LSP by 0.145 Å. The 4 membered ring made up of 2 NH_4^+ cations and 2 H_2O molecules is rigorously planar, and is 51.4° tilted from the 6 membered rings on either side as shown in Figure 3-30. The hydrogen from the NH_4 (N1 in Figure 3-32) not forming the 4 or 6 membered ring interacts with 3 fluorine atoms from 2 adjacent $\text{B}_{12}\text{F}_{12}^{2-}$ anions having H–F distances of 2.264, 2.488 and 2.770 Å. The non-ring hydrogen on O1 (O1 in Figure 3-32) also has 3 H–F interactions with distances of 2.170, 2.556, and 2.761 Å. The oxygen resting on a special position O2, (i.e. not disordered) has both hydrogens interacting with 3 fluorine atoms each with distances of 2.260, 2.862, and 2.911 Å. Finally, the water disordered about a special position, O3, has 2 interactions per hydrogen with distances (one hydrogen disordered, the other

on the inversion plane) of 2.492, 2.829, 2.664 and 2.872 Å. The $B_{12}F_{12}^{2-}$ anions are in a distorted cubic close packed arrangement as can be seen in Figure 3-31 with $B_{12}F_{12}^{2-} \odot \cdots \odot$ distances ranging from 7.051–9.760 Å as shown in Table 3-3.

3.4 Discussion

3.4.1 Synthesis of $(H_3O)_2B_{12}F_{12} \cdot nH_2O$ by Strong-Acid Cation-Exchange Resin.

Due to the aforementioned problems with known methods to synthesize $(H_3O)_2B_{12}F_{12} \cdot nH_2O$ or $H_2B_{12}F_{12}$ (Section 3.2), strong cation exchange resin was successfully used to convert highly purified $K_2B_{12}F_{12}$ into highly purified $(H_3O)_2B_{12}F_{12} \cdot nH_2O$. The resulting $(H_3O)_2B_{12}F_{12} \cdot nH_2O$ product had a light brown color from the resin (known as resin throw, or resin leech) and was demonstrated to be separated by recrystallization from dd- H_2O producing colorless $(H_3O)_2B_{12}F_{12} \cdot nH_2O$. The higher grade Purolite UWC 9126 strong acid cation exchange resin produced a material with less intense color and no observable impurity peaks by 1H NMR indicating the quality of cation exchange resin had an impact on product purity and should be considered when using resin for this application. This method allowed for preparation of $(H_3O)_2B_{12}F_{12} \cdot nH_2O$ with high cation and anion purity as determined by ICP-AES and 1H , $^{19}F[^{11}B]$, and $^{11}B[^{19}F]$ NMR respectively. Finally this method of producing $(H_3O)_2B_{12}F_{12} \cdot nH_2O$ for many applications (electrolyte, synthetic intermediate) was shown to be simple and convenient to scale for future applications.

3.4.2 Hydration/Dehydration of $(H_3O)_2B_{12}F_{12} \cdot nH_2O$ by TGA.

The $(H_3O)_2B_{12}F_{12} \cdot nH_2O$ salt exhibited 4 reversible hydration states, $n = 6, 4, 2,$ and 0 , the conditions at which each state exists were previously described. The rate at which each hydrate

phase transitions to the next phase occurs upon loss of 2 eq. of H₂O, is of interest as it allows direct to comparison with the $\text{K}_2\text{B}_{12}\text{F}_{12}\cdot 2\text{H}_2\text{O}(\text{s}) \rightarrow \text{K}_2\text{B}_{12}\text{F}_{12}(\text{s}) + 2\text{H}_2\text{O}(\text{g}) \rightarrow \text{K}_2\text{B}_{12}\text{F}_{12}\cdot 2\text{H}_2\text{O}(\text{s})$ latent porosity system investigated by Peryshkov et al.^{34,40} In the case of $\text{K}_2\text{B}_{12}\text{F}_{12}$, it hydrated in ca. 4 min taking up 2 eq. of H₂O (expanding the lattice volume by 11%) at 25 °C with $P(\text{H}_2\text{O}) = 21$ Torr, and dehydrated in ca. 21 min losing 2 eq. of H₂O at 25 °C with $P(\text{H}_2\text{O}) = 0$ Torr. The $(\text{H}_3\text{O})_2\text{B}_{12}\text{F}_{12}\cdot 6\text{H}_2\text{O}$ hydrate phase is stable at 25 °C $P(\text{H}_2\text{O}) = 6$ Torr. Comparatively the $(\text{H}_3\text{O})_2\text{B}_{12}\text{F}_{12}\cdot 6\text{H}_2\text{O}$ hydrate phase lost 2 eq. of H₂O (decreasing the lattice volume by 6.8%) to form the $(\text{H}_3\text{O})_2\text{B}_{12}\text{F}_{12}\cdot 4\text{H}_2\text{O}$ hydrate phase in 11.7 min at 55 °C with $P(\text{H}_2\text{O}) = 6$ Torr. Similarly the $(\text{H}_3\text{O})_2\text{B}_{12}\text{F}_{12}\cdot 4\text{H}_2\text{O}$ hydrate phase lost 2 eq. of H₂O to form the $(\text{H}_3\text{O})_2\text{B}_{12}\text{F}_{12}\cdot 2\text{H}_2\text{O}$ hydrate phase in 7.4 min at 120 °C with $P(\text{H}_2\text{O}) = 6$ Torr. The loss of the last 2 eq. of H₂O to form the $(\text{H}_3\text{O})_2\text{B}_{12}\text{F}_{12}\cdot 0\text{H}_2\text{O}$ hydrate phase was considerably slower, taking 72.7 min at 150 °C with $P(\text{H}_2\text{O}) = 0$ Torr. Rehydration to the hexahydrate (taking up 6 eq. of H₂O) was the slowest process taking 105.6 min, however it should be noted that rehydration was occurring while the TGA was cooling down. In a separate experiment, rehydration to the tetrahydrate from the dihydrate at 55 °C and $P(\text{H}_2\text{O}) = 6$ Torr did not gain mass after 15 min. The $(\text{H}_3\text{O})_2\text{B}_{12}\text{F}_{12}\cdot 2\text{H}_2\text{O}$ hydrate phase only began to take up H₂O once the sample was cooled to 35 °C. At 35 °C and $P(\text{H}_2\text{O}) = 6$ Torr the hydration rate of $(\text{H}_3\text{O})_2\text{B}_{12}\text{F}_{12}\cdot 2\text{H}_2\text{O}$ was 0.043 mg min⁻¹ and while cooling to 25 °C from 35 °C the hydration rate slowed to 0.033 mg min⁻¹. The $(\text{H}_3\text{O})_2\text{B}_{12}\text{F}_{12}\cdot 2\text{H}_2\text{O}$ did not take up H₂O vapor until cooled to 35 °C, which is similar to metal salts of $\text{B}_{12}\text{F}_{12}^{2-}$ that also will not take up H₂O vapor until a certain temperature is reached. The low temperature requirement for H₂O uptake occurs in these salts because the rate of H₂O escaping from the sample needs to be slower than H₂O entering the sample. The rate of both processes is controlled

by temperature and so there is a maximum temperature above which the sample will not take up H₂O vapor.

3.4.3 DFT Structure Calculations of (H₃O)₂B₁₂F₁₂ and H₂B₁₂F₁₂.

In the DFT predicted structure of (H₃O)₂B₁₂F₁₂ it was found that the H₃O⁺ ions cause lengthening of the B–F bonds (and accompanying shortening of the affected B–B bonds), and the isolated (H₃O)₂B₁₂F₁₂ molecule appears to be stable. The isolated ion pair (H₃O)⁺ B₁₂F₁₂²⁻ was also found to be stable, in contrast to the H₃O⁺ BF₄⁻ ion pair, which has been shown to spontaneously form HF and BF₃OH by MP2 and DFT calculations.⁸¹ The putative superacid H₂B₁₂F₁₂ also appears to be stable, according to these calculations, and gives further evidence that H₂B₁₂F₁₂ should be a stable and attainable synthetic target. It should be noted that the abnormally long B–B bonds of 2.06 Å, and, the abnormally short F1...F2 distances of 3.02 Å indicate that H₂B₁₂F₁₂ may be very reactive, and therefore difficult to isolate under ambient conditions.

3.4.4 Comparison of Hydrogen Bonded Networks in (H₃O)₂B₁₂F₁₂·4H₂O and (NH₄)₂B₁₂F₁₂·4H₂O Crystal Structures.

The tetrahydrate structure of both the H₃O⁺ and the NH₄⁺ salts of B₁₂F₁₂²⁻ allows for direct comparisons between the H₃O⁺ and the NH₄⁺ cations in this system. The shortest O–H...O distance in (H₃O)₂B₁₂F₁₂·4H₂O is 2.463 Å compared to the shortest N–H...O distance in (NH₄)₂B₁₂F₁₂·4H₂O of 2.794 Å, a difference of 0.331 Å. The longer N–H...O distance is empirical evidence of the significantly stronger hydrogen bond formed by H₂O with H₃O⁺ compared to NH₄⁺. Next, the (NH₄)₂B₁₂F₁₂·4H₂O only exhibits a hydrogen bonded network that extends infinitely in 1-dimension compared with a hydrogen bonded network that extends

infinitely in 2-dimensions observed in the $(\text{H}_3\text{O})_2\text{B}_{12}\text{F}_{12}\cdot 4\text{H}_2\text{O}$. The 1-dimensional network in $(\text{NH}_4)_2\text{B}_{12}\text{F}_{12}\cdot 4\text{H}_2\text{O}$ is likely the result of weaker N–H \cdots O interactions leading to more hydrogen bonding with $\text{B}_{12}\text{F}_{12}^{2-}$ anions (compare hydrogen bonding environment in Figures 3-8 and 3-32). Due the crystal structures being collected at temperatures that differ by 100 K, the $\text{B}_{12}\text{F}_{12}^{2-}$ $\odot\cdots\odot$ distances and calculated crystal densities cannot be directly compared. However, the crystal density derived from SC-XRD of $(\text{H}_3\text{O})_2\text{B}_{12}\text{F}_{12}\cdot 4\text{H}_2\text{O}$ is 5.4% more dense than $(\text{NH}_4)_2\text{B}_{12}\text{F}_{12}\cdot 4\text{H}_2\text{O}$, and the avg. $\text{B}_{12}\text{F}_{12}^{2-}$ $\odot\cdots\odot$ distances in $(\text{H}_3\text{O})_2\text{B}_{12}\text{F}_{12}\cdot 4\text{H}_2\text{O}$ are 2.1% smaller than $(\text{NH}_4)_2\text{B}_{12}\text{F}_{12}\cdot 4\text{H}_2\text{O}$.

3.4.5 Apparent Volume of Water Molecules in K^+ , NH_4^+ , and H_3O^+ Hydrated salts of $\text{B}_{12}\text{F}_{12}^{2-}$.

During the structural analysis of $(\text{H}_3\text{O})_2\text{B}_{12}\text{F}_{12}\cdot 6\text{H}_2\text{O}$, $(\text{H}_3\text{O})_2\text{B}_{12}\text{F}_{12}\cdot 4\text{H}_2\text{O}$ and $(\text{NH}_4)_2\text{B}_{12}\text{F}_{12}\cdot 4\text{H}_2\text{O}$ it was simple enough to determine the volume one water molecule occupies in the $(\text{H}_3\text{O})_2\text{B}_{12}\text{F}_{12}\cdot n\text{H}_2\text{O}$ and $(\text{NH}_4)_2\text{B}_{12}\text{F}_{12}\cdot n\text{H}_2\text{O}$ hydrated salts. The volume of 2 water molecules could be determined by taking the unit cell volume divided by Z for two different hydrate phases of the same salt, then taking the difference between the volumes per asymmetric units of each hydrate of the same salt. Using this analysis the volume of H_2O in the H_3O^+ salt in going from $(\text{H}_3\text{O})_2\text{B}_{12}\text{F}_{12}\cdot 6\text{H}_2\text{O}$ to $(\text{H}_3\text{O})_2\text{B}_{12}\text{F}_{12}\cdot 4\text{H}_2\text{O}$ is 15.4 \AA^3 . Using the same analysis for the two known hydrates of the NH_4^+ salt, the volume of H_2O in going from $(\text{NH}_4)_2\text{B}_{12}\text{F}_{12}\cdot 4\text{H}_2\text{O}$ to $(\text{NH}_4)_2\text{B}_{12}\text{F}_{12}\cdot 2\text{H}_2\text{O}$ is 34.2 \AA^3 over 100% larger volume. For comparison a similar analysis was performed for $\text{K}_2\text{B}_{12}\text{F}_{12}\cdot 2\text{H}_2\text{O}$ going to $\text{K}_2\text{B}_{12}\text{F}_{12}$ and $\text{K}_2\text{B}_{12}\text{F}_{12}\cdot 4\text{H}_2\text{O}$ going to $\text{K}_2\text{B}_{12}\text{F}_{12}\cdot 2\text{H}_2\text{O}$ yielding volumes of H_2O molecules of 17.9 \AA^3 and 28.1 \AA^3 respectively. Using the density of ice at 0 °C the calculated volume of water is 32.7 \AA^3 (calculated volume of water

at $-100\text{ }^{\circ}\text{C}$ is ca. 1% smaller) An important note to point out is that this method of determining the volume of a water molecule assumes that there is no empty space in the unit cell.

At first glance this difference of almost 100% in the volume of a water molecule between the NH_4^+ and H_3O^+ salts seems unlikely, but if analyzed differently the apparent changing size of water (caused by hydrogen bonding and other lattice interactions) makes more sense than differences in volume of the cations or $\text{B}_{12}\text{F}_{12}^{2-}$ anion. First, if one subtracts the asymmetric unit volume of $(\text{H}_3\text{O})_2\text{B}_{12}\text{F}_{12}\cdot 4\text{H}_2\text{O}$ from $(\text{NH}_4)_2\text{B}_{12}\text{F}_{12}\cdot 4\text{H}_2\text{O}$ and divides by 2 cations then each NH_4^+ cation would be 15.5 \AA^3 larger than the H_3O^+ cation, an unreasonable size difference for NH_4^+ and H_3O^+ . Literature reference for the NH_4^+ cation volume is 21 \AA^3 based on 3 different salts⁸⁴ which would indicate the H_3O^+ cation has a volume of 5.5 \AA^3 (impossibly small for H_3O^+), or the $\text{B}_{12}\text{F}_{12}^{2-}$ anion is significantly different between the two salts. A calculation from the only non-solvated crystal structure salt of $\text{B}_{12}\text{F}_{12}^{2-}$, $\text{K}_2\text{B}_{12}\text{F}_{12}$, and using a literature volume for the K^+ cation (9.86 \AA^3)⁸⁴, the volume of $\text{B}_{12}\text{F}_{12}^{2-}$ is 312 \AA^3 . If a similar analysis is performed for $\text{K}_2\text{B}_{12}\text{F}_{12}\cdot 2\text{H}_2\text{O}$, $\text{Rb}_2\text{B}_{12}\text{F}_{12}\cdot 2\text{H}_2\text{O}$, and $\text{Cs}_2\text{B}_{12}\text{F}_{12}\cdot \text{H}_2\text{O}$, all structures that do not exhibit hydrogen bonding (i.e. should have a similar H_2O volume independent of the cation as observed in $\text{K}_2\text{B}_{12}\text{F}_{12}\cdot 2\text{H}_2\text{O}$, 18 \AA^3), then the $\text{B}_{12}\text{F}_{12}^{2-}$ anion only varies in volume by at most 2.6%. Further evidence water has different apparent volume depending on hydrogen bonding is the density difference between liquid water and ice. Liquid water has a high degree of hydrogen bonding, which is why it has a higher density than solid ice. What is most interesting in the comparison presented above, the apparent size of H_2O in $(\text{H}_3\text{O})_2\text{B}_{12}\text{F}_{12}\cdot n\text{H}_2\text{O}$ and $(\text{NH}_4)_2\text{B}_{12}\text{F}_{12}\cdot n\text{H}_2\text{O}$ hydrated salts is controlled by hydrogen bonding, and, water can change its observed size by more than 100% depending on the hydrogen bonding environment. It is known that void space in

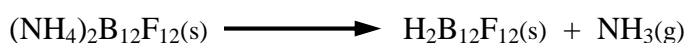
crystal lattices does occur and in many cases adventitious solvent will occupy that void space, sometimes having multiple or random orientation and/or random site occupation.

3.4.6 Attempted Synthesis of $\text{H}_2\text{B}_{12}\text{F}_{12}$ by Thermal Removal of H_2O or NH_3 and Thermal Stability of $(\text{H}_3\text{O})_2\text{B}_{12}\text{F}_{12} \cdot n\text{H}_2\text{O}$ and $(\text{NH}_4)_2\text{B}_{12}\text{F}_{12} \cdot n\text{H}_2\text{O}$.

Analysis of the DFT calculated structures of $(\text{H}_3\text{O})_2\text{B}_{12}\text{F}_{12}$ and an $(\text{NH}_4)_2\text{B}_{12}\text{F}_{12}$ analogue (see Figure 3-33) based on the $(\text{H}_3\text{O})_2\text{B}_{12}\text{F}_{12}$ structure provides a hypothetical reason as to why the synthesis of $\text{H}_2\text{B}_{12}\text{F}_{12}(\text{s})$ from $(\text{NH}_4)_2\text{B}_{12}\text{F}_{12}(\text{s})$ by the loss of 2 eq. $\text{NH}_3(\text{g})$ is plausible even though attempted thermal dehydration of $(\text{H}_3\text{O})_2\text{B}_{12}\text{F}_{12}$ did not produce $\text{H}_2\text{B}_{12}\text{F}_{12}(\text{s})$ before decomposing. The structures of $(\text{H}_3\text{O})_2\text{B}_{12}\text{F}_{12}$ and $(\text{NH}_4)_2\text{B}_{12}\text{F}_{12}$ should be very similar, however, while both cations are electrophilic, NH_4^+ is sterically hindered from interacting with the HOMO of $\text{B}_{12}\text{F}_{12}^{2-}$. The available unshared pair of electrons on the O in H_3O^+ could interact with a B–B–B (B_3) triangular face on a B_{12} cage starting a reaction. It is known that $\text{B}_{12}\text{H}_{12}^{2-}$ (and likely to a lesser extent $\text{B}_{12}\text{F}_{12}^{2-}$) should react on a B_3 triangular face since this is where the highest occupied molecular orbitals (HOMO) are located. In fact an electron rich B_3 face is the hypothetical reaction site of electrophile, F_2 , on $\text{B}_{12}\text{H}_{12}^{2-}$ during the fluorination reaction to synthesize $\text{B}_{12}\text{F}_{12}^{2-}$.³⁸ At elevated temperatures it could be possible for the oxygen in H_3O^+ to bend towards the cage and interact with the lone pair of electrons close to a B_3 face. Once this process begins, a B–O bond would begin to form and break a B–F bond in a concerted mechanism. The B–O bond would then fully form leaving an OH in place of an F on the cage as an HF bond form releasing HF. Additionally, the B–O bond is 40 kJ/mol more thermodynamically favorable than a B–F bond.⁸⁵⁻⁸⁸ The overall reaction scheme is shown below.



Conversely, in the case of $(\text{NH}_4)_2\text{B}_{12}\text{F}_{12}$ the tetrahedral geometry of the protons around the nitrogen would sterically block any possible reactions of NH_4^+ with a B_3 face. Since the reaction with a B_3 face would be blocked, the thermal loss of NH_3 shown in the scheme below should be more probable than compared to the H_3O^+ salt due steric blocking of NH_4^+ from interacting with a B_3 face.



In the TGA experiments starting from $(\text{NH}_4)_2\text{B}_{12}\text{F}_{12} \cdot 2\text{H}_2\text{O}(\text{s})$, the loss of 2 eq. of $\text{H}_2\text{O}(\text{g})$ to make $(\text{NH}_4)_2\text{B}_{12}\text{F}_{12}$ was observed. However, attempts to thermally remove 2 eq. of $\text{NH}_3(\text{g})$ to make $\text{H}_2\text{B}_{12}\text{F}_{12}(\text{s})$ decomposed the sample above 450 °C. This finding is interesting because many NH_4^+ salts are known to decompose releasing $\text{NH}_3(\text{g})$ at relatively low temperatures. A 2004 patent describes methods to make $\text{NH}_3(\text{g})$ and $\text{H}_2\text{SO}_4(\text{l})$ by thermally decomposing $(\text{NH}_4)_2\text{SO}_4$ in the presence of H_2SO_4 at ca. ≥ 280 °C.⁸⁹ Additionally, it is well known that $(\text{NH}_4)_2\text{CO}_3$, the active ingredient in smelling salts releasing $\text{NH}_3(\text{g})$, has a measurable vapor pressure of $\text{NH}_3(\text{g})$ above the solid at room temperature (vapor pressure ca. 52 Torr at 20 °C), and it fully decomposes at 60–120 °C.⁹⁰⁻⁹² Furthermore, the partially protonated salt $(\text{NH}_4)\text{HCO}_3$ will also thermally decompose to yield $\text{NH}_3(\text{g})$, H_2O and CO_2 at 100–160 °C.⁹⁰

Since the 2 eq. of H_2O are removed from $(\text{NH}_4)_2\text{B}_{12}\text{F}_{12} \cdot 2\text{H}_2\text{O}(\text{s})$, around 35–50 °C to form $(\text{NH}_4)_2\text{B}_{12}\text{F}_{12}$, H_2O could not be inhibiting the release of $\text{NH}_3(\text{g})$ through hydrogen bonding or other interaction. Yet the $(\text{NH}_4)_2\text{B}_{12}\text{F}_{12}$ salt does not release $\text{NH}_3(\text{g})$ between 50 and 450 °C, whereas other NH_4^+ salts are known to disassociate forming $\text{NH}_3(\text{g})$ and leaving behind an H^+ . The difference is that the $\text{B}_{12}\text{F}_{12}^{2-}$ anion is so weakly coordinating and has such a low proton affinity it does not hold the H^+ cation allowing the $\text{NH}_3(\text{g})$ to be released. The NH_4^+ cation is not a good

electrophile due to sterics and does not appear to react with the $B_{12}F_{12}^{2-}$ anion at temperatures near 300 °C like H_3O^+ , evidenced by the greater thermal stability of $(NH_4)_2B_{12}F_{12}$. The $B_{12}F_{12}^{2-}$ anion does not have a strong enough affinity for the H^+ to separate from $NH_3(g)$, even at temperatures in excess of 450 °C. While the $(NH_4)_2B_{12}F_{12}(s)$ salt was correctly predicted to be more thermally stable than $(H_3O)_2B_{12}F_{12}(s)$, this finding with $(NH_4)_2B_{12}F_{12}(s)$ shows the unlikely possibility of forming $H_2B_{12}F_{12}(s)$ by thermal loss of solvent molecules because the proton affinity of the $B_{12}F_{12}^{2-}$ anion is so low the proton will strongly bind with the solvent molecule, forming an ion pair of $[HB^+][B_{12}F_{12}^{2-}]$ where $B = H_2O$ or NH_3 , until the salt thermally decomposes before $H_2B_{12}F_{12}(s)$ is formed. This is yet another empirically observed bulk property manifestation of the superweak nature of the $B_{12}F_{12}^{2-}$ anion.

3.5 Summary and Conclusions

The H_3O^+ salt of $B_{12}F_{12}^{2-}$ has been synthesized cleanly starting from highly purified $K_2B_{12}F_{12}$ using a strong-acid cation-exchange resin, purified by recrystallization from water. The $(H_3O)_2B_{12}F_{12} \cdot nH_2O$ salts have exhibited four stable hydrate phases at identified temperature and humidity conditions ($n = 6, 4, 2, 0$), of which the $(H_3O)_2B_{12}F_{12} \cdot 6H_2O$ and $(H_3O)_2B_{12}F_{12} \cdot 4H_2O$ hydrate phases have been structurally characterized. Both structures exhibit extended two-dimensional hydrogen bonded networks consisting of $[H_3O^+/3H_2O]_n$ and $[H_3O^+/2H_2O]_n$ units respectively. Besides being a useful proton conductor in phosphoric acid hydrogen fuel cells the $(H_3O)_2B_{12}F_{12} \cdot nH_2O$ salt can also be used as a convenient precursor for the synthesis of other purified salts starting from pure metals or $M(OH)_x$, M_2O_x , or $M_2(CO_3)_x$ salts to make $M_x(B_{12}F_{12})_y \cdot nH_2O$ salts. This metathesis method was demonstrated by making $ZnB_{12}F_{12} \cdot 6H_2O$ from zinc metal in aqueous $(H_3O)_2B_{12}F_{12} \cdot nH_2O$.

Attempts to produce $\text{H}_2\text{B}_{12}\text{F}_{12}$ by thermally removing H_2O and/or NH_3 starting from $(\text{H}_3\text{O})_2\text{B}_{12}\text{F}_{12}\cdot n\text{H}_2\text{O}$ or $(\text{NH}_4)_2\text{B}_{12}\text{F}_{12}\cdot n\text{H}_2\text{O}$ ended in decomposition before the target compound was formed. The $(\text{H}_3\text{O})_2\text{B}_{12}\text{F}_{12}$ did not form $\text{H}_2\text{B}_{12}\text{F}_{12}$ by losing 2 eq. of H_2O but instead thermally decomposed at ca. 300 °C resulting in the formation of a new anion, $\text{B}_{12}\text{F}_{11}\text{OH}_2^-$, evidenced by NI-ESI-MS and $^{19}\text{F}[^{11}\text{B}]$ NMR spectroscopy. While the $(\text{NH}_4)_2\text{B}_{12}\text{F}_{12}$ salt exhibited a greater thermal stability, reaching 450 °C before thermal decomposition, possibly due to the sterically hindered ammonium cation unable easily attack the $\text{B}_{12}\text{F}_{12}^{2-}$ anion, also did not release $\text{NH}_3(\text{g})$ leaving behind the putative superacid $\text{H}_2\text{B}_{12}\text{F}_{12}$. Based on these attempts to produce $\text{H}_2\text{B}_{12}\text{F}_{12}$ by thermal desolvation of the acid salt of $\text{B}_{12}\text{F}_{12}^{2-}$ to evolve volatile, weak bases, it is evident that the $\text{B}_{12}\text{F}_{12}^{2-}$ anion has such a low affinity for protons that the salt decomposes before evolution of the solvent base.

The crystal lattices of $(\text{H}_3\text{O})_2\text{B}_{12}\text{F}_{12}\cdot 4\text{H}_2\text{O}$ and $(\text{NH}_4)_2\text{B}_{12}\text{F}_{12}\cdot 2\text{H}_2\text{O}$ both exhibit extensive hydrogen bonding in the crystal lattice, as well as $(\text{H}_3\text{O})_2\text{B}_{12}\text{F}_{12}\cdot 6\text{H}_2\text{O}$. Using the unit cell volumes of K^+ , NH_4^+ , and H_3O^+ salts and hydrates of $\text{B}_{12}\text{F}_{12}^{2-}$ the the apparent volume of H_2O molecules in these salt lattices was determined. The H_2O in NH_4^+ salts of $\text{B}_{12}\text{F}_{12}^{2-}$ (going from $(\text{NH}_4)_2\text{B}_{12}\text{F}_{12}\cdot 4\text{H}_2\text{O}$ to $(\text{NH}_4)_2\text{B}_{12}\text{F}_{12}\cdot 2\text{H}_2\text{O}$) is ca. 100% greater in apparent volume than in H_3O^+ salts of $\text{B}_{12}\text{F}_{12}^{2-}$ (going from $(\text{H}_3\text{O})_2\text{B}_{12}\text{F}_{12}\cdot 6\text{H}_2\text{O}$ to $(\text{H}_3\text{O})_2\text{B}_{12}\text{F}_{12}\cdot 4\text{H}_2\text{O}$). Finally, it also turns out the apparent volume of H_2O in the $(\text{NH}_4)_2\text{B}_{12}\text{F}_{12}\cdot 4\text{H}_2\text{O}$ to $(\text{NH}_4)_2\text{B}_{12}\text{F}_{12}\cdot 2\text{H}_2\text{O}$ difference is similar in volume to that of the calculated volume of H_2O molecule in ice at 0 °C.

3.6 Future Work

There are at least three experiments that would make the research of $(\text{H}_3\text{O})_2\text{B}_{12}\text{F}_{12}\cdot n\text{H}_2\text{O}$ and its hydrated phases more complete. First, measure the proton conduction of $(\text{H}_3\text{O})_2\text{B}_{12}\text{F}_{12}\cdot n\text{H}_2\text{O}$ hydrated salts in both solid and aqueous samples. This would allow direct comparison with other

proton conducting salts, and determine the viability of $(\text{H}_3\text{O})_2\text{B}_{12}\text{F}_{12}\cdot n\text{H}_2\text{O}$ hydrated salts as proton conductors in commercial applications. Second, attempt to chemically desolvate $(\text{H}_3\text{O})_2\text{B}_{12}\text{F}_{12}\cdot n\text{H}_2\text{O}$ or $(\text{NH}_4)_2\text{B}_{12}\text{F}_{12}\cdot n\text{H}_2\text{O}$ as a novel method to form the putative superacid $\text{H}_2\text{B}_{12}\text{F}_{12}$. Chemical desolvation to form the superacid $\text{H}_2\text{B}_{12}\text{F}_{12}$ will be challenging because, hypothetically, almost anything will react with $\text{H}_2\text{B}_{12}\text{F}_{12}$, making a salt, even benzene as described by Reed et al.³³ Rather than a direct chemical desolvation, the formation of $\text{H}_2\text{B}_{12}\text{F}_{12}$ might occur with a moderate temperature and a strong desiccant. For example, dried $\text{KOH}(\text{s})$ in an Abnerholden drying pistol with refluxing mesitylene to keep the sample around 165 °C. This could slowly drive off the water and trap it in a strong desiccant. Assuming there is a slight equilibrium to produce $\text{H}_2\text{O}(\text{g})$ under such dry conditions, this method would constantly shift the equilibrium towards producing more $\text{H}_2\text{O}(\text{g})$, eventually drying the sample without decomposition. Finally, the $\text{H}_2\text{B}_{12}\text{F}_{12}$ putative super acid should be synthesized using literature methods previously described (Section 3.2) in order to study and compare the properties and acidity of $\text{H}_2\text{B}_{12}\text{F}_{12}$ with other previously researched literature superacids.

3.7 Experimental

3.7.1 Reagents and Solvents:

The strong-acid cation-exchange resins used in this study were Amberlyst 15 (Rohm and Hass) and Purolite UCW9126 (The Purolite Company). The strong-acid cation-exchange resins were treated per manufacture guidelines prior to use, loaded in dd- H_2O and flushed with 20–30 BV of dd- H_2O . The compounds/reagents $\text{K}_2\text{B}_{12}\text{F}_{12}$ (Katchem spol. sr. o.), conc. hydrochloric acid (HCl) (EMD, 36.5–38% HCl , ACS grade), and conc. ammonium hydroxide (NH_4OH) (Mallinckrodt, analytical reagent grade) were used as received. The $\text{K}_2\text{B}_{12}\text{F}_{12}$ was prepared using

previously established procedures and checked for purity by ^{11}B [^{19}F], ^{19}F [^{11}B] and ^1H , NMR spectroscopy and by NI-ES-MS.³⁸ The deuterated NMR solvents/standards D_2O (Cambridge Isotopes Laboratories, Inc., 99.8% D), CD_3CN (Cambridge Isotopes Laboratories, Inc., 99.8% D, distilled from activated 3 Å molecular sieves and stored over activated 3 Å), 1,4-bis(trifluoromethyl) benzene (PTFMB) (Chemical Research Centre, Central Glass CO., LTD. 99%, distilled from activated 3 Å molecular sieves, chemical shifts; ^{19}F and ^1H are $\delta -63.80$ and $\delta 7.90$ respectively) were obtained from the indicated vendors and purified by the indicated methods. Zinc metal (reagent grade, Zn dust) was used as received. Distilled deionized water was prepared by passing distilled water with through a Barnstead Nanopure deionization system producing water with a final resistance of at least 18 MΩcm.

3.7.2 Instrumentation

TGA Analysis: Thermogravimetric analysis was performed with a TA Instruments Model 2950 TGA with Airgas UHP grade $\text{He}(\text{g})$ or liquid boil off $\text{N}_2(\text{g})$ (passed through H_2O and O_2 absorbent columns before instrument) at a flow rate of 55–60 mL min^{-1} . Data were analyzed with TA Universal Analysis Version 4.5A.

DSC Analysis: Differential scanning calorimetry was performed using a TA Instruments Model 2920 DSC with Airgas UHP grade $\text{He}(\text{g})$ or liquid boil off $\text{N}_2(\text{g})$ (passed through H_2O and O_2 absorbent columns before instrument) at a rate of 55–60 ml min^{-1} . Data were analyzed with TA Universal Analysis Version 4.5A. Samples ranged from 1.0–2.0 mg in mass and were contained in TA Instruments hermetic aluminum DSC pans with covers. Various heating rates were used to determine the thermal events and possible phase changes of $(\text{H}_3\text{O})_2\text{B}_{12}\text{F}_{12} \cdot n\text{H}_2\text{O}$.

NMR Spectroscopy: NMR spectra were taken on a 400 MHz automatic tune, Inova Varian instrument or a 300 MHz manual tune Inova Varian instrument in 5 mm NMR spectroscopy grade glass tubes. Nuclei observed for $(\text{H}_3\text{O})_2\text{B}_{12}\text{F}_{12} \cdot n\text{H}_2\text{O}$ was $^{11}\text{B}[^{19}\text{F}]$, (^{11}B frequency was 128.24 MHz and ^{19}F was 376.01 MHz on the 400 MHz instrument, ^{11}B pulse angle = 90° , pulse time = 13.5×10^{-6} s acquisition time = 0.200 s, and relaxation delay was = 0.900 s, spectral width 20491.8 Hz), and $^{19}\text{F}[^{11}\text{B}]$ (^{19}F was 376.01 MHz and ^{11}B frequency was 128.24 MHz on the 400 MHz instrument, ^{19}F pulse angle = 30° , pulse time = 4.63×10^{-6} s, acquisition time = 0.865 s, relation delay = 1.000 s, spectral width = 37878.8 Hz), and ^1H (399.7 MHz on the 400 MHz instrument).

Negative Ion Electrospray Mass Spectroscopy: Mass spectra were recorded using a 2000 Finnigan LCQ-DUO mass-spectrometer with MeCN as the carrier solvent. The instrument parameters were tuned to maximize the $\text{KB}_{12}\text{F}_{12}^-$ signal in a sample of $\text{K}_2\text{B}_{12}\text{F}_{12}$ dissolved in MeCN. Samples were on the order of 10–50 μM concentration in as received MeCN or 3:1 dd- H_2O :MeCN.

IR and Raman Analysis: Raman and FTIR analysis of $(\text{H}_3\text{O})_2\text{B}_{12}\text{F}_{12}$ was performed using a Nicolet Magna-760 FTIR/Raman spectrometer operating at a resolution of 4 cm^{-1} scanning from 400-4000 cm^{-1} using AgCl plates and a Nujol® mull. A blank of the AgCl plates was taken to determine the extent of water contamination of AgCl plates.

X-ray Crystallography: Single crystals of $(\text{H}_3\text{O})_2\text{B}_{12}\text{F}_{12} \cdot 6\text{H}_2\text{O}$ were grown by this author by slow evaporation from H_2O and SC-XRD data collection, data reduction, solution and structure refinement was performed by Stephanie R. Fiedler. Data from single crystals of

(H₃O)₂B₁₂F₁₂·6H₂O were collected using a Bruker Kappa APEX II CCD diffractometer (MoK α λ = 0.71073 Å; graphite monochromator) at T = 120(2) K. Data reduction was performed with APEX 2 suite of software from Bruker. Solution and structure refinement were performed with SHELXTL software⁹³⁻⁹⁶, a semiempirical absorption correction was applied with SADABS⁹³. Further details on the crystal structure investigation can be obtained from the ICSD Fachinformationszentrum Karlsruhe, 76344 Eggenstein-Leopoldshafen, Germany, on the depository number CSD-423408. Single crystals of (H₃O)₂B₁₂F₁₂·4H₂O were grown by collaborator Moritz Malischewski at Freie Universität Berlin, and data were collected in Berlin with a Bruker CCD 2000 diffractometer (MoK α λ = 0.71073 Å; graphite monochromator) at T = 133(2) K. Data reduction was performed with Bruker 2000 NT Software. Solution and structure refinement were performed with SHELXTL software⁹³⁻⁹⁶. Single crystals of (NH₄)₂B₁₂F₁₂·4H₂O were grown by W. Matt Jones by slow evaporation from H₂O. Data collection, data reduction, solution and structure refinement were performed by this author. Data collection performed on a Bruker Kappa APEX II CCD diffractometer (MoK α λ = 0.71073 Å; graphite monochromator) at T = 233(2) K. Data reduction was performed with APEX 2 suite of software from Bruker, a semiempirical absorption correction was applied with SCALE⁹³⁻⁹⁶. Solution and structure refinement were performed with SHELXTL software in OLEX 2, Version 1.2.5⁹⁷. All figures were generated with SHELXTL XP software.

ICP-AES: Metals analysis was performed by Bryan Brittan using a Perkin-Elmer Model 7300 DV ICP-OES, ICP-AES instrument. Elements analyzed for each sample were Ag, Al, As, Au, B, Ba, Be, Ca, Cd, Ce, Co, Cr, Cu, Fe, K, Li, Mg, Mn, Mo, Na, Ni, P, Pb, Pd, Pt, S, Sb, Se, Si, Sn, Sr, Te, Ti, Tl, U, V, W, Zn, and Zr. Samples were diluted in a mixture of metals free acids (1% v/v hydrochloric acid and 5% v/v nitric acid) to a known concentration and were an average of 3

replicates. Ytterbium was used as an internal standard and 15 interelement correction standards were used to correct for easily ionizable elements.

pH Measurement: Acidity was measured with an Orion Model 210A pH meter and Analytical Sensors Inc. pH probe; calibrated using pH 4.00 (Fisher Certified 4.00 ± 0.01 pH @ 25 °C) and pH 7.00 (EMD Traceable Standard 7.00 ± 0.01 pH 25 °C) standard buffer solutions.

3.7.3 Synthesis of $(\text{H}_3\text{O})_2\text{B}_{12}\text{F}_{12} \cdot n\text{H}_2\text{O}$ from Strong Acid Cation Exchange.

Two strong-acid ion-exchange columns of ca. 2.0 cm inner diameter and 100 cm in length were rinsed with copious amounts of dd- H_2O , then treated with 24 bed volumes of ca. 5% aqueous HCl solution at a flow rate of 4–8 BV/h to exhaustively convert the resin to the H^+ form. The resin was then rinsed until the effluent had a pH equal to the dd- H_2O as measured by a pH meter. Amberlyst 15 and Purolite UCW9126 strong cation exchange resins were treated following the same procedures. The column size and resin volume were such that < 10% of the column capacity was utilized per synthesis

The $(\text{H}_3\text{O})_2\text{B}_{12}\text{F}_{12} \cdot n\text{H}_2\text{O}$ compound was made by passing an aq. solution of 99.5+ mol% $\text{K}_2\text{B}_{12}\text{F}_{12}$, (ca. 5–10 g in 150 ml dd- H_2O) through the first H^+ form cation-exchange resin column at a flow rate of ca. 1–5 BV/h followed by dd- H_2O until the effluent had a pH equal to the dd- H_2O (usually 2 L or less of dd- H_2O was required). The collected solution was condensed to ca. 100 ml by rotary-evaporation and then passed through a second H^+ form cation-exchange column following the aforementioned procedure. A colorless to light yellow solution was dried to a light yellow solid using a rotary-evaporator, collected and ground to a powder, yield was > 95% based on starting $\text{K}_2\text{B}_{12}\text{F}_{12}$. Clear colorless crystals were obtained by recrystallization from a concentrated aqueous solution. Residual colored mother liquor was removed from

recrystallized samples by washing the crystals in a minimal volume of cold dd-H₂O, recrystallized yield was ca. 30% after washing with dd-H₂O based on starting K₂B₁₂F₁₂.

3.7.4 Purity Analysis by ¹H, ¹⁹F[¹¹B], and ¹¹B[¹⁹F] NMR Spectroscopy, and ICP-AES.

Molar equivalence of (H₃O)₂B₁₂F₁₂·*n*H₂O was determined by moles of dry K₂B₁₂F₁₂ used in the (H₃O)₂B₁₂F₁₂·*n*H₂O synthesis, dryness of K₂B₁₂F₁₂ was determined by ¹H NMR. Metal impurity was determined by ICP-AES. Purity of the B₁₂F₁₂²⁻ anion in K₂B₁₂F₁₂ before and after cation exchange was determined by ¹¹B[¹⁹F] and ¹⁹F[¹¹B] NMR spectroscopy in CD₃CN. Organic impurities and water concentration were determined by relating the ¹⁹F and ¹H NMR spectroscopy integrations relative to the internal standard PTFMB. Only PTFMB vapors were transferred to each sample by pipet to minimize oversaturation.

3.7.4.1 Thermogravimetric Analysis of (H₃O)₂B₁₂F₁₂·*n*H₂O.

Samples were from dried or recrystallized material on the order of 15–20 mg in mass and were contained in an open platinum pan. Experiments were performed with a purge of dry He(g) or N₂(g), or with gas wet with a known *P*(H₂O). A *P*(H₂O) = 6(1) Torr generated by bubbling dry gas through a saturated aqueous solution of MgCl₂ at 20 °C. The partial pressure of water under these conditions was found in literature and verified by previous tensimetric experiments.^{33,98} Due to the rapid dehydration of (H₃O)₂ B₁₂F₁₂·*n*H₂O the sample was initially equilibrated at 25 °C with *P*(H₂O) = 6(1) Torr to ensure the *n* = 6 hydrate phase was the only hydrate phase present.

3.7.5 Synthesis of Metal Salts Through $(\text{H}_3\text{O})_2\text{B}_{12}\text{F}_{12}\cdot n\text{H}_2\text{O}$: $\text{ZnB}_{12}\text{F}_{12}\cdot 6\text{H}_2\text{O}$ Proof of Concept.

Excess Zn dust was added to an unknown concentration of aq. $(\text{H}_3\text{O})_2\text{B}_{12}\text{F}_{12}\cdot n\text{H}_2\text{O}$. after the bubbling ceased indicating end of reaction, the remaining Zn metal was filtered from the solution and the resulting colorless solution was condensed in volume to ca. 5 mL. From this aqueous solution, crystals of $\text{ZnB}_{12}\text{F}_{12}\cdot 6\text{H}_2\text{O}$ were grown for SC-XRD analysis.

3.7.6 Synthesis of $(\text{NH}_4)_2\text{B}_{12}\text{F}_{12}\cdot n\text{H}_2\text{O}$ from Neutralization of $(\text{H}_3\text{O})_2\text{B}_{12}\text{F}_{12}\cdot n\text{H}_2\text{O}$.

The $(\text{NH}_4)_2\text{B}_{12}\text{F}_{12}\cdot n\text{H}_2\text{O}$ was made by W. Matt Jones by neutralization of $(\text{H}_3\text{O})_2\text{B}_{12}\text{F}_{12}\cdot n\text{H}_2\text{O}(\text{aq})$ using a slight excess of $\text{NH}_4\text{OH}(\text{aq})$. Once the reaction was complete (pH of the solution was slightly basic by pH paper or pH probe) the solution was dried to a solid and dissolved in boiling H_2O and $(\text{NH}_4)_2\text{B}_{12}\text{F}_{12}\cdot n\text{H}_2\text{O}$ was purified by slow recrystallization from water. Purity was determined by ^1H , $^{19}\text{F}[^{11}\text{B}]$, and $^{11}\text{B}[^{19}\text{F}]$ NMR spectroscopy in D_2O or dry CD_3CN .

3.8 Figures

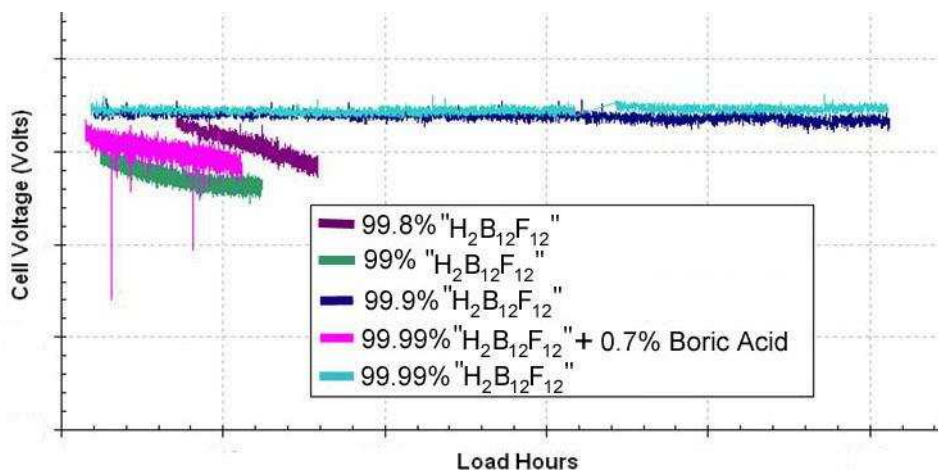


Figure 3-1. Preliminary longevity experiments in experimental fuel cells with different purity hydrogen fluoroborate acid electrolytes. Note for long life duration without a significant drop in cell voltage, the purity of " $\text{H}_2\text{B}_{12}\text{F}_{12}$ " had to be 99.9% or greater. The experiment with 99.99% pure " $\text{H}_2\text{B}_{12}\text{F}_{12}$ " and 0.7% boric acid also shows a significant decrease in cell voltage early in the experiment.⁶⁷

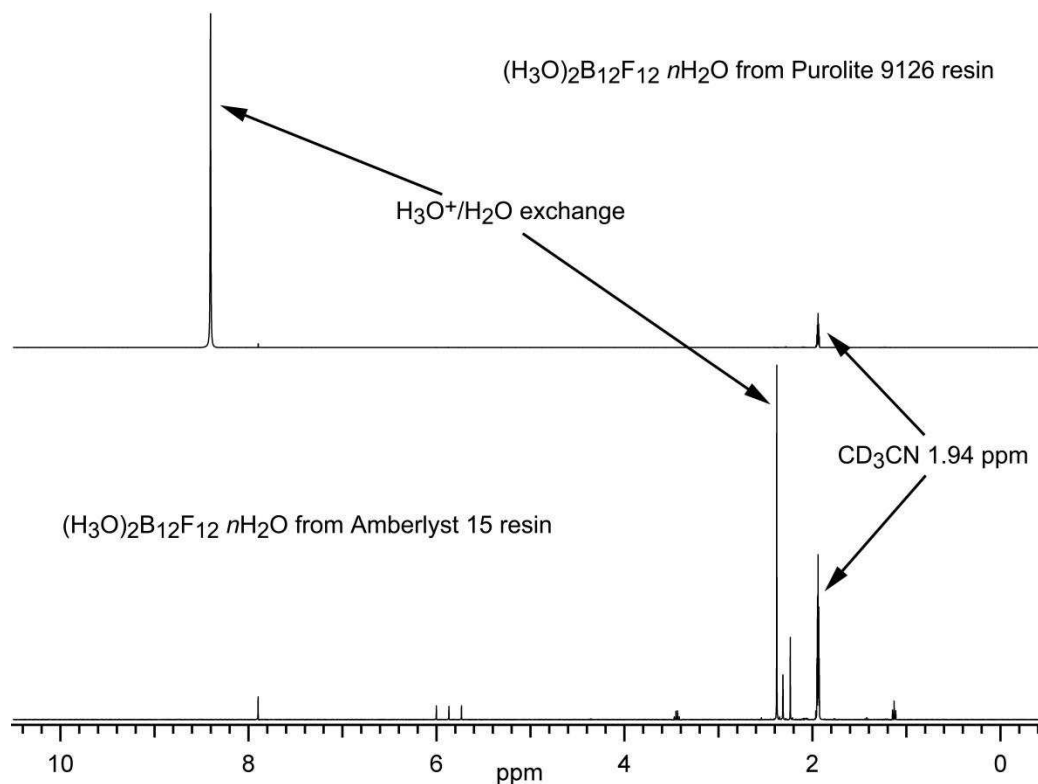


Figure 3-2. Proton NMR (400 MHz, CD₃CN, referenced to CD₂H₂CN, δ 1.94) spectra comparing impurities and qualitative concentrations in (H₃O)₂B₁₂F₁₂ · nH₂O synthesized using Amberlyst 15 and Purolite UCW 9126 cation-exchange resins. Both samples were passed through an equal size column then columns were eluted with an equal volume of water. Both samples were dried to a solid and dissolved in CD₃CN. The (H₃O)₂B₁₂F₁₂ · nH₂O appears to have more unidentifiable impurities by ¹H NMR. Note the shift in H₃O⁺/H₂O exchange is due to varying amounts of residual H₂O in each sample, the less H₂O the farther up-field the singlet peak will shift.

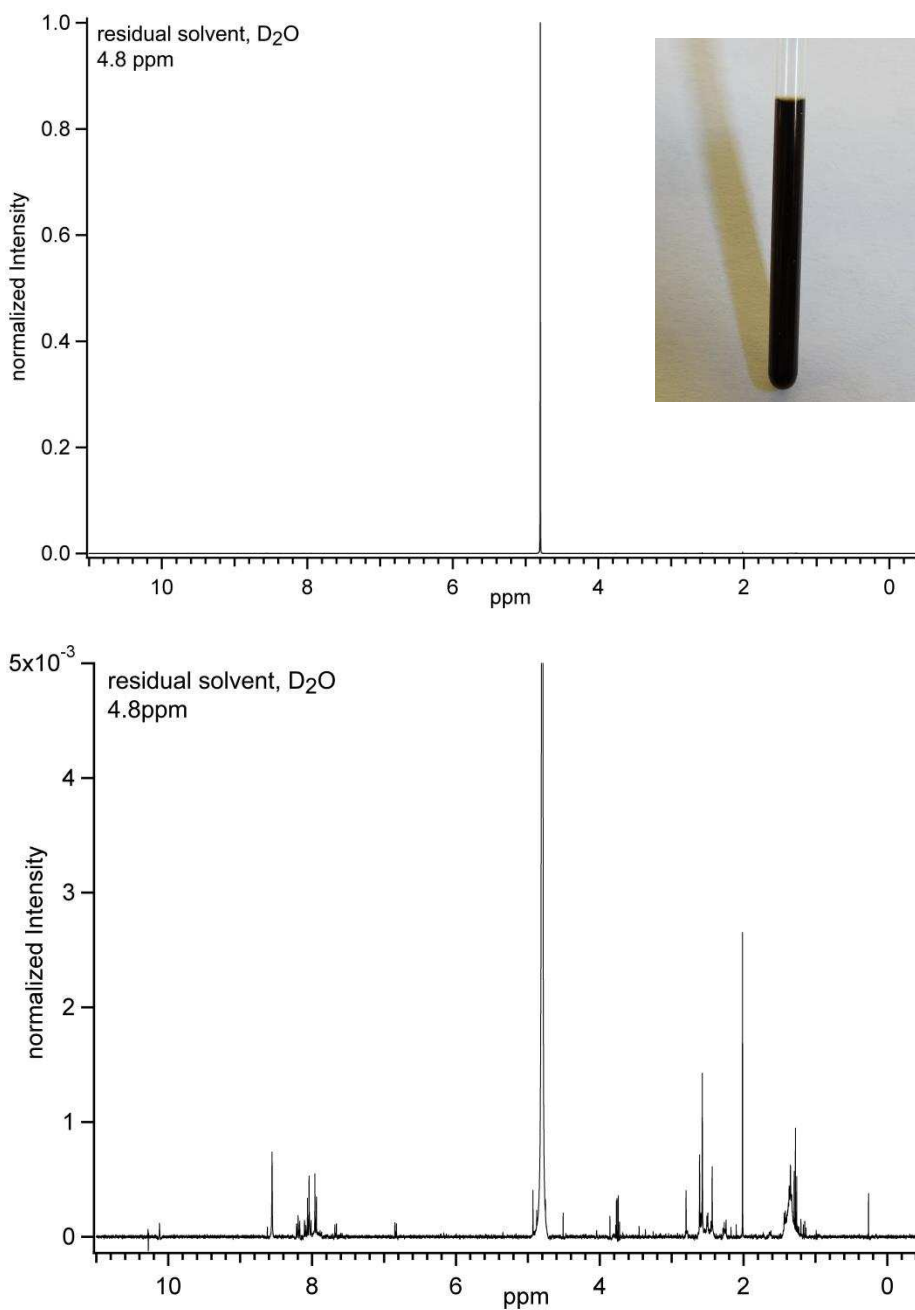


Figure 3-3. (Top) Proton NMR spectrum of impurities intentionally extracted from Amberlyst 15 resin into D₂O, normalized. Inset is image of concentrated impurities in NMR tube. (Bottom) Zoomed in image of top ¹H NMR spectrum to show other peaks visible in this sample. Even though the impurities are low in concentration (compared to peak height of residual D₂O residual solvent) the impurities are highly colored. Proton ¹H NMR, 400 MHz, referenced to HOD, δ 4.8)

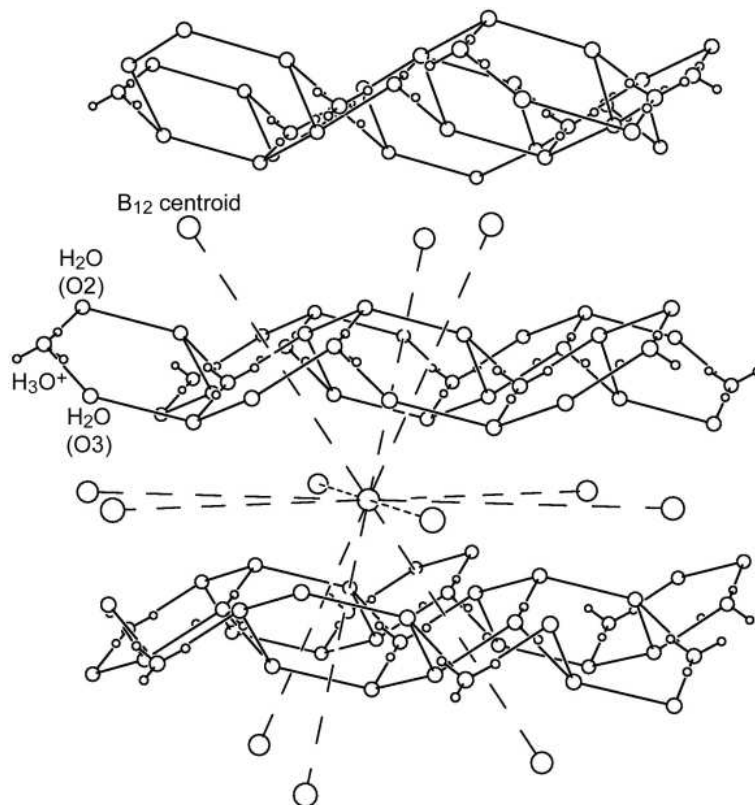


Figure 3-4. A portion of the $(\text{H}_3\text{O})_2\text{B}_{12}\text{F}_{12}\cdot 6\text{H}_2\text{O}$ structure, O atoms forming 6 membered rings through hydrogen bonding of the H_3O^+ cations and H_2O molecules. The B_{12} centroids are displayed as spheres of arbitrary size for clarity (O atoms in the rings are connected with solid lines for clarity even though they are not directly bonded). Infinite $[\text{H}_3\text{O}^+/\text{3H}_2\text{O}]_\infty$ networks intercalated between close-packed anion layers.³¹

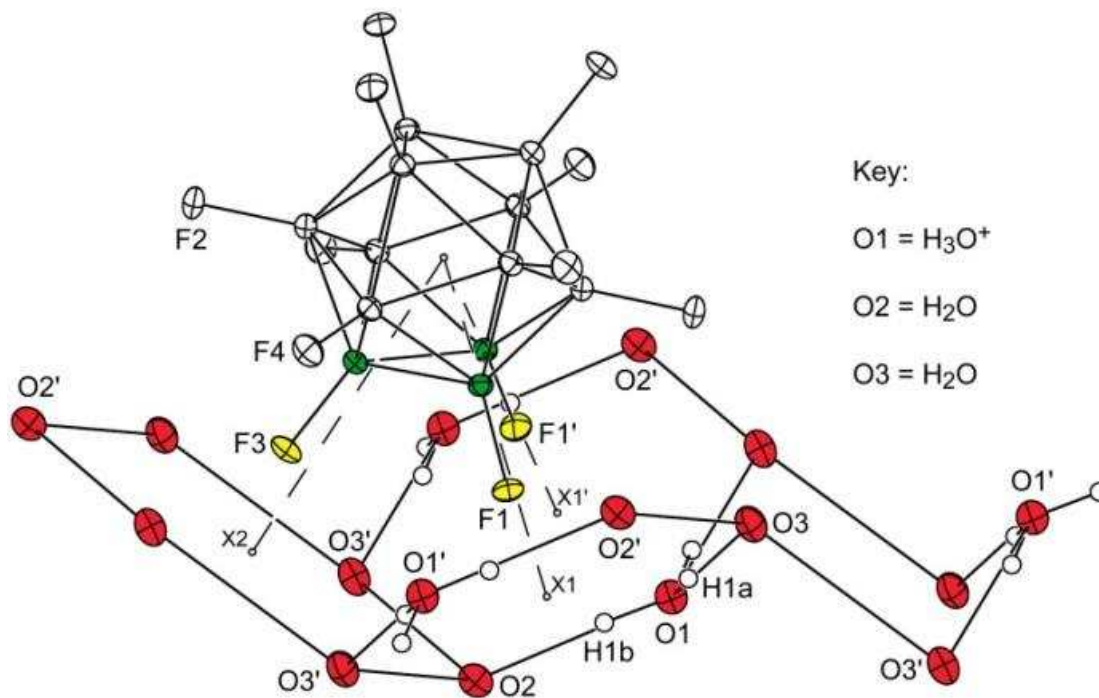


Figure 3-5. A segment of $(\text{H}_3\text{O})_2\text{B}_{12}\text{F}_{12}\cdot 6\text{H}_2\text{O}$ showing the orientation of a $\text{B}_{12}\text{F}_{12}^{2-}$ anion with respect to a triple-hexagon valley in the $[\text{H}_3\text{O}^+/\text{3H}_2\text{O}]_n$ network (50% ellipsoids for non-hydrogen atoms; only H atoms on the H_3O^+ cations are shown). The small spheres of arbitrary size labeled X1, X1', and X2 are O_6 ring centroids; the B_{12} centroid is not labeled. Also shown is the chair-conformation $[(\text{H}_3\text{O})_2(\text{H}_2\text{O})_4]^{2+}$ ring.³¹

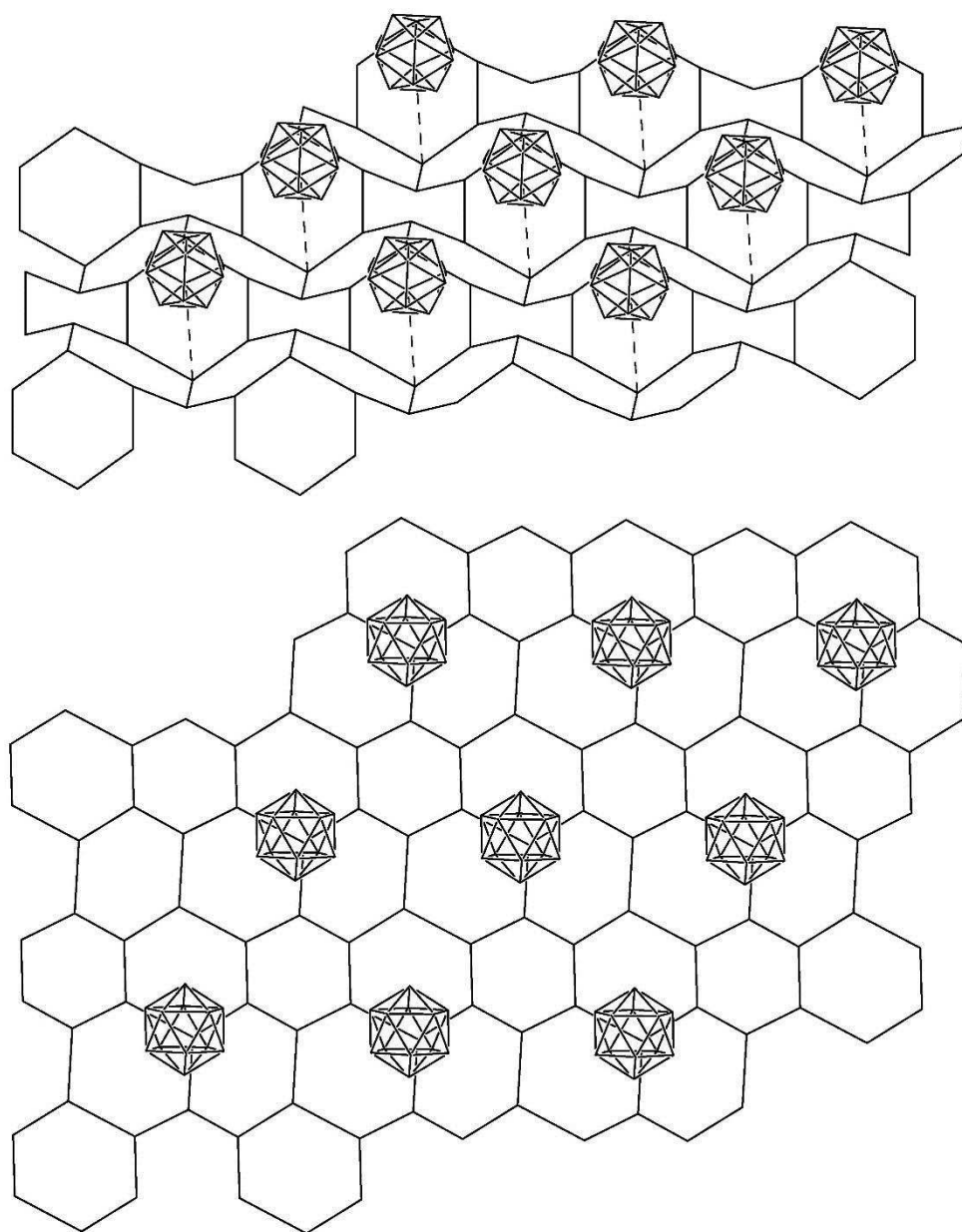


Figure 3-6. A segment of the $[\text{H}_3\text{O}^+/3\text{H}_2\text{O}]_n$ network at angle, top, and in flat projection, bottom, and one layer of $\text{B}_{12}\text{F}_{12}^{2-}$ anions in $(\text{H}_3\text{O})_2\text{B}_{12}\text{F}_{12} \cdot 6\text{H}_2\text{O}$ (H and F atoms omitted for clarity; O and B atoms depicted as points). The dotted lines connect the B_{12} centroids with O atoms at the bottoms of the triple-hexagon valleys in the network.³¹

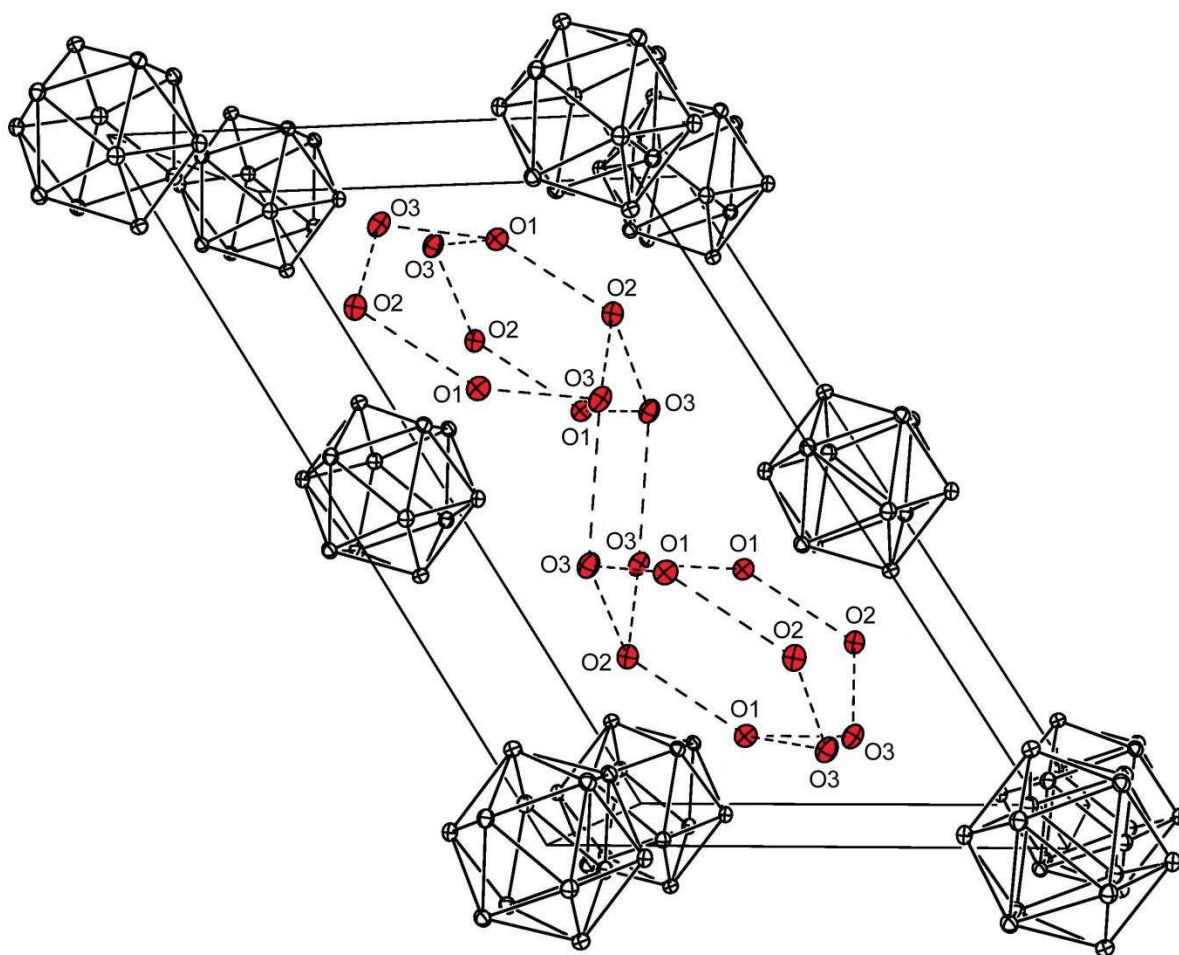


Figure 3-7. Drawing of the unit cell $(\text{H}_3\text{O})_2\text{B}_{12}\text{F}_{12}\cdot 6\text{H}_2\text{O}$ (H and F atoms omitted for clarity). There are 10 $\text{B}_{12}\text{F}_{12}^{2-}$ anions associated with this unit cell, 8 at the corners and 2 on opposite faces, for a total of 2 complete anions. There are 20 O atoms associated with this cell, 8 on faces and 12 that are completely in the cell (including 4 H_3O^+ cations (O1)). Therefore, there are 4 H_3O^+ cations and 12 complete H_2O molecules per unit cell.

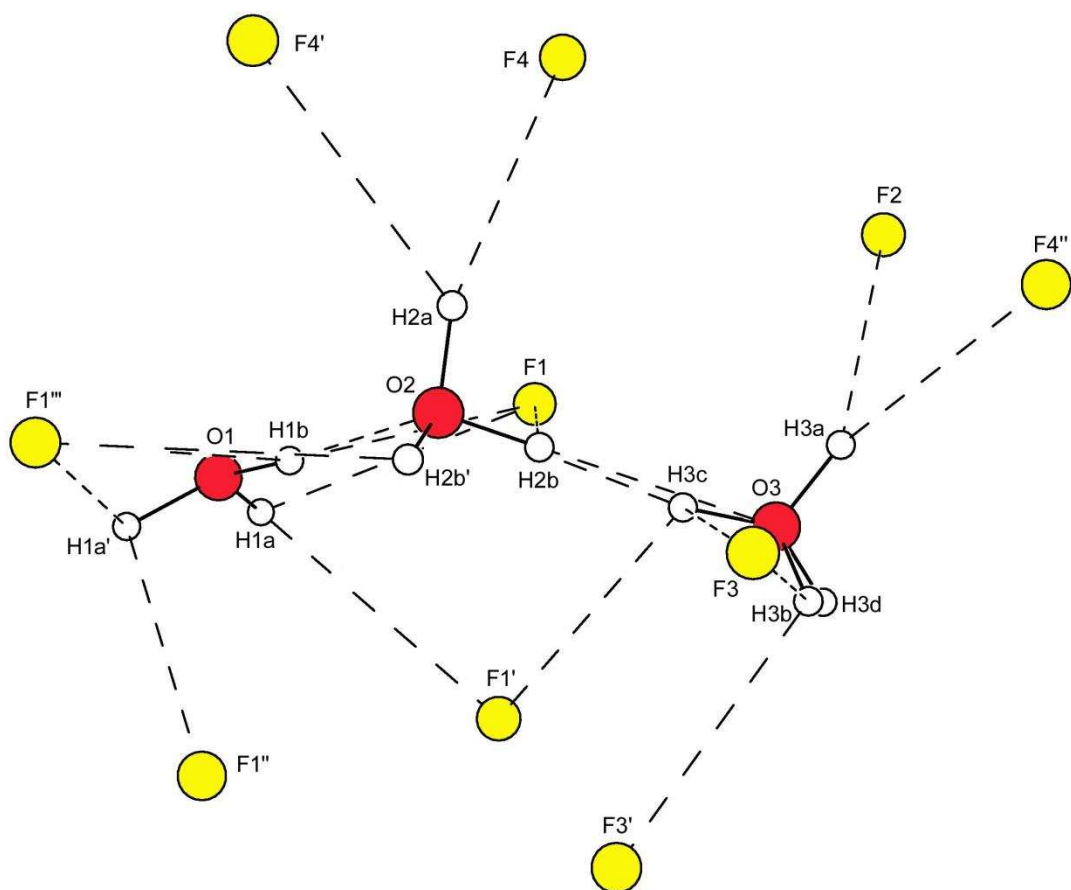


Figure 3-8. The O–H···O and O–H···F hydrogen bonds in $(\text{H}_3\text{O})_2\text{B}_{12}\text{F}_{12}\cdot 6\text{H}_2\text{O}$. Selected distances (Å; all standard errors are 0.01 Å): H1a···F1 and H1a'···F1''', 2.54; H1a···F1 and H1a'···F1'', 2.67; H1a···O3' (not shown), 1.73; H1b···F1 and H1b···F1''', 2.68; H1b···O2', 1.72; H2a···F4 and H2a···F4', 2.55; H2b···F1, 2.68; H2b···O3, 2.04; H3a···F2, 2.43; H3a···F4'', 2.25; H3b···F3, 2.35; H3b···F3', 2.67; H3c···F3, 2.57; H3c···F1', 2.70; H3c···O2, 2.09.

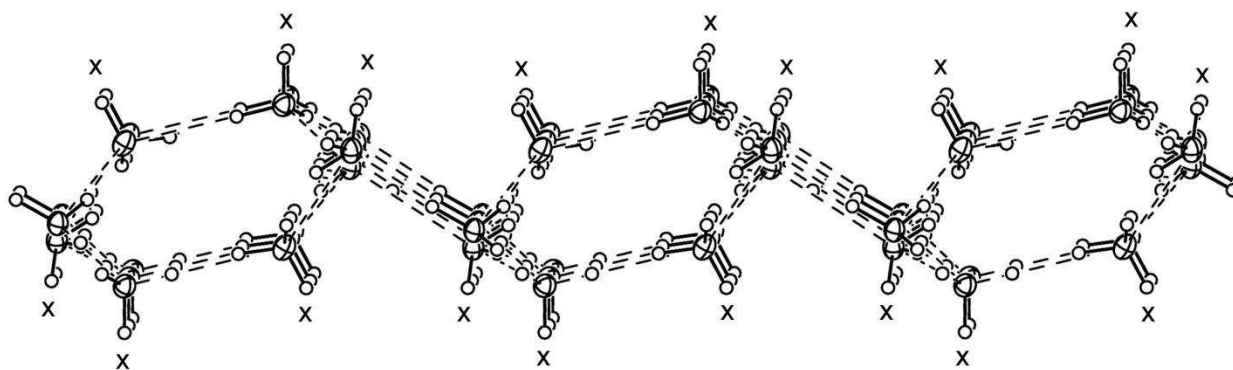


Figure 3-9. Another view of the $\text{H}_3\text{O}^+/\text{H}_2\text{O}$ layers in $(\text{H}_3\text{O})_2\text{B}_{12}\text{F}_{12}\cdot 6\text{H}_2\text{O}$. all of the H atoms pointing "up" or "down"(marked with an "X") are H2a or H3a atoms, the occupancies of which are 100%. They point towards anion F atoms, not other O atoms. Oxygen atoms shown as 50% white probability ellipsoids, hydrogens shown as white spheres of arbitrary size.

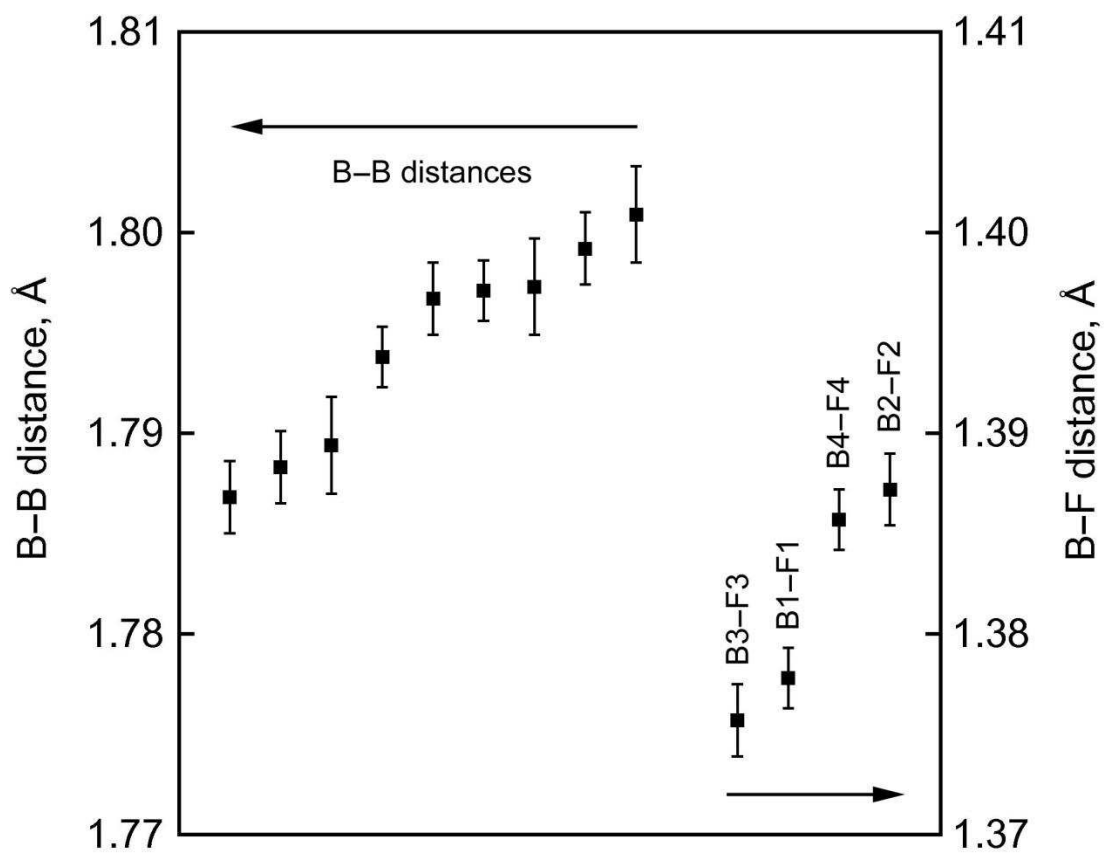


Figure 3-10. Plot of B–B and B–F distances in $(\text{H}_3\text{O})_2\text{B}_{12}\text{F}_{12} \cdot 6\text{H}_2\text{O}$ showing $\pm 3\sigma$.³¹

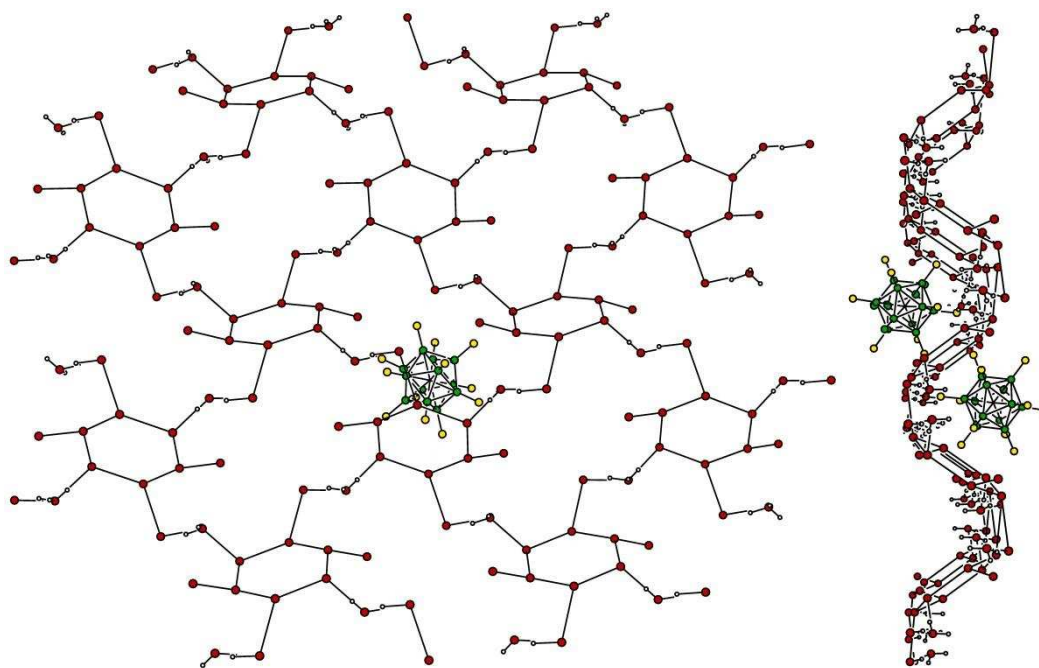


Figure 3-11. A top down view, left, and a side view, right, of the $(\text{H}_3\text{O})_2\text{B}_{12}\text{F}_{12}\cdot 4\text{H}_2\text{O}$ crystal structure collected by collaborator Dr. Prof. Konrad Seppelt. The most notable feature is the apparent hole in the 2D-hydrogen bonded network. This hydrogen bonded network is denoted L6(4)18(8) based on similar structures presented in the literature. Otherwise this structure is similar to the $(\text{H}_3\text{O})_2\text{B}_{12}\text{F}_{12}\cdot 6\text{H}_2\text{O}$ hydrate phase in that it has a CCP array of $\text{B}_{12}\text{F}_{12}^{2-}$ anions and layers of 2D-hydrogen bonded H_3O^+ cations and H_2O molecules. Hydrogens removed except those on H_3O^+ , oxygen atoms are red spheres, fluorine atoms are yellow spheres, boron atoms are green spheres, all spheres are of arbitrary size.

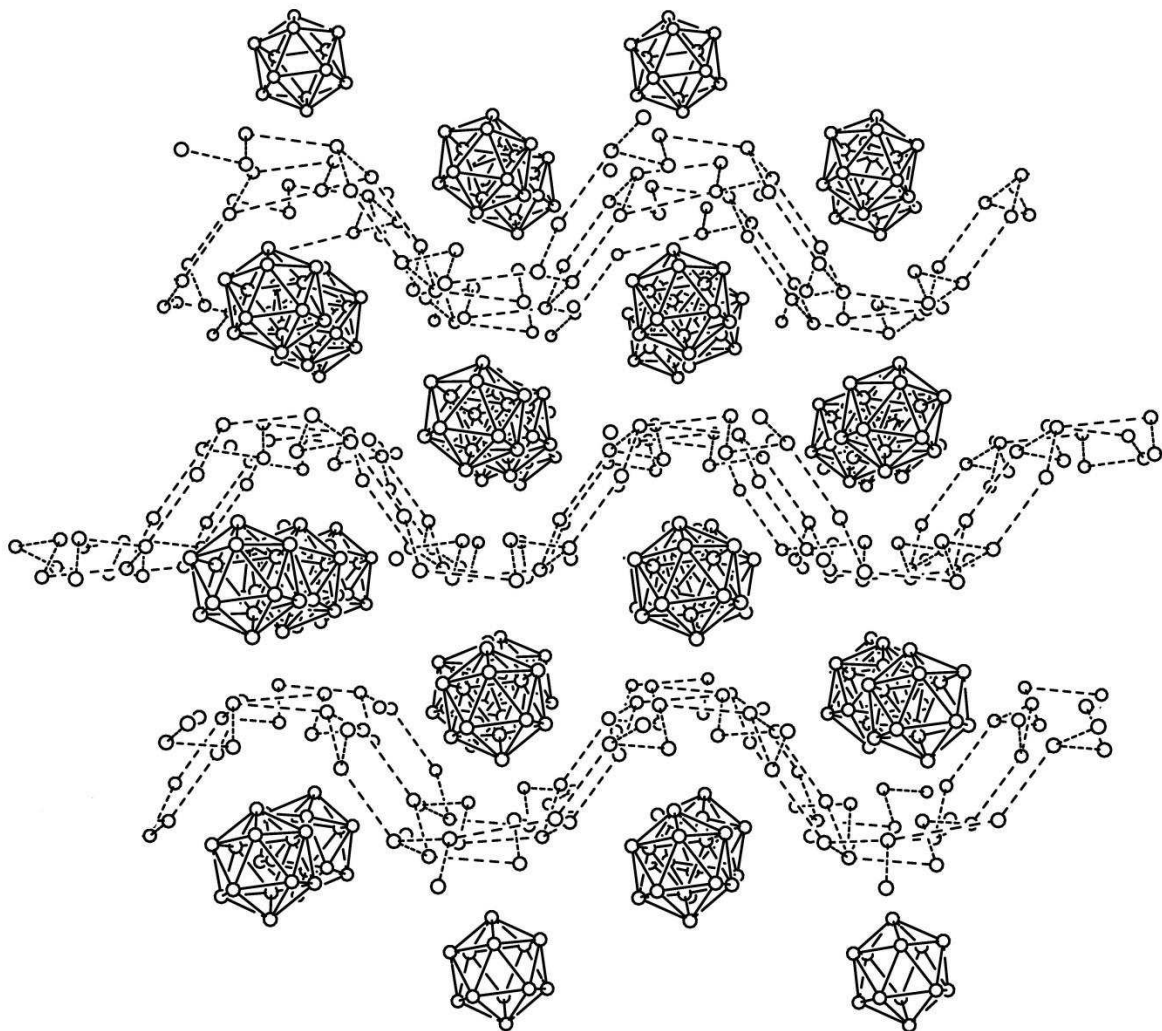


Figure 3-12. Looking through the $[\text{H}_3\text{O}^+/\text{2H}_2\text{O}]_n$ interconnected networks (hydrogens and fluorine atoms removed for clarity) illustrating the more pronounced corrugation of the $(\text{H}_3\text{O})_2\text{B}_{12}\text{F}_{12}\cdot 4\text{H}_2\text{O}$ compared to the $(\text{H}_3\text{O})_2\text{B}_{12}\text{F}_{12}\cdot 6\text{H}_2\text{O}$. Also note that the B_{12} cages are not rigorously planar between the $[\text{H}_3\text{O}^+/\text{2H}_2\text{O}]_n$ interconnected networks (compare to $(\text{H}_3\text{O})_2\text{B}_{12}\text{F}_{12}\cdot 6\text{H}_2\text{O}$ B_{12} centroids in Figure 3-4), but instead also have an oscillating pattern. Hydrogen bonded H_3O^+ and H_2O networks are connected with dashed lines, hydrogens and fluorines are removed for clarity, boron and oxygen atoms shown as spheres of arbitrary size.

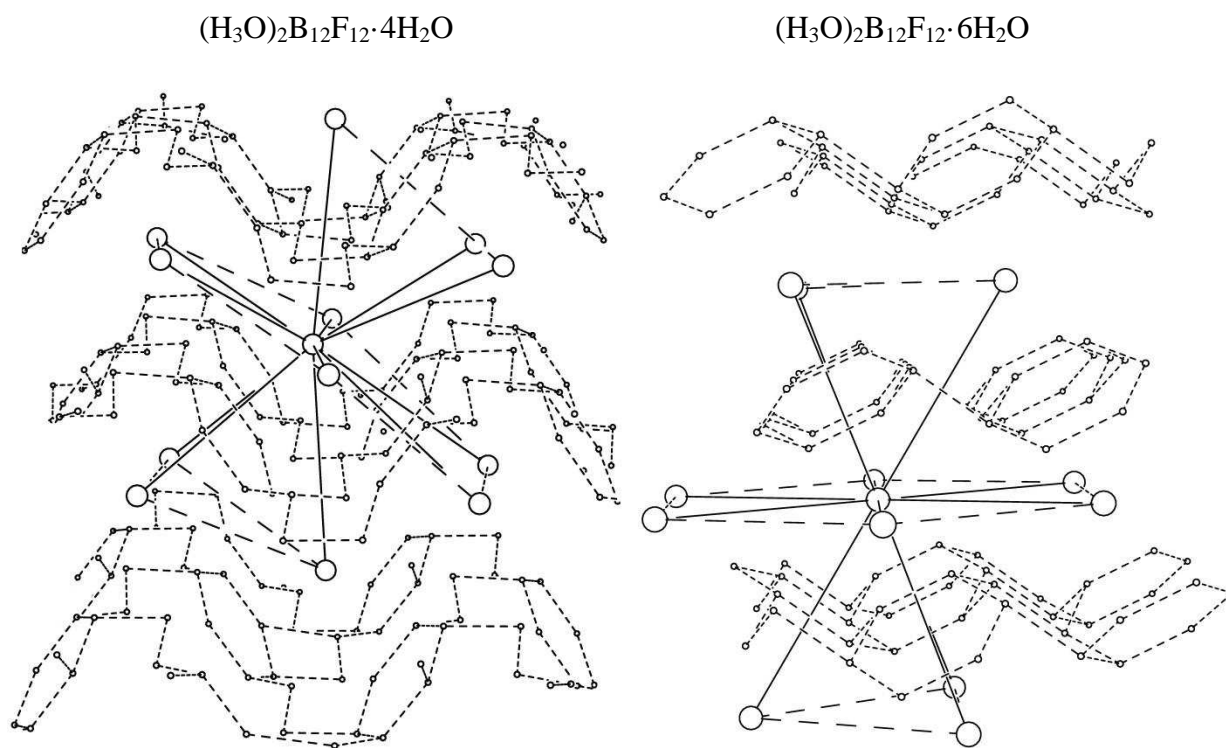


Figure 3-13. Comparison of B_{12} centroid closest neighbors in the $(\text{H}_3\text{O})_2\text{B}_{12}\text{F}_{12}\cdot 4\text{H}_2\text{O}$, left, and $(\text{H}_3\text{O})_2\text{B}_{12}\text{F}_{12}\cdot 6\text{H}_2\text{O}$, right, structures (B_{12} centroids represented by large hollow spheres of arbitrary size, hydrogens removed for clarity). Notice the $(\text{H}_3\text{O})_2\text{B}_{12}\text{F}_{12}\cdot 4\text{H}_2\text{O}$ nearest centroids are at an angle of 34.2° with respect to the direction of the $[\text{H}_3\text{O}^+/\text{2H}_2\text{O}]_n$ layers compared with $(\text{H}_3\text{O})_2\text{B}_{12}\text{F}_{12}\cdot 6\text{H}_2\text{O}$ where the nearest B_{12} centroids are parallel with the $[\text{H}_3\text{O}^+/\text{3H}_2\text{O}]_n$ layers.

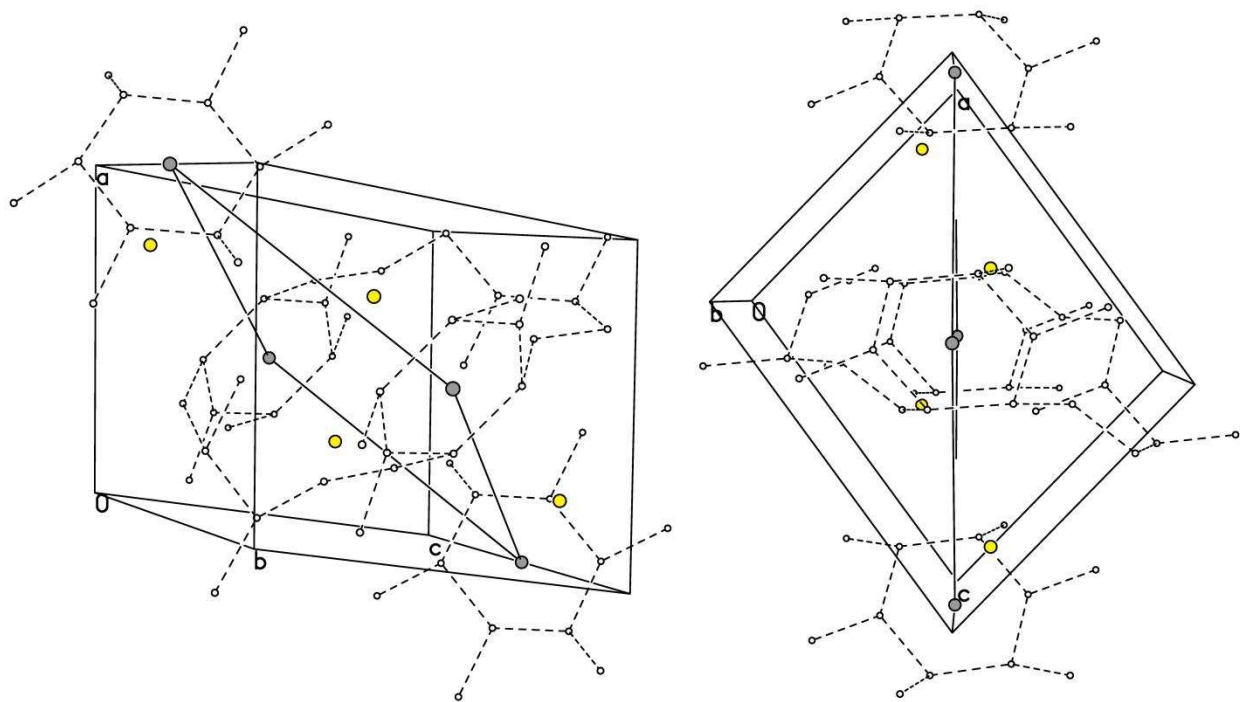


Figure 3-14. Centroids of O–H···O hydrogen bonded hexagons forming a diamond pattern within the unit cell. Left, tilted view showing the hexagon centroids on either the edge or face of the unit cell. Right, edge on view of plane showing how the B₁₂ cage centroids alternate on either side of plane and that 3 different 2 dimensional [H₃O⁺/2H₂O]_n networks pass through one unit cell. Hexagon centroids shown as grey spheres of arbitrary size, hydrogens removed from H₂O and H₃O⁺ O–H···O network for clarity, oxygen atoms shown as white spheres, B₁₂ centroids shown as yellow spheres, all spheres of arbitrary size.

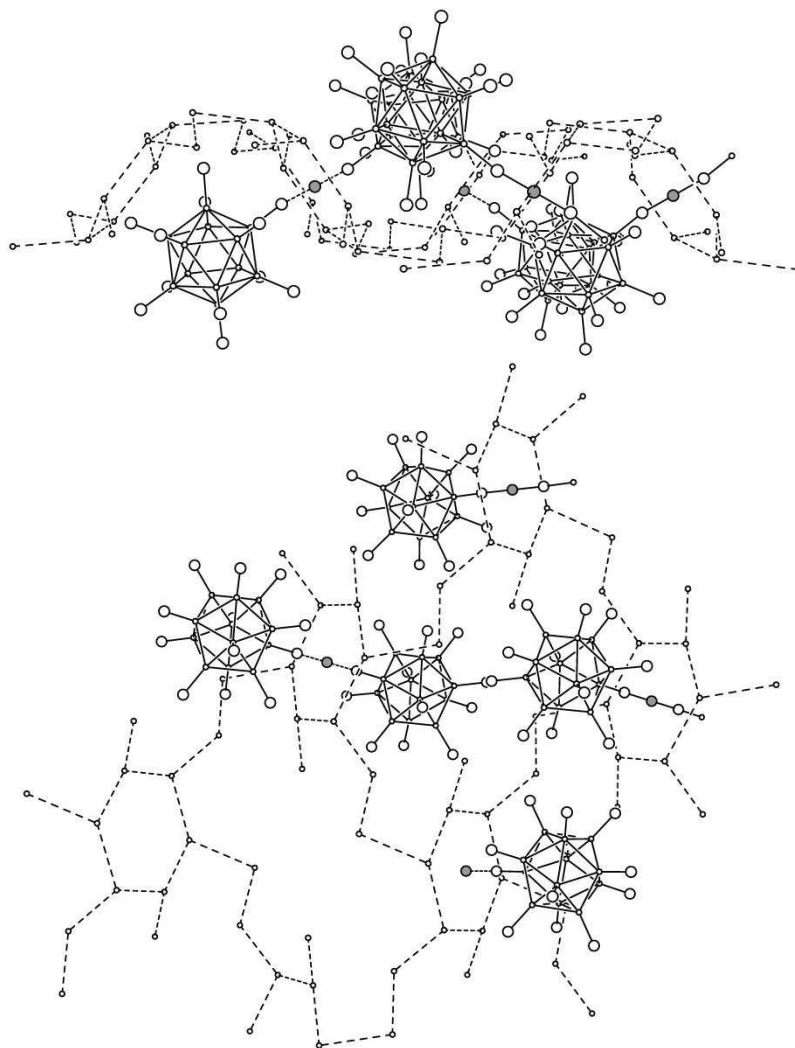


Figure 3-15. One 2 dimensional $[\text{H}_3\text{O}^+/\text{2H}_2\text{O}]_n$ network showing positioning of $\text{B}_{12}\text{F}_{12}^{2-}$ anion relative to the layer $[\text{H}_3\text{O}^+/\text{2H}_2\text{O}]_n$. (Top) Top down view showing $\text{B}_{12}\text{F}_{12}^{2-}$ off-set within a layer and B–F bond from $\text{B}_{12}\text{F}_{12}^{2-}$ anions on opposite sides of $[\text{H}_3\text{O}^+/\text{2H}_2\text{O}]$ hexagon point towards hexagon centroid. (Bottom) Same image as top rotated down 90° showing centroids of hexagons that are 1.351 \AA from a fluorine on either side of the centroid. Each $\text{B}_{12}\text{F}_{12}^{2-}$ anion only interacts with 1 hexagon centroid. The hexagons are planar with an estimated least squares distance of 0.028 \AA , and the hexagons within a side of the corrugation their mean planes are parallel and are 69.8° from the mean plane of the hexagons on the other side of the corrugation. Hexagon centroids $[\text{H}_3\text{O}^+/\text{2H}_2\text{O}]_n$ are shown as grey spheres, fluorine atoms are shown as large white spheres, boron and oxygen atoms shown as small white spheres, all spheres are of arbitrary size, hydrogens removed for clarity.

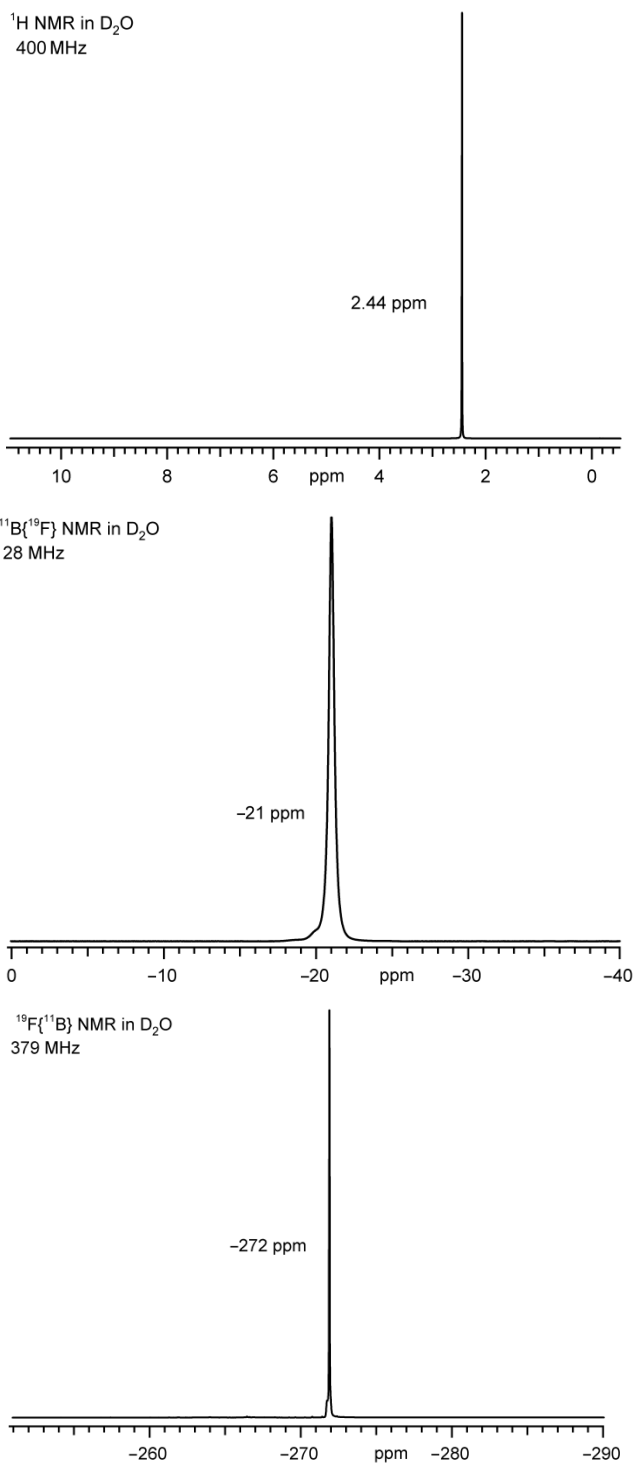


Figure 3-16. Proton, $^{11}\text{B}\{^{19}\text{F}\}$ and $^{19}\text{F}\{^{11}\text{B}\}$ NMR spectra of $(\text{H}_3\text{O})_2\text{B}_{12}\text{F}_{12} \cdot n\text{H}_2\text{O}$ in D_2O . Single peaks in all three NMR spectrums indicate a high purity of the $\text{B}_{12}\text{F}_{12}^{2-}$ anion as well as high purity with regards to solvents and other common chemical contaminants.

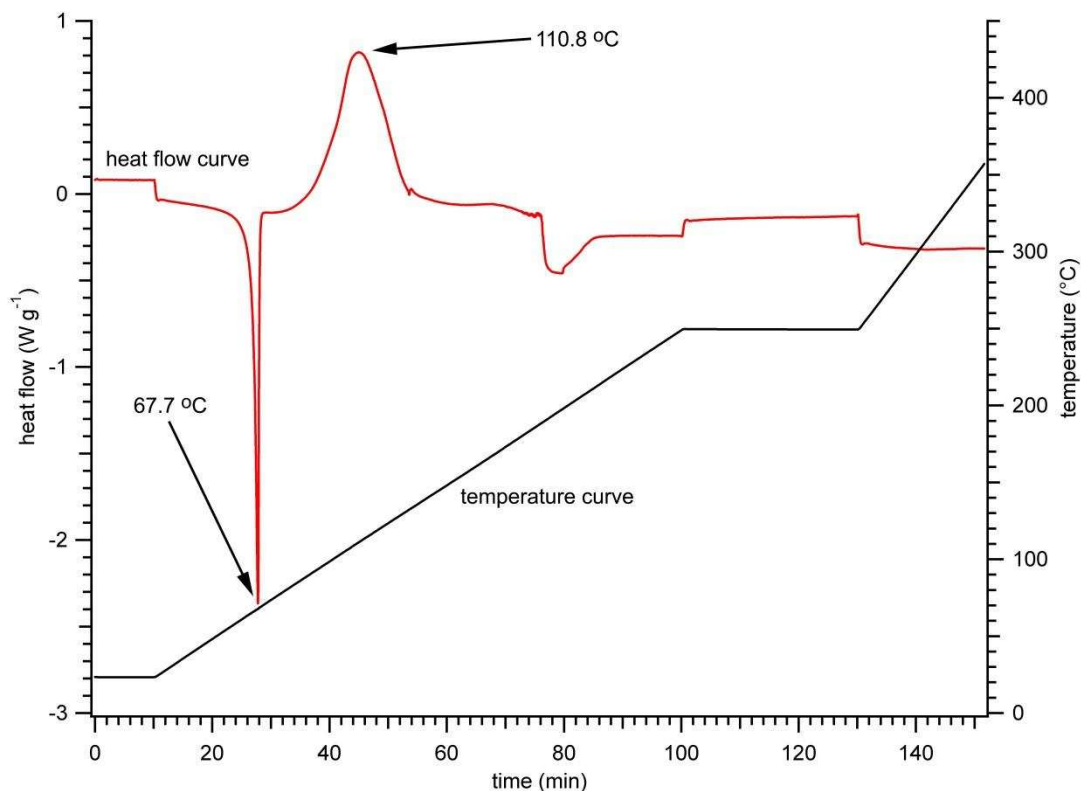


Figure 3-17. Thermogram of $(\text{H}_3\text{O})_2\text{B}_{12}\text{F}_{12}\cdot 6\text{H}_2\text{O}$ in aluminum pan. The $(\text{H}_3\text{O})_2\text{B}_{12}\text{F}_{12}\cdot 6\text{H}_2\text{O}$ appears to first melt at a $T_{max} = 67.7$ °C, preceded by a slow loss of water indicated by the gradual decrease in heat flow, the sharp endothermic event is likely melting of the sample. Then the molten sample exhibited a broad exothermic event at 110.8 °C that could be the molten acid reacting with the Al pan containing the sample.

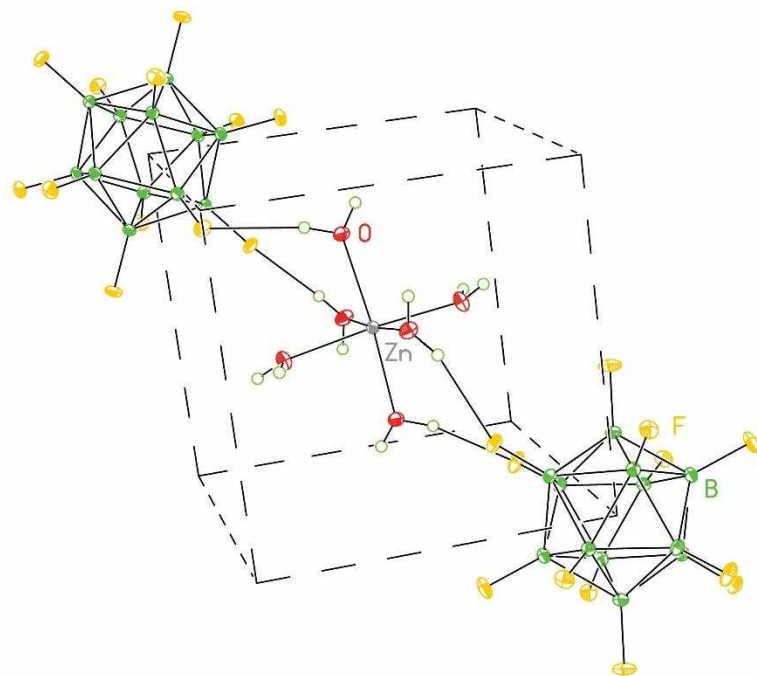


Figure 3-18. Crystal structure of $\text{ZnB}_{12}\text{F}_{12}\cdot 6\text{H}_2\text{O}$ synthesized from Zn metal and $(\text{H}_3\text{O})_2\text{B}_{12}\text{F}_{12}\cdot n\text{H}_2\text{O}$. There are 6 H_2O molecules coordinated to the central Zn^{2+} and the hydrogens from the water exhibit weak interactions with the fluorines in the $\text{B}_{12}\text{F}_{12}^{2-}$ anion. Zinc (grey), boron (green) and fluorine (yellow) shown as 50% thermal ellipsoids, hydrogens water shown as spheres of arbitrary size, other B_{12} cage centroids shown as points of the unit cell.

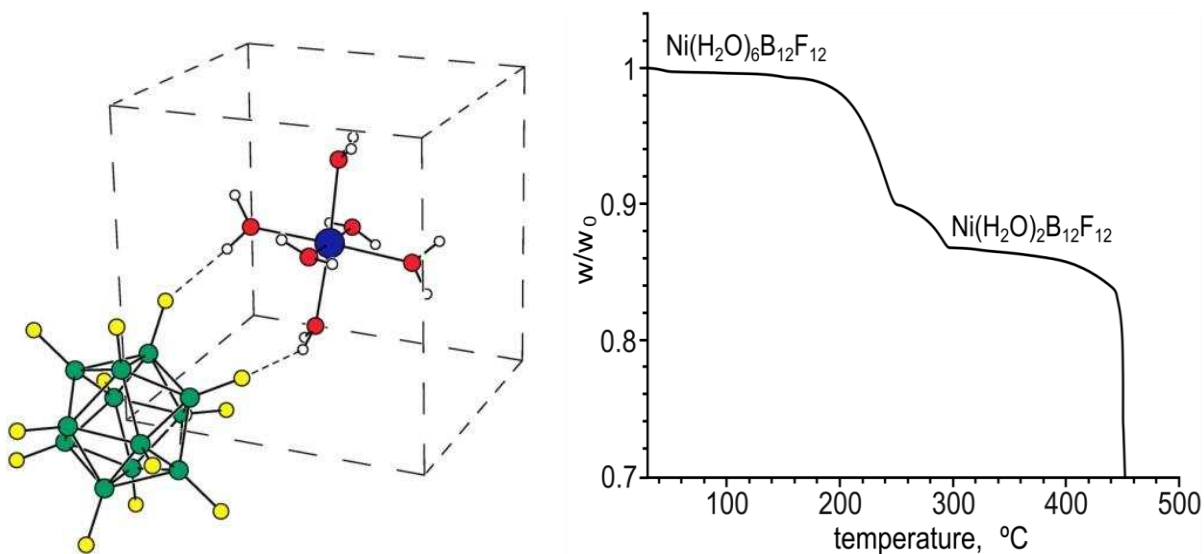


Figure 3-19. Left, generic crystal structure of $M(B_{12}F_{12}) \cdot 6H_2O$ salts (where $M = Co^{2+}, Mg^{2+}, Ni^{2+}, Zn^{2+}$), M atom (purple), oxygen atoms (red), boron (green), fluorine (yellow), hydrogen (white) are all spheres of arbitrary size. The B_{12} cage centroids are point of the unit cell. Right, thermogravimetric analysis of $Ni(B_{12}F_{12}) \cdot 6H_2O$, exhibiting decomposition when attempting to thermally dry $M(B_{12}F_{12}) \cdot 6H_2O$ salts. The sample quickly lost 4 equivalents of H_2O , however upon further heating the sample decomposed to a mass well below the mass equating to $NiB_{12}F_{12}$.

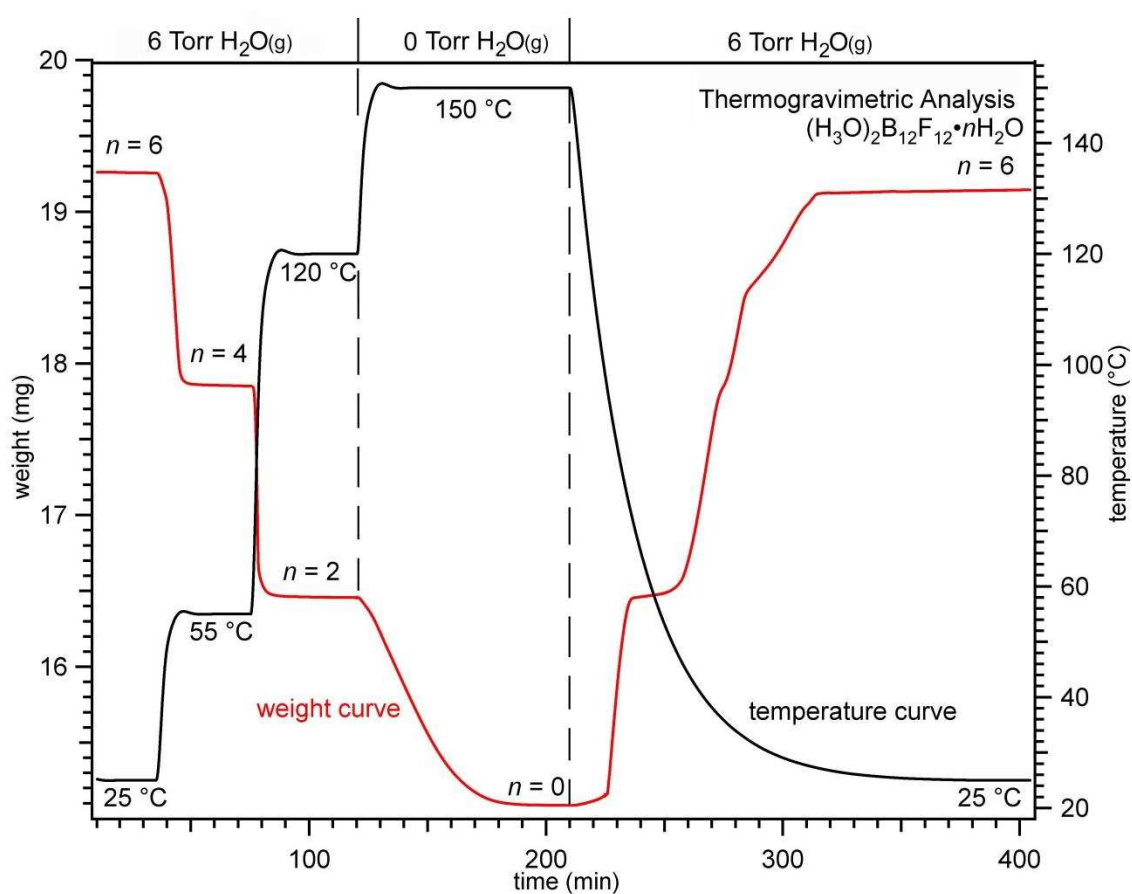


Figure 3-20. Thermogravimetric analysis of $(\text{H}_3\text{O})_2\text{B}_{12}\text{F}_{12}\cdot 6\text{H}_2\text{O}$ as a function of temperature and presence of H_2O vapor. Each hydrate phase was held isothermally at constant $P(\text{H}_2\text{O})$ for 30 min to ensure the hydrate phase was stable. The sample was initially equilibrated at $25\text{ }^\circ\text{C}$ and $P(\text{H}_2\text{O}) = 6(1)\text{ Torr}$ to ensure the major hydrate phase was $(\text{H}_3\text{O})_2\text{B}_{12}\text{F}_{12}\cdot n\text{H}_2\text{O}$ where $n = 6$.³¹

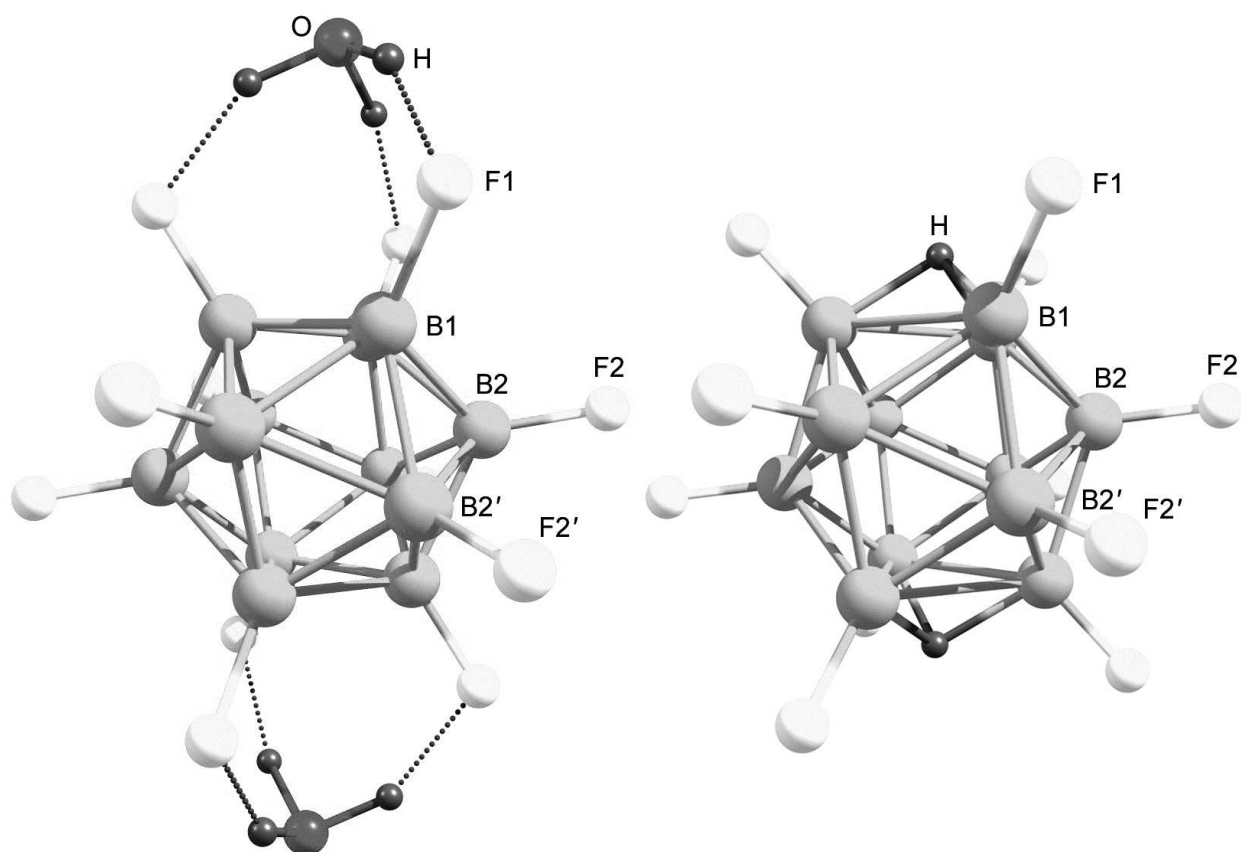


Figure 3-21. Theoretical structures of $(\text{H}_3\text{O})_2\text{B}_{12}\text{F}_{12}$, left, and $\text{H}_2\text{B}_{12}\text{F}_{12}$, right, by PBE0 DFT-predicted calculations by collaborator Dr. Alexey Popov.

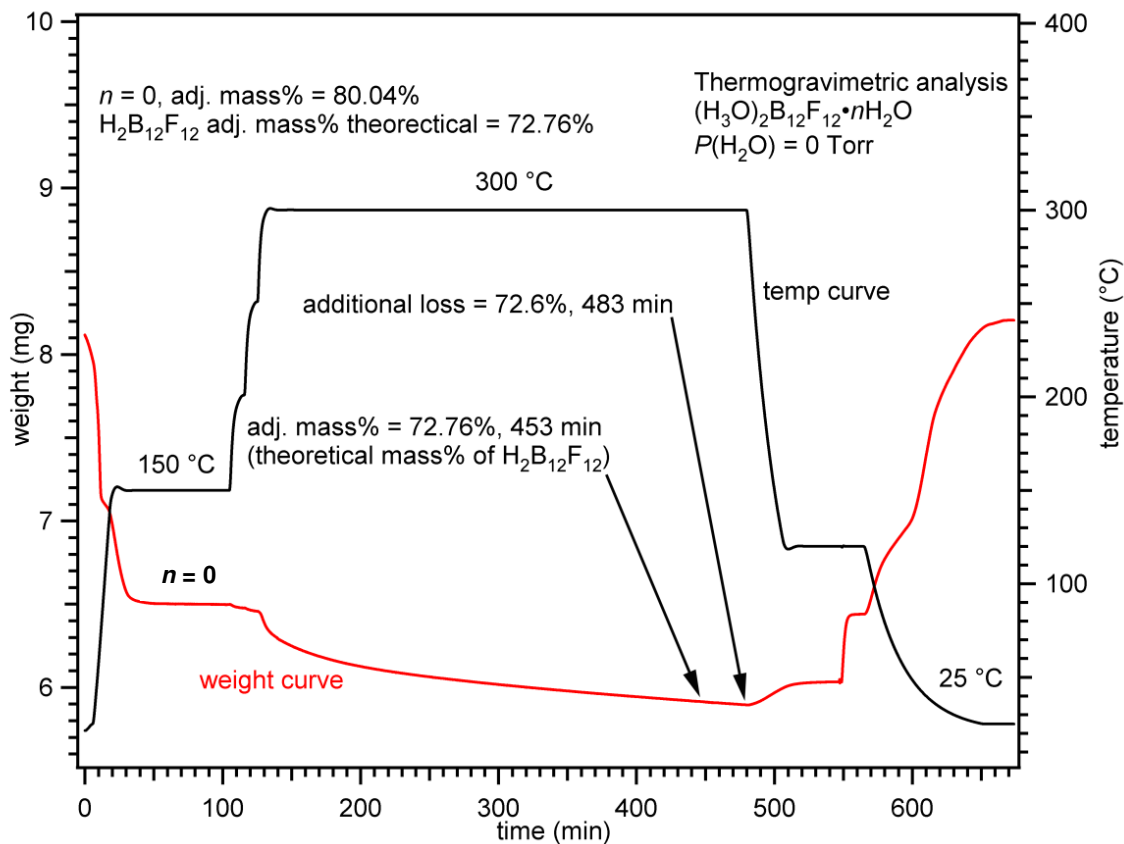


Figure 3-22. Thermogravimetric analysis of $(\text{H}_3\text{O})_2\text{B}_{12}\text{F}_{12} \cdot 6\text{H}_2\text{O}$ thermal stability experiment. The red curve is the weight curve (left axis) and the black curve is the temperature curve (right axis). The sample mass theoretically should have stayed consistent at 72.76% if the $\text{H}_2\text{B}_{12}\text{F}_{12}$ phase was stable at these conditions. Notice the mass continues to decrease past 72.76% indicating some additional mode of mass loss other than dehydration. Mass loss between the two arrows equates to 0.13% or 11 μg .

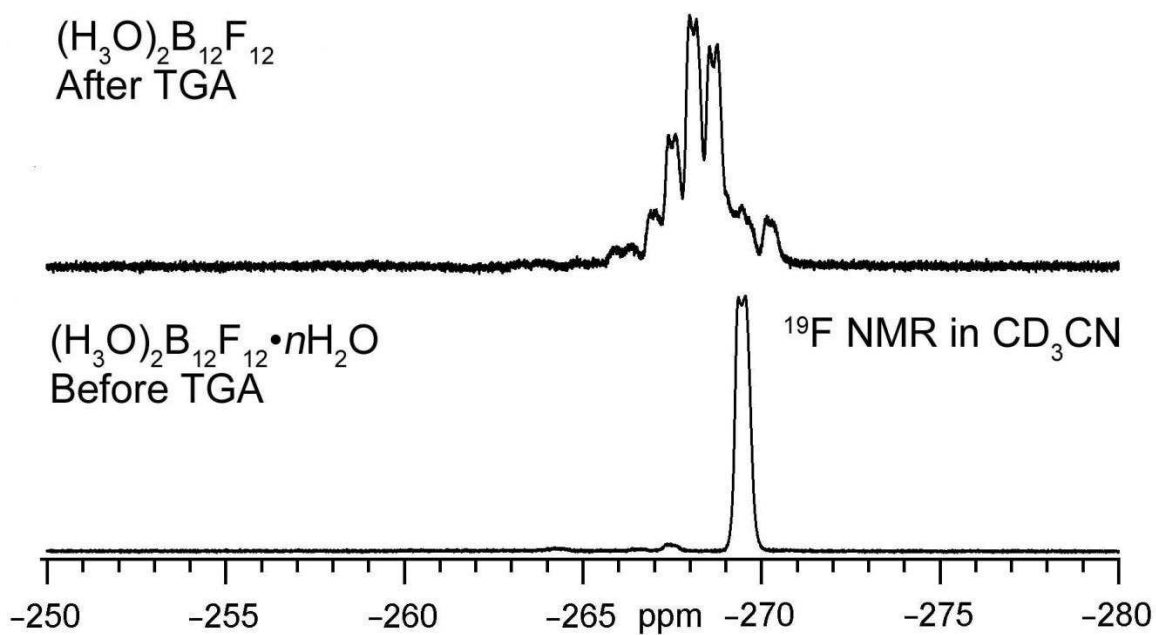


Figure 3-23. Fluorine-19 NMR spectra in CD_3CN comparison of $(\text{H}_3\text{O})_2\text{B}_{12}\text{F}_{12} \cdot n\text{H}_2\text{O}$ before and after prolonged heating at $300\text{ }^\circ\text{C}$ in a TGA experiment. Notice the formation of new peaks shifted farther up-field from $\text{B}_{12}\text{F}_{12}^{2-}$. The spectrum is not referenced, ^{19}F at 376 MHz.

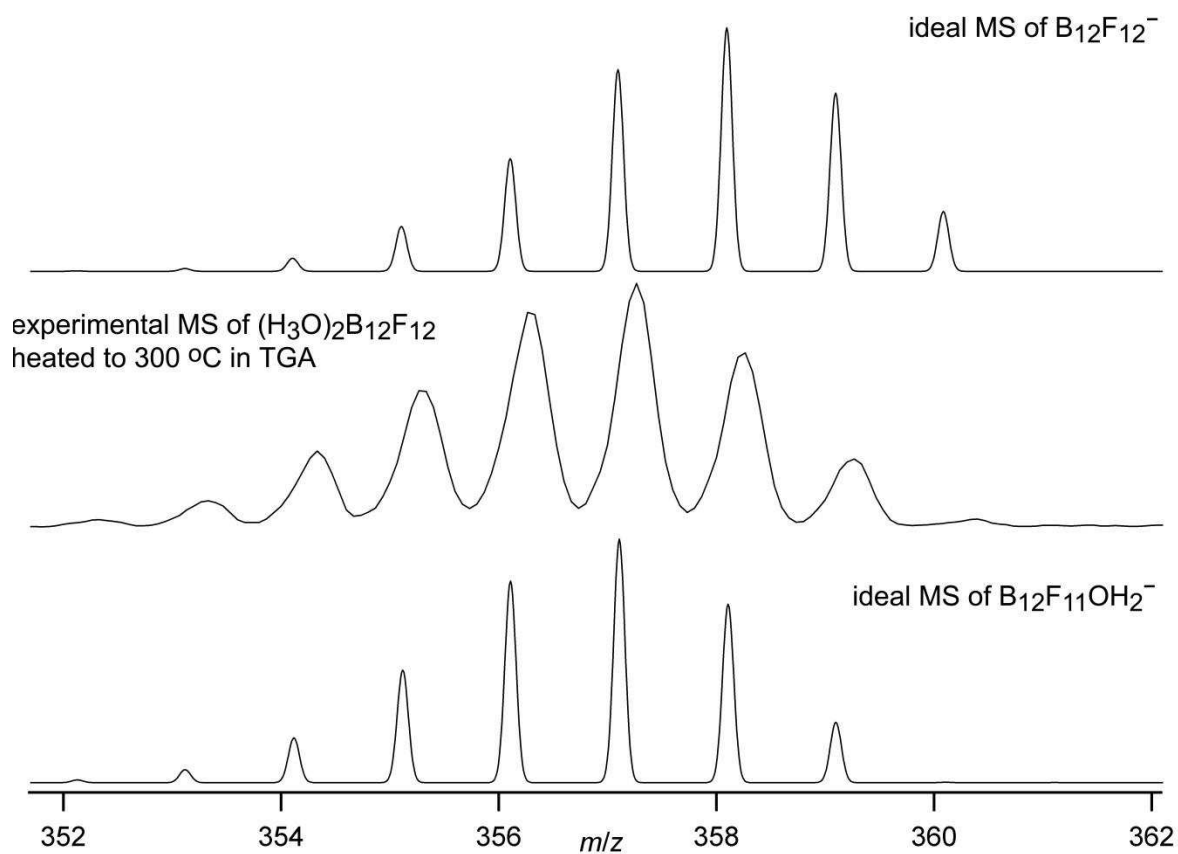


Figure 3-24. Experimental ESI-MS analysis of $(\text{H}_3\text{O})_2\text{B}_{12}\text{F}_{12}\cdot\text{OH}_2\text{O}$ after it was heated to $300\text{ }^\circ\text{C}$ in the TGA compared to idealized mass spectra for $\text{B}_{12}\text{F}_{12}^-$ ($m/z = 358$) and $\text{B}_{12}\text{F}_{11}\text{OH}_2^-$ ($m/z = 357$). Note that the isotopic peak ratio and the mass fit more closely with the $\text{B}_{12}\text{F}_{11}\text{OH}_2^-$ mass than with $\text{B}_{12}\text{F}_{12}^-$ mass.

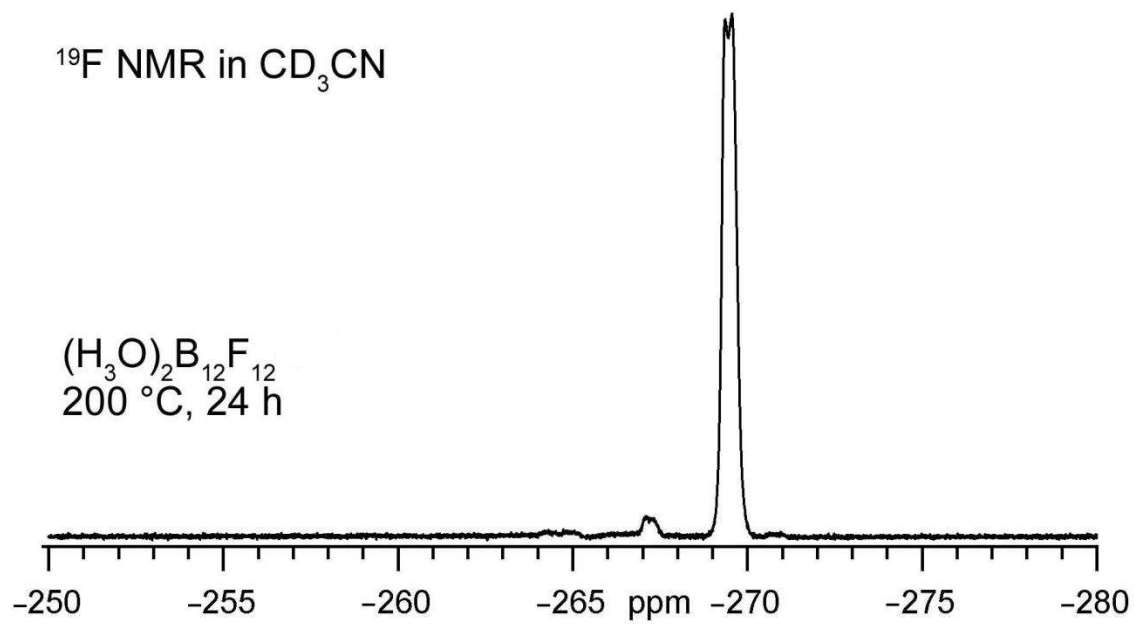


Figure 3-25. Fluorine-19 NMR spectrum of $(\text{H}_3\text{O})_2\text{B}_{12}\text{F}_{12}\cdot n\text{H}_2\text{O}$ after holding isothermal at 200 °C under dynamic vacuum for 24 h. The spectrum is not referenced, ^{19}F at 376 MHz.

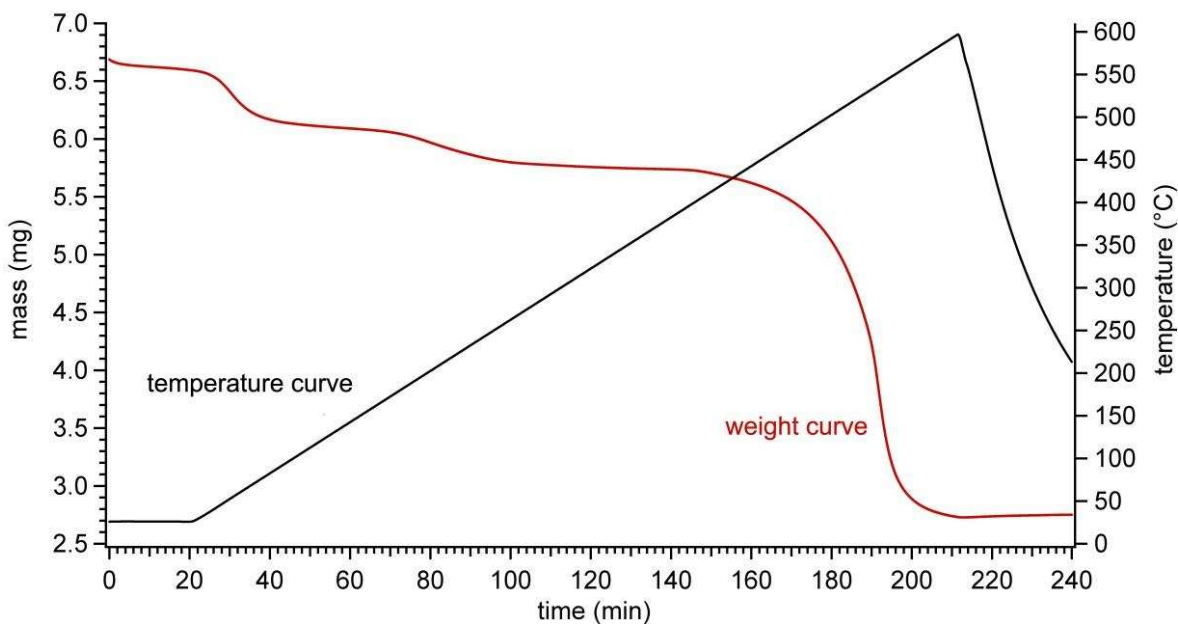


Figure 3-26. Thermogravimetric analysis of $(\text{NH}_4)_2\text{B}_{12}\text{F}_{12} \cdot n\text{H}_2\text{O}$ performed by Dimitry Peryshkov. It was believed that the first mass loss event correlated to the loss of 2 H_2O molecules and the second mass loss event correlated to the loss of the 2 NH_3 molecules leaving behind $\text{H}_2\text{B}_{12}\text{F}_{12}$, that appeared to be thermally stable up to ca. 400 °C.

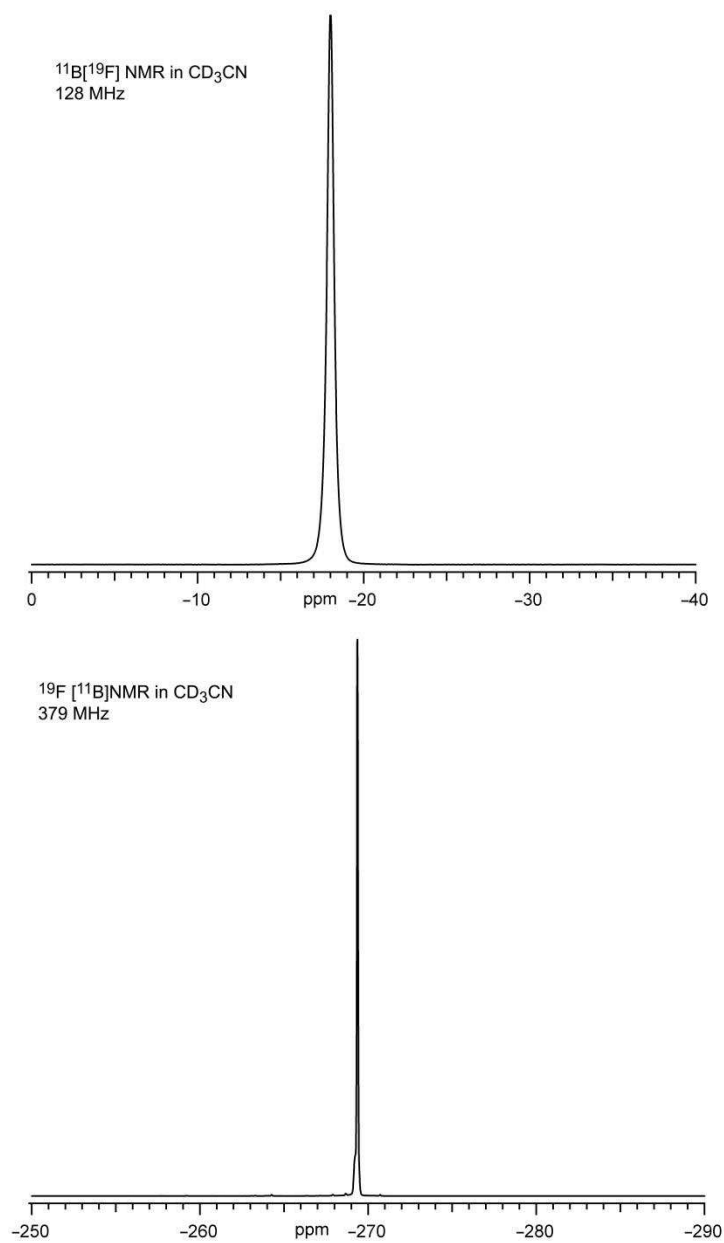


Figure 3-27. Boron-11 [^{19}F] and $^{19}\text{F}[^{11}\text{B}]$ NMR spectroscopy analysis of a sample of $(\text{NH}_4)_2\text{B}_{12}\text{F}_{12} \cdot n\text{H}_2\text{O}$ heated slowly to 200 °C then 300 °C over a 24 h span then held isothermally at 300 °C for 24 h. Top, $^{11}\text{B}[^{19}\text{F}]$ in dry CD_3CN , no standard, highly purified $\text{B}_{12}\text{F}_{12}^{2-}$ yields one ^{11}B signal. Bottom, $^{19}\text{F}[^{11}\text{B}]$ in dry CD_3CN , no standard, highly purified $\text{B}_{12}\text{F}_{12}^{2-}$ yields one ^{19}F signal. The $^{11}\text{B}[^{19}\text{F}]$ or $^{19}\text{F}[^{11}\text{B}]$ NMR spectra indicate that the $\text{B}_{12}\text{F}_{12}^{2-}$ anion remained intact after the prolonged heating at 300 °C.

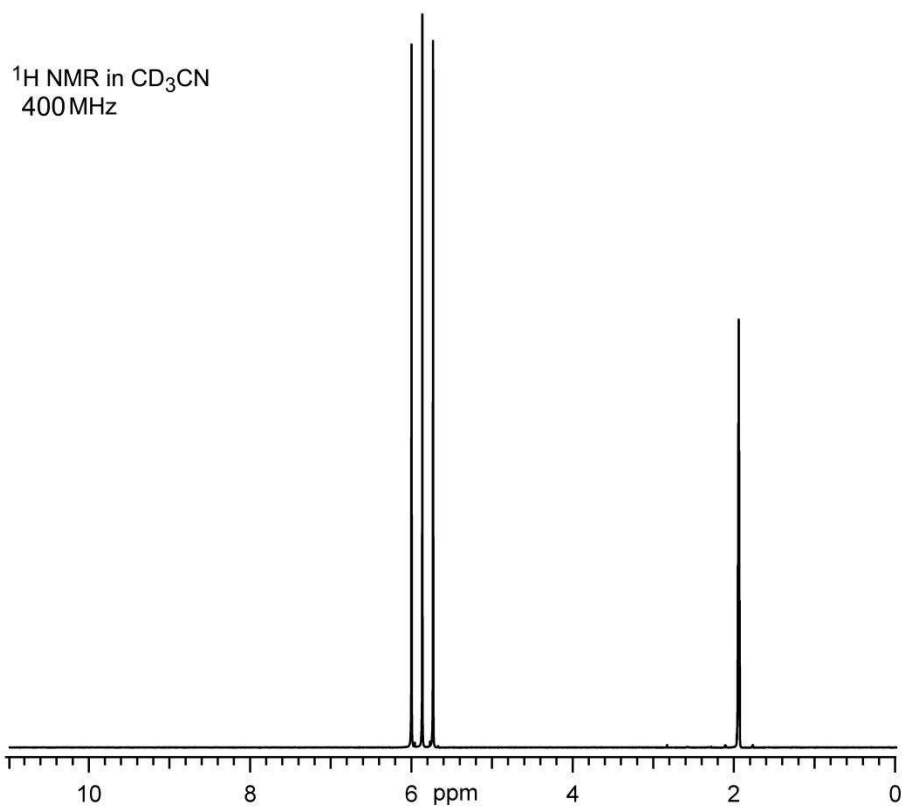


Figure 3-28. Proton NMR spectrum of a sample of $(\text{NH}_4)_2\text{B}_{12}\text{F}_{12}\cdot n\text{H}_2\text{O}$ referenced to residual proton solvent peak (CD_2HCN δ 1.94) heated slowly from 200 °C to 300 °C over a 24 h span then held isothermally at 300 °C for 24 h. Chemical shift of NH_4^+ protons = 5.93 ppm with $J_{\text{NH}} = 55.2$ Hz.

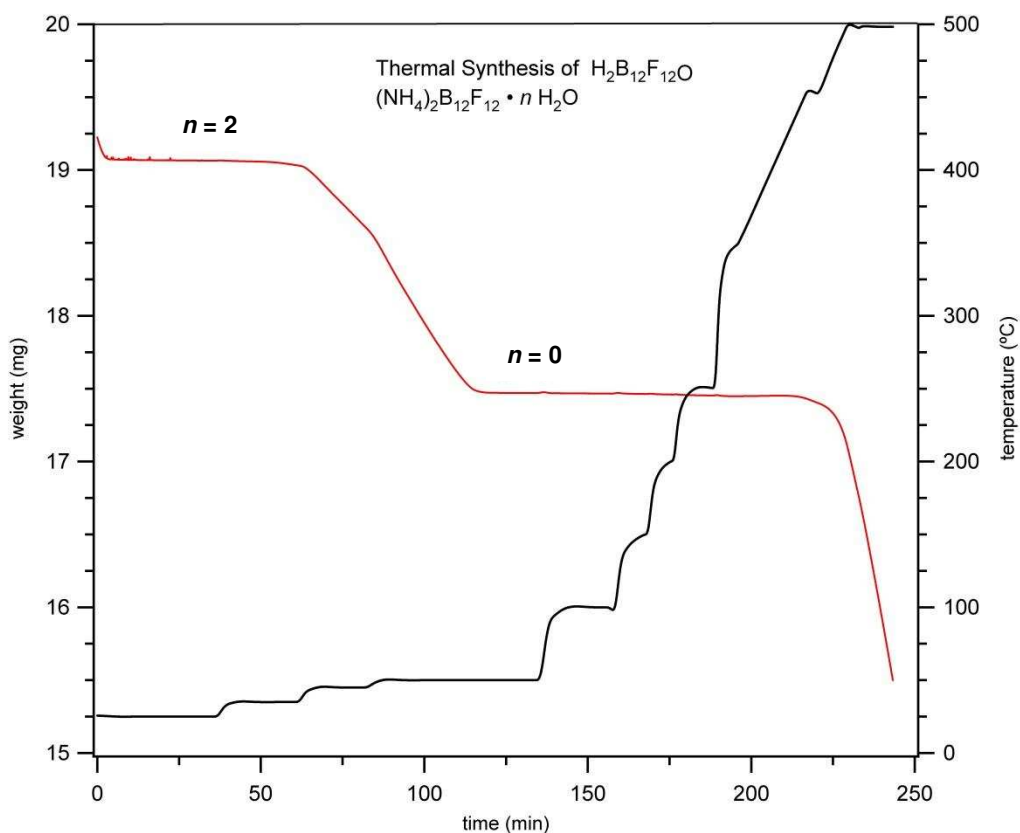


Figure 3-29. Thermogravimetric analysis of $(\text{NH}_4)_2\text{B}_{12}\text{F}_{12} \cdot 2\text{H}_2\text{O}$. The first mass loss equates to 2 eq. of H_2O and occurs slowly at a range of 35–50 °C. The $(\text{NH}_4)_2\text{B}_{12}\text{F}_{12}$ salt was stable at ca. 50 °C until ca. 450 °C. After the temperature was increased past 450 °C, the sample began to lose mass, but that mass loss continued past the theoretical mass for $\text{H}_2\text{B}_{12}\text{F}_{12}$.

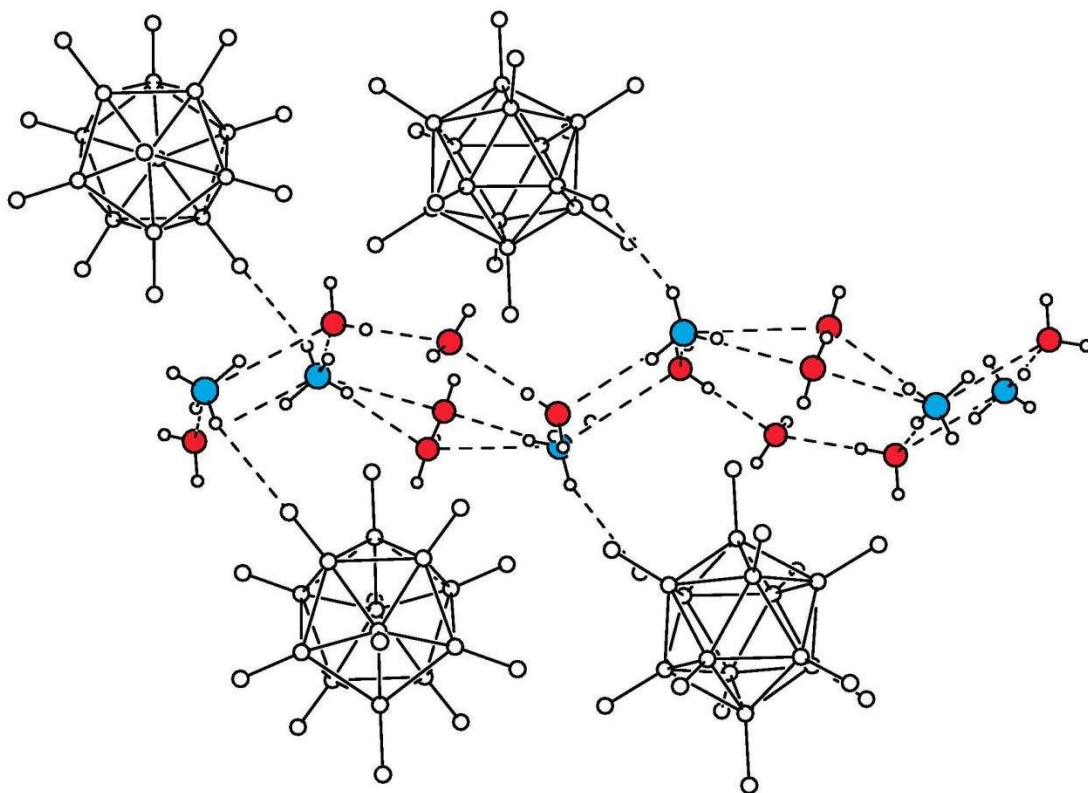


Figure 3-30. Ribbon of hydrogen bonded NH_4^+ and H_2O molecules with $\text{B}_{12}\text{F}_{12}^{2-}$ anions interacting with NH_4^+ protons. Ribbon is comprised of 4 and 6 membered rings. The 6 membered rings are made up of 2 NH_4^+ cations, 4 water molecules, one of which (O3) is disordered about a special position and the ring is not planar and deviates from the LSP by 0.15 Å. The 4 membered ring made up of 2 NH_4^+ cations and 2 H_2O molecules, is rigorously planar, and is 51.4° tilted from the 6 membered rings on either side. The $\text{N}-\text{H}\cdots\text{F}$ interactions are weak with $\text{H}-\text{F}$ distances ranging from 2.26–2.77 Å. Oxygen atoms shown as red spheres, nitrogen atoms shown as blue spheres, boron and fluorine atoms shown as large white spheres, hydrogen atoms shown as small white spheres, all spheres of arbitrary size.

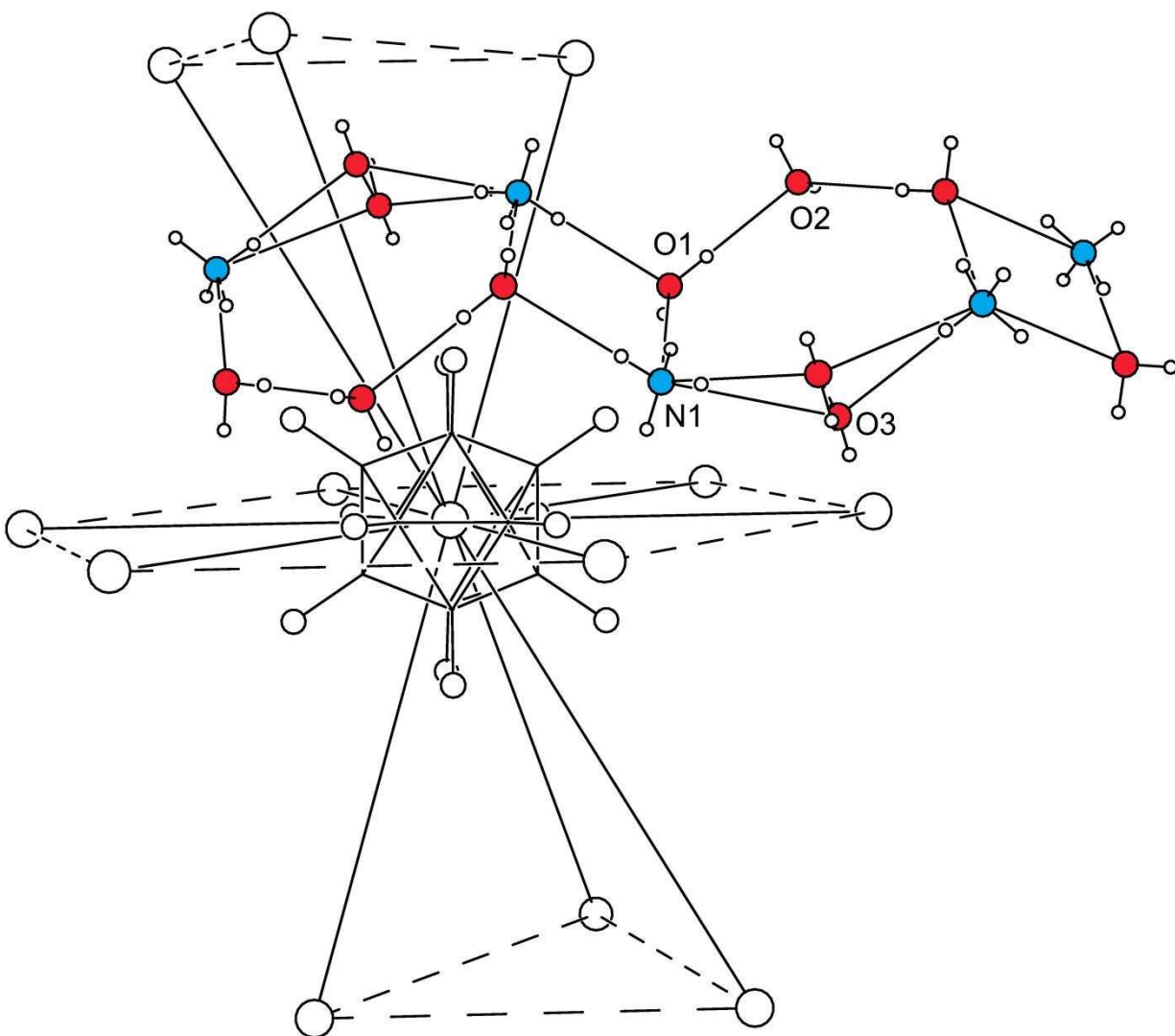


Figure 3-31. The $B_{12}F_{12}^{2-}$ anions form a cubic close packed array and are rigorously planar and parallel. The $[NH_4^+/2H_2O]_n$ interconnected ribbons fit between the layers of $B_{12}F_{12}^{2-}$ anions. The N1 coordinates to 3 adjacent H_2O molecules and the remaining H coordinates to 3 fluorine atoms from 3 $B_{12}F_{12}^{2-}$ anions. All but central B_{12} cage has been removed only showing centroid position with large white spheres of arbitrary size for clarity. Oxygen atoms shown as red spheres, nitrogen atoms shown as blue spheres, boron and fluorine atoms shown as large white spheres, hydrogen atoms shown as small white spheres, all spheres of arbitrary size.

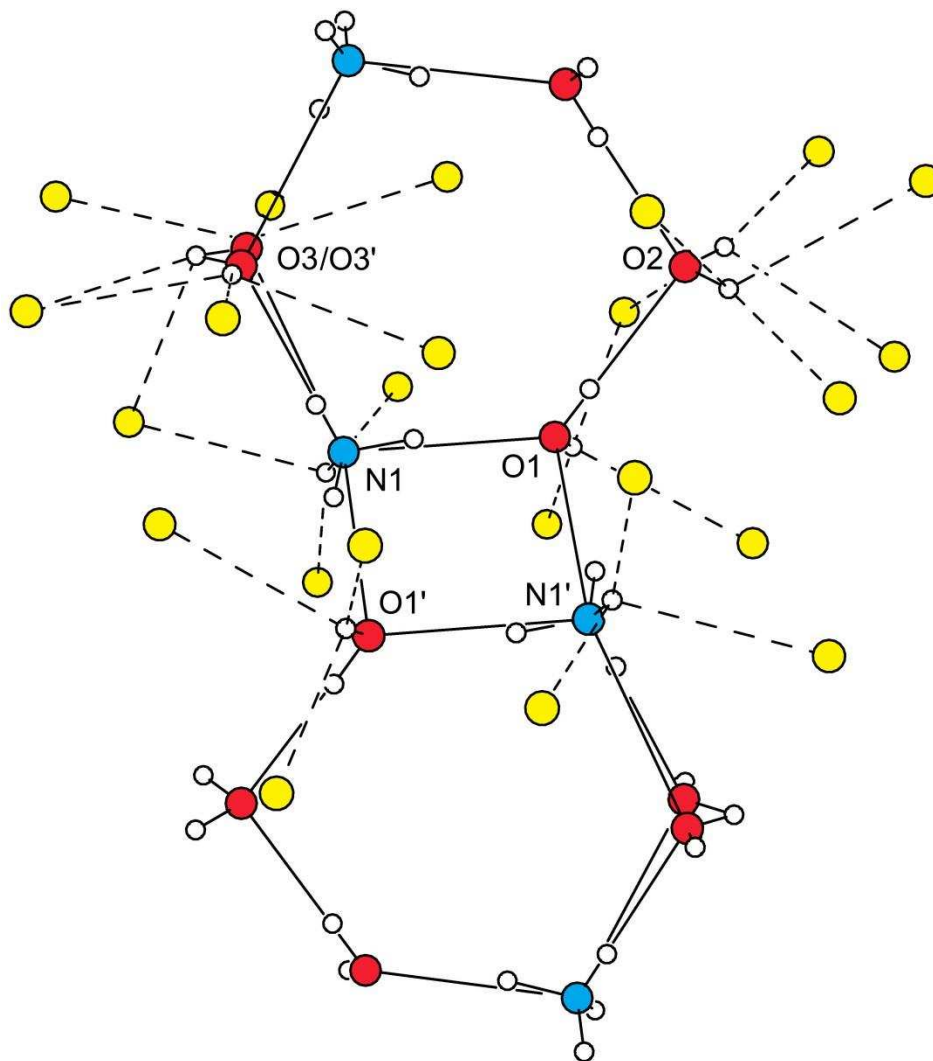


Figure 3-32. Hydrogen bonded network of $[\text{NH}_4^+/\text{2H}_2\text{O}]_n$ (all standard errors are 0.01 \AA) with $\text{N}\cdots\text{O}$ distances of 2.79 and 2.91 \AA for $\text{N1}\cdots\text{O1}$ and $\text{N1}\cdots\text{O1}'$ respectively, and $\text{N1}\cdots\text{O3}$, $\text{N1}\cdots\text{O3}'$ distances of 2.86 and 2.95 \AA respectively, and $\text{O1}\cdots\text{O2}$ distances of 2.85 \AA . There is also an extensive network of $\text{H}\cdots\text{F}$ interactions from NH_4^+ cations and H_2O molecules. The $\text{H}\cdots\text{F}$ interactions from NH_4^+ (N1) are 2.26 , 2.49 and 2.77 \AA ; $\text{H}\cdots\text{F}$ interactions from O1 are 2.17 , 2.56 , and 2.76 \AA , $\text{H}\cdots\text{F}$ interactions from O2 are 2.26 , 2.86 , and 2.91 , and $\text{H}\cdots\text{F}$ interactions from $\text{O3/O3}'$ are 2.49 , 2.66 , 2.83 , and 2.87 \AA . Oxygen atoms shown as red spheres, nitrogen atoms shown as blue spheres, fluorine atoms shown as yellow spheres, hydrogen atoms shown as small white spheres, all spheres of arbitrary size.

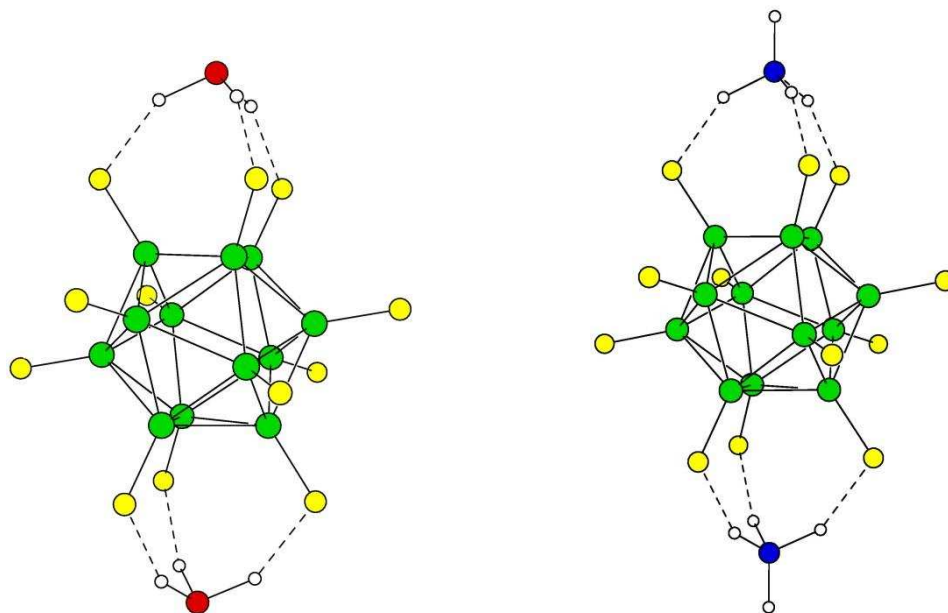


Figure 3-33. (Left) DFT predicted structure of $(\text{H}_3\text{O})_2\text{B}_{12}\text{F}_{12}$ produced by collaborator Dr. Alex Popov. (Right) hypothetical structure of $(\text{NH}_4)_2\text{B}_{12}\text{F}_{12}$ made from the $(\text{H}_3\text{O})_2\text{B}_{12}\text{F}_{12}$ atomic coordinates and replacing the oxygen atom with a nitrogen and making it tetrahedral geometry. Oxygen atoms shown as red spheres, nitrogen atoms shown as blue spheres, boron atoms shown as green spheres, fluorine atoms shown as yellow spheres, hydrogen atoms shown as small white spheres, all spheres of arbitrary size.

3.9 Tables

Table 3-1. Selected Interatomic Distances [Å] and Angles [°] for $(\text{H}_3\text{O})_2\text{B}_{12}\text{F}_{12} \cdot 6\text{H}_2\text{O}$

| | | | |
|-----------|-----------|---------------|-----------|
| B–B | 1.787(1)– | O2...O1...O3 | 125.53(2) |
| B–F | 1.801(1) | O3...O1...O3' | 96.20(4) |
| O1...O2 | 1.377(1)– | O1...O2...O3 | 112.72(2) |
| O1...O3 | 1.388(1) | O3...O2...O3' | 108.36(3) |
| O2...O3 | 2.590(1) | O1...O3...O2 | 121.58(3) |
| O3...O3' | 2.5739(8) | O1...O3...O3' | 89.70(3) |
| O2...H1b | 2.8920(8) | O2...O3...O3' | 124.89(2) |
| O2...H3c | 2.911(1) | | |
| O3...H1a | 1.72(1) | | 2.43(1) |
| O3...H2b | 2.09(1) | F2...H3a | 2.67(1) |
| F1...H1a | 1.73(1) | F3...H3b' | 2.35(1) |
| F1...H1b | 2.04(1) | F3...H3b | 2.57(1) |
| F2...H3a | 2.54(1) | F3...H3c | 2.55(1) |
| | 2.68(1) | F4...H2a | |
| | 2.43(1) | | |
| F3...H3b' | 2.67(1) | F4...H3a | 2.25(1) |

Table 3-2. Crystallographic and Data Collection Parameters for (H₃O)₂B₁₂F₁₂·6H₂O, (H₃O)₂B₁₂F₁₂·4H₂O, and (NH₄)₂B₁₂F₁₂·6H₂O.

| compound | (H ₃ O) ₂ B ₁₂ F ₁₂ ·6H ₂ O | (H ₃ O) ₂ B ₁₂ F ₁₂ ·4H ₂ O | (NH ₄) ₂ B ₁₂ F ₁₂ ·4H ₂ O |
|---|--|--|--|
| empirical formula | B ₁₂ F ₁₂ H ₁₈ O ₈ | B ₁₂ F ₁₂ H ₁₄ O ₆ | B ₁₂ F ₁₂ H ₁₆ N ₂ O ₄ |
| formula weight | 503.86 | 467.82 | 465.87 |
| habit, color | prism, colorless | needle, brown | cube, colorless |
| crystal dimensions (mm) | 0.18 × 0.18 × 0.06 | 0.40 × 0.20 × 0.15 | 0.45 × 0.28 × 0.17 |
| space group | <i>C2/m</i> | <i>P2₁/n</i> | <i>C2/c</i> |
| <i>a</i> (Å) | 14.5041(21) | 10.6533(16) | 10.5112(10) |
| <i>b</i> (Å) | 8.5208(7) | 12.845(2) | 13.3851(12) |
| <i>c</i> (Å) | 8.7025(7) | 12.592(2) | 13.3966(13) |
| <i>α</i> (deg) | 90 | 90 | 90 |
| <i>β</i> (deg) | 122.070(3) | 99.528(5) | 108.876(4) |
| <i>γ</i> (deg) | 90 | 90 | 90 |
| <i>V</i> (Å ³) | 911.36(13) | 1699.3(5) | 1783.5(3) |
| <i>Z</i> | 2 | 4 | 4 |
| <i>T</i> (K) | 120(2) | 133(2) | 233(2) |
| <i>ρ</i> _{calc} (g cm ⁻³) | 1.836 | 1.829 | 1.735 |
| <i>R</i> (<i>F</i>) (<i>I</i> > 2σ(<i>I</i>)) ^a | 0.0212 | 0.0403 | 0.0364 |
| <i>wR</i> (<i>F</i> ²) [all data] ^a | 0.0648 | 0.1102 | 0.1048 |
| min., max. e ⁻ dens., (e Å ⁻³) | -0.36, 0.20 | -0.27, 0.36 | -0.54, 0.50 |

$$^a R(F) = \frac{\sum ||F_o| - |F_c||}{\sum |F_o|}; wR(F^2) = \left(\frac{\sum [w(F_o^2 - F_c^2)^2]}{\sum [w(F_o^2)^2]} \right)^{1/2}$$

Table 3-3. The $\odot \cdots \odot$ Distances of Nearest Neighbor Centroids in $(\text{H}_3\text{O})_2\text{B}_{12}\text{F}_{12} \cdot 6\text{H}_2\text{O}$, $(\text{H}_3\text{O})_2\text{B}_{12}\text{F}_{12} \cdot 4\text{H}_2\text{O}$, and $(\text{NH}_4)_2\text{B}_{12}\text{F}_{12} \cdot 4\text{H}_2\text{O}$.

| | $(\text{H}_3\text{O})_2\text{B}_{12}\text{F}_{12} \cdot 6\text{H}_2\text{O}$ | $(\text{H}_3\text{O})_2\text{B}_{12}\text{F}_{12} \cdot 4\text{H}_2\text{O}$ | $(\text{NH}_4)_2\text{B}_{12}\text{F}_{12} \cdot 4\text{H}_2\text{O}$ |
|--|--|--|---|
| | 8.411 | 7.576 | 7.051 |
| | 8.411 | 7.576 | 7.051 |
| | 8.411 | 7.762 | 8.509 |
| | 8.411 | 8.046 | 8.509 |
| Distance from central B_{12} | 8.521 | 8.046 | 8.510 |
| centroid to 12 nearest | 8.521 | 8.198 | 8.510 |
| neighbors | 8.703 | 8.836 | 9.469 |
| | 8.703 | 8.922 | 9.469 |
| | 8.914 | 8.922 | 9.469 |
| | 8.914 | 9.221 | 9.469 |
| | 8.914 | 10.105 | 9.760 |
| | 8.914 | 10.105 | 9.760 |
| avg. (\AA) | 8.645 | 8.610 | 8.795 |
| low (\AA) | 8.411 | 7.576 | 7.051 |
| high (\AA) | 8.914 | 10.105 | 9.760 |
| crystallographic ρ (g cm^{-3}) | 1.836 | 1.829 | 1.735 |
| Z | 2 | 4 | 4 |
| volume (\AA^3) | 911.4 | 1699.4 | 1783.5 |

Table 3-4. Crystallographic O⋯O Distances Involving H₃O⁺ Ions Hydrogen Bonded to Two or Three H₂O Molecules^a.

| compound | hydronium species | (H ₃)O⋯O(H ₂), Å | (H ₂)O⋯O(H ₃)⋯O(H ₂), deg |
|---|--|--|---|
| (H ₃ O) ₂ B ₁₂ F ₁₂ ·6H ₂ O | <i>cyclo</i> -H ₁₄ O ₆ ²⁺ | 2.5739(8), 2.590(1) × 2 | 96.20(4), 125.53(2) × 2 |
| (H ₁₄ O ₆) ₂ [FeCl ₄] ₂ Cl ₂ ·C ₃₆ H ₃₆ N ₂₄ O ₁₂ ·3H ₂ O ^a | <i>cyclo</i> -H ₁₄ O ₆ ²⁺ | 2.465, 2.506 | 109.3, 110.3 |
| (H ₃ O)SbBr ₆ ·2H ₂ O ^b | (<i>cyclo</i> -H ₁₀ O ₄ ²⁺)·2H ₂ O | 2.406(2), 2.644(2), 2.689(2) | 92.0(1), 129.4(1), 135.4(1) |
| (H ₃ O)C ₉ H ₉ O ₇ S·3H ₂ O ^c | <i>cyclo</i> -H ₁₈ O ₈ ²⁺ | 2.421(2), 2.554(3) | 113.7 |
| (H ₉ O ₄)CB ₁₁ H ₆ Br ₆ ^d | H ₉ O ₄ ⁺ | 2.50(2), 2.50(2), 2.53(2) | 103.4(8), 104.0(8), 117.0(8) |

^a Standard errors for O⋯O distances and O⋯O⋯O angles are not available in those cases where they are not explicitly listed in the table.

^aVivorets, A. V.; Samsonenko, D. G.; Dybtsev, D. N.; Fedin, V. P.; Clegg, W. *J. Struct. Chem.* **2001**, *42*, 319–321.

^bHenke, H.; Kuhs, W. F. *Z. Kristallogr* **1987**, *181*, 113–126.

^cHanson, A. W. *Acta Crystallogr. C* **1987**, *43*, 296–300.

^dXie, Z.; Bau, R.; Reed, C. A. *Inorg. Chem.* **1995**, *34*, 5403–5404.

Table 3-5. Mass Changes for Hydration/Dehydration of $(\text{H}_3\text{O})_2\text{B}_{12}\text{F}_{12}\cdot 6\text{H}_2\text{O}$ Phases.

| Hydrate Phase | Mass % of | Mass % | Temp. (°C) | P(H_2O) (Torr) |
|---|--|---|---------------|-------------------------------------|
| | $(\text{H}_3\text{O})_2\text{B}_{12}\text{F}_{12}\cdot 6\text{H}_2\text{O}$ Theoretical | of $(\text{H}_3\text{O})_2\text{B}_{12}\text{F}_{12}\cdot 6\text{H}_2\text{O}$ Experimental, Figure 15 | | |
| $(\text{H}_3\text{O})_2\text{B}_{12}\text{F}_{12}\cdot 6\text{H}_2\text{O}$ | 100 | 100 | 25 | 6 |
| $(\text{H}_3\text{O})_2\text{B}_{12}\text{F}_{12}\cdot 4\text{H}_2\text{O}$ | 92.85 | 92.70 | 55 | 6 |
| $(\text{H}_3\text{O})_2\text{B}_{12}\text{F}_{12}\cdot 2\text{H}_2\text{O}$ | 85.70 | 85.47 | 120 | 6 |
| $(\text{H}_3\text{O})_2\text{B}_{12}\text{F}_{12}\cdot 0\text{H}_2\text{O}$ | 78.54 | 78.35 | 150 | 0 |
| $\text{H}_2\text{B}_{12}\text{F}_{12}$ | 72.76 | – | – | – |
| $(\text{H}_3\text{O})_2\text{B}_{12}\text{F}_{12}\cdot 6\text{H}_2\text{O}$ | 100 | 99.43 | 25 | 6 |

Table 3-6. Selected Interatomic Distances (Å) for the PBE0 DFT-predicted Structures of $\text{B}_{12}\text{F}_{12}^{2-}$, $(\text{H}_3\text{O})_2\text{B}_{12}\text{F}_{12}$, and $\text{H}_2\text{B}_{12}\text{F}_{12}$.

| distance | $\text{B}_{12}\text{F}_{12}^{2-}$ | $(\text{H}_3\text{O})_2\text{B}_{12}\text{F}_{12}$ | $\text{H}_2\text{B}_{12}\text{F}_{12}$ |
|----------|--|--|--|
| B1–B1 | 1.79 ^a [1.787(1)–1.801(1)] ^b | 1.79 | 2.06 |
| B1–B2 | | 1.79 | 1.81 |
| B1–B2' | | 1.77 | 1.80 |
| B2–B2' | | 1.82 | 1.83 |
| B1–F1 | 1.38 ^a [1.377(1)–1.388(1)] ^b | 1.41 | 1.33 |
| B2–F2 | | 1.36 | 1.34 |
| F1…F1 | 3.25 ^a [3.168(1)–3.305(1)] ^b | 3.16 | 3.64 |
| F1…F2 | | 3.24 | 3.23 |
| F1…F2' | | 3.24 | 3.02 |
| F2…F2' | | 3.26 | 3.20 |
| B–H | | | 1.40 |
| F…H | | 1.58 | 2.12 |
| O–H | | 1.01 | |

^aThese values are for all the B–B, B–F, and F–F distances for the DFT structure of $\text{B}_{12}\text{F}_{12}^{2-}$.

^bThe values in square brackets are the ranges of values from the X-ray structure of $(\text{H}_3\text{O})_2\text{B}_{12}\text{F}_{12}\cdot 6\text{H}_2\text{O}$.

Table 3-7. PBE0 DFT-optimized Coordinates for $B_{12}F_{12}^{2-}$.

| | | | |
|---|--------------|--------------|--------------|
| B | -1.524931000 | 0.000000000 | -0.762400000 |
| B | -0.470877000 | -1.451172000 | -0.762683000 |
| B | 1.233695000 | -0.896022000 | -0.762517000 |
| B | 1.233695000 | 0.896022000 | -0.762517000 |
| B | -0.470877000 | 1.451172000 | -0.762683000 |
| F | -2.761987000 | 0.000000000 | -1.379635000 |
| F | -0.852542000 | -2.626878000 | -1.382518000 |
| F | 2.236979000 | -1.617874000 | -1.382007000 |
| F | 2.236979000 | 1.617874000 | -1.382007000 |
| F | -0.852541000 | 2.626878000 | -1.382518000 |
| F | -2.236979000 | -1.617874000 | 1.382007000 |
| F | 0.852541000 | -2.626878000 | 1.382518000 |
| F | 2.761987000 | 0.000000000 | 1.379634000 |
| F | 0.852541000 | 2.626877000 | 1.382518000 |
| F | -2.236979000 | 1.617874000 | 1.382007000 |
| B | -1.233695000 | -0.896021000 | 0.762516000 |
| B | 0.470877000 | -1.451172000 | 0.762683000 |
| B | 1.524930000 | 0.000000000 | 0.762399000 |
| B | 0.470877000 | 1.451172000 | 0.762683000 |
| B | -1.233695000 | 0.896022000 | 0.762516000 |
| B | -0.000559000 | 0.000000000 | -1.704490000 |
| F | -0.001098000 | 0.000000000 | -3.087424000 |
| B | 0.000559000 | 0.000000000 | 1.704491000 |
| F | 0.001098000 | 0.000000000 | 3.087424000 |

Table 3-8. PBE0 DFT-optimized Coordinates for $(\text{H}_3\text{O})_2\text{B}_{12}\text{F}_{12}$.

| | | | |
|---|--------------|--------------|--------------|
| B | 0.000000000 | 1.034328000 | -1.320917000 |
| B | -1.471269000 | 0.849990000 | -0.319309000 |
| B | -1.471279000 | -0.850347000 | 0.319732000 |
| B | -0.000016000 | -1.699093000 | -0.321541000 |
| B | 0.894157000 | -0.514056000 | -1.321865000 |
| F | -0.000237000 | 1.826031000 | -2.485951000 |
| F | -2.621328000 | 1.514762000 | -0.598022000 |
| F | -2.621659000 | -1.514862000 | 0.597426000 |
| F | -0.000026000 | -3.026053000 | -0.609257000 |
| F | 1.581523000 | -0.910396000 | -2.485801000 |
| F | 0.000026000 | 3.026053000 | 0.609257000 |
| F | -1.581523000 | 0.910396000 | 2.485801000 |
| F | 0.000237000 | -1.826031000 | 2.485951000 |
| F | 2.621328000 | -1.514762000 | 0.598022000 |
| F | 2.621659000 | 1.514862000 | -0.597426000 |
| B | 0.000016000 | 1.699093000 | 0.321541000 |
| B | -0.894157000 | 0.514056000 | 1.321865000 |
| B | 0.000000000 | -1.034328000 | 1.320917000 |
| B | 1.471269000 | -0.849990000 | 0.319309000 |
| B | 1.471279000 | 0.850347000 | -0.319732000 |
| B | -0.894131000 | -0.513984000 | -1.321682000 |
| F | -1.581635000 | -0.910156000 | -2.485611000 |
| B | 0.894131000 | 0.513984000 | 1.321682000 |
| F | 1.581635000 | 0.910156000 | 2.485611000 |
| H | -0.785800000 | -0.456640000 | -3.767437000 |
| O | 0.000034000 | -0.005016000 | -4.207965000 |
| H | -0.000001000 | 0.903233000 | -3.772848000 |
| H | 0.785792000 | -0.456721000 | -3.767334000 |
| O | -0.000034000 | 0.005016000 | 4.207965000 |
| H | 0.785800000 | 0.456640000 | 3.767437000 |
| H | 0.000001000 | -0.903233000 | 3.772848000 |
| H | -0.785792000 | 0.456721000 | 3.767334000 |

Table 3-9. PBE0 DFT-optimized Coordinates for H₂B₁₂F₁₂.

| | | | |
|---|--------------|--------------|--------------|
| B | 1.033253000 | 0.595232000 | -1.370775000 |
| B | -0.000021000 | 1.684384000 | -0.362116000 |
| B | -1.459106000 | 0.842451000 | 0.362053000 |
| B | -1.459057000 | -0.842216000 | -0.361496000 |
| B | -0.000029000 | -1.189568000 | -1.370518000 |
| F | 1.824261000 | 1.050094000 | -2.339391000 |
| F | -0.000127000 | 3.014939000 | -0.543564000 |
| F | -2.608958000 | 1.509981000 | 0.546448000 |
| F | -2.608710000 | -1.509824000 | -0.547228000 |
| F | -0.000375000 | -2.102935000 | -2.337761000 |
| F | 2.608710000 | 1.509824000 | 0.547228000 |
| F | 0.000375000 | 2.102935000 | 2.337761000 |
| F | -1.824261000 | -1.050094000 | 2.339391000 |
| F | 0.000127000 | -3.014939000 | 0.543564000 |
| F | 2.608958000 | -1.509981000 | -0.546448000 |
| B | 1.459057000 | 0.842216000 | 0.361496000 |
| B | 0.000029000 | 1.189568000 | 1.370518000 |
| B | -1.033253000 | -0.595232000 | 1.370775000 |
| B | 0.000021000 | -1.684384000 | 0.362116000 |
| B | 1.459106000 | -0.842451000 | -0.362053000 |
| B | -1.033120000 | 0.594881000 | -1.370558000 |
| F | -1.824232000 | 1.049825000 | -2.339122000 |
| B | 1.033120000 | -0.594881000 | 1.370558000 |
| F | 1.824232000 | -1.049825000 | 2.339122000 |
| H | 0.000031000 | 0.001387000 | -2.114966000 |
| H | -0.000031000 | -0.001387000 | 2.114966000 |

Table 3-10. Mass Changes for Loss of H₂O/NH₃ From (NH₄)₂B₁₂F₁₂·2H₂O to Form H₂B₁₂F₁₂.

| Hydrate Phase | Mass % of | Mass % of | Temp. (°C) | P(H ₂ O) (Torr) |
|--|---|---|---------------|-------------------------------|
| | (NH ₄) ₂ B ₁₂ F ₁₂ ·4H ₂ O Theoretical | (NH ₄) ₂ B ₁₂ F ₁₂ ·4H ₂ O Experimental, Figure 25 | | |
| (NH ₄) ₂ B ₁₂ F ₁₂ ·4H ₂ O | 100 | - | 25 | xs liquid H ₂ O |
| (NH ₄) ₂ B ₁₂ F ₁₂ ·2H ₂ O | 92.27 | 100 | 25 | 6 |
| (NH ₄) ₂ B ₁₂ F ₁₂ | 84.53 | 91.76 | 55 | 0 |
| H ₂ B ₁₂ F ₁₂ | 77.22 | - | - | - |

Chapter 3 References

- (1) Rosenthal, M. R. *Journal of Chemical Education* 1973, 50, 331.
- (2) Beck, W.; Suenkel, K. *Chem Rev* 1988, 88, 1405.
- (3) Newbound, T. D.; Colman, M. R.; Miller, M. M.; Wulfsberg, G. P.; Anderson, O. P.; Strauss, S. H. *J Am Chem Soc* 1989, 111, 3762.
- (4) Strauss, S. H. *Chem Rev* 1993, 93, 927.
- (5) Strauss, S. H. *Chemtracts-Inorganic Chemistry* 1994, 6, 1.
- (6) Lupinetti, A. J.; Strauss, S. H. *Chemtracts-Inorganic Chemistry* 1998, 11, 565.
- (7) Reed, C. A. *Accounts of Chemical Research* 1998, 31, 133.
- (8) Krossing, I.; Raabe, I. *Angewandte Chemie International Edition* 2004, 43, 2066.
- (9) Krossing, I.; Reisinger, A. *Coordination Chemistry Reviews* 2006, 250, 2721.
- (10) Reed, C. A. *Accounts of Chemical Research* 2009, 43, 121.
- (11) Nava, M. J.; Reed, C. A. *Inorg Chem* 2010, 49, 4726.
- (12) Ivanov, S. V.; Miller, S. M.; Anderson, O. P.; Strauss, S. H. *Crystal Growth & Design* 2004, 4, 249.
- (13) Ivanova, S. M.; Ivanov, S. V.; Miller, S. M.; Anderson, O. P.; Solntsev, K. A.; Strauss, S. H. *Inorg Chem* 1999, 38, 3756.
- (14) King, B. T.; Noll, B. C.; McKinley, A. J.; Michl, J. *J Am Chem Soc* 1996, 118, 10902.
- (15) Zharov, I.; Weng, T.-C.; Orendt, A. M.; Barich, D. H.; Penner-Hahn, J.; Grant, D. M.; Havlas, Z.; Michl, J. *J Am Chem Soc* 2004, 126, 12033.
- (16) Rupich, M. W.; Foos, J. S.; Brummer, S. B. *Journal of The Electrochemical Society* 1985, 132, 119.
- (17) Koczorowski, Z.; Zagórska, I. *J Appl Electrochem* 1980, 10, 75.
- (18) Arai, J.; Matsuo, A.; Fujisaki, T.; Ozawa, K. *Journal of Power Sources* 2009, 193, 851.
- (19) GirishKumar, G.; Bailey, W. H.; Peterson, B. K.; Casteel, W. J. *Journal of The Electrochemical Society* 2011, 158, A146.
- (20) Ionica-Bousquet, C. M.; Casteel Jr, W. J.; Pearlstein, R. M.; GirishKumar, G.; Pez, G. P.; Gómez-Romero, P.; Palacín, M. R.; Muñoz-Rojas, D. *Electrochemistry Communications* 2010, 12, 636.
- (21) Ivanov, S. V.; Casteel, W. J.; Pez, G. P.; Google Patents: 2009.
- (22) Pez, G.; Ivanov, S.; Dantsin, G.; Casteel, W.; Lehmann, J. In *Google Patents; Pez Guido P, Ivanov Sergei V, Gennady Dantsin, Casteel William J Jr, Lehmann John F, AIR PRODUCTS AND CHEMICALS, INC., PENNSYLVANIA: 2007.*
- (23) Ivanov, S. V.; Casteel, W. J.; Bailey, W. H. In *Google Patents; Air Products And Chemicals, Inc.: 2011.*
- (24) Vaughey, J.; Jansen, A. N.; Dees, D. W. In *Google Patents; Uchicago Argonne, Llc: 2010.*
- (25) Polyakov, O. G.; Strauss, S. H.; Kuvychko, I. V. In *Google Patents; Synkera Technologies, Inc.: 2008.*
- (26) Chen, E. Y.-X.; Marks, T. J. *Chem Rev* 2000, 100, 1391.
- (27) Mariott, W. R.; Gustafson, L. O.; Chen, E. Y. X. *Organometallics* 2006, 25, 3721.
- (28) Bochmann, M. *Journal of Organometallic Chemistry* 2004, 689, 3982.
- (29) Bochmann, M. *Organometallics* 2010, 29, 4711.

- (30) Xie, Z. W.; Bau, R.; Reed, C. A. *Inorg Chem* 1995, 34, 5403.
- (31) Bukovsky, E. V.; Fiedler, S. R.; Peryshkov, D. V.; Popov, A. A.; Strauss, S. H. *European Journal of Inorganic Chemistry* 2012, 208.
- (32) Reed, C. A.; Fackler, N. L. P.; Kim, K.-C.; Stasko, D.; Evans, D. R.; Boyd, P. D. W.; Rickard, C. E. F. *J Am Chem Soc* 1999, 121, 6314.
- (33) Reed, C. A.; Kim, K.-C.; Stoyanov, E. S.; Stasko, D.; Tham, F. S.; Mueller, L. J.; Boyd, P. D. W. *J Am Chem Soc* 2003, 125, 1796.
- (34) Peryshkov, D. V. Dissertation, Colorado State University, 2011.
- (35) Ivanov, S. V.; Peryshkov, D. V.; Miller, S. M.; Anderson, O. P.; Rappe, A. K.; Strauss, S. H. *Journal of Fluorine Chemistry* 2012, 143, 99.
- (36) Solnstevev, K. A.; Mebel, A. M.; Votnova, N. A.; Kuznetsov, N. T.; Charkin, O. P. *Koord. Khim.* 1992, 18, 340.
- (37) Ivanov, S. V.; Miller, S. M.; Anderson, O. P.; Solntsev, K. A.; Strauss, S. H. *J Am Chem Soc* 2003, 125, 4694.
- (38) Peryshkov, D. V.; Popov, A. A.; Strauss, S. H. *J Am Chem Soc* 2009, 131, 18393.
- (39) Peryshkov, D. V.; Strauss, S. H. *Journal of Fluorine Chemistry* 2010, 131, 1252.
- (40) Peryshkov, D. V.; Popov, A. A.; Strauss, S. H. *J Am Chem Soc* 2010, 132, 13902.
- (41) Peryshkov, D. V.; Goreshnik, E.; Mazej, Z.; Strauss, S. H. *Journal of Fluorine Chemistry* 2010, 131, 1225.
- (42) Shackelford, S. A.; Belletire, J. L.; Boatz, J. A.; Schneider, S.; Wheaton, A. K.; Wight, B. A.; Ammon, H. L.; Peryshkov, D. V.; Strauss, S. H. *Org Lett* 2010, 12, 2714.
- (43) Tiritiris, I.; Schleid, T. *Zeitschrift für anorganische und allgemeine Chemie* 2003, 629, 1390.
- (44) Tiritiris, I.; Schleid, T.; Müller, K.; Preetz, W. *Zeitschrift für anorganische und allgemeine Chemie* 2000, 626, 323.
- (45) Wunderlich, J. A.; Lipscomb, W. N. *J Am Chem Soc* 1960, 82, 4427.
- (46) Her, J.-H.; Yousufuddin, M.; Zhou, W.; Jalisatgi, S. S.; Kulleck, J. G.; Zan, J. A.; Hwang, S.-J.; Bowman, R. C.; Udovic, T. J. *Inorg Chem* 2008, 47, 9757.
- (47) Derendorf, J.; Ke, Knapp, C.; Ruhle, M.; Schulz, C. *Dalton Transactions* 2010, 39, 8671.
- (48) Geis, V.; Gutsche, K.; Knapp, C.; Scherer, H.; Uzun, R. *Dalton Transactions* 2009, 2687.
- (49) Tiritiris, I.; Schleid, T. *Zeitschrift für anorganische und allgemeine Chemie* 2004, 630, 1555.
- (50) Stasko, D. J.; Perzynski, K. J.; Wasil, M. A.; Brodbeck, J. K.; Kirschbaum, K.; Kim, Y. W.; Lind, C. *Inorg Chem* 2004, 43, 3786.
- (51) Peymann, T.; Herzog, A.; Knobler, C. B.; Hawthorne, M. F. *Angewandte Chemie International Edition* 1999, 38, 1061.
- (52) Peymann, T.; Knobler, C. B.; Hawthorne, M. F. *J Am Chem Soc* 1999, 121, 5601.
- (53) A. Szytula, J. L. *Handbook of Crystal Structures and Magnetic Properties of Rare Earth Intermetallics*; CRC Press: Boca Raton, 1994.
- (54) McNaught, A. D. W., A.; Nic, M. J., J.; Kosata, B.; Updates by Jenkins, A. In *IUPAC. Compendium of Chemical Terminology*, 2nd ed. (the "Gold Book"); 2nd ed.; Blackwell Scientific Publications: Oxford, 2006.
- (55) Avelar, A.; Tham, F. S.; Reed, C. A. *Angewandte Chemie International Edition* 2009, 48, 3491.
- (56) Stoyanov, E. S.; Stoyanova, I. V.; Reed, C. A. *J Am Chem Soc* 2010, 132, 1484.
- (57) Stoyanov, E. S.; Stoyanova, I. V.; Reed, C. A. *Chemical Science* 2011, 2, 462.

- (58) Xu, J.; Izvekov, S.; Voth, G. A. *The Journal of Physical Chemistry B* 2010, 114, 9555.
- (59) Jagoda-Cwiklik, B.; Cwiklik, L.; Jungwirth, P. *The Journal of Physical Chemistry A* 2011, 115, 5881.
- (60) Takahashi, H.; Maruyama, K.; Karino, Y.; Morita, A.; Nakano, M.; Jungwirth, P.; Matubayasi, N. *The Journal of Physical Chemistry B* 2011, 115, 4745.
- (61) Stoyanov, E. S.; Kim, K. C.; Reed, C. A. *J Am Chem Soc* 2006, 128, 1948.
- (62) Bernal, I. *Comptes Rendus Chimie* 2006, 9, 1454.
- (63) Bernal, I. *Comptes Rendus Chimie* 2008, 11, 942.
- (64) Yang, Z.; Hua, S.; Hua, W.; Li, S. *The Journal of Physical Chemistry B* 2011, 115, 8249.
- (65) Knoth, W. H.; Miller, H. C.; Sauer, J. C.; Balthis, J. H.; Chia, Y. T.; Muetterties, E. L. *Inorg Chem* 1964, 3, 159.
- (66) Casteel William J Jr, I. S. V., Pez Guido P; H01B1/12 ed.; office, U. P., Ed.; Casteel William J Jr, Ivanov Sergei V, Pez Guido P: United States of America, 2006.
- (67) Motupally, S.; Kanuri, S.; Strauss, S. H.; Thrasher, J. S.; Pivovar, B.; U.S. Department of Energy, Golden Field Office: 2010.
- (68) Stoyanov, E. S.; Kim, K. C.; Reed, C. A. *Journal of Physical Chemistry A* 2004, 108, 9310.
- (69) Juhasz, M.; Hoffmann, S.; Stoyanov, E.; Kim, K.-C.; Reed, C. A. *Angewandte Chemie* 2004, 116, 5466.
- (70) Reed, C. A. *Chemical Communications* 2005, 1669.
- (71) Juhasz, M.; Hoffmann, S.; Stoyanov, E.; Kim, K. C.; Reed, C. A. *Angew Chem Int Edit* 2004, 43, 5352.
- (72) Ivanov, S. V.; Miller, S. M.; Anderson, O. P.; Solntsev, K. A.; Strauss, S. H. *J. Am. Chem. Soc.* 2003, 125, 4694.
- (73) Peryshkov, D. V.; Popov, A. A.; Strauss, S. H. *J. Am. Chem. Soc.* 2009, 131, 18393.
- (74) Peryshkov, D. V.; Goreshnik, E.; Mazej, Z.; Strauss, S. H. *J. Fluorine Chem.* 2010, 131, 1225.
- (75) Bondi, A. *The Journal of Physical Chemistry* 1964, 68, 441.
- (76) Mascial, M.; Infantes, L.; Chisholm, J. *Angewandte Chemie International Edition* 2006, 45, 32.
- (77) Infantes, L.; Motherwell, S. *CrystEngComm* 2002, 4, 454.
- (78) Infantes, L.; Chisholm, J.; Motherwell, S. *CrystEngComm* 2003, 5, 480.
- (79) Virovets, A. V.; Samsonenko, D. G.; Dybtsev, D. N.; Fedin, V. P.; Clegg, W. *Journal of Structural Chemistry* 2001, 42, 319.
- (80) Bernal, I.; Mukhopadhyay, U.; Virovets, A. V.; Fedin, V. P.; Clegg, W. *Chemical Communications* 2005, 3791.
- (81) Farcasiu, D.; Lukinskas, P. *Physical Chemistry Chemical Physics* 2000, 2, 4219.
- (82) Goldberg, I. *Journal of Inclusion Phenomena* 1984, 1, 349.
- (83) Knoth, W. H.; Miller, H. C.; England, D. C.; Parshall, G. W.; Muetterties, E. L. *J Am Chem Soc* 1962, 84, 1056.
- (84) Jenkins, H. D. B.; Roobottom, H. K.; Passmore, J.; Glasser, L. *Inorg. Chem.* 1999, 38, 3609.
- (85) Cottrell, T. L. *The Strengths of Chemical Bonds*; 2nd ed. Butterworth London, 1958.
- (86) Darwent, B. d.; 31, N. B. o. S. n., Ed. Washington, 1970.
- (87) Benson, S. W. *Journal of Chemical Education* 1965, 42, 502.
- (88) Kerr, J. A. *Chem Rev* 1966, 66, 465.

- (89) Hansen, T. O. In Google Patents; Hansen Tor, Oeystein: 2004.
- (90) House Jr, J. E. Inorganic and Nuclear Chemistry Letters 1980, 16, 185.
- (91) House Jr, J. E. Thermochemica Acta 1980, 40, 225.
- (92) Muehling, J. K.; Arnold, H. R.; House Jr, J. E. Thermochemica Acta 1995, 255, 347.
- (93) Sheldrick, G. M.; Bruker AXS: Madison, WI, 2003.
- (94) Sheldrick, G. M.; 6.15 ed.; Bruker AXS: Madison, WI, 2004.
- (95) Sheldrick, G. M.; Bruker AXS: Madison, WI, 2006.
- (96) Sheldrick, G. M. Acta Crystallographica Section A 2008, 64, 112.
- (97) Dolomanov, O. V.; Bourhis, L. J.; Gildea, R. J.; Howard, J. A. K.; Puschmann, H. Journal of Applied Crystallography 2009, 42, 339.
- (98) Kou, Y.; Schmidt, S. J. Food Chemistry 1999, 66, 253.

Chapter 4.

New or Improved Syntheses of the $B_{12}H_{11}(NH_3)^-$ and $B_{12}F_{11}(NH_3)^-$ Anions and the 1,2-, 1,7-, and 1,12- Isomers of $B_{12}H_{10}(NH_3)_2$ and $B_{12}F_{10}(NH_3)_2$ and Their Spectroscopic and Structural Characterization

4.1 Introduction and Justification

The Strauss research group at Colorado State University has a longstanding interest in the synthesis and application of highly-fluorinated superweak anions (i.e., extremely weakly coordinating anions^{1,2}), including the polyhedral carborane and borane anions 1-R-CB₁₁F₁₁⁻,³ B₁₂F₁₂²⁻,^{4,5} and B₁₂F₁₁(NH₃)⁻.⁶ (The term superweak anion, conceptually the conjugate base of an actual or hypothetical superacid, was introduced by Strauss at an ACS National Meeting symposium on weakly coordinating anions organized by Strauss and C. A. Reed in 1998.^{7,8}) The primary use of these particular superweak anions has been to generate and study highly reactive cations or cation-like species such as Cu(CO)₄⁺,⁹ Rh(η⁶-C₆H₆)(CO)₂⁺,¹⁰ and Al(CH₃)₂⁺.¹¹

However, there are other potential uses for molecules or molecular ions containing a high weight% of naturally-occurring boron (and therefore a relatively high weight% of ¹⁰B) that have nothing to do with reactive cations.¹² Three of the most important uses are boron neutron capture therapy (BNCT),¹³⁻¹⁶ thermal neutron detectors (TNDs) for homeland security applications,¹⁷ and extractants for nuclear waste.¹⁸ For applications such as these, derivatization of the borane cluster is desirable (i.e., derivatization other than per-*B*-fluorination). Instead of only one site of substitution in 1-R-CB₁₁F₁₁⁻ (i.e., the C atom), the monoammonio anions B₁₂H₁₁(NH₃)⁻,¹⁹ B₁₂F₁₁(NH₃)⁻,⁶ and B₁₂Cl₁₁(NH₃)⁻²⁰ have three sites of substitution (i.e., the three N–H bonds) and the diammonio compounds 1,2-, 1,7-, and 1,12-B₁₂H₁₀(NH₃)₂ have six sites of substitution

(see Figure 4-1 for the IUPAC numbering scheme for B₁₂ clusters. A non-nuclear application is the preparation of anions for ionic liquids.^{21,22} Another non-nuclear application is as starting materials for the preparation of non-linear optical materials.^{23,24} These applications may or may not benefit from per-*B*-fluorination depending on the nature of the other components with which they are mixed or to which they are attached (e.g., peptides and other biomolecules for BNCT and the scintillators and polymers used for TNDs, etc.). A final non-nuclear application, a new project in the Strauss-Boltalina group, is the use of polymerizable derivatives of the per-*B*-fluorinated mono- and diammonio clusters (i.e., derivatives with polymerizable hydrocarbyl substituents on the N atoms) to form protective polymeric coatings on anodes for secondary lithium-ion batteries while at the same time allowing high lithium-ion mobility through the coating.

The amination of alkali metal salts of B₁₂H₁₂²⁻ with hydroxylamine-*O*-sulfonic acid to produce B₁₂H₁₁(NH₃)⁻ and the three isomers of B₁₂H₁₀(NH₃)₂ was reported by Hertler and Raasch in 1964¹⁹ (they were part of the Muetterties group at the Dupont Central Research and Development Department that was influential in developing the chemistry of polyhedral boranes²⁵). By modern standards, the isomers of B₁₂H₁₀(NH₃)₂ were not well separated and were not well characterized (high-field NMR spectroscopy and efficient separation methods were not available in the 1960s²⁶).

A number of papers (including the original Hertler and Raasch paper¹⁹) have reported the *N*-alkylation of B₁₂H₁₁(NH₃)⁻.^{14-16,18,21-24,26} However, only two papers about any of the isomers of B₁₂H₁₀(NH₃)₂ have appeared since Hertler and Raasch's 1964 paper. The first paper reported the partial separation of B₁₂H₁₀(NH₃)₂ isomers into 1,7-B₁₂H₁₀(NH₃)₂ and an inseparable mixture of 1,2- and 1,12-B₁₂H₁₀(NH₃)₂ as well as their ¹H and ¹¹B NMR spectra.²⁶ The second paper

reported the X-ray structure of 1,7- $B_{12}H_{10}(NH_3)_2 \cdot 0.5H_2O$.²⁷ Three of the goals, regarding the $B_{12}H_{10}(NH_3)_2$ isomers, of the work reported in this chapter were (i) to prepare the isomers of $B_{12}H_{10}(NH_3)_2$ in higher yield and higher purity than previously reported, (ii) to prepare their per-B-fluorinated counterparts, and (iii) to characterize all six compounds by multinuclear NMR spectroscopy, including and single-crystal X-ray diffraction.

The direct fluorination of $CsB_{12}H_{11}(NH_3)$ in anhydrous HF (aHF) with 20/80 F_2/N_2 , reported by Strauss and co-workers in 2003,⁶ is not very efficient. The reaction was carried out in a Monel reactor in a batch process. The yield was a modest 41%. Moreover, only ca. 0.8 g of $CsB_{12}H_{11}(NH_3)$ could be fluorinated per batch, because the use of elevated pressures of F_2/N_2 resulted in cluster degradation and even lower yields. The other two goals of the work reported in this chapter were (i) to scale up the fluorination reaction to 2 g of $KB_{12}H_{11}(NH_3)$ using MeCN in a glass round-bottom flask instead of aHF in a Monel reactor, and to do so without sacrificing the yield or purity of the final product, $KB_{12}F_{11}(NH_3)$, and (ii) to obtain a precise single-crystal X-ray structure of a salt of the $B_{12}F_{11}(NH_3)^-$ monoanion.

With the exception of the determination of the X-ray structure of 1,2- $B_{12}F_{10}(NH_3)_2$, all five of the goals mentioned above have been achieved.

4.2 Results and Discussion

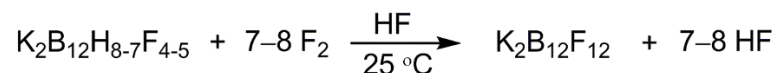
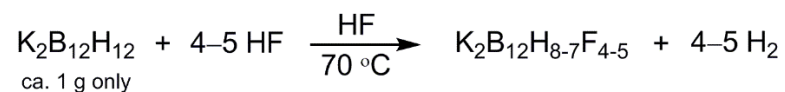
This section is broken into three parts, (I) the improved and efficient fluorination of $B_{12}H_{11}(NH_3)^-$ to $B_{12}F_{11}(NH_3)^-$ and the precise X-ray structure $NaB_{12}F_{11}(NH_3) \cdot 4H_2O$, (II) the improved synthesis, purification, and spectroscopic characterization of the three isomers of $B_{12}H_{10}(NH_3)_2$ and their per-B-fluorinated counterparts, and (III) the X-ray structures of 1,2-, 1,7- and 1,12- $B_{12}H_{10}(NH_3)_2$ and 1,7- and 1,12- $B_{12}F_{10}(NH_3)_2$. Parts I and III describe work for which

the author of this dissertation is responsible. Part II describes work that was done by a Plan B M.S. student in the Strauss-Boltalina group, Amanda M. Pluntze, under the direct supervision and day-to-day assistance of the author of this dissertation. The author is responsible for 50% of this work. All of it will be described in this dissertation because except in a few cases it is impossible to separate the work done by the author and by Amanda Pluntze and because Ms. Pluntze was not required to write a Master's thesis.

4.2.1 Improved and Efficient Fluorination of $B_{12}H_{11}(NH_3)^-$.

4.2.1.1 Background.

A species believed at the time to be $B_{12}F_{12}^{2-}$ was reported by Muetterties and co-workers in 1962²⁸ but was subsequently shown, by the same Dupont group, to be $B_{12}(OH)F_{11}^{2-}$.²⁹ The first successful per-*B*-fluorination of $B_{12}H_{12}^{2-}$ to produce $B_{12}F_{12}^{2-}$ was reported by Konstantin Solntsev and co-workers at the Russian Academy of Sciences in 1992.³⁰ They treated $Cs_2B_{12}H_{12}$ with supercritical aHF at 550 °C to produce $Cs_2B_{12}F_{12}$ in 38% yield.³⁰ In 2003 Strauss, Solntsev, and co-workers reported an improved synthesis of $K_2B_{12}F_{12}$ in 72% recrystallized yield using the reaction scheme shown below. The HF used was aHF and the F_2 used was 20/80 F_2/N_2 . The reaction vessel was a 150 mL Monel cylinder equipped with a vacuum tight valve



that could be safely heated to 70 °C. The scale of the reaction was limited to ca. 1 g of $K_2B_{12}H_{12}$ due to the finite volume of the reactor and because it was found that F_2 partial pressures above 1

atm caused extensive cluster decomposition leading to low yields. Furthermore, the two-step reaction sequence, plus workup and recrystallization of the product, took nearly a week to complete. It is significant for the reader to note that each B–H bond that reacts with a molecule of F_2 in the second reaction shown above produces a B–F bond *and a molecule of HF* as a byproduct.

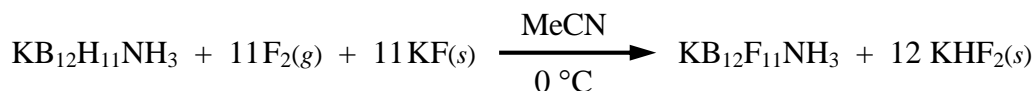
In 2009 Peryshkov, Popov, and Strauss reported a greatly improved synthesis of $K_2B_{12}F_{12}$ in 74% recrystallized yield.⁵ They bubbled 20/80 F_2/N_2 continuously through a mixture of $K_2B_{12}H_{12}$ and a large excess of solid KF in cold MeCN containing 2% v/v H_2O in a Pyrex round-bottom flask (the H_2O was added to ensure that all of the $K_2B_{12}H_{12}$ was in solution at the start of F_2 fluorination). The continuous flow of F_2 allowed the scale of the reaction to be increased to 10 g $K_2B_{12}H_{12}$ without sacrificing the purity or yield of the product. In addition, the reaction time was significantly shortened. Approximately 15 g of 99.5+% pure $K_2B_{12}F_{12}$ was prepared, using ordinary Pyrex glassware, in less than two days.⁵

A critical feature of the Peryshkov improved synthesis was the addition of a large excess of solid KF to the reaction mixture in order to scavenge the 12 equivalents of HF byproduct per mole of $B_{12}F_{12}^{2-}$ produced (note that both KF and KHF_2 are essentially insoluble in anhydrous MeCN). Peryshkov et al. found that, in the absence of KF, *the buildup of HF inhibited the F_2 fluorination of $B_{12}H_{12-x}F_x^{2-}$ clusters*, especially as x approached 12, as shown in Figure 4-2, which has been adapted from a figure in Peryshkov's paper.⁵ They performed a conclusive control experiment in which 2% v/v aHF was added to the reaction mixture before starting the addition of F_2 . This reaction was even slower than the reaction without added KF, which was slower than the reaction with added KF. There was no doubt that the presence of HF inhibited

the per-*B*-fluorination of $B_{12}H_{12}^{2-}$ by F_2 in MeCN, even though, as discussed above, 100% HF can slowly fluorinate $B_{12}H_{12}^{2-}$ all by itself to a mixture of $B_{12}H_8F_4^{2-}$ and $B_{12}H_7F_5^{2-}$.⁴

4.2.2 Efficient per-*B*-fluorination of $B_{12}H_{11}(NH_3)^-$ with F_2/N_2 in MeCN.

As discussed in the Introduction to this chapter, the fluorination of $B_{12}H_{11}(NH_3)$ dissolved in aHF with 20/80 F_2/N_2 in a Monel reactor is time intensive and could be scaled up. In order to "greatly improve" the synthesis of $KB_{12}F_{11}(NH_3)$ it seemed logical to apply the "Peryshkov" conditions (minus the H_2O_2 purification step for reasons described in Chapter 2) to $KB_{12}H_{11}(NH_3)$ as the substrate. The expected reaction is shown below.



Excess solid KF (to absorb the HF byproduct as it is formed) was added to 2 g of $KB_{12}H_{11}(NH_3)$ dissolved in 150 mL of MeCN at 0 °C, and the mixture was bubbled with 20/80 F_2/N_2 for several hours. Small 8–10 μL aliquots were withdrawn periodically, worked up as described in the Experimental Section, and used to obtain a negative-ion electrospray ionization (NI-ESI) mass spectrum. The relative concentrations of $B_{12}H_{11-n}F_n(NH_3)^-$ anions present in the reaction mixture (and in other reaction mixtures to be discussed below) at various times during the F_2 fluorination were determined using the mass spectrum for each aliquot as follows. Mass spectra of B_{12} -containing species give rise to isotopologue patterns such as the example shown in Figure 4-3 for $B_{12}F_{11}(NH_3)^-$. These patterns are due to the 19.9(7)% ^{10}B and 80.1% ^{11}B isotopes in naturally-occurring boron. Fluorine-19 is 100% abundant and ^1H and ^{14}N are 99.6+% abundant in naturally occurring samples of these elements, so their contributions to the relative

intensities of the individual isotopologues (hereinafter "isotops") in the isotope patterns for any of the $B_{12}H_{11-n}F_n(NH_3)^-$ anions are negligible. By convention, the single m/z value for the isotope pattern is taken to be the most intense m/z peak in the pattern, the peak for the anion with two ^{10}B and ten ^{11}B atoms, which is, ideally, 28.4% of the total intensity for all of the isotops in the isotope pattern. Thus, for mass spectral purposes, "the mass" of $B_{12}F_{11}(NH_3)^-$ is taken to be 356 amu (for comparison, the actual weighted-average molecular mass of $B_{12}F_{11}(NH_3)^-$ is 355.745 amu and the exact mass of $(^{10}B_2^{11}B_{10})F_{11}(NH_3)^-$ is 356.128 amu). The m/z 356 peak for $(^{10}B_2^{11}B_{10})F_{11}(NH_3)^-$ in Figure 4-3 is flanked by the m/z 355 and 357 peaks for $(^{10}B_3^{11}B_{10})F_{11}(NH_3)^-$ and $(^{10}B_1^{11}B_{11})F_{11}(NH_3)^-$, respectively, with, ideally, 23.4 and 21.0% intensity, respectively.

For the purposes of the work reported in this dissertation, the relative intensities of different isotops in a given mass spectrum were determined by summing the absolute intensities for the three most intense peaks in each isotope pattern. In order to take into account the differences in ESI sensitivity coefficients as a function of n , the following control experiment was performed. An equimolar mixture of 99+% pure $KB_{12}H_{11}(NH_3)$ and $KB_{12}F_{11}(NH_3)$ in MeCN was injected into the mass spectrometer. The $B_{12}F_{11}(NH_3)^-/B_{12}H_{11}(NH_3)^-$ "sum-of-the-three-most-intense-isotope-peaks" relative intensity ratio was 9.635. It was assumed that the relative sensitivity coefficients varied linearly in 11 increments from 1.000 to 9.635 for $n = 0$ to $n = 11$, and the absolute-intensity sums were scaled by the corresponding sensitivity-coefficient factor for the purpose of estimating the relative concentration of each $B_{12}H_{11-n}F_n(NH_3)^-$ anion in a mixture. Therefore, the relative concentrations are only known precisely to the extent that this assumption is valid. However, in the analysis that follows, small uncertainties in relative concentrations will have no impact on the overall interpretation of the results.

The mass spectra taken at several time intervals for the direct fluorination of a 2 g sample of $\text{KB}_{12}\text{H}_{11}(\text{NH}_3)$ in 0 °C MeCN using 20/80 F_2/N_2 in the presence of a large excess of solid KF are shown in the top set of spectra in Figure 4-4. After bubbling the F_2/N_2 gas mixture through the vigorously stirred reaction mixture for 5 h, a mixture of $\text{B}_{12}\text{H}_{11-n}\text{F}_n(\text{NH}_3)^-$ anions were present, with $n = 8, 9, 10$ (the most abundant species), and 11 (the desired product, nearly as abundant at this time as the anion with $n = 10$). Also present in the 5 h spectrum are low-intensity isotop patterns for $\text{NaB}_{12}\text{F}_{11}(\text{NH}_2)^-$ and $\text{KB}_{12}\text{F}_{11}(\text{NH}_2)^-$ at m/z 378 and 394, respectively (note that sodium and potassium, like fluorine, are monoisotopic). These species, the isotop patterns for which are indicated with asterisks in some of the spectra in Figures 4-4 and 4-7, are observed with variable relative intensities that probably depend on (i) concentration and (ii) the exact workup of each sample taken from the reaction mixture. Importantly, there is also an m/z 179 isotop pattern with spacing between the isotops of only 0.5 amu. This is due to a small amount of $\text{B}_{12}\text{F}_{12}^{2-}$ that serves as an internal relative intensity standard.

After 7 h, the only $\text{B}_{12}\text{H}_{11-n}\text{F}_n(\text{NH}_3)^-$ anions present were those with $n = 10$ and 11, the initial interpretation of which is that the 11-step fluorination of the $\text{B}_{12}\text{H}_{11}(\text{NH}_3)^-$ starting material was approaching completion. However, there were at least four relatively-abundant B_{12} -containing dianionic species present in the m/z 180–220 region, the identities of which have not been ascertained (none of them is due to $\text{B}_{12}\text{HF}_{10}(\text{NH}_2)^{2-}$, $\text{B}_{12}\text{F}_{11}(\text{NH}_2)^{2-}$, $\text{NaB}_{12}\text{HF}_{10}(\text{NH})^{2-}$, $\text{KB}_{12}\text{HF}_{10}(\text{NH})^{2-}$, $\text{NaB}_{12}\text{F}_{11}(\text{NH})^{2-}$, or $\text{KB}_{12}\text{F}_{11}(\text{NH})^{2-}$, the m/z values for which would be 168.5, 177.5, 179.5, 187.5, 188.5, and 196.5, respectively). More importantly, the *relative* intensity of the $\text{B}_{12}\text{F}_{12}^{2-}$ internal-standard isotop pattern in the 7 h spectrum is clearly much higher, relative to the sum of the intensities of the $\text{B}_{12}\text{HF}_{10}(\text{NH}_3)^-$ and $\text{B}_{12}\text{F}_{11}(\text{NH}_3)^-$ isotop patterns, than in the 5 h spectrum. This is shown more clearly in Figure 4-5. The unambiguous meaning of this is that

the $\text{B}_{12}\text{HF}_{10}(\text{NH}_3)^-$ and $\text{B}_{12}\text{F}_{11}(\text{NH}_3)^-$ anions were not stable over time in this reaction mixture and were decomposing to unknown sets of products, some of which may have been $\text{B}_{12}\text{F}_{11}(\text{NHF})^{2-}$ (m/z 186.5) and $\text{B}_{12}\text{F}_{11}(\text{NF}_2)^{2-}$ (m/z 195.5), the isotop patterns for which are indicated with the letter *y* in Figure 4-4. After 9 h, there was virtually no $\text{B}_{12}\text{HF}_{10}(\text{NH}_3)^-$ and $\text{B}_{12}\text{F}_{11}(\text{NH}_3)^-$ left in the reaction mixture (although there may be some $\text{NaB}_{12}\text{F}_{11}(\text{NH}_2)^-$, or $\text{KB}_{12}\text{F}_{11}(\text{NH}_2)^-$ present), and a different set of B_{12} -containing dianionic decomposition species were evident in the m/z ca. 180–200 region.

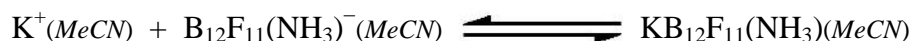
The net result is that the "Peryshkov" conditions are ineffective (to say the least) for the F_2 fluorination of $\text{B}_{12}\text{H}_{11}(\text{NH}_3)^-$ in cold MeCN *with excess KF*. Before a solution of $\text{B}_{12}\text{F}_{11}(\text{NH}_3)^-$ containing negligible amounts of other $\text{B}_{12}\text{H}_{11-n}\text{F}_n(\text{NH}_3)^-$ anions can be produced (i.e., before the fluorination is complete), virtually all of the $\text{B}_{12}\text{F}_{11}(\text{NH}_3)^-$ that formed had decomposed.

The bottom set of mass spectra in Figure 4-4 show the F_2 fluorination of $\text{KB}_{12}\text{H}_{11}(\text{NH}_3)$ in 0 °C MeCN *without added KF* after 5 and 7 h. The amounts of $\text{KB}_{12}\text{H}_{11}(\text{NH}_3)$ starting material and MeCN used and the rate at which F_2/N_2 was bubbled through the solution were the same as in the "with added KF" experiment just described. The only difference was the absence of solid KF in the reaction mixture. The fluorination was nearly complete after 5 h and was as complete as could be measured by mass spectrometry after 7 h. Although no $\text{B}_{12}\text{F}_{12}^{2-}$ internal standard was present in this experiment, the absolute intensities of the $n = 10$ and 11 isotop patterns indicate little or no decomposition between 5 and 7 h. Furthermore, the isolated yield of $\text{KB}_{12}\text{F}_{11}(\text{NH}_3)$ product, after workup, was ca. 60-70%. The absence of solid KF in the reaction mixture, and the concomitant buildup of the byproduct HF over time, apparently inhibited the decomposition of the highly-fluorinated anions $\text{B}_{12}\text{HF}_{10}(\text{NH}_3)^-$ and/or $\text{B}_{12}\text{F}_{11}(\text{NH}_3)^-$.

Similar experiments were performed with smaller amounts of $\text{KB}_{12}\text{H}_{11}(\text{NH}_3)$ starting material, which allowed complete or nearly-complete fluorination to be achieved in ca. 2 h. The mass spectra (not shown) were analyzed in the same way as described above. Plots of the average value of n for all $\text{B}_{12}\text{H}_{11-n}\text{F}_n(\text{NH}_3)^-$ cluster anions present vs. time are shown in Figure 4-6. The decomposition of $\text{B}_{12}\text{HF}_{10}(\text{NH}_3)^-$ and/or $\text{B}_{12}\text{F}_{11}(\text{NH}_3)^-$ anions that occurred in the presence of excess solid KF notwithstanding, the rates of fluorination with and without added KF are about the same. In fact, the fluorination was slightly faster *without* added KF, particularly between 1 and 2 h, which means that *fluorination was slightly faster as the concentration of byproduct HF increased over time*, exactly the opposite of what was observed by Peryshkov in the F_2 fluorination of $\text{K}_2\text{B}_{12}\text{H}_{12}$ in cold MeCN. This observation begs the question "could HF increase the rate of reaction of $\text{B}_{12}\text{H}_{11-n}\text{F}_n(\text{NH}_3)^-$ anions with F_2 even though it decreases the rate of reaction of $\text{B}_{12}\text{H}_{12-n}\text{F}_n^{2-}$ anions with F_2 ?"

To explore this unexpected result further, two reactions were performed with ca. 1.3% v/v (10.1 equiv based on starting $\text{KB}_{12}\text{H}_{11}(\text{NH}_3)$) and 1.8% v/v% (13.0 equiv based on starting $\text{KB}_{12}\text{H}_{11}(\text{NH}_3)$) aHF added to solutions of 2 g of $\text{KB}_{12}\text{H}_{11}(\text{NH}_3)$ in 150 mL of 0 °C anhydrous MeCN, both in the absence of solid KF. The mass spectra of samples taken from these two experiments are shown in Figures 4-7 and 4-8, and plots of the average value of n for all $\text{B}_{12}\text{H}_{11-n}\text{F}_n(\text{NH}_3)^-$ cluster anions present at a particular time vs. time are shown in Figure 4-9. Figure 4-7 also includes some mass spectra from the "without KF" samples that were used to obtain the mass spectra shown at the bottom of Figure 4-4 except that the samples injected into the mass spectrometer for the spectra shown in Figure 4-7 were 10 times more concentrated (i.e., the "without added KF" and "without added HF" samples were from the same fluorination reaction. Comparison of these two sets of spectra demonstrates that the relative intensities of the

$B_{12}F_{11}(NH_3)_2^-$ and $KB_{12}F_{11}(NH_2)_2^-$ isotop patterns at m/z 356 and 394, respectively, are concentration dependent, presumably because the ion-pair association equilibrium shown below is shifted to the right as the solution becomes more concentrated (i.e., the equilibrium quotient $K_{eq} = [KB_{12}F_{11}(NH_3)]/[K^+][B_{12}F_{11}(NH_3)^-]$ requires that the concentration ratio $[KB_{12}F_{11}(NH_3)]/[B_{12}F_{11}(NH_3)^-]$ will increase as the solution becomes more concentrated):



In the "without added HF/without added KF" reaction, the concentration of HF was zero at the start of fluorination and increased over time. In the two "with added HF" reactions, the concentration of HF at the beginning of the fluorination was approximately equal to the final concentration of HF in the "without added HF" reaction and increased to twice that concentration when the fluorinations were complete. If HF increased the rate of fluorination, the "with added HF" reactions should go to completion faster than the "without added HF" reaction. The results shown in Figures 4-7, 4-8, and 4-9 are unambiguous and conclusive. When HF was added to a cold MeCN solution of $KB_{12}H_{11}(NH_3)$, *the rate of F_2 fluorination increased significantly*. Fluorination was complete in only half-to-two-thirds of the time required to reach completion when HF was not added to the solution (i.e., 3 or 4 h vs. 6 h). Although previous work by Peryshkov et al. had shown that HF *inhibits* the F_2 fluorination of $B_{12}H_{12}^{2-}$ and *promotes* the decomposition of $B_{12}F_{12}^{2-}$ by F_2 ,⁵ this work has demonstrated that HF *accelerates* the F_2 fluorination of $B_{12}H_{11}NH_3^-$ and *protects* the perfluorinated product $B_{12}F_{11}(NH_3)^-$ from decomposition in the presence of F_2 . This work has made it clear that optimal direct per-*B*-fluorination conditions can be very different, in fact completely opposite, for different types of

borane (and possibly carborane) clusters. This phenomenon was not, and could not have been, anticipated in advance.

4.2.3 Single Crystal X-ray Structure of $\text{Na}(\text{H}_2\text{O})_4\text{B}_{12}\text{F}_{11}(\text{NH}_3)$: Evidence for $\text{NH}\cdots\text{F}$ Hydrogen Bonding.

It is instructive to consider the structure of this hydrated salt of the $\text{B}_{12}\text{F}_{11}(\text{NH}_3)^-$ anion before addressing the possible reasons that HF protects it from decomposition during the F_2 fluorination reactions in MeCN.

Single crystals of $\text{Na}(\text{H}_2\text{O})_4\text{B}_{12}\text{F}_{11}(\text{NH}_3)$ were grown by slow evaporation from a MeCN/ H_2O solution containing the $\text{B}_{12}\text{F}_{11}\text{NH}_3^-$ anion and both K^+ and Na^+ cations. X-ray diffraction data were collected using a Bruker Kappa APEX II CCD diffractometer, $\text{MoK}\alpha$ radiation ($\lambda = 0.71073 \text{ \AA}$), and a graphite monochromator at 120(2) K. Data reduction, solution, and refinement methods are discussed in Experimental Section.

The structure of $\text{Na}(\text{H}_2\text{O})_4\text{B}_{12}\text{F}_{11}(\text{NH}_3)$ consists of discrete $\text{B}_{12}\text{F}_{11}(\text{NH}_3)^-$ anions, two types of Na^+ cations on inversion centers, and four molecules of H_2O . A thermal-ellipsoid drawing of the anion is shown in Figure 4-10. Plots of the B–B distances in $\text{Na}(\text{H}_2\text{O})_4\text{B}_{12}\text{F}_{11}(\text{NH}_3)$ (this work), $\text{B}_{12}\text{H}_{11}(\text{NH}=\text{CH}(\text{p}-\text{C}_6\text{H}_4\text{OMe}))$,¹⁴ $(4\text{-NH}_2\text{-1-Me-1,2,4-triazolium})_2\text{B}_{12}\text{F}_{12}$,³¹ and $(1\text{-Et-3-Me-imidazolium})_2\text{B}_{12}\text{H}_{12}$ ³² are shown in Figure 4-11. It is clear that the effect of fluorination on both ammonioborane(1–) and borane(2–) icosahedral anions is to expand the B_{12} cage. Assuming that the B_{12} cages are ideal icosahedra, with an edge length equal to the average B–B distances of 1.797 \AA for $\text{Na}(\text{H}_2\text{O})_4\text{B}_{12}\text{F}_{11}(\text{NH}_3)$ and 1.773 \AA for $\text{B}_{12}\text{H}_{11}(\text{NH}=\text{CH}(\text{p}-\text{C}_6\text{H}_4\text{OMe}))$, the volume of the former is 4.1% larger than the volume of the latter (the volume of an icosahedron with an edge length of x is $(5/12)(3 + 5^{1/2})x^3$). A DFT calculation by collaborator Dr. Alexey A. Popov

(IFW, Dresden, Germany) on the hypothetical C_{5v} isomer of $B_{12}H_6F_6^{2-}$ anion is in harmony with these results: the B_1 – $B_{\text{upper belt}} (B_{\text{ub}})$ distance (involving BF vertexes) is 1.799 Å, significantly longer than the $B_{\text{lower belt}} (B_{\text{lb}})$ – B_{12} distance of 1.775 Å.

The structure of $Na(H_2O)_4B_{12}F_{11}(NH_3)$ has a one-dimensional hydrogen bonding network of $B_{12}F_{11}NH_3^-$ anions (bonding through the NH_3 group) and four H_2O molecules in the crystal lattice as shown in Figure 4-12. The four O atoms of the H_2O molecules form a nearly square-planer O_4 tetrameric ring, shown in detail in Figure 4-13, with $O\cdots O$ distances that range from 2.738(3) to 2.789(3) Å (average 2.762 Å), interior angles of 84.3, 84.4, 94.6, and 96.3°, and an average deviation of the O atoms from the O_4 least-squares plane of 0.016 Å. The two $N\cdots O$ distances are 2.844(3) and 2.891(3) Å; the $O\cdots N\cdots O$ angle is 128.2(1)°.

The B_{12} centroid \cdots centroid ($\odot\cdots\odot$) distances range from 7.331 to 9.745 Å and average 8.279 Å. These centroids form nearly-planar layers, with deviations of the B_{12} centroid from the least-squares plane of centroids of only 0.026 Å. The relative orientations of the one dimensional hydrogen bonded network of $B_{12}F_{11}NH_3^-$ anions and H_2O tetramers is shown in Figure 4-14. The H_2O tetramer centroids are co-linear, and the line of H_2O tetramer centroids makes an angle of 79.3° with respect to the B_{12} centroid least-squares plane. The H_2O tetramer centroids are 4.865 Å apart along the line of these centroids, and these lines are 11.324 Å apart within a layer of B_{12} centroids. The plane of the H_2O tetramer is tilted 33° with respect to the line of tetramer centroids and is tilted 47.2° with respect to the B_{12} centroid least-squares plane. The relative orientations of the lines and planes can be seen in Figure 4.14.

The two unique octahedral NaO_2F_4 coordination spheres in $Na(H_2O)_4B_{12}F_{11}(NH_3)$, which are shown in Figure 4-15, consist of four F atoms from four different anions and two O atoms from two H_2O molecules. The sum of bond valences^{33,34} for the Na^+ cations are 1.09 and 1.16.

Interestingly, in the structure of $\text{Na}_2(\text{H}_2\text{O})_4\text{B}_{12}\text{F}_{12}$, with fewer H_2O molecules per Na^+ ion, the distorted octahedral coordination spheres consist of four O atoms and two F atoms.³⁵ The differences between the two structures are that the four H_2O molecules in $\text{Na}_2(\text{H}_2\text{O})_4\text{B}_{12}\text{F}_{12}$ form infinite chains of edge-sharing NaO_4 distorted tetrahedra with no hydrogen bonding between the H_2O molecules, and the four H_2O molecules in $\text{Na}(\text{H}_2\text{O})_4\text{B}_{12}\text{F}_{11}(\text{NH}_3)$ form infinite chains of $(\text{H}_2\text{O})_4$ hydrogen-bonded tetramers. The infinite chains in the two structures are compared in Figure 4-16.

Figure 4-17 shows a drawing of the structure that emphasizes the hydrogen bonding in the X-ray structure of $\text{Na}(\text{H}_2\text{O})_4\text{B}_{12}\text{F}_{11}(\text{NH}_3)$ between the NH_3 group H atoms and two H_2O molecules and two F atoms from a neighboring $\text{B}_{12}\text{F}_{11}\text{NH}_3^-$ anion. The $\text{NH}\cdots\text{OH}_2$ distances are 1.96 and 1.99 Å. The bifurcated $\text{NH}\cdots\text{FB}$ distances are 2.29 and 2.40 Å. It is significant that one of the ammonio group H atoms forms bifurcated hydrogen bonds with two F atoms, even in the presence of four H_2O molecules per $\text{B}_{12}\text{F}_{11}\text{NH}_3^-$ anion and even considering the much stronger $\text{BF}\cdots\text{Na}^+$ interactions that exist in this structure. Strong hydrogen bonding between an ammonio group H atom and F^- in MeCN or the surface F^- ions in solid KF, for which the $\text{H}\cdots\text{F}$ hydrogen bonding in the structure of $\text{NaB}_{12}\text{F}_{11}\text{NH}_3\cdot 4\text{H}_2\text{O}$ is a model, is discussed in the part of this chapter that follows.

4.2.4 Why Does HF protect $\text{B}_{12}\text{F}_{11}(\text{NH}_3)^-$ From Decomposition in the Presence of F_2 ?

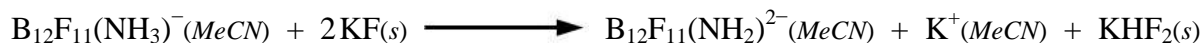
It is clear from the mass spectroscopic data shown in Figures 4-4 and 4-5 that $\text{B}_{12}\text{F}_{11}(\text{NH}_3)^-$ (and possibly other $\text{B}_{12}\text{H}_{11-n}\text{F}_n(\text{NH}_3)^-$ species) is not stable in cold MeCN containing F_2 in the presence of solid KF. As the eleven-step per-*B*-fluorination of $\text{B}_{12}\text{H}_{11}(\text{NH}_3)^-$ progressed over time from $n = 0$ to $n = 11$, one would have expected the concentration of $\text{B}_{12}\text{F}_{11}(\text{NH}_3)^-$ to

increase at the expense of the concentrations of $\text{B}_{12}\text{H}_2\text{F}_9(\text{NH}_3)^-$ and $\text{B}_{12}\text{HF}_{10}(\text{NH}_3)^-$, as was the case when no solid KF was present (e.g., the 5 h and 7 h "no KF added" mass spectra in Figure 4-4). However, when KF was present the concentrations of $\text{B}_{12}\text{H}_2\text{F}_9(\text{NH}_3)^-$, $\text{B}_{12}\text{HF}_{10}(\text{NH}_3)^-$, and $\text{B}_{12}\text{F}_{11}(\text{NH}_3)^-$ all decreased relative to the $\text{B}_{12}\text{F}_{12}^{2-}$ internal intensity standard between 5 h and 7 h, and after 9 h no $\text{B}_{12}\text{F}_{11}(\text{NH}_3)^-$ was detected by mass spectrometry. The concentrations of $\text{B}_{12}\text{H}_2\text{F}_9(\text{NH}_3)^-$ and $\text{B}_{12}\text{HF}_{10}(\text{NH}_3)^-$ are expected to increase and then decrease over time as the average value of n increases, but the concentration of $\text{B}_{12}\text{F}_{11}(\text{NH}_3)^-$ should only increase over time unless it is being converted to other products, that is, unless it is being decomposed, presumably by F_2 .

Significantly, it appears that the rate of decomposition of $\text{B}_{12}\text{F}_{11}(\text{NH}_3)^-$ is faster, or at least not slower, than the rates of decomposition of intermediate $\text{B}_{12}\text{H}_{11-n}\text{F}_n(\text{NH}_3)^-$ anions with 10 or fewer F atoms. Otherwise, little or no $\text{B}_{12}\text{F}_{11}(\text{NH}_3)^-$ would have been present at any time during the reaction. This is in sharp contrast to the relative stabilities of $\text{B}_{12}\text{H}_{12-n}\text{F}_n^{2-}$ anions in MeCN solution in the presence of F_2 and solid KF. Peryshkov et al. reported that the mol% yield of $\text{K}_2\text{B}_{12}\text{F}_{12}$ was significantly higher when the starting material was an 80/20 mixture of $\text{K}_2\text{B}_{12}\text{H}_8\text{F}_4/\text{K}_2\text{B}_{12}\text{H}_7\text{F}_5$ (92 mol%) rather than $\text{K}_2\text{B}_{12}\text{H}_{12}$ (74%; the F_2 fluorination conditions in cold MeCN were the same).⁵ This was attributed to the oxidative decomposition of $\text{B}_{12}\text{H}_{12-n}\text{F}_n^{2-}$ anions with small values of n . This was a sensible result, because $\text{B}_{12}\text{F}_{12}^{2-}$ should be much more resistant to oxidation than $\text{B}_{12}\text{H}_{12}^{2-}$ or $\text{B}_{12}\text{H}_{12-x}\text{F}_x^{2-}$ anions with small values of n .

Ivanov et al. reported that $\text{B}_{12}\text{F}_{11}(\text{NH}_3)^-$ is much more acidic in H_2O than $\text{B}_{12}\text{H}_{11}(\text{NH}_3)^-$ (the $\text{p}K_a$ of $\text{B}_{12}\text{F}_{11}(\text{NH}_3)^-$ was found to be 9.6, about the same as for aqueous HCO_3^-).⁶ The deprotonated species $\text{B}_{12}\text{F}_{11}(\text{NH}_2)^{2-}$ was stable indefinitely in alkaline H_2O and was isolated as crystalline $[\text{N}(n\text{-Bu})_4]_2[\text{B}_{12}\text{F}_{11}(\text{NH}_2)]$, which was stable indefinitely on the benchtop.⁶ A tentative

explanation for the relatively rapid decomposition of $B_{12}F_{11}(NH_3)^-$ by F_2 in the presence of solid KF but not in the absence of solid KF is as follows: (i) $B_{12}F_{11}(NH_3)^-$ is easier to deprotonate than $B_{12}HF_{10}(NH_3)^-$, which is easier to deprotonate than $B_{12}H_2F_9(NH_3)^-$, etc. (i.e., with more F atoms, $B_{12}F_{11}(NH_3)^-$ is a stronger acid than $B_{12}HF_{10}(NH_3)^-$, which is a stronger acid than $B_{12}H_2F_9(NH_3)^-$, etc.); (ii) the presence of solid KF removes the HF byproduct formed in the F_2 fluorination reaction by forming solid KHF_2 (both KF^{36} and KHF_2 have negligible solubility in anhydrous MeCN) and also removes H^+ from $B_{12}F_{11}(NH_3)^-$ to form $B_{12}F_{11}(NH_2)^{2-}$ and solid KHF_2 ; (iii) $B_{12}F_{11}(NH_2)^{2-}$ reacts with F_2 to form both $B_{12}F_{11}(NHF)^{2-}$ and $B_{12}F_{11}(NF_2)^{2-}$, which decompose relatively rapidly to BF_4^- , among other cluster degradation products; (iv) in the absence of solid KF, the buildup of HF in solution prevents the deprotonation of $B_{12}F_{11}(NH_3)^-$ to $B_{12}F_{11}(NH_2)^{2-}$ and hence inhibits the decomposition of $B_{12}F_{11}(NH_3)^-$. The proposed decomposition sequence can be summarized in the three reactions shown below.



Species with m/z values that correspond to $B_{12}F_{11}(NHF)^{2-}$ and $B_{12}F_{11}(NF_2)^{2-}$ were present in the 9 h "KF added" spectrum in Figure 4-4 (i.e., isotop patterns at 186.8 and 195.5). However, it has not been possible to isolate and more fully characterize/identify these species, presumably because they decompose during the workup of the reaction mixture, and for this reason the presence of $B_{12}F_{11}(NHF)^{2-}$ and $B_{12}F_{11}(NF_2)^{2-}$ must remain tentative. It is possible that F_2 causes

the decomposition of $B_{12}F_{11}(NH_2)^{2-}$ without the intermediacy of $B_{12}F_{11}(NHF)^{2-}$ or $B_{12}F_{11}(NF_2)^{2-}$. Nevertheless, it is clear that during the latter stages of the F_2 fluorination of $KB_{12}H_{11}(NH_3)$ in 0 °C MeCN with excess KF, the formation and decomposition of $B_{12}F_{11}(NH_3)^-$ occur at similar rates.

4.2.5 Why Does the Presence of HF Accelerate the F_2 Fluorination of $B_{12}H_{11}(NH_3)^-$?

In order to address this question, it is useful to first review the answer proposed by Peryshkov et al. to the question: Why does HF *inhibit* the F_2 fluorination of $B_{12}H_{12}^{2-}$ in cold MeCN?⁵ In their 2009 paper in *J. Am. Chem. Soc.* Peryshkov et al. proposed that HF either solvates or protonates $B_{12}H_{12-n}F_n^{2-}$ species on the most basic B_3 triangular faces of the cluster, which would be the faces with the greatest number of remaining B–H bonds. It was also proposed that fluorination occurred at the interface of the bubbles of F_2/N_2 and the solution, and that protonation of faces with B–H bonds would orient those faces *away* from the gas bubble, *into* the MeCN solution (note that the title of Peryshkov's 2009 paper is "Direct Perfluorination of $K_2B_{12}H_{12}$ in Acetonitrile Occurs at the Gas Bubble-Solution Interface and Is Inhibited by HF. Experimental and DFT Study of Inhibition by Protic Acids and Soft, Polarizable Anions").⁵ This would inhibit fluorination by preventing the Lewis acidic F_2 molecule from forming an acid–base complex with that face of the cluster. This proposal is summarized in Figure 4-18.

If fluorination of $B_{12}H_{11}(NH_3)^-$ also occurs on the surface of F_2/N_2 bubbles, then the presence of HF would be expected to have a similar effect, *inhibiting* fluorination by preventing F_2 from forming a complex with B_3 faces containing B–H bonds. But this is not what is observed. The presence of HF accelerates fluorination. There must be other ways that HF can act during the fluorination of $B_{12}H_{11}(NH_3)^-$ to more than overcome any inhibition caused by blocking B_3 faces

from F₂ complexation. Furthermore, whatever these countervailing effects might be, why would they not be operative in the fluorination of B₁₂H₁₂²⁻?

If the overall mechanism of the B–H to B–F transformations are essentially the same for B₁₂H₁₂²⁻ and B₁₂H₁₁(NH₃)⁻, then the opposite effects of HF must be rooted in the structurally and electronic differences of the two clusters. They have different overall charges: 2- and 1-. They have and very different charge distributions: B₁₂H₁₂²⁻ is spherically symmetric and B₁₂H₁₁(NH₃)⁻ can be thought of as a zwitterion, with a 2- cluster with a 1+ appendage. Nevertheless, at this point in time there is no compelling explanation for the observed difference in the effect of HF. It is likely that additional experiments and DFT calculations will provide the necessary evidence to clarify the situation. While many hypothesis can be developed to explain this unanticipated phenomenon such as (i) B₁₂H₁₁(NH₃)⁻ forms strong hydrogen bonds to multiple HF molecules in solution effectively lowering the HF concentration available to block B₃ faces, (ii) the –NH₃⁺ moiety on the B₁₂ cage changes the electronic nature of the B₁₂ cage such that HF build-up no longer slows fluorination of B–H bond to B–F with F₂, or (iii) the accumulation of HF (or addition of HF) increases the dielectric strength of the MeCN or the increase of protic acid (or both) increase the rate of fluorination of B–H bond to B–F with F₂, a phenomenon known in fluorination of organic compounds in solvent with F_{2(g)}.³⁷⁻⁴¹ The last hypothesis would indicate that the rate of fluorination of K₂B₁₂H₁₂ slowing down as HF builds up (or is added) is the outlier and that fluorination of B₁₂H₁₁NH₃⁻ is more similar to organic compounds in solvent with F_{2(g)}. However, without further control experiments coupled with DFT calculations, all hypotheses have equal merit, and further speculation without additional, carefully controlled experiments is of little value.

4.2.6 Improved Synthesis, Purification, and Spectroscopic Characterization of the Isomers of $B_{12}H_{10}(NH_3)_2$ and $B_{12}F_{10}(NH_3)_2$.

During the synthesis of $KB_{12}H_{11}NH_3$ from $K_2B_{12}H_{12}$ and hydroxylamine-*O*-sulfonic acid as described by Hertler and Raasch, ca. 30% of the recovered product is 3 isomers of $B_{12}H_{10}(NH_3)_2$.¹⁹ The neutral isomers, 1,2-, 1,7-, and 1,12- $B_{12}H_{10}(NH_3)_2$ can be separated by a liquid-liquid extraction separation method with ethyl acetate and dd- H_2O , developed by Ms. Plunzte. This separates the more polar product species from the amination reaction mixture ($KB_{12}H_{11}NH_3$, 1,2- $B_{12}H_{10}(NH_3)_2$ and residual $K_2B_{12}H_{12}$) from the less polar species (1,7- $B_{12}H_{10}(NH_3)_2$, 1,12- $B_{12}H_{10}(NH_3)_2$, with a small amount of 1,2- $B_{12}H_{10}(NH_3)_2$). Figure 4-19 shows the $^{11}B[^1H]$ decoupled NMR of the organic and aqueous layers for such a separation. Table 4-3 shows the 1H ($-NH_3$ protons only) and ^{15}N ppm shifts of each compound as determined by HSQC. Using these peak assignments, integration of the 1D 1H - ^{15}N NMR spectrum of the crude material shows that of the converted products of the amination reaction are 70% is $KB_{12}H_{11}NH_3$ and 30% is a mixture of the three diammonio isomers, specifically 3, 22, and 5% as the 1,12-, 1,7-, and 1,2- $B_{12}H_{10}(NH_3)_2$ respectively. The physical isolation of the isomers by gradient flash chromatography resulted in overall 2.5, 11, and 2.7% yields of the 1,12-, 1,7-, and 1,2- $B_{12}H_{10}(NH_3)_2$ respectively. New synthesis methods to target greater yields of the diammonio boranes by Ms. Plunzte had some success but were not repeated and will not be discussed further here. The separation process afforded all three isomers in pure form, as verified by single crystal X-ray crystallography.

4.2.7 NMR Characterization of 1,2-, 1,7-, and 1,12- Isomers of $B_{12}H_{10}(NH_3)_2$ and $B_{12}F_{10}(NH_3)_2$.

The NMR chemical shifts and coupling constants for the 1,2-, 1,7-, and 1,12- isomers of $B_{12}H_{10}(NH_3)_2$ and $B_{12}F_{10}(NH_3)_2$ are listed in Table 4-3. The 1H NMR spectra of 1,2-, 1,7-, and 1,12- $B_{12}H_{10}(NH_3)_2$ exhibit broad signals because of the quadrupolar nature of ^{11}B , ^{10}B , and ^{14}N . Recording ^{11}B -coupled and -decoupled 1H spectra allowed many of the $J(^{11}B^1H)$ values to be determined.

Although ^{15}N is only 0.4% naturally abundant, it was possible to determine $\delta(^{15}N)$ values for 1,2-, 1,7-, and 1,12- $B_{12}H_{10}(NH_3)_2$ using 2D 1H - ^{15}N HSQC NMR spectroscopy.⁴² This pulse sequence, which is commonly used for the structural analysis of proteins, has also been used to study boron-nitrogen compounds containing NH bonds such as the amino borane $B(NH(CH_3)_3)$.⁴³ The spectra recorded in this work represent the first time that 1H - ^{15}N HSQC NMR has been used to study polyhedral boranes with NH moieties. Figure 4-20 shows the NH region of the normal 1H and 1D 1H - ^{15}N HSQC NMR spectra of a crude amination reaction mixture containing 1,2-, 1,7-, and 1,12- $B_{12}H_{10}(NH_3)_2$ (ca. 30 mol% combined) and $KB_{12}H_{11}(NH_3)$ (ca. 70 mol%). The relative mole ratios of 1,2-, 1,7-, and 1,12- $B_{12}H_{10}(CH_3)_2$ in the product mixture, 0.23:1.00:0.14, respectively, were determined from the integrated intensities of the resonances in the HSQC spectrum. The ^{15}N resonances for the ammonio N atoms are clearly evident in the 2D spectrum. They are relatively broad because the ammonio N atoms are bonded to quadrupolar ^{11}B or ^{10}B atoms.

Figure 4-21 shows 1H - ^{15}N HSQC NMR spectra of purified samples of 1,2-, 1,7-, and 1,12- $B_{12}H_{10}(NH_3)_2$. The sample of 1,12- $B_{12}H_{10}(NH_3)_2$ contains a small amount of the monoammonio borane salt $KB_{12}H_{11}(NH_3)$ because, as discussed above, these two compounds are

very soluble in H₂O and are extremely difficult to separate. These spectra provide the best evidence for the relative purity of the three isomers.

4.2.8 Fluorination of B₁₂H₁₀(NH₃)₂ Isomers.

The per-*B*-fluorination of the isomers of B₁₂H₁₀(NH₃)₂ was accomplished using a mixture of the three isomers and using each of the individual purified isomers. The method of direct fluorination was, with minor modifications, the "without added KF" method developed for the F₂ fluorination of B₁₂H₁₁(NH₃)⁻ in cold MeCN: continuously bubbling 20/80 F₂/N₂ through a cold MeCN solution of the compound(s) in the presence of an increasing concentration of byproduct HF as the ten B–H fluorination steps proceeded to completion. This method was found to be efficient, one interpretation of which is that the presence of HF protected B₁₂F₁₀(NH₃)₂ isomers from decomposition caused by F₂ via the intermediacy of putative B₁₂F₁₀(NH₃)(NHF)⁻ and/or B₁₂F₁₀(NH_{2-n}F_n)₂²⁻ species. However, experiments designed to test this hypothesis were not performed, since results from fluorination of KB₁₂H₁₁NH₃ indicated such a protective effect with HF was occurring. The reaction conditions are similar to fluorination of KB₁₂H₁₁NH₃ in MeCN at 0 °C. Yields of each isomer have yet to be determined; however the crude yield of a mixture of isomers is nearly identical to the fluorination of KB₁₂H₁₁NH₃. The identity of the isomers formed has been initially characterized by single crystal X-ray structures of 1,2-, 1,7- and 1,12-B₁₂H₁₀(NH₃)₂ and 1,7- and 1,12-B₁₂F₁₀(NH₃)₂ (some are preliminary structures due to severe solvent or other impurity disorder), and by ¹⁹F[¹¹B], ¹¹B[¹⁹F], and ¹H NMR spectroscopy of isolated compounds.

4.2.9 The X-ray Structures of 1,2-, 1,7- and 1,12- $B_{12}H_{10}(NH_3)_2$ and 1,7- and 1,12- $B_{12}F_{10}(NH_3)_2$.

Single crystals of 1,2- $(NH_3)_2B_{12}H_{10}$ (grown from ethyl acetate), 1,7- $(NH_3)_2B_{12}H_{10}$ (grown from dd- H_2O), 1,12- $(NH_3)_2B_{12}H_{10}$ (grown from MeCN), 1,7- $(NH_3)_2B_{12}F_{10}$ (grown from MeCN), and 1,12- $(NH_3)_2B_{12}F_{10}$ (grown from MeCN) were grown by slow evaporation of solvent in air by Amanda Pluntze. The crystal structures of 1,2- $(NH_3)_2B_{12}H_{10}$, 1,7- $(NH_3)_2B_{12}H_{10}$, 1,12- $(NH_3)_2B_{12}H_{10}$, and 1,7- $(NH_3)_2B_{12}F_{10}$ were collected by the author of this dissertation using the Bruker Kappa APEX II CCD diffractometer at Colorado State University. The crystal structure of 1,12- $(NH_3)_2B_{12}F_{10}$ was collected using synchrotron X-ray source at Argonne National Laboratory, Advanced Photon Source, ChemMatCARS, station 15-ID-B. The 50% thermal ellipsoid plots of the 1,2-, 1,7- and 1,12- $B_{12}H_{10}(NH_3)_2$ B_{12} anions are shown in Figure 4-22, important crystallographic information is shown in Table 4-4. All of the structures have either solvent (MeCN, H_2O , or ethyl acetate) in the lattice of methyl amide (CH_3CONH_2) and so direct comparisons of packing efficiency or other structural motifs such as hydrogen bonding interactions etc. is of little value. However, with the exception of 1,7- $B_{12}H_{10}(NH_3)_2$, these are the first, to the best of this authors knowledge, crystal structures of these four diammonio compounds.

4.3 Summary and Conclusions

Synthesis and isolation of the monoammonio compound $KB_{12}H_{11}NH_3$ was accomplished as well as synthesis, isolation, and characterization of the three diammonio isomers 1,2-, 1,7- and 1,12- $B_{12}H_{10}(NH_3)_2$. Crystal structures (some preliminary) of the diammonio isomers 1,2-, 1,7-

and 1,12-B₁₂H₁₀(NH₃)₂ compounds were also collected, for the first time further proving the identity of 1,2-, and 1,12-B₁₂H₁₀(NH₃)₂, never before published structures.

The scaled fluorination of KB₁₂H₁₁NH₃ into KB₁₂F₁₁NH₃ was accomplished in anhydrous MeCN at 0 °C with 20/80 F₂/N₂(g). The fluorination proceeds to completion with the addition of excess KF, and when excess KF is used, the KB₁₂F₁₁NH₃ product decomposes prior to the fluorination being complete, an unanticipated and completely opposite phenomenon when compared to the fluorination of K₂B₁₂F₁₂ in MeCN at 0 °C with 20/80 F₂/N₂(g) by Peryshkov. Furthermore, when anhydrous HF is added to the anhydrous MeCN before the start of the fluorination reaction, the fluorination of KB₁₂H₁₁NH₃ in MeCN at 0 °C with 20/80 F₂/N₂(g) occurs at a faster rate. The reaction rate enhancement effects of anhydrous HF on the fluorination of KB₁₂H₁₁NH₃, are at this time still unknown, but should be explored further.

A crystal structure of NaB₁₂F₁₁NH₃·4H₂O has been collected and has a 4H₂O tetramer that hydrogen bonds with the –NH₃ group on the B₁₂ cage. The 4H₂O tetramer and –NH₃ hydrogen bonded network extend through the lattice infinitely in one dimension. Additionally, the Na⁺ in the NaB₁₂F₁₁NH₃·4H₂O structure has a coordination sphere of four fluorine atoms from four adjacent B₁₂ cages and only two oxygen atoms from adjacent H₂O molecules, a surprising result when considering typical metal interaction with oxygen and fluorine.

Finally, fluorination of a mixture of the 1,2-, 1,7- and 1,12-B₁₂H₁₀(NH₃)₂ diammonio isomers appears to be similar to KB₁₂H₁₁NH₃ in that it does not go to completion in the presence excess KF. By using a similar method to that of fluorinating KB₁₂H₁₁NH₃, a mixture of 1,2-, 1,7- and 1,12-B₁₂H₁₀(NH₃)₂ was fluorinated and subsequently separated into separate isomers, each isomer was characterized by NMR and single crystal X-ray structures of the 1,7- and 1,12-B₁₂F₁₀(NH₃)₂ have been collected.

It appears from this work that the mechanism of fluorination of $\text{KB}_{12}\text{H}_{11}\text{NH}_3$ and the three diammonio isomers, 1,2-, 1,7- and 1,12- $\text{B}_{12}\text{H}_{10}(\text{NH}_3)_2$, is different from that reported by Peryshkov, and that further control experiments are required to determine these differences.

4.4 Future Work

Multiple experiments are necessary to elucidate the surprising phenomenon that $\text{KB}_{12}\text{H}_{11}\text{NH}_3$ will completely fluorinate forming $\text{KB}_{12}\text{F}_{11}\text{NH}_3$ in the presence of > 10 equiv of HF, a result exactly opposite to the complete fluorination of $\text{K}_2\text{B}_{12}\text{H}_{12}$ forming $\text{K}_2\text{B}_{12}\text{F}_{12}$. The first desired experiment is to take an equal molar mixture of $\text{KB}_{12}\text{H}_{11}\text{NH}_3$ and $\text{K}_2\text{B}_{12}\text{H}_{12}$ in anhydrous MeCN with 10-12 equiv of HF. The first problem such an experiment is that $\text{K}_2\text{B}_{12}\text{H}_{12}$ has low solubility in anhydrous MeCN, which is why 2.4% H_2O is typically added during the first step of the fluorination of $\text{K}_2\text{B}_{12}\text{H}_{12}$. If necessary a minimal amount of water could be added to the anhydrous MeCN to get $\text{K}_2\text{B}_{12}\text{H}_{12}$, however, it may also be the case that the added HF would raise the dielectric strength of the MeCN enough to dissolve the $\text{K}_2\text{B}_{12}\text{H}_{12}$. If in this experiment $\text{K}_2\text{B}_{12}\text{H}_{12}$ still completely fluorinates without a drastic decrease in the rate than other control experiments are required. First, attempt to fluorinate $\text{K}_2\text{B}_{12}\text{H}_{12}$ in anhydrous MeCN with addition of anhydrous HF, since Peryshkov always used added H_2O in his fluorinations in MeCN, if he used aqueous HF instead of anhydrous HF, this could have a drastic effect on solvent properties. Next fluorinate a single isomer of $\text{B}_{12}\text{H}_{10}(\text{NH}_3)_2$, preferably 1,12- because then only one type of B-H is being fluorinated during the reaction. Finally, some DFT calculations such as which B_3 face would be the lowest energy for protonation of $\text{B}_{12}\text{H}_{11}\text{NH}_3^-$ and $\text{B}_{12}\text{HF}_{10}\text{NH}_3^-$, do those positions change in a higher dielectric medium, and does the $-\text{NH}_3$ electronic effects on the B_{12} cage change the way B-H bonds and B_3 faces interact with HF, or F_2 in MeCN would aid in

determining the unanticipated, reproducible result that $\text{B}_{12}\text{H}_{11}\text{NH}_3^-$ fluorinates faster in the presence of HF.

4.5 Experimental

4.5.1 Reagents and Solvents

Potassium dodecahydro-*closo*-dodecaborate ($\text{K}_2\text{B}_{12}\text{H}_{12}$) (Air Products and Chemicals Inc., purified of methanol by H_2O azeotropic removal washing/drying cycles till methanol was not observed by ^1H NMR spectroscopy). The MeCN (Fisher, ACS grade with $< 0.01\%$ water) was used as received, or, anhydrous MeCN was prepared by drying with > 20 vol% 3 Å molecular sieves, 48 h with agitation, distill under $\text{N}_2(\text{g})$ (Airgas cylinder, UHP grade, 99.999%) bubble room temperature solvent with $\text{N}_2(\text{g})$ 30 min to deoxygenate, F_2/N_2 gas mixture (20%/80% $\pm 5\%$, Matheson Tri-gas), liquid anhydrous HF, (Air Products and Chemical,), hydroxylamine-*O*-sulfonic acid (Acros, 97%), KOH (Fisher, ACS grade pellets, 84%), and ethyl acetate (Fisher, ACS grade), KHCO_3 (Fisher, Certified ACS grade) were used as received. The deuterated NMR solvents D_2O (Cambridge Isotopes Laboratories, Inc., 99.8% D), and CD_3CN (Cambridge Isotopes Laboratories, Inc., 99.8% D), were used as received. In certain cases as indicated anhydrous was used CD_3CN (dried with > 20 vol% activated 3 Å molecular sieves, distilled and stored over activated 3 Å under $\text{N}_2(\text{g})$). Distilled deionized water (dd- H_2O) was prepared by passing distilled water with through a Barnstead Nanopure deionization system producing water with a final resistance of at least 18 MΩcm.

4.5.2 Instrumentation

NMR Spectroscopy: NMR spectra were taken on a 400 MHz automatic tune, Inova Varian instrument or a 300 MHz manual tune Inova Varian instrument in 5 mm NMR spectroscopy grade glass tubes. Samples were dissolved in as received D₂O or CD₃CN as indicated. Nuclei observed for KB₁₂H₁₁NH₃, KB₁₂F₁₁NH₃, and KB₁₂F₁₁NH_{3-x}R_x (R = C₃H₅) were ¹¹B[¹⁹F], (¹¹B frequency was 128.24 MHz and ¹⁹F was 376.01 MHz on the 400 MHz instrument, ¹¹B pulse angle = 90°, pulse time = 13.5 × 10⁻⁶ s acquisition time = 0.200 s, and relaxation delay was = 0.900 s, spectral width 20491.8 Hz), and ¹⁹F[¹¹B] (¹⁹F was 376.01 MHz and ¹¹B frequency was 128.24 MHz on the 400 MHz instrument, ¹⁹F pulse angle = 30°, pulse time = 4.63 × 10⁻⁶ s, acquisition time = 0.865 s, relation delay = 1.000 s, spectral width = 37878.8 Hz), and ¹H (399.7 MHz on the 400 MHz instrument).

Negative Ion Electrospray Mass Spectroscopy: Mass spectra were recorded using a 2000 Finnigan LCQ-DUO mass-spectrometer with MeCN as the carrier solvent. The instrument parameters were tuned to maximize the KB₁₂F₁₂⁻ signal in a sample of K₂B₁₂F₁₂ dissolved in MeCN. Samples were on the order of 10–50 μM concentration in as received MeCN or 3:1 dd-H₂O:MeCN. Samples that were known to be acidic were neutralized with 1 drop (ca. 50 μL) of saturated aqueous KHCO₃ solution.

X-ray Crystallography: Single crystals of NaB₁₂F₁₁NH₃·4H₂O were grown by the author of this dissertation by slow evaporation from H₂O. Data collection, data reduction, solution and structure refinement were performed by this author. Data collection performed on a Bruker

Kappa APEX II CCD diffractometer (MoK α λ = 0.71073 Å; graphite monochromator) at $T=120(2)$ K. Data reduction was performed with APEX 2 suite of software from Bruker, a semiempirical absorption correction was applied with SCALE⁴⁴⁻⁴⁷. Solution and structure refinement were performed with SHELXTL software in OLEX 2, Version 1.2.5⁴⁸. All figures were generated with SHELXTL XP software.

Single crystals of 1,2-(NH₃)₂B₁₂H₁₀ (grown from ethyl acetate), 1,7-(NH₃)₂B₁₂H₁₀ (grown from dd-H₂O), 1,12-(NH₃)₂B₁₂H₁₀ (grown from MeCN), 1,7-(NH₃)₂B₁₂F₁₀ (grown from MeCN), and 1,12-(NH₃)₂B₁₂F₁₀ (grown from MeCN) were grown by slow evaporation of solvent in air by Amanda M. Pluntze. The crystal structures of 1,2-(NH₃)₂B₁₂H₁₀, 1,7-(NH₃)₂B₁₂H₁₀, 1,12-(NH₃)₂B₁₂H₁₀, and 1,7-(NH₃)₂B₁₂F₁₀ were collected by the author of this dissertation using the Bruker Kappa APEX II CCD diffractometer and the same software described above. The crystal structure of 1,12-(NH₃)₂B₁₂F₁₀ was collected using synchrotron X-ray source at Argonne National Laboratory, Advanced Photon Source, ChemMatCARS, station 15-ID-B. Data were collected using a Bruker Kappa APEX II CCD diffractometer employing synchrotron radiation and a diamond (1 1 1) monochromator (λ = 0.41328 Å) at $T=120(2)$ K and a Bruker D8 goniometer scanning through ω and ϕ rotation. Absorption and other corrections were applied using SCALE.⁴⁶ The structure was solved using direct methods and refined (on F^2 , using all data) by a full-matrix, weighted least-squares process.^{44,45,47} Standard Bruker control and integration software (APEX II) was employed, and Bruker SHELXTL software was used with Olex 2 for structure solution, refinement, and molecular graphics.^{45,47,48}

4.5.3 Synthesis of $\text{KB}_{12}\text{H}_{11}\text{NH}_3$.

Solid $\text{K}_2\text{B}_{12}\text{H}_{12}$, 10.0 g (45.5 mmol), and ca 2 eq. of hydroxylamine-*O*-sulfonic acid 11.0 g (93.8 mmol) were added to a 100 mL round bottom flask with a Teflon® stir-bar and dissolved in ca. 70 mL of dd- H_2O . The solution was refluxed for 3 h then cooled to room temperature and neutralized with 10% aqueous KOH. Approximately 4 times the volume of absolute ethanol was added to the neutralized solution forming a white precipitate of potassium sulfate. The mixture was then cooled to 4 °C for 13 h. The white precipitate was filtered from the solution. The solution was then again chilled for 2 h and filtered to remove any remaining white precipitate. The solution was dried to a solid by rotary-evaporation and further dried by heating to ca. 60 °C and removing volatiles with vacuum.

Once the filtrate was dried, the crude product was dissolved in 95 mL of dd- H_2O and the diammonio products were separated from the monoammonio products by liquid-liquid extraction with ethyl acetate. The aqueous layer was treated with 4 additions of 40 mL each ethyl acetate and 2 additions of 50 mL each. All of the ethyl acetate layers were combined and washed with 50 mL of dd- H_2O . The ethyl acetate solutions were collected into a single sample and dried to a solid. Similarly, the aqueous solutions were collected into a single sample and dried to a solid. Both samples were dried by rotary-evaporation and further dried by removing all volatiles under vacuum. The ethyl acetate layer containing a small amount of 1,2- $(\text{NH}_3)_2\text{B}_{12}\text{H}_{10}$, 1,7- $(\text{NH}_3)_2\text{B}_{12}\text{H}_{10}$ and 1,12- $(\text{NH}_3)_2\text{B}_{12}\text{H}_{10}$ dried down to 2.17 g of a white solid. The aqueous layer containing a small amount of 1,2- $(\text{NH}_3)_2\text{B}_{12}\text{H}_{10}$, $\text{KB}_{12}\text{H}_{11}\text{NH}_3$ and some $\text{K}_2\text{B}_{12}\text{H}_{12}$ dried down to 6.91 g of white solid. The dried aqueous layer was dissolved in MeCN and filtered through glass fiber filter paper to remove the $\text{K}_2\text{B}_{12}\text{H}_{12}$ resulting in 6.05 g of $\text{KB}_{12}\text{H}_{11}\text{NH}_3$ with a small amount

of 1,2-(NH₃)₂B₁₂H₁₀ detectable by ¹¹B NMR. Final yield of purified KB₁₂H₁₁NH₃ based on starting K₂B₁₂H₁₂ = 67%. The chemical shifts of KB₁₂H₁₁NH₃ in D₂O are; ¹¹B[¹H] signals δ -6.53(1), δ -15.5 (5), δ -16.4(5), and δ -19.7(1), ¹H[¹¹B] signals δ 0.99(1), δ 1.15(5), δ 1.39(5), and NH₃ δ 4.67. The ¹¹B and ¹H chemical shifts of the 1,2-(NH₃)₂B₁₂H₁₀, 1,7-(NH₃)₂B₁₂H₁₀ and 1,12-(NH₃)₂B₁₂H₁₀ in D₂O are shown in Table 4-3. It should be noted that KB₁₂H₁₁NH₃ and the 1,2- and 1,7 isomers of (NH₃)₂B₁₂H₁₀, are extremely hygroscopic and difficult to dry, they should be stored in desiccator of dry atmosphere glovebox to keep powdery, and consistent mass.

4.5.4 Synthesis of KB₁₂F₁₁NH₃ in anhydrous MeCN.

In an inert atmosphere glovebox dried KB₁₂H₁₁NH₃ 2.0g (10.2 mmol) was added to a 250 mL round bottom flask with a Teflon® stir-bar to which 150 mL of anhydrous MeCN was added. The mixture was capped, removed from the glovebox and cooled to 0 °C. Once cooled the solution was slowly bubbled with F₂/N₂ gas mixture 20/80, the outflow of which went to a separate fluorination of K₂B₁₂H₁₂ prepared as previously described (Chapter 2). The outflow of the fluorination of K₂B₁₂H₁₂ went to an aqueous solution of KI to indicate when not all F₂ was being consumed. The reaction was allowed to bubble slowly with F₂/N₂ gas mixture for 4 h, after which time the flow of F₂/N₂ stopped and both reactors were purged with N₂(g) for 30 minutes to remove any F₂(g). A small sample is taken (8–20 μL, diluted in 10 mL MeCN) and the reaction progress was monitored by Ni-ESI-MS. Once determined complete solid KHCO₃, 30-40 g, and ca. 100 mL dd-H₂O was added and stirred until the solution was neutral and two layers formed. Crude yield after drying down the MeCN layer 3.26 g, ca. 80 yield. To purify the KB₁₂F₁₁NH₃, it was extracted from the ethyl acetate as KB₁₂F₁₁NH₂⁻ with 10% KOH, leaving any K₂B₁₂F₁₂ in the organic layer. The KOH solution was acidified with HCl, and the KB₁₂F₁₁NH₃ extracted once

more into ethyl acetate following the procedure described in Chapter 2 to purify $\text{K}_2\text{B}_{12}\text{F}_{12}$. Purified yields vary due to incomplete extraction of the $\text{KB}_{12}\text{F}_{11}\text{NH}_3$ into ethyl acetate, but range from 60-70% before any recrystallization. The chemical shifts of $\text{KB}_{12}\text{F}_{11}\text{NH}_3$ in CD_3CN are; $^{11}\text{B}[^{19}\text{F}]$ signals $\delta -14.7(1)$, $\delta -17.1(10)$, $\delta -34.1(1)$, $^{19}\text{F}[^{11}\text{B}]$ signals $\delta -263.2(1)$, $\delta -264.3(5)$, $\delta -270.8(5)$ relative to $\text{K}_2\text{B}_{12}\text{F}_{12}$ $\delta -269.5(12)$, and $^1\text{H}(\text{NH}_3)$ $\delta 5.72$ (broad).

4.5.5 Synthesis of $\text{KB}_{12}\text{F}_{11}\text{NH}_3$ with ca. 2.0% HF in anhydrous MeCN.

Reactions involving anhydrous HF were prepared using the same procedure described above. Once the stoppered 250 mL flask with the Teflon® stir bar, $\text{KB}_{12}\text{H}_{11}\text{NH}_3$, 2.0g (10.2 mmol), and 150 mL anhydrous MeCN was removed from the glove box, it was attached to a stainless steel vacuum line with access to anhydrous HF. The entire $\text{KB}_{12}\text{H}_{11}\text{NH}_3/\text{MeCN}$ reaction mixture was cooled to $-196\text{ }^\circ\text{C}$ with liquid nitrogen, and put under vacuum to transfer the liquid anhydrous HF. Liquid anhydrous HF was slowly transferred under vacuum into a calibrated FEP tube and condensed in a NaCl water ice bath (ca. $-5\text{ }^\circ\text{C}$), once the correct amount of HF was condensed the, it was transferred to the $-196\text{ }^\circ\text{C}$ reaction mixture and slowly (ca. 1 h) warmed to ca. $-35\text{ }^\circ\text{C}$ to melt the MeCN allowing the HF to mix into the reaction. After the reaction was completely liquid at $-35\text{ }^\circ\text{C}$, the solution was warmed to $0\text{ }^\circ\text{C}$ and the fluorination was promptly started, following similar procedure described above.

4.5.6 Separation of 1,2-, 1,7-, and 1,12- $(\text{NH}_3)_2\text{B}_{12}\text{X}_{10}$ (X = H, F).

Column chromatography on a silica gel stationary phase was used to separate the three isomers, monitored by thin layer chromatography (TLC) using a potassium permanganate/ethanol stain. Gradient elution was used starting with 4:1 ethyl acetate:hexanes to

elute the 1,12 isomer. Subsequently the eluent was switched to a 2:1 ethyl acetate:hexanes mixture, allowing the 1,7 isomer to elute. Any residual $\text{KB}_{12}\text{H}_{11}\text{NH}_3$ in the mixture was removed by switching the eluent to 100% ethyl acetate, and lastly methanol was used to collect the 1,2 isomer. The compounds were dried using a rotary evaporator followed by overnight vacuum treatment.

4.5.7 Synthesis of 1,2-, 1,7-, and 1,12- $(\text{NH}_3)_2\text{B}_{12}\text{F}_{10}$.

The fluorination of a mixture of 1,2-, 1,7-, and 1,12- $(\text{NH}_3)_2\text{B}_{12}\text{F}_{10}$ was performed following the same method as described for fluorination of $\text{KB}_{12}\text{H}_{11}\text{NH}_3$ described in Section 4.5.4, with the major differences being the scale and the starting material. The starting material for this reaction was the mixture of $(\text{NH}_3)_2\text{B}_{12}\text{F}_{10}$ isomers isolated in the ethyl acetate layer from the amination description in Section 4.5.3. The scale of the reaction was 1 g of the mixture of $(\text{NH}_3)_2\text{B}_{12}\text{F}_{10}$ isomers with 50–75 mL anhydrous MeCN.

Figures 4.6

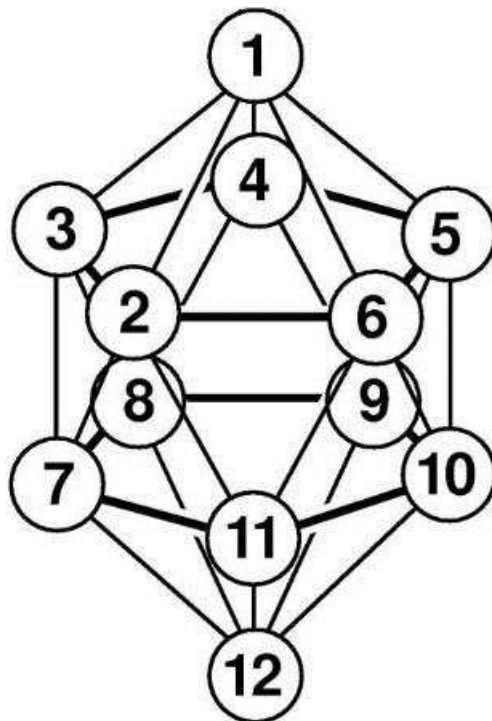


Figure 4-1. The IUPAC numbering scheme for icosahedral B₁₂ clusters.

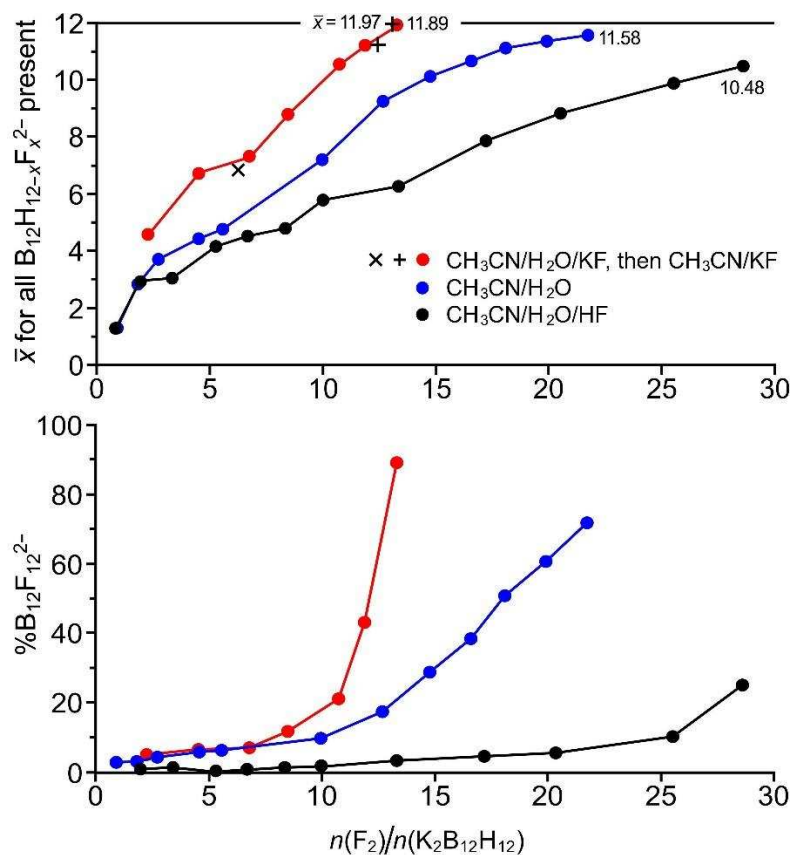


Figure 4-2. The average value of x for all $\text{B}_{12}\text{H}_{12-x}\text{F}_x^{2-}$ clusters present (top graph) and the $\%\text{B}_{12}\text{F}_{12}^{2-}$ present (bottom graph) vs. the number of equivalents of F_2 added per mole of $\text{K}_2\text{B}_{12}\text{F}_{12}$ during reactions of $\text{K}_2\text{B}_{12}\text{H}_{12}$ with 20/80 F_2/N_2 in MeCN (adapted from a figure in ref 5). The rate at which F_2/N_2 was bubbled through the reaction mixture was different for each of the experiments shown but was constant throughout each individual experiment. Therefore, the mole ratio $n(\text{F}_2)/n(\text{K}_2\text{B}_{12}\text{H}_{12})$ is directly proportional to time, but on a different scale for each reaction.

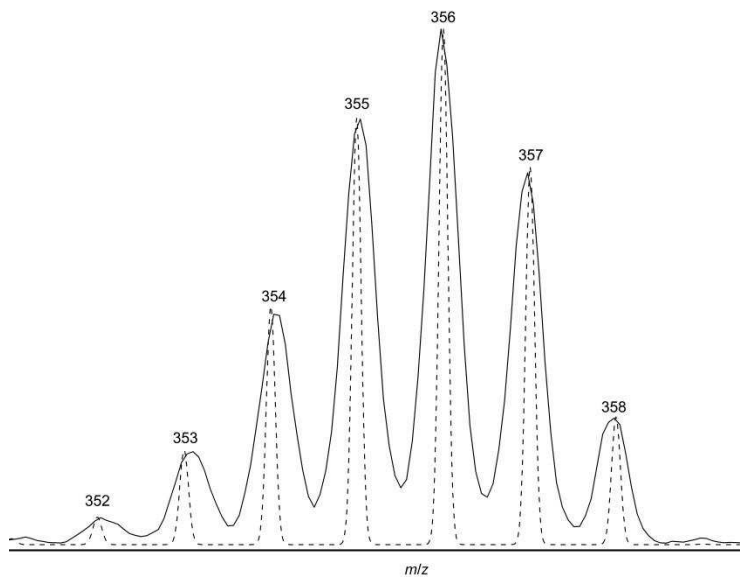


Figure 4-3. Experimental (solid line) NI-ESI-MS and calculated (dashed line) isotopologue patterns for mass spectra of $B_{12}F_{11}(NH_3)^-$. The peaks at m/z 355, 356, and 357 correspond to anions with $^{10}B_3^{11}B_9$, $^{10}B_2^{11}B_{10}$, and $^{10}B_1^{11}B_{11}$ polyhedral clusters, respectively, the calculated percent intensities of which are 23.4, 28.4, and 21.0%, respectively. The sum of the experimental intensities for these three peaks for different $B_{12}H_{11-n}F_n(NH_3)^-$ anions in a mixture of anions, when corrected for their (estimated) different sensitivity coefficients, were used to determine the relative abundances of the different anions in a mixture of $B_{12}H_{11-n}F_n(NH_3)^-$ anions.

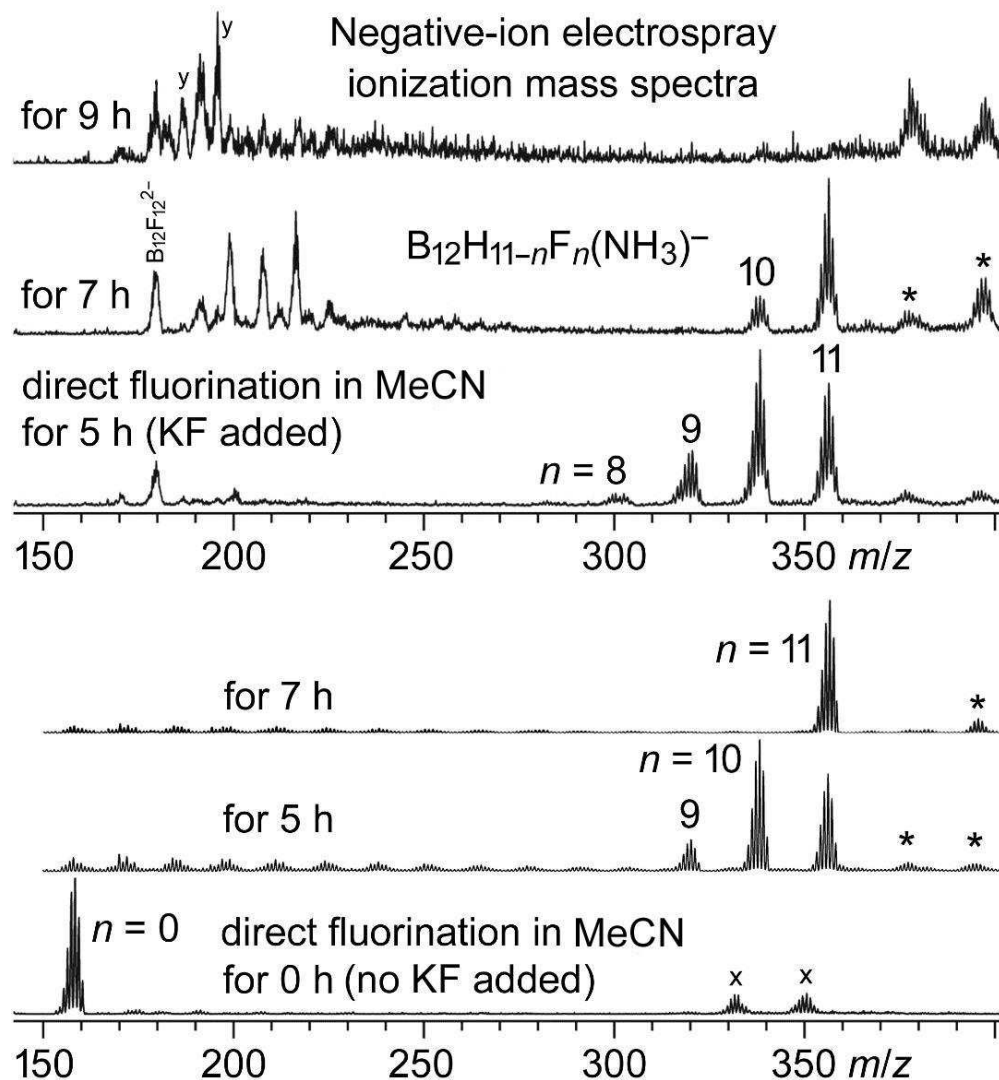


Figure 4-4. NI-ESI mass spectra of aliquots removed at the indicated times from 20/80 F_2/N_2 fluorination reactions of $KB_{12}H_{11}(NH_3)$ in 0 °C MeCN with and without a large excess of KF added to the reaction mixture. The isotop patterns indicated by asterisks at m/z 378 and 394 are due to $NaB_{12}H_{11}(NH_2)^-$ and $KB_{12}H_{11}(NH_2)^-$, respectively. The isotop patterns indicated by the letter x at m/z ca. 331 and 350 are due to adventitious impurities remaining in the mass spectrometer injection system from a different experiment by a different operator. They are not due to $B_{12}HF_{10}(NH_3)^-$ (m/z 338) and $B_{12}F_{11}(NH_3)^-$ (m/z 356). The isotop patterns indicated by the letter y are discussed in the text.

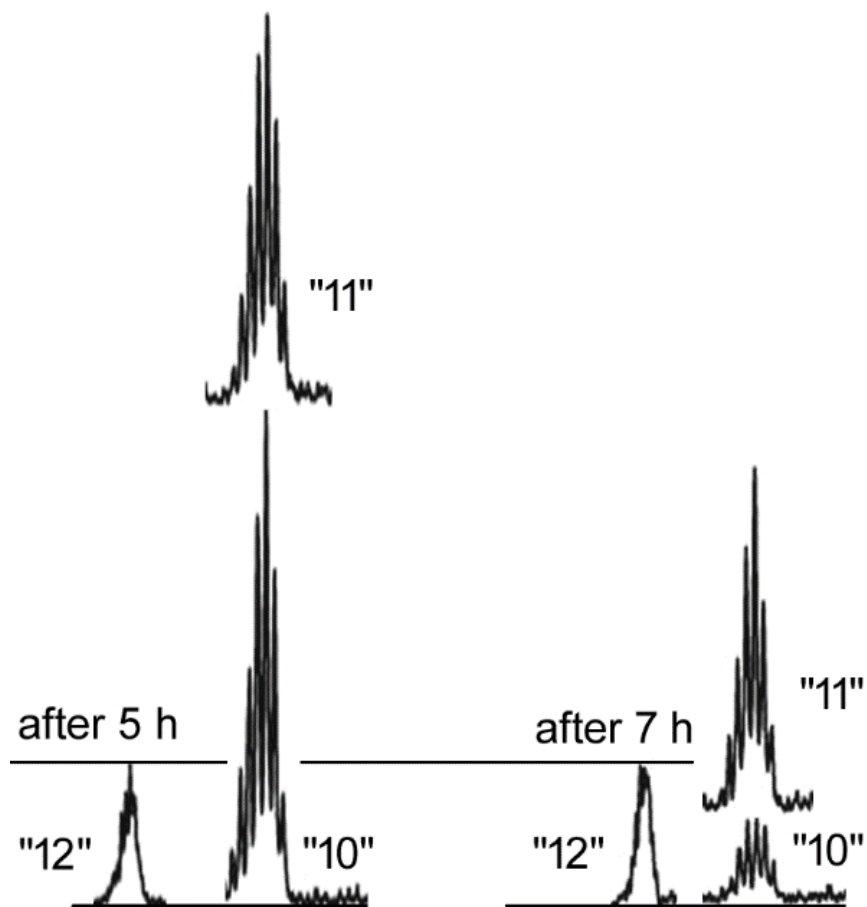


Figure 4-5. Comparison of the relative amounts of $B_{12}F_{12}^{2-}$ ("12"), $B_{12}HF_{10}(NH_3)^-$ ("10"), and $B_{12}F_{11}(NH_3)^-$ ("11") present after 5 and 7 h in the F_2 fluorination depicted in the top set of mass spectra in Figure 2. The total amount of $B_{12}HF_{10}(NH_3)^-$ and $B_{12}F_{11}(NH_3)^-$ present after 5 h is twice as much as the amount present after 7 h.

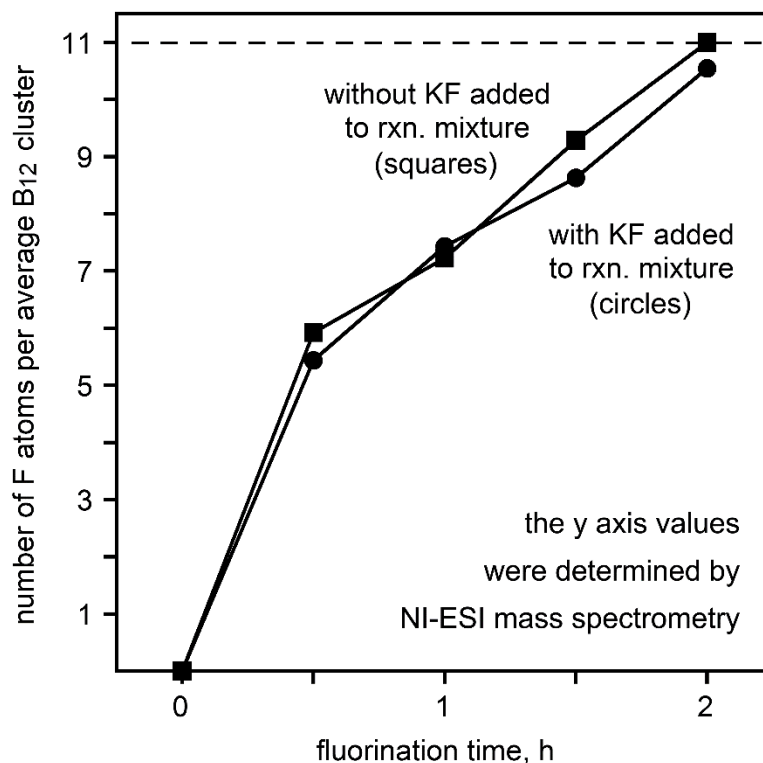


Figure 4-6. The number of F atoms per average $B_{12}H_{11-n}F_n(NH_3)^-$ anion (i.e., \bar{n}) present at various times during the F_2 fluorination of $KB_{12}H_{11}(NH_3)^-$ in $0^\circ C$ MeCN with and without excess KF added to the reaction mixture. These conditions are the same as those used for the 2.0 g scale fluorinations from which the mass spectra shown in Figure 4-4 were obtained, but the mass spectra used to determine the \bar{n} values in this graph were from fluorination reactions with only 0.6 g of $KB_{12}H_{11}(NH_3)^-$ starting material. That is why the reaction times for these fluorinations are ca. three times smaller than for the 2.0 g scale fluorinations (i.e., 2 h instead of ca. 7 h).

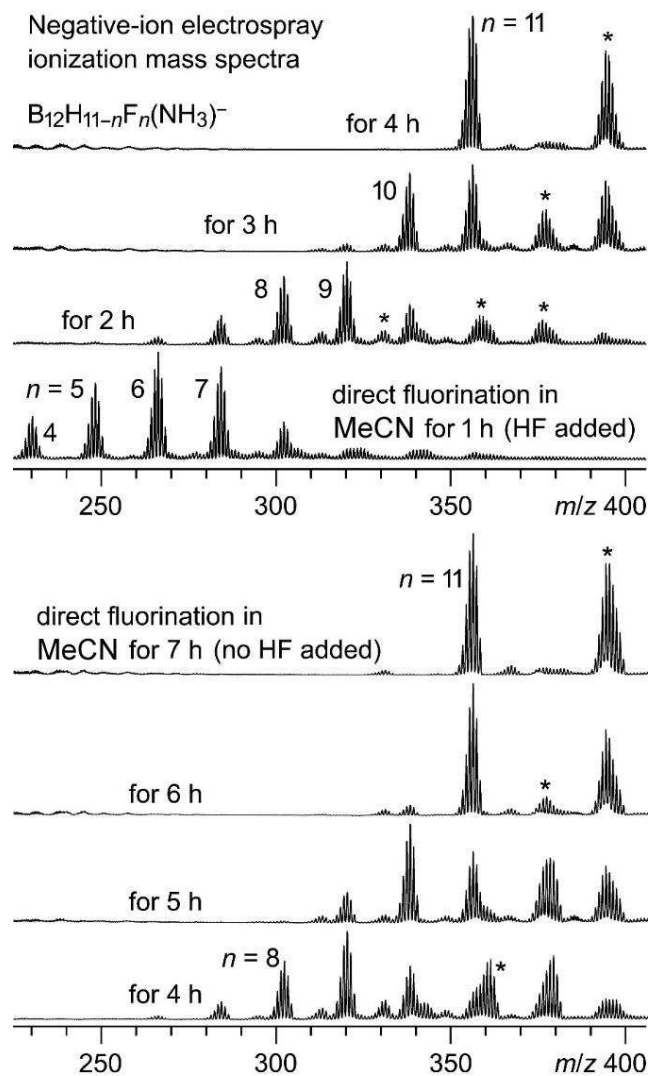


Figure 4-7. NI-ESI mass spectra of aliquots removed at the indicated times from 20/80 F_2/N_2 fluorination reactions of $KB_{12}H_{11}(NH_3)$ in 0 °C MeCN with and without 1.3% v/v aHF added to the reaction mixture. The isotop patterns indicated by asterisks at m/z 378 and 394 are due to $NaB_{12}H_{11}(NH_2)^-$ and $KB_{12}H_{11}(NH_2)^-$, respectively. Note that the "No HF added" spectra are from the same fluorination experiment as those used to collect the "No KF added" spectra shown in Figure 4-4. For the spectra shown here, the samples injected into the mass spectrometer were ca. 10 times more concentrated. Comparison of the two sets of spectra demonstrates that the relative intensities of the $B_{12}F_{11}(NH_3)_2^-$ and $K B_{12}F_{11}(NH_3)_2^-$ isotop patterns at m/z 356 and 394, respectively, are concentration dependent.

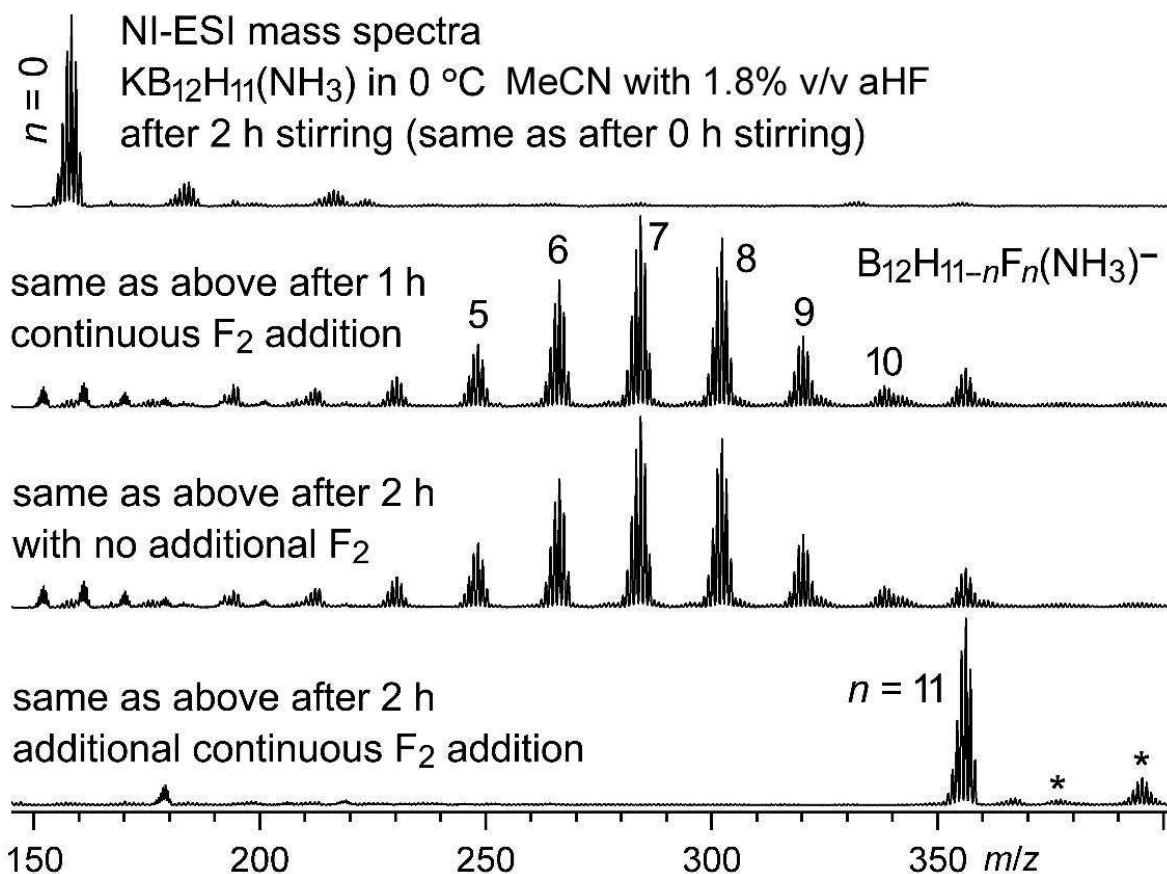


Figure 4-8. NI-ESI mass spectra of samples of withdrawn from an experiment to determine if HF in cold MeCN can fluorinate $B_{12}H_{11-n}F_n(NH_3)^-$ species with $n = 0$ and with $n = 5-10$. After 2 h stirring in 1.8% v/v HF/MeCN, 0 °C, the $\text{KB}_{12}\text{H}_{11}\text{NH}_3$ remained unchanged. The solution was treated with 20/80 $\text{F}_2/\text{N}_2(\text{g})$ for 1 h. The partially fluorinated mixture of $B_{12}H_{11-n}F_n(NH_3)^-$ anion species was left in the HF MeCN solution for 2 h, again remaining unchanged. Finally, the mixture was treated with 20/80 $\text{F}_2/\text{N}_2(\text{g})$ for 2 h longer making the only $B_{12}F_{11}NH_3^-$ by NI-ESI.

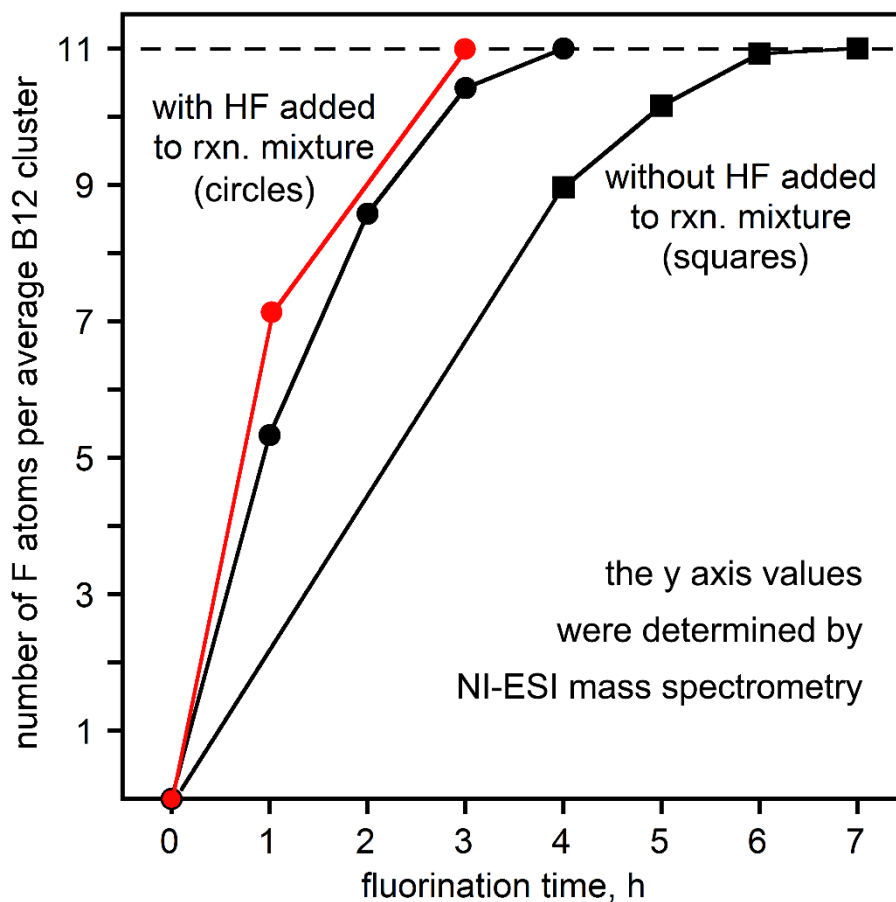


Figure 4-9. The number of F atoms per average $B_{12}H_{11-n}F_n(NH_3)^-$ anion (i.e., \bar{n}) present at various times during the F_2 fluorination of $KB_{12}H_{11}(NH_3)^-$ in 0 °C MeCN with and without 2.0% v/v HF added to the reaction mixture. These results were obtained from the mass spectra shown in Figures 4-7 and 4-8. The concentration of HF was ca. 10% higher at the beginning of the experiment depicted with red data points (i.e., ca. 2.2% added HF instead of 2.0% added HF).

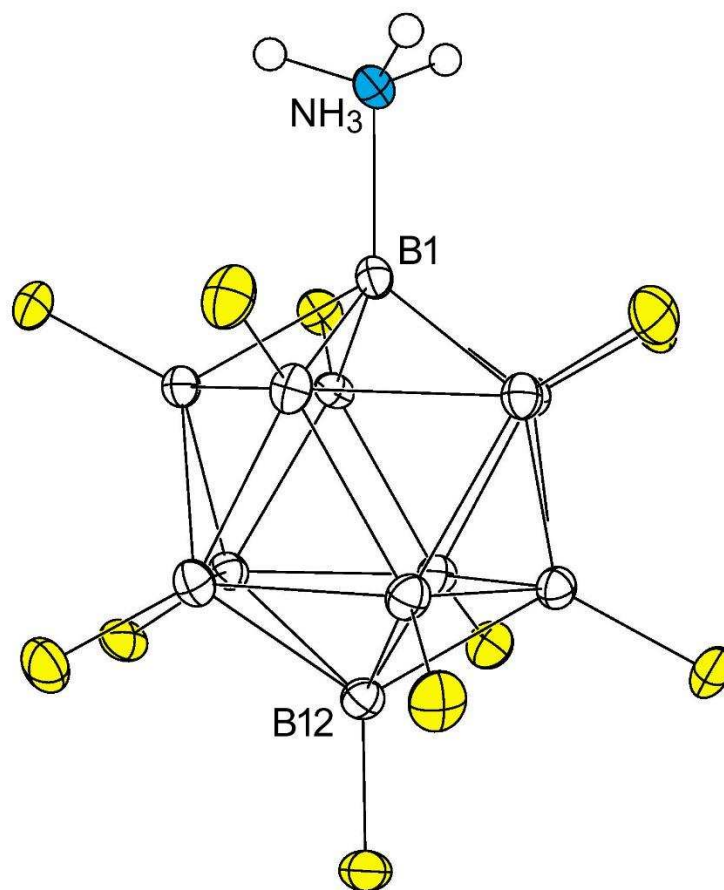


Figure 4-10. Thermal ellipsoid plot of the ammonioborane anion in the X-ray structure of $\text{Na}(\text{H}_2\text{O})_4\text{B}_{12}\text{F}_{11}(\text{NH}_3)$ (50% probability ellipsoids except for H atoms, which are shown as spheres of arbitrary size; F atoms highlighted in yellow).

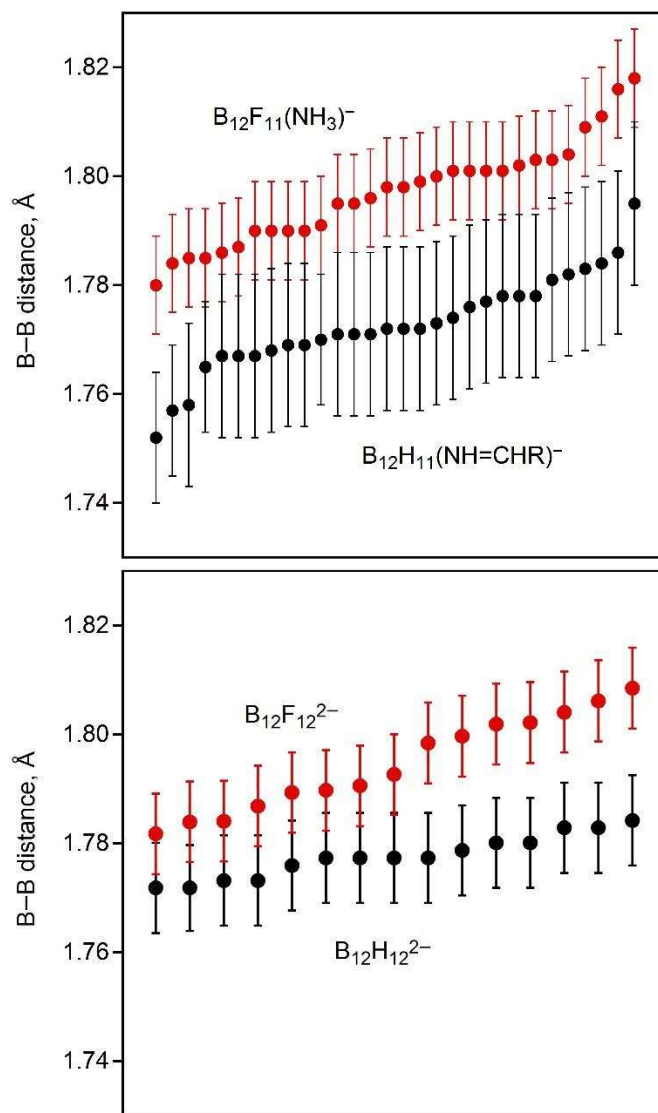


Figure 4-11. Plots of the B–B distances in the X-ray structures of $Na(H_2O)_4B_{12}F_{11}(NH_3)$ (this work), $B_{12}H_{11}(NH=CH(p-C_6H_4OMe))$,¹⁴ $(4-NH_2-1-Me-1,2,4-triazolium)_2B_{12}F_{12}$,³¹ and $(1-Et-3-Me-imidazolium)_2B_{12}H_{12}^{2-}$ ³² (the error bars shown are $\pm 3\sigma$).

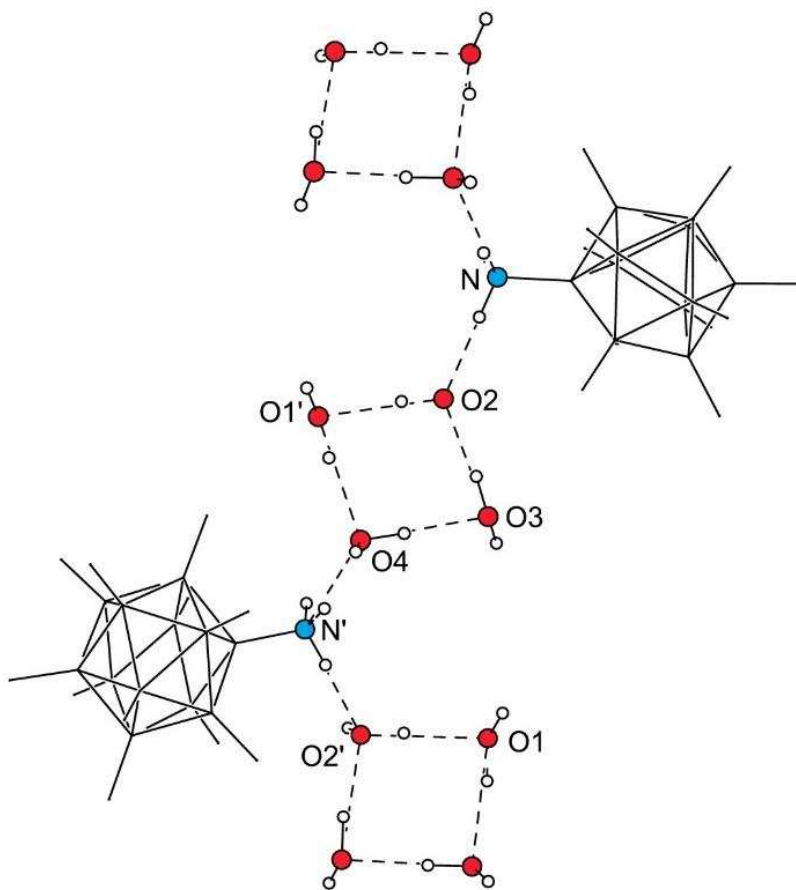


Figure 4-12. The one-dimensional hydrogen bonding network in the X-ray structure of $\text{Na}(\text{H}_2\text{O})_4\text{B}_{12}\text{F}_{11}(\text{NH}_3)$ showing the hydrogen bonding between the NH_3 group and the four H_2O molecules (the B and F atoms are represented as dimensionless points for clarity). The four H_2O molecules form a nearly square-planer tetrameric ring with an average $\text{O}-\text{H}\cdots\text{O}$ distance of 2.76 Å, interior $\text{O}\cdots\text{N}\cdots\text{O}$ angles of 84.3, 84.4, 94.6, and 96.3°, and an average deviation of the four O atoms from their least-squares plane of 0.016 Å. The $\text{N}-\text{H}\cdots\text{O}$ distances average 2.87 Å; the $\text{O2}\cdots\text{N}\cdots\text{O4}$ angle is 128.2°.

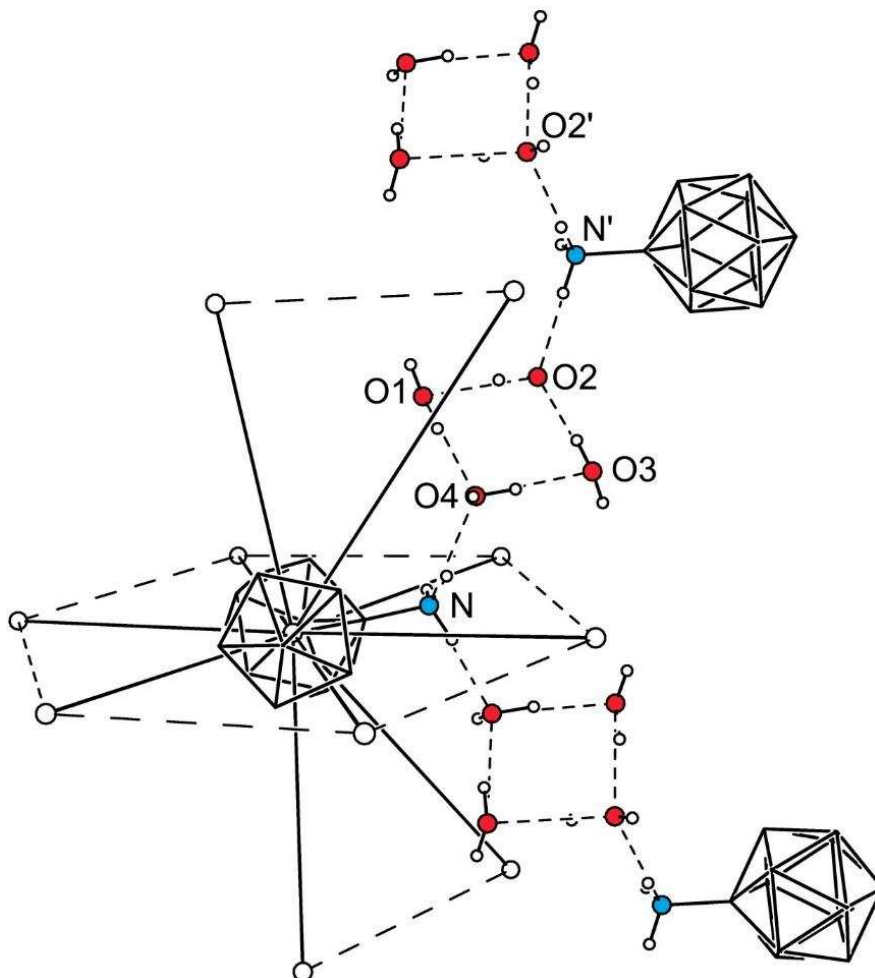


Figure 4-13. The location of the $B_{12}F_{11}NH_3^-$ anion relative to its nearest neighbor anions in the X-ray structure of $NaB_{12}F_{11}NH_3 \cdot 4H_2O$ (the B_{12} centroids (\odot) shown as spheres of arbitrary size, the B_{12} cages are shown as line drawings, and the F atoms have been removed for clarity). The $\odot \cdots \odot$ distances range from 7.331 to 9.745 Å and average 8.279 Å. The one dimensional hydrogen-bonded H_2O tetramers are hydrogen bonded to the $B_{12}F_{11}NH_3^-$ anions through planar, pseudo-hexagonal arrays planes of B_{12} cages.

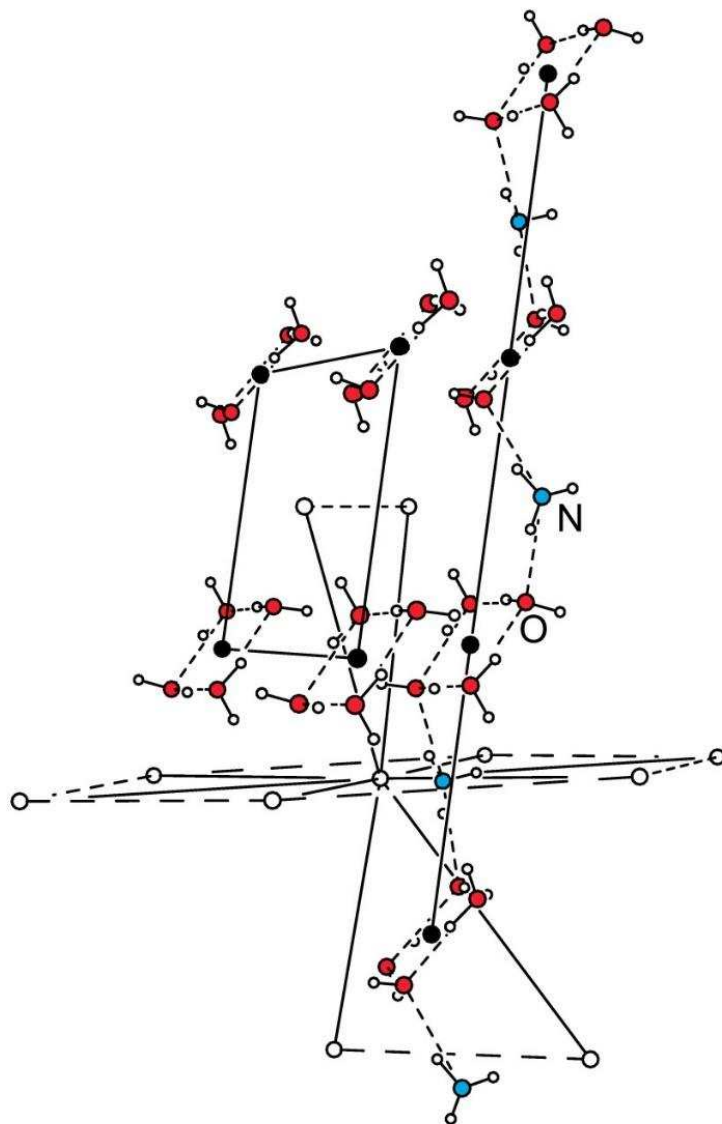


Figure 4-14. The location of the $B_{12}F_{11}NH_3^-$ anions relative to their nearest neighbor anions in the X-ray structure of $Na(H_2O)_4B_{12}F_{11}(NH_3)$ (the B_{12} centroids are shown as white spheres of arbitrary size and the H_2O tetramer centroids are shown as black spheres of arbitrary size). The one dimensional hydrogen-bonded H_2O tetramers are hydrogen bonded to the $B_{12}F_{11}NH_3^-$ anions through planar, pseudo-hexagonal arrays planes of B_{12} cages. Columns of the H_2O tetramer centroids have a perpendicular distance of 4.865 \AA from the next column. The columns are 11.324 \AA apart within a layer and make an angle of 79.3° with the plane of B_{12} centroids. The H_2O tetramer is tilted 33° from the plane formed by the centroids of the H_2O tetramers.

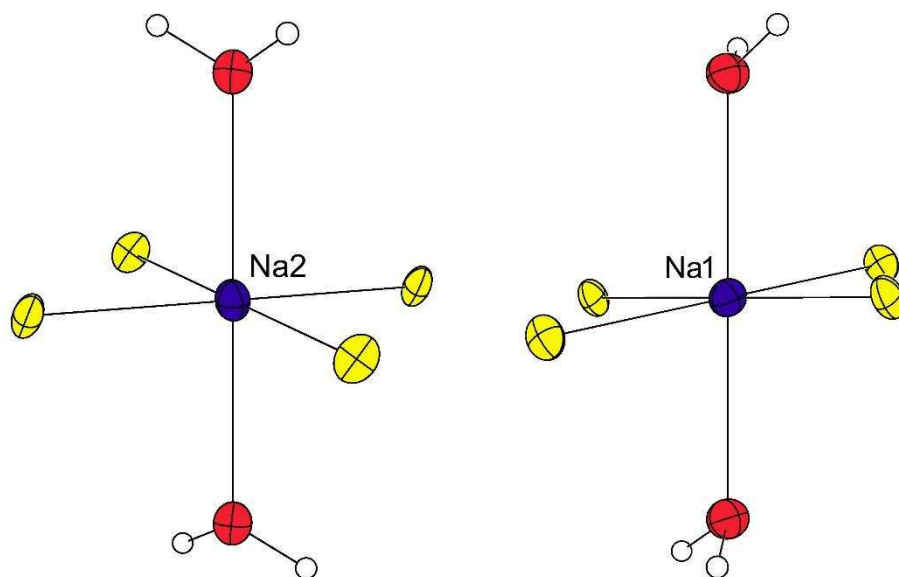


Figure 4-15. Drawing of the NaF_4O_2 coordination spheres in the X-ray structure of $\text{Na}(\text{H}_2\text{O})_4\text{B}_{12}\text{F}_{11}(\text{NH}_3)$ (50% probability ellipsoids; F atoms highlighted in yellow; O atoms highlighted in red). The Na^+ ions sit on centers of inversion. The sets of Na1–F and Na2–F distances are 2.294(1)/2.456(1) and 2.281(1)/2.386(1) Å, respectively. The two unique Na1–O and Na2–O distances are 2.338(1) and 2.331(1) Å, respectively. The two unique Na1–O and Na2–O distances are 2.338(1) and 2.331(1) Å, respectively. The $\text{O}\cdots\text{O}$ vector in the Na1 and Na2 coordination units subtend angles of 7.2 and 8.0°, respectively, from the respective F_4 least-squares planes. The sum of bond valences for Na1 and Na2 are 1.09 and 1.16, respectively.

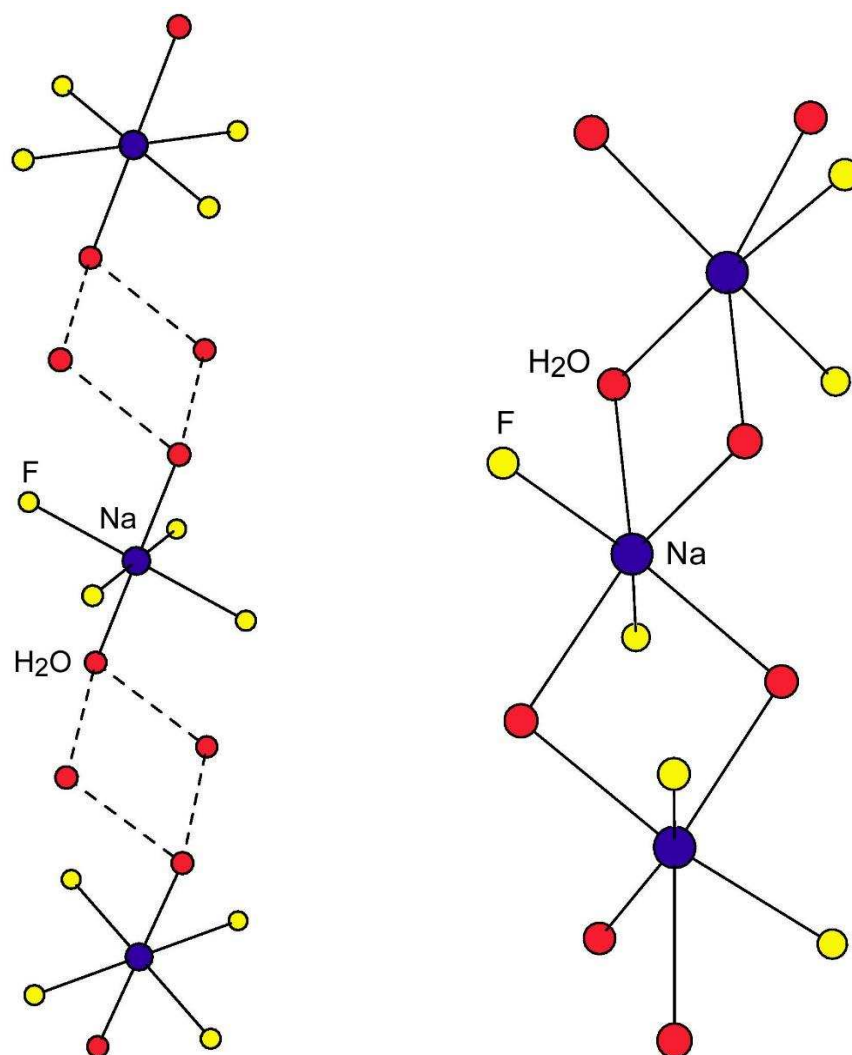


Figure 4-16. Comparison of the infinite chains of NaF_4O_2 and NaF_2O_4 moieties in the X-ray structures of $\text{Na}(\text{H}_2\text{O})_4\text{B}_{12}\text{F}_{11}(\text{NH}_3)$ (left, this work) and $\text{Na}_2(\text{H}_2\text{O})_4\text{B}_{12}\text{F}_{12}$ (right, ref XX), respectively (the H_2O molecule H atoms have been omitted for clarity; F and O atoms and Na^+ cations are highlighted in yellow, red, and purple, respectively). The H_2O molecules in $\text{Na}(\text{H}_2\text{O})_4\text{B}_{12}\text{F}_{11}(\text{NH}_3)$ form hydrogen-bonded tetramers; individual H_2O molecules do not bridge the Na^+ cations. The H_2O molecules in $\text{Na}_2(\text{H}_2\text{O})_4\text{B}_{12}\text{F}_{12}$ bridge the Na^+ cations and are not hydrogen-bonded to one another.

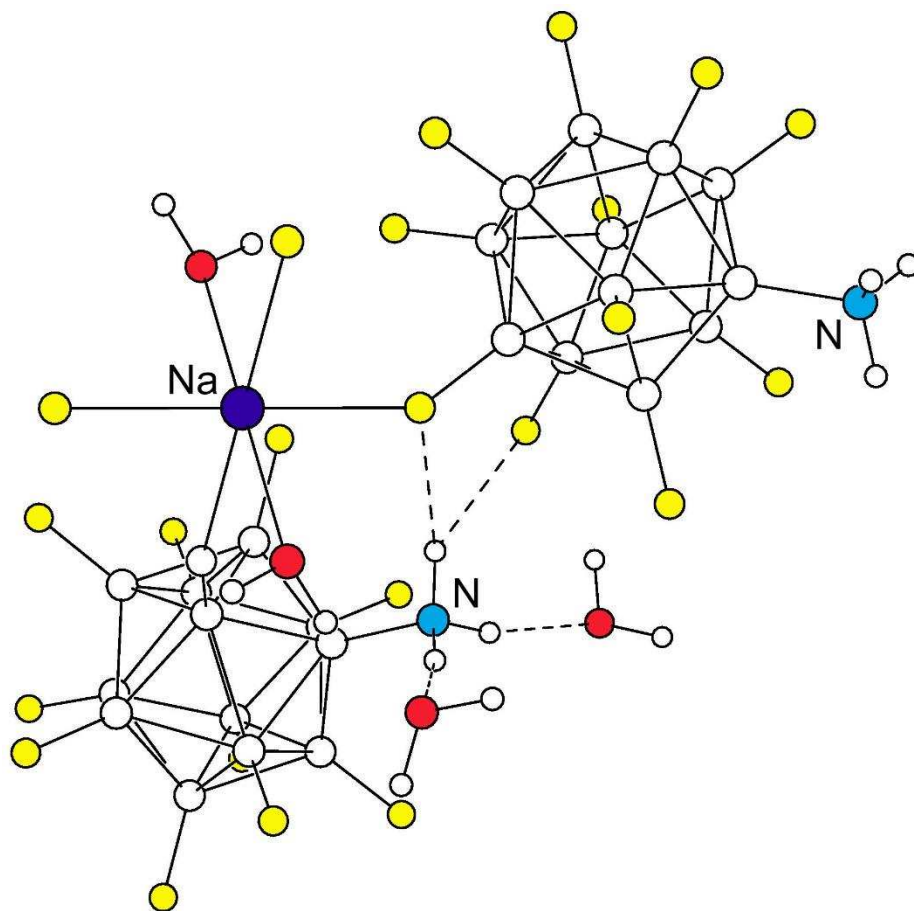


Figure 4-17. Drawing of the X-ray structure of $\text{Na}(\text{H}_2\text{O})_4\text{B}_{12}\text{F}_{11}(\text{NH}_3)$ emphasizing the hydrogen bonding between the $-\text{NH}_3$ H atoms and two H_2O molecules and two F atoms from a neighboring $\text{B}_{12}\text{F}_{11}\text{NH}_3^-$ anion (F, O, N, and Na atoms highlighted in yellow, red, light blue, and purple). The $\text{NH}\cdots\text{OH}_2$ distances are 1.96 and 1.99 Å. The bifurcated $\text{NH}\cdots\text{FB}$ distances are 2.29 and 2.40 Å.

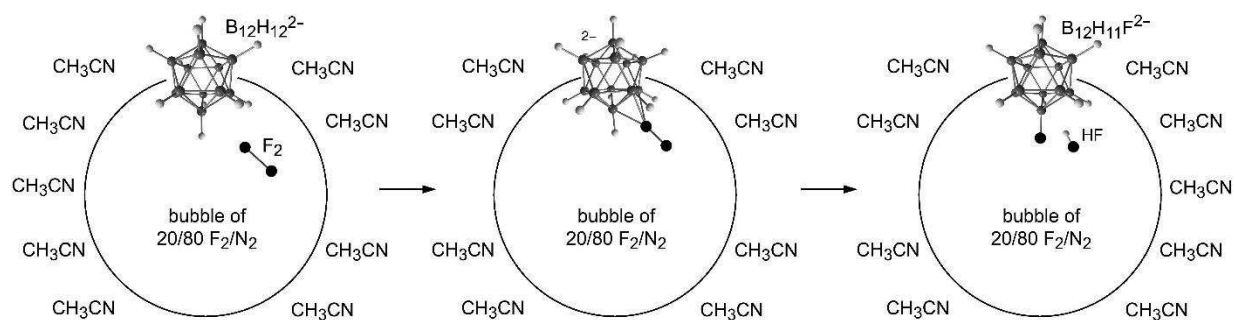


Figure 4-18. Proposed reaction scheme for the fluorination of $B_{12}H_{12}^{2-}$ on the surface of a bubble of F_2/N_2 gas in acetonitrile. The size of the bubble is not to scale. The fraction of the anion that extends into the bubble is arbitrary. Reproduced from ref 5.

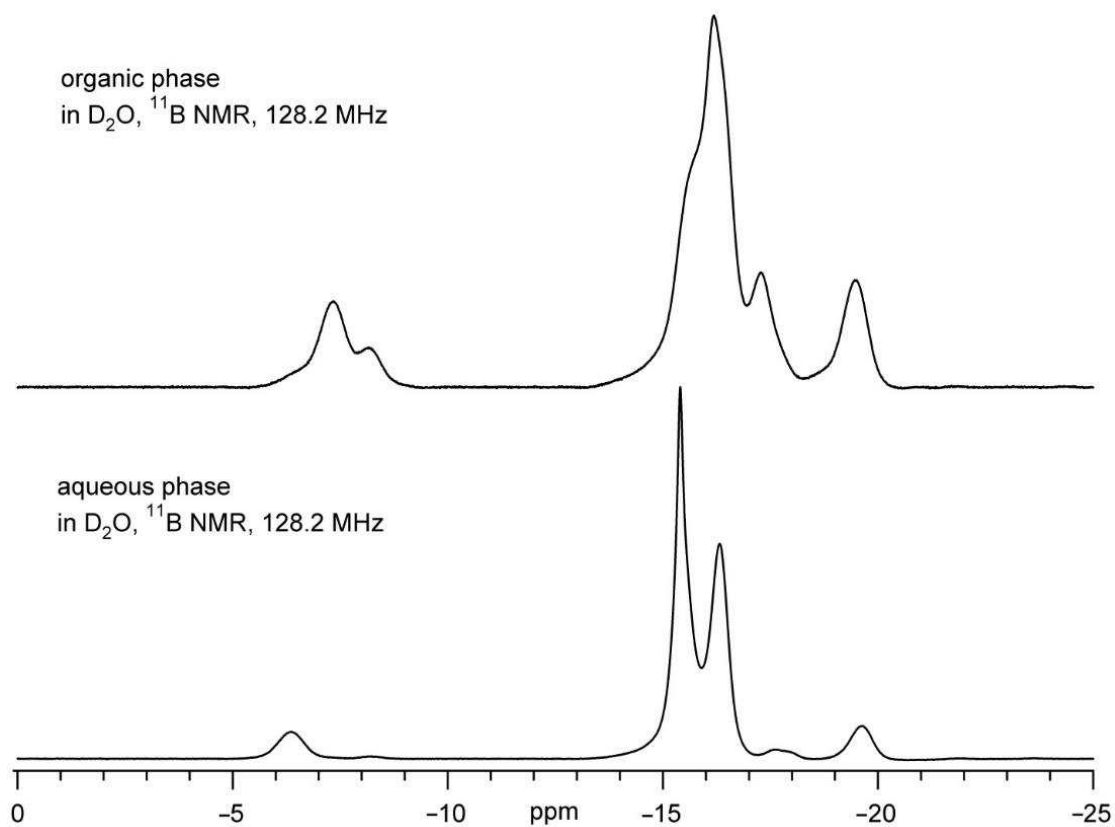


Figure 4-19. (Top) The ^{11}B NMR spectra of compounds 1,7- and 1,12- $(\text{NH}_3)_2\text{B}_{12}\text{H}_{10}$ soluble in the organic phase. (Bottom) The ^{11}B NMR spectra of compounds $\text{KB}_{12}\text{H}_{11}\text{NH}_3$, 1,2- $(\text{NH}_3)_2\text{B}_{12}\text{H}_{10}$, and $\text{K}_2\text{B}_{12}\text{H}_{12}$, soluble in the aqueous phase.

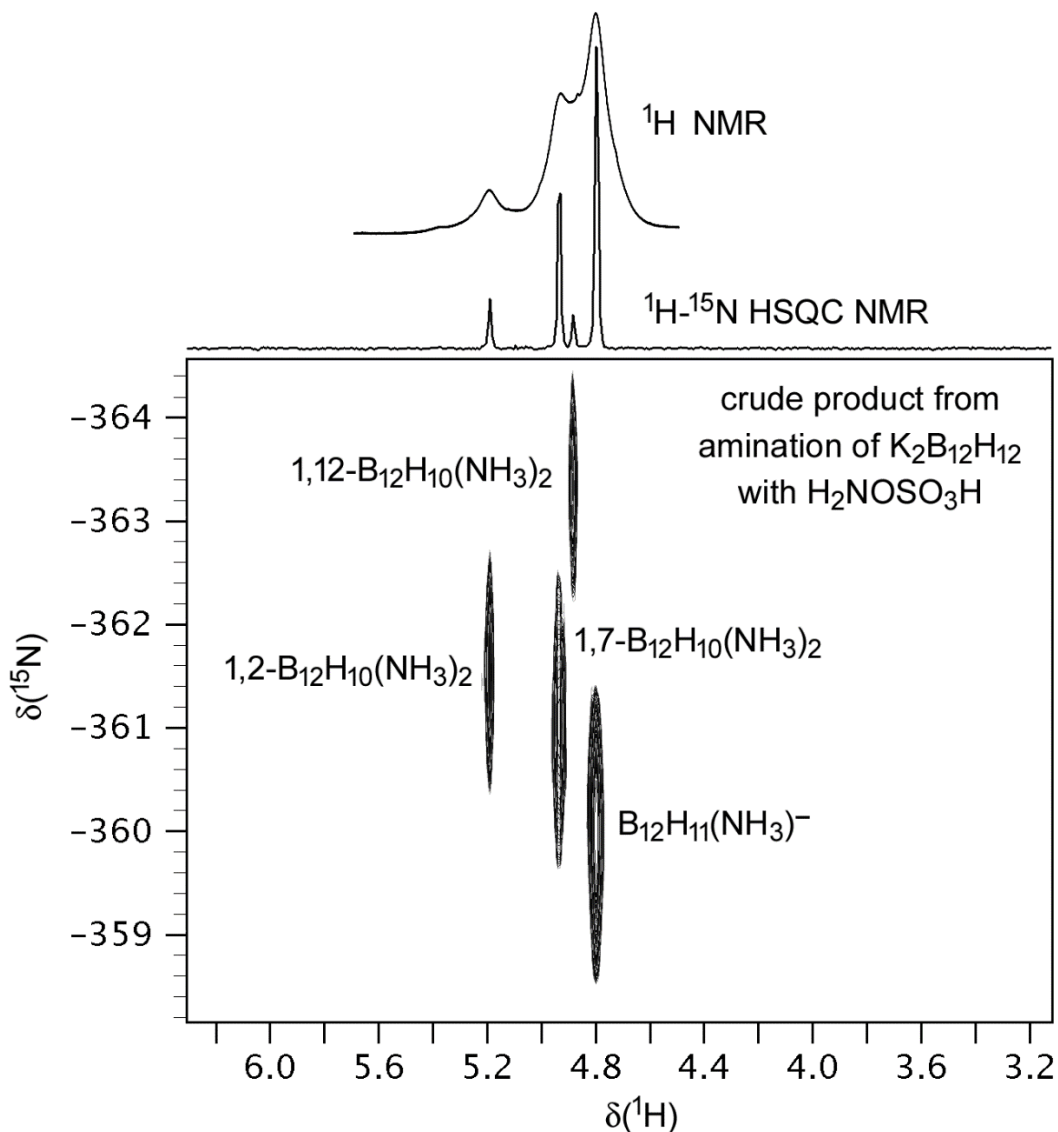


Figure 4-20. The NH region of the ^1H - ^{15}N heteronuclear single quantum correlation (HSQC) NMR spectrum of a CD_3CN solution of the crude product from a reaction of $\text{H}_2\text{NOSO}_3\text{H}$ and $\text{K}_2\text{B}_{12}\text{H}_{12}$ in aqueous base. The HSQC spectrum only shows resonances for H atoms bonded to ^{15}N (0.4% natural abundance). For comparison, the normal ^1H NMR spectrum of the mixture, showing the broad resonances for H atoms bonded to quadrupolar ^{14}N (99.6% natural abundance, $I = 1$), is superimposed on the HSQC spectrum at the top. The relative mole ratios of 1,2-, 1,7-, and 1,12- $\text{B}_{12}\text{H}_{10}(\text{CH}_3)_2$ in the product mixture, 0.23:1.00:0.14, respectively, were determined from the integrated intensities of the resonances in the HSQC spectrum.

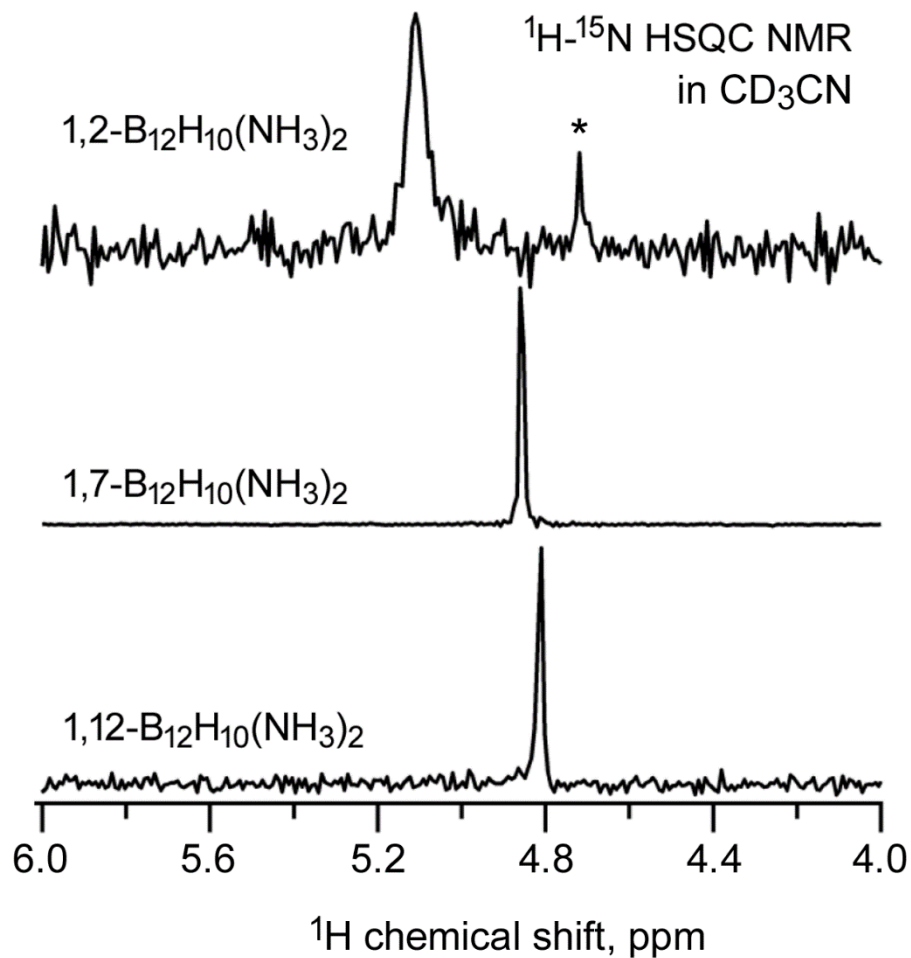


Figure 4-21. The NH region of the ^1H - ^{15}N heteronuclear single quantum correlation (HSQC) NMR spectra of purified samples of 1,2-, 1,7-, and 1,12- $\text{B}_{12}\text{H}_{10}(\text{CH}_3)_2$. The resonance marked with an asterisk in the spectrum of 1,12- $\text{B}_{12}\text{H}_{10}(\text{CH}_3)_2$ is due to the $\text{B}_{12}\text{H}_{11}(\text{NH}_3)$ anion.

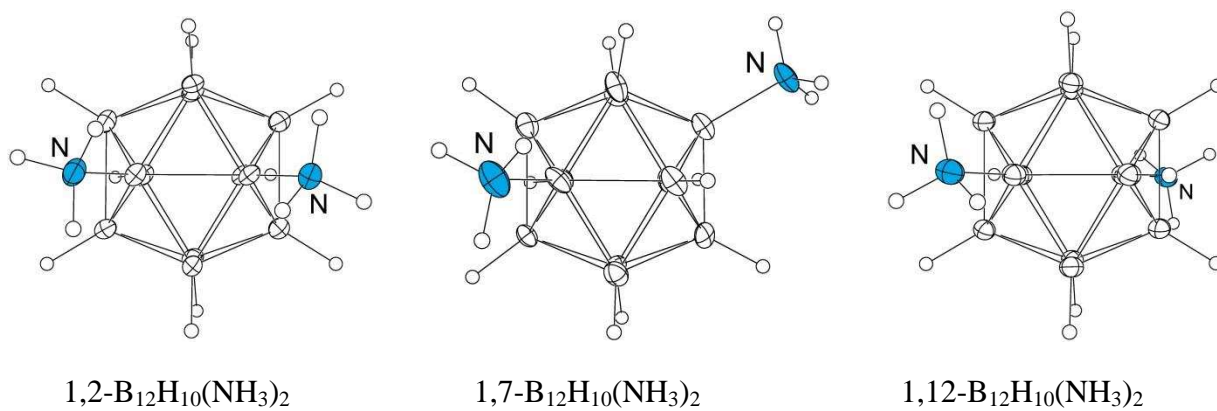


Figure 4-22. Thermal ellipsoid plots (50% probability) of the three isomers of $B_{12}H_{10}(NH_3)_2$ borate cage compounds. Single crystal X-ray structures of the three protic and 1,7- and 1,12- $B_{12}F_{10}(NH_3)_2$ compounds have been collected. In all cases there was no disorder in the B_{12} cage, however, disordered incorporated solvent or acetamide reduced the quality statistics of these crystal structures.

Tables 4.7

Table 4-1. Crystallographic data collection and refinement parameters for NaB₁₂F₁₁NH₃·4H₂O

| | |
|--|---|
| empirical formula | B ₁₂ H ₁₁ F ₁₁ NNaO ₄ |
| formula weight (g mol ⁻¹) | 450.81 |
| habit, color | plate, colorless |
| crystal system, space group | monoclinic, <i>P2₁/c</i> |
| crystal size (mm) | 0.112 × 0.290 × 0.356 |
| <i>a</i> (Å) | 9.7451(8) |
| <i>b</i> (Å) | 11.324(1) |
| <i>c</i> (Å) | 14.587(1) |
| <i>α</i> (deg) | 90 |
| <i>β</i> (deg) | 100.652(5) |
| <i>γ</i> (deg) | 90 |
| <i>V</i> (Å ³) | 1582.0(2) |
| <i>Z</i> | 4 |
| <i>T</i> (K) | 120(2) |
| ρ_{calc} (g cm ⁻³) | 1.893 |
| $R(F)$ ($I > 2\sigma(I)$) ^a | 0.0283 |
| $wR(F^2)$ [all data] ^a | 0.0815 |
| GOF | 1.059 |

^a $R(F) = \Sigma||F_o| - |F_c|| / \Sigma|F_o|$; $wR(F^2) = (\Sigma[w(F_o^2 - F_c^2)^2] / \Sigma[w(F_o^2)^2])^{1/2}$

Table 4-2. Selected interatomic distances (Å) and angles (deg) for NaB₁₂F₁₁NH₃·4H₂O^a

| | |
|----------------------------------|--------------------------|
| B ₁ -N | 1.524(2) |
| B ₁ -B _{ub} | 1.780(3)-1.796(3) |
| B _{ub} -B _{ub} | 1.799(3)-1.818(3) |
| B _{ub} -B _{lb} | 1.785(3)-1.801(3) |
| B _{lb} -B _{lb} | 1.790(3)-1.804(3) |
| B _{lb} -B12 | 1.785(3)-1.801(3) |
| B _{ub} -F _{ub} | 1.376(2)-1.384(2) |
| B _{lb} -F _{lb} | 1.380(2)-1.395(2) |
| B12-F12 | 1.388(2) |
| N-H | 0.894(17)-0.928(17) |
| (N)H···F; N-H···F | 2.29, 2.40; 123.4, 149.1 |
| (N)H···O; N-H···O | 1.96; 1.99; 163.6; 165.6 |

^a Abbreviations: ub = upper belt (B2-B6 or F2-F6); lb = lower belt (B7-B11 or F7-F11).

Table 4-3. NMR chemical shifts and coupling constants (Hz) for 1,2-, 1,7-, and 1,12-B₁₂H₁₀(NH₃)₂ and for B₁₂F₁₀(NH₃)₂^a

| parameter | 1,2-BH ^b | 1,7-BH ^b | 1,12-BH ^b | 1,2-BF ^c | 1,7-BF ^c | 1,12-BF ^c |
|--|---------------------|---------------------|----------------------|---|----------------------|----------------------|
| δ ¹¹ B | -8.3, ca. -16, | -7.4, -15.8, | -8.3, | -13.8 ^d | -14.0(2) | -16.3(10) |
| | ca. -16, -17.9, | 16.5, -17.4, | -16.2 | -15.1 ^d , -16.1 ^d | -16.2(6) | -30.4(2) |
| | -19.5 | -19.6 | — | -33.1(2) | -32.8(2) | |
| $J(^{11}\text{B}^1\text{H})$ | n.a., ca. 130, | n.a., n.o., | n.a., 126 | — | — | — |
| | ca. 130, n.o., | n.o., n.o., | — | — | — | — |
| | 137 | 135 | — | — | — | — |
| δ ¹ H(B) | 1.05, 1.11, | 1.12, 1.21, | 1.39 | — | — | — |
| | 1.41, 1.53 | 1.37, 1.60 | — | — | — | — |
| δ ¹⁹ F | — | — | — | -256.1(2) | -258.4(2) | -263.5(10) |
| | — | — | — | -257.8,(2) -263.2(4) | -262.0(2), -263.8(4) | — |
| | — | — | — | -269.0(2) | -269.7(2) | — |
| $J(^{11}\text{B}^{19}\text{F})^{\text{d}}$ | — | — | — | — | — | — |
| δ ¹⁵ N | -361.6 | -360.0 | -361.0 | — | — | — |
| δ ¹ H(N) | 5.11 | 4.87 | 4.81 | 6.4 | 5.8 | 5.9 |

^a Abbreviations: BH = B₁₂H₁₀(NH₃)₂; BF = B₁₂F₁₀(NH₃)₂; n.o. = not observable, n.a. = not applicable (for B atoms bonded to the NH₃ groups). The order of δ ¹¹B and $J(^{11}\text{B}^1\text{H})$ and of δ ¹⁹F and $J(^{19}\text{F}^{11}\text{B})$ values in consecutive lines are listed in the same order. For comparison, the δ ¹¹B, δ ¹H, and $J(^{11}\text{B}^1\text{H})$ values for K₂B₁₂H₁₂ in D₂O are -15.6, 1.2, and 124 Hz, respectively.

^b Spectra taken in D₂O

^c These peaks are not well resolved but integrate to 10 boron atoms relative to 2 boron atoms at δ -33.1

^d Due to the quadrupolar effects of ¹⁰B and ¹¹B, NMR experimental methods have yet to resolve the $J(^{11}\text{B}^{19}\text{F})$ coupling in these compounds.

Table 4-4. Crystallographic data collection and refinement parameters for 1,2-, 1,7-, and 1,12-B₁₂H₁₀(NH₃)₂ and for 1,7- and 1,12-B₁₂F₁₀(NH₃)₂^a

| | 1,2-BH·4CH ₃ CO ₂ C ₂ H ₅ ^c | 1,7-BH·H ₂ O | 1,12-BH·2MeCN | 1,7-BF·4CH ₃ CONH ₂ | 1,12-BF·6CH ₃ CONH ₂ ^c |
|---|--|--|---|--|---|
| empirical formula | B ₁₂ H ₄₂ C ₁₆ N ₂ O ₈ | B ₁₂ H ₁₈ N ₂ O | B ₁₂ C ₄ H ₂₂ N ₄ | B ₁₂ C ₈ H ₂₆ F ₁₀ N ₆ O ₄ | B ₁₂ C ₁₂ H ₃₆ F ₁₀ N ₈ O ₆ |
| formula weight (g mol ⁻¹) | 520.25 | 191.88 | 255.98 | 590.07 | 708.18 |
| habit, color | plate, colorless | plate, colorless | plate, colorless | plate, colorless | plate, colorless |
| crystal system | monoclinic | orthorhombic | monoclinic | triclinic | triclinic |
| space group | <i>C2/c</i> | <i>Pna2₁</i> | <i>C2/c</i> | <i>P$\bar{1}$</i> | <i>P$\bar{1}$</i> |
| crystal size (mm) | 0.47 × 0.29 × 0.08 | 0.31 × 0.47 × 0.74 | 0.10 × 0.13 × 0.19 | 0.03 × 0.18 × 0.31 | dimensions not taken |
| <i>a</i> (Å) | 25.6542(15) | 22.850(5) | 15.6291(12) | 8.5238(4) | 9.0567(5) |
| <i>b</i> (Å) | 12.8429(6) | 10.2195(17) | 10.7931(8) | 9.5041(5) | 10.1952(6) |
| <i>c</i> (Å) | 23.9393(14) | 9.2643(14) | 9.3545(7) | 17.3394(9) | 10.3951(6) |
| <i>α</i> (deg) | 90 | 90 | 90 | 90.560(3) | 61.8970(10) |
| <i>β</i> (deg) | 111.994(4) | 90 | 92.507(4) | 96.742(3) | 73.8840(10) |
| <i>γ</i> (deg) | 90 | 90 | 90 | 110.061(3) | 85.3450(10) |
| <i>V</i> (Å ³) | 7313.4(7) | 2163.4(7) | 1576.5(2) | 1308.45(11) | 812.00(8) |
| <i>Z</i> | 12 | 4 | 4 | 2 | 1 |
| <i>T</i> (K) | 120(2) | 120(2) | 120(2) | 100(2) | 100(2) |
| <i>ρ</i> _{calc} (g cm ⁻³) | 1.194 | 1.135 | 1.079 | 1.498 | 1.457 |
| <i>R</i> (<i>F</i>) (<i>I</i> > 2σ(<i>I</i>)) ^b | 0.1064 | 0.0489 | 0.0387 | 0.0406 | 0.0520 |
| <i>wR</i> (<i>F</i> ²) [all data] ^b | 0.3128 | 0.1134 | 0.1091 | 0.0983 | 0.2029 |
| GOF | 1.387 | 1.012 | 1.034 | 1.017 | 3.949 |
| min., max. e ⁻ dens., (e Å ⁻³) | -0.80, 1.73 | -0.21, 0.21 | -0.18, 0.21 | -0.35, 0.30 | -0.59, 0.78 |

^a Abbreviations: BH = B₁₂H₁₀(NH₃)₂; BF = B₁₂F₁₀(NH₃)₂. ^b $R(F) = \sum ||F_o| - |F_c|| / \sum |F_o|$; $wR(F^2) = (\sum [w(F_o^2 - F_c^2)^2] / \sum [w(F_o^2)^2])^{1/2}$

^c Preliminary structure.

Chapter 4 Reference

- (1) Strauss, S. H. *Chem. Rev.* **1993**, *93*, 927.
- (2) Krossing, I.; Raabe, I. *Angew. Chem.* **2004**, 2066.
- (3) Ivanov, S. V.; Rockwell, J. J.; Polyakov, O. G.; Gaudinski, C. M.; Anderson, O. P.; Solntsev, K. A.; Strauss, S. H. *J. Am. Chem. Soc.* **1998**, *120*, 4224.
- (4) Ivanov, S. V.; Miller, S. M.; Anderson, O. P.; Solntsev, K. A.; Strauss, S. H. *J. Am. Chem. Soc.* **2003**, *125*, 4694.
- (5) Peryshkov, D. V.; Popov, A. A.; Strauss, S. H. *J. Am. Chem. Soc.* **2009**, *131*, 18393.
- (6) Ivanov, S. V.; Davis, J. A.; Miller, S. M.; Anderson, O. P.; Strauss, S. H. *Inorg. Chem.* **2003**, *42*, 4489.
- (7) *Chem. Eng. News*, March 31.
- (8) Lupinetti, A. J.; Strauss, S. H. *Chemtracts–Inorg. Chem.* **1998**, *11*, 565.
- (9) Ivanova, S. M.; Ivanov, S. V.; Miller, S. M.; Anderson, O. P.; Solntsev, K. A.; Strauss, S. H. *Inorg. Chem.* **1999**, *38*, 3756.
- (10) Lupinetti, A. J.; Havighurst, M. D.; Miller, S. M.; Anderson, O. P.; Strauss, S. H. *J. Am. Chem. Soc.* **1999**, *121*, 11920.
- (11) Ivanov, S. V.; Rappe, A. K.; Strauss, S. H. *manuscript in preparation* **2005**.
- (12) Sivaev, I. B.; Bregadze, V. I.; Sjöberg, S. *Collect. Czech. Chem. Commun.* **2002**, *67*, 679.
- (13) Hawthorne, M. F. *Pure Appl. Chem.* **1991**, 63.
- (14) Sivaev, I. B.; Bruskin, A. B.; Nesterov, V. V.; Antipin, M. Y.; Bregadze, V. I.; Sjöberg, S. *Inorg. Chem.* **1999**, *38*, 5887.
- (15) Genady, A. R. *Acta Chim. Slov.* **2012**, *59*, 89.
- (16) El-Zaria, M. E.; Genady, A. R.; Nakamura, H. *New J. Chem.* **2010**, *34*, 1612.
- (17) Bertrand, G. H. V.; Hamel, M.; Sguerra, F. *Chem. Eur. J.* **2014**, *20*, 15660.
- (18) Bernard, R.; Cornu, D.; Gruner, B.; Dozol, J. F.; Miele, P.; Bonnetot, B. *J. Organomet. Chem.* **2002**, *657*, 83.
- (19) Hertler, W. R.; Raasch, M. S. *J. Am. Chem. Soc.* **1964**, *86*, 3661.
- (20) Bolli, C.; Derendorf, J.; Jenne, C.; Scherer, H.; Sindlinger, C. P.; Wegener, B. *Chem. Eur. J.* **2014**, *20*, 13783.
- (21) Justus, E.; Voge, A.; Gabel, D. *Eur. J. Inorg. Chem.* **2008**, 5245.
- (22) Justus, E.; Rischka, M.; Wishart, J. F.; Werner, K.; Gabel, D. *Chem. Eur. J.* **2008**, *14*, 1918.
- (23) Bernard, R.; Cornu, D.; Baldeck, P. L.; Daslavsky, J.; Letoffe, J. M.; Scharff, J. P.; Miele, P. *Dalton Trans.* **2005**, 3065.
- (24) Bernard, R.; Cornu, D.; Scharff, J. P.; Chiriach, R.; Miele, P. *Inorg. Chem.* **2006**, *45*, 8743.
- (25) Muetterties, E. L.; Knoth, W. H. *Polyhedral Boranes*; M. Dekker: New York, 1969.
- (26) Gruner, B.; Bonnetot, B.; Mongeot, H. *Coll. Czech. Chem. Commun.* **1997**, *62*, 1185.
- (27) Dudenkov, I. V.; Zhizhin, K. Y.; Chernyavskii, A. S.; Katser, S. B.; Goeva, L. V.; Sergienko, V. S.; Solntsev, K. A.; Kuznetsov, N. T. *Russ. J. Inorg. Chem.* **2000**, *45*, 1864.
- (28) Knoth, W. H.; Miller, H. C.; England, D. C.; Parshall, G. W.; Muetterties, E. L. *J. Am. Chem. Soc.* **1962**, *84*, 1056.
- (29) Knoth, W. H.; Miller, H. C.; Sauer, J. C.; Balthis, J. H.; Chia, Y. T.; Muetterties, E. L. *Inorg. Chem.* **1964**, *3*, 159.

- (30) Solntsev, K. A.; Mebel, A. M.; Votnova, N. A.; Kuznetsov, N. T.; Charkin, O. P. *Koord. Khim.* **1992**, *18*, 340.
- (31) Belletire, J. C.; Schneider, S.; Shackelford, S. A.; Peryshkov, D. V.; Strauss, S. H. *J. Fluorine Chem.* **2011**, *132*, 925.
- (32) Shackelford, S. A.; Belletire, J. L.; Boatz, J. A.; Schneider, S.; Wheaton, A. K.; Wight, B. A.; Hudgens, L. M.; Ammon, H. L.; Strauss, S. H. *Org. Lett.* **2009**, *11*, 2623.
- (33) Brown, I. D.; Altermatt, D. *Acta Cryst.* **1985**, *B41*, 244.
- (34) Brown, I. D. *Chem. Rev.* **2009**, *109*, 6858.
- (35) Peryshkov, D. V.; Bukovsky, E. V.; Lozinšek, M.; Folsom, T. C.; Heyliger, D. L.; Strauss, S. H. *Manuscript in preparation*.
- (36) Wynn, D. A.; Roth, M. M.; Pollard, B. D. *Talanta* **1984**, *31*, 1036.
- (37) Chambers, R. D.; Skinner, C. J.; Hutchinson, J.; Thomson, J. *Journal of the Chemical Society, Perkin Transactions I* **1996**, 605.
- (38) Chambers, R. D.; Skinner, C. J.; Thomson, J.; Hutchinson, J. *Journal of the Chemical Society, Chemical Communications* **1995**, 17.
- (39) L. Coe, P.; M. Stuart, A.; J. Moody, D. *Journal of the Chemical Society, Perkin Transactions I* **1998**, 1807.
- (40) Chirakal, R.; Vasdev, N.; Schrobilgen, G. J.; Nahmias, C. *Journal of Fluorine Chemistry* **1999**, *99*, 87.
- (41) Taylor, S. D.; Kotoris, C. C.; Hum, G. *Tetrahedron* **1999**, *55*, 12431.
- (42) Pascal, S. M. *NMR Primer: an HSQC-Based Approach with Vector Animations*; IM Publications: West Sussex, UK, 2008.
- (43) Wrackmeyer, B.; Kupce, E.; Koster, R.; Seidel, G. *Magn. Reson. Chem.* **1992**, *30*, 393.
- (44) Sheldrick, G. M.; 6.15 ed.; Bruker AXS: Madison, WI, 2004.
- (45) Sheldrick, G. M. *Acta Crystallographica Section A* **2008**, *64*, 112.
- (46) Sheldrick, G. M.; Bruker AXS: Madison, WI, 2003.
- (47) Sheldrick, G. M.; Bruker AXS: Madison, WI, 2006.
- (48) Dolomanov, O. V.; Bourhis, L. J.; Gildea, R. J.; Howard, J. A. K.; Puschmann, H. *Journal of Applied Crystallography* **2009**, *42*, 339.

Chapter 5.

Single-Crystal X-ray Structural Characterization of C₆₀ Derivatives with Perfluoroalkyl and Related Perfluorinated Substituents: Seven Isomers of C₆₀(CF₃)₁₀ and 1,9-C₆₀(cyclo-CF₂(2-C₆F₄)), a Faux Hawk Fullerene with PCBM-like Properties

5.1 Introduction and Justification

The first fullerene derivative with multiple CF₃ groups to be structurally characterized by X-ray crystallography was 1,3,7,10,14,17,23,28,31,40-C₆₀(CF₃)₁₀.^{1,2} Figure 5-1 shows this structure along with two Schlegel diagrams, one of which shows cage C–C bond distances in pm. (A Schlegel diagram is a two-dimensional representation of a three-dimensional polyhedron created by distorting it in such a way that it can be laid out flat so that no edges cross.^{3,4} For C₆₀, this involves choosing one of the 12 pentagons and extending it in a rubber-sheet fashion such that it becomes a frame for the other 11 pentagons and 20 hexagons.) The *pmp*³*mpmp* addition-pattern abbreviation denotes a ribbon of edge-sharing *meta* (*m*) and *para* (*p*) C₆(CF₃)₂ hexagons (note that each shared edge is a C(sp³)–C(sp²) bond). This seminal paper and others that followed⁵ showed conclusively that C₆₀(CF₃)_n compounds, in general (there are only two exceptions), have "ribbon" addition patterns with *p-m-p* and/or *p-p-p* (i.e., *p*³) segments (as described above) along with, in some cases, one or two isolated *p*-C₆(CF₃)₂ hexagons.² For example, the only isomer known for the composition C₆₀(CF₃)₂ is *p*-C₆₀(CF₃)₂ (i.e., 1,7-C₆₀(CF₃)₂), and the three known isomers of C₆₀(CF₃)₄ are *p*³-, *pmp*-, and *p,p*-C₆₀(CF₃)₄.⁵ These observations are in sharp contrast to the earlier prediction of Taylor that the CF₃ groups in C₆₀(CF₃)_n derivatives occupy a string of contiguous cage C atoms.^{6,7}

The six previously known isomers of $C_{60}(CF_3)_{10}$, plus the six new isomers prepared by Strauss-Boltalina group Ph.D. student Bryon W. Larson⁸ and structurally characterized by the author of this dissertation, are listed in Table 5-1.⁹⁻¹⁵ Schlegel diagrams for the six previously known isomers, which are abbreviated 60-10-1 through 60-10-6, are shown in Figure 5-2.² The first part of the abbreviation refers to the fullerene, C_{60} . The second part refers to the number of CF_3 groups. The third part is an arbitrary isomer number or letter. Isomer numbers are given for those compounds with experimentally-verified addition patterns (i.e., verified by X-ray crystallography). The only exception to this "isomer-number" rule is that 60-10-1, which was first reported in 2005¹ and only structurally characterized in 2015 as part of this dissertation research, was tentatively assigned its now-verified addition pattern in 2007 on the basis of its ^{19}F NMR spectrum, first reduction potential ($E_{1/2}(0/-)$ value), and DFT relative energy and $E(LUMO)$ value. The numbered abbreviations refer to both (i) a particular compound of C_{60} with 10 CF_3 groups and (ii) the addition pattern of that compound in general, regardless of substituent. For example, 60-10-7, which is not included in this table, would denote the as-yet-unknown isomer of $C_{60}(CF_3)_{10}$ with the same addition pattern as a structurally-characterized isomer of $C_{60}(C_2F_5)_{10}$, which has been assigned the abbreviation 60-10-7- C_2F_5 .⁵ As another example, the unknown compound 1,3,7,10,14,17,23,-28,31,40- $C_{10}H_{10}$ would be abbreviated 60-10-3-H. Note that; (i) 60-10-1 had a tentatively-assigned and now proven addition pattern consisting of a p^3mpmp ribbon and an isolated $p-C_6(CF_3)_2$ hexagon, (ii) 60-10-3 has an mp^3m ribbon segment that surrounds a fulvene-like portion of the C_{60} cage that is isolated from the remaining π system, (iii) 60-10-6 has an addition pattern consisting of a p^3mp ribbon and a separate pmp ribbon, and (iv) 60-10-4 has an unusual addition pattern consisting of two p^3m^2 loops. The significance of the

isolated fulvene portion of the 60-10-3 π system will be discussed later in this chapter. Finally, note also that C_{60} has 30 π bonds and $C_{60}(CF_3)_{10}$ isomers have 25 π bonds.

The six previously known isomers of $C_{60}(CF_3)_{10}$ have played an important role in fullerene chemistry for several reasons. First, they comprise the first example of a fullerene(X) $_n$ composition of *any* fullerene with *any* substituent X with more than four well-characterized isomers for a given value of n . Second, their addition patterns were precisely known, in five cases by X-ray crystallography. (This is not a trivial reason; there are literally hundreds of millions of possible isomers for the composition $C_{60}X_{10}$.¹⁶). Third, their electrochemical properties were studied by cyclic voltammetry in the same laboratory under the same conditions (i.e., identical solvent, electrolyte, electrodes, cell design, and potential-sweep rate), and all six had reversible (i.e., quasi-reversible) first reductions (and some had second and even third reversible reductions).¹⁰ Fourth, and most importantly, their first reduction potentials (i.e., $E_{1/2}(0/-)$ values) varied over an unexpectedly large range of 0.50 V. The previous largest range of $E_{1/2}(0/-)$ values for *structurally-characterized* isomeric fullerene derivatives was 0.15 V for three isomers of $C_{70}Bn_2$.¹⁷ Two other examples are three isomers of $C_{60}F_{36}$ $\Delta E_{1/2}(0/-) = 0.080$ V¹⁸ and two structurally-characterized isomers of $C_{60}(CH_2Ph)_4$ $\Delta E_{1/2}(0/-) = 0.050$ V.¹⁹ The unprecedented large range of $E_{1/2}(0/-)$ values for $C_{60}(CF_3)_{10}$ isomers (hereinafter known as 60-10 isomers or simply as 60-10's) and a detailed analysis of their addition patterns, their DFT-predicted $E(LUMO)$ values, and the "shapes" of their DFT-predicted LUMOs led to an understanding of what factors most affect $E_{1/2}(0/-)$ values for fullerene derivatives. The unprecedented and surprising conclusion was that the addition pattern, specifically how the addition pattern effects the number and proximity of non-terminal double bonds in pentagons (see below), had a much greater influence on the reduction potential of a given compound than

the number of electron-withdrawing CF_3 substituents. That is why it was important to confirm the previously, but tentatively, assigned addition pattern of 60-10-1 and to structurally characterize the six new isomers. When the spectroscopic and electrochemical properties of the six new isomers are studied in detail, in future work, the knowledge of their addition patterns, determined in this work by X-ray crystallography, will be used to further understand how fullerene addition patterns affect fullerene electronic properties.

In addition, it was recently discovered that the compound 1,9- $\text{C}_{60}(\text{cyclo-CF}_2(2-\text{C}_6\text{F}_4))$, prepared by former Strauss-Boltalina group student Dr. Long K. San,²⁰ exhibited charge-carrier yield \times mobility performance in organic photovoltaic (OPV) active-layer blends with poly-3-hexylthiophene that rivaled the blends of the industry-standard fullerene acceptor phenyl- C_{61} -butyric acid methyl ester (PCBM). The structure of this unusual fullerene derivative was reasonably well established by spectroscopic evidence. Nevertheless, the author of this dissertation undertook the determination of its structure by X-ray crystallography, especially because the performance of fullerene acceptors in OPV devices is widely believed to be a function of, among other factors, their aggregation behavior, especially the number of electronically coupled nearest-neighbors and their three-dimensional arrangement.²¹⁻³² For this reason, the solid-state molecular packing patterns of 1,9- $\text{C}_{60}(\text{cyclo-CF}_2(2-\text{C}_6\text{F}_4))$, 60-10-1, and the six new isomers of $\text{C}_{60}(\text{CF}_3)_{10}$ will also be discussed in detail in this chapter.

5.2 Results

5.2.1 Three new isomers of $C_{60}(CF_3)_{10}$.

The six new isomers of $C_{60}(CF_3)_{10}$, arbitrarily numbered 60-10-8 through 60-10-13, are listed in Table 5-1. X-ray collection and refinement parameters and some derived results (densities, molecular packing arrangements, and ranges of fullerene centroid...centroid ($\odot \cdots \odot$) distances) for 60-10-1 and the six new isomers are listed in Tables 5-2 and 5-3. Crystals of 60-10-1 were grown by Strauss-Boltalina group member Tyler C. Clikeman. Data collection, structure solution, and refinement for 60-10-1 were carried out by the author of this dissertation. Crystals for the six new isomers of $C_{60}(CF_3)_{10}$ were grown by former Strauss-Boltalina group member Dr. Bryon W Larson. Diffraction data were collected, and the structures were initially solved, by the author of this dissertation with the assistance of Strauss-Boltalina research group Post-doctoral student Dr. Igor V. Kuvychko for 60-10-8, 60-10-9, and 60-10-10. Final refinements were performed by the author. Diffraction data collections, structure solutions, and final refinements for 60-10-11, 60-10-12, and 60-10-13 were performed by the author (and, in the case of 60-10-11, with the assistance of Dr. Yu-Sheng Chen at the Advanced Photon Source at Argonne National Lab, where the synchrotron X-ray diffraction data for 60-10-11 were collected by the author). All of the six new structures consist of a complete $C_{60}(CF_3)_{10}$ molecule in the asymmetric unit (i.e., all 100 atoms are unique). The structure of 60-10-1 consists of two independent molecules (i.e., 200 unique atoms).

Schlegel diagrams of the six new isomers are shown in Figure 5-3. Schlegel diagrams for all eleven isomers with "ribbon" addition patterns (i.e., all isomers except 60-10-4) are shown together for easier comparison in Figure 5-4. Thermal ellipsoid plots of the two unique 60-10-1

molecules are shown in Figure 5-5. Thermal ellipsoid plots of the six new isomers are shown in Figure 5-6. The six new isomers of $C_{60}(CF_3)_{10}$ are asymmetric, as is 60-10-1. Only one enantiomer is shown for each structure in Figures 5-3, 5-4, and 5-5.

The six new isomers exhibit addition patterns that follow the general trends described above for the previously known 60-10 isomers^{1,10-12,15} and other $C_{60}(CF_3)_n$ derivatives.⁵ The p^3mp,pmp addition pattern of 60-10-8 is strikingly similar to the addition pattern of 60-10-6. Both molecules have identical p^3mp ribbons, and their pmp ribbons both involve the same three hexagons. The $pmpmpmp,p$ addition patterns of 60-10-9 and 60-10-13 are related to the single-ribbon $pmpmpmpmp$ addition pattern of 60-10-5. Both 60-10-5 and 60-10-13 have the same $pmpmpmpmp$ fragment, but the "last two" CF_3 groups are on different $p-C_6(CF_3)_2$ hexagons. In the case of 60-10-5, the last $p-C_6(CF_3)_2$ hexagon links up with the $pmpmpmpmp$ ribbon to generate an additional $m-C_6(CF_3)_2$ hexagon; in the case of 60-10-13, the last $p-C_6(CF_3)_2$ hexagon is an isolated $p-C_6(CF_3)_2$ hexagon.

Unlike a planar molecule such as $m-C_6H_4(CF_3)_2$ and $p-C_6H_4(CF_3)_2$, in which the CF_3 groups are well separated from one another, the curvature of the C_{60} cage, plus the distortions introduced by converting 10 cage $C(sp^2)$ atoms into $C(sp^3)$ atoms, force the CF_3 groups in $m-C_6(CF_3)_2$ and $p-C_6(CF_3)_2$ hexagons and in 1,3- $C_5(CF_3)_2$ pentagons into close proximity. Furthermore, in general, CF_3 groups in $C_{60}(CF_3)_n$ derivatives exhibit staggered conformations with respect to their three underlying cage C–C bonds. These two structural features result in $F\cdots F$ interatomic distances of ca. 2.5–2.9 Å directly over each shared hexagon or pentagon, as shown in Figure 5-7 for a fragment of the structure of 60-10-12. The distortions to the icosahedral C_{60} cage by adding 10 CF_3 groups can be seen in Figure 5-8.

5.2.2 Molecular Structure of 1,9-C₆₀(cyclo-CF₂(2-C₆F₄)).

Single crystals of 1,9-C₆₀(cyclo-CF₂(2-C₆F₄)) suitable for X-ray diffraction were grown by former Strauss-Boltalina group member Dr. Long K San by slow evaporation of a carbon disulfide solution as described in Chapter 1, reference 20. Even after multiple crystallization attempts and slow crystal growth, 1,9-C₆₀(cyclo-CF₂(2-C₆F₄)) recovered crystals were always small (less than 50 ± μm on a side), resulting in poor diffraction on the Bruker Apex II single crystal instrument at The Colorado State University, Department of Chemistry, Central Instrument Facility. The best single crystal diffraction data set of 1,9-C₆₀(cyclo-CF₂(2-C₆F₄)) was collected using the synchrotron X-ray source at the Advanced Photon Source at Argonne National Lab by Dr. Yu-Sheng Chen at $T = 15(2)$ K. The final solution and refinement was determined by the author of this dissertation. The crystal structure of 1,9-C₆₀(cyclo-CF₂(2-C₆F₄)), a 50% probability ellipsoid plot is shown in Figure 5-9, exhibits a disorder of the entire molecule (not shown), and has one unique 1,9-C₆₀(cyclo-CF₂(2-C₆F₄)) unit in the asymmetric unit. This molecule has been nick-named faux hawk due to its resemblance to a faux hawk hair style, also shown in Figure 5-9.

5.3 Discussion

5.3.1 Fullerene Cage C–C Distances, The Distinction Between Single and Double Bonds.

Plots of the 90 cage C–C bond distances in the X-ray structures of 60-10-1 (only one of the two nearly identical independent molecules) and 60-10-9 vs. the corresponding DFT-optimized C–C distances are shown in Figure 5-10. These plots indicate that the DFT code used by our

collaborator,³³⁻³⁷ Dr. Alexey A. Popov, reproduces the X-ray determined structures quite well, within $\pm 3\sigma$.

In the discussion that follows, it is important to understand the distinction between cage C–C single and double bonds in underivatized fullerenes and the difficulty in distinguishing cage C–C single and double bonds in fullerene derivatives. Figure 5-11, reproduced from reference 1, shows plots of cage C–C distances in 60-10-3 and in Balch and Olmstead's precise structure of C_{60} in crystals of $C_{60}\cdot Pt(OEP)\cdot 2C_6H_6$ ³⁸. The terms "single" and "double" bonds are, of course, artificial but useful constructs since all cage C–C bonds in underivatized fullerenes have some double-bond character. All fullerenes have exactly 12 pentagons,³⁹ and in C_{60} that gives rise to 60 single bonds (pentagon-hexagon edges, also known as 5,6 bonds) and 30 double bonds (hexagon-hexagon edges, also known as 6,6 bonds). However, in 60-10-3 three of the four shortest cage C–C bonds, which are clearly "double" bonds, are 5,6 bonds, and are known generically as DBIPs (double-bonds in pentagons). Two other short 5,6 bonds, C11–C29 and C13–C30, are DBIPs that have *two* C(sp²) nearest neighbors, and they are known as non-terminal DBIPs, or *nt*-DBIPs.¹⁰ This is to distinguish them from terminal DBIPs (*t*-DBIPs), which have only one C(sp²) nearest neighbor and arise whenever there is a *meta*-C₆(CF₃)₂ hexagon in the ribbon of edge-sharing *m*- and *p*-C₆(CF₃)₂ hexagons.

5.3.2 The Electronic Consequences of Non-Terminal Double Bonds in Pentagons (*nt*-DBIPs).

Figure 5-12 shows that $C_{60}(CF_3)_n$ isomers span a wide range of reduction potentials not only for $n = 10$ but for each even value of n from $n = 6$ to $n = 12$.¹⁰ It is possible to pick an isomer for each n such that $E_{1,2}(0/-)$ increases as n increases (this was the expectation of most fullerene scientists before the publication of reference 10), but it is also possible to pick isomers such that

$E_{1/2}(0/-)$ decreases as n increases. Furthermore, it is possible to pick isomers for $n = 2$ to $n = 12$ that result in a saw-tooth plot as n increases. One of the main discoveries reported in reference 10 is that the LUMOs of $C_{60}X_n$ derivatives have large contributions from the p- π orbitals on or near the nt -DBIP cage C atoms, and that, all other things being equal, $E(\text{LUMO})$ values decrease (and $E_{1/2}(0/-)$ values increase) as the LUMO becomes more delocalized over the fullerene π system. Thus, $C_{60}X_n$ derivatives with multiple nt -DBIPs, and especially with nt -DBIPs in close proximity, have the most extensively delocalized LUMOs and are the best electron acceptors.

Figure 5-13 shows Schlegel diagrams for 60-10-1, 60-10-2, and 60-10-3 with red-highlighted nt -DBIPs and two representations of their respective DFT-predicted LUMOs (these DFT calculations were published in the Popov-Boltalina-Strauss 2007 "Frontier Orbital" paper in *J. Am. Chem. Soc.*¹⁰). The three LUMOs differ significantly in their degree of delocalization, and the $E_{1/2}(0/-)$ values decrease from 60-10-1 to 60-10-2 to 60-10-3 as the degree of delocalization decreases (i.e., the compounds become harder to reduce as the LUMO becomes more localized, a sensible result if a "particle-in-a-box" analogy is invoked).¹⁰ The compounds 60-10-2 and 60-10-3 have the same two nt -DBIPs. In 60-10-3, however, the LUMO is confined to the isolated fulvene fragment. In 60-10-2, the fulvene fragment is in conjugation with the rest of the fullerene π system. The result is that the LUMO in 60-10-2 is more delocalized than the LUMO in 60-10-3, and 60-10-2 is 0.15 V easier to reduce than 60-10-3. In 60-10-1, the isolated p - $C_6(\text{CF}_3)_2$ hexagon gives rise to a third nt -DBIP, and the proximity of this double bond to the two nt -DBIPs in the fulvene fragment results in a much more extensively delocalized LUMO than in 60-10-2. The net result is that 60-10-1 is 0.25 V easier to reduce than 60-10-2, and 0.40 V easier to reduce than 60-10-3. Therefore, the electronic properties of fullerene(X) $_n$ isomers (i.e., for a given X and a given value of n) are an extremely sensitive function of the addition pattern: the molecular

structures of isomers 60-10-1 and 60-10-3 only differ by shifting *one, and only one*, CF₃ group to a new position four cage C atoms away, and, this difference leads to the aforementioned change in $E_{1/2}(0/-)$ by 0.40 V.

With this in mind, the addition patterns of the new 60-10 isomers, determined by the author of this dissertation, their electrochemical $E_{1/2}(0/-)$ values, measured by Strauss-Boltalina group Ph.D. student Bryon W. Larson, and listed in Table 5-4, and the DFT results of Alexey Popov listed in Table 5-1 will be seen to be entirely consistent with the conclusions published in reference 10 regarding LUMOs and *nt*-DBIPs (i.e., regarding LUMOs and addition patterns).

Figure 5-14 shows a comparison of the addition patterns of 60-10-8 and 60-10-6. These two isomers have two *nt*-DBIPs in common in the p^3 portion of their respective addition patterns. These *nt*-DBIPs are in conjugation and, together with a 6:6 double bond, form a fulvene-like moiety on the surface of the cages. The compound 60-6-1, with a p^3mp , has the same fulvene moiety with two *nt*-DBIPs.¹⁰ This fulvene moiety "anchors" the LUMO to that portion of each molecule, as also shown in Figure 5-14. The remaining *nt*-DBIP in each molecule is remote from the fulvene and does not appear to influence the location or cage-C atom contributions to the LUMOs, unlike the situation in 60-10-1, where the third *nt*-DBIP is close to the fulvene moiety and produces a more delocalized LUMO. In harmony with the similar remote location of the third *nt*-DBIP and similarly shaped LUMO for 60-10-8 and 60-10-6, their electrochemical $E_{1/2}(0/-)$ values relative to $C_{60}^{0/-}$, are similar, 0.47(1) V for 60-10-8 and 0.41(1) V, for 60-10-6. Note that 60-10-1, with its more extensively delocalized LUMO, is a significantly better electron acceptor ($E_{1/2}(0/-) = 0.65(1)$ V $C_{60}^{0/-}$).

The isolated fulvene moiety in 60-10-3, a key to its much poorer electron accepting properties, was discussed above. New isomer 60-10-12 also has an isolated fulvene moiety, but

in addition it has another *nt*-DBIP that contributes to its LUMO, as shown in Figure 5-14, unlike the situation in 60-10-3. Therefore, it comes as no surprise that 60-10-12 is a better electron acceptor ($E_{1/2}(0/-) = 0.37(1) \text{ V C}_{60}^{0/-}$) than 60-10-3 ($E_{1/2}(0/-) = 0.16(1) \text{ V C}_{60}^{0/-}$).

The DFT-predicted $E(\text{LUMO})$ for 60-10-11 is -5.090 eV , only 39 meV higher than 60-10-1. Based on this, it should be the second-best electron acceptor of the structurally characterized 60-10 isomers, and that prediction will be tested in future work. It is easy to see why this compound is predicted to be such a good electron acceptor. Its addition pattern gives rise to four *nt*-DBIPs, three of which are spatially similar to the three *nt*-DBIPs in 60-10-1. These three *nt*-DBIPs in 60-10-11 combine to form a very delocalized LUMO, as shown in Figure 5-15. Interestingly, the fourth *nt*-DBIP in 60-10-11, which is spatially closer to the fulvene *nt*-DBIPs than the third but is actually more remote than the third as far as π conjugation is concerned, does not contribute to the LUMO. For this reason, Dr. Alexey Popov also calculated the LUMO+1 orbital for 60-10-11. Figure 5-15, clearly shows that this orbital is "anchored" to the fourth *nt*-DBIP, a satisfying result as far as the link between *nt*-DBIPs and a $\text{C}_{60}(\text{CF}_3)_{10}$ LUMO (and now LUMO+1) is concerned.

5.3.3 Solid-State Packing of $\text{C}_{60}(\text{CF}_3)_{10}$ Isomers.

Even though molecules of $\text{C}_{60}(\text{CF}_3)_{10}$ are not as spherically symmetric as C_{60} , most 60-10 isomers that crystallize without lattice solvent molecules adopt either an idealized cubic close-packed (CCP) or hexagonal close-packed (HCP) structure. This is true of new structures 60-10-9, 60-10-10, and 60-10-12, as shown in Figure 5-16, as well as the previously reported structures 60-10-3,¹ 60-10-4,¹¹ and 60-10-6.¹⁵

When a molecule of chloroform is also present in the asymmetric unit, as in the structure of 60-10-8, the solid-state packing of fullerene moieties is not close packed, as shown in Figure 5-17. In this case each 60-10-8 molecule has 15 nearest-neighbor fullerenes. The range of distances between the fullerene centroids (\odot) is large, from 9.852 to 16.009 Å. Surprisingly, the shortest of these distances is shorter than the unique $\odot \cdots \odot$ distance in cubic C_{60} at 110 K, 9.936 Å.⁴⁰ On the other hand, even with a molecule of chloroform-*d* in the asymmetric unit, the 60-10-11 molecules in the structure of 60-10-11·CDCl₃ pack in an HCP array, with only 12 nearest neighbors, as shown in Figure 5-16.

The packing efficiency of fullerene derivatives in the solid state may be one of the factors that controls the mobility of electrons present in fullerene domains in organic photovoltaic active materials (these electrons are produced by exciton dissociation during photoillumination). In this regard, it is interesting that the six solvent-free close-packed structures listed in the preceding paragraph, although they consist of isomer molecules with identical molecular formulas, exhibit subtle differences in their densities, from 1.992 g cm⁻³ for 60-10-9 to 2.073 g cm⁻³ for 60-10-4 (both sets of data were collected at 110 ± 10 K). This must be due to subtle differences in intermolecular interactions, both attractive and repulsive, caused by the different addition patterns. The ranges of $\odot \cdots \odot$ distances for 60-10-9, 60-10-10, and 60-10-12 are listed in Table 5-3. The ranges for 60-10-3, 60-10-4, and 60-10-6 are 10.187–14.232, 9.878–12.634, and 10.952–14.472 Å, respectively. There is a correlation, albeit not a very strong one, between the mean $\odot \cdots \odot$ distance and the crystal density, as shown graphically in Figure 5-18. In contrast, there is no meaningful correlation between the density and either the median $\odot \cdots \odot$ distance or the standard deviation of the 12 $\odot \cdots \odot$ distances (for 60-10-3, 60-10-4, and 60-10-6 these

parameters are [12.143 and 1.016 Å], [12.100 and 0.912 Å], and [11.441 and 0.988 Å], respectively).

Finally, the solid-state fullerene packing in the structure of 60-10-13, which does not contain solvent molecules, is not close-packed, as shown in Figure 5-19. Nevertheless, the density of crystals of 60-10-13 is ca. 0.6% higher than the densities of crystals of the HCP structures 60-10-9 and 60-10-10, 1.992 and 1.993 g cm⁻³, respectively. Although HCP and CCP are the most dense ways to pack spheres in three-dimensional space, the nearly equal, if not higher, density of 60-10-13 reinforces the concept that 60-10 molecules are "fuzzy" spheres with "fluorous" patches on parts of the fullerene surface, and the hard sphere (i.e., the surfaces) of the C₆₀ cores does not come into van der Waals contact with the hard spheres of most of its neighbors in the lattice. This is shown in Figure 5-20, in which the fluorous regions between molecules of 60-10-13 and, for comparison, 60-10-9 are emphasized. Despite the similarities, there is at least one important difference. The closest approach of neighboring molecules in 60-10-13, with a ⊙⋯⊙ distance of 10.126 Å, does not involve efficient π-π interactions between parallel polygons on the two molecules. In contrast, in 60-10-9 and in the other close-packed structure, the closest approach has a ⊙⋯⊙ distance of 9.703 Å (as mentioned above, shorter than in cubic C₆₀) and does involve a pair of parallel all-C(sp²) hexagons, with perpendicular displacements of 3.24 ± 0.02 Å from the C atoms of one hexagon to the least-squares plane of the other, distances that are shorter than the 3.35 Å separation of the all-C(sp²) hexagonal planes in graphite.

5.3.4 Solid-State Packing of 1,9-C₆₀(*cyclo*-CF₂(2-C₆F₄)) and Comparison with Single-Crystal X-ray Structures of PCBM and PCBM-like Molecules.

The structure of 1,9-C₆₀(*cyclo*-CF₂(2-C₆F₄)) is shown in Figure 5-9. It is compared with the molecular structure of PCBM in Figure 5-21. The two substituents have nearly the same number of non-hydrogen atoms, 13 for 1,9-C₆₀(*cyclo*-CF₂(2-C₆F₄)) and 14 for PCBM, but the faux hawk substituent is clearly the more compact. The 1.632(2) Å C1–C9 bond in PCBM is only marginally longer than the 1.610(5) Å distance in 1,9-C₆₀(*cyclo*-CF₂(2-C₆F₄)), and fullerene cage atoms C1 and C9 are only slightly less pyramidalized in PCBM (POAV $\theta_p = 17.1^\circ \times 2$) than in 1,9-C₆₀(*cyclo*-CF₂(2-C₆F₄)) ($\theta_p = 18.9$ and 19.1°).

There are two solvent-free X-ray structures of PCBM: a single-crystal structure determined using data collected at 100(2) K²² and a structure determined from powder X-ray diffraction data applying a collected at 298(2) K.²³ Both have the same space group, the same nearest-neighbor crystal packing as shown in Figure 5-22 and, despite the difference in temperature, have densities (i.e., unit cell volumes) that differ by only 0.64(3)%. This is somewhat surprising because most organic crystals exhibit a larger percentage-increase in density between 300 and 100 K, typically 3–6%.²⁴ For example, the density increases over this temperature range for benzene, naphthalene, and the *F3m3* polymorph of C₆₀ are 5.1, 7.8, and 2.0%, respectively.²⁴ This may indicate that solvent-free PCBM is packed as tightly as possible at 25 °C, even more so than C₆₀.

The solvent-free solid-state packing of 1,9-C₆₀(*cyclo*-CF₂(2-C₆F₄)) and PCBM²² are shown in Figures 5-23 and 5-24, respectively. In both cases the C₆₀ cage centroids (⊙) form rigorously-planar layers that are stacked in the third dimension. In the structure of 1,9-C₆₀(*cyclo*-CF₂(2-C₆F₄)), the stacking direction is parallel to the crystallographic *c* axis, as shown in Figure 5-25.

Significantly, the numbers of nearest neighbor molecules in the two structures are different. There are only seven (7) nearest neighbor fullerene molecules in crystalline solvent-free PCBM, with $\odot \cdots \odot$ distances of 9.95–10.28 Å. The mean and median distances are 10.17 and 10.24 Å, respectively. On the other hand, there are ten (10) nearest neighbors in the structure of 1,9- $C_{60}(\text{cyclo-CF}_2(2-C_6F_4))$, with $\odot \cdots \odot$ distances of 9.74–10.34 Å. The mean and median distances are 10.09 and 10.05 Å, respectively. The result is that the density of crystalline 1,9- $C_{60}(\text{cyclo-CF}_2(2-C_6F_4))$, 1.885 g cm⁻³, is 15.6% higher than the 1.631 g cm⁻³ density of solvent-free PCBM, even though the molar masses of the two compounds, 918.67 g mol⁻¹ for 1,9- $C_{60}(\text{cyclo-CF}_2(2-C_6F_4))$ and 910.83 g mol⁻¹ for PCBM, differ by only 1.1%. Although the diffraction data reported here for 1,9- $C_{60}(\text{cyclo-CF}_2(2-C_6F_4))$ were collected at 15(2) K, unit cell parameters were also determined at 120(2) K, and the unit cell volume was only 0.64% larger at 120(2) K than at 15(2) K. If the 120 K density is considered, then the density of crystalline 1,9- $C_{60}(\text{cyclo-CF}_2(2-C_6F_4))$ is 14.8% higher than crystalline solvent-free PCBM at 100 K.

It is widely believed that the aggregation behavior of OPV acceptor fullerenes in the solid state, especially the number of electronically coupled nearest neighbors and their three-dimensional arrangement, are among the key factors that determine charge transport properties in the fullerene domains in Type II heterojunction solar cells.^{22,23,25-32,41,42} Accordingly, the determination of the number of nearest neighbor fullerenes is important, and it depends on the choice of the maximum relevant $\odot \cdots \odot$ distance beyond which fullerene–fullerene electronic coupling is probably negligible. After the seven closest PCBM molecules surrounding each molecule of PCBM in the solvent-free structure,²² shown in Figure 5-22, the two next shortest $\odot \cdots \odot$ distances are 11.61 and 13.23 Å. On what basis should one decide whether or not the 11.61 Å molecule should be considered to be an electronically-relevant nearest neighbor? The

criterion used here is as follows. Consider that the 11.61 Å distance is too long for effective electronic coupling because the closest cage surface... cage surface distance ($C_{\text{cage}}\cdots C_{\text{cage}}$) between these two PCBM molecules is 5.03 Å (and these two C_{cage} atoms are close to lying on the $\odot\cdots\odot$ vector). In contrast, the closest $C_{\text{cage}}\cdots C_{\text{cage}}$ distances for PCBM molecules with $\odot\cdots\odot$ separations of 10.28 and 10.24 Å are 3.23 and 3.32 Å, respectively, approximately the same as the 3.35 Å interplanar separation in graphite.⁴³ For 1,9- $C_{60}(\text{cyclo-CF}_2(2-C_6F_4))$, the closest $C_{\text{cage}}\cdots C_{\text{cage}}$ distance between two molecules with separations of 10.34 Å is 3.38 Å, and the next closest $\odot\cdots\odot$ distances are 14.00 Å. Therefore, the two centroids that are 10.34 Å from the central centroid belong to faux hawk fullerene molecules counted among the ten nearest neighbors around each faux hawk molecule.

Interestingly, the perpendicular spacing between the rigorously-planar layers of centroids are smaller, not larger, in the structure of solvent-free PCBM, 5.89 and 6.46 Å, than in the structure of 1,9- $C_{60}(\text{cyclo-CF}_2(2-C_6F_4))$, 6.96 and 8.71 Å. Due to offsets of the C_{60} centroid layers relative to one another, the interlayer spacings are not an important metric from the standpoint of electron mobility. The $\odot\cdots\odot$ distances, $C_{\text{cage}}\cdots C_{\text{cage}}$ distances, and their three-dimensional arrangement are important.

It may come as a surprise that the $\odot\cdots\odot$ distances in PCBM crystals containing solvent molecules can be, on average, shorter, not longer, than in the solvent-free structure discussed above, even when there are as many PCBM nearest neighbors. In the 123 K single-crystal structure of PCBM.0.5CS₂,²⁵ seven $\odot\cdots\odot$ distances span the range 9.86–10.27 Å and average 10.08 Å. There are two unique PCBM molecules in the 90 K structure of PCBM·0.5C₆H₅Cl, they both have seven nearest neighbors, and the mean $\odot\cdots\odot$ distances are 10.01 and 10.02 Å (the two ranges are 9.84–10.14 and 9.95–10.06 Å, respectively).³¹ In the 123 K structure of

ThCBM·1.25CS₂, in which a nearly-isosteric thienyl five-membered ring has replaced the phenyl group in PCBM, there are two unique ThCBM molecules.²⁵ One has seven nearest neighbors with a mean $\odot \cdots \odot$ distance of 10.03 Å (the range is 9.98–10.19 Å) and the other has *ten* nearest neighbors with a mean $\odot \cdots \odot$ distance of 9.99 Å (the range is 9.84–10.19 Å).²⁵ Finally, in the 90 K structure of PCBM·*o*-C₆H₄Cl₂, the one exception that proves the rule, there are only six, not seven, $\odot \cdots \odot$ distances, although the mean distance is still small, only 10.01 (the range is 10.00–10.22 Å). Whatever space is taken up by solvent molecules in structures of PCBM and related molecules, the fullerene–fullerene interactions can be as strong and as extensive as in solvent-free structures. It remains to be seen whether the presence of *all* types of solvent molecules, not just the ones examined so far, and/or the presence of other so-called "impurities" in fullerene domains *always* have a deleterious effect on electron mobility in blended donor-acceptor thin films and/or on power conversion efficiencies of OPV devices made with such films.

5.4 Experimental Section

5.4.1 Reagents and Solvents/Instrumentation

Samples were provided by Strauss-Boltalina group members Dr. Bryon W. Larson, Dr. James B. Whitiker, Dr. Long K. San, or Tyler C. Clikeman. Synthesis, purification and characterization of C₆₀(CF₃)₁₀-X compounds and 1,9-C₆₀(*cyclo*-CF₂(2-C₆F₄)) can be found in references. All crystalline samples suitable for signal crystal X-ray diffraction analysis were provided to the author.

X-ray Crystallography: Single crystals of 60-10-8, 60-10-9, 60-10-10, 60-10-12, and 60-10-13 were grown as previously described, data were collected at Colorado State University. Samples were mounted on a Mylar loop with paratone oil. Data from single crystals were collected using

a Bruker Kappa APEX II CCD diffractometer (MoK α λ = 0.71073 Å; graphite monochromator) at T = 120(2) K, with the exception of 60-10-12, it was collected at T = 100(2) K. Data reduction was performed with APEX 2 suite of software from Bruker. Solution and structure refinement were performed with SHELXTL software⁴⁴⁻⁴⁷, or OLEX 2, Version 1.2.5.⁴⁸ A semiempirical absorption correction was applied with SADABS⁴⁴. All figures were generated with SHELXTL XP software.^{45,49}

Single crystals of 60-10-1, 60-10-11, and faux hawk were grown as previously described, data sets were collected at Advanced Photon Source, Argonne National Laboratory, Lemont IL, Using Synchrotron Radiation Source, Beamline 15-ID-B, ChemMatCARS. Samples were mounted on glass fiber filament with paratone oil. Data from single crystals were collected at 100(2) K with the exception of faux hawk, it was collected at 15(2) K, using synchrotron radiation (λ = 0.41328 Å) with a diamond (111) monochromator, a Bruker D8 goniometer, and Bruker CCD detector controlled by Bruker APEX II software. Data reduction was performed with APEX 2 suite of software from Bruker. Solution and structure refinement were performed with SHELXTL software⁴⁴⁻⁴⁷, or OLEX 2, Version 1.2.5.⁴⁸ A semiempirical absorption correction was applied with SADABS⁴⁴. All figures were generated with SHELXTL XP software.^{45,49}

5.5 Figures

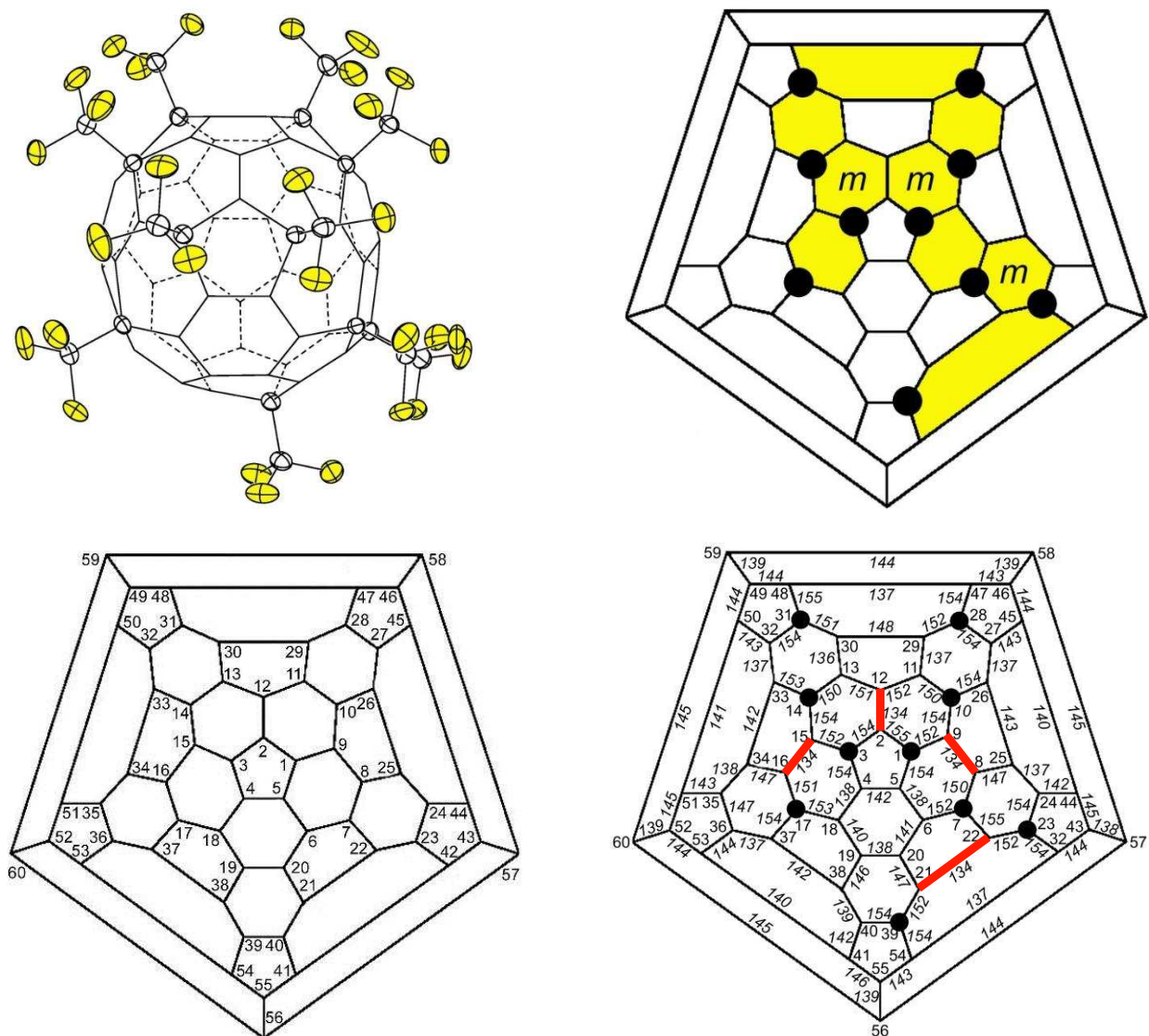


Figure 5-1. The structure of and Schlegel diagrams for 1,3,7,10,14,17,23,28,31,40- $C_{60}(CF_3)_{10}$ (60-10-3; 50% probability ellipsoids for some atoms; F atoms highlighted in yellow in the thermal ellipsoid plot). The black circles in the Schlegel diagrams indicate the cage C atoms to which the CF_3 groups are attached. The pmp^3mpmp ribbon is highlighted in yellow in the upper Schlegel diagram, and the *meta*- $C_6(CF_3)_2$ hexagons are indicated with the letter *m*. The lower Schlegel diagrams show IUPAC locants, cage C–C bond distances in pm, and the four shortest C–C bonds highlighted in red. The standard errors (σ) for the C–C bond distances in this structure are 0.3 pm and therefore $\pm 3\sigma$ is ca. ± 1 pm. Adapted to figures published in ref 1.

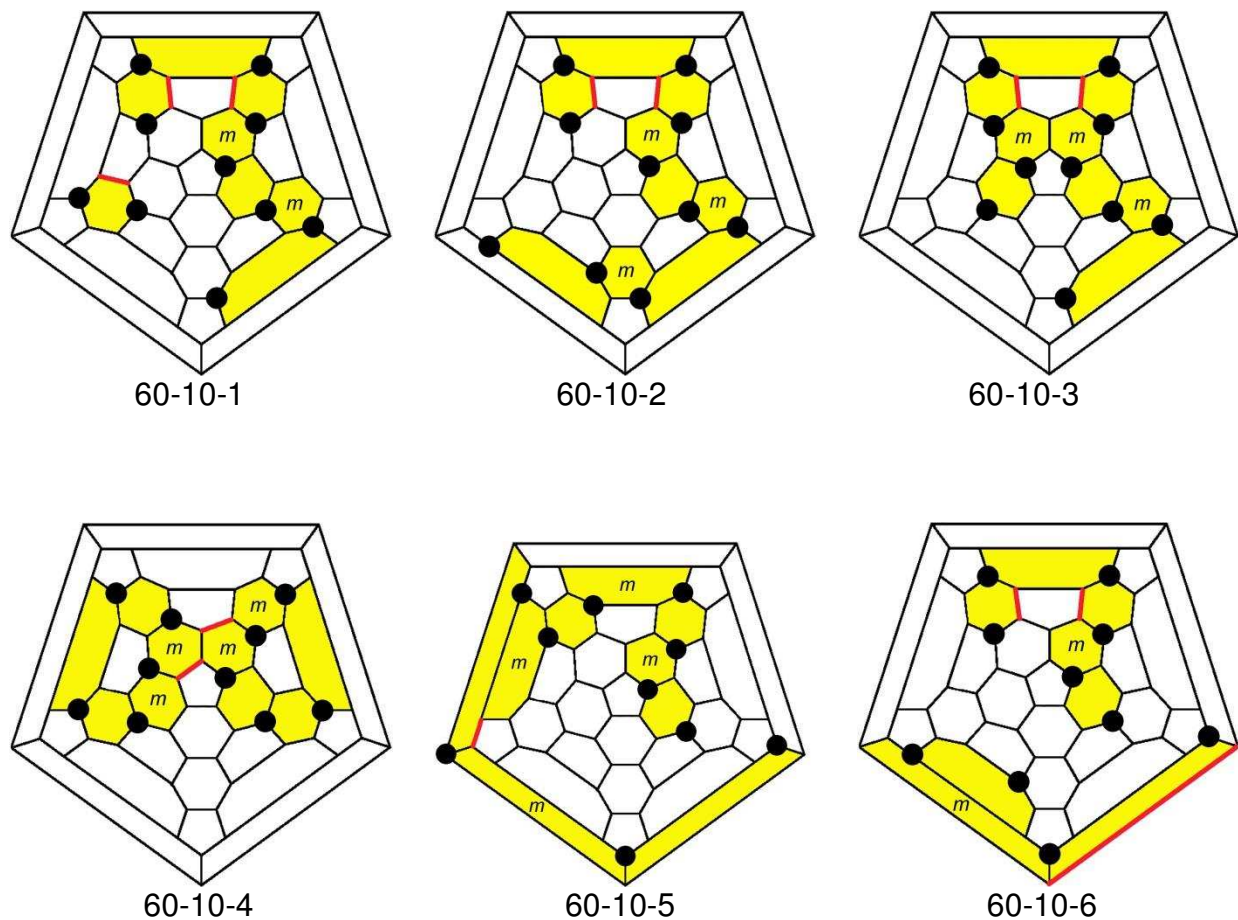


Figure 5-2. Schlegel diagrams for the previously known isomers of $C_{60}(CF_3)_{10}$. The black circles indicate the cage C atoms to which the CF_3 groups are attached. The ribbons or loops of edge-sharing *meta*- and *para*- $C_6(CF_3)_2$ hexagons and isolated *p*- $C_6(CF_3)_2$ hexagons are highlighted in yellow, and the *meta*- $C_6(CF_3)_2$ hexagons are indicated with the letter *m*. The bonds highlighted in red are non-terminal double bonds in pentagons (*nt*-DBIPs; see text). Adapted from drawings published in ref 2

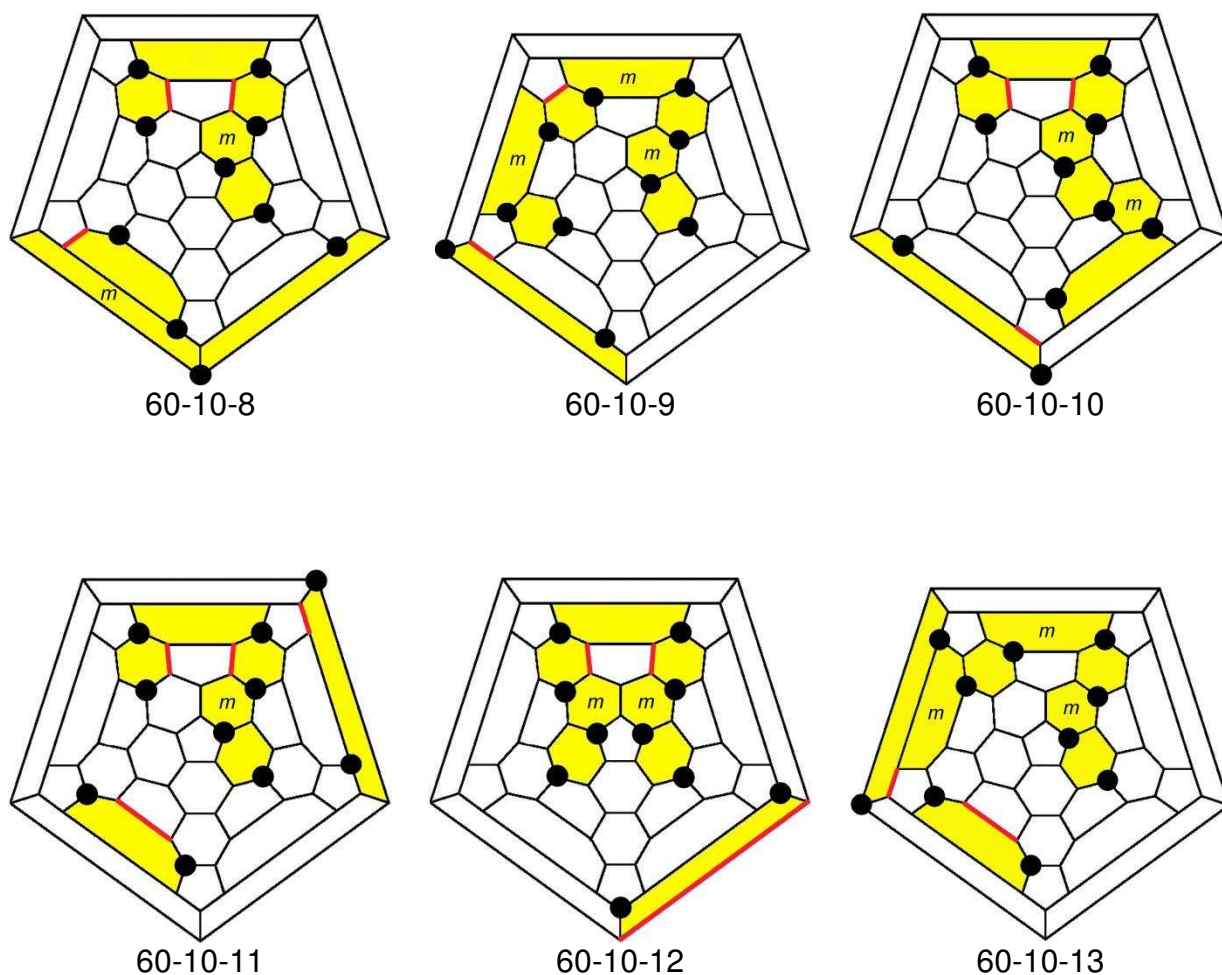


Figure 5-3. Schlegel diagrams for the structurally characterized new isomers of $C_{60}(CF_3)_{10}$. (See Table 5-1 for a key to the abbreviations 60-10-8 through 60-10-13.) The black circles indicate the cage C atoms to which the CF_3 groups are attached. The ribbons of edge-sharing *meta*- and *para*- $C_6(CF_3)_2$ hexagons and the isolated *p*- $C_6(CF_3)_2$ hexagons are highlighted in yellow, and the *meta*- $C_6(CF_3)_2$ hexagons are indicated with the letter *m*. The bonds highlighted in red are non-terminal double bonds in pentagons (*nt*-DBIPs see text). The most precise structure is that of 60-10-9, with C–C distance esd's of 0.003 Å.

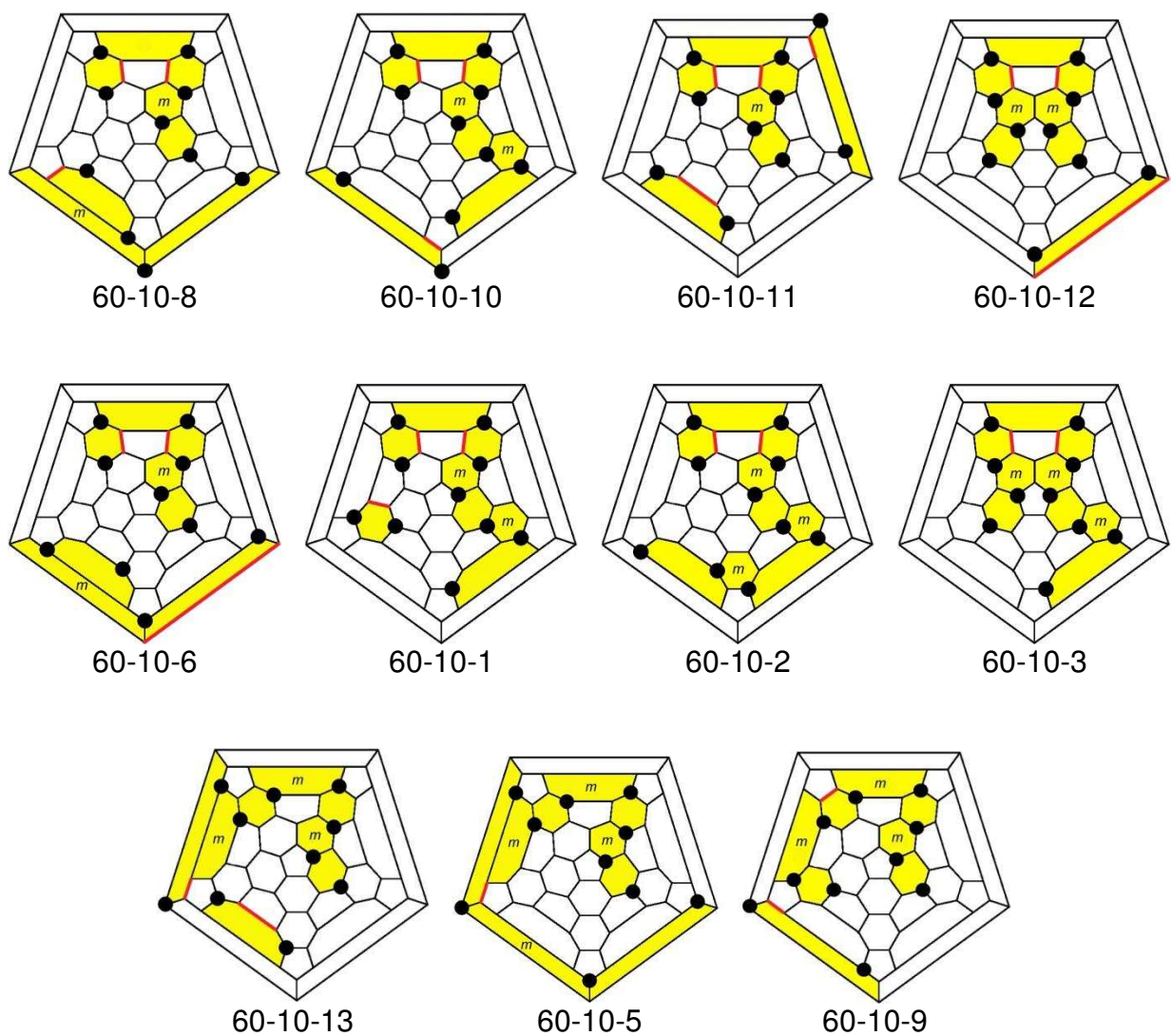


Figure 5-4. Schlegel diagrams arranged to compare and contrast the addition patterns of structurally characterized isomers of $C_{60}(CF_3)_{10}$. The first four relevant comparisons are vertical: 60-10-8 with 60-10-6; 60-10-10 with 60-10-1; 60-10-11 with 60-10-2; and 60-10-12 with 60-10-3. The bottom row allows a horizontal comparison of the addition patterns of 60-10-9, 60-10-5, and 60-10-13 to be made.

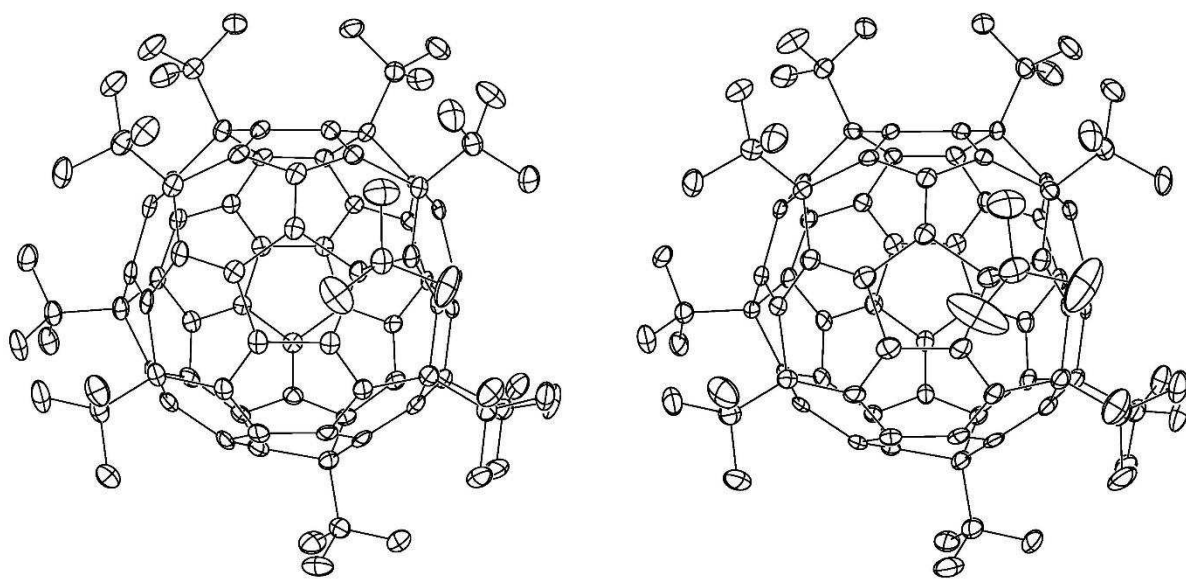


Figure 5-5. X-ray crystallographic 50% thermal ellipsoid plots of the two unique C₆₀(CF₃)₁₀ molecules in the structure of 1,6,11,16,18,24,27,36,41,57-C₆₀(CF₃)₁₀ (60-10-1).

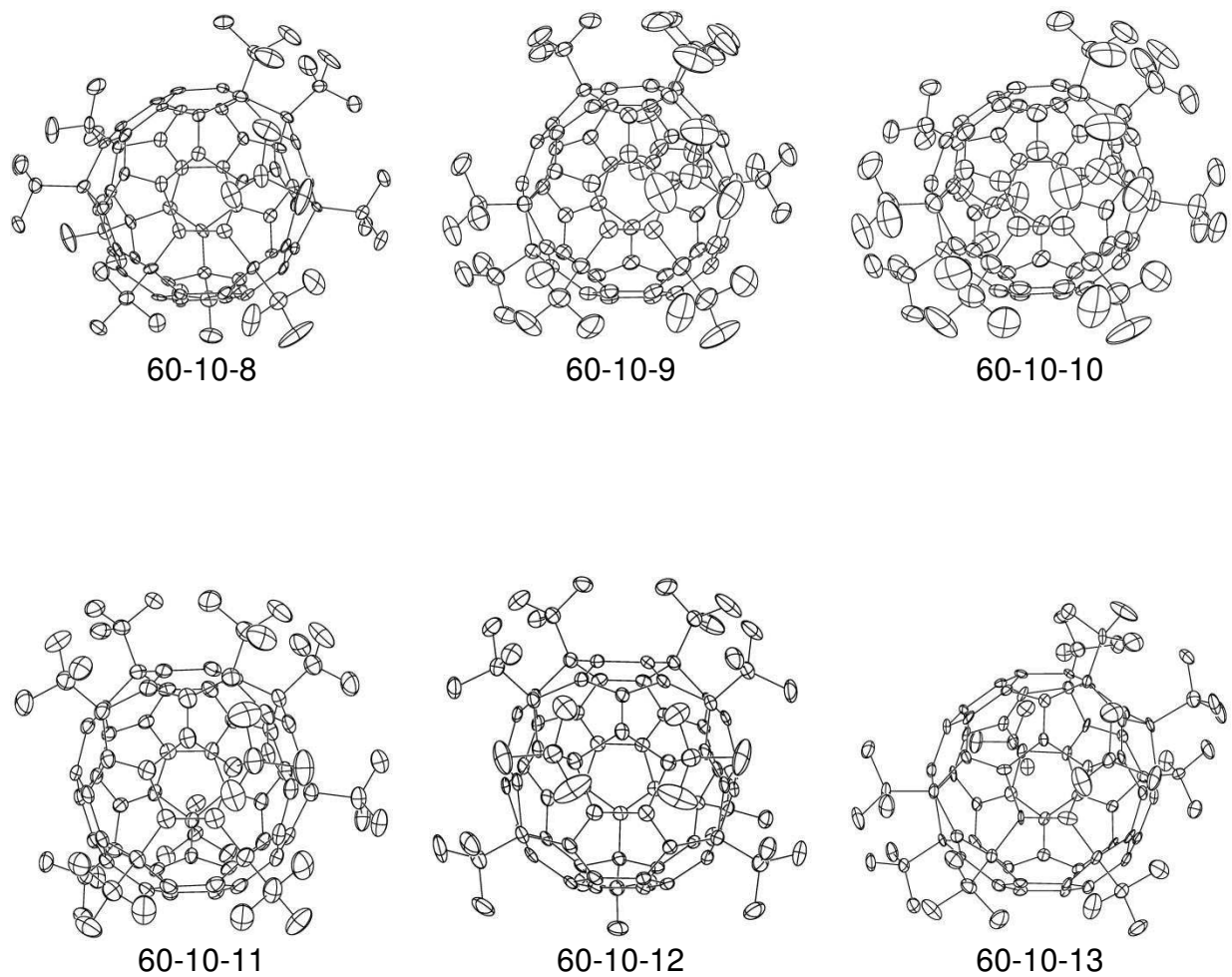


Figure 5-6. X-ray crystallographic 50% thermal ellipsoid plots of the six structurally-characterized new isomers of C₆₀(CF₃)₁₀. The CHCl₃ and CDCl₃ molecules of solvation in the structures of 60-10-8 and 60-10-11, respectively, are omitted for clarity.

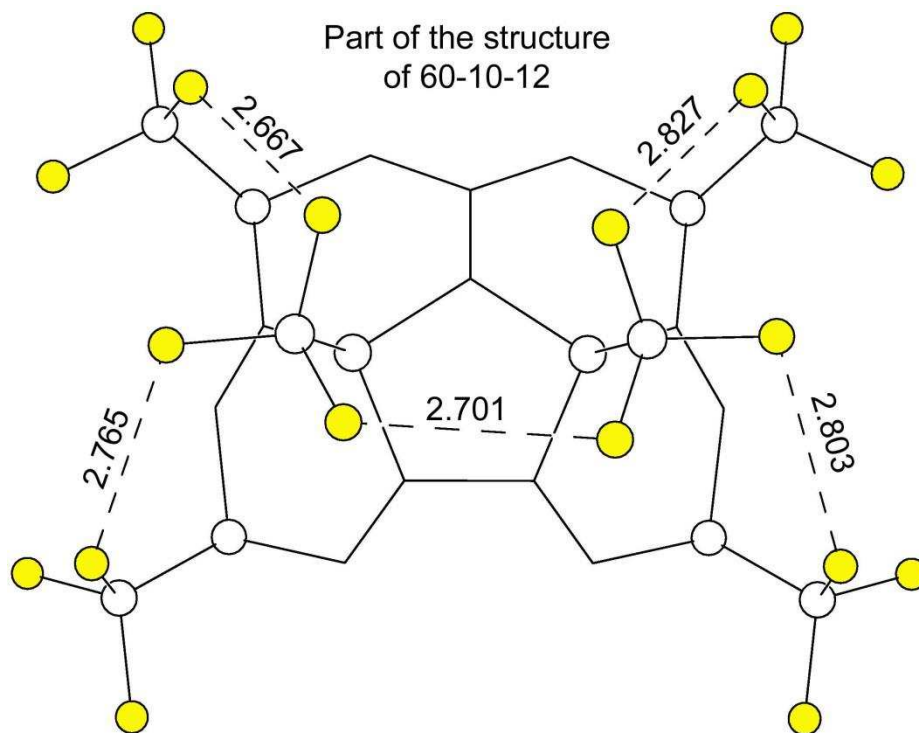


Figure 5-7. A portion of the X-ray structure of 60-10-12. The CF_3 groups that are not on the central pentagon are staggered with respect to the underlying cage C–C bonds. Their F–C–C–C torsion angles are 57.9 – 59.1° . The two CF_3 groups sharing the central pentagon have conformations that are significantly rotated with respect to being staggered. Their torsion angles are 16.1 and 24.0° . The F···F interatomic distances shown are in Å (the standard error for each distance is 0.003 Å).

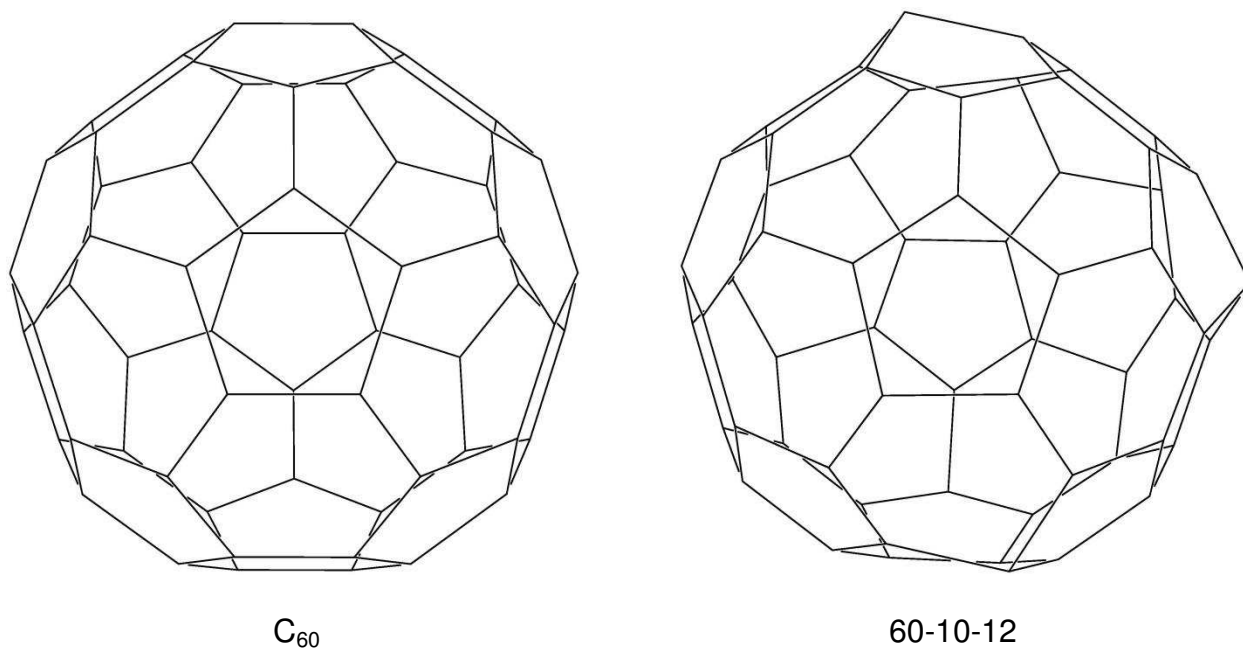


Figure 5-8. Comparison of the structures of underivatized C_{60} (left) and the fullerene cage in the structure of 60-10-12 (right; CF_3 groups omitted for clarity). The coordinates for the 60 unique $C(sp^2)$ atoms in C_{60} (i.e., no crystallographic symmetry) are from ref 14. Note the significant distortion of the fullerene cage in 60-10-12, which has 50 $C(sp^2)$ and 10 $C(sp^3)$ atoms.

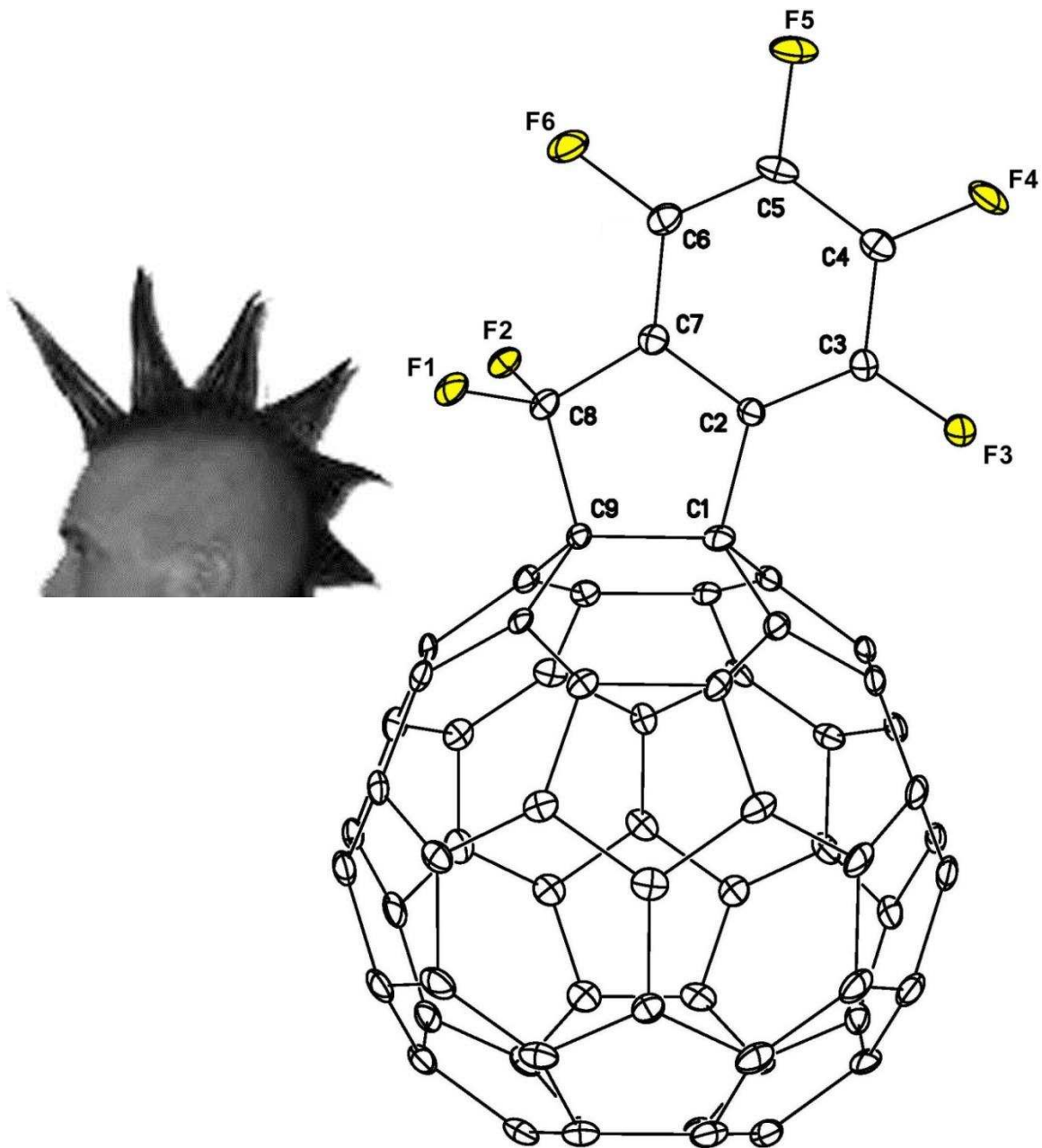


Figure 5-9. Comparison of the structure of 1,9-C₆₀(*cyclo*-CF₂(2-C₆F₄)) (50% probability ellipsoids) with a photograph of a particular type of faux hawk hairstyle. The resemblance led to the "faux hawk" nickname of 1,9-C₆₀(*cyclo*-CF₂(2-C₆F₄)).

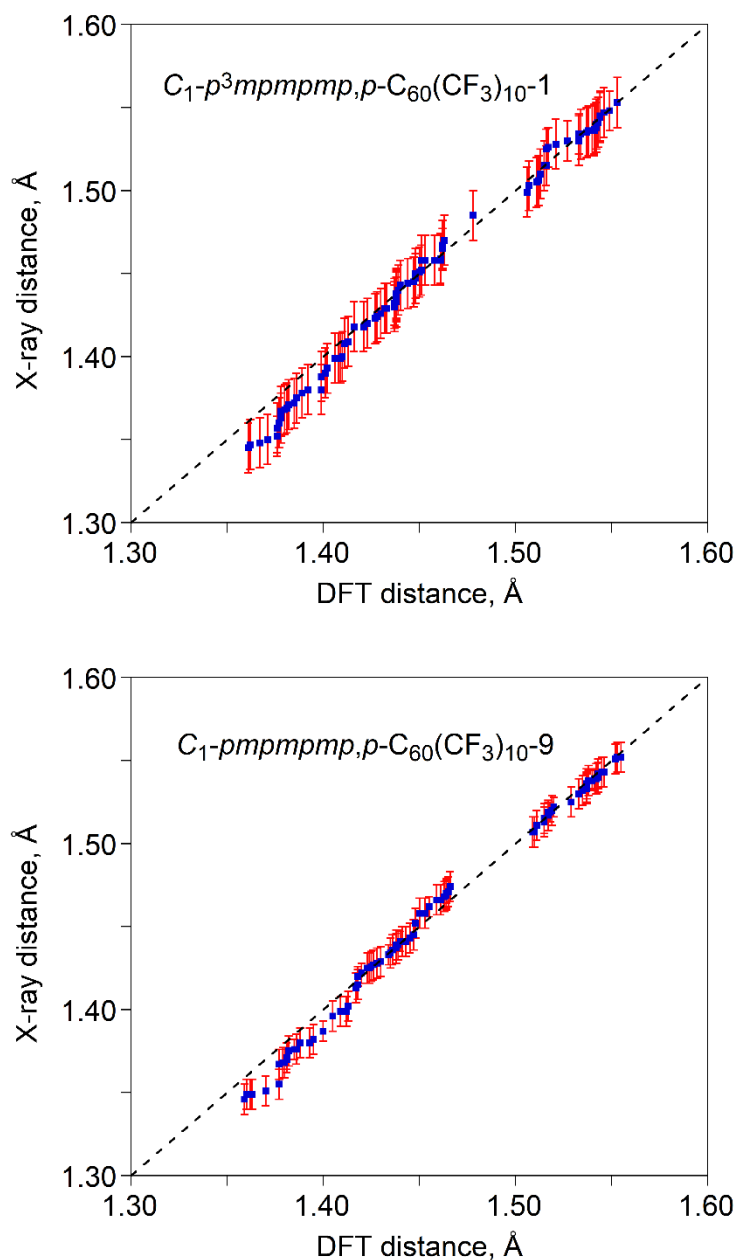


Figure 5-10. Plots of the X-ray vs. DFT-optimized cage C–C distances in the structures of 60-10-1 and 60-10-9. The error bars shown in both plots represent $\pm 3\sigma$. The DFT calculations were performed by Dr. Alexey A. Popov at the PBE/TZ2P level using PBE functional and the Priroda code.³³⁻³⁷

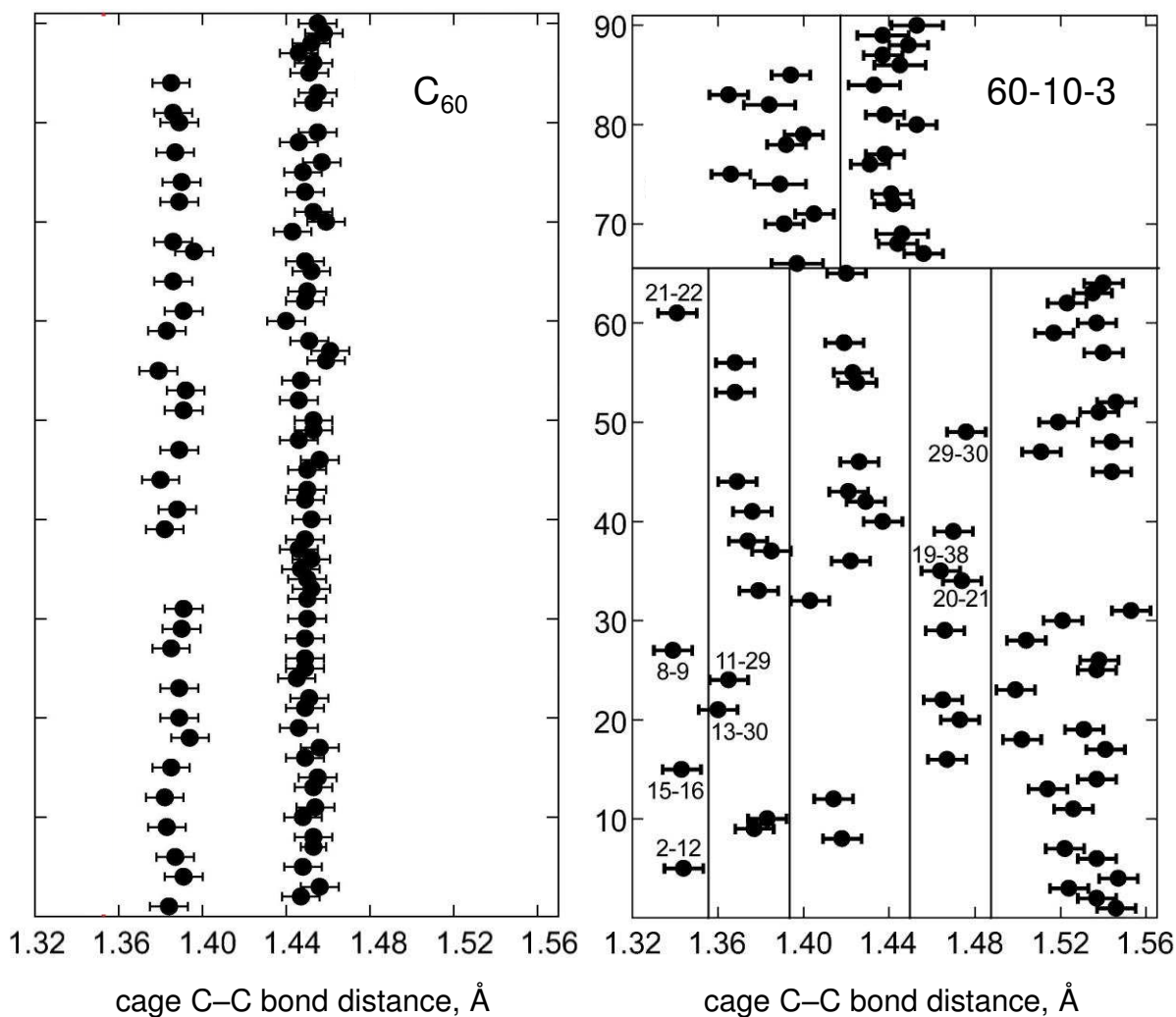


Figure 5-11. Plots of the X-ray diffraction determined cage C–C bond distances in the C_{60} molecule in $C_{60}\cdot Pt(OEP)\cdot 2C_6H_6$ (ref 38) and in 1,3,7,10,14,17,23,28,31,40- $C_{60}(CF_3)_{10}$ (60-10-3; reference 1). The non-terminal double bonds in pentagons in 60-10-3 are C11–C29 and C13–C30, which are part of the isolated fulvene fragment in this compound. The error bars shown in both plots represent $\pm 3\sigma$.

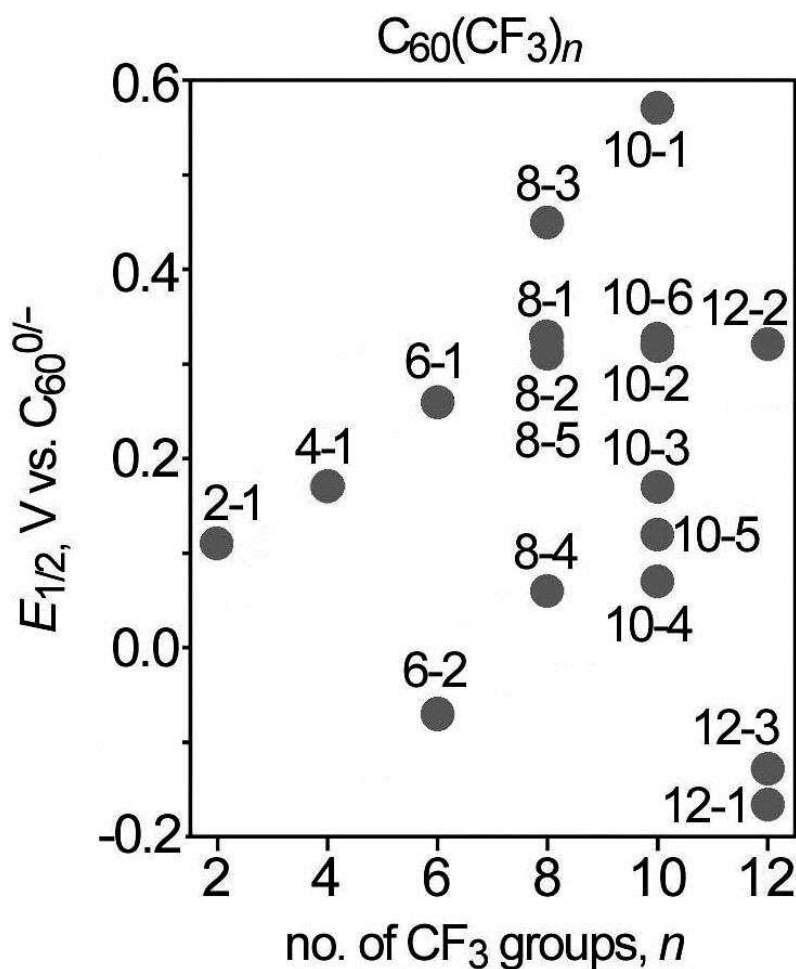


Figure 5.12. Experimental first reduction potentials (electrochemical $E_{1/2}(0/-)$ values) of 18 $C_{60}(CF_3)_n$ compounds with $n = 2$ (one isomer), 4 (one isomer), 6 (two isomers), 8 (five isomers), 10 (six isomers), and 12 (three isomers). This plot was redrawn using data published in ref 10. The sensitivity of $E_{1/2}^{(0/-)}$ to the addition pattern is underscored by the fact that three of these compounds, 60-6-2, 60-12-1, and 60-12-3, are *harder* to reduce than C_{60} itself, including two compounds with 12 strongly-electron-withdrawing CF_3 groups. This plot does not include $E_{1/2}^{(0/-)}$ values for the six new $C_{60}(CF_3)_{10}$ isomers. Those values are listed in Table 5-4.

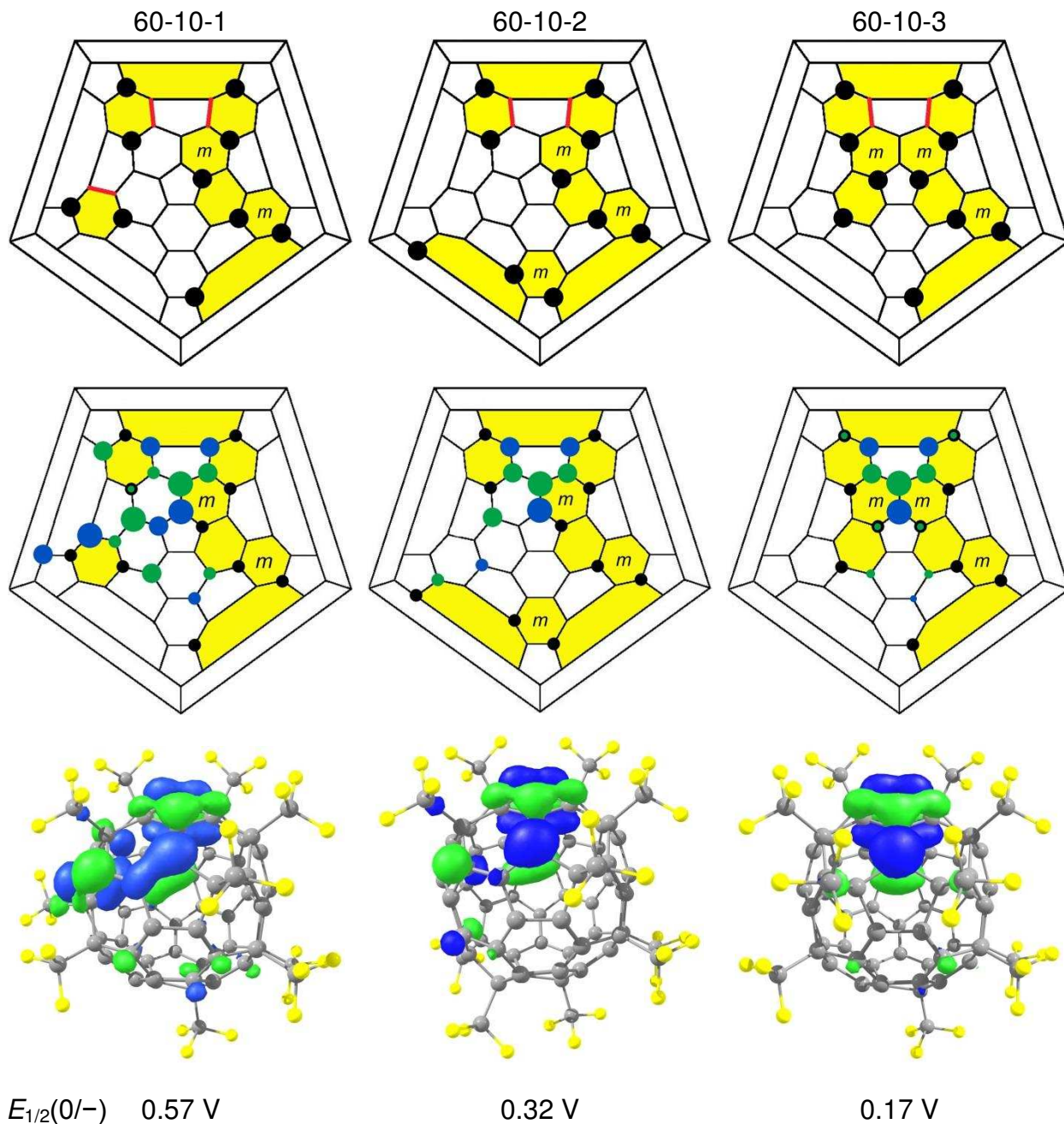


Figure 5.13. Schlegel and LUMO diagrams showing the *nt*-DBIPs (highlighted in red) and the DFT-predicted cage C atom contributions to the LUMOs for 60-10-1, 60-10-2, and 60-10-3. The black circles in the Schlegel diagrams indicate cage C atoms to which the CF₃ groups are attached. The blue (+) and green (-) circles represent the upper lobes of the π atomic orbitals for each cage C atom scaled approximately to its contribution to the LUMO. The $E_{1/2}^{(0/-)}$ values shown are vs. C₆₀^{0/-} (0.1 M N(*n*-Bu)₄BF₄ in CH₂Cl₂; data from ref 10).

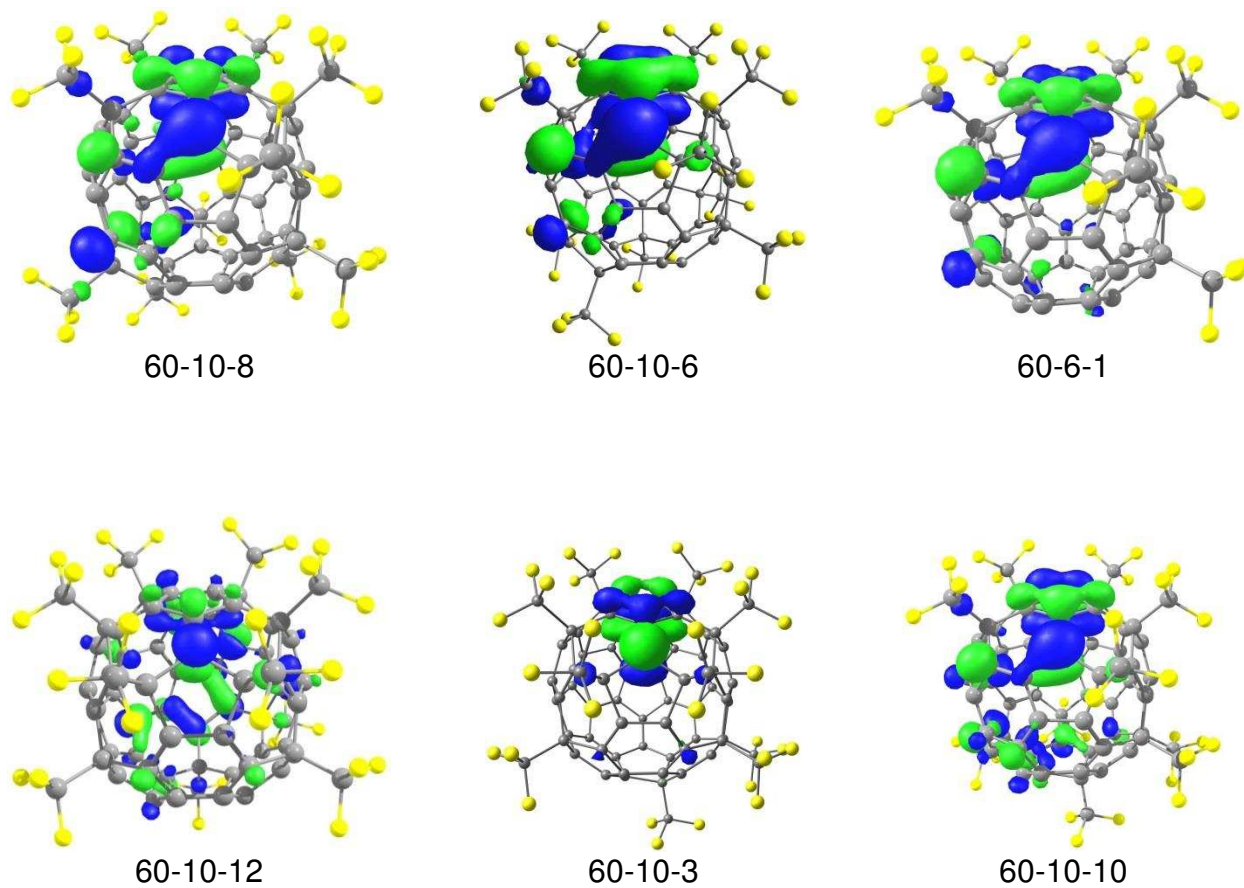


Figure 5-14. (Top) Comparison of the DFT-predicted LUMOs of new compound 60-10-8 with the previously reported compounds 60-10-12 and 60-6-1. (Bottom) Comparison of the DFT-predicted LUMOs of new compounds 60-10-12 and 60-10-10 with the previously reported compound 60-10-3. The LUMO diagrams were provided by Dr. Alexey A. Popov.

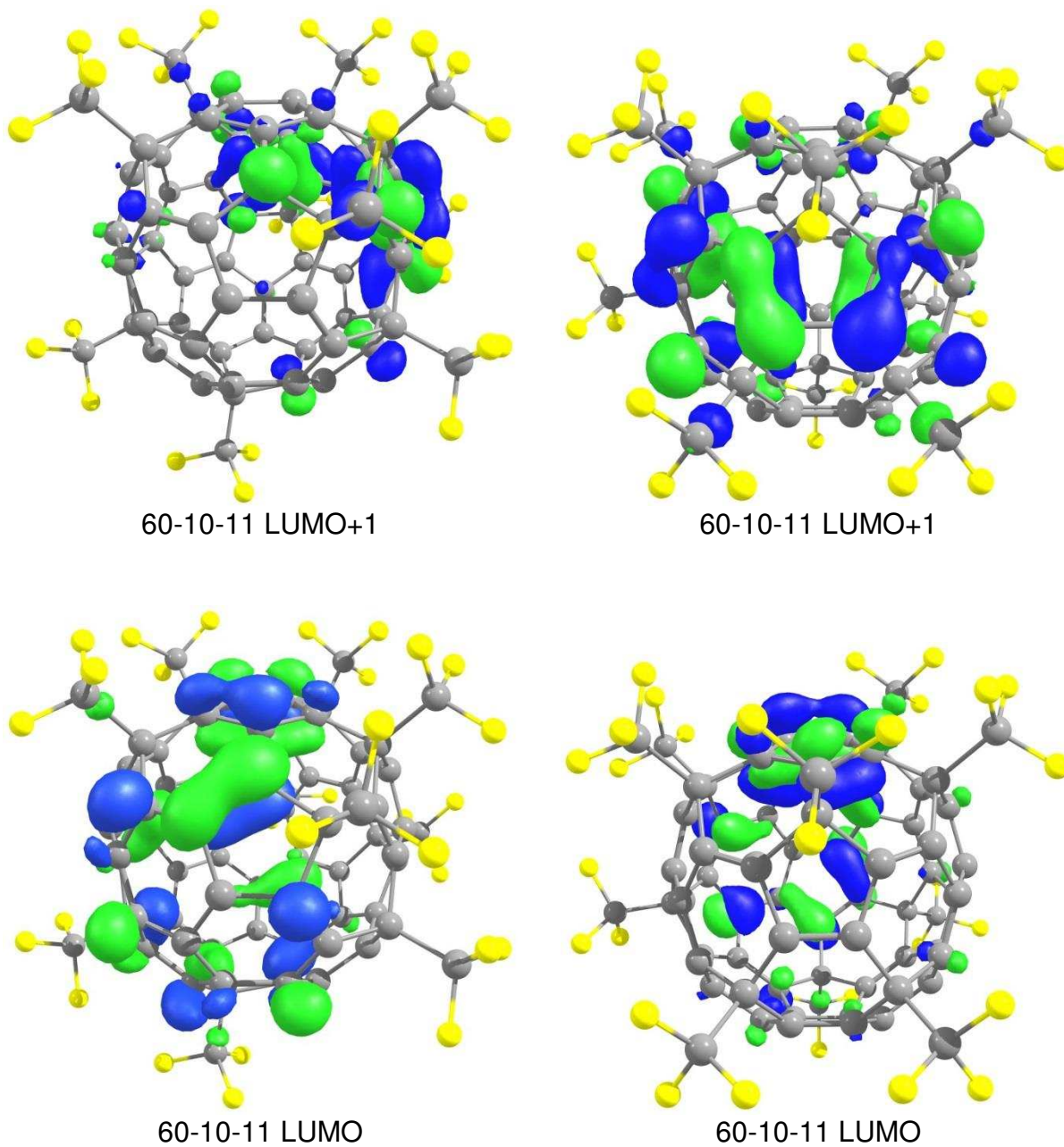


Figure 5-15. Drawings of two orientations of the LUMO and LUMO+1 for $C_{60}(CF_3)_{10}$ isomer 60-10-11. The LUMO diagrams were provided by Dr. Alexey A. Popov.

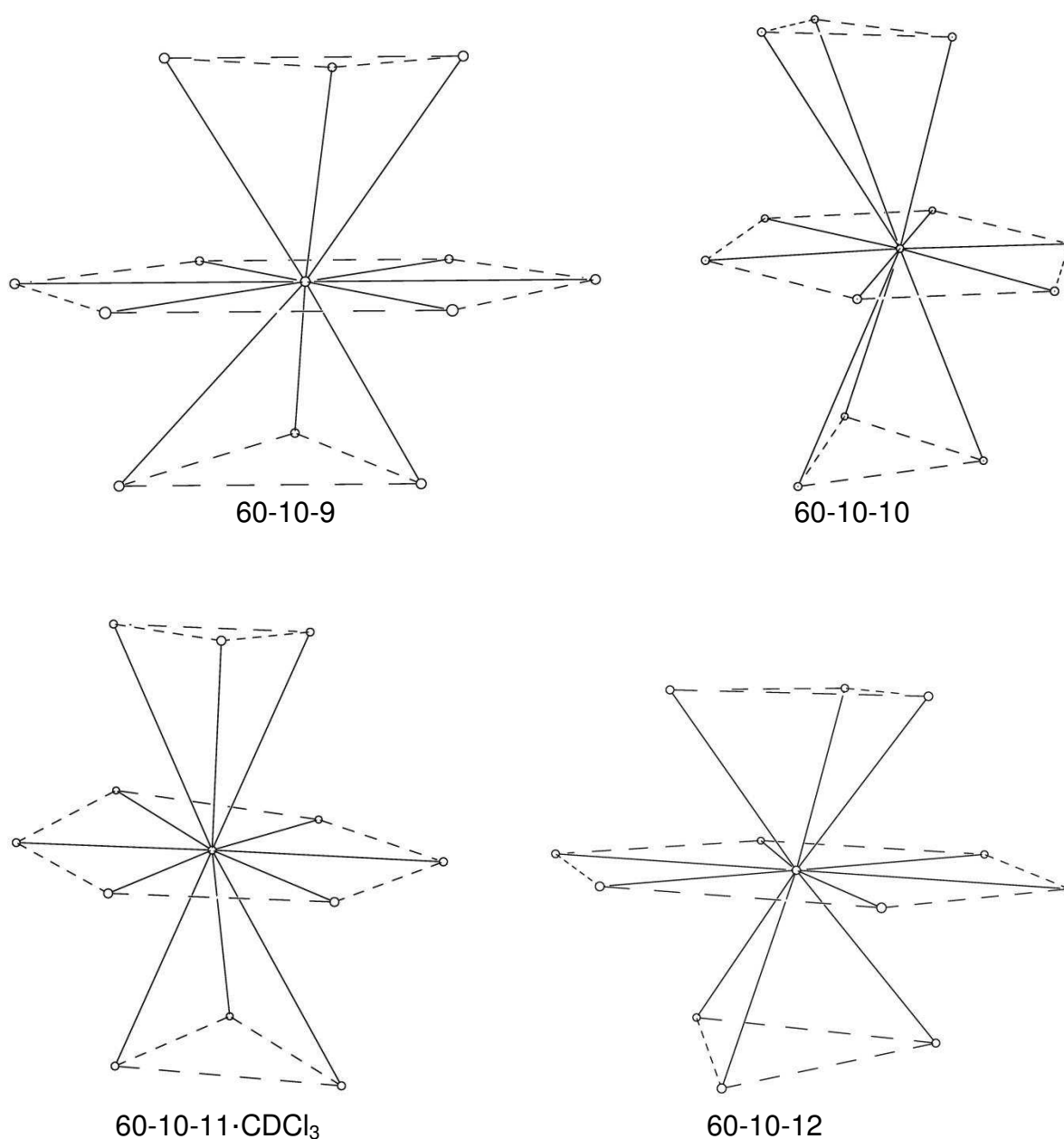


Figure 5-16. Molecular packing in the X-ray structures of four of the new 60-10 isomers. The fullerene centroids (\odot) are shown as spheres of arbitrary size. The CDCl₃ solvent molecules in the structure of 60-10-11·CDCl₃ have been omitted for clarity. The packing pattern for 60-10-12 is cubic close-packed. The packing patterns for the other three structures are hexagonal close-packed. The ranges of $\odot \cdots \odot$ distances are listed in Table 5-3.

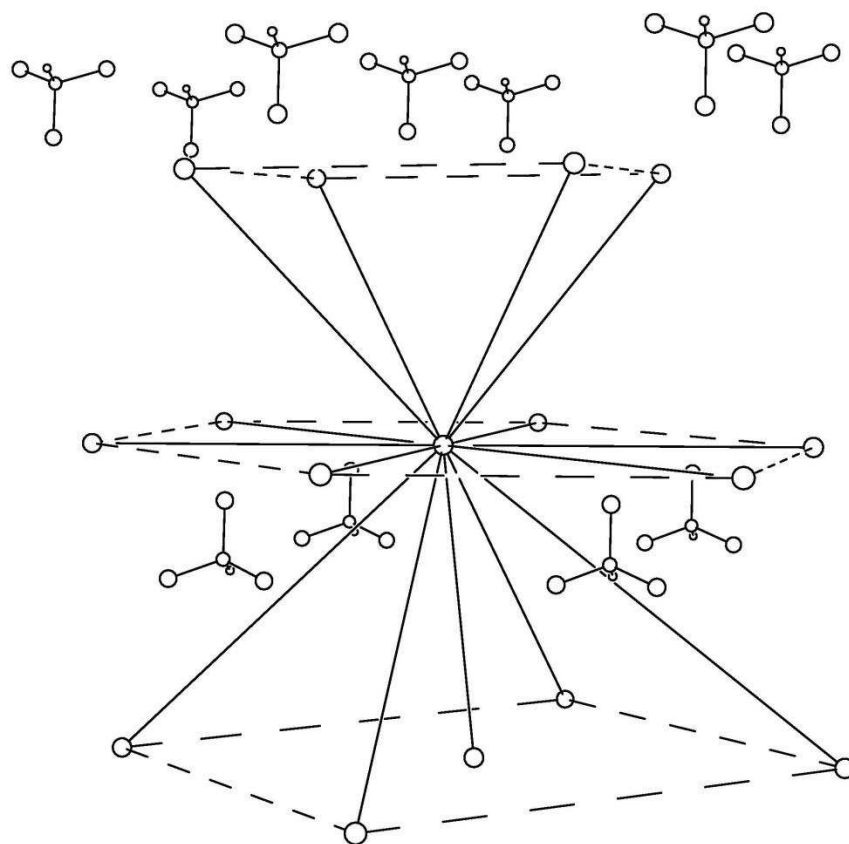


Figure 5-17. Molecular packing pattern for the X-ray structure of 60-10-8-CHCl₃. The fullerene centroids (⊙) are shown as spheres of arbitrary size. Also shown are 11 molecules of CHCl₃. The shortest ⊙⋯⊙ distance, depicted as a nearly vertical solid line, is 9.852 Å. The other 14 ⊙⋯⊙ distances shown as solid lines span the range 11.271–16.009 Å.

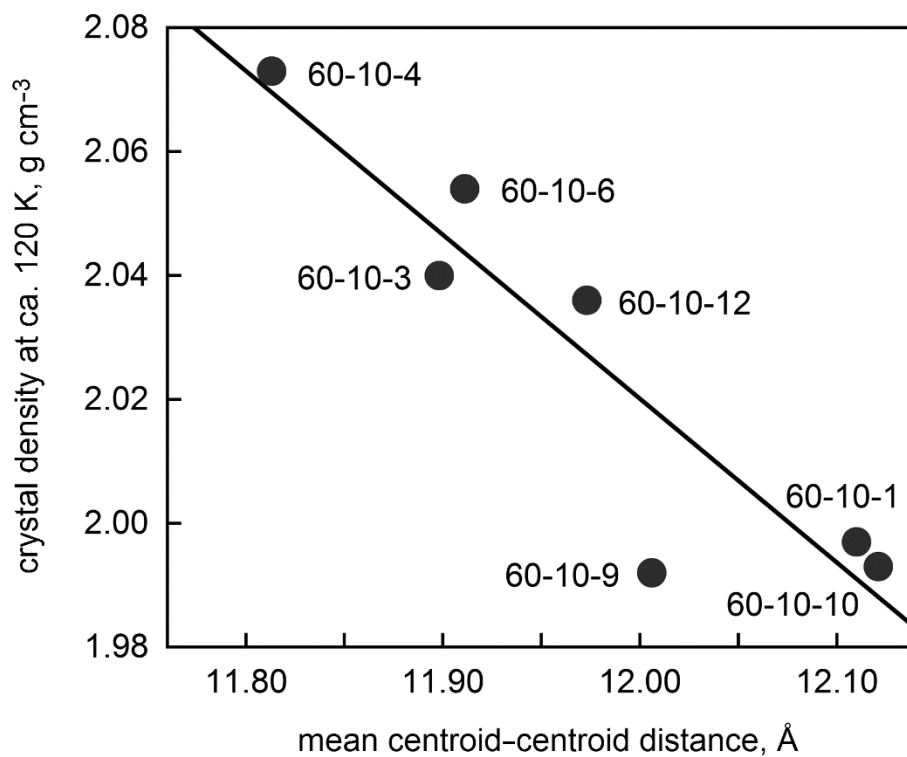


Figure 5-18. Graph showing the approximately linear correlation of crystal density of solvent-free close-packed structures vs. the mean centroid-centroid distance for seven 60-10 X-ray structures. The data for all seven structures were collected at ca. 120 K (110 ± 10 K). The structures of 60-10-3, 60-10-4, and 60-10-6 were reported in refs 1, 11, and 15, respectively.

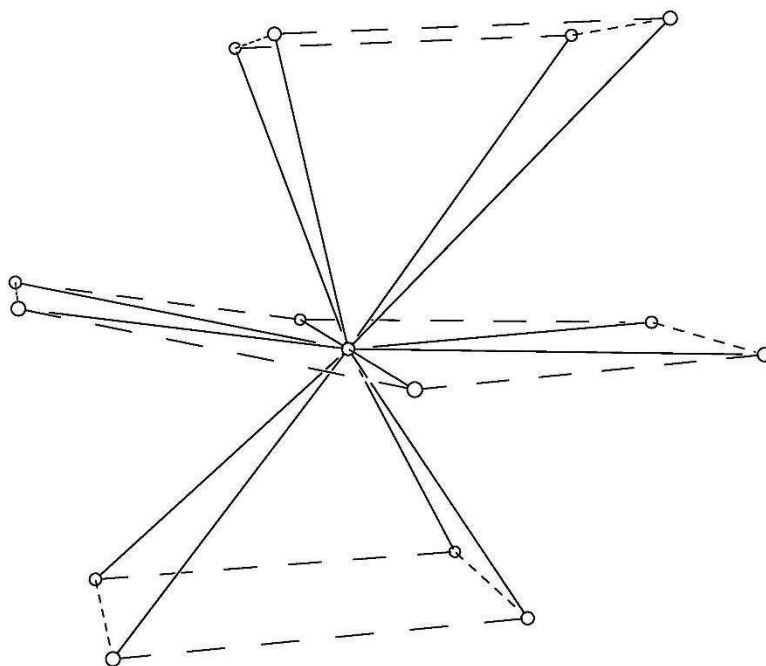


Figure 5-19. Molecular packing in the X-ray structure of 60-10-13. The fullerene centroids (\odot) are shown as spheres of arbitrary size. The range of the $\odot \cdots \odot$ distances shown as 14 solid lines is 10.126–14.414 Å. Even though the molecular packing for 60-10-13 is not close-packed, its density (2.004 g cm^{-3}) is ca. 0.6% higher than the densities of 60-10-9 and 60-10-10, which are close-packed (1.992 and 1.993 g cm^{-3} , respectively).

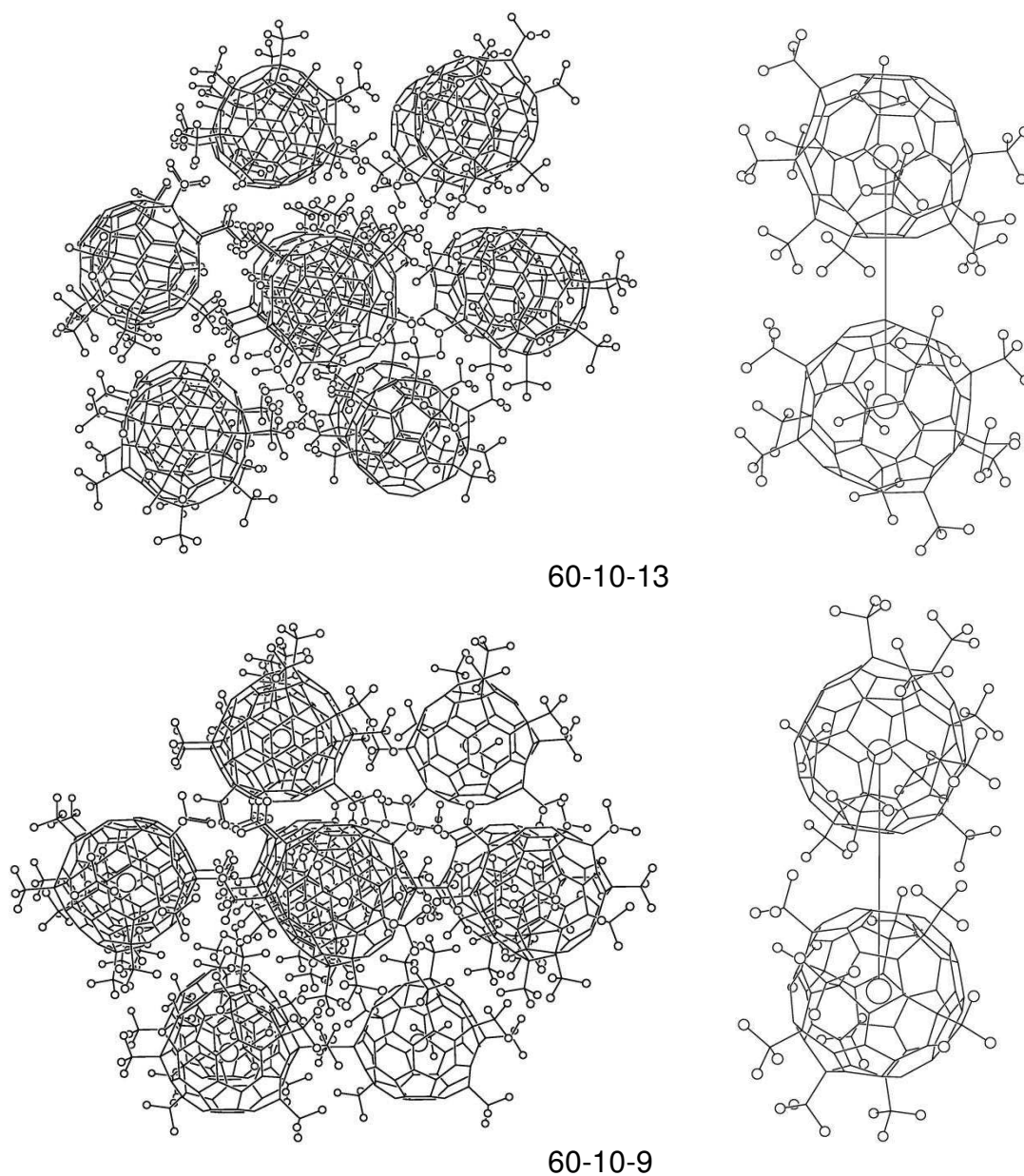


Figure 5-20. Packing of 60-10 molecules in the X-ray structures of 60-10-13 (top) and 60-10-9 (bottom). Only the F atoms and fullerene centroids (\odot) are shown as spheres of arbitrary size (small and large, respectively). The interactions of CF_3 groups on neighboring molecules prevents close π - π interactions in all cases in the structure of 60-10-13 and in all but one case in 60-10-9. Pairs of molecules with the shortest $\odot \cdots \odot$ distance in each structure are also shown ($\odot \cdots \odot = 10.126 \text{ \AA}$ for 60-10-13 and 9.703 \AA for 60-10-9). Note that the pair of neighboring molecules shown for 60-10-9 have an overlapping and rigorously parallel hexagon-hexagon π - π interaction with an interplanar spacing of $3.24 \pm 0.02 \text{ \AA}$.

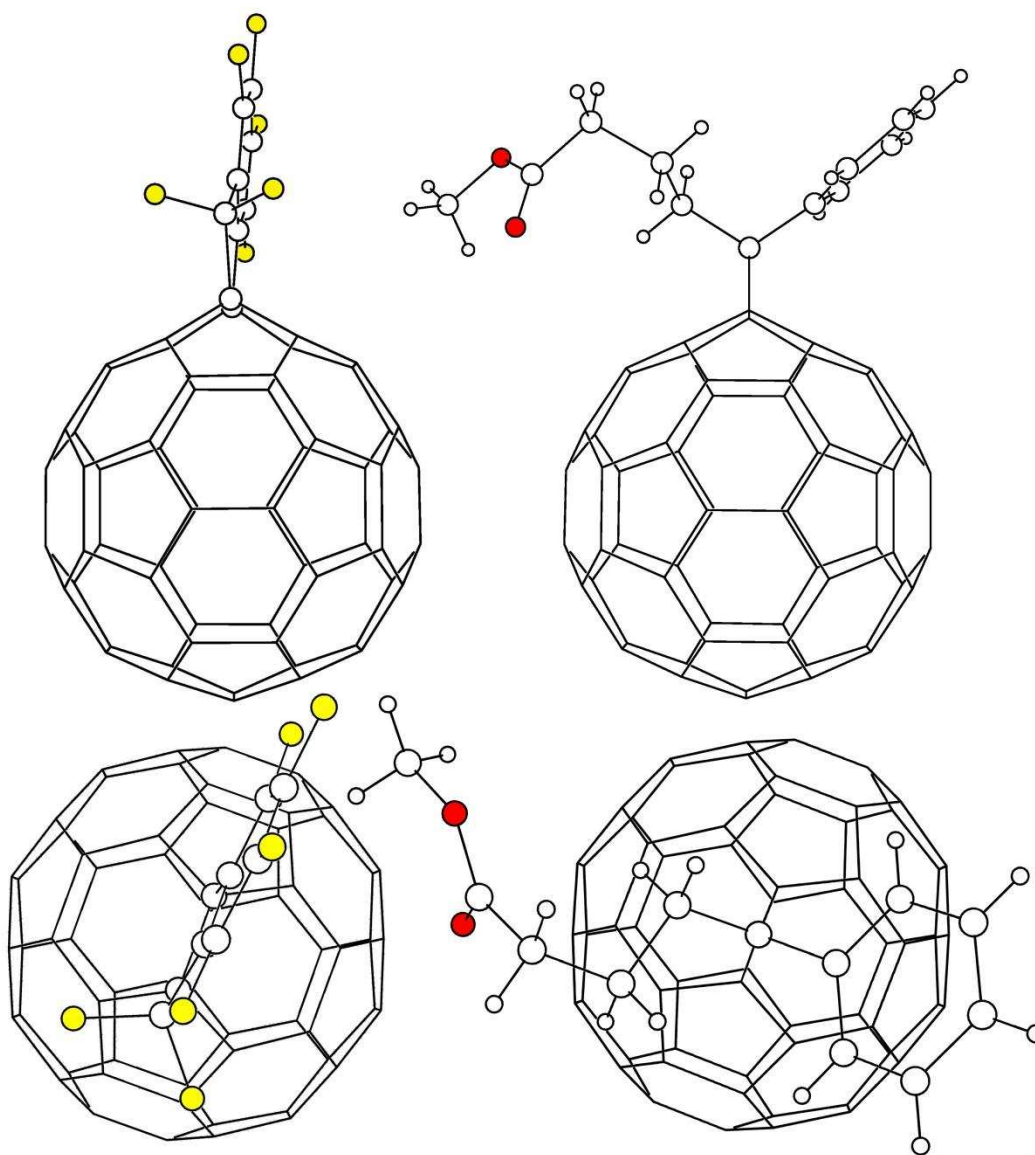


Figure 5-21. Comparison of the molecular structures of the faux hawk fullerene 1,9-C₆₀(*cyclo*-CF₂(2-C₆F₄)) (left, this work) and PCBM (right, ref 21). The large and small white spheres represent C and H atoms, respectively; the red and yellow spheres represent O and F atoms, respectively. The fullerene cages and the substituent atoms in the two structures are scaled equally.

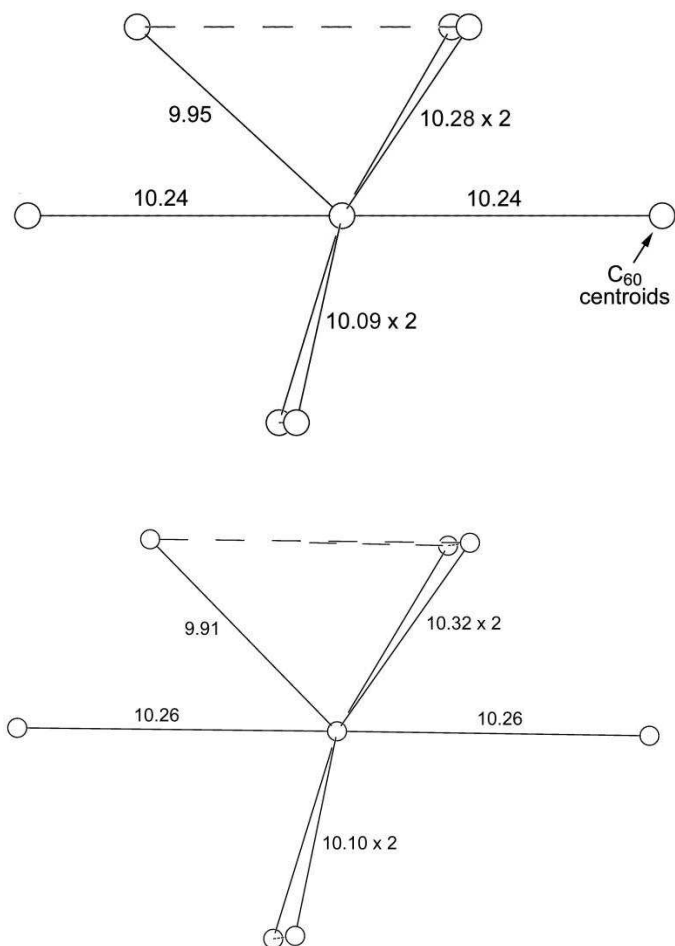


Figure 5-22. Comparison of the nearest-neighbor centroid packing patterns in the single-crystal X-ray structure (top; data collected at 100 K; ref 21) and the powder X-ray diffraction structure (bottom; data collected at 300 K; ref 22) of solvent-free PCBM (PCBM = phenyl-C₆₁-butyric acid methyl ester). The averages of the seven nearest-neighbor distances are 10.17 (top) and 10.18 Å (bottom).

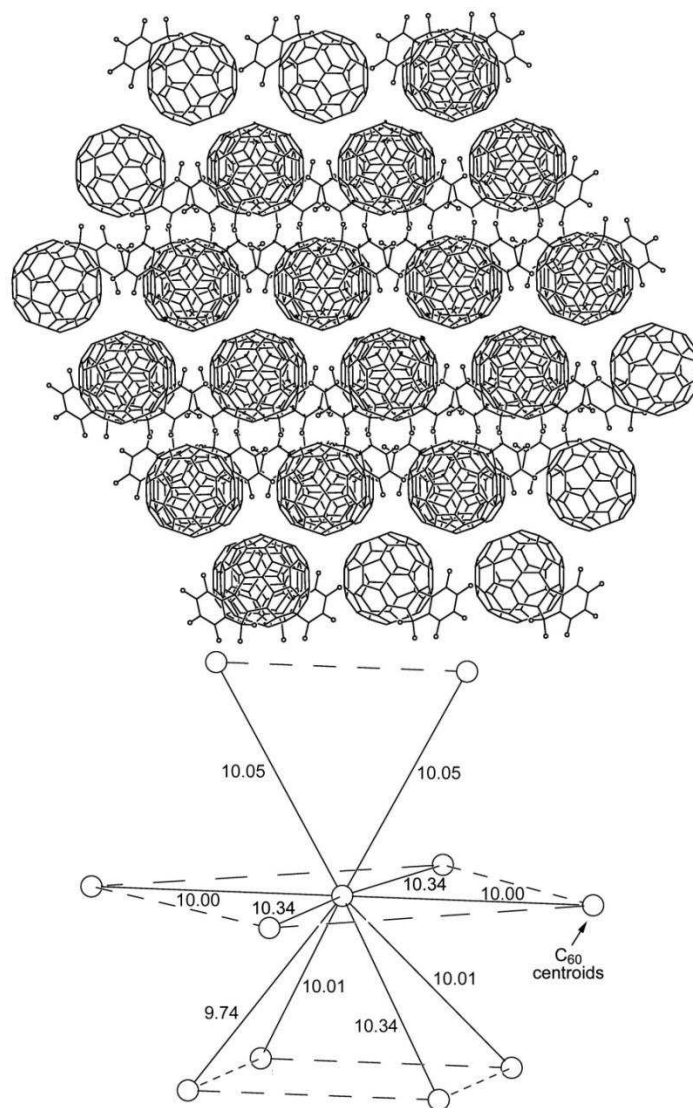


Figure 5-23. The packing of molecules of the faux hawk fullerene determined by single-crystal X-ray diffraction. The molecules are arranged in layers with rigorously co-planar C₆₀ cage centroids. The layers are stacked in the direction parallel to the long axis of the page, which in this case is parallel to the crystallographic *c* axis. Each faux hawk fullerene molecule is surrounded by 10 nearest neighbor molecules with C₆₀ centroid···centroid distances that range from 9.74 to 10.34 Å (avg 10.09 Å). The lower centroid diagram is only slightly turned and tilted from the orientation of molecules in the upper packing diagram for clarity.

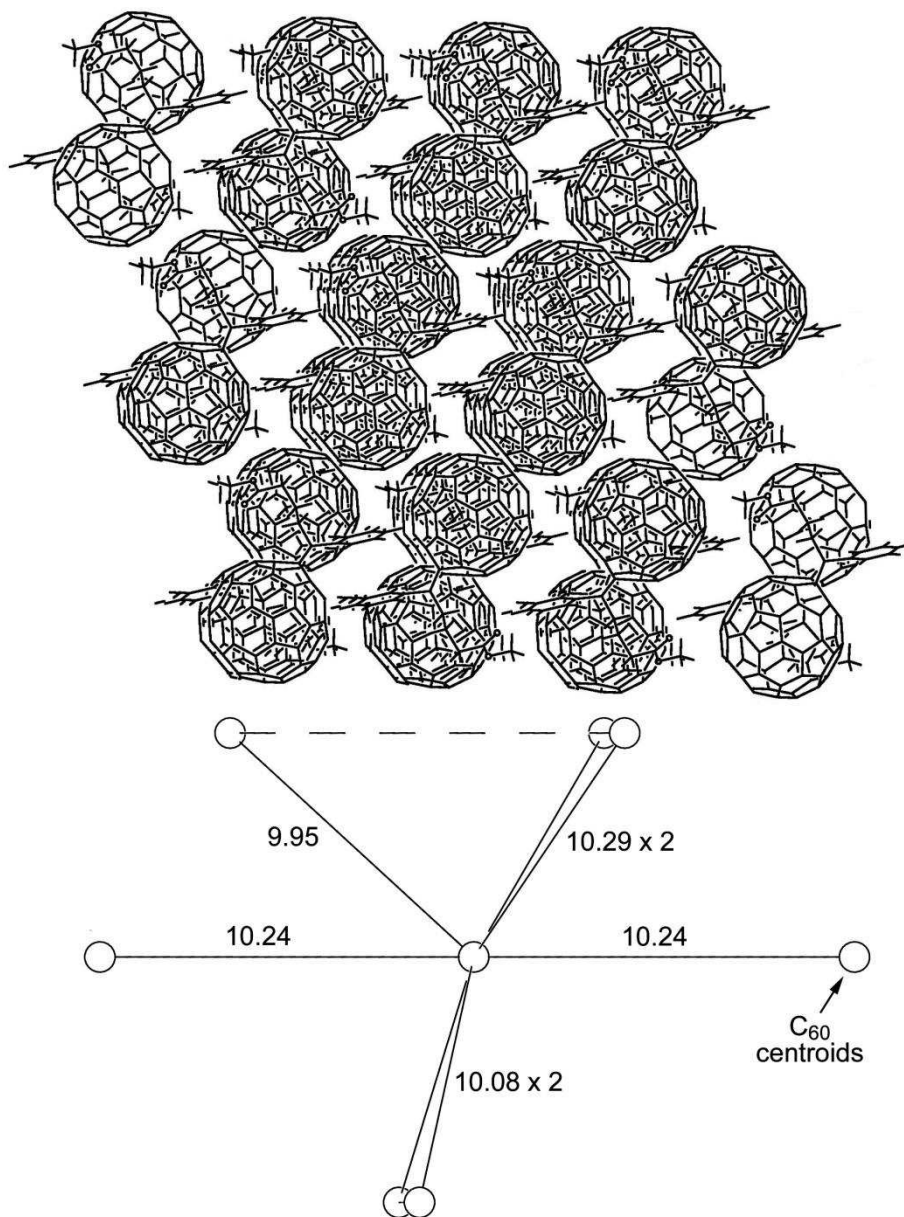


Figure 5-24. The packing of molecules of PCBM in the solvent-free structure determined by single-crystal X-ray diffraction. The molecules are arranged in layers with rigorously co-planar C₆₀ cage centroids. The layers are stacked in the direction parallel to the long axis of the page. Each PCBM molecule is surrounded by 7 nearest neighbor molecules with centroid···centroid distances that range from 9.95 to 10.28 Å (avg. 10.17 Å). The orientations of the centroids in the lower diagram and the molecules in the upper packing diagram are the same.

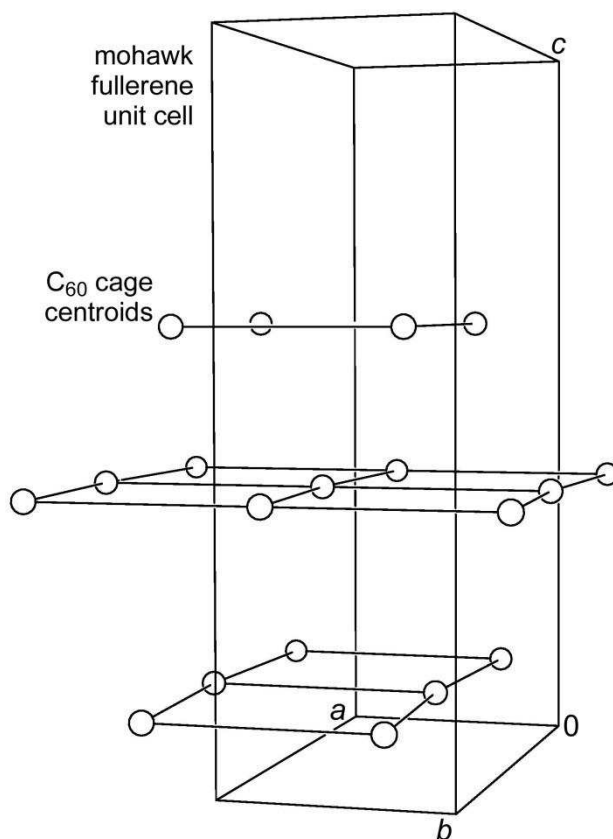


Figure 5-25. Unit cell and packing pattern of the C_{60} cage centroids in the crystal structure of the faux hawk fullerene $1,9-C_{60}(\text{cyclo-}CF_2(2-C_6F_4))$. The rigorously planar, approximately square arrays of centroids are stacked along the crystallographic c axis.

Tables 5.6

Table 5-1. Previously Known and New C₆₀(CF₃)₁₀ Compounds^a

| abbreviation ^b | addition-pattern ^c | IUPAC lowest locants ^d | synthesis and isolation ref | X-ray ref | ¹⁹ F NMR ref | DFT predictions ^e | |
|---------------------------|--|-----------------------------------|-----------------------------|-----------|-------------------------|-----------------------------------|---------------------|
| | | | | | | rel. energy, kJ mol ⁻¹ | <i>E</i> (LUMO), eV |
| 60-10-1 | <i>C</i> ₁ - <i>p</i> ³ <i>mpmp</i> , <i>p</i> | 1,6,11,16,18,24,27,36,41,57 | 1 | t.w. | 1 | 9.22 | -5.129 |
| 60-10-2 | <i>C</i> ₁ - <i>p</i> ³ <i>mpmpmp</i> | 1,6,11,16,18,24,27,36,54,60 | 1 | 12 | 1 | 0.06 | -4.894 |
| 60-10-3 | <i>C</i> ₁ - <i>pmp</i> ³ <i>mpmp</i> | 1,3,7,10,14,17,23,28,31,40 | 1 | 1 | 1 | 4.56 | -4.754 |
| 60-10-4 | <i>C</i> ₂ -(<i>p</i> ³ <i>m</i> ² -loop) ² | 1,6,12,15,18,23,25,41,45,57 | 10 | 11 | 10 | 7.60 | -4.529 |
| 60-10-5 | <i>C</i> ₁ - <i>pmpmpmpmpmp</i> | 1,6,11,16,18,26,36,41,44,57 | 10 | 10 | 10 | 1.25 | -4.638 |
| 60-10-6 | <i>C</i> ₁ - <i>p</i> ³ <i>mp</i> , <i>pmp</i> | 1,6,11,18,24,27,33,51,54,60 | 10 | 15 | 10 | 0.00 | -4.922 |
| 60-10-8 | <i>C</i> ₁ - <i>p</i> ³ <i>mp</i> , <i>pmp</i> | 1,6,11,16,18,28,31,36,44,58 | 8 | t.w. | 8 | 16.03 | -4.983 |
| 60-10-9 | <i>C</i> ₁ - <i>pmpmpmpmp</i> , <i>p</i> | 1,6,11,18,24,27,34,50,52,55 | 8 | t.w. | 8 | 17.36 | -4.829 |
| 60-10-10 | <i>C</i> ₁ - <i>p</i> ³ <i>mpmp</i> , <i>p</i> | 1,6,11,16,18,24,27,36,50,60 | 8 | t.w. | 8 | 20.55 | -4.924 |
| 60-10-11 | <i>C</i> ₁ - <i>p</i> ³ <i>mp</i> , <i>p</i> , <i>p</i> | 1,6,11,14,18,24,27,31,53,56 | 8 | t.w. | 8 | 29.60 | -5.090 |
| 60-10-12 | <i>C</i> ₁ - <i>pmp</i> ³ <i>mp</i> , <i>p</i> | 1,3,7,10,14,17,28,31,43,55 | 8 | t.w. | 8 | 15.41 | -4.867 |
| 60-10-13 | <i>C</i> ₁ - <i>pmpmpmpmp</i> , <i>p</i> | 1,6,11,16,18,26,36,44,47,59 | 8 | t.w. | 8 | 18.46 | -4.938 |

^a The previously known isomers of C₆₀(CF₃)₁₀ are 60-10-1 through 60-10-6; t.w. = this work. ^b The first part of the abbreviation refers to the fullerene, C₆₀. The second part refers to the number of CF₃ groups. The third part is an arbitrary isomer number or letter. ^c The addition pattern abbreviations refer to a ribbon of edge-sharing *meta*- (*m*) and *para* (*p*) C₆(CF₃)₂ hexagons (each shared edge is a C(sp³)-C(sp²) bond). ^d According to the Schlegel diagram shown in Figure 5-1 (see references 13,14 for IUPAC-approved nomenclature rules for C₆₀ and C₇₀ compounds). ^e The DFT results were obtained by the Strauss-Boltalina Group DFT collaborator Dr. Alexey A. Popov. The methodology he used for these calculations is described in many Popov, Boltalina, Strauss, et al. publications, including refs 5 and 9..

Table 5-2. Crystal data, structure refinement parameters, density, and fullerene centroid...centroid ($\odot \cdots \odot$) distances for faux hawk fullerene and 60-10-1.^a

| compound abbreviation | faux hawk fullerene ^a | 60-10-1 ^a |
|--|----------------------------------|-----------------------------|
| crystal system | orthorhombic | triclinic |
| space group, <i>Z</i> | <i>Pbca</i> , 8 | $P\bar{1}$, 4 ^a |
| <i>a</i> , (Å) | 9.9998(6) | 12.2718(6) |
| <i>b</i> , (Å) | 20.6538(12) | 20.2702(11) |
| <i>c</i> , (Å) | 31.3512(2) | 21.0715(11) |
| α , (deg) | 90 | 113.4700(10) |
| β , (deg) | 90 | 101.5240(10) |
| γ , (deg) | 90 | 90.0410(10) |
| <i>V</i> , (Å ³) | 6475.1(7) | 4692.2(4) |
| ρ_{calc} (g cm ⁻³) | 1.885 | 1.997 |
| <i>T</i> , (K) | 15(2) | 100(2) |
| <i>R</i> (<i>F</i>) (<i>I</i> > 2 σ (<i>I</i>)) ^b | 0.0732, | 0.0567, |
| <i>wR</i> (<i>F</i> ²) [all data] ^b | 0.1633 | 0.1420 |
| GOF | 1.121 | 1.002 |
| close-packed lattice? | not close-packed | not close-packed |
| $\odot \cdots \odot$ distances, (Å) | 9.74–10.34 | 9.703–13.741 |
| mean $\odot \cdots \odot$ distance, [Å (σ)] | 10.09 (0.20) | 12.006 (1.149) |
| median $\odot \cdots \odot$ distance, (Å) | 10.03 | 12.144 |

^a The chemical formula and formula weight for the faux hawk fullerene (FHF) are C₇₀F₃₀ (i.e., 1,9-C₆₀(*cyclo*-CF₂(2-C₆F₄))) and 1410.70 g mol⁻¹, respectively; The chemical formula and formula weight for 60-10-1 are C₇₀F₃₀ (i.e., 1,6,11,16,18,24,27,36,41,57-C₆₀(CF₃)₁₀; *pmpmpmp,p*-C₆₀(CF₃)₁₀) and 1410.70 g mol⁻¹, although the asymmetric unit contains two independent 60-10-1 molecules. ^b $R(F) = \Sigma||F_o| - |F_c|| / \Sigma|F_o|$; $wR(F^2) = (\Sigma[w(F_o^2 - F_c^2)^2] / \Sigma[w(F_o^2)^2])^{1/2}$

Table 5-3. Crystal data, structure refinement parameters, density, and fullerene centroid...centroid ($\odot \cdots \odot$) distances for new $C_{60}(CF_3)_{10}$ isomers^a

| compound abbreviation ^b | 60-10-8·CHCl ₃ | 60-10-9 | 60-10-10 | 60-10-11·CDCl ₃ | 60-10-12 | 60-10-13 |
|---|---------------------------|----------------|----------------|----------------------------|----------------|------------------|
| crystal system | triclinic | triclinic | monoclinic | triclinic | monoclinic | orthorhombic |
| space group, <i>Z</i> | $P\bar{1}$, 2 | $P\bar{1}$, 2 | $C2/c$, 8 | $P2_1/c$, 4 | $P2_1/n$, 4 | $P2_12_12_1$, 4 |
| <i>a</i> , (Å) | 11.532(1) | 12.1441(6) | 46.403(6) | 12.253(1) | 17.794(1) | 11.525(1) |
| <i>b</i> , (Å) | 12.088(1) | 12.3855(7) | 12.115(2) | 24.771(3) | 13.1545(8) | 19.760(2) |
| <i>c</i> , (Å) | 19.854(2) | 17.3822(9) | 17.249(3) | 17.001(2) | 20.108(1) | 20.527(2) |
| α , (deg) | 72.791(4) | 93.614(3) | 90 | 90 | 90 | 90 |
| β , (deg) | 74.569(5) | 96.249(3) | 104.164(7) | 106.035(3) | 102.099(2) | 90 |
| γ , (deg) | 85.305(5) | 114.298(2) | 90 | 90 | 90 | 90 |
| <i>V</i> , (Å ³) | 2548.3(4) | 2351.9(2) | 9402(2) | 4959.2(8) | 4602.0(5) | 4674.6(9) |
| ρ_{calc} (g cm ⁻³) | 1.994 | 1.992 | 1.993 | 2.051 | 2.036 | 2.004 |
| <i>T</i> , (K) | 120(2) | 120(2) | 120(2) | 100(2) | 100(2) | 120(2) |
| <i>R</i> (<i>F</i>) (<i>I</i> > 2σ(<i>I</i>)) ^c | 0.0628 | 0.0520 | 0.0458 | 0.0716 | 0.0445 | 0.0401 |
| <i>wR</i> (<i>F</i> ²) [all data] ^c | 0.2285 | 0.1556 | 0.1436 | 0.2217 | 0.1123 | 0.1038 |
| GOF | 0.975 | 1.036 | 1.057 | 0.985 | 1.017 | 1.028 |
| idealized lattice packing | not close-packed | HCP | HCP | HCP | CCP | not close-packed |
| $\odot \cdots \odot$ distances, (Å) | 9.852–16.009 | 9.703–13.741 | 10.073–14.346 | 10.078–14.661 | 10.203–13.958 | 10.126–14.414 |
| mean $\odot \cdots \odot$ distance, [Å (σ)] | 13.232 (2.110) | 12.006 (1.149) | 12.121 (1.465) | 12.244 (1.268) | 11.973 (1.353) | 12.455 |
| median $\odot \cdots \odot$ distance, (Å) | 12.198 | 12.144 | 12.115 | 12.327 | 11.953 | 11.881 |

^a Except for 60-10-8·CHCl₃ and 60-10-11·CDCl₃, the chemical formulas and formula weights are C₇₀F₃₀ and 1410.70 g mol⁻¹, respectively. For 60-10-8·CHCl₃, the chemical formula is C₇₀HCl₃F₃₀ and the formula weight is 1530.07 g mol⁻¹. For 60-10-11·CDCl₃, the chemical formula is C₇₀Cl₃DF₃₀ and the formula weight is 1531.07 g mol⁻¹. ^b See Table 5-1 and Figures 5-3 and 5-4 for IUPAC lowest locants and Schlegel diagrams, respectively, for these compounds. ^c HCP = hexagonal close-packed; CCP = cubic close-packed. ^c $R(F) = \Sigma||F_o| - |F_c|| / \Sigma|F_o|$; $wR(F^2) = (\Sigma[w(F_o^2 - F_c^2)^2] / \Sigma[w(F_o^2)^2])^{1/2}$

Table 5-4. First Reduction Potentials, Gas-Phase Electron Affinities, and DFT-Predicted LUMO Energies for C₆₀(CF₃)₁₀ Isomers^a

| compound | $E_{1/2}(0/-)$, V vs. C ₆₀ ^{0/-} | DFT $E(\text{LUMO})$, eV |
|-----------------|---|---------------------------|
| C ₆₀ | 0.00 | -4.379 |
| 60-10-1 | 0.65 | -5.129 |
| 60-10-2 | 0.38 | -4.894 |
| 60-10-3 | 0.16 | -4.754 |
| 60-10-4 | — | -4.529 |
| 60-10-5 | 0.12 | -4.638 |
| 60-10-6 | 0.41 | -4.922 |
| 60-10-8 | 0.47 | -4.983 |
| 60-10-9 | — | -4.867 |
| 60-10-10 | — | -4.938 |
| 60-10-11 | — | -4.867 |
| 60-10-12 | 0.37 | -4.938 |
| 60-10-13 | 0.42 | -4.938 |

^a The $E_{1/2}(0/-)$ values were determined by cyclic voltammetry by Strauss-Boltalina Ph.D. student Bryon W. Larson.⁸ Uncertainties are ± 0.01 V. Several compounds have not been studied as of this writing. The DFT $E(\text{LUMO})$ values were calculated by Dr. Alexey A. Popov and are also listed in Table 5-1.

Table 5-5. Interatomic distances (Å) and angles (deg) for the X-ray and DFT-optimized structures of the faux hawk fullerene 1,9-C₆₀(*cyclo*-CF₂(2-C₆F₄))

| parameter | X-ray | DFT |
|-----------|--------------------|-----------|
| C1–C9 | 1.610(5) | 1.608 |
| C1–C2 | 1.538(6) | 1.531 |
| C2–C7 | 1.374(6) | 1.395 |
| C7–C8 | 1.482(5) | 1.496 |
| C8–C9 | 1.572(5) | 1.587 |
| F1···F6 | 2.997(6) | 3.088 |
| F2···F6 | 3.151(6) | 3.088 |
| C2–C1–C9 | 102.6(3) | 103.6 |
| C2–C1–C | 109.5(3); 115.8(3) | 114.3 × 2 |
| C8–C9–C1 | 105.2(3) | 105.5 |
| C8–C9–C | 109.2(3); 113.6(3) | 114.5 × 2 |
| C1–C2–C7 | 113.0(3) | 112.9 |
| C2–C7–C6 | 121.4(4) | 121.8 |
| C2–C7–C8 | 111.7(4) | 111.6 |
| C7–C8–C9 | 106.4(3) | 106.4 |

Chapter 5 References

- (1) Kareev, I. E.; Kuvychko, I. V.; Lebedkin, S. F.; Miller, S. M.; Anderson, O. P.; Seppelt, K.; Strauss-Boltalina, S. H.; Boltalina, O. V.: Synthesis, Structure, and ^{19}F NMR Spectra of 1,3,7,10,14,17,23,28,31,40- $\text{C}_{60}(\text{CF}_3)_{10}$. *J. Am. Chem. Soc.* **2005**, *127*, 8362-8375.
- (2) Boltalina, O. V.; Popov, A. A.; Kuvychko, I. V.; Shustova, N. B.; Strauss-Boltalina, S. H.: Perfluoroalkylfullerenes. *Chem. Rev.* **2015**, *115*, 1051-1105.
- (3) Kupitz, Y. S.: On the existence of a combinatorial Schlegel diagram of a simplicial unstacked 3-polytope with a prescribed set of vertices. *Discrete Math.* **1993**, *120*, 121-134.
- (4) Heimann, R. B.: The use of Schlegel maps to describe dissolution features on crystals. *J. Mater. Sci. Lett.* **1995**, *14*, 811-812.
- (5) Boltalina, O. V.; Kuvychko, I. V.; Shustova, N. B.; Strauss-Boltalina, S. H.: Perfluoroalkylation of Fullerenes. In *Handbook of Carbon Nanomaterials, Volume 1, Syntheses and Supramolecular Systems*; Desouza, F., Kadish, K. M., Ed.; World Scientific: Singapore, 2011; pp 101-143 and references therein.
- (6) Darwish, A. D.; Avent, A. G.; Abdul-Sada, A. K.; Taylor, R.: [60]- and [70]Fullerenes are trifluoromethylated across 5:6-bonds. *Chem. Commun.* **2003**, 1374-1375.
- (7) Darwish, A. D.; Abdul-Sada, A. K.; Avent, A. G.; Martsinovich, N.; Street, J. M.; Taylor, R.: Novel addition in trifluoromethylation of [70]fullerene. *J. Fluorine Chem.* **2004**, *125*, 1383-1391.
- (8) Larson, B. W., Colorado State University, 2015.
- (9) Kareev, I. E.; Popov, A. A.; Kuvychko, I. V.; Shustova, N. B.; Lebedkin, S. F.; Bubnov, V. P.; Anderson, O. P.; Seppelt, K.; Strauss-Boltalina, S. H.; Boltalina, O. V.: Synthesis and X-ray or NMR/DFT Structure Elucidation of Twenty-One New Trifluoromethyl Derivatives of Soluble Cage Isomers of C_{76} , C_{78} , C_{84} , and C_{90} . *J. Am. Chem. Soc.* **2008**, *130*, 13471-13489.
- (10) Popov, A. A.; Kareev, I. E.; Shustova, N. B.; Stukalin, E. B.; Lebedkin, S. F.; Seppelt, K.; Strauss-Boltalina, S. H.; Boltalina, O. V.; Dunsch, L.: Electrochemical, Spectroscopic, and DFT Study of $\text{C}_{60}(\text{CF}_3)_n$ Frontier Orbitals ($n = 2-18$): The Link between Double Bonds in Pentagons and Reduction Potentials. *J. Am. Chem. Soc.* **2007**, *129*, 11551-11568.
- (11) Kareev, I. E.; Lebedkin, S. F.; Popov, A. A.; Miller, S. M.; Anderson, O. P.; Strauss-Boltalina, S. H.; Boltalina, O. V.: 1,6,12,15,18,23,25,41,45,57-Decakis(trifluoromethyl)-1,6,12,15,18,23,-25,41,45,57-decahydro($\text{C}_{60}\text{-I}_h$)[5,6]fullerene. *Acta Crystallogr.* **2006**, *E62*, o1501-o1503.
- (12) Kareev, I. E.; Lebedkin, S. F.; Miller, S. M.; Anderson, O. P.; Strauss-Boltalina, S. H.; Boltalina, O. V.: 1,6,11,16,18,26,36,44,48,58-Decakis(trifluoromethyl)-1,6,11,16,18,26,36,44,48,58-decahydro($\text{C}_{60}\text{-I}_h$)[5,6]fullerene benzene 2.5-solvate. *Acta Crystallogr.* **2006**, *E62*, o1498-o1500.
- (13) Cozzi, F.; Powell, W. H.; Thilgen, C.: Numbering of Fullerenes. *Pure Appl. Chem.* **2005**, *77*, 843-923.
- (14) Powell, W. H.; Cozzi, F.; Moss, G. P.; Thilgen, C.; Hwu, R. J. R.; Yerin, A.: Nomenclature for the $\text{C}_{60}\text{-I}_h$ and $\text{C}_{70}\text{-D}_{5h(6)}$ Fullerenes (IUPAC Recommendations 2002). *Pure Appl. Chem.* **2002**, *74*, 629-695.

- (15) Shustova, N. B.; Peryshkov, D. V.; Popov, A. A.; Boltalina, O. V.; Strauss-Boltalina, S. H.: 1,6,11,18,24,27,33,51,54,60-Decakis(trifluoromethyl)-1,6,11,18,24,27,33,51,54,60-decahydro-(C₆₀-Ih)[5,6]fullerene. *Acta Cryst.* **2007**, *E63*, o3129.
- (16) Fujita, S.: Soccerane Derivatives of Given Symmetries. *Bull. Chem. Soc. Japan* **1990**, *63*, 3215-3223.
- (17) Kadish, K. M.; Gao, X.; Gorelik, O.; Van Caemelbecke, E.; Suenobu, T.; Fukuzumi, S.: Electrogeneration and characterization of (C₆H₅CH₂)₂C-70. *J. Phys. Chem. A* **2000**, *104*, 2902-2907.
- (18) Paolucci, D.; Paolucci, F.; Marcaccio, M.; Carano, M.; Taylor, R.: Electrochemistry of perfluorinated fullerenes: the case of three isomers of C₆₀F₃₆. *Chem. Phys. Lett.* **2004**, *400*, 389-393.
- (19) Kadish, K. M.; Gao, X.; Caemelbecke, E. V.; Suenobu, T.; Fukuzumi, S.: Electrosynthesis and Structural Characterization of Two (C₆H₅CH₂)₄C₆₀ Isomers. *J. Am. Chem. Soc.* **2000**, *122*, 563-570.
- (20) San, L. K.: Strong Fullerene and Polycyclic Aromatic Hydrocarbon Electron Acceptors with Perfluorinated Substituents. Colorado State University, 2015.
- (21) Paternò, G.; Warren, A. J.; Spencer, J.; Evans, G.; García Sakai, V.; Blumberger, J.; Cacialli, F.: Micro-focused X-ray diffraction characterization of high-quality [6,6]-phenyl-C₆₁-butyric acid methyl ester single crystals without solvent impurities. *J. Mater. Chem.* **2013**, *1*, 5619-5623.
- (22) Casalegno, M.; Zanardi, S.; Frigerio, F.; Po, R.; Carbonera, C.; Marra, G.; Nicolini, T.; Raos, G.; Meille, S. V.: Solvent-free phenyl-C₆₁-butyric acid methyl ester (PCBM) from clathrates: insights for organic photovoltaics from crystal structures and molecular dynamics. *Chem. Commun.* **2013**, *49*, 4525-4527.
- (23) MacKenzie, R. C. I.; Frost, J. M.; Nelson, J.: A numerical study of mobility in thin films of fullerene derivatives. *J. Chem. Phys.* **2010**, *132*, 06904_1-6.
- (24) Cheung, D. L.; Troisi, A.: Theoretical Study of the Organic Photovoltaic Electron Acceptor PCBM: Morphology, Electronic Structure, and Charge Localization. *J. Phys. Chem. C* **2010**, *114*, 20479-20488.
- (25) Choi, J. H.; Honda, T.; Seki, S.; Fukuzumi, S.: Relationship between crystal packing and high electron mobility in the single crystal of thienyl-substituted methanofullerene. *Chem. Commun.* **2011**, *47*, 11213-11215.
- (26) Oberhofer, H.; Blumberger, J.: Revisiting electronic couplings and incoherent hopping models for electron transport in crystalline C₆₀ at ambient temperatures. *Phys. Chem. Chem. Phys.* **2012**, *14*, 13846-13852.
- (27) Nardes, A. M., Ferguson, A.J., Whitaker, J. B., Larson, B. W., Larsen, A. E., Maturová, K., Graf, P. A., Boltalina, O. V., Strauss-Boltalina S. H., Kopidakis N.: Beyond PCBM: Understanding the Photovoltaic Performance of Blends of Indene-C₆₀ Multiadducts with Poly(3-hexylthiophene). *Adv. Funct. Mater.* **2012**.
- (28) Gajdos, F.; Oberhofer, H.; Dupuis, M.; Blumberger, J.: On the Inapplicability of Electron-Hopping Models for the Organic Semiconductor Phenyl-C₆₁-butyric Acid Methyl Ester (PCBM). *J. Phys. Chem. Lett.* **2013**, *4*, 1012-1017.
- (29) Rispen, M. T.; Meetsma, A.; Rittberger, R.; Brabec, C. J.; Sariciftci, N. S.; Hummelen, J. C.: Influence of the solvent on the crystal structure of PCBM and the efficiency of MDMO-PPV:PCBM 'plastic' solar cells. *Chem. Commun.* **2003**, 2116-2118.

- (30) Tummala, N. R.; Mehraeen, S.; Fu, Y.-T.; Risko, C.; Brédas, J.-L.: Materials-Scale Implications of Solvent and Temperature on [6,6]-Phenyl-C₆₁-butyric Acid Methyl Ester (PCBM): A Theoretical Perspective. *Adv. Funct. Mater.* **2013**, *23*, 5800-5813.
- (31) Tassone, C. J.; Ayzner, A. L.; Kennedy, R. D.; Halim, M.; So, M.; Rubin, Y.; Tolbert, S. H.; Schwartz, B. J.: Using Pentaarylfullerenes to Understand Network Formation in Conjugated Polymer-Based Bulk-Heterojunction Solar Cells. *J. Phys. Chem. C* **2011**, *115*, 22564-22571.
- (32) Kennedy, R. D.; Halim, M.; Khan, S. I.; Schwartz, B. J.; Tolbert, S. H.; Rubin, Y.: Crystal-Packing Trends for a Series of 6,9,12,15,18-Pentaaryl-1-hydro[60]fullerenes. *Chem. Eur. J.* **2012**, *18*, 7418-7433.
- (33) Perdew, J. P.; Burke, K.; Ernzerhof, M.: Generalized Gradient Approximation Made Simple. *Phys. Rev. Lett.* **1996**, *77*, 3865-3868.
- (34) Laikov, D. N.: Fast Evaluation of Density Functional Exchange-Correlation Terms Using the Expansion of the Electron Density in Auxiliary Basis Sets. *Chem. Phys. Lett.* **1997**, *281*, 151-156.
- (35) Laikov, D. N.; Ustynuk, Y. A.: *Russ. Chem. Bull.* **2005**, *54*, 820.
- (36) Granovsky, A. A.: Firefly. v. 8.0.0 ed., 2013.
- (37) Schmidt, M. W.; Baldrige, K. K.; Boatz, J. A.; Elbert, S. T.; Gordon, M. S.; Jensen, J. H.; Koseki, S.; Matsunaga, N.; Nguyen, K. A.; Su, S. J.; Windus, T. L.; Dupuis, M.; Montgomery, J. A.: *J. Comput. Chem.* **1993**, *14*, 1347-1363.
- (38) Olmstead, M. M.; de Bettencourt-Dias, A.; Lee, H. M.; Pham, D.; Balch, A. L.: Interactions of metalloporphyrins as donors with the electron acceptors C60, tetracyanoquinomethane (TCNQ) and trinitrofluorenylidene malonitrile. *Dalton Trans.* **2003**, 3227-3232.
- (39) Fowler, P. W.; Manolopoulos, D. E.: *An Atlas of Fullerenes*; Dover: Mineola, NY, 2006.
- (40) Liu, S.; Lu, Y.-J.; Kappes, M.; Ibers, J. A.: The Structure of the C60 Molecule: X-Ray Crystal Structure Determination of a Twin at 110 K. *Science* **1991**, *254*, 408-410.
- (41) Savenije, T. J.; Ferguson, A. J.; Kopidakis, N.; Rumbles, G.: Revealing the Dynamics of Charge Carriers in Polymer:Fullerene Blends Using Photoinduced Time-Resolved Microwave Conductivity. *J. Phys. Chem. C* **2013**, *117*, 24085-24103.
- (42) Ferguson, A. J.; Kopidakis, N.; Shaheen, S. E.; Rumbles, G.: Dark Carriers, Trapping, and Activation Control of Carrier Recombination in Neat P3HT and P3HT:PCBM Blends. *J. Phys. Chem. C* **2011**, *115*, 23134-23148.
- (43) Grzegorzczak, W. J.; Savenije, T. J.; Dykstra, T. E.; Piris, J.; Schins, J. M.; Siebbeles, L. D. A.: Temperature-Independent Charge Carrier Photogeneration in P3HT-PCBM Blends with Different Morphology. *J. Phys. Chem. C* **2010**, *114*, 5182-5186.
- (44) Sheldrick, G. M.: SADABS, v. 2.10 – A program for area detector absorption corrections. Bruker AXS: Madison, WI, 2003.
- (45) Sheldrick, G. M.: *SHELXTL*. 6.15 ed.; Bruker AXS: Madison, WI, 2004.
- (46) Sheldrick, G. M.: APEX2, v. 2.0-2. Bruker AXS: Madison, WI, 2006.
- (47) Sheldrick, G. M.: A short history of SHELX. *Acta Crystallographica Section A* **2008**, *64*, 112-122.
- (48) Dolomanov, O. V.; Bourhis, L. J.; Gildea, R. J.; Howard, J. A. K.; Puschmann, H.: OLEX2: a complete structure solution, refinement and analysis program. *Journal of Applied Crystallography* **2009**, *42*, 339-341.
- (49) Sheldrick, G. M.: SHELXTL, v. 6.12 UNIX. Bruker AXS: Madison, WI, 2001.

Chapter 6.

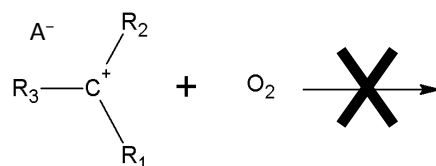
Versatile Robust Metal Reactor for High Temperature Trifluoromethylation of PAHs and Fullerenes; X-ray Structural Characterization of PAH(CF₃)*n* and Related Compounds and Insights into the Mechanism of Radical Substitution

6.1 Introduction and Justification

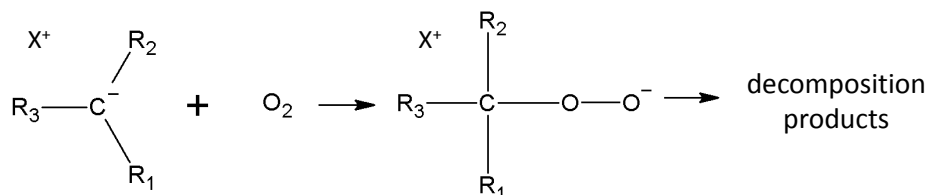
Replacement of legacy silicon and metal based electronic components in common electronic devices such as, semiconductors, field effect transistors, light emitting diodes and photovoltaics with rationally designed, tuned organic materials or hybrids promises many added benefits. Novel, sustainable, earth-abundant organic electronic materials will lead to lower-cost, lower-weight, flexible electronic devices. Besides being earth abundant, organic electronic materials can be, and already are, being solution processed rather than requiring energy intensive purification, growth of large single crystals, and further etching and processing.¹ Furthermore, organic electronic materials hold the promise of functioning in ways metal and semi-metal based semiconductors cannot, especially when considering the possible 3D architectures of self-assembled organic electronic materials.²

New organic electronic materials need to be electronically, thermally, chemically, and photo-stable for use in devices. Currently, one of the areas with the greatest need for new materials is air, or more accurately oxygen stable *n*-type organic semiconductors.³ To rationally design such molecules requires an understanding of why stable, *n*-type organic electronic materials are so hard to produce. A look at why stable *p*-type organic electronic materials are easier to produce is beneficial for this discussion. A *p*-type material (organic or metallic) is electron deficient and has the absence of an electron (known as a hole) allowing the remaining electrons mobility as well as

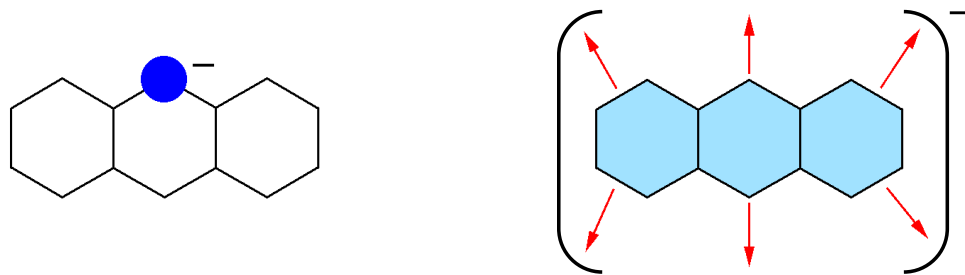
the hole. Additionally, a *p*-type material being electron deficient, is not particularly reactive towards the ubiquitous oxidizing agent, oxygen (O₂). As an example the tertiary carbo-cation salt shown below would not be particularly reactive with O₂, and the carbo-cation could be further stabilized by electron donating R groups.



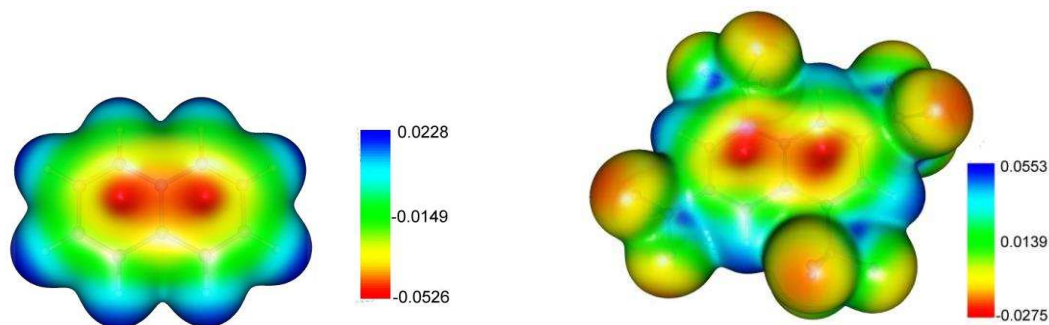
Conversely, *n*-type materials have extra electrons and are thus typically reactive towards O₂ first forming a peroxy-intermediate as the first step of the decomposition mechanism shown below.



The reactivity of *n*-type organic electronic materials makes sense when thought of from an organic synthesis standpoint. In typical organic synthesis, localized regions that are highly charged on a molecule are exploited to preferentially react with another compound, or itself forming a new compound. Ways to mitigate the reactivity of these highly charged, localized regions, is to delocalize the charge over many atoms. Shown below to the left is an anthracene core with a localized, highly charged, region of electron density illustrated as a blue circle. To the right is an anthracene with an equal amount of charge, distributed over the entire anthracene core.



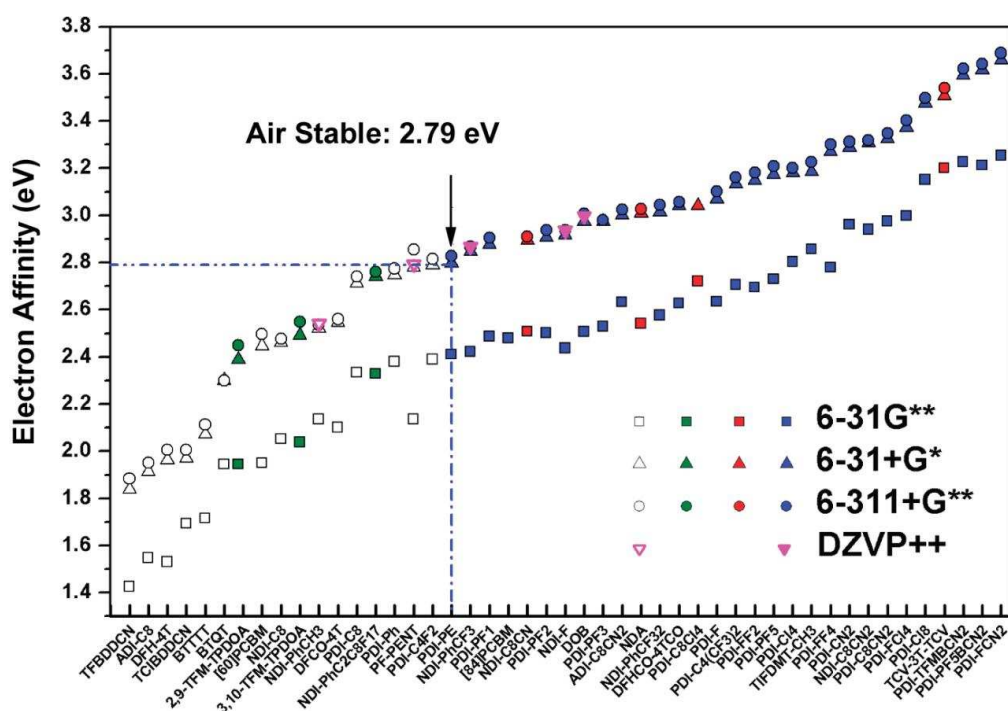
The charge delocalization effectively lowers the charge density at any given location on the anthracene core making it less reactive. Electron delocalization is possible with strongly electron withdrawing substituents and an electronically conjugated system drawing electron density away from the localized area. As an example of the effects electron withdrawing groups such as CF_3 can have on the electron density of a polycyclic aromatic hydrocarbon, below is the calculated electron density map of naphthalene (left) compared to naphthalene with 4 CF_3 substituted in a symmetric pattern (right).⁴ It should be noted that the colors appear the same in both density maps, but the scales are different for the naphthalene and the naphthalene with 4 CF_3 groups.



Notice how the core of the naphthalene with 4 CF_3 substituents is about half as negative as the core of the unsubstituted naphthalene. The combination of π -conjugation and electron withdrawing properties of the CF_3 groups effectively lowered the charge density in the center of the naphthalene molecule. Besides delocalizing the charge, it has been shown in many instances that the presence of electron withdrawing groups such as halogen atoms, perfluoroalkyl (R_F) groups, nitro groups and cyano groups on polyaromatic hydrocarbons (PAH) enhances the (i)

electron acceptor properties (formation of *n*-type material), (ii) solid state charge carrier mobilities, and (iii) air stability.⁵⁻⁹

A synthetic target for air-stable *n*-type organic materials has been hypothesized by Chang et al. based on comparing experimental air stability of materials in organic field effect transistors (OFET), to their DFT-predicted gas-phase electron affinities.³ This hypothetical gas-phase electron affinity limit for air-stable *n*-type organic electronic materials was derived from the figure shown below where filled in markers indicate sufficient air stability.³



While not every compounds (listed on the x-axis, all abbreviations described in reference 3 where figure was taken) with a DFT-predicted gas-phase electron affinity less that 2.8 eV exhibited poor air stability in an OFET device, this is a reasonable target to aim for when synthesizing air stable *n*-type organic semiconductor materials.

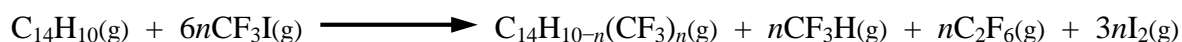
The electron withdrawing ability of the added substituent and its reactivity is critical in designing organic *n*-type materials, that will be stable towards O₂, other compounds, and materials the organic *n*-type may encounter.¹⁰⁻¹³ The synthetic methodologies and electron

withdrawing capabilities of R_F groups, and their effects on fullerenes, have been studied extensively in the Strauss-Boltalina research group.¹⁴⁻¹⁹ More recently, the substitution of R_F groups onto PAHs has been explored in the Strauss-Boltalina research group, and in fact a number of these PAH cores highly substituted with R_F groups, typically CF_3 groups, do exhibit measured gas-phase electron affinities ≥ 2.8 eV.^{4,5,20-22} A foreseeable problem with using many CF_3 groups as electron withdrawing groups to enhance the air stability of n -type semiconducting properties of PAHs, is that the bulky CF_3 groups are going to augment the PAH crystal structure likely pushing the arene rings farther apart making electronic communication between adjacent rings less probable.^{23,24}

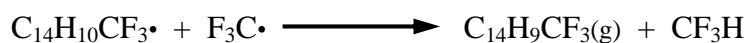
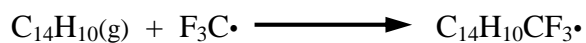
The next important parts of this research, that will be presented in this dissertation chapter are, (i) improving the reaction methods used to make these trifluoromethyl polycyclic aromatic hydrocarbons ($PAH(CF_3)_n$), for reasons that will be explained, (ii) further understanding the free radical reaction method employed at high temperatures with $CF_3I(g)$ to synthesize these $PAH(CF_3)_n$'s and, (iii) compare multiple solvent free $PAH(CF_3)_n$ crystal structures in search of trends (benificial or not) in structural motifs and intermolecular distances.

6.2 Synthesis of $PAH(CF_3)_n$ in Sealed Glass Ampoules.

The published method to make $PAH(CF_3)_n$ previously demonstrated in the Strauss-Boltalina research group is to combine the desired PAH and CF_3I gas in a sealed glass ampoule, and heat to temperatures at or above 300 °C holding isothermal for 1–24 h.^{4,5,20-22} The unbalanced reaction scheme for the radical mechanism is shown below.



The reaction scheme presented is not balanced because it is a free radical reaction initiated by thermal hemolytic cleavage of the C–I bond in CF₃I forming F₃C• and I• radicals. The proposed reaction mechanism, is first addition of a F₃C• radical to the PAH, and then removal of the hydrogen from the newly formed sp³ carbon of the intermediate radical species by another radical. The putative mechanism is described in the reaction scheme below for the substitution of one hydrogen atom with one F₃C moiety.



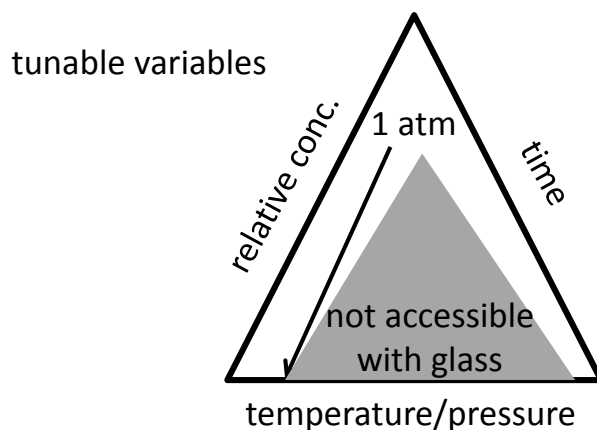
Direct evidence for this reaction method by structural characterization of intermediate species will be shown in a later section of this chapter. For this radical reaction to make appreciable quantities of products with one or more F₃C substitutions, the entire reaction (and hence the entire reactor ampoule) must be at or near the same temperature of > 300 °C. Previously this reaction was performed in a set-up similar to the diagram in in Figure 6-1. If the entire reactor is not at or above 300 °C then the starting PAH or low substituted PAH(CF₃)_n will simply sublime and condense in the cold zone halting further reaction. This is sometimes a useful technique purposefully employed to limit the number of F₃C substitutions. After the radical reaction is complete, the ampoule is cooled to RT, broken open and all material is dissolved in DCM or similar polar organic solvent and worked up to remove I₂(s) either by reaction with copper metal or aqueous Na₂S₂O₄ and liquid-liquid extraction, then ultimately separating single compounds and isomers by HPLC.

6.2.1 Problems Associated with Glass Ampoule Reactor Based Reaction Set-up.

The synthesis and separation method described above has, in the past, worked well for producing many compounds and isomers of PAH(CF₃)*n*'s for proof of concept, and initial characterization of these compounds as good electron acceptors. Thermal ellipsoid plots of the SC-XRD structures of a select number of compounds and isomers produced by the sealed glass ampoule synthesis and HPLC separation method is shown in Figure 6-2. The naming of these compounds throughout this dissertation chapter is a four letter designation of the PAH starting material, the number of F₃C substitutions, and the isomer number for that particular number of F₃C substitutions. The isomer number is arbitrary and is consecutive starting from 1 for the first isomer discovered. Table 6-1 lists the starting PAH, and the 4 letter designation for each PAH used throughout this text.

The sealed glass ampoule method allowed for "proof of concept" for the generalize reaction of PAHs with CF₃I at temperatures in excess of 300 °C. However, the glass ampoules posed problems for continued use, further development, and possible scaling of the reactions. The glass ampoules could only be safely operated at pressures around 2 atm internal pressure; 1 atm of pressure exerting force on the outside of the ampoule meaning the actual internal pressure was 1 atm above atmospheric pressure. For reference, the important physical properties for transferring and using CF₃I are; (i) melting point of CF₃I is -110 °C, (ii) boiling point is -22.5 °C, and (iii) the vapor pressure at 25 °C is 3,296.5 Torr (4.34 atm, 63.74 psi).²⁵ The pressure limitation of the glass ampoules required extra care in loading them, being careful to not over pressurize the ampoule with CF₃I, and ensuring the reaction temperature and pressure were not such that too much pressure would build inside the ampoule causing it to rupture. Furthermore, each ampoule had to be fabricated, by trained personnel, initially having a valve so the ampoule could be

loaded with PAH solid, evacuated of air and then loaded with the appropriate amount of CF_3I gas. With the ampoule loaded and the valve closed the ampoule was cooled to $-196\text{ }^\circ\text{C}$ and flame sealed. While this method was performed by multiple researchers in the Strauss-Boltalina research group, it was quickly evident that the learning curve in fabricating suitable glass ampoules, loading them with the proper amount of CF_3I , and then adequately sealing the ampoules, required considerable practice and skill. Additionally, due to the pressure limitations, the total amount of CF_3I added was fixed based on the volume of the ampoule and temperature of the reaction, thereby limiting the equivalence of CF_3I , or total reaction size. Finally, the softening temperature of glass also limited to the maximum temperature of reaction to ca. $450\text{ }^\circ\text{C}$. These limitations of the glass ampoule limited the tunable variables used to optimize current reactions and test new PAHs. A schematic of the limits of the glass ampoule on the tunable variables is shown below.



The limits on tunable variables also did not allow for experimentation of high melting point PAHs such as coronene ($\text{C}_{24}\text{H}_{12}$) with a melting point of $435.8\text{ }^\circ\text{C}$.²⁶ Because glass ampoules required considerable skill to fabricate and seal, and the pressure limitations of the glass construction, a new, safer more robust reactor design was sought. Replacing glass ampoules with a metal reactor would improve safety, increase reaction scale, reproducibility, as well as augment

the number of tunable variables. This section of this chapter will describe efforts to find a low-cost, reusable, off-the-shelf reactor to replace sealed glass ampoules for the reasons discussed above. Furthermore, initial testing and comparison to similar reaction in sealed glass ampoules will be discussed to demonstrate the suitability of the metal reactor.

6.2.2 Design Requirements For New PAH(CF₃)_n Synthesis Reactor.

The new reactor design required the following: (i) more robust construction that can handle pressures up to 1,000 psi (51,714 Torr or 68 atm) and temperatures greater than 450 °C, for larger variable regimes and for a large engineering factor of safety, (ii) reusable reactor, not requiring skilled glass blowing for fabrication before every experiment, (iii) ability to take in and out of inert atmosphere glovebox to use different, reactive starting materials or other types of reactions with CF₃I, and (iv) ability to place entire reactor (or parts where reaction is taking place) into hot zone for extended period of time. The design requirements described above require a material stronger, and more thermally robust than glass, very likely metal. Two problems quickly become evident with metal parts and a metal reactor, (i) metal valves typically have polymer seats and valve stem packing making their maximum working temperature around 240 °C depending on the polymer used for the seat material, and (ii) most metal alloys react with one or more reactant or product in the reaction. The most corrosive species in the reactor is I₂(g) at high temperatures and pressures, has a measured corrosion rate of greater than 1.0 mm/y for gaseous or aqueous solutions of I₂(g).²⁷ This corrosivity and compatibility needs to be taken into account for all of the wetted parts of the reactor (i.e., parts that can come in contact with the reactants and products).

Valves that can be safely and routinely operated at temperatures in excess of 450 °C do exist, and employ soft metal as the valve seat material and graphite, Grafoil® or other graphite

impregnated materials as the valve packing material. An initial cost survey for such valves yielded estimates ranging from ca. \$430 to over \$10,000 depending on the materials used in the internal and external parts. Besides performing at elevated temperatures, the wetted parts of the valve also needed to be constructed of materials that are not reactive with the reagents or products in order for the valve to be reusable. To combat reactor corrosion, the valve and reactor can be constructed of materials resistant to I_2 corrosion but at a significant cost increase. As an example, a ½" NPT, quarter turn ball valve, quoted by Triad Processing Equipment; if the valve body, connection ends, and shut-off ball are constructed of 316 stainless steel with the proper high temperature packing materials then the cost of the valve is \$1,290; however, if the valve body, connection ends, and shut-off ball are constructed of Inconel 625 (an I_2 resistant alloy) with the proper high temperature packing materials the cost of the valve increases to \$10,350. Due to the rapid cost increases with reactor construction from corrosion resistant metals, another, less expensive method to minimize corrosion of the reactor is preferred.

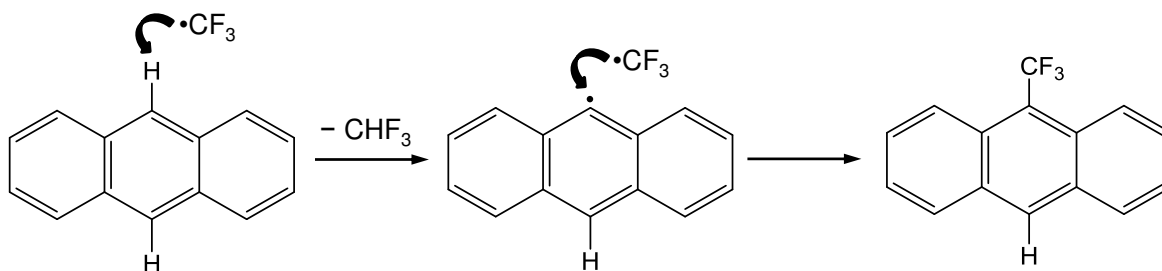
Another technique to combat the corrosivity of the byproduct $I_2(g)$, is to add an additive that will irreversibly react with the $I_2(g)$ as its produced, thereby limiting its contact with the metal reactor, minimizing reactor corrosion. From previous work, it was already known that adding Cu metal as a catalyst to promote the thermal hemolytic cleavage of the C-I bond in CF_3I also had the added benefit of reacting with $I_2(g)$ forming CuI_2 . Two separate reactions in glass ampoules, one with and one without Cu metal additive, show the effectiveness of copper metal at scavenging $I_2(g)$. The two resulting sealed ampoules are shown in Figure 6-3. The final design requirement, as in any engineering project, is low cost, the reactor should be inexpensive and preferably an off the shelf item that can be replaced from time to time. With the high pressures

and temperatures planned for this reactor, it is optimal that the reactor be replaced after so many reactions or years to prevent metal fatigue and premature failure of the reactor.

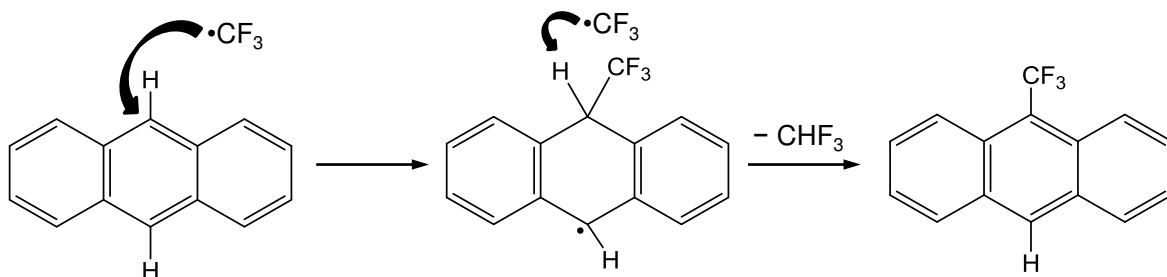
6.3 Structural Evidence for the Free Radical Substitution Mechanism on PAHs by $\text{CF}_3\cdot$ Radicals.

The free radical reaction of CF_3I and PAHs at elevated temperature has been known to work and has been utilized extensively by the Strauss-Boltalina research group to make many strong electron accepting $\text{PAH}(\text{CF}_3)_n$'s.^{4,5,20-22} During the initial research of making many strong electron accepting compounds the mechanism of how the $\text{F}_3\text{C}\cdot$ replaces the H atom on the PAH core has been somewhat of a mystery. As previously described, it is known that $\text{F}_3\text{C}\cdot$ radicals are formed by thermal homolytic cleavage of the C–I bond in CF_3I at temperatures at or above 300 °C. There are two possible pathways shown below as Radical Scheme 1 and 2 with ANTH as the PAH, that can explain the radical substitution of a hydrogen atom on a PAH. Depending on the melting point and vapor pressure of the starting PAH, the reaction could take place completely in the gas phase, or on the surface of liquid PAH in the sealed reactor, independent of the reactor construction material.

Radical Scheme 1



Radical Scheme 2

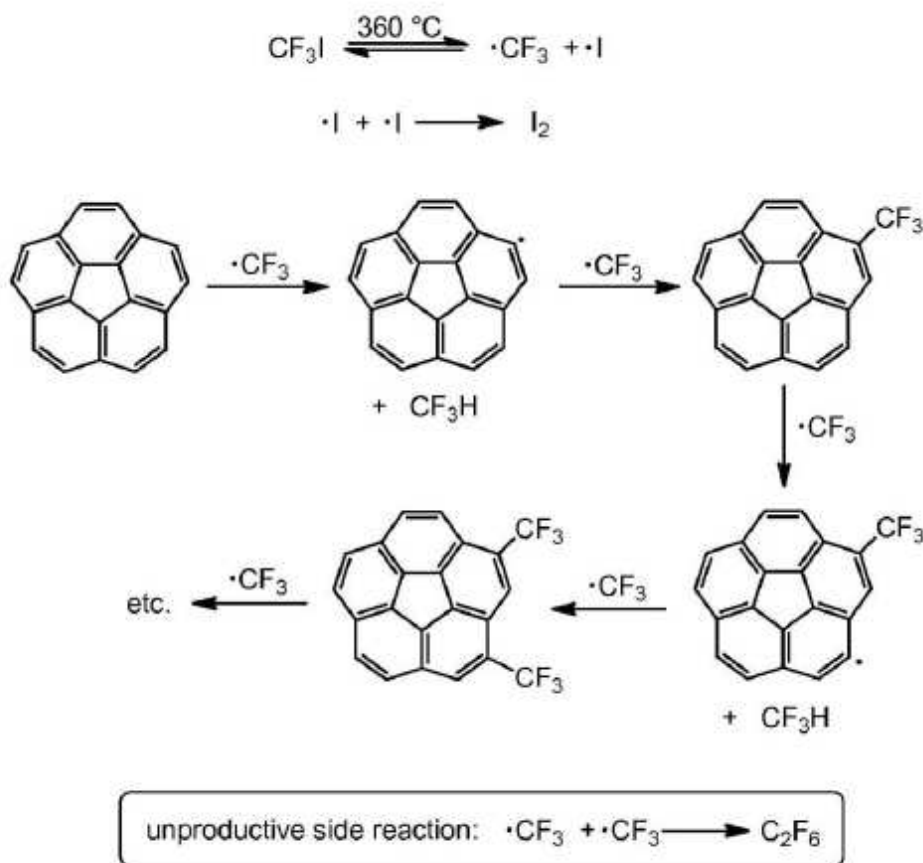


Radical Scheme 1 is initiated by an $\text{F}_3\text{C}\cdot$ coming into close proximity to interact with a PAH and then react with the PAH and remove a hydrogen atom, forming $\text{F}_3\text{C}-\text{H}$ and leaving the $\text{PAH}\cdot$ as a radical. The $\text{PAH}\cdot$ radical at this point could shift the location of the radical through resonance until the radical is localized at the lowest energy location. Then a second $\text{F}_3\text{C}\cdot$ would eventually come in contact with the $\text{PAH}\cdot$ forming a $\text{F}_3\text{C}-\text{PAH}$ bond. Depending on the PAH, shifting of the radical may or may not be observed. Radical Scheme 2, again starting with an $\text{F}_3\text{C}\cdot$ coming into close proximity and reacting with a PAH. However, in Radical Scheme 2, the $\text{F}_3\text{C}\cdot$ adds to the PAH forming a temporary sp^3 carbon radical intermediate rather than removing an H atom. The $\text{F}_3\text{C}-\text{PAH}\cdot$ then interacts with a second $\text{F}_3\text{C}\cdot$ radical that removes the H atom forming $\text{F}_3\text{C}-\text{H}$ and $\text{F}_3\text{C}-\text{PAH}$ reforming the sp^2 carbon in the PAH core.

A tentative reaction mechanism was previously described (Kuvychko et al. *Angew. Chem. Int. Ed.* 2012, reference 3) basically following Radical Scheme 1, (the formation of a $\text{PAH}\cdot$ and CF_3H) as shown in an excerpt and figure from the Supporting Information below.

"Tentative mechanistic scheme for the formation of $\text{C}_5-\text{C}_{20}\text{H}_5(\text{CF}_3)_5$ from $\text{C}_{20}\text{H}_{10}$ and CF_3I . To the best of our knowledge, the gas-phase transformation of aromatic

C–H bonds into C–CF₃ moieties with CF₃ radicals derived from homolytic thermolysis of CF₃I is unprecedented. A plausible, but tentative, mechanistic scheme is shown below.



It shows the removal of an H atom by a CF₃ radical to form a CF₃H and C₂₀H₉ radical followed by the formation of the new C–CF₃ bond trapping the C₂₀H₉ radical by another CF₃ radical."

In the corannulene work no evidence was given to justify a preferred mechanistic pathway. In a later publication (Kuvycho et al. *Angew. Chem. Int. Ed.* 2013, reference 5) it was stated that CF₃H was observed as a reaction product as well as I₂. While this evidence does lend credibility to the thermal homolytic free radical formation of F₃C• and I• required to initiate the mechanism

described by Kuvycho et al. both Radical Schemes described above are still equally valid given the described evidence.

It should also be noted that neither Radical Scheme presented above takes into account the reactivity of $I\cdot$ and only presumes that $I\cdot$ must react with $I\cdot$ forming the clearly visible purple product I_2 . However, the reactivity of $I\cdot$ should not be immediately discounted, as it could play an important role during the reaction. The problem with trying to find evidence for the reactivity and participation of $I\cdot$ in the radical reaction is that at the temperatures the reaction takes place, any CF_3I , HI , $PAH-I$ or other possible iodine containing compounds formed, have weak bond energies and would themselves likely undergo thermal hemolytic cleavage, reforming $F_3C\cdot, I\cdot$, or $PAH\cdot$. So while it is unlikely that any intermediate "trapped" CF_3I , HI , or $PAH-I$ compounds will be isolated from these reactions, $I\cdot$ could still be playing a role in keeping the radical reaction going, removing atoms or groups from highly reactive sp^3 carbon intermediates, or further initiating radicalization, forming $F_3C\cdot$ or $PAH\cdot$ that do lead to products.

The best direct evidence for either radical scheme is structural evidence (1H , ^{19}F and ^{13}C NMR in combination with mass spectra, or SC-XRD) of a product compound that could have only formed from one of the intermediate radicals described in Radical Scheme 1 or 2. However, the compound suggesting one scheme over the other would not be a typical PAH with substituted CF_3 groups, but rather a trapped intermediate compound and would only be useful to further elucidate the reaction mechanism. For example, evidence for Radical Scheme 1 would come from a compound that was a $PAH-PAH$ dimer with no CF_3 groups indicating that a $PAH\cdot$ reacted with a second $PAH\cdot$, or something other than a $F_3C\cdot$. This hypothetical compound would suggest the $F_3C\cdot$ removed an H atom forming F_3C-H leaving a $PAH\cdot$ that further reacted with a $PAH\cdot$ or PAH . Were Reaction Scheme 1 the preferred mechanism, then PAH_n polymers would

likely also result. Similarly, evidence for Radical Scheme 2 would come from a compound that had two CF_3 groups added onto two separate sp^3 carbons indicating that a $\text{F}_3\text{C}\cdot$ reacted with a PAH, formed the first sp^3 carbon, an intermediate then the $\text{F}_3\text{C-PAH}\cdot$ reacted with a second $\text{F}_3\text{C}\cdot$ forming a neutral compound and a second sp^3 carbon. Due to the possibilities with free radical reactions these two hypothetical compounds or a number of other possible compounds would further explain the preferred radical mechanism utilized in these reactions; and could allow further optimization of such reactions.

6.4 Single Crystal X-ray Structural and Packing Analysis of $\text{PAH}(\text{CF}_3)_n$'s and Related Compounds.

Organic semiconductor and conductor compounds, regardless of the application, must have a few commonalities in order to function properly. First they must be stable during operation, i.e. while conducting electrons for *n*-type organic semiconductors, and holes for *p*-type organic semiconductors. Since all compounds in this dissertation are electron acceptors, all discussions will only be about *n*-type or electron conducting organic semiconductor compounds. This stability during conduction requirement entails being stable as the neutral compound or as the anion intermediate formed during the conduction process. The stability during conduction is determined by physical properties of the compounds such as electron affinity, ionization potential, oxidation/reduction potentials etc as well as the electrochemical stability of any impurities, or additives in the material. Furthermore the rate of conduction needs to be reasonable for the desired application. This requires that the compound does not form an electron or hole trapped state that slows the conduction process, and that the molecules are in close enough proximity to allow electron conduction.

The structural characteristics of a particular compound can be easily determined and compared to determine, if in a series of compounds, trends can be seen that would indicate this or that compound would be a better or worse conductor. Such an analysis would be based on distances and relative orientation of the closest neighboring molecules in a solvent free crystal structure. Such an analysis on 1,4,5,8,9,10-hexakis(trifluoromethyl)anthracene (ANTH-6-1), 1,4,5,8-tetrakis(trifluoromethyl)acridine (ACRD-4-1), 1,3,5,7-tetrakis(trifluoromethyl)azulene (AZUL-4-1), 1,3,5,7-tetrakis(trifluoromethyl)naphthalene (NAPH-4-1), 1,4,5,8-tetrakis(trifluoromethyl)phenazine (PHNZ-4-2), as well as 10,11,12,13-benzo[*b*]triphenylene (TRPH(C₄F₄)) will be presented in this chapter. While experimental solid state conductivities of these compounds has yet to be realized, an initial hypothesis of what compound(s) in the series should have better electrical conductivity relative to the other compounds based on analysis of the closest neighbors in each crystal structure will be discussed.

6.5 Results

6.5.1 Metal Reactor for High Pressure, High Temperature Reactions of CF₃I and PAH.

The replacement metal reactor was conceived, designed, and initially tested by the author of this dissertation chapter. Some reactions using the metal reactor were performed by fellow Strauss-Boltalina group member, Nicholas J. Deweerd, directed by the author of this dissertation, and some of the data collected by Nicholas Deweerd will be shown to illustrate the feasibility and differences between the sealed glass ampoules and the metal reactor. After considerable research into high temperature valves and “off-the-shelf” components that will satisfy the engineering requirements of this reactor, a valve from High Pressure Equipment was found to be well suited to 50 mg to 1 g scale reactor, a schematic of this reactor and valve is shown in Figure

6-4. This valve and tube with a cap making up the entire reactor (hereafter referred to as the *metal reactor*) are ideal for this high temperature reaction for multiple reasons, (i) the valve, tube and cap are constructed of heavy walled 316 stainless steel and are rated to pressures up to 20,000 psi of continuous use, (ii) the valve seals when closed with a metal to metal seat and will function properly up to 550 °C, (iii) the valve packing in the valve stem is made of a flexible graphite, Grafoil®, and can withstand temperatures up to 500 °C, (iv) the exterior of the valve stem incorporates heat dissipating fins to ensure the valve packing does not get too hot and prematurely degrade causing a leak, (v) the reactor tube and cap are inexpensive and replaceable, so as the reactor is used and worn due to slow reaction with I₂(g) and other compounds in the reactor these parts can be replaced, and (vi) the reactor tube and valve are commercial, off the shelf products and are relatively inexpensive. Finally, larger size tubes can be obtained for the same valve to scale the reaction; a schematic of the larger tube with the same valve is shown in Figure 6-5. The larger metal reactor will not be discussed further in this chapter.

A simplified procedure to use this reactor is as follows; (i) remove reactor tube from the valve to load the solid PAH and the copper powder I₂ scavenger, (ii) thread reactor onto valve, evacuate and add CF₃I quantitatively by pressure volume additions, (iii) close valve sealing the contents of the reactor below the valve seat, (iv) insert the metal reactor assembly into a tube furnace past the valve seat to ensure the reaction is at a nearly constant temperature.

6.5.2 Testing the High Pressure High Temperature Metal Reactor to Make PAH(CF₃)_n.

To test the reactor, a PAH that has been used many times with success in making significant conversion of products in the glass ampoules, anthracene (ANTH), was employed. Additionally, coronene (CORO), which trifluoromethylation in the glass sealed ampoules was not efficient with respect to the conversion of the starting material into products, was also tested in the metal

reactor. The glass ampoule and metal reactor experimental conditions for ANTH and CORO are shown in Table 6-2. The reactor was also tested using C₆₀ and C₇₀ as the starting materials to make trifluoromethylfullerenes (TMF), a different type of strong organic electron acceptor researched by the Strauss-Boltalina research group. Experimental details and preliminary results of the fullerene reactions are also tabulated in Table 6-2 to further illustrate the capabilities of this metal reactor.

The reaction of ANTH with CF₃I in the metal reactor formed many products and isomers, converting most of the ANTH to products with CF₃ groups. The ANTH reaction had 13.4 equiv of CF₃I creating a pressure in the reactor of greater than 11,003 Torr, assuming no reaction causing the pressure to decrease. The resulting crude mixture was considered too complex to attempt to separate by HPLC. Any single compound separated from this reaction would be in quantities too low to characterize. The ¹H and ¹⁹F NMR spectra of the crude ANTH reaction mixture collected from the metal reactor compared to previously isolated ANTH-6-1 are shown in Figures 6-6 and 6-7 respectively. The comparison to purified ANTH-6-1 demonstrates the significant number of products and isomers generated by this reaction method.

Two reactions of CORO with CF₃I were performed in the metal reactor both producing products with CF₃ groups. The first reaction had 34.3 equiv of CF₃I creating a pressure in the reactor of greater than 17,000 Torr, assuming no reaction causing the pressure to decrease. The crude product mixture was collected, separated from Cu powder and CuI solid and analyzed by HPLC to quantify the number of compounds and isomers formed. The analytical HPLC is shown in Figure 6-8. The ¹H and ¹⁹F NMR spectra of the crude reaction mixture are shown in Figures 6-9 and 6-10 respectively. After separating 17 fractions from the crude product, which HPLC trace is shown in Figure 6-8 (multiple separations to get enough material), it was determined that

most of them represented compounds of general formula $\text{H}_2\text{CORO}(\text{CF}_3)_{7-9}$, i.e., dihydrocoronene derivatives. Mr. Deweerd was able to grow single crystals of two of those fractions suitable for SC-XRD structural characterization. The two crystal structures are shown in Figure 6-11. Important crystallographic data for those crystal structures are shown in Table 6-3. Both structures obtained from this reaction had broken aromaticity due to additions of CF_3 groups rather than substitutions. One CORO structure had 5 CF_3 substitutions and 2 CF_3 additions and is designated $\text{H}_2\text{CORO-7-1}$. The other CORO compound structurally characterized had 6 CF_3 substitutions and 2 CF_3 additions and is designated $\text{H}_2\text{CORO-8-1}$. Both compounds have the same pattern of $\text{sp}^2 \text{CF}_3$, $\text{sp}^3 \text{CF}_3$, $\text{sp}^3 \text{CF}_3$, and $\text{sp}^2 \text{CF}_3$ shown in Figure 6-11.

The second CORO reaction performed by Mr. Deweerd with 7 equiv of CF_3I in the metal reactor (pressure in the reactor of 7,008 Torr, assuming no reaction causing the pressure to decrease) produced fewer products as shown by an analytical HPLC trace in Figure 6-12. The compounds produced also had no products or isomers with sp^3 carbons evidenced by narrower chemical shifts in both ^1H and ^{19}F NMR, spectra are shown in Figures 6-13 and 6-14 respectively. No pure products have been isolated from this reaction mixture at this time.

Reactions with C_{60} and C_{70} were also performed with the metal reactor. The C_{70} reaction and both analytical HPLCs were performed by Mr. Deweerd. The C_{60} reaction with 40.4 equiv CF_3I (pressure in the reactor of 8503 Torr, assuming no reaction causing the pressure to decrease) showed low conversion to C_{60} cages with 12 or more CF_3 additions. The analytical HPLC and ^{19}F NMR of the crude mixture from the reaction of C_{60} and CF_3I in the metal reactor are shown in Figures 6-15 and 6-16 respectively. There was a significant amount (ca. 50% integrated intensity of HPLC peaks) of unreacted C_{60} in the crude reaction mixture as evidenced by the second peak in the HPLC having a retention time range of 6.5–7.5 min, equal to that of C_{60} under

these conditions. The reaction of C_{60} with CF_3I in the metal reactor did appear to be partially selective in making a particular, known isomer of $C_{60}(CF_3)_{12}$ with S_6 symmetry. This particular isomer has low solubility in most organic solvents and precipitated out as a yellow/brown solid from toluene or benzene solutions used to rinse the crude reaction mixture from the metal reactor. The ^{19}F NMR spectrum and Schlegel diagrams showing the addition pattern of the 12 CF_3 additions to C_{60} is shown in Figure 6-17 for this compound.

A reaction with C_{70} and 20 equiv of CF_3I (pressure in the reactor of 3608 Torr, assuming no reaction causing the pressure to decrease) was the last substrate tested in this series of preliminary studies in the metal reactor. The crude reaction mixture with C_{70} showed less conversion, only 12%, and no selectivity for a particular compound unlike what was observed for the C_{60} reaction. The analytical HPLC shown in Figure 6-18, shows mostly unreacted C_{70} at retention time range of 9–10 min. The ^{19}F NMR spectrum shown in Figure 6-19 did not show any peaks related to $C_{70}(CF_3)_{2n}$ (where $n > 1$); most likely due to the presence of multiple products with low symmetry, the only observable signal corresponded to C_6F_6 at $\delta = -164.9$. However, a mass spectrum, of the crude reaction mixture, shown in Figure 6-20, did show compounds of $C_{70}(CF_3)_{2n}$ where n ranged from 7–10. In this case the mass spectrum is not a representative assessment of the entire sample because of analyte suppression of the harder-to-ionize C_{70} compounds with fewer CF_3 additions. There are likely $C_{70}(CF_3)_{2n}$ compounds in the sample where $n < 7$, however because those compounds would be harder to reduce, in the presence of the higher homologues, they do not ionize as easily and do not show up in the mass spectrum. Subsequent experiments with C_{70} substrate showed steady improvements in the conversion and improved selectivity, but will not be discussed further at this point.

The metal reactor has been tested with two PAH substrates, ANTH, and CORO, and two fullerene substrates, C₆₀ and C₇₀. For all 4 substrates, products with CF₃ were observed by one or more analytical techniques. These initial experiments were a proof of concept type, aimed at attesting the metal reactor as a replacement for the sealed glass ampoules.

6.5.3 Single Crystal X-ray Structures of Intermediate Compounds as Evidence of Proposed Radical Substitution Mechanism.

The two H₂CORO(CF₃)_n compounds, isolated by Nicholas Deweerd using the metal reactor and two other compounds isolated from different reactions, performed by different members of the Strauss-Boltalina research group have similar crystal structural motifs that give evidence for one of the radical substitution methods. Synthesis and isolation of the two H₂CORO(CF₃)_n compounds have already been described. A reaction starting from tetracene (TETR) reacted with CF₃I, in the gas phase in an sealed glass ampoule, (experimental conditions can be found in Table 5.2) produced an H₂TETR(CF₃) compound. The reaction was carried out by former group member Igor Kuvychko, separated by HPLC and crystallized from MeCN by former Masters student Amanda Pluntze. The crystal structure was collected, solved, and refined by the author of this dissertation. The H₂TETR(CF₃)₈ compound has broken aromaticity with two sp³ carbon atoms, one with geminal F₃C groups and one with a F₃C and H atom. The two sp³ carbons are *para* to one another in the TETR core. The compound is denoted as H₂TETR-8-1. The crystal structure is shown in Figure 6-21, important crystallographic information is shown in Table 6-3, the bond distances and angles of the sp³ in the H₂TETR(CF₃)₈ structure compared to typical bond lengths and angles of sp³ carbon atoms is shown in Table 6-4. The sp³ carbon with geminal CF₃ additions has F₃C–C bond lengths of 1.562 and 1.569 Å and bond angles of the F₃C–C–CF₃ 109.5°. The sp³ carbon with a CF₃ and H atom has a F₃C–C bond length of 1.546 Å and bond

angle of the F_3C-C-H 107.8° . Due to the sp^3 carbons, the H_2 tetracene core is bent at the two sp^3 carbons 15.8° from planarity.

The second compound with two sp^3 carbon atoms was $H_2ANTH_2(BnF)_2$, produced in a reaction starting from ANTH with $BnFI$, in DMSO with Cu metal, experimental conditions can be found in Table 6-2.²⁸ further experimental and characterization of compounds produced by similar reactions as those employed to make $H_2ANTH_2(BnF)_2$ can be found in Dr. San's dissertation, Chapter 2 reference 28. The reaction was carried out and separated by former group member Long K San, the crystal structure was collected, solved, and refined by Strauss-Boltalina group member Tyler Clikeman, but is shown here as further evidence of the radical mechanism. The SC-XRD structure of $H_2ANTH_2(BnF)_2$ dimer shown in Figure 6-22 has two sp^3 carbon atoms per H_2ANTH core, *para* to one another. Important crystallographic information and bond lengths and angles of the sp^3 carbons in $H_2ANTH_2(BnF)_2$ can be found in Table 6-3 and 6-4 respectively. The sp^3 carbon atom with the CF_3 addition and H atom has F_3C-C bond length of 1.536 \AA and bond angle of 105.7° . The sp^3 carbon with an H atom and adjacent H_2ANTH core has a $C-C$ bond length of 1.588 \AA and bond angle of 107.4° . Due to the sp^3 carbons, the H_2ANTH cores are bent 33.7° from planarity at the two sp^3 carbons.

Further structural evidence of the radical mechanism is demonstrated by the crystal structures of $H_2CORO(CF_3)_{7-1}$ and $H_2CORO(CF_3)_{8-1}$ compounds, each with two sp^3 carbon atoms *ortho* to each other, formed in the metal reactor with 34.4 equiv of CF_3I at $450^\circ C$ for 4 h. Both of these H_2CORO compounds have the same segment of two CF_3 additions, *ortho* to each other and two CF_3 substitutions two carbons away from either side of the two CF_3 additions, as shown in Figure 6-11. In the $H_2CORO(CF_3)_{7-1}$ structure, the two F_3C-C bond lengths are 1.522 and 1.523 \AA and bond angles range from 100.5° to 110.4° . The geometry about these carbon atoms in both

crystal structures are an average due to the disorder in the two sp^3 carbon atoms found in both structures. The disorder is shown in Figure 6-23. In the $H_2CORO(CF_3)_8-1$ structure, the two F_3C-C bond lengths are 1.535 and 1.536 Å and the bond angles range from 107.8° to 110.7° . The two CF_3 additions cause the normally rigorously planar CORO core to deform from planarity. The $H_2CORO(CF_3)_7-1$ and $H_2CORO(CF_3)_8-1$ H_2CORO cores deviate from planarity by 0.049 Å and 0.116 Å from their respective least squares planes.

The disorder in the $H_2CORO(CF_3)_7-1$ and $H_2CORO(CF_3)_8-1$ crystal structures makes it less certain that there are two sp^3 carbon atoms in the compound. However, a 1H NMR of the $H_2CORO(CF_3)_8-1$ compound shown in Figure 6-24 exhibits hydrogen signal at δ between 5.0 and 5.5, a chemical shift correlating to an sp^3 carbon atom with a strong electron withdrawing group.

All four of these compounds have at least one sp^3 carbon with a CF_3 addition and a hydrogen atom. The hydrogen atom likely originated from the starting PAH. The crystallographic evidence for the carbons in all four structures being sp^3 based on bond angles and distances makes it likely that these are accurate models of the SC-XRD data. Additionally, the SC-XRD crystal structure of the $H_2CORO(CF_3)_8-1$ is further substantiated by changes the appropriate shifts in the 1H NMR spectrum that indicates an sp^3 carbon bearing a proton and a CF_3 group.

6.5.4 Single Crystal X-ray Structural Analysis of $PAH(CF_3)_n$'s and Related Compounds.

For the reasons described above, the structural characterization of these $PAH(CF_3)_n$'s is important for determining their plausibility as organic electronic acceptor compounds. The author of this text has structurally characterized 4 solvent free $PAH(CF_3)_n$ and one compound with a C_4F_4 substitution and compared packing and structural properties to a $PAH(CF_3)_n$ previously characterized in the Strauss-Boltalina research group, 1,4,5,8,9,10-

hexakis(trifluoromethyl)anthracene (ANTH-6-1). The exact synthesis, purification, and characterization were carried out by other Strauss-Boltalina group members and will be annotated appropriately. The compounds are denoted with a 4 letter abbreviation of the base PAH, shown in Table 6-1, and then the number of CF₃ substitutions and finally an arbitrary isomer number (isomer number assigned by order of isolation and discovery). The 4 PAH(CF₃)*n*'s discussed here are 1,4,5,8-tetrakis(trifluoromethyl)acridine (ACRD-4-1), 1,3,5,7-tetrakis(trifluoromethyl)azulene (AZUL-4-1), 1,3,5,7-tetrakis(trifluoromethyl)naphthalene (NAPH-4-1), 1,4,5,8-tetrakis(trifluoromethyl)phenazine (PHNZ-4-2), as well as 10,11,12,13-benzo[*b*]triphenylene (TRPH(C₄F₄)).

The ACRD-4-1 compound synthesized by previous group member Long K. San was synthesized in a sealed glass ampoule with acridine and CF₃I gas, and separated by HPLC. The symmetric isomer ACRD-4-1 crystallized as large colorless plates by slow evaporation from a solution of DCM. The ACRD-4-1 structure is as expected, but the entire molecule is disordered as shown in Figure 6-25 due to flipping of the molecule about the long axis. The ACRD core is nearly planar with an average deviation of only 0.006 Å from a least squares plane of the core atoms. The ACRD-4-1 molecules are stacked in layers where the layers are tilted 29.2° and rotated 64.7° from molecules in adjacent columns of molecules. The centroids of these layers either fall in the center of the unit cell or on unit cell vertices as shown in Figure 6-26. The layers are separated by 4.193 Å from each other measured from planes of the centroids; however molecules that actually overlap each other in columns are separated by 8.386 Å. The ACRD-4-1 molecules within the layers and have centroid···centroid (⊙···⊙) distances of 9.764, 10.65 and 10.67 Å.

The ANTH-6-1 compound was synthesized, separated, and crystallized by a previous post-doctoral student in the Strauss-Boltalina research group, Igor Kuvychko. Dr. Kuvychko also collected the crystal structure, solution, and refinement. The ANTH-6-1 compound was synthesized in a sealed glass ampoule with anthracene and CF_3I gas, and separated by HPLC. Crystals suitable for SC-XRD of ANTH-6-1 were grown by slow evaporation of a MeCN solution. The ANTH-6-1 structure is not of high quality but does allow for analysis of the intermolecular interactions and core deformation. The crystal structure analysis is presented here for completeness in the series of $\text{PAH}(\text{CF}_3)_n$'s. The ANTH core in ANTH-6-1 is not rigorously flat and has a deviation of 0.08 Å from a least squares plane of the core carbon atoms. Additionally the core has a slight bend of 7.2° at the 9,10 positions of the ANTH as shown in Figure 6-27. The greatest amount of overlap between the two ANTH cores in a column, shown in Figure 6-28, has an average perpendicular distance of 3.766 Å. The ANTH-6-1 packs in a pseudo-hexagonal array in the layers and have $\odot \cdots \odot$ distances of 10.29, 11.20 and 14.21 Å as shown in Figure 6-28.

The AZUL-4-1 compound has been previously published in *Chem. Comm.* 2014, with the author of this dissertation as a co-author.²⁰ The AZUL-4-1 compound was synthesized, separated, and crystallized by fellow graduate student Tyler T. Clikeman. The AZUL-4-1 compound was synthesized in a sealed glass ampoule with azulene and CF_3I gas, and separated by HPLC; crystals suitable for SC-XRD were grown by slow evaporation of a DCM solution. The crystal structure was collected, solved, and refined by the author of this dissertation. The AZUL-4-1 crystal structure has a disorder commonly found in symmetrically substituted azulene crystal structures, where the AZUL core can flip about the short axis of the molecule taking up the same volume in either orientation. A 50% thermal ellipsoid plot of a single AZUL-4-1 and of

the disordered segment is shown in Figure 6-29. Besides the disorder the AZUL-4-1 appears to be similar to the other PAH(CF₃)_n structures, the AZUL core is planar to 0.007 Å of a least squares plane of the core carbon atoms, it packs in columns with 8.083 Å distance between overlapping AZUL cores. The next layer below is 4.028 Å away but there is no aromatic overlap with that layer due to a complete molecule slip in the next layer. The AZUL cores in a single layer are rigorously planar and have ⊖⋯⊖ distances of 8.906 Å in two directions, molecules in the other two directions are not co-planar. A figure of the columns from the side and looking down on the columns is shown in Figure 6-30. The disorder in the AZUL core is left in intentionally to show that the disorder did not change the molecular packing of the columns.

The NAPH-4-1 compound has been previously published in *Chem. Euro J.* 2014, with the author of this dissertation as a co-author.⁴ The NAPH-4-1 compound was synthesized, separated, and crystallized by previous graduate student Long K. San. The NAPH-4-1 compound was synthesized in a sealed glass ampoule with naphthalene and CF₃I gas, and separated by HPLC. Crystals suitable for SC-XRD were grown by slow evaporation of a carbon disulfide solution. The crystal structure was collected, solved, and refined by the author of this dissertation. Two molecules within a layer are shown in Figure 6-31. The distances between the closest overlapping parallel planes in the NAPH structure is 3.75 Å, decreased from 4.23 Å observed in the parent NAPH structure.²⁹ In this case, the addition of CF₃ groups actually increases intermolecular interactions through a F–H close contacts of 2.649 Å and an F–NAPH centroid distance of 3.089 Å, both acting to draw the adjacent molecules within a layer of parallel molecules closer together. The F–NAPH centroid and F–H interactions are also shown in Figure 6-31. The overall packing of the NAPH-4-1 in the crystal structure is a common herringbone pattern as shown in two orientations in Figure 6-32. The layers are rotated 83.6° from adjacent

layer The only co-planar NAPH cores in a layer are in one direction due to the rotation of the adjacent layer, the $\odot \cdots \odot$ distances between those NAPH centroids is 9.201 Å.

The PHNZ-4-2 compound was synthesized by former Strauss-Boltalina group post-doctoral member, Igor Kuvychko, separated, and crystallized by fellow graduate student, Karlee P. Castro. The PHNZ-4-2 compound was synthesized in a sealed glass ampoule with phenazine and CF_3I gas, and separated by HPLC. Crystals suitable for SC-XRD were grown by slow evaporation of a MeCN solution. The crystal structure was collected, solved, and refined by the author of this dissertation. The PHNZ-4-2 crystal structure did not have any disorder, as shown in Figure 6-33, and is also arranged in columns. Molecules within a column were separated by 15.82 Å $\odot \cdots \odot$. The nearest molecule in an adjacent column is 7.561 Å as measured from the plane of the two PHZN cores. The nearby columns are tilted 20.2° and rotated 81.6° from molecules in the adjacent column as shown in Figure 6-33. The six nearest neighbors in a pseudo-hexagonal layer of PHNZ cores (similar to that shown in the ANTH-6-1, Figure 6-28) have $\odot \cdots \odot$ distances of 10.15 or 12.72 Å with the centroids of those PHZN cores being planar. This structure is not herringbone but rather columns of molecules as shown in Figure 6-34, where molecules are separated from the neighboring columns well as separated from molecules within the column by greater than 7 Å in either direction.

The TRPH(C_4F_4) compound was synthesized and isolated by current Strauss-Boltalina group Ph.D. student Kerry P. Rippey, The TRPH(C_4F_4) compound was synthesized in a sealed Monel metal reactor with metal plugs at both ends with triphenylene and $\text{I-CF}_2\text{CF}_2\text{CF}_2\text{CF}_2\text{-I}$ liquid, and separated by HPLC (the full synthetic and separation method has been submitted at the time of writing this dissertation). Crystals suitable for SC-XRD were grown by slow evaporation of a toluene solution. The crystal structure was collected, solved, and refined by the author of this

dissertation. The TRPH(C₄F₄) crystal structure did not have any disorder as showing in Figure 6-35. The TRPH(C₄F₄) molecules are rigorously planar and form columns alternating end to end that have a plane to plane distance of 3.396 Å, also shown in Figure 6-35. The adjacent columns are either shifted up 1.404 Å or down 1.992 Å, still leaving a plane to plane distance between molecules in every column of 3.396 Å (i.e. the columns are staggered up and down from one another). The columns do appear to form pseudo-hexagonal packed layers, but due to the shift up or down in adjacent columns, in fact only 3 columns are co-planar as shown in figure 6-36. The three co-planer columns have $\odot \cdots \odot$ distances of 12.37 Å. The TRPH(C₄F₄) crystal structure has significant TRPH-TRPH core overlap as shown in Figure 6-37.

6.6 Discussions

6.6.1 Metal Reactor for High Pressure, High Temperature Reactions of CF₃I with Either PAH or Fullerene Based Reactants.

The use of the metal reactor described above resulted in conversion to PAH(CF₃)_n and TMF when used as a drop-in replacement instead of sealed glass ampoules for synthesis of these compounds. After multiple experiments with ANTH, CORO, C₆₀, and C₇₀ the metal reactor has been found to be a suitable reaction set-up to produce highly substituted PAH(CF₃)_n's or trifluoromethylfullerenes. However, as expected, the reaction conditions need to be optimized for the metal reactor. The most significant differences between the metal reactor and the glass ampoules found so far are as follows: (i) the volume of the metal reactor is fixed and is relatively small compared with the sealed glass ampoules, (ii) the metal reactor allows for significantly more equiv of CF₃I and greater pressures to be used, and (iii) Use of copper powder to scavenge I₂(g) to minimize damage to the metal reactor. The small volume is problematic for scaling the

reactions; however, a larger reactor tube can be put on the same valve when scaling the reaction is needed, as shown in Figure 5.5. The metal reactor allows for increased equiv of CF_3I , and greater pressures were shown to be beneficial for improving conversion to products, particularly those with high substitution degree. The increased pressure (and/or equiv of CF_3I) was also found to yield the new product types, i.e., dihydro-PAHs, that have lost aromaticity in the PAH substrates (i.e. forming sp^3 carbons with either 2 CF_3 groups or a CF_3 and H atom).

The increased pressure and equiv of CF_3I did not have a negative effect on the synthesis of TMFs from C_{60} or C_{70} starting material. The C_{60} and C_{70} reactions both had conversion to highly substituted $\text{C}_{60}(\text{CF}_3)_n$ and $\text{C}_{70}(\text{CF}_3)_n$ products. The highly substituted $\text{C}_{60}(\text{CF}_3)_n$ and $\text{C}_{70}(\text{CF}_3)_n$ products are the compounds known to be difficult to separate with the traditional HPLC method since the highly substituted $\text{C}_{60}(\text{CF}_3)_n$ and $\text{C}_{70}(\text{CF}_3)_n$ products have nearly the same retention times in all known HPLC conditions.^{30,31} Unless a mixture of highly substituted $\text{C}_{60}(\text{CF}_3)_n$ or $\text{C}_{70}(\text{CF}_3)_n$ products is the desired outcome, the metal reactor synthetic method will need to be optimized further for fullerene substrates. However, it should be pointed out that even under non-optimized conditions, the particular isomer of $\text{C}_{60}(\text{CF}_3)_{12}\text{-S}_6$ was made in observable quantities (i.e. greater than 5 mg) and isolated. The reaction conditions could be optimized further to increase the yield of this particular compound, and likely others. For example, preliminary data (not shown here) indicate that high selectivity can be achieved in the case of C_{70} trifluoromethylation, leading to the synthesis of highly desirable functional compounds $\text{C}_{70}(\text{CF}_3)_8$ and $\text{C}_{70}(\text{CF}_3)_{10}$.

Evidence of the loss of aromaticity and greater conversion to sp^3 carbons at higher pressures for PAH substrates was shown by the reaction of ANTH with 13.4 equiv of CF_3I and 2 separate reactions of coronene with different amounts of CF_3I . The metal-reactor reaction of ANTH

mimicked previously reported sealed glass ampoule reactions in scale, equiv of CF₃I, reaction time, and temperature. However, the pressure during the metal-reactor reaction, assuming no reaction took place would have been 11,000 Torr, higher than that observed in a sealed glass ampoule. As a result, the metal-reactor ANTH reaction generated many compounds and isomers by ¹H and ¹⁹F NMR (Figures 6-6 and 6-7 respectively) and appeared to generate many compounds that had sp³ carbons evidenced by the ¹H NMR spectrum having peaks in the δ 3.5 to 6.5 range.

The coronene reaction with 34.3 equiv of CF₃I was held isothermally for 3 h at 450 °C. Assuming no reaction took place the pressure of CF₃I in the reactor at 450 °C was 17,288 Torr (ca. 334 psi, or 22.7 atm), much greater than the 1-2 atm in the sealed glass ampoules. The HPLC trace in Figure 6-8 shows the significant number of compounds and isomers formed from this coronene CF₃I reaction. From that crude reaction mixture, 2 pure fractions were collected by HPLC separation by Mr. Deweerd, and crystallized into 2 separate compounds, a coronene derivative with 5 substitutions and 2 additions, and a coronene derivative with 6 substitutions and 2 additions. The crystal structures give evidence to the identity of both these compounds are shown in Figure 6-11. The second reaction with coronene and 7 equiv of CF₃I (equating to a maximum pressure of 7000 Torr assuming no reaction) did not appear to form any sp³ carbons based on ¹H or ¹⁹F NMR analysis of the crude reaction mixture. By HPLC, there still appeared to be a significant number of different compounds (and isomers), but little if any broken aromaticity was observed. The HPLC trace of the second coronene reaction with 7 equiv of CF₃I is shown in Figure 6-12, the ¹H and ¹⁹F NMR spectra are shown in Figures 6-13 and 6-14 respectively.

A tentative hypothesis as to why the increased pressure during the CF_3I radical reaction causes an increase in the products with sp^3 carbon atoms is that the greater pressure creates an environment with a greater concentration of $\text{CF}_3\cdot$ and $\text{I}\cdot$ radicals. The greater concentration of radicals creates a reaction condition where the frequency of two radicals meeting is much greater, and thus radical recombination can happen much faster. Simply assuming the difference in pressure of the sealed glass ampoule reactions and the metal reactor reactions are an indication of the difference in radical concentrations for each reaction type, then the radical concentration in the metal reactor would be ca. 1,000–1,700 times as great as the sealed glass ampoule reactions.

Besides the concentration of $\text{F}_3\text{C}\cdot$ created at high pressures in the metal reactor (and high concentrations), the $\text{I}\cdot$ concentration may become important in controlling the radical mechanism, and possible products in terms of radical initiation, propagation and termination. A recent review of trifluoromethylation with $\text{F}_3\text{C}\cdot$ by Studer (*Angew. Chem. Int. Ed.* 2012), discusses the possible importance of $\text{I}\cdot$ in trifluoromethyl substitution of arenes with CF_3I .³² Studer suggests that rather than being a spectator radical, $\text{I}\cdot$ reacts with the $\text{F}_3\text{C-PAH}\cdot$ intermediate forming a transient intermediate neutral $\text{F}_3\text{C-PAH-I}$ molecule that at high temperatures rearomatizes to the $\text{F}_3\text{C-PAH}$ by eliminating HI , and thereby completing the substitution. Relating this to the results from the metal reactor, if the concentration of $\text{I}\cdot$ is important to fully substitute the hydrogen atom rather than just requiring two CF_3 groups per CF_3 substitution, then the addition of excess copper should cause increased appearance of addition products rather than substitution products. The copper powder would be competing for the $\text{I}\cdot/\text{I}_2(\text{g})$ during the reaction and once the $\text{I}\cdot/\text{I}_2(\text{g})$ concentration is below a critical value, CF_3 substitution may cease and CF_3 addition may become the dominate pathway. Considering the possibility that

formation of the CF₃ substitution products depends on the I•/I₂(g) concentration, further optimization and possibly a different I₂(g) scavenger may need to be found.

Further evidence for complications in the free radical reactions with F₃C• radicals, was found in an early work by Whittle and co-workers, who have shown that F₃C• radicals (generated from thermal hemolytic cleavage of hexafluoroacetone, CF₃COCF₃, forming 2 equiv of CF₃• and CO) reacted with aromatic molecules (benzene, toluene, *o*-xylene) only forming CF₃ addition products, but not substitutions products.³³⁻³⁶ For the discussion presented in this dissertation, Whittle's work in which CF₃• formed addition products in the absence of I• could be considered a perfect control experiment to ascertain the role of I• in the CF₃ substitution reaction. Additionally, Whittle and co-workers found that F₃C• reactions with benzene become reversible at temperature ≥ 140 °C, meaning F₃C• can add and be removed during the reaction, further complicating this reaction.^{34,35} Finally, Whittle et al. found that hydrogen abstraction from benzene with F₃C• forming C₆H₅• and CF₃H *does not occur*.³³ This does not preclude such a hydrogen abstraction pathway in larger PAHs that have the ability to stabilize the radical by delocalizing the radical over more atoms. At the same time, Whittle's observation agree with the structural evidence presented in this dissertation chapter that the F₃C• reacts with a PAH forming a F₃C-PAH• rather than a PAH• and CF₃H.

Due to the possibility of the metal reactor surface reaction with I₂(g), a byproduct formed during the reaction, copper powder has to be added to protect the metal reactor by sequestering I₂(g). However, it is known that metals will affect the dissociation energy of F₃C-I. For example, the bond dissociation energy (BDE) of the C-I bond in F₃C-I is 221 kJ/mol at 298 K.^{33-35,37} Yet in the presence of Ag(111) the BDE of the C-I bond in F₃C-I lowered by ca. 29 kJ/mol.³⁷ Furthermore, it was found that CF₃I will adsorb and desorb to Ag(111) (and likely other metals)

which changes the amount of CF_3I in the gas phase at any given time, further complicating this reaction. Because copper powder is added to prolong the useable life of the metal reactor, the temperature required to initiate the reaction through C–I bond homolysis of CF_3I to $\text{F}_3\text{C}\cdot$ and $\text{I}\cdot$ is different compared to sealed glass ampoules (in the absence of metal promoter). Furthermore, it is unknown at this time if the stainless steel metal reactor is further augmenting the temperature at which thermal homolysis of the F_3C –I bond occurs and what effect that would have on the reaction.

Thus far the metal reactor has produced compounds that have CF_3 groups either added to or substituted on PAH or fullerene starting compounds. The metal reactor does allow for much greater pressures, which can cause the formation of complex mixtures of many different compounds that could be challenging for isolation in pure form. Furthermore, the increased pressure of CF_3I and copper powder could be increasing the likelihood of favoring CF_3 additions rather than CF_3 substitutions. The metal reactor requires copper metal powder (or some other I_2 scavenger) to remove $\text{I}_2(\text{g})$ during the reaction, which changes the reaction conditions. The copper powder and surface impurities on the copper such as adsorbed H_2O and CuO , can also have an effect on conversion, separation, and products formed and will need to be further investigated.

In summary, even at this early stage of testing and troubleshooting its performance, it is clear that the new metal reactor designed by the author possesses several advantages over the previously used sealed glass reactors. It can be used with high and low pressures and mixtures of gases if one of the gases is condensable. Additionally, the metal reactor is more conducive to monitor the volatile products (CF_3H , C_2F_6 and others) to further elucidate the reaction mechanism and/or progress of a particular reaction.

6.6.2 Structural Evidence of Intermediate Compounds in Support of a Proposed Radical Substitution Mechanism.

Four crystal structures have been presented in this chapter that all have the same structural motif of an sp^3 carbon atom with a bound F_3C group and hydrogen atom. This structure in a final compound indicates that Radical Scheme 2 (formation of $F_3C-PAH\cdot$ with an sp^3 carbon containing intermediate) is likely the second step in the radical reaction mechanism after the F_3C-I undergoes thermal hemolytic cleavage forming $F_3C\cdot$ and $I\cdot$. The four crystal structures presented have strong structural evidence of an sp^3 carbon based on geometry and bond lengths. Bond distances and angles of the $H_2ANTH_2(Bn_F)_2$ and $H_2TETR(CF_3)_{8-1}$ structure are shown in Table 6-4, bond distances and angles for the two $H_2CORO(CF_3)_n$ are not shown due to the disorder in the sp^3 carbons causing spurious bond lengths and angles. However, the disorder in those positions and the CF_3 groups pointing nearly perpendicular relative to the coronene ring could only realistically be caused by sp^3 carbon atoms in those positions. Further corroborating 1H spectra of the $H_2CORO(CF_3)_{8-1}$ indicate there is at least one sp^3 carbon with a F_3C group and H atom. Based on the 4 crystal structures resulting from PAHs reacted with CF_3I or Bn_FI in; (i) DMSO ($H_2ANTH_2(Bn_F)_2$), (ii) sealed glass ampoule ($H_2TETR(CF_3)_{8-1}$), or (iii) the metal reactor ($H_2CORO(CF_3)_{7-1}$ and $H_2CORO(CF_3)_{8-1}$) presented in this chapter; there is strong evidence to suggest that Radical Scheme 2 is the likely mechanism of the free radical substitution of H with CF_3 on a PAH from multiple reaction conditions.

The mechanism for the reaction between F_3C-I and PAH very likely initiates by thermal homolysis of the F_3C-I bond at or near temperatures of 300 °C with the formation of $F_3C\cdot$ and $I\cdot$. Based on the structural evidence presented it is likely that $F_3C-PAH\cdot$ with an sp^3 carbon is a transient intermediate. Because any formed CF_3I , HI , $PAH-I$ or other possible iodine containing

intermediates are not likely to be found as a product, the role of the I• is not assumed to play a role in this mechanism, but is noted that it could still be important in the overall substitution reaction. Finally, the work of Whittle et al. suggests that $F_3C\cdot$ can reversibly react with benzene and presumably the larger PAHs presented in this dissertation chapter. With that in mind, a tentative hypothesis for the free radical reaction of F_3C-I and a PAH at temperatures above which F_3C-I homiletically cleaves is that the reaction will be a continually changing system until the reaction is cooled to the point reactions stop occurring, essentially "freezing out" the products in the system when a lower temperature limit is reached.

6.6.3 Single Crystal X-ray Structural Analysis of PAH(CF₃)_n's and Related Structures.

Solvent free single crystal structures of ACRD-4-1, ANTH-6-1, AZUL-4-1, NAPH-4-1, PHNZ-4-1, and TRPH(C₄F₄) have been presented along with distances to the closets adjacent molecules in the crystal structure. Closest neighboring molecules above and below, along with a qualitative estimate of molecular overlap, and closet neighbor side to side are tabulated in Table 6-7 for each compound. For all the reasons mentioned in the introduction of this chapter, close distances to nearest neighbors and possibility of good aromatic overlap are necessary to realize the desired electronic properties of these organic electronic compounds. A quick glance at Table 6-7 shows that the first 5 PAHs, with 4 or 6 CF₃ substituents either have poor molecular overlap within a column, or there is complete overlap but at distances too long for low energy electron conduction. The reason the poor overlap or long distance to nearest neighbors is likely due to the bulky CF₃ groups. While the CF₃ groups are excellent, highly stable, strong electron withdrawing substituents, they are also bulky and repel nearby molecules (due to the repulsion of electron rich CF₃ groups on adjacent molecules) in the crystal structure.^{23,24} Only in one case (NAPH-4-1) out of the five presented with CF₃ groups, was any significant attractive interaction found. It so

happens that NAPH-4-1 has shorter distances between adjacent molecules in a co-planar layer compared to the crystal structure of naphthalene.²⁹

Conversely the TRPH(C₄F₄) crystal structure had close aromatic distances within a column (3.396 Å), approaching the accepted inter-planer distances in graphite of 3.35 Å.³⁸ Contrasting some of the features of the TRPH(C₄F₄) compared to the 5 PAH(CF₃)_n's demonstrates some physical characteristics of TRPH(C₄F₄) that are likely necessary for minimizing inter-planar distances in solid state structures of PAHs. The TRPH(C₄F₄) properties that allow it to pack so densely are (i) the C₄F₄ substitution is co-planar with the triphenylene core and does not increase the Z dimension of the molecule, (ii) the C₄F₄ substitution makes the TRPH(C₄F₄) molecule polar and in the structure stacks rotated by 180° from the above and below molecules (i.e. head to tail), and (iii) there is significant aromatic overlap allowing significant interaction between two molecules.

While the PAH(CF₃)_n compounds presented do have high electron accepting properties, are thermally, chemically and photo-chemically stable, and can be synthesized and purified relatively easily, they do not, appear by a crystal structure analysis to be conducive to electron mobility in the solid state. Most of the possible uses of these strong electron withdrawing PAHs such as organic semiconductors, organic light emitting diodes, and organic photovoltaics, all require moderate electron mobility in the solid state. Other uses such as room-temperature, organic, metal-like conductors require exceptional electron mobility. For either application, the electron mobility in the solid state has to be related to the efficiency of molecular packing, and the PAH(CF₃)_n's presented should be considerably less conducive in the solid state compared to the TRPH(C₄F₄) based on the structural analysis presented in this dissertation.

6.7 Summary and Conclusions:

Synthesis of strong electron accepting PAHs through a radical reaction with CF_3I gas has produced a number of promising $\text{PAH}(\text{CF}_3)_n$'s that are valuable for studying properties of new *n*-type organic semiconductors. The previous sealed glass ampoule reaction method was great for initially making the compounds as a proof of concept. However, it was quickly realized that this method requires personnel skilled in glass blowing and accurate gas transfer to ensure the glass ampoule is not over pressurized creating an unsafe situation. Furthermore the glass ampoule limited the maximum pressure and equivalence of CF_3I when designing reaction conditions. As a replacement a metal reactor comprised of a metal valve and tube, or metal reactor, that was closed at one end was found as an "off-the-shelf" replacement for the sealed glass ampoule. The metal reactor can handle temperatures up to $550\text{ }^\circ\text{C}$ and pressures up to 1×10^6 Torr (20,000 psi). The initial experiments with anthracene, coronene, C_{60} and C_{70} substrates, CF_3I gas and excess copper powder demonstrated the metal reactor does substitute CF_3 groups for hydrogens on PAHs and add CF_3 groups to fullerenes. The greater pressures and addition of copper powder certainly change the reaction since more products sp^3 result from the metal reactor than the sealed glass ampoule. Further optimization of the metal reactor for a particular PAH or fullerene target molecule will be required. Since the metal reactor is safer, more robust, and reusable, performing many reactions to optimize reaction conditions will be less time consuming and safer than with sealed glass ampoules.

Four $\text{PAH}(\text{CF}_3)_n$ compounds structurally characterized by SC-XRD synthesized using CF_3I , and three different reaction methods yielded compounds that had at least one sp^3 carbon atom with a F_3C moiety and hydrogen atom. The bond distances and angles for all 4 structures, and the orientation of the CF_3 on the putative sp^3 carbon atom give strong evidence for the formation of

sp^3 carbon atoms, from an aromatic compound indicating a loss of aromaticity. The sp^3 carbon atom with a F_3C moiety and hydrogen atom suggests a reaction mechanism of addition of a $F_3C\cdot$ first to the PAH forming a $F_3C-PAH\cdot$ intermediate. at some later time, the $F_3C-PAH\cdot$ undergoes rearomization of the PAH either by another $F_3C\cdot$ removing the hydrogen or through an addition of $I\cdot$ and then elimination of HI as described in the literature. Based on these crystal structures, it is believed that the addition of $F_3C\cdot$ happens first, and with that in mind, new reaction methods could be employed to more selectively synthesize the desired compounds.

Finally, the crystal structures of 5 $PAH(CF_3)_n$'s and $TRPH(C_4F_4)$ were contrasted to determine structural properties that affect the aromatic overlap and inter-planar distances of these strong electron accepting compounds in the solid state. It was determined that the $TRPH(C_4F_4)$, with inter-planar distances of 3.396 Å, approaching that of graphite, has three important physical characteristics that promote short interplanar distances. These three physical characteristics are (i) the C_4F_4 substitution does not greatly change the Z dimension of the triphenylene core, (ii) the C_4F_4 moiety makes the $TRPH(C_4F_4)$ have a dipole causing the molecule to orient with a 180° rotation relative to molecules above and below (iii) the triphenylene core is still relatively open allowing for significant aromatic overlap. Comparatively the 5 $PAH(CF_3)_n$'s presented have little overlap or complete overlap at distances too great for electronic communication between overlapping layers. Based on this finding, when attempting to design new organic electronic compounds, the structural characteristics of $TRPH(C_4F_4)$ should be taken into account.

6.8 Future Work

Important future experiments regarding the metal reactor include using larger, more thermally stable PAHs to determine if the reactor works for other large PAHs that were unsuccessful in the sealed glass ampoules. Perform reactions with a mixture of CF_3I and $N_2(g)$

(or other inert gas) to determine if the increased pressure is changing the reaction or just the concentration of CF_3I . Also test new $\text{I}_2(\text{g})$ scavengers that do not change the reaction by changing the thermal homolysis temperature of the C–I bond, CF_3I adsorption/desorption kinetics, $\text{I}\cdot/\text{I}_2$ scavenging etc.) as much as copper powder. Determine if $\text{I}\cdot$ is important to eliminate HI and rearomatize the PAH core after the CF_3 addition, by a control experiment hexafluoroacetone as the $\text{F}_3\text{C}\cdot$ radical generator removing $\text{I}\cdot$ from the reaction. Finally, to determine if CF_3 can be removed from a F_3C –PAH during the reaction a second control experiment with only a single $\text{PAH}(\text{CF}_3)_n$ heated to a temperature or many temperatures to see if it is thermally stable once produced.

6.9 Experimental:

6.9.1 Reagents and Solvents:

All reagents and solvents were used as received unless otherwise noted. Anthracene (TCI America, 94%), coronene (TCI America, > 95%), C_{60} (MTR Ltd. 99.50%), C_{70} (MTR Ltd. 98+%), copper powder (Strem, 99% copper powder), 1-iodotrifluoromethane (SynQuest Labs), heptane (Fisher Scientific, ACS grade), dichloromethane (Fisher Scientific, ACS grade), toluene (Fisher Scientific, ACS grade) chloroform-*d* (CDCl_3 , Cambridge Isotopes Laboratories, Inc. 99.8% D), toluene-*d*₈ ($\text{C}_6\text{D}_5\text{CD}_3$, Cambridge Isotopes Laboratories, Inc. 99.5% D), benzene-*d*₆ (C_6D_6 , Cambridge Isotopes Laboratories, Inc. 99.5% D), 1,4-bis(trifluoromethyl)benzene (Chemical Research Centre, Central Glass, CO. LTD. 99%), perfluorobenzene (C_6F_6 , Sigma Aldrich, 99%).

6.9.2 Instrumentation:

HPLC: All HPLC analysis were performed by Nicholas J. Deweerd using a Shimadzu LC-6AD with a SPD-201A UV-vis detector operating on two wavelengths, 300 nm and 370 nm. The columns used were either a semi-preparative COSMOSIL Buckyprep column (10 × 250 mm, Nacalai Tesque) or a semi-preparative COSMOSIL Buckyprep-M column (10 × 250 mm, Nacalai Tesque) as described. Eluent solvents were either heptane or toluene.

Negative Ion Electrospray Mass Spectroscopy: Mass spectra were recorded using a Finnigan LTQ-LC/MS-MS mass-spectrometer with an electrospray ionization source, or a 2000 Finnigan LCQ-DUO mass-spectrometer with an electrospray ionization source. Samples were on the order of 10–50 μ M concentration in toluene (fullerene based compounds) or MeCN (PAH based compounds).

NMR Spectroscopy: All NMR spectra were taken on a Varian INOVA 400 MHz automatic tune instrument in 5 mm NMR spectroscopy grade glass tubes. Nuclei observed were ^{19}F and ^1H at a frequency of 376.01 MHz and 399.7 MHz respectively. Both nuclei used 1 s relaxation time and 60° pulse angle. Experiments were performed in CDCl_3 , toluene- d_8 , or C_6D_6 as described. Proton NMR spectra were referenced to the residual proton peaks in each NMR solvent (CHCl_3 $\delta = 7.27$ (singlet), CHD_2 peak in toluene- d_8 $\delta = 2.09$ (pentet), C_6HD_5 $\delta = 7.16$ (singlet)). The ^{19}F spectra were referenced to added C_6F_6 $\delta = -164.9$ (singlet) or added 1,4-bis(trifluoromethyl)benzene $\delta = -66.4$ (singlet).

X-ray Crystallography: Single crystals of ACRD-4-1, ANTH-6-1, AZUL-4-1, H_2TETR -8-1, NAPH-4-1, PHNZ-4-2 and TRPH(C_4F_4) were grown as previously described, data were collected at Colorado State University. Samples were mounted on a Mylar loop with paratone

oil. Data from single crystals of were collected using a Bruker Kappa APEX II CCD diffractometer (MoK α λ = 0.71073 Å; graphite monochromator) at T = 120(2) K. Data reduction was performed with APEX 2 suite of software from Bruker. Solution and structure refinement were performed with SHELXTL software³⁹⁻⁴², or OLEX 2, Version 1.2.5.⁴³ A semiempirical absorption correction was applied with SADABS³⁹. All figures were generated with SHELXTL XP software.^{40,44}

Single crystals of H₂ANTH₂-(Bn_F)₂, H₂CORO(CF₃)₇₋₁ and H₂CORO(CF₃)₈₋₁ were grown as previously described, data were collected at Argonne National Laboratory, Advanced Photon Source, Lemont IL, Using Synchrotron Radiation Source, Beamline 15-ID-B, ChemMATCARS. Samples were mounted on glass fiber filament with paratone oil. Data from single crystals of were collected at 100(2) K using a synchrotron radiation (λ = 0.41328 Å) with a diamond (111) monochromator, a Bruker D8 goniometer, and Bruker CCD detector controlled by Bruker APEX II software. Data reduction was performed with APEX 2 suite of software from Bruker. Solution and structure refinement were performed with SHELXTL software³⁹⁻⁴², or OLEX 2, Version 1.2.5.⁴³ A semiempirical absorption correction was applied with SADABS³⁹. All figures were generated with SHELXTL XP software.^{40,44}

6.9.3 Synthesis with Anthracene and CF₃I in Metal Reactor

Anthracene powder (55.4 mg, 0.331 mmol) and copper powder (2.37 g, 37 mmol) were added to the metal reactor in air and CF₃I (4.18 mmol) was loaded into the metal reactor anaerobically. The reactor was placed in preheated (360 °C) tube furnace and held isothermally for 3 h, after which time the reactor was promptly removed and cooled to room temperature with convection in ca. 25 min. The cooled reactor was opened and washed with five aliquots (10 mL ea.) of DCM. The DCM rinses were combined, filtered to remove any copper or CuI₂ powder,

and then dried by rotary evaporation. The DCM soluble mass = 0.148 g, 81% crude yield assuming 6 CF₃ substitutions.

6.9.4 Synthesis of H₂CORO(CF₃)₇-1 and H₂CORO(CF₃)₈-1 in Metal Reactor

Coronene powder (50.2 mg, 0.167 mmol) and copper powder (4.55 g, 72 mmol) were added to the metal reactor in air and CF₃I (5.72 mmol) was loaded into the metal reactor anaerobically. The reactor was placed in preheated (450 °C) tube furnace and held isothermally for 4 h, after which time the reactor was promptly removed and cooled to room temperature with convection in ca. 25 min. The cooled reactor was opened and washed with five aliquots (10 mL ea.) of toluene. The toluene rinses were combined, filtered to remove copper or CuI₂ powder and then dried by rotary evaporation. Toluene soluble mass = 0.093 g, 78% crude yield assuming 6 CF₃ substitutions.

6.9.5 Synthesis with C₆₀ and CF₃I in Metal Reactor

The C₆₀ powder (49.2 mg, 0.068 mmol) and copper powder (1.81 g, 28 mmol) were added to the metal reactor in air and CF₃I (2.75 mmol) was loaded into the metal reactor anaerobically. The reactor was placed in preheated (450 °C) tube furnace and held isothermally for 3 h, after which time the reactor was promptly removed and cooled to room temperature with convection in ca. 25 min. The cooled reactor was opened and washed with five aliquots (10 mL ea.) of toluene. The toluene rinses were combined, filtered to remove any copper or CuI₂ powder, and then dried by rotary evaporation. The toluene soluble mass = 0.084 g, 81% crude yield assuming 12 CF₃ substitutions. The C₆₀(CF₃)₁₂-S₆ isomer was isolated by filling the metal tube of the metal tube reactor with 10–12 mL toluene and sonicating for 10 min repeating process 3 times. The toluene was then poured into a vial and dried to a yellow brown solid weighing ca. 20 mg. Due

to the visible yellow brown residue on the inside of the metal tube after the sonication extraction, a total mass and yield of $C_{60}(CF_3)_{12}-S_6$ isomer was never determined.

6.9.6 Synthesis with C_{70} and CF_3I in Metal Reactor

The C_{70} powder (50.0 mg, 0.059 mmol) and copper powder (2.11 g, 33 mmol) were added to the metal reactor in air and CF_3I (1.19 mmol) was loaded into the metal reactor anaerobically. The reactor was placed in preheated (450 °C) tube furnace and held isothermally for 1 h, after which time the reactor was promptly removed and cooled to room temperature with convection in ca. 25 min. The cooled reactor was opened and washed with 5 aliquots (10 mL ea.) of toluene. The toluene rinses were combined, filtered to remove any copper or CuI_2 powder, and then dried by rotary evaporation. The toluene soluble mass = 0.023 g 12% crude yield assuming 12 CF_3 substitutions.

6.8 Figures

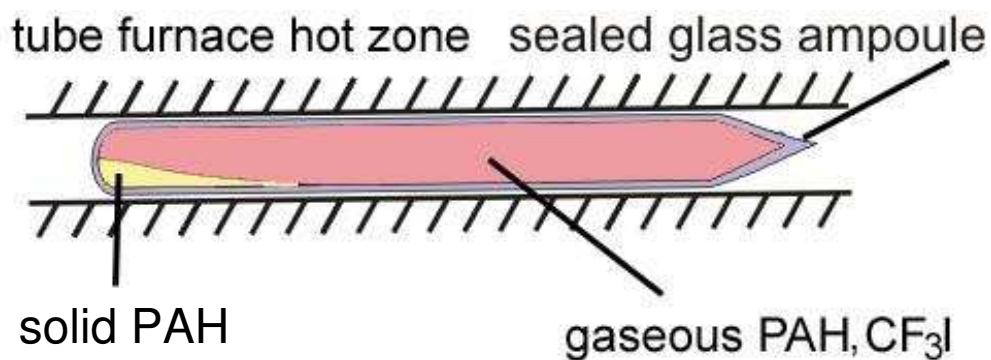


Figure 6-1. Diagram of a reaction set-up of PAH and gaseous CF₃I in a sealed glass ampoule completely contained in a furnace. The reaction is initiated by thermal homolysis of the C–I bond in F₃CI forming F₃C• and I• radicals. The F₃C• radical then reacts with the liquid or gaseous PAH. The entire glass ampoule must be contained in the hot zone of the tube furnace otherwise the PAH or PAHs with a low number of CF₃ substitutions will sublime and condense in the colder regions of the glass ampoule, halting reaction.

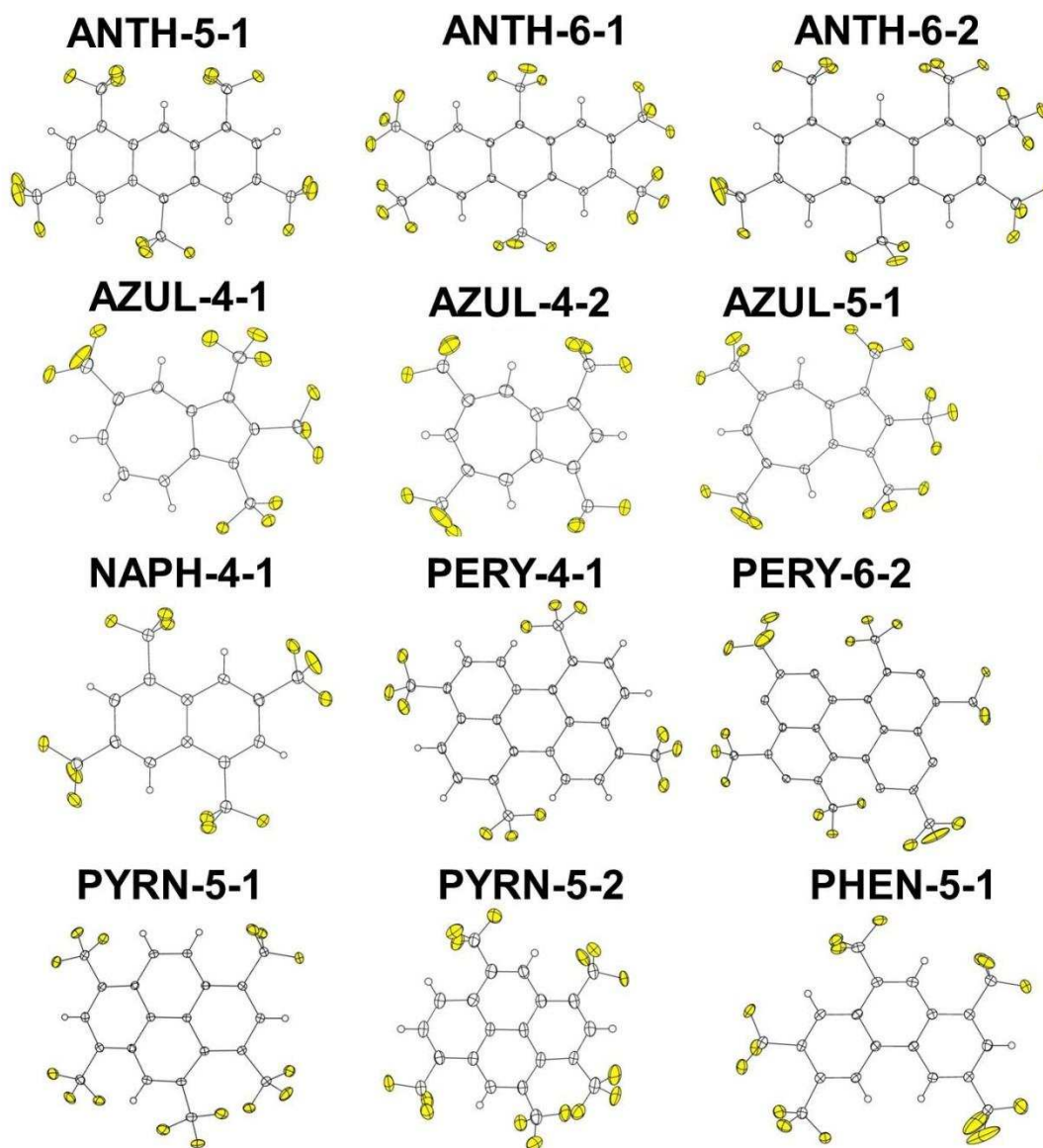


Figure 6-2. Thermal ellipsoid plots of a selection of trifluoromethylated polycyclic aromatic hydrocarbons (PAH(CF₃)_n) produced in sealed glass ampoules. The naming of these compounds throughout this dissertation chapter is a four letter designation of the starting PAH, the number of CF₃ substitutions, and the isomer number for that particular number of CF₃ substitutions (isomer number is arbitrary and is consecutive starting from 1 for the first isomer discovered).



Figure 6-3. Two separate reactions of PAH with CF_3I . (Top) Sealed glass ampoule only contained the PAH and CF_3I gas, note the purple iodine color. (Bottom) Sealed glass ampoule of a separate reaction of the same PAH with CF_3I with added Cu metal powder, note the absence of purple iodine. These reactions were completed and photographs were taken by fellow Strauss-Boltalina group member, Kerry Rippy.

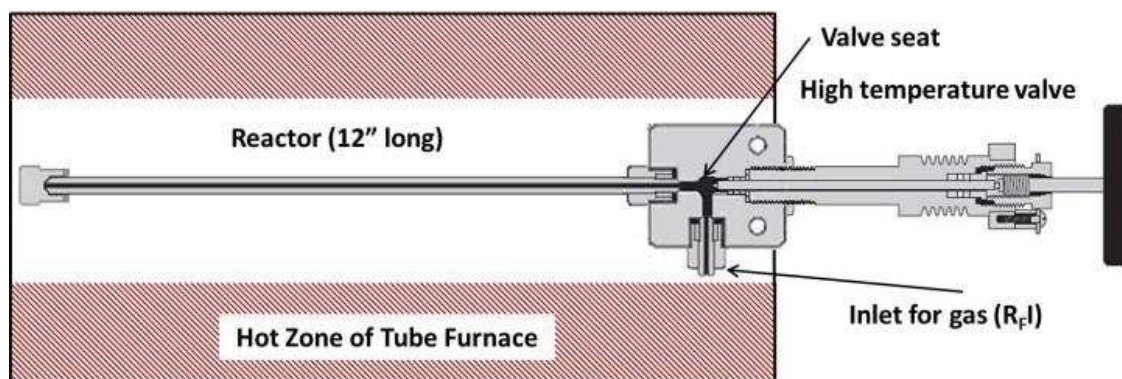


Figure 6-4. The valve is such that the body of the valve can be heated while the valve packing stem is lengthened to remove it from the constant heat source. The valve has heat dissipating fins and the packing is composed of Grafoil® allowing the packing to still be heated to over 500 °C, even though it is extended away from the direct heat source. This valve and reactor is rated up to 20,000 psi when the valve is open or closed for an added margin of safety. After insertion of the reactor into the tube furnace suitable refractory material is used to seal the tube furnace to minimize temperature fluctuations throughout the heating cycle.

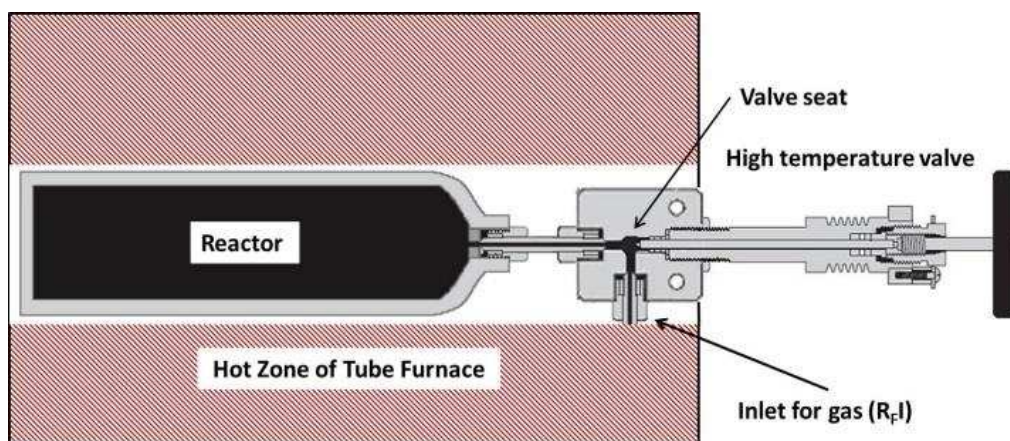


Figure 6-5. The valve can be the same as the smaller reactor. The reactor could be scaled such that the maximum amount of product can be made per batch constrained only by the largest tube furnace in the Strauss-Boltalina research group. The effective heating zone in the largest furnace is I.D. = 9 cm, length 36 cm.

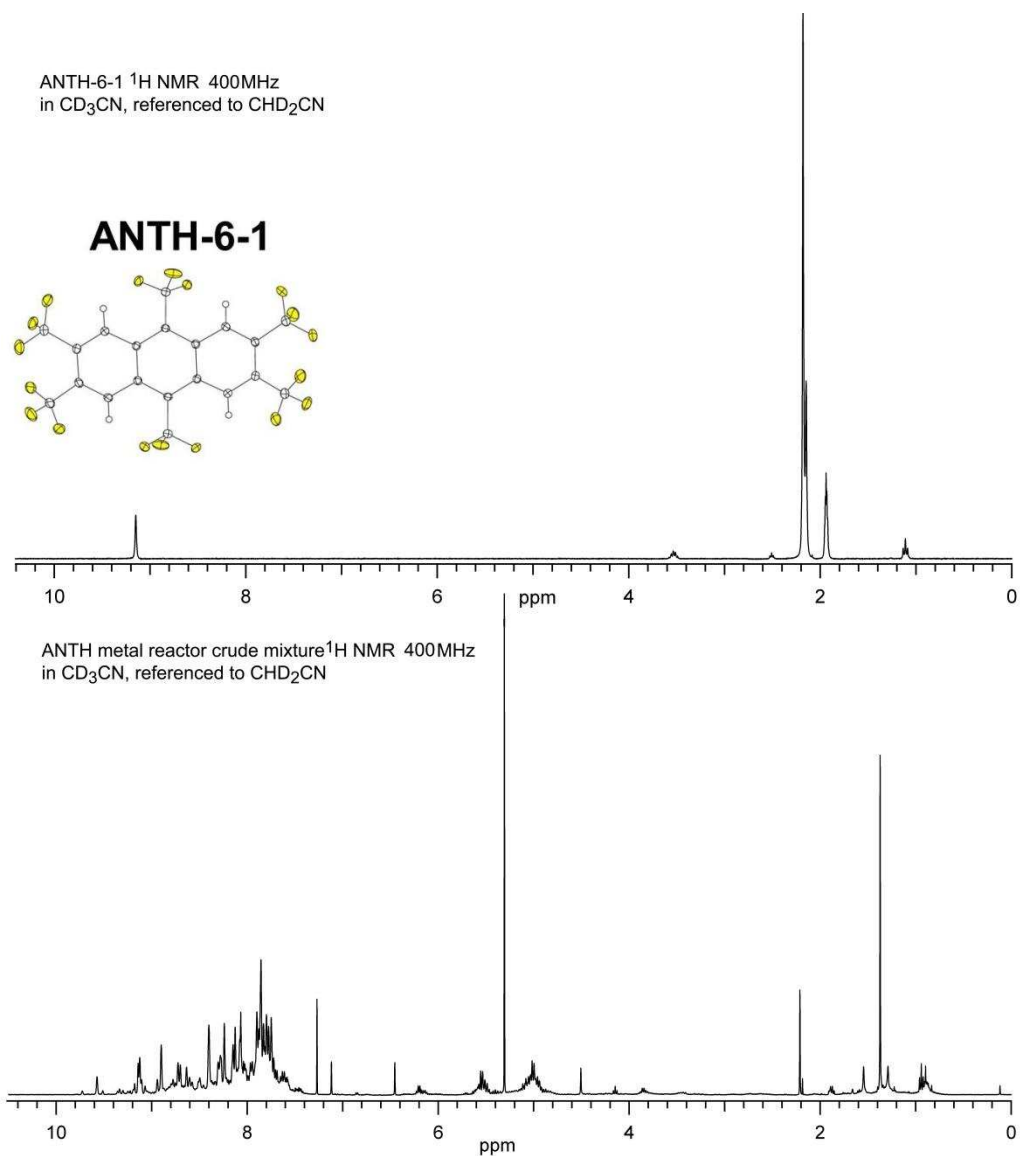


Figure 6-6. (Top) Proton NMR spectra of purified ANTH-6-, the only signal corresponding to ANTH-6-1 is $\delta = 9.17$ for the 4 equivalent hydrogens. (Bottom) Proton NMR spectrum of the crude the reaction mixture of ANTH with 13 equiv CF_3I , in the metal reactor, 360°C , 3 h. The crude reaction mixture from the metal reactor had many compounds and isomers and was deemed too complex, and the recovered individual compounds would be too small to attempt to separate by HPLC and analyze. This does demonstrate successful reaction with ANTH and CF_3I in the metal reactor.

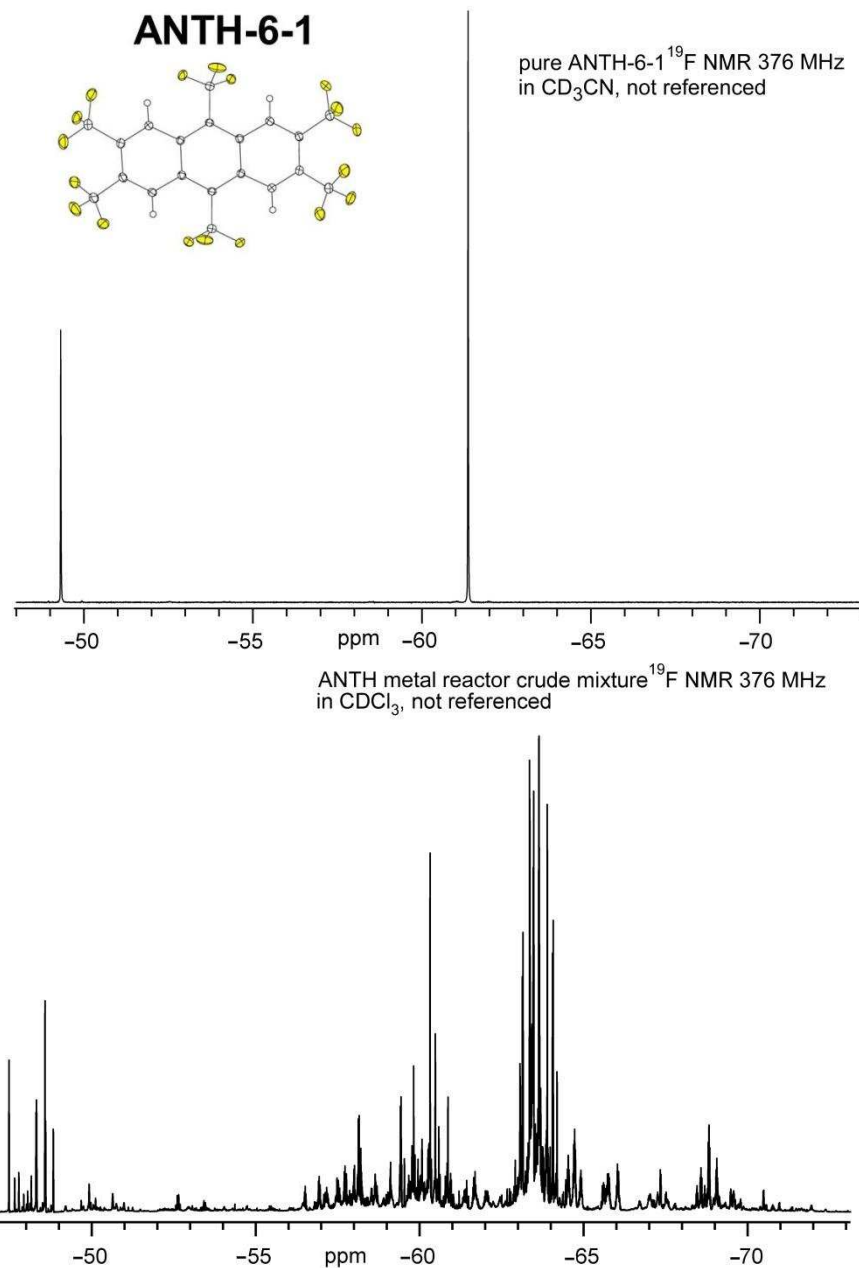


Figure 6-7. (Top) Fluorine-19 NMR spectra of purified ANTH-6-1. (Bottom) The crude reaction mixture from a reaction of ANTH with 13 equiv CF_3I , in the metal reactor, 360 °C, 3 h. The crude reaction mixture from the metal reactor had many compounds and isomers and was deemed too complex. Attempts to separate by HPLC would have produced individual compounds in quantities too small to analyze. This does demonstrate successful reaction with ANTH and CF_3I in the metal reactor.

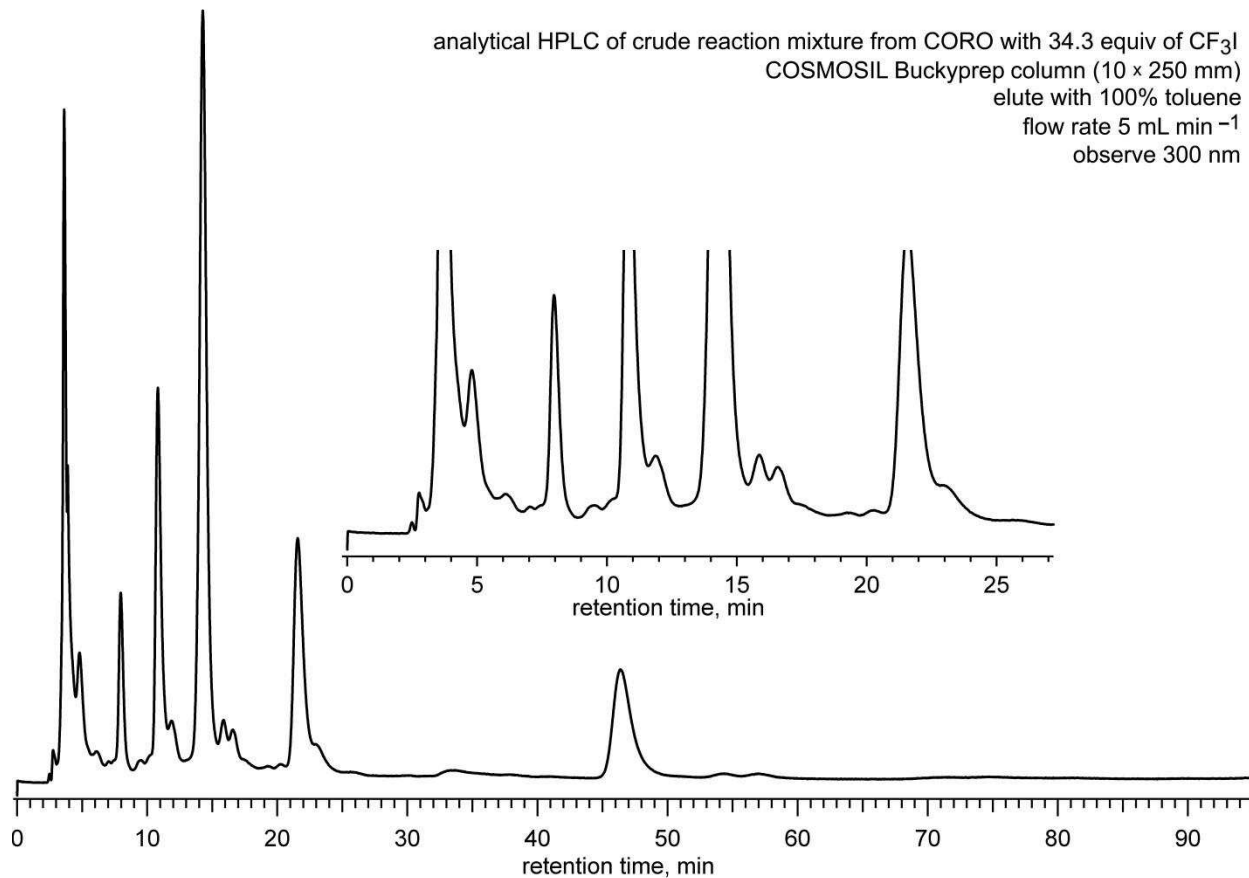


Figure 6-8. Representative HPLC trace of the crude reaction mixture from the coronene reaction in the metal tube reactor with excess Cu powder 34.3 equiv of CF₃I, at 450 °C for 4 h. Multiple nearly pure fractions were collected by HPLC and of the collected fractions two formed crystals characterized structurally by SC-XRD. The HPLC trace and separation were performed by fellow graduate student Nicholas Deweerd. Heptane was used as the eluent to give the best peak separation

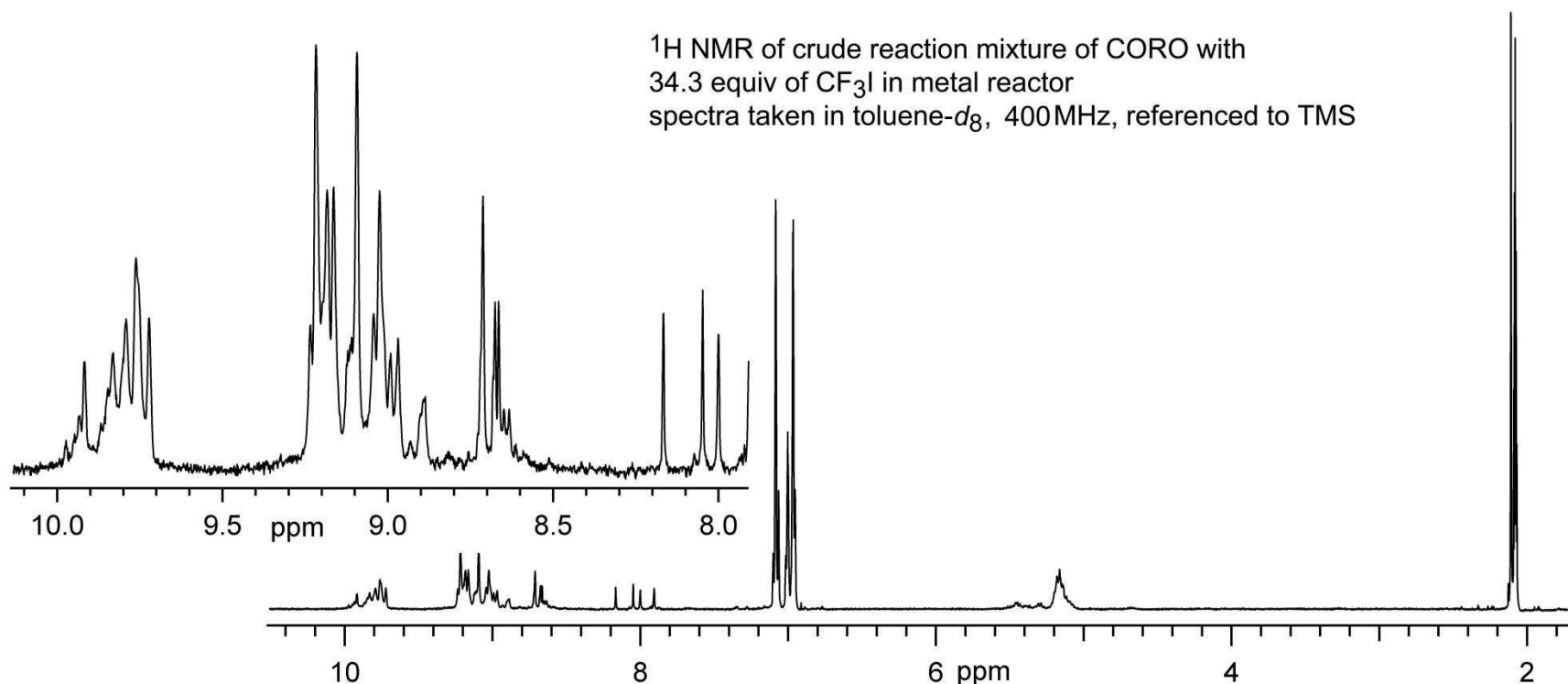


Figure 6-9. The ¹H NMR spectrum of the crude reaction mixture from the coronene reaction in the metal tube reactor with excess Cu powder 34.3 equiv of CF₃I, at 450 °C for 4 h. The crude reaction mixture from the metal reactor had many compounds and isomers. The chemical shift range from $\delta = 7.8$ to 10 is expected for hydrogens on sp² carbon atoms in a coronene molecule. The peaks $\delta = 5.0$ to 5.6 are hydrogens on sp³ carbon atoms in a coronene molecule with broken aromaticity. The broadness of the peaks is due to the large number of compounds and isomers in the crude mixture. This reaction mixture was partially separated using HPLC by fellow graduate student Nicholas Deweerd. Two of the separated compounds were fractions pure enough to grow single crystals suitable for SC-XRD.

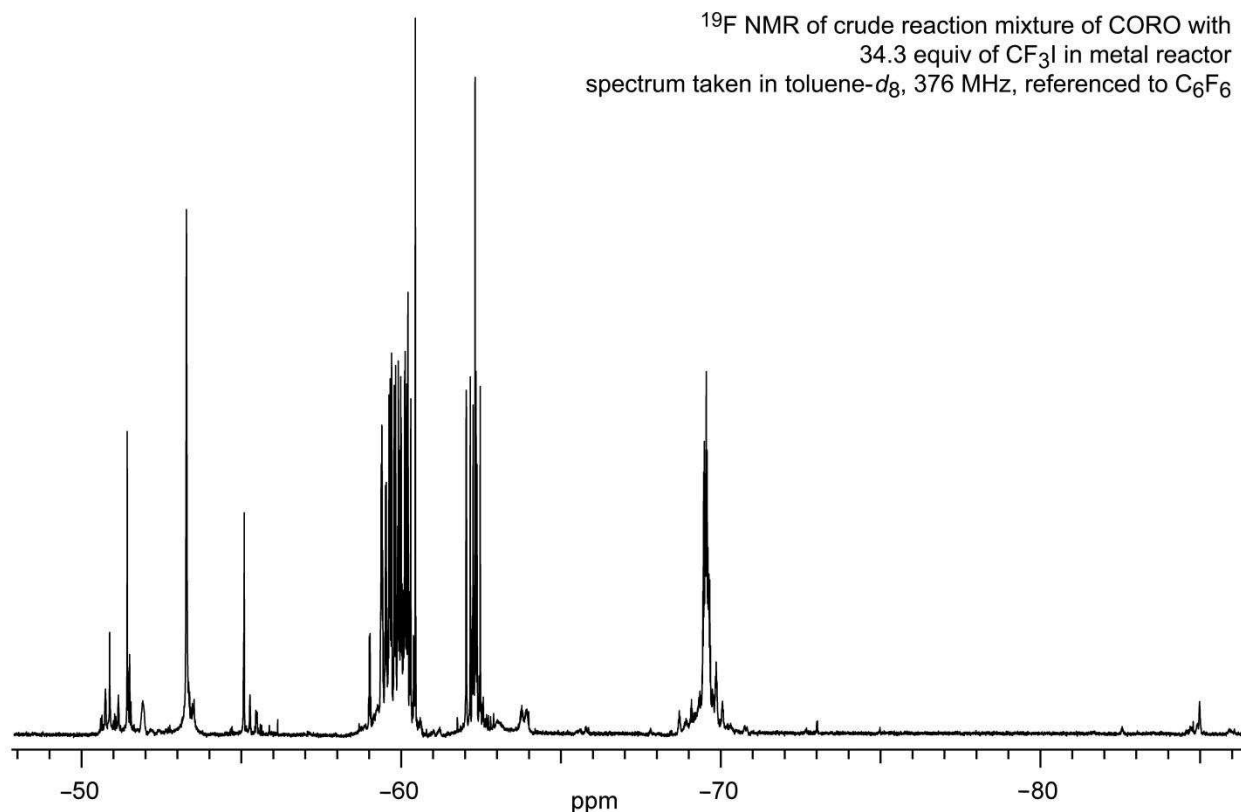


Figure 6-10. Fluorine-19 NMR spectrum of crude reaction mixture from the coronene reaction in the metal tube reactor with excess Cu powder 34.3 equiv of CF₃I, at 450 °C for 4 h. The crude reaction mixture from the metal reactor has many compounds and isomers. The broad chemical shift range for this reaction mixture is believed to arise from the many compounds and isomers and the formation of sp³ carbon atoms in the reaction that are bonded to CF₃ groups. This reaction mixture was partially separated using HPLC by fellow graduate student Nicholas Deweerdt. Two of the separated compounds were fractions pure enough to grow single crystals suitable for SC-XRD.

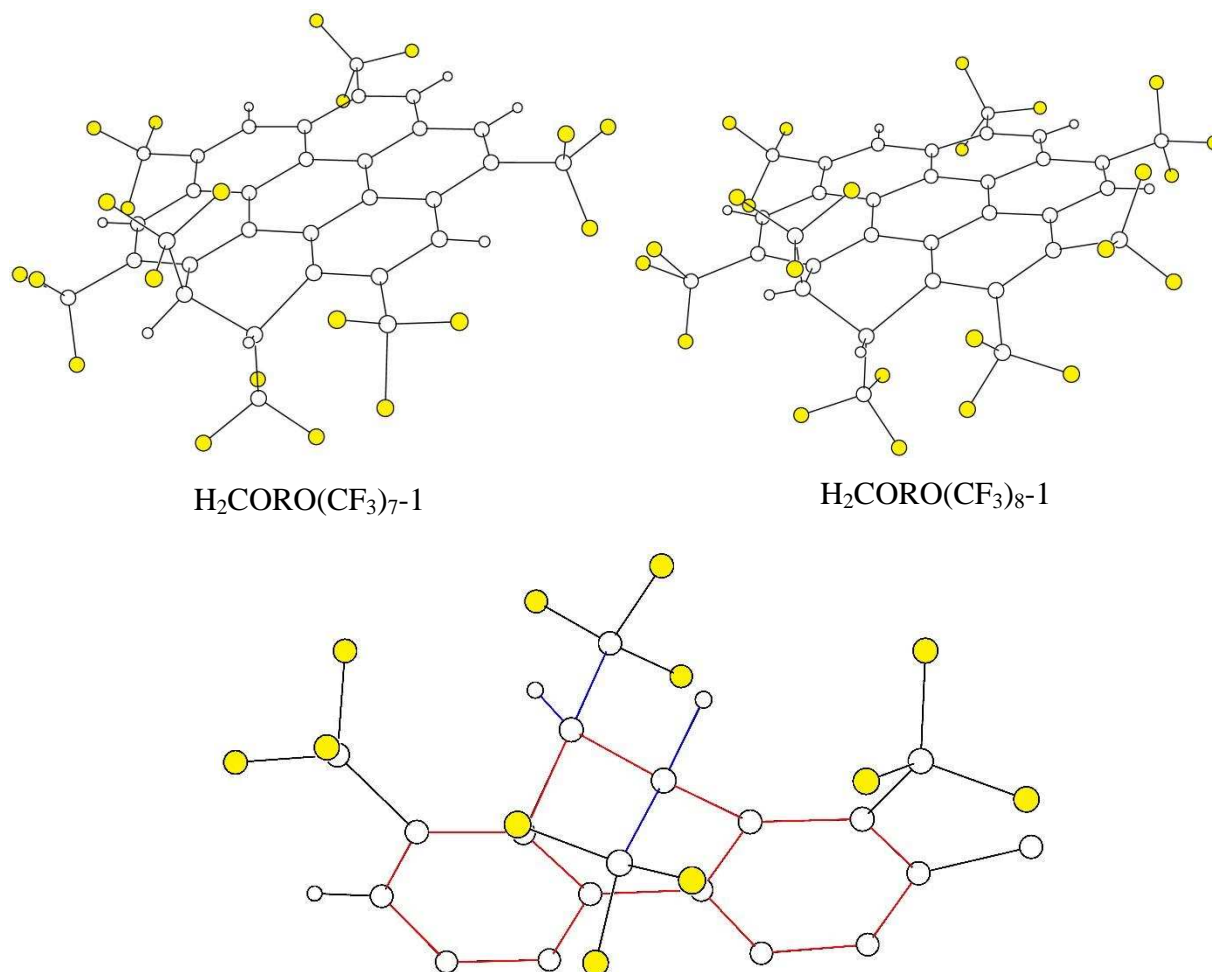


Figure 6-11. (Top) Single crystal X-ray structures of coronene derivatives collected by HPLC separation, and crystallized for SC-XRD. The SC-XRD was performed by Tyler Clikeman and Kerry Rippey with synchrotron radiation at Argonne National Laboratory, Advanced Photon Source. The two structures shown above are coronene derivatives with broken aromaticity. The compound on the left has 5 substitutions of CF_3 and 2 additions of CF_3 and the compound on the right has 6 substitutions of CF_3 and 2 additions of CF_3 . (Bottom) The broken aromaticity has the same pattern for both molecules shown in the lower figure, note part of the coronene structure has been removed for clarity. All atoms are shown as spheres of arbitrary size, F atoms are yellow spheres, carbon atoms are large white spheres and H atoms are small white spheres. The H_2CORO is lined with red bonds and the sp^3 carbon bonds are blue.

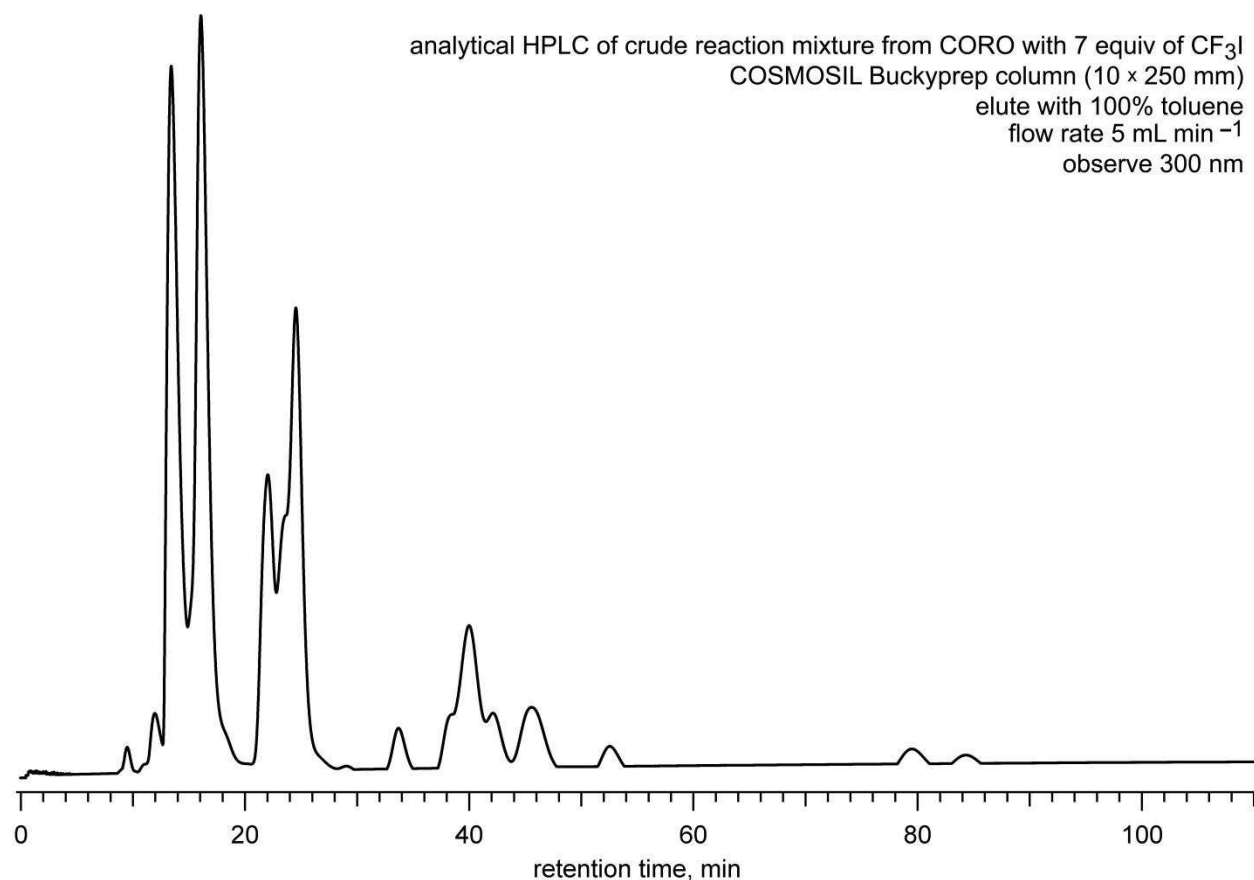


Figure 6-12. Representative HPLC trace of the crude reaction mixture of the coronene reaction in the metal tube reactor with excess copper powder, 7 equiv of CF₃I, at 450 °C for 4 h. The HPLC trace and separation was performed by fellow graduate student Nicholas Deweerd. Note that this HPLC was run with 100% toluene compared to the first HPLC in Figure 6-8, which was run in 100% heptane. The toluene has the effect of making CORO compound elute faster and with less separation than in heptane.

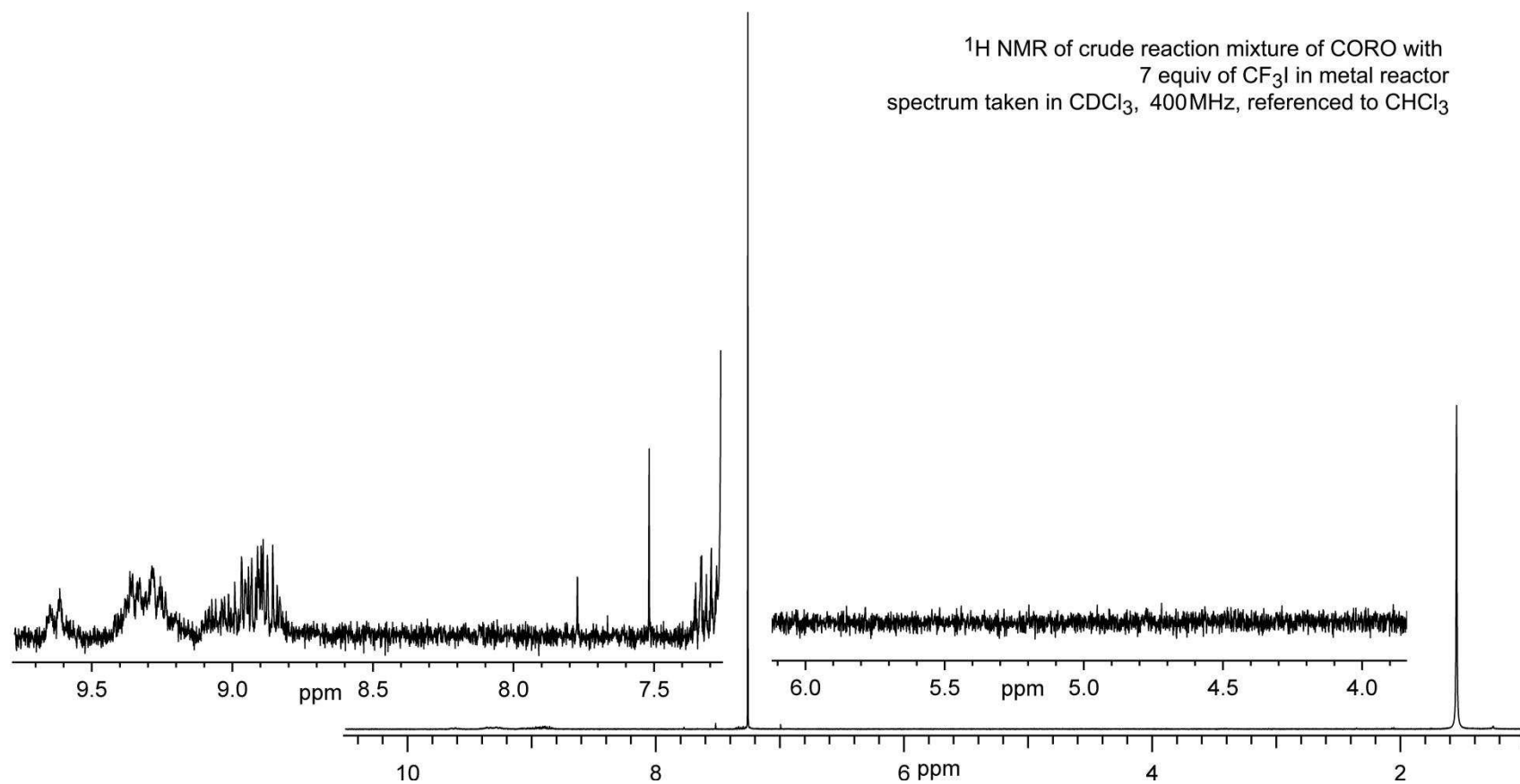


Figure 6-13. The ¹H NMR spectrum of the crude reaction mixture of the coronene reaction in the metal tube reactor with excess copper powder, 7 equiv of CF₃I, at 450 °C for 4 h. Note that the number of ¹H NMR signals is considerably lower and in a much narrower range than the spectrum shown in Figure 6-8. Additionally, there are no peaks in the range of $\delta = 4$ to 6, an indication that there was no formation of sp² carbon atoms in this crude reaction mixture.

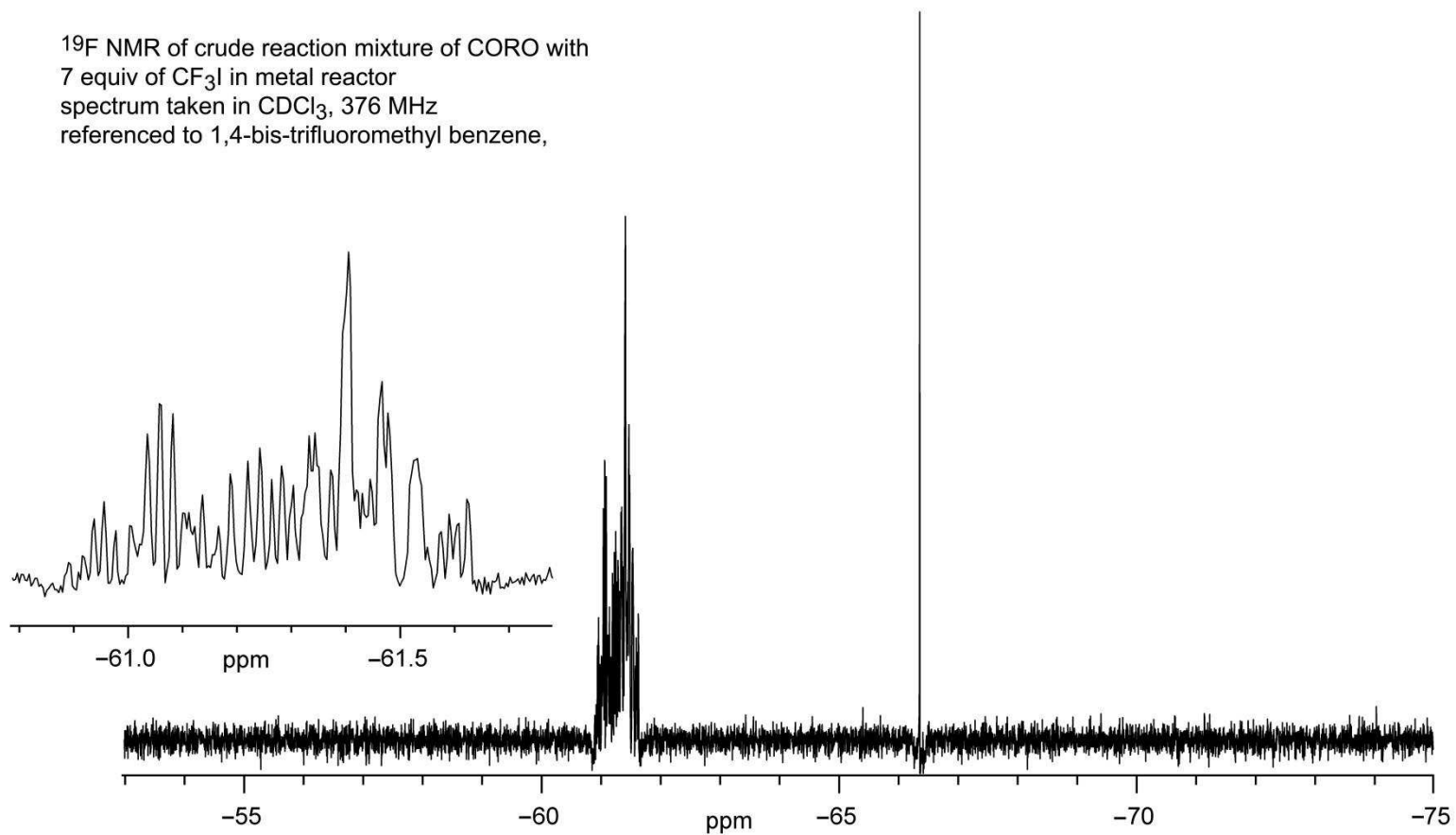


Figure 6-14. The ¹⁹F NMR spectrum of the crude reaction mixture of the coronene reaction in the metal tube reactor with excess copper powder, 7 equiv of CF₃I, at 450 °C for 4 h. Note that the number of ¹⁹F NMR signals is considerably lower and in a much narrower range than the spectrum shown in Figure 6-8. The spectrum is referenced to 1,4-bis-trifluoromethyl benzene (singlet to the left of the complex multiplet) at $\delta = -66.4$.

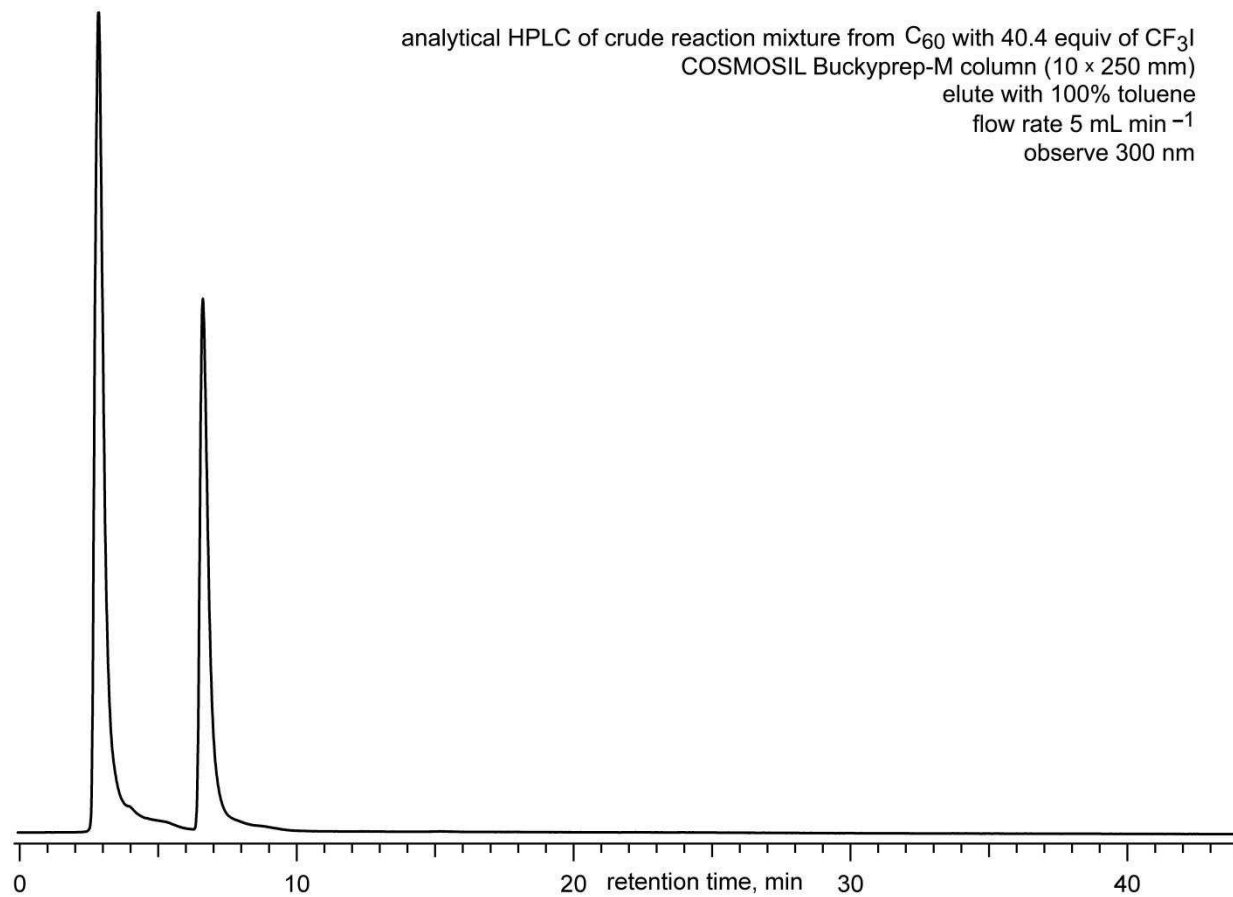


Figure 6-15. Analytical HPLC of the crude reaction mixture produced in the metal reactor starting with C₆₀ and 40.4 equiv of CF₃I, at 450 °C for 3 h. The peak at a retention time range of 6–8 min is due to unreacted C₆₀. The peak at retention time range 2–6 min is a mixture of co-eluting C₆₀(CF₃)_n compounds where *n* ranges from 12–18 additions.

^{19}F NMR of crude reaction mixture of C_{60} with
40.4 equiv of CF_3I in metal reactor
spectrum taken in CDCl_3 , 376 MHz
referenced to C_6F_6

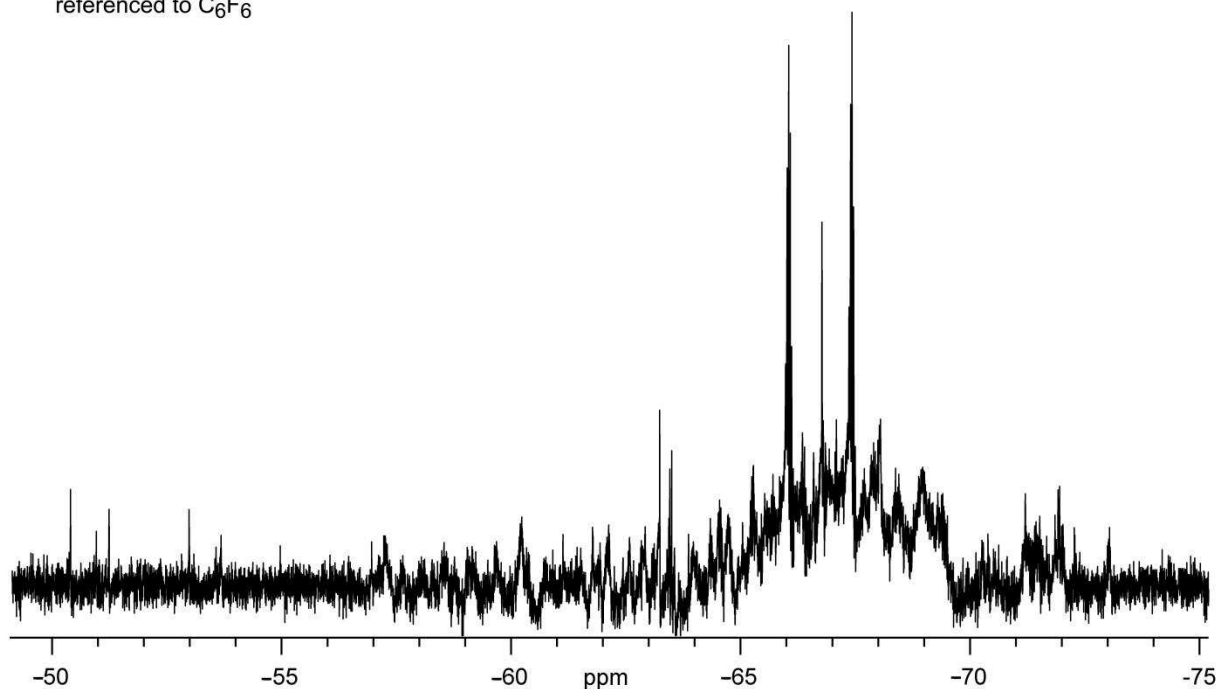


Figure 6-16. The ^{19}F NMR spectrum of the crude reaction mixture produced in the metal reactor starting with excess copper C_{60} and 40.4 equiv of CF_3I , at $450\text{ }^\circ\text{C}$ for 3 h. The spectrum was taken in CDCl_3 and referenced to C_6F_6 , $\delta = -164.9$. The two tall peaks at $\delta = -66.1$ and -67.4 correspond to a particular $\text{C}_{60}(\text{CF}_3)_{12}$ isomer with S_6 symmetry. Overall the crude reaction mixture had low conversion and formed many products, with the largest single product being $\text{C}_{60}(\text{CF}_3)_{12}\text{-}S_6$.

^{19}F NMR of isolated $\text{C}_{60}(\text{CF}_3)_{12}$ compound from metal reactor
 reaction with 40.4 equiv CF_3I
 spectrum taken in C_6D_6 , 376 MHz, referenced to C_6F_6

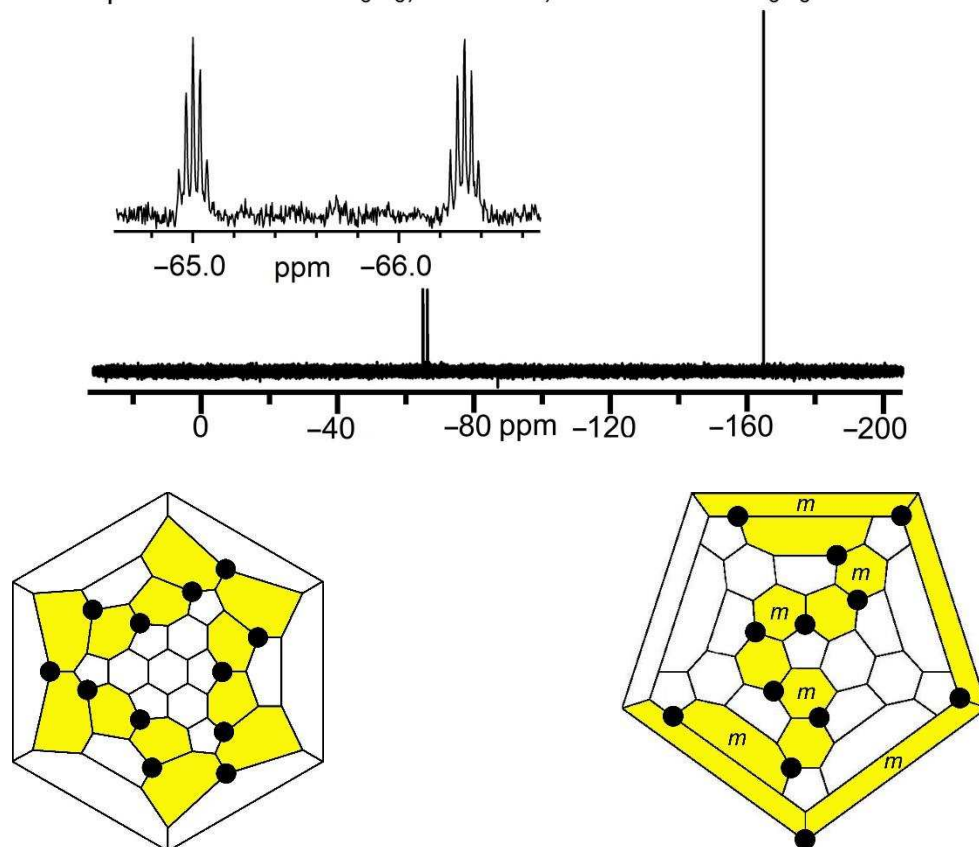


Figure 6-17. (Top) The ^{19}F NMR spectrum of the largest single product from the crude reaction mixture produced in the metal reactor starting with excess copper C_{60} and 40.4 equiv of CF_3I , at $450\text{ }^\circ\text{C}$ for 3 h was $\text{C}_{60}(\text{CF}_3)_{12}\text{-S}_6$. This isomer of 12 CF_3 additions is particularly thermodynamically favored, has high symmetry, and was preferentially collected due to its low solubility in most organic solvents. (Bottom) Two Schlegel diagrams indicating the CF_3 addition positions are shown below the spectrum. The left Schlegel diagram shows the symmetry of the addition pattern down the 3-fold symmetric axis of the C_{60} cage. The right Schlegel diagram is looking down the 5-fold symmetric axis of the C_{60} cage. The 5-fold symmetry is more typically shown in the Strauss-Boltalina group to describe the addition pattern to a C_{60} molecule. The NMR spectrum was collected in C_6D_6 using C_6F_6 as a chemical shift standard with $\delta = -164.9$.

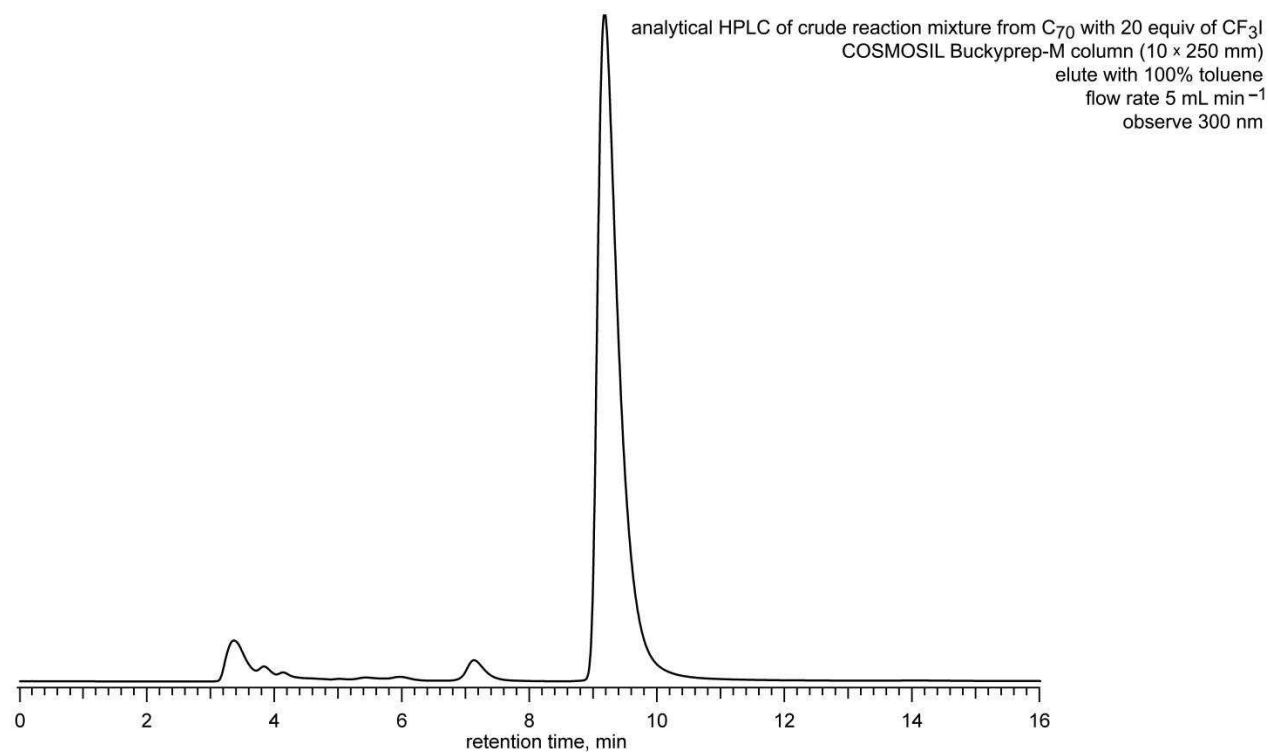


Figure 6-18. Analytical HPLC of the crude reaction mixture produced in the metal reactor starting with excess copper, C₇₀ and 20 equiv of CF₃I at 450 °C for 1 h. The tallest peak at a retention time range of 9–10 min is from unreacted C₇₀. The peaks before the C₇₀ are mixtures of co-eluting C₇₀(CF₃)_n compounds where *n* ranges from 14–20 additions.

¹⁹F NMR of crude reaction mixture of C₇₀ with
20 equiv of CF₃I in metal reactor
spectra taken in CDCl₃, 376 MHz, referenced to C₆F₆

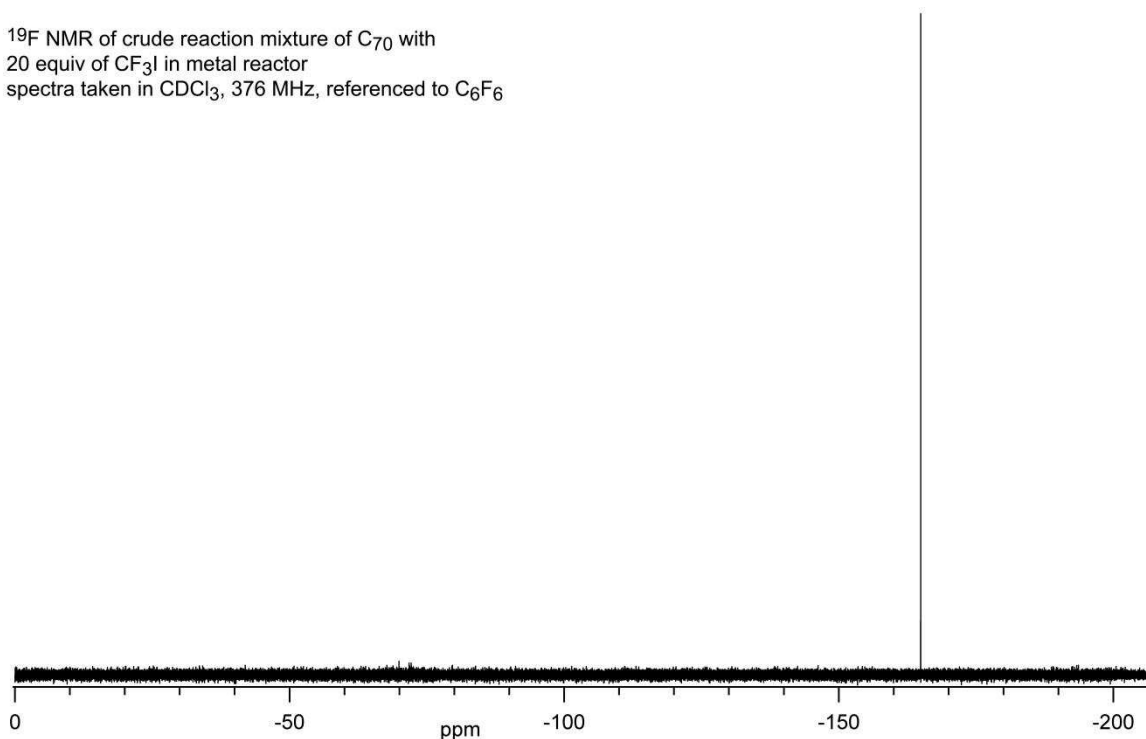


Figure 6-19. The ¹⁹F NMR spectrum of the crude reaction mixture produced in the metal reactor starting with excess copper, C₇₀ and 20 equiv of CF₃I at 450 °C for 1 h. The spectrum was taken in CDCl₃ and referenced to C₆F₆, δ = -164.9, the only visible peak in the spectrum. There is virtually no signal from the products due to low conversion to C₇₀(CF₃)_{2n} (where *n* > 1), and the C₇₀ that was converted to C₇₀(CF₃)_{*n*} products was converted to *n* = 14–20 compounds. In addition to making many compounds, the number of possible isomers for 14–20 additions of CF₃ groups to a C₇₀ cage is very large. The low ¹⁹F signal is due to low concentration of any one particular compound.

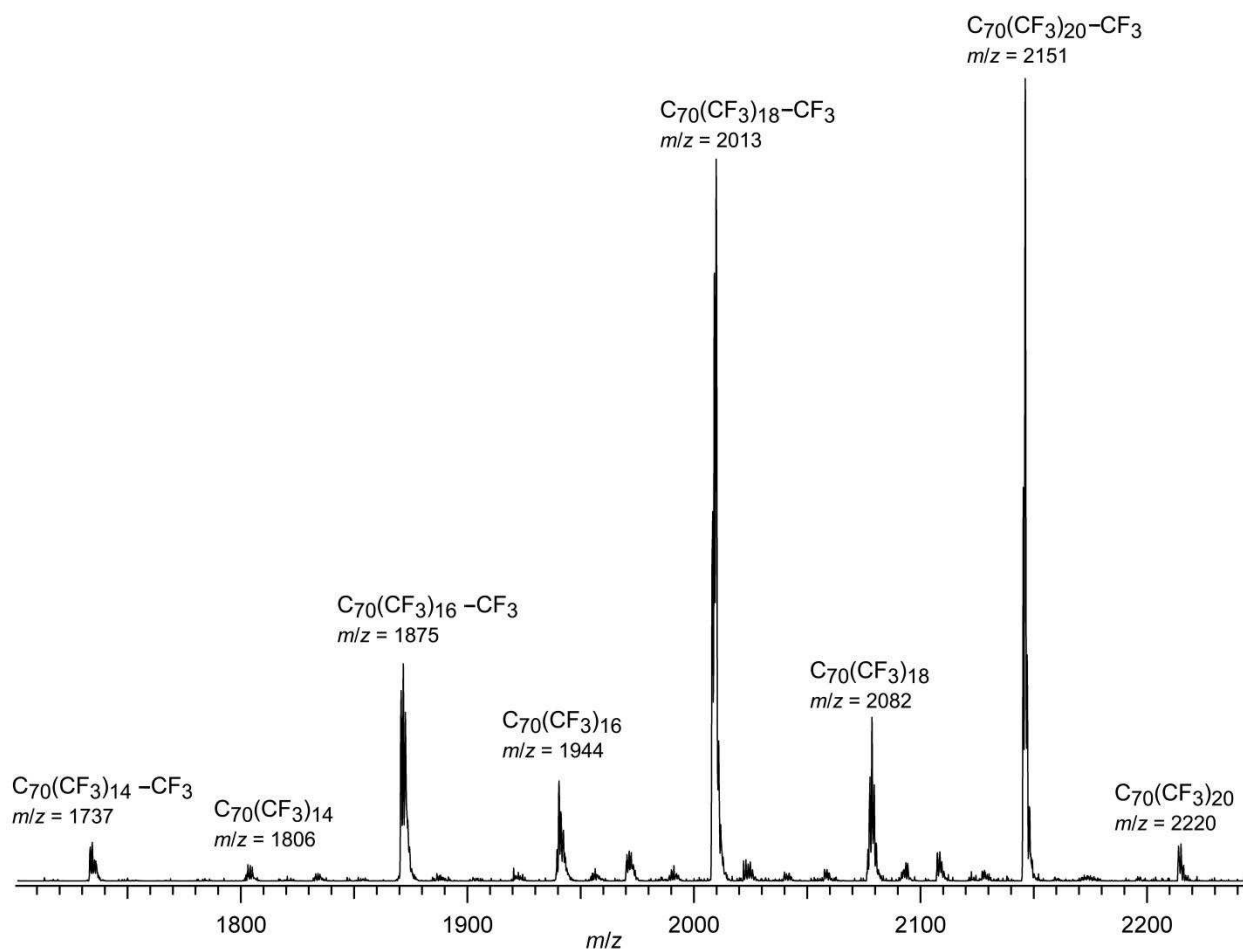


Figure 6-20. The ESI mass spectrum of the crude reaction mixture produced in the metal reactor starting with excess copper, C_{70} and 20 equiv of CF_3I at 450 °C for 1 h. The ESI-MS is not representative of the entire sample because the ESI ionization source is not well suited for ionizing fullerene species with low additions of CF_3 groups. This mass spectrum does demonstrate that the reaction in the metal reactor did produce some $C_{70}(CF_3)_n$ species where $n = 14-20$.

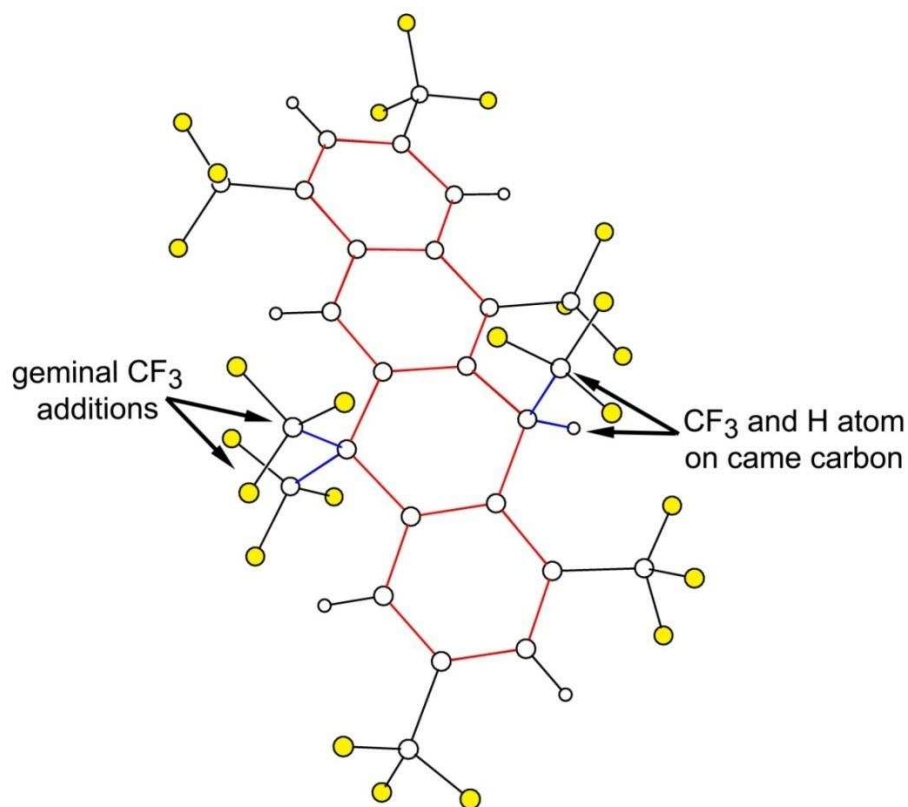


Figure 6-21. Single crystal XRD structure of H₂TETR-8-1 with 2 sp³ carbon atoms *para* to one another on an interior ring of the PAH. The sp³ carbon with geminal CF₃ additions has F₃C–C bond lengths of 1.562 and 1.569 Å and bond angle of 109.5°. The sp³ carbon with an CF₃ and H atom has a F₃C–C bond length of 1.546 Å and bond angle of 107.8°. Due to the sp³ carbon atoms, the H₂-tetracene core is bent at the two sp³ carbon atoms 15.8° from planarity. This crystal structure is evidence of a radical reaction mechanism where the F₃C• reacts with a PAH core first forming a F₃C–PAH• intermediate. Then a second F₃C• radical reacts with the F₃C–PAH• intermediate and either removes the H atom forming F₃C–PAH, or some other reaction occurs that allows geminal F₃C groups. All atoms are shown as spheres of arbitrary size, F atoms are yellow spheres, carbon atoms are large white spheres and H atoms are small white spheres. The H₂ANTH is lined with red bonds and the sp³ carbon bonds are blue.

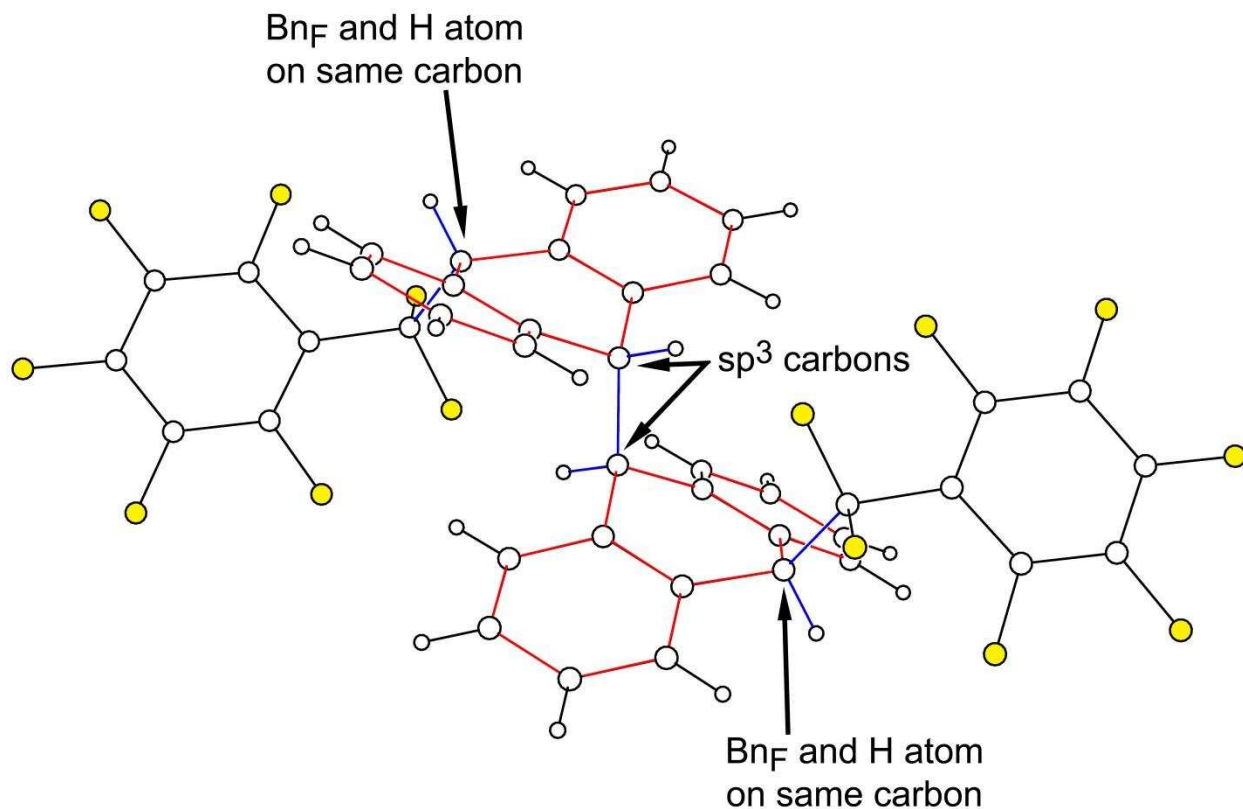


Figure 6-22. Single crystal XRD structure of $\text{H}_2\text{ANTH}_2(\text{BnF})_2$ dimer with 2 sp^3 carbon atoms per H_2ANTH core, *para* to one another. The sp^3 carbon with CF_3 addition and H atom has $\text{F}_3\text{C}-\text{C}$ bond length of 1.536 Å and bond angle of 105.7°. The sp^3 carbon with an H atom and adjacent H_2ANTH core has a $\text{C}-\text{C}$ bond length of 1.588 Å and bond angle of 107.4°. Due to the sp^3 carbon atoms, the H_2ANTH cores are bent at the two sp^3 carbon atoms 33.7° from planarity. This crystal structure is also evidence of a radical reaction mechanism where the $\text{F}_3\text{C}\cdot$ reacts with a PAH core first forming a $\text{F}_3\text{C}-\text{PAH}\cdot$ intermediate. Then in this case the $\text{F}_3\text{C}-\text{PAH}\cdot$ radical reacted with another $\text{F}_3\text{C}-\text{PAH}\cdot$ intermediate or an ANTH that was then terminated with a $\text{F}_3\text{C}\cdot$. All atoms are shown as spheres of arbitrary size, F atoms are yellow spheres, carbon atoms are large white spheres and H atoms are small white spheres. The H_2ANTH is lined with red bonds and the sp^3 carbon bonds are blue.

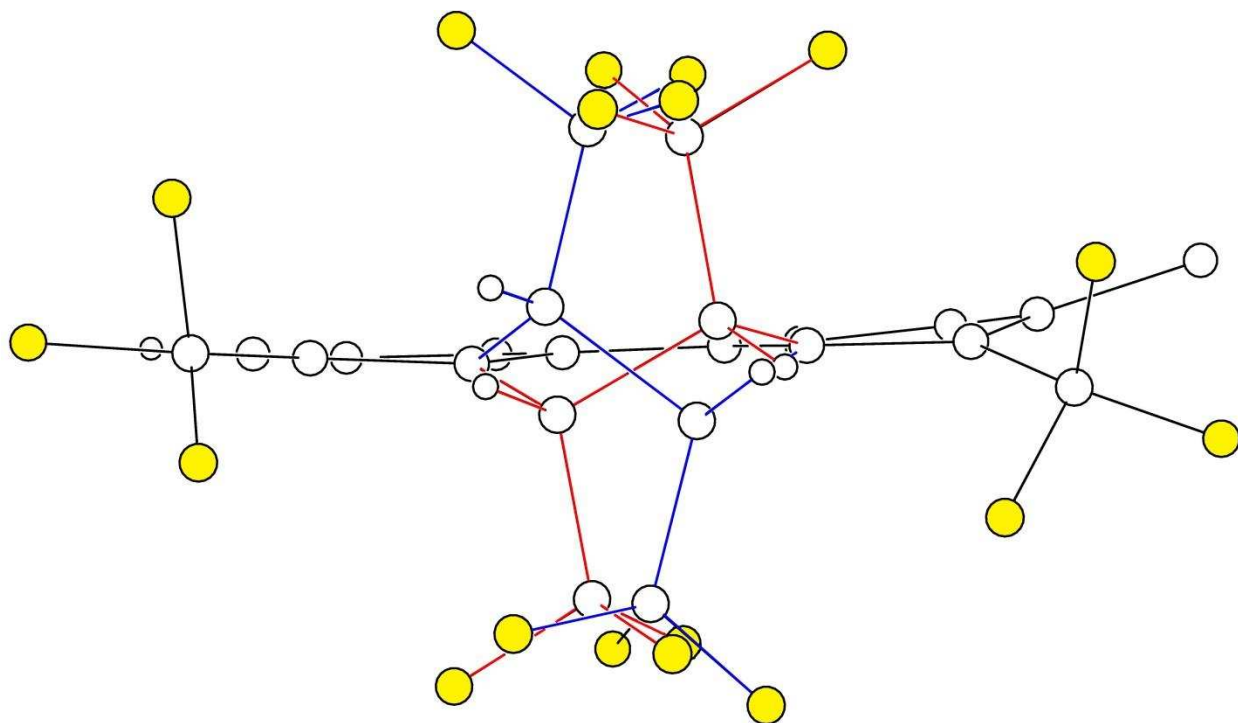


Figure 6-23. The disordered CF_3 groups on *ortho* sp^3 carbon atom present in both H_2CORO structures. The red lined bonds indicate one orientation of the molecule and the blue lined bonds indicate the other orientation of the molecule. All atoms are shown as spheres of arbitrary size, the yellow spheres are F atoms, large white spheres are C atoms and small white spheres are H atoms. The entire CORO unit and other CF_3 groups are not shown for clarity.

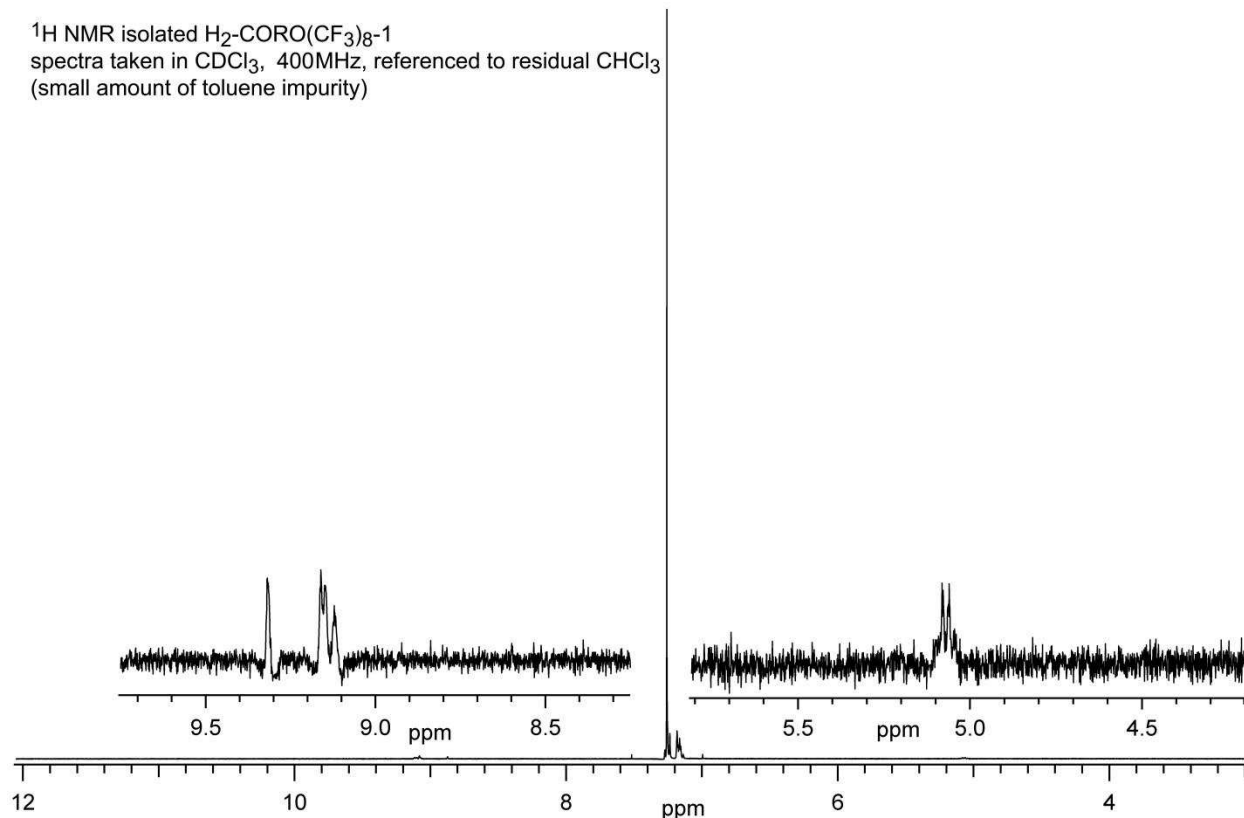


Figure 6-24. The ¹H NMR of isolated H₂CORO(CF₃)₈-1 in CDCl₃. The peaks at $\delta = 5.05$ (d), $\delta = 9.15$ (s), $\delta = 9.17$ (two singlets), and $\delta = 9.32$ (s) belong to the six hydrogen atoms on H₂CORO(CF₃)₈-1. The integration values are (from right to left) 2:1:2:1. The four hydrogen signals between $\delta 9.0$ and 9.5 are from the 4 remaining aromatic hydrogens; the two hydrogen signals between $\delta 5.0$ and 5.5 are from the two hydrogen atoms attached to C–CF₃ carbon atoms. The ¹H NMR was taken in CDCl₃ and the sample had a small toluene impurity. The spectrum is referenced to the residual CHCl₃ peak at $\delta = 7.27$.

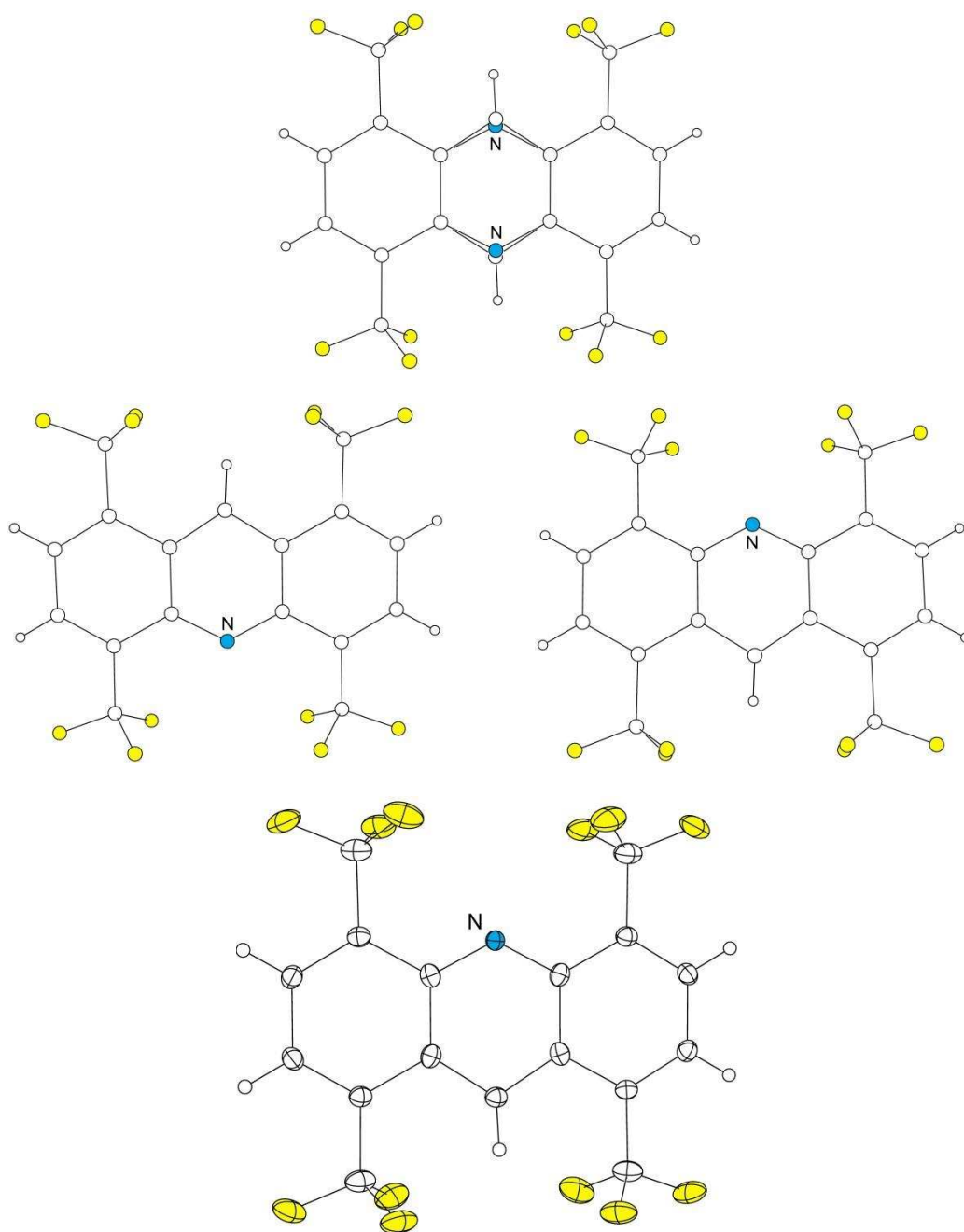


Figure 6-25. (Top) The disorder in the ACRD core of ACRD-4-1 in the single crystal X-ray structure. (Bottom) A thermal ellipsoid plot (50% thermal ellipsoids) of ACRD-4-1. No other disorder was observed in this structure. The fluorine atoms are colored yellow, nitrogen atom is colored blue, carbon atoms are large white spheres of thermal ellipsoids, and the hydrogen atoms are small white spheres of arbitrary size.

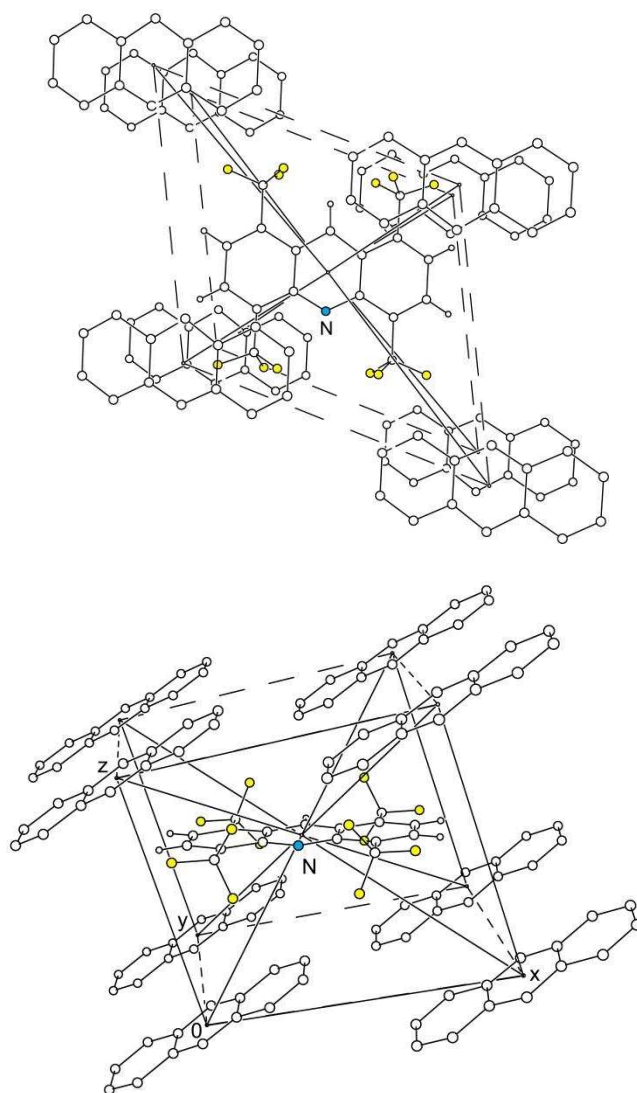


Figure 6-26. Layers of ACRD-4-1 in the crystal structure. (Top) Looking through the layers showing the PAH core overlap. (Bottom) Looking side on through the layers, the center layer makes an angle of 29.2° with the layers above and below. The centroids of the ACRD cores in the layers either fall in the center of the unit cell or on a vertex. Due to the disorder of the ACRD core the carbon and nitrogen atoms there is no reason to differentiate the nitrogen atoms and carbon atoms in the molecules. The fluorine atoms are colored yellow, nitrogen atom is colored blue the carbon atoms are large white spheres and the hydrogen atoms are small white spheres, all of arbitrary size.

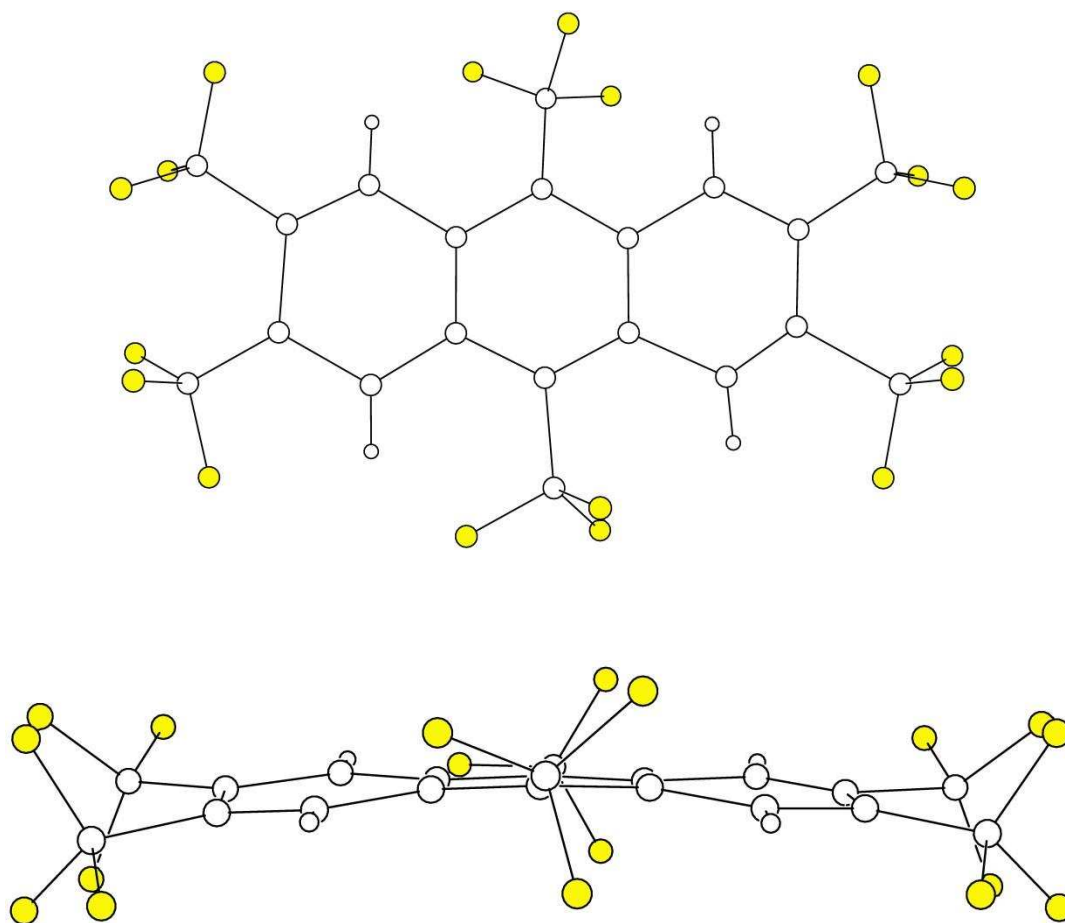


Figure 6-27. Preliminary single crystal X-ray structure of ANTH-6-1. (Top) A top down view of a single ANTH-6-1 molecule. (Bottom) Side view of a single ANTH-6-1 molecule showing the slight bend of 7.2° in the ANTH-6-1 core. The ANTH core is not rigorously planar and has an average deviation of 0.08 \AA from a least squares plane of the core carbon atoms. The yellow spheres are fluorine atoms, large white spheres are carbon atoms, and small white spheres are hydrogen atoms.

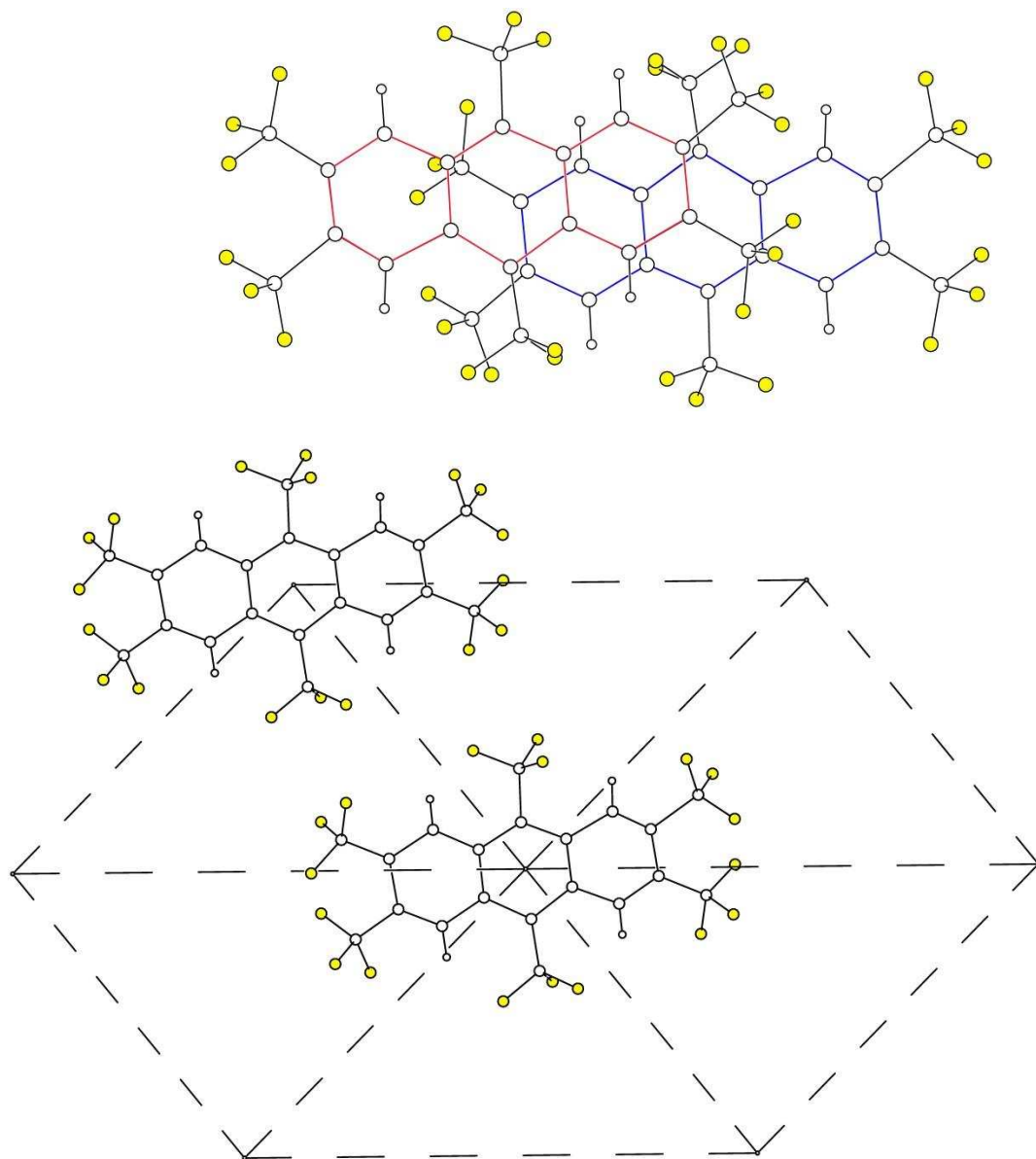


Figure 6-28. (Top) The overlap of the closest ANTH-6-1 molecules in a single column of ANTH-6-1 molecules. (Bottom) The pseudo-hexagonal packing of ANTH-6-1 within a single layer of ANTH-6-1 molecules. The nearest atoms to an ANTH-6-1 aromatic core have an average distance of 3.766 Å. The nearest ANTH-6-1 $\odot \cdots \odot$ distance in a single layer is 10.29 Å. Fluorine atoms are yellow spheres, carbon atoms are large white spheres, hydrogen atoms are small white spheres, centroids are marked with the smallest white spheres.

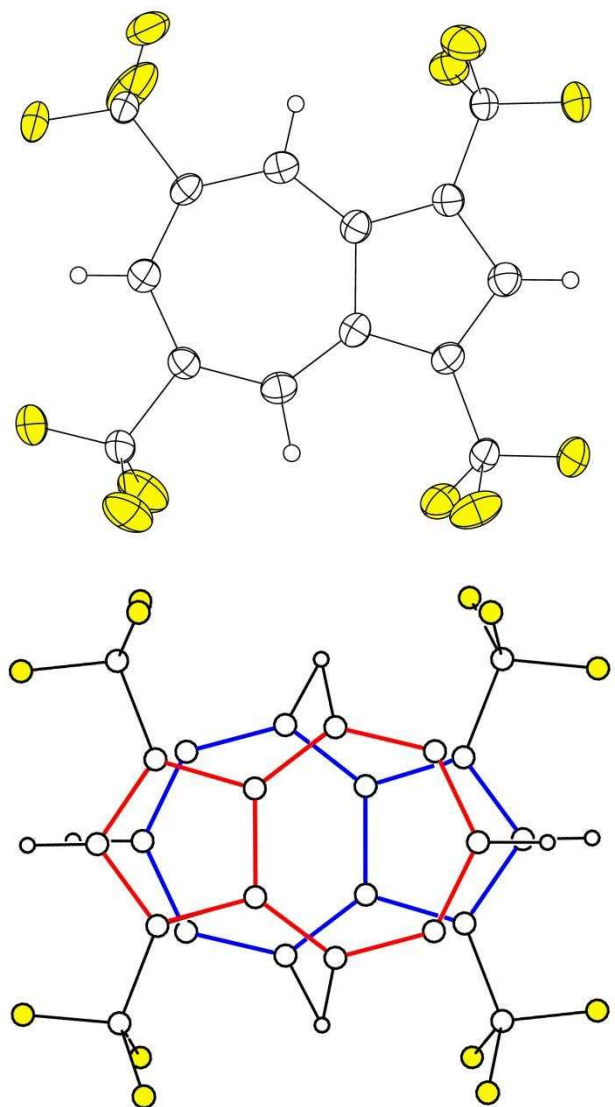


Figure 6-29. (Top) The 50% thermal ellipsoid plot of a single AZUL-4-1 molecule from the single crystal X-ray structure of AZUL-4-1. (Bottom) The disorder in the AZUL core in this crystal structure. The red outline is one orientation the blue outline the other orientation. This a common disorder in symmetrically substituted AZUL crystal structures because the molecule takes up nearly the same volume in either orientation. The yellow ellipsoids or spheres in both figures are fluorine atoms, large white ellipsoids or spheres are carbon atoms, smaller white sphere in both figures are hydrogen atoms.

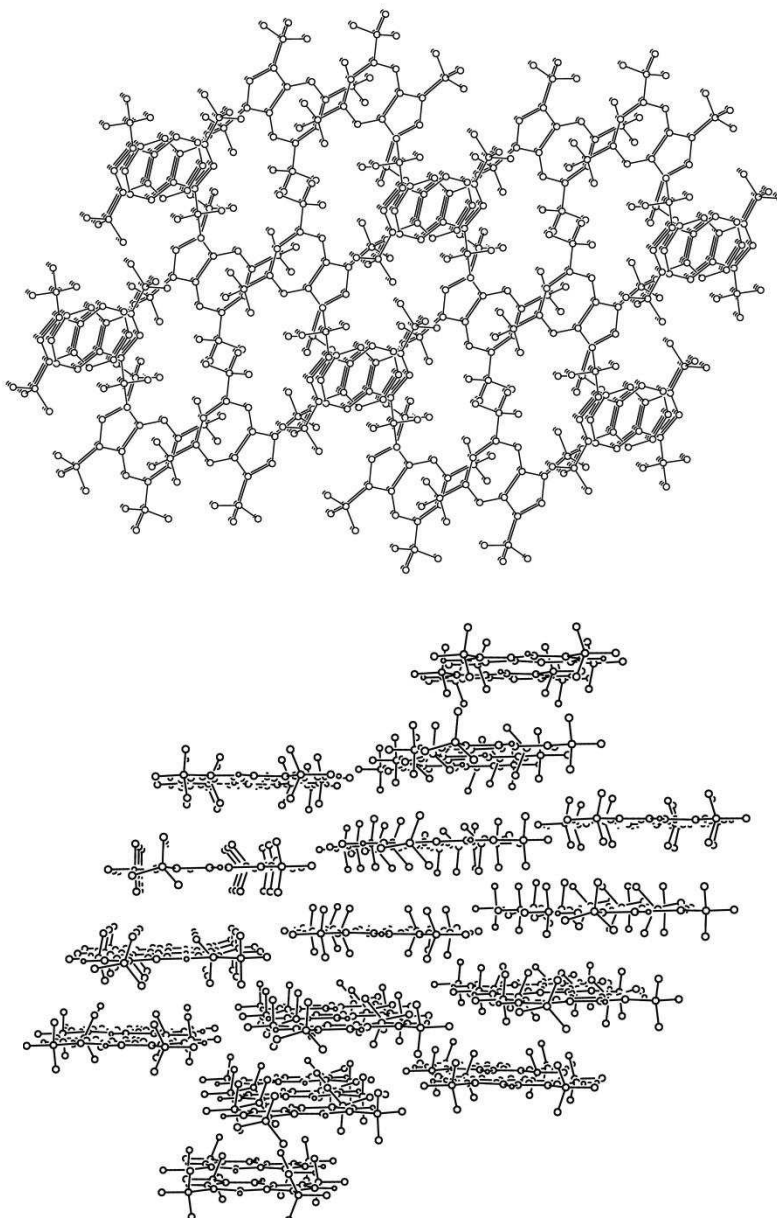


Figure 6-30. (Top) Columns of AZUL-4-1 molecules in the single crystal X-ray structure. Note that the disordered AZUL-4-1 does not take up any more space in the packing of the columns. (Bottom) Side view of the top image showing the spacing between layers. The spacing between overlapping layers is 8.083 Å, but the next closest layer is 4.028 Å down but shifted one column to either side. The molecules into and out of the page are co-planer and have C...C distances of 8.906 Å. All atoms are shown as white spheres of an arbitrary size; hydrogens have been removed for clarity.

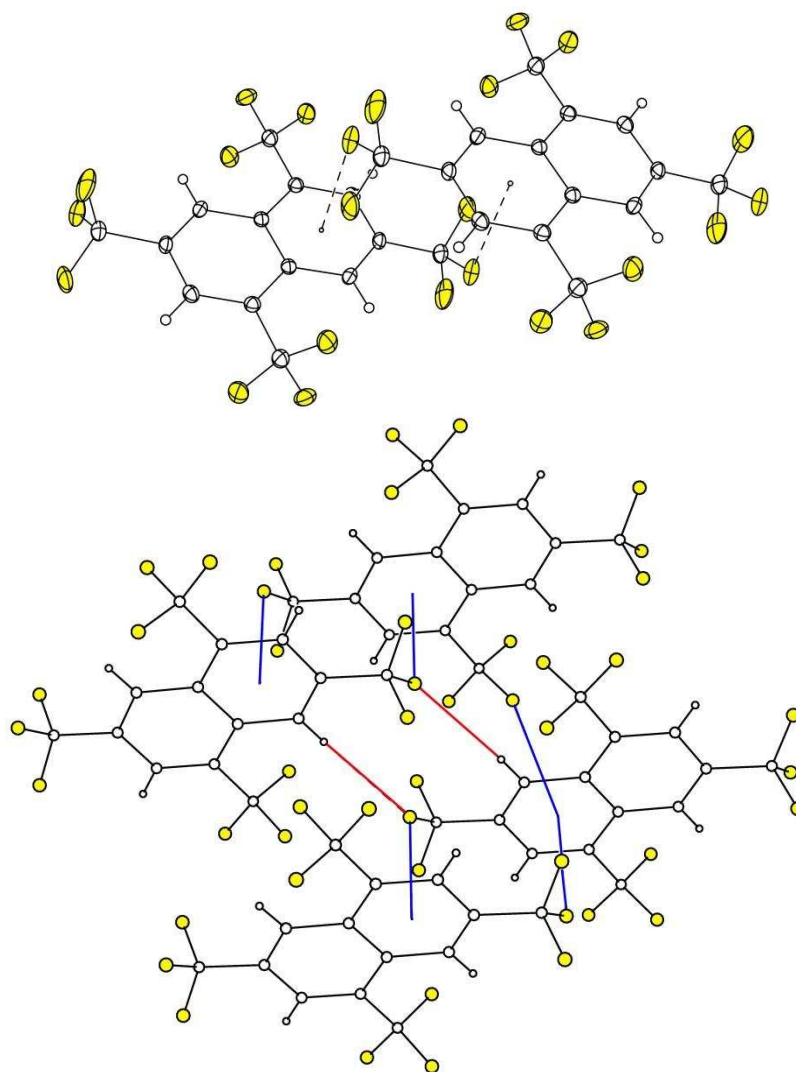


Figure 6-31. (Top) Two NAPH-4-1 molecules in a layer staggered from the single crystal X-ray structure of NAPH-4-1, 50% thermal ellipsoids. Each NAPH core is nearly planar with 0.016 Å average deviations from a least squares plane of the core atoms. There are two weak interactions that make the NAPH-4-1 have closer $\odot \cdots \odot$ distances than in unsubstituted naphthalene. A weak fluorine atom to centroid interaction with a distance of 3.089 Å, and a weak fluorine atom to hydrogen atom interaction with a distance of 2.649 Å. (Bottom) The weak fluorine interaction with the centroid of a benzene ring in an adjacent NAPH-4-1 (highlighted blue), and with an H atom on adjacent molecules (highlighted red). Yellow spheres or thermal ellipsoids are fluorine atoms, white spheres or thermal ellipsoids are carbon atoms, hydrogen atoms are small white spheres.

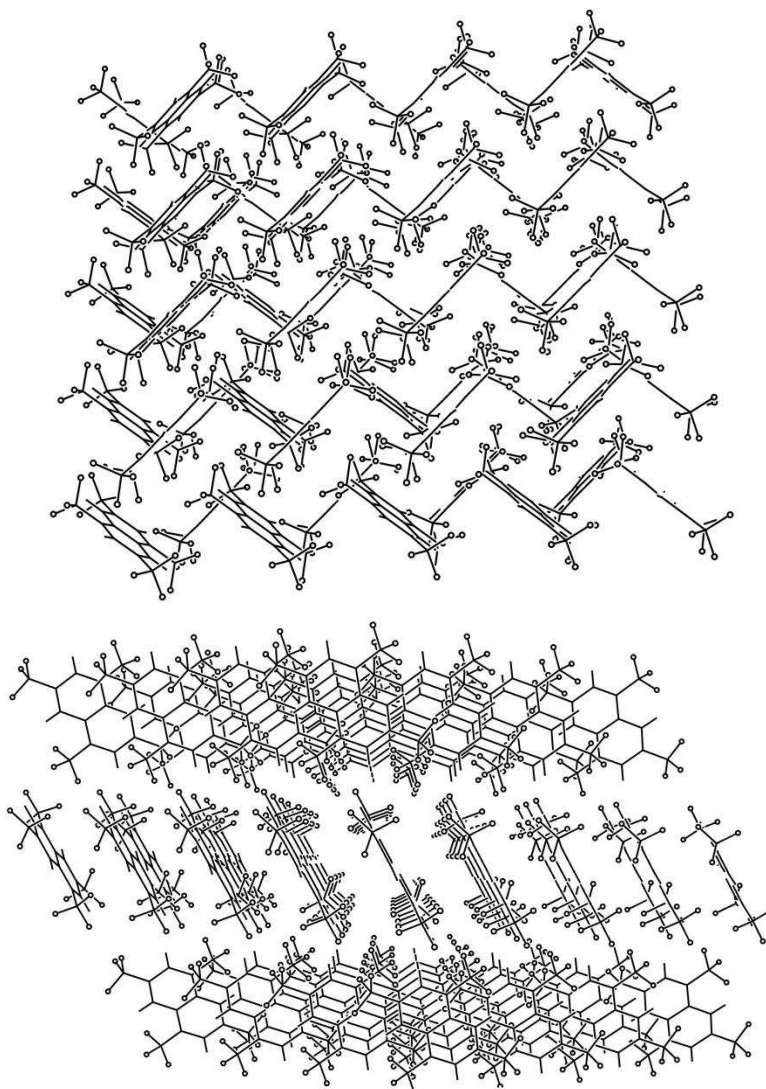


Figure 6-32. (Top) The NAPH-4-1 structure exhibits a herringbone packing where layers are rotated 83.6° from adjacent layers shown in the top layer. (Bottom) The NAPH cores within a layer are parallel to one another, but due to the CF_3 groups the layers do not have any aromatic overlap due to a rotation of 83.6° as shown in the lower figure. All carbon and fluorine atoms are spheres of arbitrary size, hydrogen atoms removed for clarity.

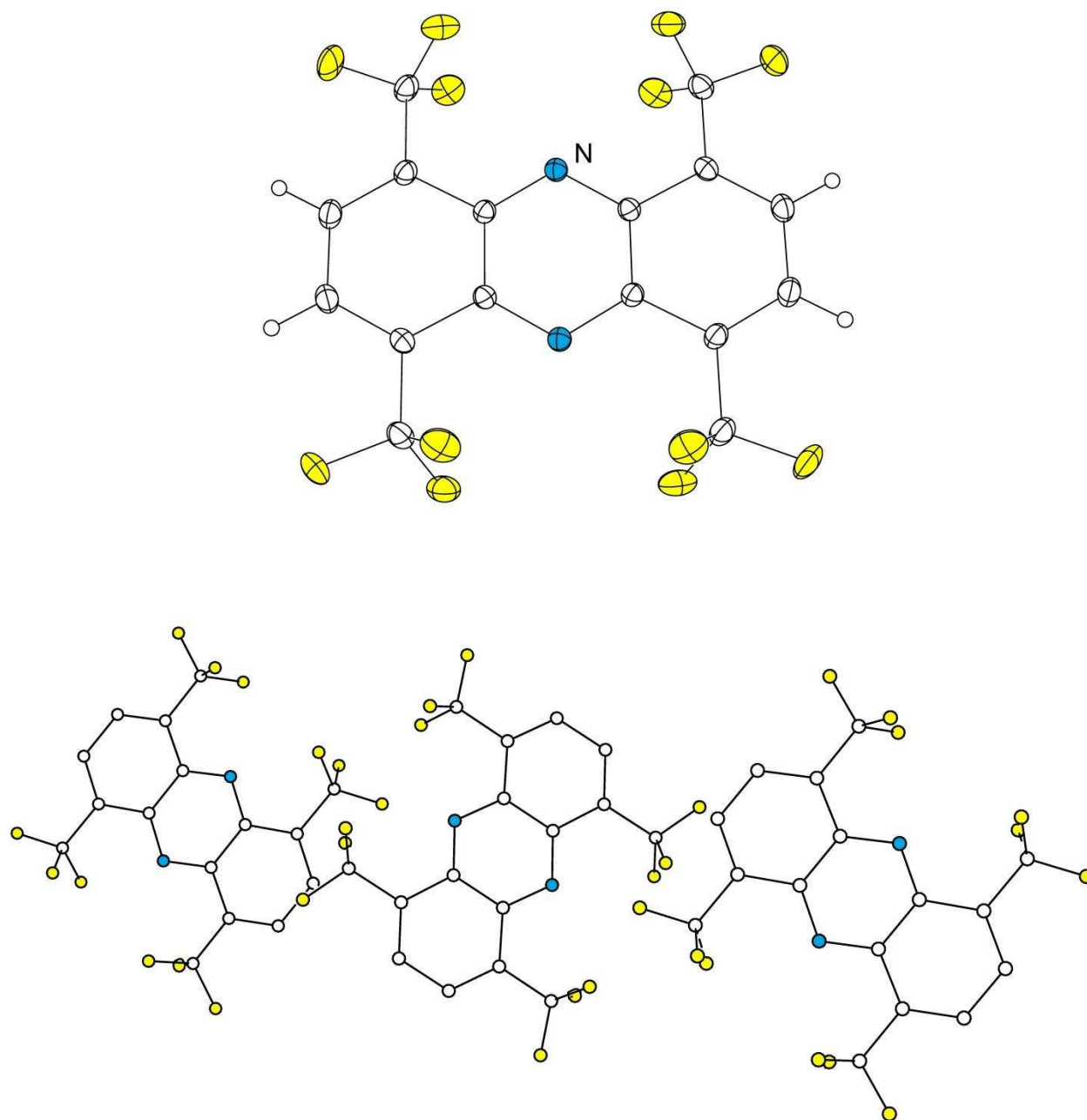


Figure 6-33. (Top) The single crystal X-ray structure of PHNZ-4-1 structure did not exhibit any disorder, 50% thermal ellipsoid plot with yellow fluorine atoms, blue nitrogen atoms, white carbon atoms, and colorless spheres of arbitrary size for the hydrogen atoms. (Bottom) Three PHZN-4-1 molecules (hydrogens removed for clarity) in a single layer illustrating the 81.6° rotation from nearby molecules. There is also a tilt of 20.2° between PHNZ cores nearest each other. The centroids of the PHNZ cores in a layer are rigorously planar.

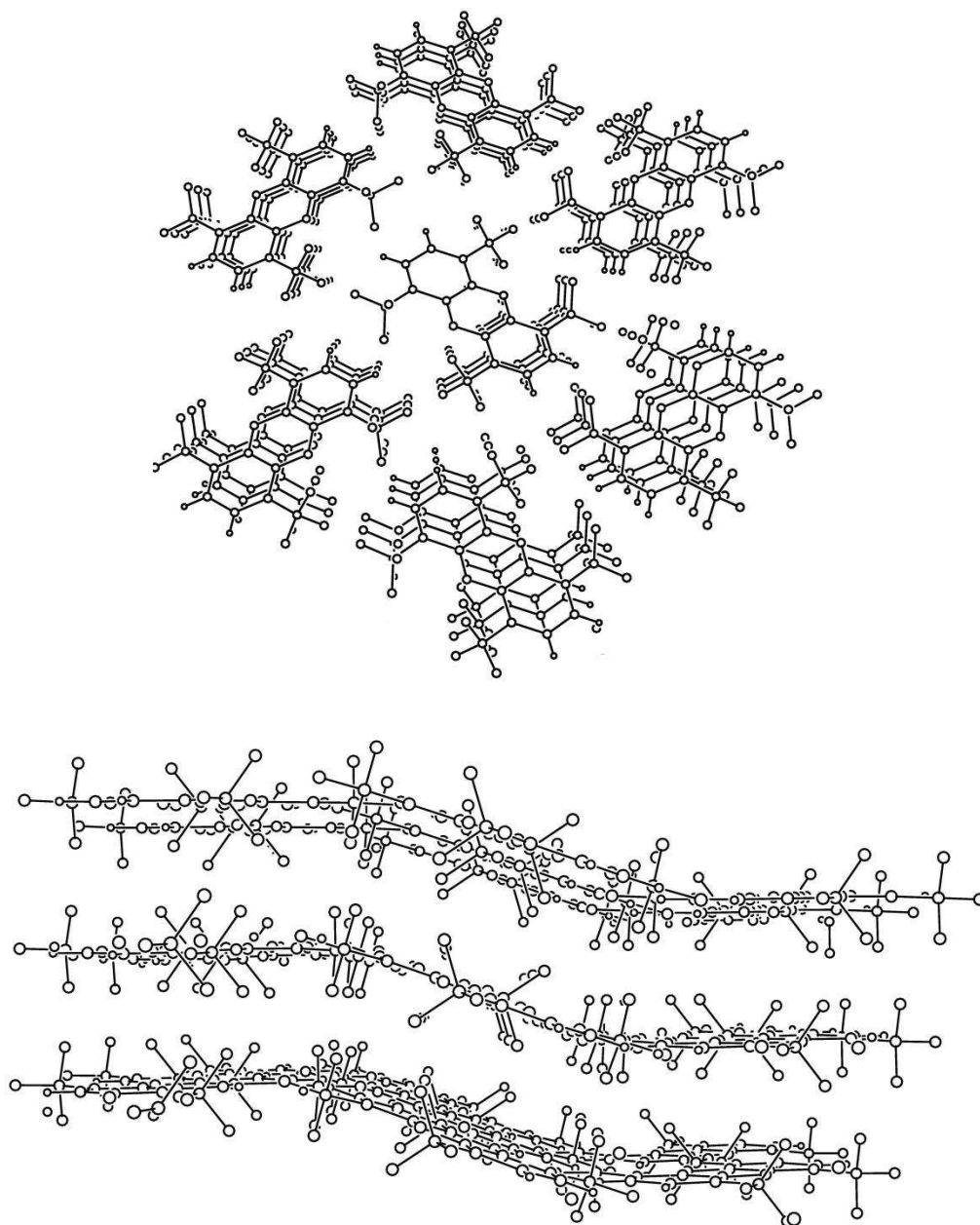


Figure 6-34. (Top) The PHZN-4-1 layers are in a pseudo-hexagonal array similar to ANTH-6-1, with $\odot \cdots \odot$ distances of 10.15 or 12.72 Å. When rotated 90° the pseudo-hexagonal array forms layers separated by 7.561 Å. (Bottom) The tilt down between adjacent molecules in a single layer is 20.2°. The fluorine, carbon, and nitrogen atoms are shown as white spheres of arbitrary size; the hydrogens have been removed for clarity.

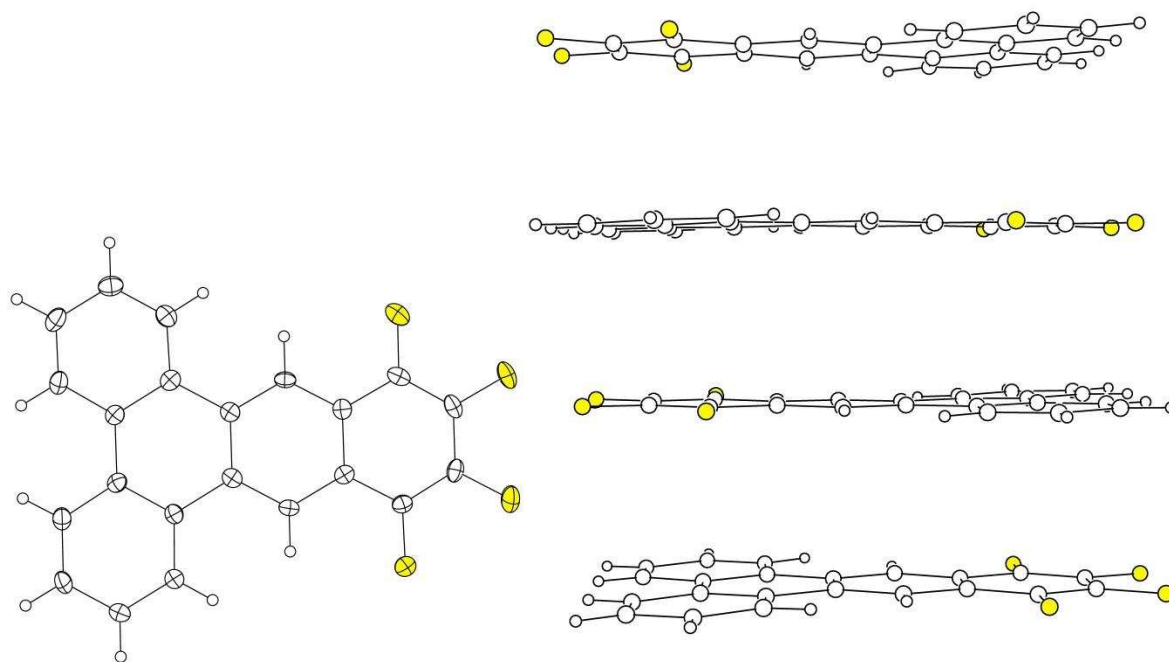


Figure 6-35. (Left) The TRPH(C₄F₄) single crystal X-ray structure did not exhibit any disorder; the left figure is the thermal ellipsoid plot with 50% thermal ellipsoids. (Right) Four TRPH(C₄F₄) molecules in a single column, note how they stack rotated 180° from one another (head to tail). The mean plane to mean plane distance between the TRPH cores is 3.396 Å. The triphenylene core only deviates from a least squares plane of all carbon atoms by 0.019 Å. For both figures fluorine atoms are yellow, carbon atoms are white and hydrogen atoms are small white spheres of arbitrary size.

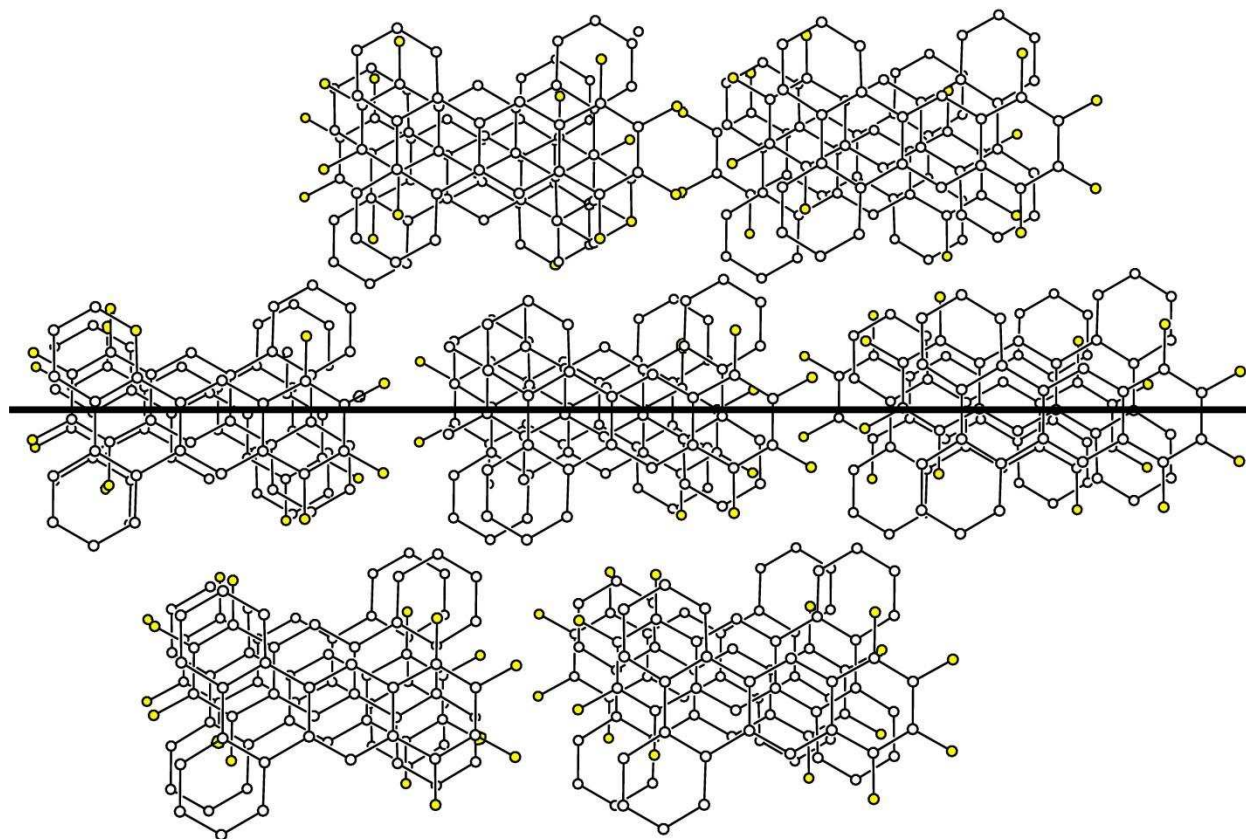


Figure 6-36. Pseudo-hexagonal array of TRPH(C₄F₄) molecules. The columns of molecules under the black line are co-planar and have $\ominus \cdots \ominus$ distances of 12.37 Å. The columns of TRPH(C₄F₄) molecules above and below the black line are either 1.404 Å above or 1.992 Å below the molecules under the black line. All molecules in this figure still maintain a distance of 3.396 Å between the TRPH(C₄F₄) molecule above it and below it within a column. The yellow spheres are fluorine atoms, white spheres are carbon atoms, hydrogen atoms removed for clarity.

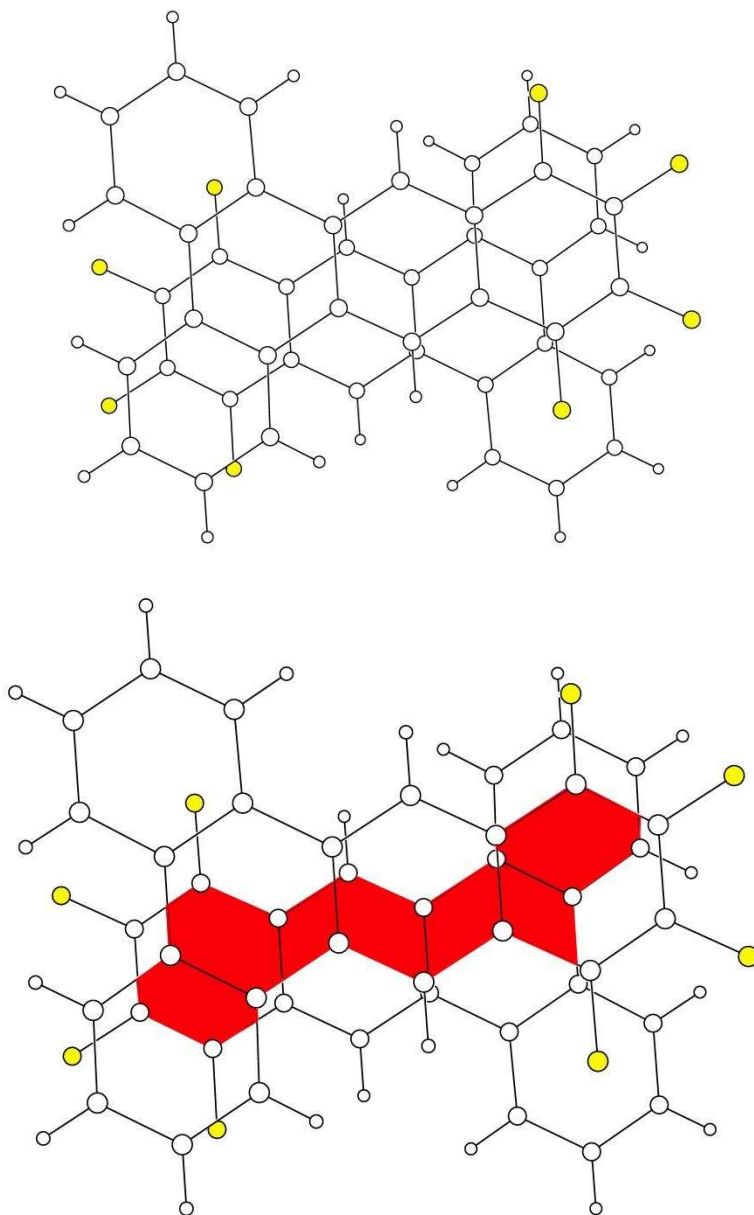
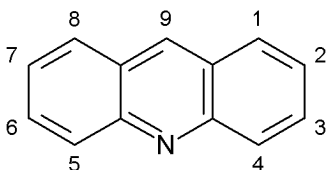
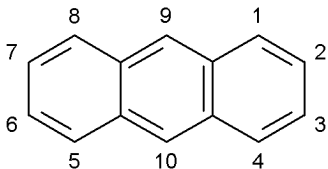
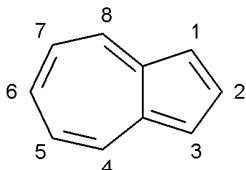
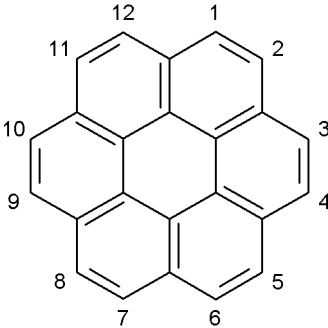
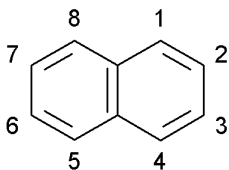


Figure 6-37. (Top) The TRPH(C₄F₄) crystal structure exhibits the closest distance with aromatic overlap of 3.396 Å, and also has significant aromatic overlap. (Bottom) The extent of aromatic overlap of two TRPH(C₄F₄) in a column. All atoms are shown as spheres of arbitrary size, fluorine atoms are yellow, carbon atoms are large white spheres, and hydrogen atoms are small white spheres.

6.9 Tables

Table 6-1. Polycyclic Aromatic Hydrocarbons and Polyatomic Polycyclic Aromatic

Hydrocarbons Discussed in Chapter 5

| name | abbreviation used in this dissertation | chemical formula | structure and numbering |
|-------------|--|------------------|---|
| acridine | ACRD | $C_{13}H_9N$ |  |
| anthracene | ANTH | $C_{14}H_{10}$ |  |
| azulene | AZUL | $C_{10}H_8$ |  |
| coronene | CORO | $C_{24}H_{12}$ |  |
| naphthalene | NAPH | $C_{10}H_8$ |  |

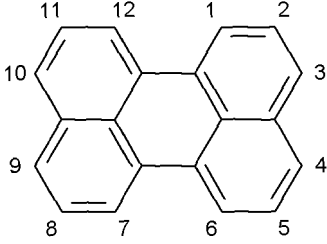
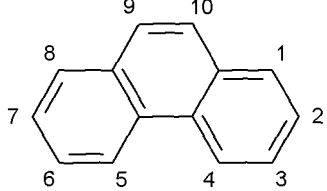
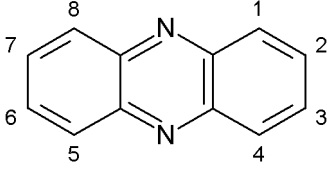
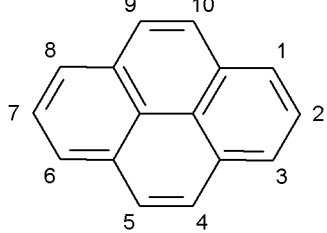
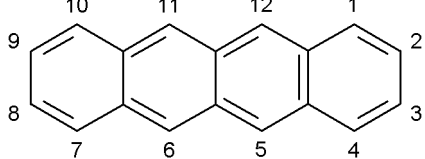
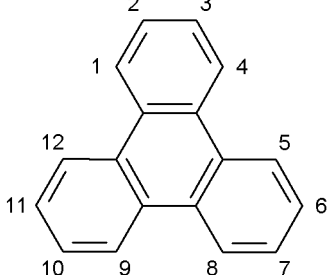
| | | | |
|--------------|------|----------------|--|
| perylene | PERY | $C_{20}H_{12}$ |  |
| phenanthrene | PHEN | $C_{14}H_{10}$ |  |
| phenazine | PHNZ | $C_{12}H_8N_2$ |  |
| pyrene | PYRE | $C_{16}H_{10}$ |  |
| tetracene | TETR | $C_{18}H_{12}$ |  |
| triphenylene | TRPH | $C_{18}H_{12}$ |  |

Table 6-2. Reactions for Making PAH(CF₃)_n and TMF

| reaction | reactor | mass of PAH, mg (mmol) | CF ₃ I:PAH equiv | Cu powder: PAH equiv | temperature/time (°C/h) | reaction pressure (Torr) | crude % conversion |
|--|--------------------------------|------------------------|---|----------------------|-------------------------|--------------------------|--------------------|
| ANTH + CF ₃ I ^a | glass ampoule | 178 (0.99) | 12 | – | 360/24 | 760-1000 ^c | 20% ^d |
| CORO + CF ₃ I ^b | glass ampoule | 5.3 | 25 | – | 360/24 | 760-1000 ^c | 15.2% ^d |
| CORO + CF ₃ I ^b | glass ampoule | 5.4 | 24 | – | 275-300/23 | 760-1000 ^c | none soluble |
| CORO + CF ₃ I ^b | glass ampoule | 17.8(0.06) | 25 | 0.4 | 300/0.083 | 760-1000 ^c | 13.4% ^d |
| TETR + CF ₃ I ^b | glass ampoule | 73.3 (0.32) | 31.8 | – | 360/7 | 760-1000 ^c | 79% ^d |
| ANTH + CF ₃ I + Cu metal powder | metal reactor | 55.4 (0.31) | 13.4 | 120 | 360/3 | 11,003 | 81% ^d |
| CORO + CF ₃ I + Cu metal powder | metal reactor | 50.2 (0.17) | 34.3 | 429 | 450/4 | 17,288 | 78% ^d |
| CORO + CF ₃ I + Cu metal powder ^e | metal reactor | 100 (0.33) | 7 | 100 | 450/4 | 7008 | 12% ^d |
| C ₆₀ + CF ₃ I + Cu metal powder | metal reactor | 49.2(0.07) | 40.4 | 417 | 450/3 | 8503 | 79% ^f |
| C ₇₀ + CF ₃ I + Cu metal powder ^e | metal reactor | 50(0.06) | 20 | 600 | 450/1 | 3608 | 12% ^f |
| ANTH+ Bn _F I + Cu metal powder (in DMSO) ^g | airfree tube with DMSO solvent | 50 | 2 (Bn _F I, perfluorobenzyl iodide) | 3 | 140/24 | 760 | < 10% |

^a From *Angew. Chem. Int. ed.* **2013**, 52, 4871, reference 5.

^b Unpublished reaction performed by Dr. Kuvychko.

^c Reaction pressure reported as a range because sealed glass ampoule volume not known.

^d Percent conversion calculated based on an average product having 6 CF₃ substitutions.

^e Reaction performed by Mr. Deweerdt.

^f Percent conversion calculated based on an average product having 12 CF₃ additions.

^g Reaction performed by Dr. San, reference 28.

Table 6-3. Important Crystallographic Data for H₂CORO-(CF₃)₇-1, H₂CORO-(CF₃)₈-1, H₂ANTH₂-(Bn_F)₂, and H₂TETR-8-1

| compound | H ₂ CORO-(CF ₃) ₇ -1 | H ₂ CORO-(CF ₃) ₈ -1 | H ₂ ANTH ₂ -(Bn _F) ₂ | H ₂ TETR-8-1 |
|--|--|--|---|--|
| empirical formula | C ₃₁ F ₂₁ H ₇ | C ₃₂ F ₂₄ H ₆ | C ₄₂ F ₁₄ H ₂₀ | C ₂₆ F ₂₄ H ₆ |
| formula weight | 778.35 | 846.35 | 790.58 | 774.31 |
| habit, color | rod, colorless | rod, light yellow | plate, colorless | cube, colorless |
| crystal dimensions (mm) | 0.23 × 0.13 × 0.03 | 0.15 × 0.10 × 0.03 | 0.59 × 0.47 × 0.19 | 0.28 × 0.26 × 0.20 |
| space group | <i>P</i> 2 ₁ / <i>n</i> | <i>P</i> $\bar{1}$ | <i>P</i> $\bar{1}$ | <i>P</i> 1 |
| <i>a</i> (Å) | 13.4625(6) | 8.1278(4) | 7.4018(11) | 10.350(2) |
| <i>b</i> (Å) | 7.9058(3) | 13.1666(6) | 10.6440(15) | 13.060(3) |
| <i>c</i> (Å) | 14.4223(6) | 13.8141(7) | 10.7240(15) | 16.150(3) |
| α (deg) | 90 | 73.1890(10) | 94.667(3) | 66.69(3) |
| β (deg) | 117.7620(10) | 89.6170(10) | 104.049(3) | 76.14(3) |
| γ (deg) | 90 | 79.1220(10) | 90.993(4) | 79.81(3) |
| <i>V</i> (Å ³) | 1358.30(10) | 1387.91(12) | 816.3(2) | 1938.2 |
| <i>Z</i> | 2 | 2 | 1 | 3 |
| <i>T</i> (K) | 100(2) | 100(2) | 100(2) | 120(2) |
| ρ_{calc} (g cm ⁻³) | 1.991 | 2.025 | 1.608 | 1.990 |
| <i>R</i> (<i>F</i>) (<i>I</i> > 2 σ (<i>I</i>)) ^a | 0.0612 | 0.0442 | 0.0419 | 0.0495 |
| <i>wR</i> (<i>F</i> ²) [all data] ^a | 0.1566 | 0.1270 | 0.1044 | 0.1457 |
| min., max. e ⁻ dens., (e Å ⁻³) | -0.42, 0.49 | -0.38, 0.44 | -0.21, 0.22 | -0.60, 0.79 |

^a $R(F) = \frac{\sum ||F_o| - |F_c||}{\sum |F_o|}$; $wR(F^2) = \left(\frac{\sum [w(F_o^2 - F_c^2)^2]}{\sum [w(F_o^2)^2]} \right)^{1/2}$

Table 6-4. Bond Lengths and Angles of sp³ Carbons in H₂ANTH₂(Bn_F)₂, and H₂TETR(CF₃)₈-1^a

| compound | H ₂ ANTH ₂ -(Bn _F) ₂ | H ₂ TETR(CF ₃) ₈ -1 ^b |
|---|---|--|
| 1 st sp ³ carbon, distance 1 (Å) ^b | 1.518 | 1.511 |
| distance 2 (Å) | 1.521 | 1.512 |
| distance 3 (Å) | 1.588 | 1.546 |
| angle 1 (X- sp ³ -ANTH) (°) ^c | 107.4 | 107.8 |
| angle 2 (ring-sp ³ -ring) (°) ^c | 111.1 | 116.1 |
| 2 nd sp ³ carbon, distance 1 (Å) ^b | 1.521 | 1.534 |
| distance 2 (Å) | 1.523 | 1.544 |
| distance 3 (Å) | 1.536 | 1.562 |
| distance 4 (Å) | – | 1.569 |
| angle 1 (X- sp ³ -ANTH) (°) ^c | 106.9 | 109.5 |
| angle 2 (ring-sp ³ -ring) (°) ^c | 112.4 | 115.1 |
| typical sp ³ carbon bond distance (Å) | 1.54 ⁴⁵ | |
| typical sp ³ carbon bond angle (°) | 109.5 ⁴⁶ | |

^a Only distances and angles shown for H₂ANTH₂(Bn_F)₂ and H₂TETR(CF₃)₈-1. Disorder in H₂CORO(CF₃)_n structures requires sp³ carbons to be constrained and restrained affecting experimental bond distances and angles.

^b Only C–C distances are shown, all hydrogen positions calculated using a rider model so C–H distances are not experimental data.

^c Only showing X–C–CF₃ angle (where X = H or CF₃) and angle from two ring carbons with sp³ carbon.

Table 6-5. Important Crystallographic Data for, ACRD-4-1, ANTH-6-1, AZUL-4-1, and NAPH-4-1,

| compound | ACRD-4-1 | ANTH-6-1 ^a | AZUL-4-1 | NAPH-4-1 |
|---|--|--|--|--|
| empirical formula | C ₁₇ F ₁₂ H ₅ N | C ₂₀ F ₁₈ H ₄ | C ₁₄ F ₁₂ H ₄ | C ₁₄ F ₁₂ H ₄ |
| formula weight | 451.22 | 586.22 | 400.17 | 400.17 |
| habit, color | plate, colorless | needle, colorless | plate, violet | plate, colorless |
| crystal dimensions (mm) | 0.39 × 0.19 × 0.13 | 0.18 × 0.09 × 0.08 | 0.22 × 0.18 × 0.02 | 0.26 × 0.15 × 0.05 |
| space group | <i>P</i> 2 ₁ / <i>n</i> | <i>P</i> 1̄ | <i>P</i> 1̄ | <i>P</i> 2 ₁ / <i>n</i> |
| <i>a</i> (Å) | 9.7637(5) | 10.2874(9) | 8.9064(4) | 6.6592(7) |
| <i>b</i> (Å) | 8.3857(5) | 11.1995(10) | 9.5245(4) | 6.3490(6) |
| <i>c</i> (Å) | 10.6501(6) | 17.2771(15) | 13.4137(6) | 15.7170(17) |
| <i>α</i> (deg) | 90 | 104.985(6) | 105.240(2) | 90 |
| <i>β</i> (deg) | 117.156(3) | 101.131(6) | 101.204(2) | 91.099(5) |
| <i>γ</i> (deg) | 90 | 97.343(6) | 101.091(2) | 90 |
| <i>V</i> (Å ³) | 775.86(8) | 1853.2(3) | 1040.70(8) | 664.38(12) |
| <i>Z</i> | 2 | 4 | 3 | 2 |
| <i>T</i> (K) | 120(2) | 120(2) | 120(2) | 120(2) |
| ρ_{calc} (g cm ⁻³) | 1.931 | 2.101 | 1.916 | 2.000 |
| <i>R</i> (<i>F</i>) (<i>I</i> > 2σ(<i>I</i>)) ^b | 0.0372 | 0.2308 | 0.0497 | 0.0339 |
| <i>wR</i> (<i>F</i> ²) [all data] ^b | 0.1067 | 0.4617 | 0.1283 | 0.0833 |
| min., max. e ⁻ dens., (e Å ⁻³) | -0.27, 0.51 | -0.97, 1.21 | -0.59, 0.83 | -0.29, 0.51 |

^a Preliminary structure

$$^b R(F) = \frac{\sum ||F_o| - |F_c||}{\sum |F_o|}; wR(F^2) = \left(\frac{\sum [w(F_o^2 - F_c^2)^2]}{\sum [w(F_o^2)^2]} \right)^{1/2}$$

Table 6-6. Important Crystallographic Data for, and PHNZ-4-1, and TRPH(C₄F₄)

| compound | PHNZ-4-1 | TRPH(C ₄ F ₄) |
|--|---|--|
| empirical formula | C ₁₆ F ₁₂ H ₄ N ₂ | C ₂₂ F ₄ H ₁₀ |
| formula weight | 452.21 | 350.30 |
| habit, color | prism, yellow | plate, colorless |
| crystal dimensions (mm) | 0.50 × 0.20 × 0.17 | 0.88 × 0.05 × 0.02 |
| space group | <i>P</i> 2 ₁ / <i>c</i> | <i>P</i> $\bar{1}$ |
| <i>a</i> (Å) | 5.4811(3) | 6.823(3) |
| <i>b</i> (Å) | 15.8196(8) | 9.388(4) |
| <i>c</i> (Å) | 9.3584(4) | 12.374(5) |
| α (deg) | 90 | 108.987(12) |
| β (deg) | 102.978(2) | 93.214(12) |
| γ (deg) | 90 | 102.002(13) |
| <i>V</i> (Å ³) | 790.73(7) | 726.5(5) |
| <i>Z</i> | 2 | 2 |
| <i>T</i> (K) | 120(2) | 120(2) |
| ρ_{calc} (g cm ⁻³) | 1.899 | 1.829 |
| <i>R</i> (<i>F</i>) (<i>I</i> > 2 σ (<i>I</i>)) ^a | 0.0366 | 0.0930 |
| <i>wR</i> (<i>F</i> ²) [all data] ^a | 0.0945 | 0.1213 |
| min., max. e ⁻ dens., (e Å ⁻³) | -0.24, 0.52 | -0.23, 0.22 |

^a $R(F) = \frac{\sum ||F_o| - |F_c||}{\sum |F_o|}$; $wR(F^2) = \left(\frac{\sum [w(F_o^2 - F_c^2)^2]}{\sum [w(F_o^2)]} \right)^{1/2}$

Table 6-7. Nearest Crystallographic Neighbors in ACRD-4-1, ANTH-6-1, AZUL-4-1, NAPH-4-1, PHNZ-4-1, and TRPH(C₄F₄)

| compound | ACRD-4-1 | ANTH-6-1 | AZUL-4-1 | NAPH-4-1 | PHNZ-4-1 | TRPH(C ₄ F ₄) |
|----------------------------------|----------|----------|----------|----------|----------|--------------------------------------|
| nearest overlapping molecule (Å) | 8.39 | 3.766 | 8.083 | 3.75 | 15.82 | 3.39 |
| amount of overlap ^a | complete | < 50% | complete | < 50% | complete | > 50%, |
| nearest molecule in a layer (Å) | 9.76 | 10.29 | 8.906 | 9.201 | 10.15 | 12.37 |

^a For the purpose of this text overlap will be quantified as complete, < 50%, > 50%, or none.

Chapter 6 References

- (1) Forrest, S. R. *Nature* 2004, 428, 911.
- (2) Zhang, X.; Bauerle, P.; Aida, T.; Skabara, P.; Kagan, C. *Organic Electronics for a Better Tomorrow: Innovation, Accessibility, Sustainability, Chemical Sciences and Society Summit (CS3)*, 2012.
- (3) Chang, Y.-C.; Kuo, M.-Y.; Chen, C.-P.; Lu, H.-F.; Chao, I. *The Journal of Physical Chemistry C* 2010, 114, 11595.
- (4) San, L. K.; Bukovsky, E. V.; Kuvychko, I. V.; Popov, A. A.; Strauss-Boltalina, S. H.; Boltalina, O. V. *Chemistry – A European Journal* 2014, 20, 4373.
- (5) Kuvychko, I. V.; Castro, K. P.; Deng, S. H. M.; Wang, X.-B.; Strauss-Boltalina, S. H.; Boltalina, O. V. *Angewandte Chemie International Edition* 2013, 52, 4871.
- (6) Tang, M. L.; Bao, Z. *Chemistry of Materials* 2010, 23, 446.
- (7) Anthony, J. E.; Facchetti, A.; Heeney, M.; Marder, S. R.; Zhan, X. *Advanced Materials* 2010, 22, 3876.
- (8) Yoon, M.-H.; Facchetti, A.; Stern, C. E.; Marks, T. J. *J Am Chem Soc* 2006, 128, 5792.
- (9) Babudri, F.; Farinola, G. M.; Naso, F.; Ragni, R. *Chemical Communications* 2007, 1003.
- (10) Schmidbauer, S.; Hohenleutner, A.; König, B. *Advanced Materials* 2013, 25, 2114.
- (11) Schmidbauer, S.; Hohenleutner, A.; König, B. *Beilstein Journal of Organic Chemistry* 2013, 9, 2088.
- (12) Seifert, R.; Rabelo de Moraes, I.; Scholz, S.; Gather, M. C.; Lüssem, B.; Leo, K. *Organic Electronics* 2013, 14, 115.
- (13) Sun, H.; Putta, A.; Billion, M. *The Journal of Physical Chemistry A* 2012, 116, 8015.
- (14) Boltalina, O. V.; Popov, A. A.; Kuvychko, I. V.; Shustova, N. B.; Strauss-Boltalina, S. H. *Chem. Rev.* 2015, 115, 1051.
- (15) Coffey, D. C.; Larson, B. W.; Hains, A. W.; Whitaker, J. B.; Kopidakis, N.; Boltalina, O. V.; Strauss-Boltalina, S. H.; Rumbles, G. *The Journal of Physical Chemistry C* 2012, 116, 8916.
- (16) Kuvychko, I. V.; Whitaker, J. B.; Larson, B. W.; Folsom, T. C.; Shustova, N. B.; Avdoshenko, S. M.; Chen, Y. S.; Wen, H.; Wang, X. B.; Dunsch, L.; Popov, A. A.; Boltalina, O. V.; Strauss-Boltalina, S. H. *Chem. Sci.* 2012, 3, 1399.
- (17) Shustova, N. B.; Peryshkov, D. V.; Kuvychko, I. V.; Whitaker, J. B.; Larson, B. W.; Dunsch, L.; Chen, Y. S.; Seppelt, K.; Popov, A. A.; H., S. S.; Boltalina, O. V. *Chem. Commun.* 2010, 47, 875.
- (18) Wang, X.-B.; Chi, C.; Zhou, M.; Kuvychko, I. V.; Seppelt, K.; Popov, A. A.; Strauss-Boltalina, S. H.; Boltalina, O. V.; Wang, L.-S. *J. Phys. Chem. A* 2010, 114, 1756.
- (19) Popov, A. A.; Kareev, I. E.; Shustova, N. B.; Stukalin, E. B.; Lebedkin, S. F.; Seppelt, K.; Strauss-Boltalina, S. H.; Boltalina, O. V.; Dunsch, L. *J. Am. Chem. Soc.* 2007, 129, 11551.
- (20) Clikeman, T. T.; Bukovsky, E. V.; Kuvychko, I. V.; San, L. K.; Deng, S. H. M.; Wang, X.-B.; Chen, Y.-S.; Strauss-Boltalina, S. H.; Boltalina, O. V. *Chemical Communications* 2014, 50, 6263.
- (21) Kuvychko, I. V.; Dubceac, C.; Deng, S. H. M.; Wang, X.-B.; Granovsky, A. A.; Popov, A. A.; Petrukhina, M. A.; Strauss-Boltalina, S. H.; Boltalina, O. V. *Angewandte Chemie International Edition* 2013, 52, 7505.

- (22) Kuvychko, I. V.; Spisak, S. N.; Chen, Y.-S.; Popov, A. A.; Petrukhina, M. A.; Strauss-Boltalina, S. H.; Boltalina, O. V. *Angewandte Chemie International Edition* 2012, 51, 4939.
- (23) Mottishaw, J. D.; Sun, H. *The Journal of Physical Chemistry A* 2013, 117, 7970.
- (24) Sun, H.; Tottempudi, U. K.; Mottishaw, J. D.; Basa, P. N.; Putta, A.; Sykes, A. G. *Crystal Growth & Design* 2012, 12, 5655.
- (25) McCain, W. C.; Macko, J. In *Halon Options Technical Working Conference* 1999, p 242.
- (26) Torres, L. A.; Campos, M.; Martínez, M.; Rojas, A. *The Journal of Chemical Thermodynamics* 2009, 41, 957.
- (27) Sandvik Materials Technology Website; Vol. 2014.
- (28) San, L. K., Colorado State University, 2015.
- (29) Capelli, S. C.; Albinati, A.; Mason, S. A.; Willis, B. T. M. *The Journal of Physical Chemistry A* 2006, 110, 11695.
- (30) Whitaker, J. B., Colorado State University, 2013.
- (31) Larson, B. W., Colorado State University, 2013.
- (32) Studer, A. *Angewandte Chemie International Edition* 2012, 51, 8950.
- (33) Chamberlain, G. A.; Whittle, E. *Transactions of the Faraday Society* 1971, 67, 2077.
- (34) Charles, S. W.; Pearson, J. T.; Whittle, E. *Transactions of the Faraday Society* 1961, 57, 1356.
- (35) Charles, S. W.; Whittle, E. *Transactions of the Faraday Society* 1960, 56, 794.
- (36) Pritchard, G. O.; Pritchard, H. O.; Schiff, H. I.; Trotman-Dickenson, A. F. *Transactions of the Faraday Society* 1956, 52, 849.
- (37) Junker, K. H.; Sun, Z. J.; Scoggins, T. B.; White, J. M. *The Journal of Chemical Physics* 1996, 104, 3788.
- (38) Girifalco, L. A.; Lad, R. A. *The Journal of Chemical Physics* 1956, 25, 693.
- (39) Sheldrick, G. M.; Bruker AXS: Madison, WI, 2003.
- (40) Sheldrick, G. M.; 6.15 ed.; Bruker AXS: Madison, WI, 2004.
- (41) Sheldrick, G. M.; Bruker AXS: Madison, WI, 2006.
- (42) Sheldrick, G. M. *Acta Crystallographica Section A* 2008, 64, 112.
- (43) Dolomanov, O. V.; Bourhis, L. J.; Gildea, R. J.; Howard, J. A. K.; Puschmann, H. *Journal of Applied Crystallography* 2009, 42, 339.
- (44) Sheldrick, G. M.; Bruker AXS: Madison, WI, 2001.
- (45) Muller, P.; Herbst-Irmer, B.; Spek, A. L.; Schneider, R.; Sawaya, M. R. *Crystal Structure Refinement: A Crystallographer's Guide to SHELXL*; International Union of Crystallography, Oxford Science Publications, 2006.
- (46) Brown, T., L.; LeMay, H. E., Jr.; Bursten, B. E.; Burdge, J., R. *Chemistry The Central Science*; 8th ed.; Prentice Hall, NJ, 2000.

Chapter 7.

Preparation and Characterization of Silicon Nanoparticles by Anaerobic Wet Milling

7.1 Introduction and Justification

Comminution by mechanical attrition (grinding) is a routine method to reduce particle size which is beneficial for: increasing surface area and reactivity of a material, increasing solubility, maximizing solids loading, thickening and stabilizing slurries/suspensions, intimate homogenization of powdered materials, homogenizing particle size and morphology, and top down manufacture of nanoparticles.¹⁻¹⁰ The desirability of nanoparticles for a host of reasons makes them attractive synthetic targets; however, commonly employed bottom-up synthesis, while well-established, is sensitive to many variables and requires exceptional control over solvent, reagents and any possible contaminants (known or otherwise), temperatures, reaction time, pH, surfactants, and other additives for reproducibility.¹¹⁻¹³ Top-down grinding of materials to form nanoparticles is attractive from the standpoint of cost, and, in certain materials, the usage of the nanoparticles will tolerate irregular morphology and larger size distribution of milled nanoparticles.^{5-7,9,10} The properties that make nanoparticles attractive (rapid solubility, increased suspension properties, rapid reaction rates, high surface areas) also make them difficult to synthesize in high purity. For example, nanoparticles have the inherent property of having a significant portion of the per-mass or per-volume composition of the material as surface material which necessitates exacting control of all components that could affect the surface chemistry during nanoparticle formation. Whether via solution based, bottom-up synthesis or top-down grinding based methods; in both cases any and all compounds that can interact with the nascent surface have the possibility of reacting and contaminating the particle surface. Simple, top-down

grinding methods with precise control over all reagents and contaminants are required to make further strides in this field.

The grinding method most discussed in literature, which is easily adapted to anaerobic conditions, is a ball mill either inside an inert atmosphere glovebox, or charging a ball mill jar in an inert atmosphere and then sealing with an inert gas. While it is simple to adapt a ball mill to a glovebox, presumably without even opening the glovebox face, ball mills themselves are ill-suited for efficient production of high purity nanoparticles.^{1-3,14} First, ball mills are known to have poor efficiency when grinding a material below ca. 1 μm , this is due to simple statistics, the chances of a ball in the milling jar striking a particle in such a way that particle fracture occurs decreases as the particle size decreases, requiring considerably longer milling times for marginal decrease in particle size.^{3,14} Second, a ball mill relies on high-energy impact to fracture particles, in the process, damaging the milling media, and milling jar over time and is known to contaminate the sample with measurable amounts of the milling balls or milling jar materials.¹⁻³ Due to contamination concerns milling balls and jars must be chosen carefully in order to not inadvertently react or contaminate the sample.

A mill design well suited to efficiently grinding materials to fine particulate size, 10–1 μm size and easily into the nm range, is a stirred media mill, sometimes called an attritor mill or stirred ball mill.^{1,14,15} The attritor mill imparts energy to fine milling media in a stationary vessel through a rotating mixer, maximizing the mechanical energy imparted to the milling media and material.^{1,3} It has been claimed that a stirred media mill can grind a material up to 10 times faster compared to a conventional ball mill.^{3,16} The grinding process occurs by a cyclic mechanism of increasing lattice defects generated through severe plastic deformation of the sample particles during grinding via various particle- mill, media, and particle interactions until a critical potential

energy point in an individual particle is reached, such that further imparted energy from the mill causes particle fracture. A stirred media mill can operate with a sample suspended in a solvent or dry sample allowing fine control over what contacts the freshly exposed reactive material during the grinding process. However, the stirred media mill is not without its problems, due to its high-energy transfer and rapid grinding of a sample, rapid amorphization can occur if care is not taken to prevent aggregation and agglomeration of fine particles that limit further particle fracture. Factors affecting grinding rate, ultimate grinding limit and other grinding dynamics of a stirred media mill have been explored by Peukert et al. and others at length.^{14,15,17-25} Peukert et al. show that grinding efficiency in stirred media mill applications depends on multiple variables including milling time, mill media loading percent, agitator tip velocity, temperature, and the ability of the milling fluid and additives to stabilize the particles against agglomeration.^{15,17-19,21,24} Various additives to stabilize the suspension and mitigate agglomeration by means of electrostatic, steric or electrosteric stabilization have been shown to allow further particle size reduction to occur compared to systems without such additives.^{15,18,24} This concept is logical from the stand point of the system changing to minimize the surface potential (Figure 7-1).^{26,27} The nascent particle surfaces generated during grinding are quite reactive and therefore the surface potential is greatly increased during milling. At some point it becomes more favorable (under the conditions created during grinding) for a sample to agglomerate into larger particles, thereby reducing the generated surface potential. In many respects this shift to minimize surface potential is similar to micelles in a solution forming a predictable size based on properties of the aqueous and lipid portions, type and quantity of surfactant, and any salt or buffer additives, the system will change to minimize the surface potential under that particular set of conditions. The major difference being that during comminution of a sample in a mill the set of conditions is

dynamic throughout the milling cycle, i.e., as more fresh surface is exposed, chemical reactions, physisorption, and particle agglomeration can augment the surface and can further change the overall surface potential.

Peukert et al. also describe a “true” grinding limit that is reached when crystallites become too small for a critical number of lattice defects to be generated in the particle.²¹ It is necessary to know the true grinding limit of a particular system to minimize significant amorphization. The authors go on to describe an “apparent” grinding limit that is controlled by the stability of the suspension and how the suspension can hinder reaching the true grinding limit by being too viscous, decreasing energy transfer from milling media to particles and significant inter-particle interaction leading to agglomeration. While stirred media mills have been used extensively to produce nanoparticles, and many research groups have investigated what experimental factors are important for reaching the smallest particle size, this author has found no indication that a research group has successfully adapted a stirred media mill to an inert atmosphere for complete inert atmosphere operation. The following chapter will show that even though the milling slurry in a stirred media mill under aerobic conditions is constantly covered with solvent (and any possible additives) atmospheric oxygen can have a significant impact on the resultant product.

The quite reactive element oxygen, in 200,000 ppm abundance in air, readily reacts with most metals and metalloids, especially with the freshly exposed surfaces produced during grinding. Butyagin and coworkers showed that Si ball milled in an atmosphere of 100 Torr of O_{2(g)}, will irreversibly bind (likely through chemical reaction) 17.5 wt% oxygen, and silicon powder activated by ball milling in vacuum and then exposed to the same amount of O_{2(g)} still irreversibly bound 1.1% oxygen.²⁸ Production of top-down nanoparticles via an anaerobic milling method is quite attractive for many applications: formation of metal nanoparticles for

increased volumetric energy densities of liquid and solid fuels, and explosives,^{4,29-33} formation of cold-welded single component powders and multi-component intermetallic powders,^{16,34,35} and quantum confined suspension stable nanoparticles.³⁶⁻³⁸ The effect on milling efficacy caused by adventitious oxygen present during the grinding of metals (no matter the mill design) is of interest since most metals form a surface oxide coating that would affect the agglomeration rates of these particles, affecting the ultimate particle size as well as the purity of the sample. In some cases this highly-reactive, nascent particle surface has been exploited to form new chemical bonds. The purity and surface chemistry of the new species is also affected by any undesired side reactions. Mitchell and Koch et al. used silicon with oxygen or various reactive organic solvents in a ball mill to concurrently mill the silicon into nanoparticles and form Si-C and Si-O bonds on the surface of the particles to produce a variety of air-stable, luminescent, passivated silicon nanoparticles.³⁶⁻³⁸

To determine what effects an oxygen containing atmosphere had on milling dynamics in a stirred media mill, this author along with fellow graduate student Karlee P. Castro, undergraduate student Brent M. Wyatt, and Advisor Steven H. Strauss adapted a stirred media mill to a strictly anaerobic atmosphere. Together with the aforementioned colleagues, the effect oxygen has on milling metallurgical grade Si was studied and here the author of this dissertation presents the results. To accomplish this research the Strauss research group members mentioned above took on the task to completely adapt a Netzsch MiniCer stirred media mill to an enclosed inert gas glovebox and determine what effect oxygen had on the grinding dynamics of MGS. A schematic of the circulating stirred media mill used in this research is shown in Figure 7-2. The design and planning of adapting the stirred media mill to an inert atmosphere glovebox was performed by the author of this dissertation and Prof. Strauss. The execution of the plan to put

the mill in the glovebox was undertaken by the author of this dissertation, Karlee P Castro, Brent M. Wyatt and Steven H. Strauss. A description of the engineering and adaptations required to put the mill and components in the glove box is described in the experimental section. Milling experiments were performed by the author of this dissertation and Karlee P. Castro. Material characterization was performed by many individuals and will be described in the experimental section.

Metallurgical grade Si was chosen as the test material because, while it does have an initial surface covering of SiO₂, the large increase in surface area created by the milling process rendered this small amount of initial oxide coating insignificant. Also, freshly exposed Si would rapidly react with any available O₂(g), making surface oxide or other surface silicon bonds easily distinguished by XPS. Milling dynamics was investigated by milling MSG rigorously air and moisture-free and by intentionally adding surface passivating aromatic compounds (pyrene) during the anaerobic grinding of MGS samples. Anaerobic experiments were also compared to aerobic milled samples produced under similar conditions. Both anaerobic and aerobic samples were analyzed by BET N₂(g) specific surface area, aerobic and anaerobic powder XRD, O₂(g) titration and reaction experiments, and XPS.

7.2 Results

Handle all metals milled anaerobically with caution: samples were extremely pyrophoric; samples poured through air reacted rapidly ranging in severity from heating and glowing orange to igniting particulate mid-air causing a fireball. Unless otherwise noted anaerobic samples were treated anaerobically and manipulated in an N₂(g) or Ar(g) environment. Milled samples were analyzed by BET surface area analysis, powder XRD, (sometimes as a paste in

highly purified grease to protect from oxygen), SEM, TEM, and XPS to determine effects of milling time, solvent, additives, and oxygen content. Dynamic light scattering was used to determine approximate particle size, compare size distribution, and to further substantiate the BET surface area measurements. It was known from SEM and TEM that the milled particles were solid particles that were irregular in shape (i.e. without internal surface area due to porous particles), SEM and TEM images of A-H/M-5.5h are shown in Figures 7-3 and 7-4. All of the samples inspected by SEM looked similar to A-H/M-5.5h. Collected data for all milled MGS samples, as well as milling parameters are summarized in Table 7-1. Milling parameters listed in Table 7-1 include aerobic anaerobic, mill solvent, seal fluid solvent, milling time, additives, as well as measured BET surface area, and percent Si-C and Si-O bonding determined by XPS.

7.2.1 Anaerobic Powder XRD Method.

Due to the reactivity of some of these milled materials it was necessary to find a method to perform PXRD analysis in an anaerobic or nearly anaerobic environment. The transfer of the samples and purging of the PXRD instrument X-ray protection enclosure would have been painstaking and still not afforded a sufficiently anaerobic environment for these materials. Instead the anaerobically milled powders were coated with a high purity grease (Apiezon Type N) to act as a short term oxygen barrier. The grease method was tested with known samples to determine its effect on the resulting data (see results in Figure 7-5). Apiezon grease is highly purified aliphatic only based grease. Since the samples were milled in heptane it was suspected that the Apiezon Type N grease would not react with the milled silicon samples. A control experiment was performed on a sample immediately prepared and again on the same sample 52 days later to confirm that the grease was protecting the sample and no significant change in the

observed PXRD pattern had occurred shown in Figure 7-6. As expected the PXRD of samples mixed with Apiezon grease attenuated the peak height and slightly broadened the peak widths compared to samples dispersed on top of high-vacuum silicon grease. However, for the purposes of this study determination of crystallinity was still possible with the observed measurements as shown in Figures 7-5 and 7-6. Diffraction peaks for 1 h milled samples (AA-H-1h and AA-M/P-1h) showed decreased but measurable diffraction peaks but all samples milled for longer than 1 h showed very weak diffraction peaks.

7.2.2 Anaerobic Milling of Metallurgical Grade Silicon in Heptane.

The three milling experiments performed in dry, air-free heptane in an inert atmosphere glovebox produced dark gray to black solids that were reactive with oxygen. In addition to the three anaerobic milling experiments in dry, air-free heptane, two additional anaerobic experiments were performed to probe how much batch to batch contamination was transferred after normal cleaning; the first with dry, air-free heptane as the milling fluid and mesitylene as the seal fluid to determine “impurity” leeching from the seal fluid (AA-H/M-5.5h) and a second experiment with dry, air-free heptane as the seal fluid and mill fluid (AA-H-5.5h) to determine cross contamination between batches with small quantities of impurities. The AA-H-5.5h experiment was also doubled as a convenient method to remove contaminants from the slurry lines and sonicator flow cell, and is included as further data.

The five samples free of deliberate and adventitious slurry stabilizing species had similar BET surface areas (Table 7-1, Figure 7-7) indicating mechano-chemical equilibrium was reached quickly. The surface area changed little with time while the crystallite size decreased rapidly; the AA-H-4h sample had almost an identical powder XRD pattern to the AA-H-5h sample,

suggesting similar crystallite sizes. Further evidence of decreasing crystallite size is given by comparing TEM images of AA-H-1h to those of AA-H-5h as shown in Figures 7-8 and 7-9. The TEM images demonstrate that the bulk of the particles were amorphous with the agglomerated particles having a size range on the order of 10–200 nm in size. The remaining crystallites embedded in the amorphous agglomerated particles identified by darkfield TEM also shown in Figures 7-4, 7-8 and 7-9, range in size from 2–50 nm comparable to crystallites sizes observed in Si ball milling research.³⁹

The surface chemistry of samples AA-H/M-5.5h, AA-H-5.5h, AA-H-1h, AA-H-3h, and AA-H-5h was examined using XPS. See Figure 7-10 for AA-H-1h, AA-H-3h, and AA-H-5h. All samples contained silicon, carbon, and oxygen and all samples except AA-H/M-5.5h and AA-H-1h had a small (≤ 5 atomic %) amount of fluorine present (Table 7-2). The silicon spectra contained 3 peaks: ca. 99.5 eV associated with Si^0 ⁴⁰⁻⁴³, ca. 100.5 eV assigned to Si-C ⁴⁴⁻⁴⁶, and ca. 101.5 associated with Si_xO_y ^{41,47}. Sample AA-H/M-5.5h exhibited significantly different silicon binding than the other samples; of the silicon present, 38% was Si-C , 9% was Si-O , and 53% was Si^0 . For all other samples milled anaerobically in heptane the silicon was in the same three bonding environments, but the amount of each was: Si-C 12–24%, Si-O 5–7%, and Si^0 72–81%. After one hour of milling there was 12% Si-C and 7% Si-O , after that first hour there was a slight increase in the amount of Si-C to 17% and almost no change in the Si-O (6%) and these values are nearly the same after 5 hours (Table 7-1)

Three carbon binding environments were observed: ca. 283.5 eV for Si-C ^{44,46}, ca. 285.0 eV for C-C/C-H , and ca. 286.5 eV for C-O . Samples AA-H-1h, AA-H-3h, and AA-H-5h were sputtered to remove surface hydrocarbon contamination, changes in the analyzed XPS peaks before and after the sputter treatment of the samples can be seen in Figure 7-11. The total amount

of carbon bonding did decrease for all samples after the sputter treatment, but all three binding environments remained. A small (≤ 4 atomic %) nitrogen peak was present after sputtering. Despite the fact that these samples were milled anaerobically, oxygen was present at 3–12% of the total and had two binding environments: C–O at ca. 532 eV and Si–O at ca. 533.8 eV.

Attempts to understand the reactivity of the silicon surface of the anaerobically milled particles led to multiple gas uptake experiments of anaerobically milled Si powder with various gases. During the BET surface area analysis in $N_2(g)$ (99.999%) samples did not exhibit any irreversible sorption of $N_2(g)$ gas indicating that silicon nitride was not being rapidly formed. Post treatment experiments of AA-H/M-5.5h (specific surface area = $295 \text{ m}^2\text{g}^{-1}$) with oxygen exhibited 5.1% by mass irreversible absorption in 5,128 min. Most of that mass was taken up quickly as shown in the successive gas uptake curves in Figure 7-12. Similar experiments by Butyagin et al.²⁸ with anaerobically milled silicon showed a 1.1% mass increase by mass until equilibrium pressure was reached (time not reported). While the oxygen uptake by AA-H/M-5.5h is ca. 4.6 times greater than in the Butyagin experiment, it should be noted that the AA-H/M-5.5h sample has ca. 110 times greater surface area than samples described by Butyagin. A second oxygen post treatment experiment with AA-H-5.5h exposed to air showed a 2.6% mass increase in ca. 5,760 min (AA-H-5.5h specific surface area = $70 \text{ m}^2\text{g}^{-1}$). Interestingly the anaerobic AA-H-5.5h sample absorbed ca. 68% of the total oxygen mass in the first 10 min, and during this time the sample and vial in which it was contained warmed to the touch. A final experiment demonstrating the reactivity of these anaerobically milled samples with oxygen was performed by simply pouring ca. 50 mg sample of anaerobic AA-H-5.5h from a vial (sample prepared in a vial in an argon atmosphere glovebox so the vial was filled with argon) through air causing

orange sparks and an ensuing fireball. The resulting powder was a brown color instead of the original grey black color.

To determine if water vapor in air was reacting at all with the anaerobically milled MGS, a fresh sample of anaerobic AA-H/M-5.5h was treated with ca. 4 Torr of water vapor (low vapor of $\text{H}_2\text{O}(\text{g})$ to inhibit condensing H_2O on the glass) and in ca. 6 h the pressure dropped 3.5 Torr. The sample itself did not actually take up mass; it is believed the observed pressure drop was due to exposing the rigorously dry glassware to the water vapor. A final experiment to determine if a sample treated with $\text{O}_2(\text{g})$ would then take up $\text{H}_2\text{O}(\text{g})$ was also performed; again the total pressure of $\text{H}_2\text{O}(\text{g})$ taken up was 8.85 Torr, but the mass of the sample only increased by 0.2%. Based on these experiments it is likely that the anaerobically milled Si reacts rapidly with $\text{O}_2(\text{g})$ but not with $\text{H}_2\text{O}(\text{g})$.

7.2.3 Anaerobic Milling of Metallurgical Grade Silicon in Mesitylene with Pyrene Additive.

Two anaerobic batches were milled in dry, air-free mesitylene with 9.0 wt/wt% pyrene additive (relative to Si mass) as an aromatic stabilizer to determine the effects aromatic compounds have on milling silicon. The two milling experiments performed in dry, air-free mesitylene in an inert atmosphere glovebox produced dark gray to black solids that were reactive with oxygen, but not to the extent that the heptane milled samples were reactive with oxygen. If rapidly exposed to air, the mesitylene/pyrene milled samples would warm and, in some instances, visible smoke was observed. The sample did change in color from grey/black to brown, no sparks or flame were observed. The two anaerobic batches (AA-M/P-1h, AA-M/P-2h, AA-M/P-5h, AA-M/P-6h) produced 4 samples exhibiting surface area growth with increased milling time; a trend commonly observed in attritor milling experiments. The 1, 2, and 5 hour

milled samples had increasing BET surface areas while the 6 hour milled sample had a BET surface area lower than the 5 hour sample as shown in Figure 7-13, indicating that particle agglomeration was becoming the dominant interaction stopping overall particle fracture. Also from Figure 7-13, as expected, the MGS continued to lose crystallinity from AA-M/P-1–6 h of milling time. Surface chemical species analysis of the AA-M/P-5h sample by XPS revealed a small amount of Si–O bonding (11% of the total Si), and significant Si–C bonding (33% of the total Si), no other species were observed by XPS.

Post treatment of AA-M/P-5h with O₂(g) was also performed, it displayed rapid initial uptake of O₂(g), but quickly stopped taking up O₂(g) as can be seen in the gas uptake curves in Figure 7-14. The O₂(g) was added in small quantifiable doses so an overall rate of O₂(g) uptake is not known, but a rate trend and a final amount of O₂(g) taken up was determined, the total amount of O₂(g) taken up equated to 0.9% by mass. This equates to 18% of the O₂(g) taken up by AA-H/M-5.5h indicating the mesitylene/pyrene sample was more passivated towards O₂(g) reactions than anaerobic material milled only in heptane (AA-H/M-5.5h). Since the O₂(g) uptake by AA-M/P-5h no water uptake experiments were performed on it or other mesitylene/pyrene milled samples.

The surface of AA-M/P-5h was studied with XPS; spectra are shown in Figure 7-15. Silicon, carbon, and oxygen were all present in this sample with the same binding environments which were observed for the samples milled anaerobically in heptane. Of the silicon present 33% was Si–C, 11% was Si–O, and 56% was Si⁰. Compared to the samples milled anaerobically in heptane AA-M/P-5h contained a much higher amount of carbon, 62% of the total elemental composition as shown in Table 7-2.

7.2.4 Aerobic Milling of Metallurgical Grade Silicon in Heptane.

The aerobic milling in as received heptane yielded a brown powder that was not noticeably reactive with air. Both samples milled aerobically in heptane, A-H/M-5.5h and A-H-5h, were studied using XPS. Sample A-H/M-5.5h contained 33% silicon, 35% carbon, and 32% oxygen as a sum of bonding environments for each element as shown in Table 7-2. Sample A-H-5h contained 36% silicon, 32% carbon, and 33% oxygen as a sum of bonding environments for each element as shown in Table 7-2. The silicon spectra contained peaks for Si^0 at ca. 99.5 eV, Si-C at ca. 100.5 eV, Si_xO_y at ca. 102 eV, and a peak at ca. 103.5 eV for SiO_2 ^{41,44,47}. The amounts of silicon for each type of bonding environment in A-H/M-5.5h are: 46% Si^0 , 13% Si-C, and 41% Si-O as shown in Table 7-1. The amounts of silicon for each type of bonding environment in A-H-5h are: 28% Si^0 , 19% Si-C, and 53% Si-O as shown in Table 7-1. In the carbon spectra, the same peaks are observed that were present in the anaerobically heptane milled samples. Sample A-H/M-5.5h contained the same two oxygen peaks (ca. 532 and 533.8 eV) that were seen in samples milled anaerobically. Sample A-H-5h contained three oxygen peaks at 531.5 eV, 533 eV, and 534.2 eV as shown in Figure 7-17.

7.2.5 Aerobic Milling of Metallurgical Grade Silicon in Mesitylene with Pyrene Additive.

The aerobic milling in as received mesitylene with 9% wt/wt pyrene yielded a brown powder that was not noticeably reactive with air. Sample A-M/P-5h was studied by XPS the results of which can be seen in Figure 7-15. The silicon spectrum contained the same peaks as were seen in the aerobic heptane milled samples. The amounts of silicon were: Si^0 31%, Si-C 34%, Si-O 35%. The carbon spectrum contained two peaks at 285 eV and 286.4 eV, the Si-C peak is likely

contained within the C–C/C–H peak at 285 eV. The oxygen spectrum contains two peaks at 532.5 eV and 533.8 eV.

7.2.6 DLS Particle Size Analysis of Milled Metallurgical Grade Silicon Samples.

Comparable 1 h and 5 h milled MGS samples were tested for particle size range by DLS to ascertain the mean particle size and the total range of particle sizes. Shown in Figure 7-16 is the collected data compared for 5 samples compared, AA-H-1h, AA-H-5h, AA-M/P-1h, AA-M/P-5h, and A-H-5h, samples were dispersed in 200 proof ethanol. The distribution in Figure 7-16 is the average of 3 measurements for each sample. Notice from Figure 7-16 that all 5 samples, independent of additives and milling time, exhibit similar mean particle size and particle size distribution. For all samples measured by DLS the data obtained was considered "quality" by the Malvern software. Based on the DLS analysis in absolute EtOH, all of the samples measured had a minimum particle size starting around 70 ± 5 nm and depending on the additives a maximum particle size ranging up to 600 ± 175 nm.

7.3 Discussion

During the milling experiments a low volume percentage of sample compared to milling media to: (i) decrease time required to reach mechano-chemical equilibrium in experiments where that was the desired target, (ii) minimize particle-particle interaction/agglomeration, and (iii) minimize changes in milling efficiency when multiple samples were removed. Milling efficiency is dependent on the ratio of milling media to sample. The milling media in the mill chamber on a percent volume basis started at ca. 94% milling media for all experiments, and

when samples, roughly half the mass of the original starting material were removed, the percent volume of milling media went up to 97%, a change of only 3%.

For experiments investigating surface protection with aromatic compounds pyrene was chosen as the additive because it could physiochemically adsorb to the nascent Si surface, and during the continued milling in aromatic mesitylene solvent, act as a surface stabilizing additive allowing further particle break down. Previous studies have shown that aromatic compounds, typically benzene, interact with certain faces of Si when rigorously cleaned, and can form strong chemisorption interactions.⁴⁸ The pyrene was thought to react with or adsorb to the Si surface thereby protecting the Si surface and allowing further comminution.

7.3.1 Anaerobic vs. Aerobic Milling of Metallurgical Grade Silicon Without Surface Passivating Additives.

The apparent effect oxygen (or air) had on stabilizing the slurry against agglomeration during the milling process was quite dramatic. The anaerobically milled MGS in dry, air-free heptane reached mechano-chemical equilibrium rapidly with little measurable change in surface area between the 1 h milling time and 5 hour milling time as shown in Figure 7-7. As expected the increased milling time past mechano-chemical equilibrium was reached only further amorphized the MGS without significant changes to particle size, confirmed by BET surface area measurements. The A-H-5h sample had a similar amount of crystallinity compared to AA-H-5h as determined by PXRD, but had a BET surface area over four times greater than the AA-H-5h sample. This suggests that in aerobic conditions, even though the MGS was being milled in a slurry of heptane, enough available oxygen was present to react with the silicon surface forming Si-O bonds changing the surface of the particles. The partially oxidized surface was adequate to

mitigate inter-particle interaction and agglomeration allowing further particle fracture. The amount of oxide present on the MGS after milling aerobically and anaerobically was compared using XPS; when milled aerobically 35–53% of the total Si present was in the form of an oxide while after anaerobic milling 5–7% of the total Si present was bound to oxygen. Furthermore, anaerobically milled samples were apparently forming more Si–C bonds than aerobically milled samples observed at ca. 283.5 eV (see Figures 7-18 and 7-10). One can reasonably assume that reaction of Si with heptane molecules in the dry, air-free heptane only milled samples is especially difficult as it requires activation/cleavage of a strong C–H or C–C bond at near room temperature, a reaction that is likely to be thermodynamically unfavorable under these conditions unless the nascent Si surface were catalyzing such reaction. The XPS results confirm a low degree of Si–C bond formation in the anaerobically milled samples, indicating that the freshly exposed Si is likely not catalytically activating C–H or C–C bond cleavage based on the moderate percent of Si–C bonding present. However, under the conditions created during the milling process, it is likely more energetically favorable to cold-weld smaller particles together forming larger agglomerates minimizing the overall surface potential compared to the surface potential of an equal mass of smaller Si particles. This hypothesis would also explain the time independent specific surface area for the AA-H-1–5 h anaerobic, heptane only milled samples. The cold-welding of smaller particles is likely the thermodynamically more favorable way to minimize the surface potential of the milled particles. Nevertheless, with such a high concentration of heptane in the mill chamber, the formation of Si–C bonds from reaction with heptane is likely a kinetic product. The ability of the nascent Si surface to activate C–H or C–C bonds at or near room temperature as evidenced by XPS is interesting and could be further utilized to protect the Si surface from rapid reaction with air.

Further evidence of the different surface chemistry for the anaerobically milled samples compared to the aerobically milled samples was shown by the differences in forming a suspension in solution. After drying the AA-H-5h and A-H-5h samples, attempts to suspend the particles in dry, air-free heptane with a probe sonicator yielded quite different results; the AA-H-5h sample formed a suspension that did not settle out in a matter of tens of minutes compared with aerobic milled A-H-5h sample that settled out almost immediately. The AA-H-5h sample was shown by XPS to have very little oxygen, (Si–O = 6% of the total Si) some Si–C bonding (18% of the total Si), indicating the addition of carbonaceous species to the surface of the MGS particles. The addition of carbonaceous groups to the surface of the MGS milled particles was likely beneficial for suspending the particles in heptane. On the other hand, the A-H-5h sample had 53% of all Si in Si–O or SiO₂ bonding environments by XPS and only 19% of all Si was in Si–C bonding environments as shown in Figure 7-18. Based on this data, it is no surprise that the much more hydrophilic Si–O surface of the A-H-5h sample would not suspend in heptane despite the fact that both samples had similar amounts of Si–C bonding.

To examine how strongly carbonaceous groups were bound to the Si-surface, evacuation of the milled samples was carried out. Silicon–carbon bonds were present even after evacuating the milled sample on a high-vacuum line (ca. 10^{-5} Torr) for greater than 12 h which would remove any weakly bound or physisorbed heptane. After removing all volatiles by vacuum, XPS spectra were obtained that still exhibited Si–C bonds. Once initial spectra were obtained the samples were sputtered and XPS analysis was repeated. Interestingly, after sputtering, while the total percent of carbon decreased, the component Si–C of the carbon peaks was more pronounced as shown in Figure 7-11. This suggests that normally observed carbon surface contamination had been removed leaving behind mostly carbonaceous species that exhibited Si–C bonds. No

precedent has been found in the literature for the formation of bonds between silicon and aliphatic carbon compounds by mechano-chemical means alone. The Mitchell group milled silicon with a ball mill in octane, 1-octene, and 1-octyne and found evidence of C–H bonds by FT-IR for 1-octene and 1-octyne milled silicon, but not in octane milled silicon.^{36,37,49}

In all of the anaerobically milled samples there was no XPS peak present at ca. 103.5 eV for SiO₂. However, there was typically a peak present at ca.102 eV which would likely be due to a silicon suboxide species, i.e., Si_xO_y^{41,47} (see Figure 7-10). Despite the anaerobic milling conditions, some surface bound oxygen remained and it cannot be determined whether this was from: (i) the initial SiO₂ layer on the MGS, (ii) due to reactions with the small amount (≤ 1 ppm) O_{2(g)} in the anaerobic milling atmosphere, or, (iii) another unknown source of adventitious oxygen.

When samples were milled anaerobically without the surface reactive carbon species, most had a small (≤ 5 atomic %) amount of fluorine present. The only possible fluorine source in the glovebox this author had identified was the Viton® tubing used for transporting the slurry from the overhead stirrer to the sonicator and back to the mill. One hypothesis regarding the source of the fluorine was that the nascent silicon surface could be so reactive after a short time in the mill that it reacted with the normally inert Viton® tubing and started to leach or remove compounds (like plasticizer) from the tubing. In the C 1s XPS spectra there was no evidence of C–F bonds, but given the low level of fluorine present, these peaks could have been below the detection limit. The high reactivity of nascent silicon surfaces was corroborated further by the presence of fluorine and Si–C bonds in samples milled anaerobically in heptane.

Samples that were milled anaerobically (in an N_{2(g)} atmosphere) in heptane and then sputtered in the XPS showed the presence of a small (≤ 4 atomic %) amount of nitrogen. Silicon

surfaces free of contaminants is known to react with nitrogen during milling to form silicon nitrides, however, this process was shown to be slow.⁵⁰ The reason that this peak was only apparent after sputtering is not clear, but may not be observed without sputtering due to the hydrocarbon surface contamination.

7.3.2 Anaerobic Milling of Metallurgical Grade Silicon With and Without Surface Passivating Additives.

All of the anaerobically milled samples appeared to be reactive with $O_2(g)$ based on visual inspection when exposed to air, and based on observed pressure decrease when anaerobic samples were treated with $O_2(g)$. Not surprisingly, the anaerobically milled material with surface passivating additives was less reactive with $O_2(g)$, likely due to greater passivation of the MGS surface. Direct comparison of XPS data for anaerobic milled samples with and without surface passivating additives shows similar small amounts of Si–O bonding (AA-H-5h Si–O = 6%, AA-M/P-5h Si–O = 11%), but, a marked increase in Si–C bonding in the sample with surface passivating additives (AA-H-5h Si–C = 18%, AA-M/P-5h Si–C = 33%). The slow reaction rate with $O_2(g)$ post-treatment and the greater Si–C bonding in the anaerobic milled sample with surface passivating additives indicates that in the absence of oxygen and in the presence of a reactive organic material more Si–C bonding did occur.

7.3.3 Milling Time for Anaerobic Milling of Metallurgical Grade Silicon Without Surface Passivating Additives Compared to Anaerobic With Surface Passivating Additives.

Milling time did not appear to make much difference in the measured BET surface in the anaerobic experiments without surface passivating additives (AA-H-1h, AA-H-2h, AA-H-3h,

AA-H-4h, AA-H-5h, AA-H-5.5h). In the AA-H-1–5h series of anaerobic milled samples with no additive the crystallinity rapidly decreased forming mostly amorphous particles with small crystallites embedded in solid amorphous particles. In the AA-H-5.5h sample, the BET surface area was $70 \text{ m}^2\text{g}^{-1}$ compared to the AA-H-1–5h series the average BET surface area of $40 \pm 5 \text{ m}^2\text{g}^{-1}$, which indicates a difference in these samples. While the percentage of Si–O and Si–C bonding were nearly the same for these samples based on the Si bonding environments, the overall carbon was 12% greater in the AA-H-5.5h sample. This additional carbon could have been further mitigating particle agglomeration during milling allowing a greater level of particle reduction without the formation of Si–C bonds. By XPS as shown in Figure 7-10, these samples all had less than 10% Si–O bonding ($6.5 \pm 0.5\%$) and Si–C bonding near 20% ($15.0 \pm 3.0\%$). The anaerobic samples milled for 1, 2, 3, 4, and 5 h in heptane had almost no increase in BET surface area indicating there was little to no stabilization of the slurry and therefore particle fracture quickly reached a maximum and particle agglomeration (likely through cold-welding) became the dominate process. The two competing rates, particle fracture by milling action, and particle agglomeration by inter-particle interaction combined to create a particle size equilibrium.

In contrast, the samples milled anaerobically with surface passivating additives exhibited an increase in measured BET surface area with increased milling time, going from AA-M/P-1h = $75 \text{ m}^2\text{g}^{-1}$ to AA-M/P-5h = $258 \text{ m}^2\text{g}^{-1}$. The AA-M/P-6h milled sample had a measured BET surface area of $205 \text{ m}^2\text{g}^{-1}$, decreased from the 5 h sample indicating the minimum particle size had been reached, and agglomeration had become the dominant rate, likely due to increased inter-particle interactions. The aromatic surface passivating species were superior at stabilizing the slurry compared to heptane alone, allowing further particle reduction. The anaerobic samples milled for 1, 2 and 5 h with surface passivating species showed increased

BET surface area with increased milling time, indicating further particle fracture was occurring between those times.

7.3.4 Anaerobic vs. Aerobic Milling of Metallurgical Grade Silicon with Surface Passivating Additives.

Interestingly, samples milled anaerobically with the same surface passivating additives had measured BET surface areas greater than samples milled aerobically, AA-M/P-5h, AA-M/P-6h had specific surface areas of 258 and 205 m^2g^{-1} respectively while A-M/P-5h, A-M/P-6h has specific surface areas of 130 and 140 m^2g^{-1} respectively. However, the presence of oxygen did not appear to preclude or diminish the formation of Si–C bonding. Aerobic milled MGS with surface passivating additives exhibited significant Si–O formation with nearly the equal amounts of Si–C bonding compared to anaerobically milled MGS with surface passivating additives (AA-M/P-5h Si–O = 11%, Si–C = 33%, A-M/P-5h Si–O = 35%, Si–C = 34%) as shown in Figure 7-15. Based on bond enthalpies, an Si–O bond is stronger than an Si–C bond by 67 kJ/mol indicating the formation of significant Si–C bonding in aerobically milled samples with surface passivating additives is likely a kinetic phenomenon. The increase in Si–C bonding when milled with surface passivating additives likely arose due to the significantly greater concentration of carbon containing molecules compared to $\text{O}_2(\text{g})$ during milling. The process of Si–C bond formation likely occurs as follows; once an MGS particle fractures exposing the nascent surface, the more available carbon additives or solvent react even though reaction with $\text{O}_2(\text{g})$ would be the thermodynamically preferred reaction. This result also indicates that while Si–O bonds are more thermodynamically favorable, they are not as good at mitigating surface potential allowing further particle size reduction compared with aromatic carbon compounds for MGS milled

samples. This result regarding additives versus oxygen should be taken into account when milling any metal powder aerobically; the presence of oxygen and formation of metal oxide could be limiting the minimum particle size more than the intentional additives added to augment the surface potential.

Under the milling conditions presented here, regardless of oxygen, milling solvent, and surface passivating additives all samples milled for 5 or 5.5 h reached nearly the same level of amorphization as shown in the PXRD in Figure 7-18. The specific surface area of each of these samples spans a range of over 7 times from the lowest specific surface area to the greatest. This wide range of specific surface area and corresponding particle sizes was produced by variations in additives, solvent and oxygen presence.

7.3.5 DLS Experiments Do Not Appear To Correlate With BET Surface Area Measurements of Metallurgical Grade Silicon Nanoparticles.

The DLS particle size distribution measurements appear to be counter to the BET surface area measurements for the 5 samples tested by DLS. Assuming the surface area can be directly correlated to particle size (this assumption requires that the particles be non-porous, which appears to be the case for the samples inspected by TEM). Table 7-3 shows the results for samples measured by DLS, measured by BET surface area, and calculated particle size based on BET specific surface area assuming solid spheres with monodisperse distribution, and the particle size range obtained by DLS in absolute ethanol. From Table 7-3 note the large disparity in calculated monodisperse particle size based on BET specific surface area and the mean DLS particle size for each sample, the DLS particle size is 3 to 23 times as large as the calculated size based on BET specific surface area measurements. This large difference between these two

methods for deriving particle size does have a number of variables that could account for these observed differences. As a control experiment a sample of silica-gel with a BET surface area of ca. $500 \text{ m}^2\text{g}^{-1}$ (Sigma Aldrich, 70-230 mesh, 60 \AA , for column chromatography), was measured by this author to have a BET surface area of $550 \text{ m}^2\text{g}^{-1}$, a difference of 10%.

The discrepancy of the particle size based on DLS and particle size calculated from measured BET surface area could be caused by many of the assumptions. First, the calculated particle size based on BET specific surface area assumes the sample is comprised of spherical monodisperse particles, which is known not to be the case from SEM and TEM. In fact, SEM and TEM show thin plates of irregular shape which would have a much greater surface area to volume ratio compared to a sphere, so small changes in actual particle size of thin irregular sheets would have a significant change in the measured BET surface area. Similarly, the calculations used to obtain particle size from the changes in scattering patterns in the DLS experiment assume spherical particles, which again these samples are known to not be spherical. Also, for the DLS experiments\ samples were dispersed in ethanol which could have reacted with the reactive surface of the anaerobic samples or otherwise changed the surface potential of the samples causing agglomeration. Such agglomeration in the ethanol suspension would artificially increase the particle size. Attempts to repeat the DLS measurement in air-free heptane resulted in unreliable data due to rapid particle settling, even at low concentrations. Based on the SEM and TEM images and the BET surface area measurements it seems the DLS measurements in ethanol are not an accurate representation of the true particle size of these samples.

7.4 Summary and Conclusion

Stirred media mills can be used in a top-down approach to produce irregularly shaped silicon nanoparticles. When milling silicon, the presence of surface passivating additives including oxygen or aromatic carbon containing species mitigates agglomeration and leads to a dramatic increase in specific surface area, and corresponding decrease in average particle size. Particle amorphization occurs rapidly in a stirred media mill, within two hours crystallite size is on the order of 2–50 nm regardless of whether surface passivating additives are present. Nascent silicon surfaces produced by this mill under anaerobic conditions are sufficiently reactive to result in the formation of Si–C bonds when milled in a relatively inert solvent such as heptane. Interestingly, when milled aerobically in either heptane or mesitylene the silicon still forms a significant amount of Si–C bonds as well as Si–O bonds, indicating selection of mill fluid and additives should be considered carefully, and that, when milling silicon, and likely all metalloids and metals, significant metal oxygen formation does occur in the absence of other surface passivation in stirred media mills. When milled anaerobically with carbon based solvents and/or carbon containing reactive aromatic species, the silicon forms mostly Si–C bonds with very little Si–O. Due to the lack of surface passivation the resulting material is highly reactive once dried to a solid in the absence of $O_2(g)/H_2O(g)$. The silicon milled anaerobically with aromatic additives is less reactive with $O_2(g)$ than silicon milled anaerobically in heptane, but does still exhibit some reactivity with residual $O_2(g)$ in controlled experiments. Finally, the nascent silicon surface produced by this milling method was reactive with typically non-reactive solvents, any oxygen present and aromatic additives; this empirically derived knowledge should be used as a guide

when choosing milling conditions for producing silicon nanoparticles or any metal nanoparticle of an oxygen reactive metal with a particular particle size and chemically modified surface.

7.5 Future Work

While the Strauss-Boltalina group no longer has access to the Netzsch MiniCer Laboratory stirred media mill, there are some follow-on experiments that would be an interesting addition to this research. First, repeat the aerobic and anerobic milling of the metallurgical grade silicon with even more reactive organic additives and solvents to try and more completely surface passivate the Si nanoparticles. Reactive additives can include aldehydes, amides, and alkenes, more reactive solvents could include cyclohexene, ethylene carbonate, or propylene glycol. With new additives, different chemistry could be occurring on the surface of the nanoparticles. Further attempts should be made to characterize what is on the surface of the nanoparticles by solid state NMR, or attenuated total reflectance FT-IR analysis of the surface. Depending on the residual surface chemistry, nano particles produced with this type of chemically modified surface could be further reacted to augment their surface chemistry for a particular application.

Since so many practical uses of nanoparticles have been optimized for regular-shaped nanoparticles, methods to make regular shaped and low size distribution nano-scale materials by top-down-milling would be advantageous over bottom-up-solution methods. Methods to polish the irregular shaped particles produced by this type of milling method, either during the milling process or in a secondary milling process would be of great interest in for many applications requiring expensive bottom-up synthesized nanoparticles. This polishing can be accomplished by further wearing and fracture of the particles (similar to polishing a metal surface with finer and finer grit sand paper) or by a chemical polishing method.

7.6 Experimental

7.6.1 Necessary Design Parameters, Requirements for Mill and Rotary Evaporator and Requirements for Anaerobic, Moisture Free Atmospheric Conditions.

All milling operations employed a continuous flow Netzsch MiniCer Laboratory stirred media mill (loaned to the Strauss-Boltalina by Kratos LLC.) with yttrium stabilized zirconium oxide lining, and Netzsch SiLi yttrium stabilized zirconium oxide milling media ranging from 0.3–0.4 mm. The mill had a grinding chamber volume ca. 160 mL, with a cylindrical slotted mixer blade, a 150 μm separator screen, double mechanical seals separating the grinding tank from motor bearings by means of ca. 80 psi seal fluid, and an inline QSonica 700 W, 20 kHz sonicator with an 85 mL low-flow cell with a 1.27 cm diameter probe, programmed to run throughout the milling procedure for 3 min at 30% of peak amplitude in intervals every 10 min, see schematic and slurry flow direction in Figure 7-2.

The goal of this project was to be able to mill bulk silicon particles (nominally 170–325 mesh) slurried in an anaerobic, anhydrous solvent under anaerobic conditions. For the purpose of this project, an anaerobic atmosphere was defined as an $\text{N}_2(\text{g})$ atmosphere with ≤ 1 ppm oxygen ($\text{O}_2(\text{g})$) and ≤ 1 ppm water vapor ($\text{H}_2\text{O}(\text{g})$). For this application the mill was a Netzsch Minicer circulation laboratory scale attritor mill, the reasons for using this mill compared to other mills is described in this chapter. To this end, an existing Vacuum Atmospheres HE-453-4 glovebox (hereinafter abbreviated "GB") was modified to house the Netzsch Minicer mill (hereinafter referred to as "the mill"), mill-related equipment, and the Büchi rotary evaporator. The modifications were planned by this author and Professor Steven Strauss; the execution of the

plan was performed by this author, Professor Steven H. Strauss fellow graduate student Karlee P. Castro, and undergraduate student Brent M. Wyatt. The design, planning execution and troubleshooting required several months to complete. The mill, having been manufactured in Germany had many non-American parts and fittings that required adapters. Furthermore, multiple correspondences with Netzsch technical staff indicate a mill like this has never been previously completely enclosed in an inert atmosphere system as described below. A photograph of the GB before modification is shown in Figure 7-19. A general reference for the principles of GB design and use is given in Shriver, D. F.: "The manipulation of air-sensitive compounds", ref 52.

Photographs of the Netzsch Minicer mill and related equipment are shown in Figure 7-20. These six pieces of equipment are; (i) the mill, (ii) the seal-fluid pressure tank and pump (mounted to the same stand), (iii) the slurry tank, (iv) the peristaltic pump, (v) the sonicator and its electrical power/control unit, and (vi) the main electrical control unit. A diagram of the flow direction and circulation route of the slurry during the milling process is shown in Figure 7-2. A diagram of the electrical connections is shown in Figure 7-21, and cooling water connections, seal fluid connections, and inert gas connection is shown Figure 7-22 of the Netzsch Minicer mill in its unaltered state is shown for comparison to modifications.

Proper function of the mill requires the following to be supplied; (i) 230 VAC, 15 A electrical connection for main electrical control unit and overhead stirrer, (ii) 120 VAC, 15 A for sonicator, (iii) 80–100 psi N₂ gas line for the pressurized seal-fluid tank, (iv) cooling water lines in and return lines for the mill, slurry tank and pressurized seal-fluid tank, and (v) physical access to most pieces of equipment to use, change settings or repair during the use of the mill. All of these inputs were required to be put through the GB wall in such a way that the GB could

still attain a dry air-free environment and allow function of the mill. Additionally, some of these inputs had to be flexible to allow the mill to tilt and move during operation shown in Figure 7-20.

7.6.1.1 Considerations and Solutions for Electrical Requirements and Feedthroughs for Mill.

The biggest considerations when bringing power into the GB is safety (electrifying an aluminum glovebox) and making sure the port or bulkhead connector would not leak gas into the GB. Both of these problems were solved by finding the proper bulkhead connector that was hermetically sealed, could be sealed through the aluminum wall, and ensuring the wiring was all performed correctly and properly grounded. The main electrical control unit required 230 VAC electrical power. Since the CSU high-voltage service is nominally 208 VAC, (typical of 2 hot legs of a 3 phase commercial electrical system actual readings 210–214 VAC) a voltage booster was required. To compensate for the lower voltage a Jefferson 416-1121-000 (0.25 kVA) buck-boost transformer was installed to boost the CSU line voltage from 208 V to 230 V, actual readings 230–232 V, as shown in Figure 7-23. The Minicer manual provided by Netzsch specified a 20 amp circuit for the main control unit, but this was not consistent with the size (i.e., the diameter) of the individual wires in the primary power cord of the main electrical unit. The wires in the primary power cord were labeled with a European code for wires that could handle current of 10 A at 250 VAC, (the cross-sectional area of these copper (Cu) wires is 1 mm²). Furthermore, the sum of the currents specified in the Netzsch manual for the mill (4.0 amp), the peristaltic pump (1.2 amp), and the seal-fluid pump (2.5 amp) was only 7.7 amp. Therefore, a 240 VAC, 15 amp circuit breaker was installed on the outside of the GB for the primary 230 V power cord coming from the Jefferson transformer shown in Figure 7-23. The circuit breaker was mounted such that it would act as the main power switch for the mill and an emergency

shutdown switch in reach of the main user if necessary during a milling operation inside the GB. The transformer and circuit breaker and their position on the GBN are shown in Figure 7-23. The other components requiring power (probe sonicator and overhead stirrer) were connected to their own separate circuits and were not part of the main breaker shut off.

The main 230 V power cord (from the 240 VAC, 15 A breaker) then continued, via a Pave Technology electrical bulkhead connector through an aluminum (Al) panel (hereinafter referred to as "the Al panel"), shown in Figure 7-24, mounted inside a metal double gang junction box on the roof of the GB shown in Figure 7-25. Specifications for the Pave Technology bulkhead connector are shown in Figure 7-24. On the inside of the GB a metal double gang junction box with NEMA L6-20 receptacle and plug, shown in Figure 7-26, was used to safely connect and disconnect the main power from the main control unit when necessary. A secondary movable, metal double gang junction box with cover that was attached to the plug (inside the GB) was used to connect the original main power cord for the Netzsch electrical control unit and the original power cord for the slurry-pot overhead stirrer to 230 VAC 15A line coming into the GB. All metal boxes and the aluminum GB were grounded to ensure no shock hazard was possible.

Exiting the Netzsch main electrical control unit are four wires carrying 230 V to (i) the mill motor, (ii) the seal-fluid pump, (iii) the seal-fluid-tank pressure sensor, and (iv) the peristaltic "feed" pump shown in Figures 7-22 and 7-27. Other electrical equipment in the GB were powered by existing 120 V outlets, including the sonicator power/control unit, the LED lights installed above the seal-fluid unit and the mill, the Büchi rotary evaporator and its variable-temperature bath, and a fan to mix the GB atmosphere as high-purity nitrogen gas was purged through the GB before, during, and after milling.

7.6.1.2 Considerations and Solutions for Cooling Water Requirements and Feedthroughs for Mill, and Seal Fluid Lines.

Any fluid transport occurring in the GB for mill operation (i.e. cooling water and seal fluid) had to be robust enough that it would not break or leak requiring the GB to be disassembled to clean and repair. The slurry pot, mill, and pressurized seal-fluid tank required a constant circulation of cooling water to maintain the desired temperature of the slurry and the seal fluid during the milling operation. The fittings and materials used for circulating water in a dry air-free glovebox had to be such that they were durable enough not to break over time and did not slowly leak moisture during continued use. Flexible plastic tubing could not be used for the cooling water lines inside the GB because water vapor ($\text{H}_2\text{O}(\text{g})$) will diffuse through any polymeric elastomer (for example, the permeability to $\text{O}_2(\text{g})$ and $\text{H}_2\text{O}(\text{g})$ at 25 °C are $4.5 \times 10^{-11} \text{ cm}^2/\text{s}\cdot\text{Torr}$ and $2.2 \times 10^{-9} \text{ cm}^2/\text{s}\cdot\text{Torr}$, respectively for Teflon®/FEP (e.g., Viton®)^{1,2} and $5.0 \times 10^{-14} \text{ cm}^2/\text{s}\cdot\text{Torr}$ and $9.3 \times 10^{-11} \text{ cm}^2/\text{s}\cdot\text{Torr}$, respectively, for poly(vinylidene) chloride (e.g., Tygon®)).^{1,3} Additionally the water lines attached to the mill had to be flexible to allow the mill to articulate without leaking or coming loose during operation. Finally, since the mill and components were a product of Germany, the cooling water plumbing parts and threads on the mill and other components were all British Standard Pipe Taper (BSPT, seal is made on the threads) threads or British Standard Pipe Parallel (BSPP, seal is made with a secondary gasket) threads requiring adaptors and Teflon® sealing tape to adapt all connections to National Pipe Thread (NPT, seal is made on the threads). While BSPT and BSPP threads are not mechanically inferior to NPT threads in anyway known to this author, they are harder to find in the correct sizes. The seal fluid lines only contained the seal fluid, which was going to be made anhydrous

and oxygen free prior to bringing into the GB, so the tubing only needed to be flexible, durable unlikely to kink or break and resistant to the seal fluid. To save money, ¼" PTFE-lined stainless steel braided hose was used for the seal fluid lines (about 20% the cost of convoluted stainless-steel lines).

The flexible tubing chosen for cooling water was Swaglok ⅜" I.D. convoluted 316L stainless-steel-core flexible tubing with braided stainless-steel sheathing for protection, close up view in Figure 7-26. The tubing was connected to the mill components using ⅜" stainless-steel Swaglok fittings with adaptors when necessary. Bringing the cooling water from the source outside the GB through the Al roof panel was accomplished using ½" NPT 316 stainless steel bulkhead connectors with ¼" thick Teflon® gaskets (1⅜" OD) purchased from ALSCO Industrial Products, Inc. and ½" NPT Swagelok B-45F8 brass ball valves, both of which are shown in Figure 7-28, the assembled units can be seen in Figure 7-26. Several photographs of the cooling-water lines and their connections to the mill, slurry pot, and seal-fluid tank are shown in Figures 7-29 and 7-30. These photographs also show all of the seal fluid and cooling water lines connected to the mill.

Note that the use of Viton® tubing to circulate the solvent/nanoparticle slurry via the peristaltic pump did not present a problem. Solvent vapor would already be present in the GB atmosphere during milling, so a small amount of added solvent vapor due to solvent-vapor diffusion through the Viton® tubing would not degrade the anaerobic atmosphere with O₂(g) or H₂O(g).

7.6.1.3 Considerations and Solutions for High Pressure N₂ Gas Feedthrough for Mill.

The mill required 80-100 psi of inert gas supplied to the seal fluid tank to maintain a certain pressure in the pressurized seal fluid tank and seal fluid lines. The pressurized seal fluid acts as a high pressure barrier inside the mill to ensure no mill contents leaks into the bearings and motor. If the mechanical seal separating the milling chamber and bearings should be compromised the high pressure seal fluid would leak in rather than the slurry in the mill seeping into the motor bearings causing damage. The 80–100 psi N₂ gas was connected to the seal fluid tank via ¼" Cu tubing, appropriate brass Swagelok fittings, and a brass Swagelok bulkhead connector sealed through a hole in the Al roof panel as shown in Figure 7-25. The Cu tubing supplied N₂(g) via a tank of ultra-high-purity (UHP) N₂(g) outside the GB connected with a 2-stage high purity gas regulator to ensure the outlet pressure did not drift as the N₂(g) tank pressure (inlet of the regulator) decreased. The pressure and seal fluid level sensor threaded into the top of the seal fluid tank and had to be accessible to add or exchange the seal fluid.

7.6.1.4 Positioning of Mill and Components in the GB While Keeping Them as Accessible as Required.

The greatest difficulty by far was to position all of the mill components in the GB such that they could be accessed either as they would be outside of the GB or modified in such a way that they could be accessed inside the GB. For instance, the mill itself had to be right in front of the GB gloves and accessible for easy set-up and cleaning. The peristaltic pump had to be within reach to set-up the Viton® tubing in the pump head, however, the power and control to the

peristaltic pump was performed at the main control unit. The pressurized seal fluid tank only needed to be accessed when the when a new seal fluid was being used, or when it needed to be repaired. Because of the low frequency of needing to access the seal fluid tank and pump the entire stand was placed on the far left of the gloves, left of the mill in Figure 7-29. The seal fluid tank was oriented so that the sight-level on the pressure tank could be read by a person working on the left side of the glovebox. The seal-fluid pressure tank was lowered in the mounted stand so that the large threaded cap and seal-fluid level sensor shown in Figure 7-31 could be loosened, removed, and re-tightened even with the limited reach of a person working on the left side of the GB. The sonicator control box needed to be accessed through the touch screen only, so it was suspended in the back of the GB from a Unistrut® rack shown in Figure 7-32, and a remote power switch shown in Figure 7-27 was created to turn the unit on and an extension was added to the touch screen stylus so it could be used from the gloves. Similarly the sonicator probe and flow cell were suspended to keep it up and out of the way. The main control/power unit was turned sideways to access the control buttons shown in Figure 7-30 with the GB gloves, however, the main power shut off could not be accessed in this orientation (see power off switch and emergency stop button in top left Figure 7-20), hence using the breaker as the power off switch.

7.6.1.5 Adapting Büchi RII Rotary Evaporator for use in Inert Atmosphere Glovebox.

The Büchi RII rotary evaporator was also put into the GB so the bulk of the solvent could be removed rapidly from the milling slurry in the inert atmosphere. The rotary evaporator was used normally with the exception of the solvent collection and the heating bath. The variable-temperature bath was filled with Thomas silicone oil instead of water. The silicon oil was

pretreated to remove traces of O₂(g) or other volatiles by heating to 150 °C under vacuum for 24 h. The vacuum was connected through Tygon® tubing in the GB to a brass valve and sealed brass bulkhead connector to another brass valve exterior of the GB. The exterior brass valve was connected to a large cold trap and diaphragm vacuum pump. The double valve for the vacuum to the rotary evaporator was to ensure that no accidental opening of one valve would compromise the GB atmosphere.

7.6.1.6 Final Mill Operation in the GB

Overall the Netzsch mill and components functioned inside the GB as they did outside of the GB. The additional engineering and adaptations to allow this inert atmosphere operation of the Netzsch mill were not cumbersome and did not impede the use or operation of the mill compared to when the mill was on the benchtop. The only notable difference is during cleaning of the mill, in the GB cleaning the mill chamber and the slurry tank was more difficult. However, the greatest drawback to having the mill in the GB was if/when the mill required repair. On one occasion the power inverter in the main control unit that controlled power to the mill motor, became inoperable and to repair the power inverter GB had to be disassembled to access the main control unit and replace and reprogram the power inverter. While all possible scenarios halting the use of this mill in the GB could not be planned for, most possible problems were planned for, and the 9 times the mill was used in the GB, only one of those times it did not function due to a faulty power inverter.

7.6.2 Reagents and Solvents

The MGS was obtained from Marietta Minerals (Si = $98.9 \pm 0.20\%$, major impurities Fe = $0.35 \pm 0.30\%$, Al = $0.20 \pm 0.15\%$, Ca = $0.12 \pm 0.06\%$), through Kratos LLC. Prior to milling, the silicon powder was hand ground in air, and sieved to a size range of 45–90 μm . Dry, air-free heptane (Fisher, HPLC grade submicron filtered) was prepared by refluxing over sodium metal for ca. 12 h, and then distilled under $\text{N}_2(\text{g})$. Dry, air-free mesitylene (Alfa Aesar, 98+%) was prepared by refluxing over sodium metal for ca. 12 h, and then distilled under $\text{N}_2(\text{g})$. Sample names and milling conditions are listed in Table 1. The milling process and all subsequent manipulations of the anaerobic milled silicon took place in an $\text{N}_2(\text{g})$ or $\text{Ar}(\text{g})$ (Airgas, UHP grade used as received) atmosphere glovebox for anaerobic samples. The quality of the atmosphere (concentration of oxygen and solvent) was determined by the length of time an exposed 25 W tungsten filament light bulb stayed on in the glovebox.⁵¹ The atmosphere was sufficiently pure to keep the light bulb on continuously for at least 24 h prior to any milling or handling of anaerobically milled silicon indicating combined concentrations of $\text{O}_2(\text{g})$ and $\text{H}_2\text{O}(\text{g})$ at or below 5 ppm.⁵²

7.6.3 Instrumentation and Material Analysis Techniques.

BET: Anaerobic specific surface area analysis was performed via BET methods using specially designed air-free “pear-shaped” flasks.⁵³ The flasks had narrow necks minimizing the volume of gas exposed to a gradient temperature (i.e. temperature change going from room temperature to liquid N_2 temperature). This method of BET analysis required a two temperature measurement of the final pressure in the flask. The gas used was $\text{N}_2(\text{g})$ (Airgas, UHP, 99.999%) and the sample

was cooled to liquid N₂(g) temperatures. The silicon sample was added to the flask in a glovebox and then further dried by vacuum (<10⁻⁵ Torr) at 20 °C for at least 16 h. Samples were ca. 1.00 g in mass, and the sample volume was corrected for in the final pressure measurement. The data was plotted as $P_{eq}/n(P_0 - P_{eq})$ vs. P_{eq}/P_0 and fit to a linear equation where the slope, intercept, and the moles of N₂ required to form a monolayer was calculated⁵³, and the specific surface area was determined using a surface area for N₂ of 1.62 m² molecule⁻¹.⁵⁴ At least 5 nitrogen additions were performed per sample, more additions were performed when required to keep the P_{eq}/P_0 in the linear range of 0.05–0.30.⁵³ In all cases the linear fit through the 5 or more data points had an $R^2 > 0.999$.

H₂O(g) and O₂(g) Gas uptake Experiments: For oxygen uptake experiments industrial grade O₂(g) (Airgas 99.5%) was used as received. For water uptake experiments distilled deionized water (Barnstead Nanopure filtration and deionizer system, final resistance greater than 18 MΩcm) was freeze, pump, thaw, degassed three times to remove any dissolved gases. A fresh sample of milled, dried MGS was transferred to an air-free test tube in an N₂(g) or argon-filled glovebox and attached to a glass manifold with a #9 o-ring joint. Keeping the sample rigorously anaerobic all volatiles were again removed by vacuum, 10⁻⁵ Torr for ca. 12 h. The sample was then exposed to measured doses of O₂(g) or H₂O(g). In the case of H₂O(g) experiments, the H₂O(g) was held isothermally at a temperature of 19 °C, just below room temperature to ensure no water vapor would condense in the air-free sample tube leading to erroneous mass changes.

Powder XRD: Data were collected on a Scintag X-2 powder X-ray diffractometer, with Cu Kα radiation ($\lambda = 0.154$ nm) at 40 mA and 45 kV, a tube divergent slit width of 2 mm and a tube scatter slit width of 4 mm. The instrument is equipped with a Peltier detector with a scatter slit

width of 0.5 mm and a reference slit width of 0.2 mm. The experimental setup was a standard Bragg-Brentano geometry with a stationary sample stage. Each sample was scanned from 5°–90° or 10°–80° in 0.02° step increments with 1.00 s collection per step. Samples that were aerobic were sprinkled onto a thin film of high vacuum silicon grease applied to a standard glass microscope slide or mixed in mortar and pestle with Apiezon Type N grease in air and spread as a paste to a standard microscope slide.

Air-free powder XRD: Instrument and experimental set up were the same as previously described. Samples were prepared by grinding/mixing a weighed sample of the milled MGS in a weighed amount of Apiezon Type N grease in a N₂(g) or argon filled glovebox. All milled MGS samples were 0.106 ± 0.008 g and all amounts of Apiezon Type N grease were 0.260 ± 0.007 g. The mixture of milled MGS powder and grease was ground in a clean, dry agate mortar and pestle inside the glovebox until a smooth brown paste formed. The paste was then removed from the glovebox and spread as a film covering ca. the middle half of the surface area on a standard glass microscope slide.

TEM: Transmission electron microscopy was performed on a JEOL JEM-2100F field emission transmission electron microscope by Dr. Roy Geiss. Samples were dispersed in ethanol (Pharmco-AAPER 200 proof, ACS/USP grade) or isopropyl alcohol (Fisher, 99.999%) in air with a bath sonicator for ca. 10 min. The dispersion settled for ca. 1 min then the solution was added drop-wise to TEM grids (Ted Pella, part #01840, pure carbon on 200 mesh Cu), and allowed to dry in air for ca. 10 min. The grids with samples were then attached to a double tilt holder and subjected to ca. 10⁻³ Torr vacuum until the pressure equilibrated (indicating little to

no residual alcohol remained). Samples were imaged at 200 keV, images were captured and manipulated with Gatan Microscopy Suite, Version 2.31.734.0. To simplify the crystalline region and crystallite size analysis most TEM images were collected in darkfield view with the beam at an arbitrary angle and then rotated 90° from the initial angle.

SEM: Scanning electron microscopy was performed on a JEOL JSM-6500F field emission scanning electron microscope by Dr. Roy Geiss. Samples were dispersed in ethanol (Pharmco-AAPER 200 proof, ACS/USP grade) or isopropyl alcohol (Fisher, 99.999%) in air with a bath sonicator for ca. 10 min. The dispersion settled for ca. 1 min then the solution was added dropwise to TEM grids (Ted Pella, part #01840, pure carbon on 200 mesh Cu), and allowed to dry in air for ca. 10 min.

XPS: X-ray photoelectron spectroscopy (XPS) experiments were performed on a PHI-5800 system using a monochromatic Al K α X-ray source by Karlee P. Castro. A takeoff angle of 45° was used for all analyses and an electron neutralizer set to 5 μ A for anaerobic samples and 35 μ A for aerobic samples was used to partially offset sample charging. High resolution spectra were collected using 0.1 eV/step, 100 ms/step, 23.50 eV pass energy, and a spot size of 0.8 \times 2 mm. CasaXPS Version 2.3.16 was used to analyze all data. Silicon and carbon spectra were fit with a Tougaard background and oxygen spectra were fit with a Shirley background, using an average width of 5 and 70% Gaussian 30% Lorentzian peak shapes. After fitting the C 1s spectrum, all peaks were shifted by setting the C–C/C–H peak to 285.0 eV to charge correct all binding energies. The metallic silicon Si⁰ environment was fit with both a 2p_{1/2} and 2p_{3/2} peak, the other Si environments were fit with single peaks.

Anaerobic samples were loaded onto the sample holder in a N₂(g) or argon-atmosphere glovebox and transferred into either a transfer bag or a glass jar. When using a transfer bag, the bag was opened over the flush of nitrogen exiting the sample introduction chamber and the sample holder transferred into the instrument and started under vacuum as quickly as possible, typically within 30 seconds. When using the glass jar with a plastic lid and the seam covered in parafilm, the glass jar was opened under a flush of argon and the sample holder transferred into the instrument under a flush of argon and then immediately started under vacuum. For samples that were sputtered to remove surface hydrocarbon contamination, an argon-ion gun within the XPS operated at 2 kV for 0.1 min was used.

DLS: Dynamic light scattering was performed on a Malvern Zetasizer Nano ZS with a 633 nm laser source operating in backscatter mode with a source detector angle of 173°. Samples were dispersed in 200 proof ethanol (Pharmco-AAPER 200 proof, ACS/USP) by breaking up clumps in an agate mortar and pestle and then further dispersion with sonication for 10–15 min in a bath sonicator. Samples were diluted until a quality experiment was achieved. Samples were tested in 1.5 mL PMMA ISO 9001-14001 Certified, disposable cuvettes (GMBH, Cat. No. 759085D) at 25 °C and were held isothermally at 25 °C for 2 min prior to the experiment. For each sample 3 measurements of 12–15 runs per measurement were utilized (number of runs depending on sample concentration, determined by instrument for each sample).

7.6.4 Anaerobic Milling in Heptane

Dry, air-free heptane (Fisher, HPLC grade submicron filtered) was prepared by refluxing over sodium metal for ca. 12 h, and then distilled under N₂(g). Except for sample AA-H/M-5.5h

dry, air-free heptane was also used as the seal fluid in the Netzsch MiniCer mill. For sample AA-H/M-5.5h dry, air-free mesitylene was used as the seal fluid. The mill was charged with ca. 130 mL of 0.3–0.4 mm Netzsch SiLi beads. Once the mill was ramped up to 4104 rpm and the heptane was circulating, ground, sieved MGS powder (ca. 20 g) was added to the slurry tank over a 5 min period, followed by more heptane (ca. 150 mL). Once all MGS was added the inline sonicator was started and continued until the end of the milling cycle. For the AA-H-1h and AA-H-2h experiment, after 1 h of milling, approximately half of the slurry material was removed from the mill by taking the outflow material till the slurry bucket was nearly empty, this produced sample AA-H-1h. An equal volume of dry, air-free heptane was added to the slurry bucket and the milling continued for an additional 1 h to make the AA-H-2h sample. The 2 h sample material was removed by taking the outflow material till the slurry bucket was nearly empty, adding dry, air-free heptane to the slurry tank, milling for 10 additional minutes, and then taking the outflow material until the slurry bucket was empty. Both of the second set of outflows were collected and treated as the 2 h sample. These two slurries (1 h and 2 h) were collected in separate flasks and dried to a powder by rotary evaporation in the glovebox. A similar procedure was followed for milling, collecting and drying samples AA-H-3h and AA-H-4h. The AA-H-5h sample was milled, collected with two flushes of dry, air-free heptane, collected and dried as a single sample. After the samples were dried to a powder they were sealed in their respective flasks, removed from the glovebox and all volatiles were removed by vacuum ($<10^{-5}$ Torr) at 20 °C for ca. 15 h.

7.6.5 Anaerobic Milling in Mesitylene with Pyrene Additive

Dry, air-free mesitylene (Alfa Aesar, 98+%) was prepared by refluxing over sodium metal for ca. 12 h, and then distilled under $N_2(g)$. Dry, air-free mesitylene was also used as the seal fluid in the Netzsch MiniCer mill. Pyrene (0.99 mmols, Alfa Aesar 98%, used as received) was mixed with ca. 460 mL of mesitylene for ca. 15 h in the glovebox. The mesitylene solution of pyrene was then added to the slurry tank following the same procedure described in the heptane milling experiments. Samples were removed following the heptane procedure as well, except with dry, air-free mesitylene to wash through the mill. Besides using a solution of pyrene in mesitylene all other milling parameters and handling procedures were the same as previously described. One batch was milled for 1 h, removed ca. half the slurry and the second portion was taken at 2 h (AA-M/P-1h and AA-M/P-2h respectively) and second batch was milled for 5 h, removed ca. half the slurry and the second portion was taken at 6 h (AA-M/P-5h and AA-M/P-6h respectively).

7.6.6 Aerobic Milling of Silicon in Heptane

The aerobic milling of silicon took place outside of the glovebox using the same Netzsch MiniCer mill. Mesitylene was used as the seal fluid to mill sample A-H/M-5.5h. Heptane was used as the seal fluid to mill sample A-H-5h. The mill was operated as previously described with the following exceptions: heptane was used as received, rotary evaporation was performed outside the glovebox, powder XRD and BET samples were prepared in air, XPS sample films were transferred to the XPS sample chamber under aerobic conditions. The A-H/M-5.5h XPS

sample film was prepared in 1,2,3-trichloropropane and the A-H-5h XPS sample film was prepared in heptane.

7.6.7 Aerobic Milling of Silicon in Mesitylene with Pyrene Additive

The aerobic milling of silicon took place outside of the glovebox using the same Netzsch MiniCer mill and produced samples A-M/P-5h and A-M/P-6h. The mill was operated as previously described with the following exceptions: mesitylene was used as received, rotary evaporation was performed outside the glovebox, powder XRD and BET samples were prepared in air, XPS sample film was prepared in 1,2,3-trichloropropane and transferred to the XPS sample chamber under aerobic conditions.

7.7 Figures

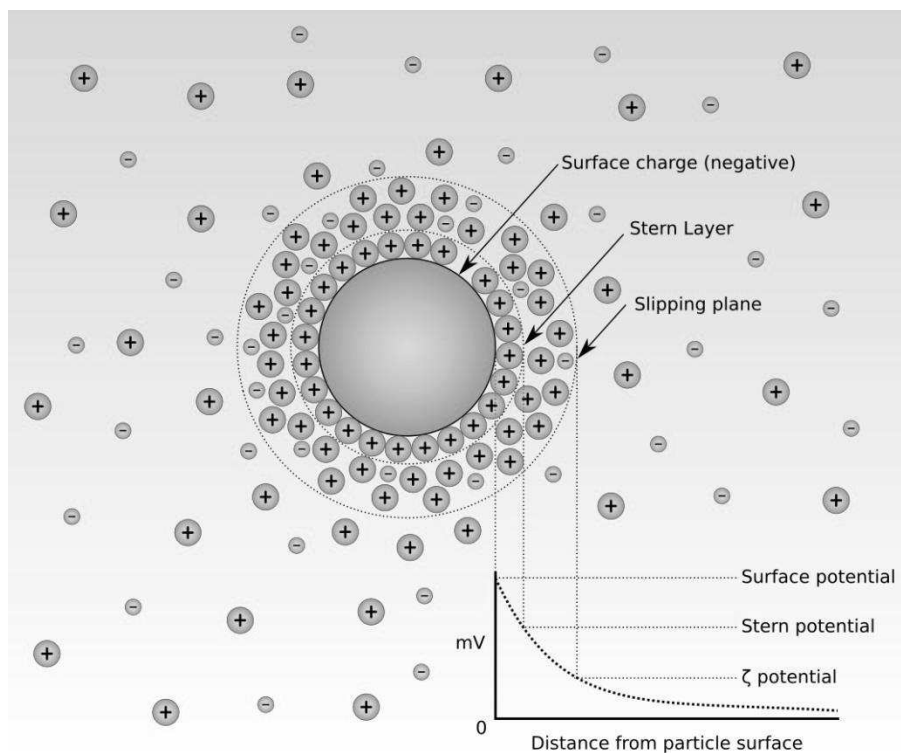


Figure 7-1. Diagram showing different regions of surface potential of a particle suspended in a solution. In this diagram the particle is negatively charged attracting positive charges to the immediate surface that slowly (if at all) exchange with the solution, this layer is known as the Stern Layer, and has a related Stern potential. Outside the Stern Layer is a more labile layer that exchanges more rapidly with the solution and has its own associated potential known as the Zeta potential (ζ – potential). The Zeta potential can be measured directly and is determined by the suspended particle (which determines the Stern layer), the solvent, any additives (buffers, surfactants, and other physiochemical interacting species) and other particles and their associated layers suspended in solution. The ζ – potential also dictates how stable a suspension is with low values of ζ indicate rapid flocculation and high values indicate a stable suspension/colloid.^{26,55}

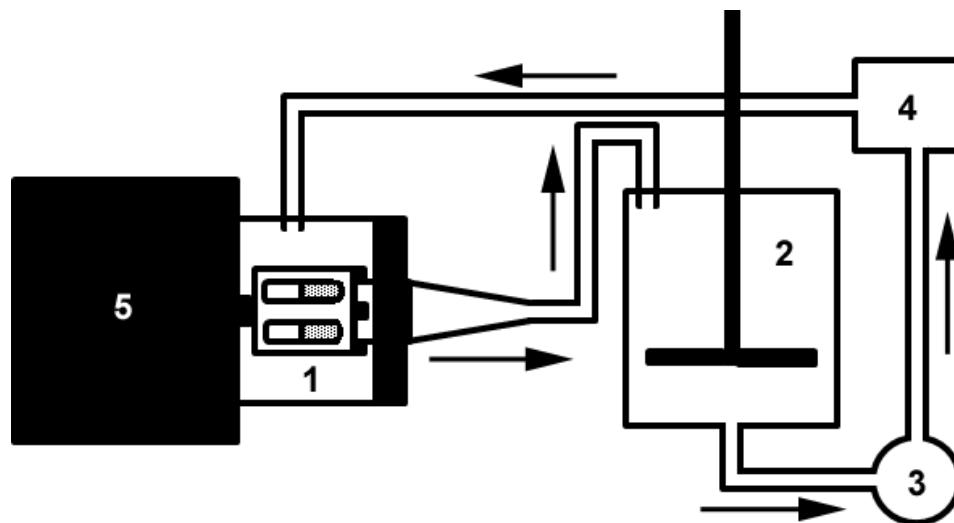


Figure 7-2. Schematic of Netzsch MiniCer Laboratory mill, arrows indicate direction of flow. (1) 160 mL water cooled milling chamber with double mechanical pressurized fluid seal, slotted cylinder mixer blade, 150 μm separator screen, (2) slurry tank with overhead mixer, samples and additives were added via slurry tank, (3) peristaltic slurry pump with 1/8" I.D. Viton® tubing, (4) low-flow sonicator cell with 1/2" diameter probe, (5) mill motor.

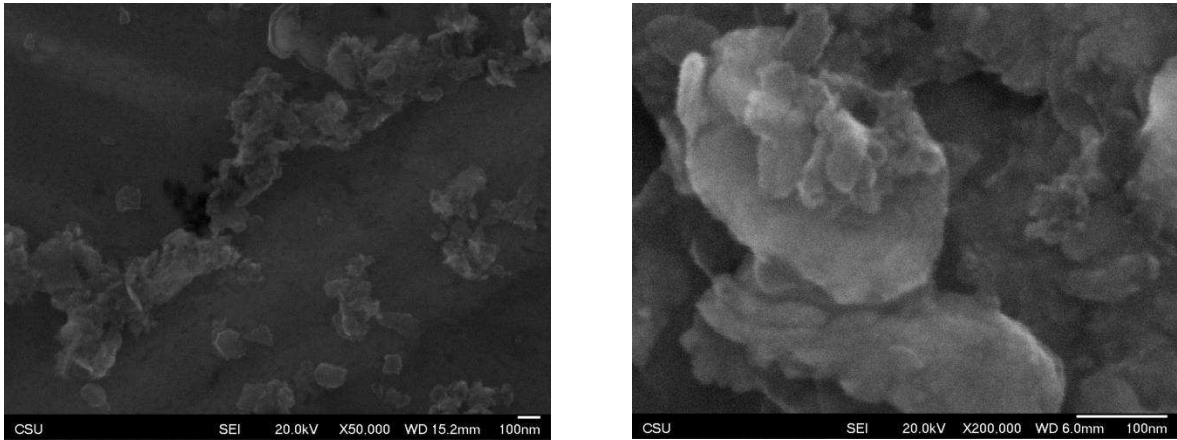


Figure 7-3. Scanning electron microscopy images of A-H/M-5.5h aerobic milled MGS particles. (Left) Image is 50,000X at 20.0 kV looking at many irregular shaped particles. Note the large distribution of sizes and that most particles appear to have flat jagged surfaces. (Right) Image 200,000X at 20 kV, many small particles adhered to the surface of a larger particle form a larger agglomerate particle. These SEM images illustrate the morphology and broad particle size range of the MGS after milling.

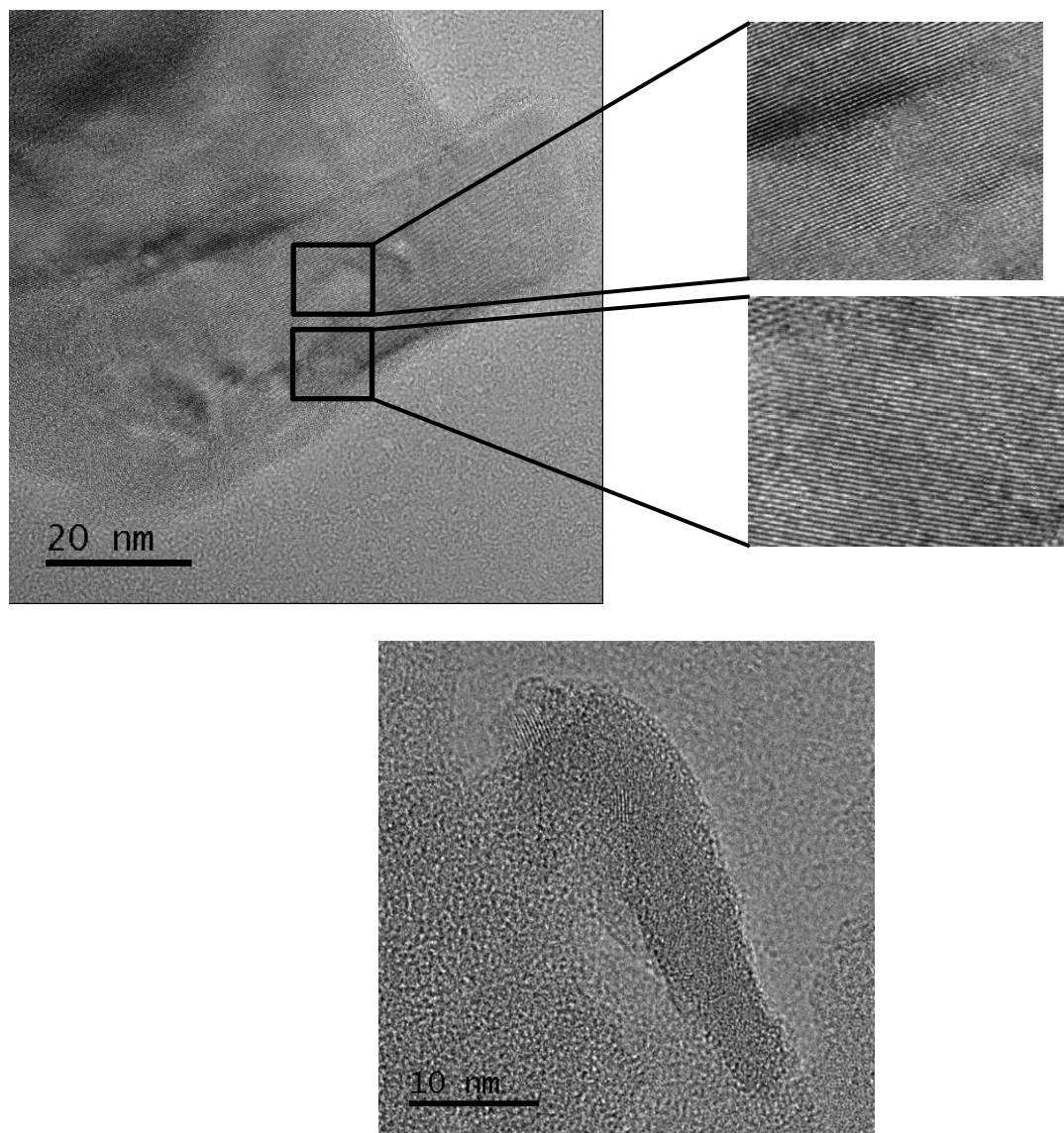


Figure 7-4. Transmission electron microscopy images of A-H/M-5.5h aerobically milled MGS. (Top) Multiple crystalline regions in multiple orientations in the same particle due to the milling process. Between these two regions is an area that is random and amorphous. These are multiple crystalline regions created/combined by the milling process with amorphous regions in-between the crystalline regions. (Bottom) Another example that the sample is mostly amorphous with very small but identifiable Si crystallites imbedded in a continuous amorphous particle. Two crystallites were measured indicated by black lines, the top having a length of 3.1 nm and the bottom a length of 1.9 nm in the long dimension perpendicular to the image.

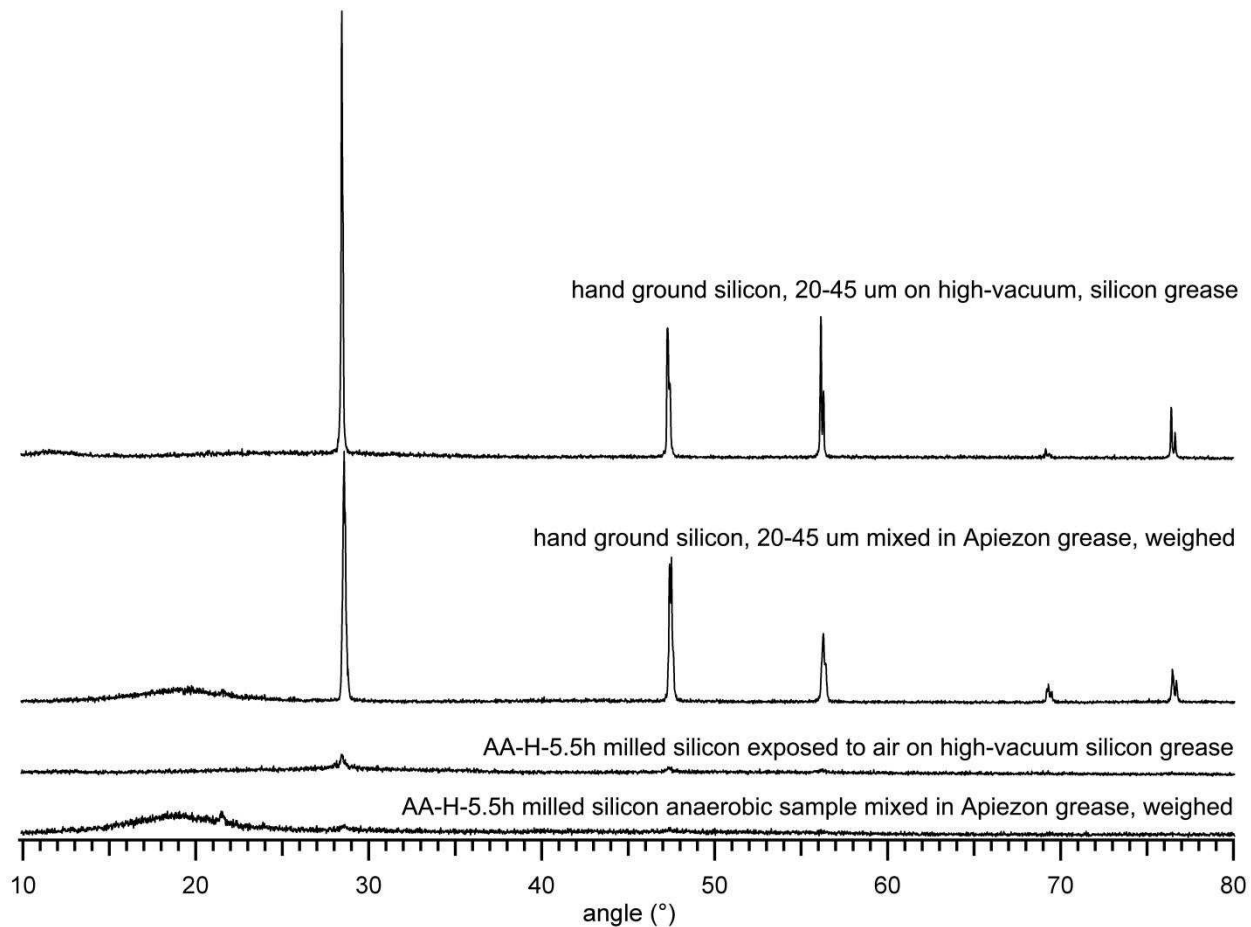


Figure 7-5. Comparison of two silicon powder samples analyzed by powder XRD to determine the effect of preparing the sample as a paste intimately mixed with Apiezon Type N grease. Hand ground metallurgical silicon ranging in size from 20–45 μm , and AA-H-5.5h dispersed onto a thin film of high-vacuum grease spread on a glass microscope slide compared to the same materials mixed with Apiezon Type N grease forming a homogenous paste and spread onto a glass microscope slide. The samples in Apiezon grease were weighed as well as the quantity of Apiezon grease, (the hand ground sample was mixed with Apiezon grease but not treated anaerobically). Notice the decrease in peak heights and broadening of peak widths for both the hand ground and AA-H-5.5h when mixed with Apiezon grease. While some signal attenuation was observed, this was acceptable to determine relative crystallinity of these samples while keeping the sample anaerobic during the XRD experiment.

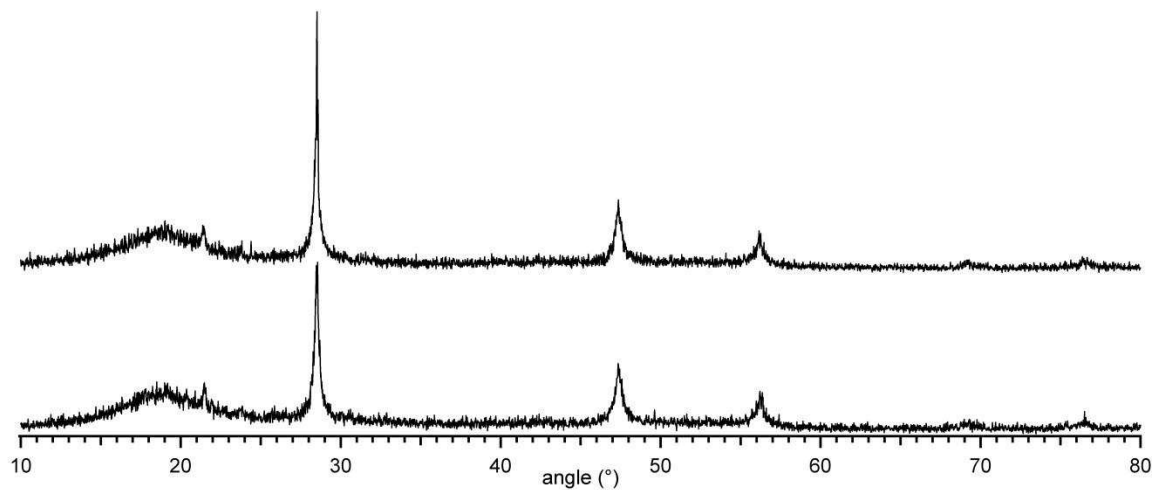


Figure 7-6. Powder XRD pattern of AA-H-1h in Apiezon Type N grease, the bottom pattern is after milling and drying the sample, the top pattern is the exact same powder XRD sample after 52 days, the sample was left intact, on the slide, in open air during those 52 days.

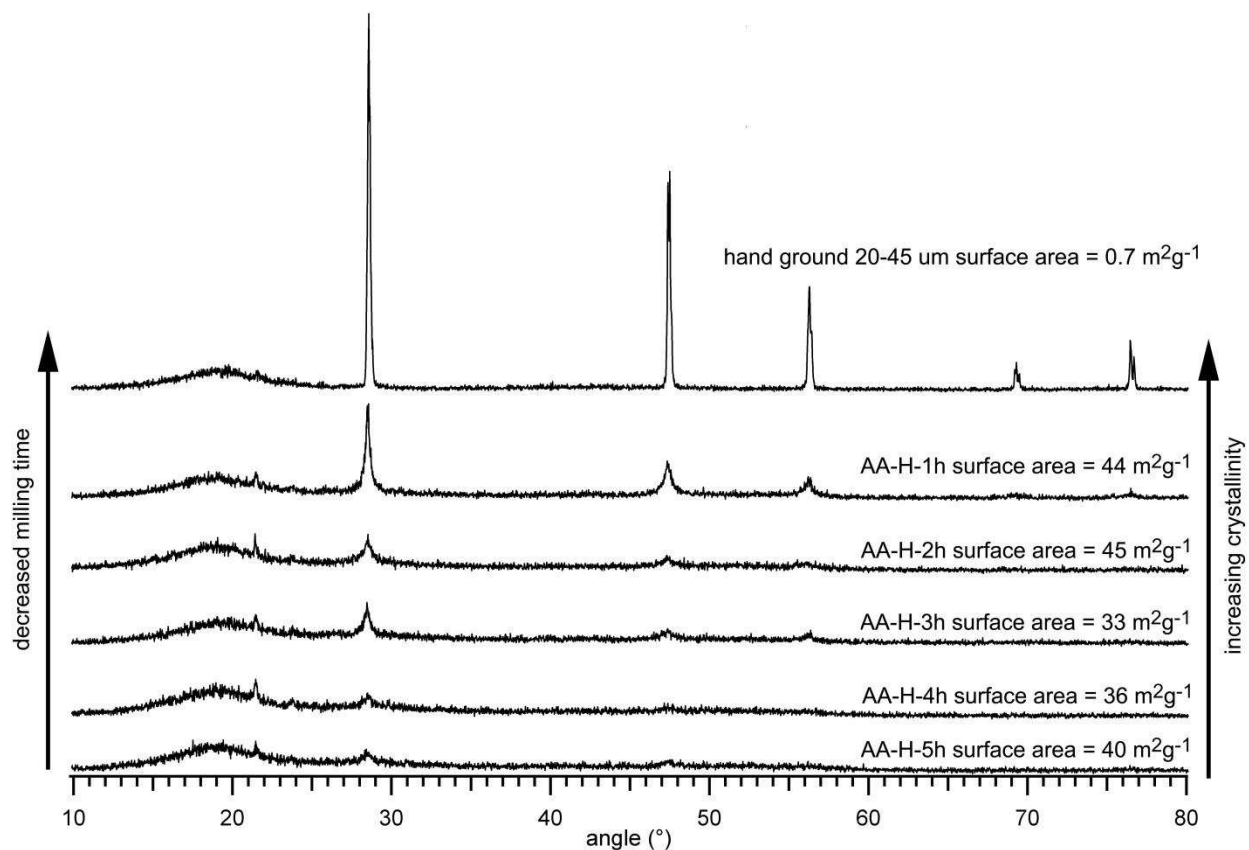


Figure 7-7. Anaerobic powder XRD of AA-H-1–5h compared to hand ground silicon powder ranging in particle size from 20–45 μm . The 1–5 h milled samples were milled anaerobically and treated rigorously anaerobic. The hand ground sample of metallurgical silicon was prepared by mixing in Apeizon Type N grease, same as the other 5 samples, but was not treated anaerobically. Note the similar surface areas for all 5 samples. Also note the decrease in crystallinity with increased milling time.

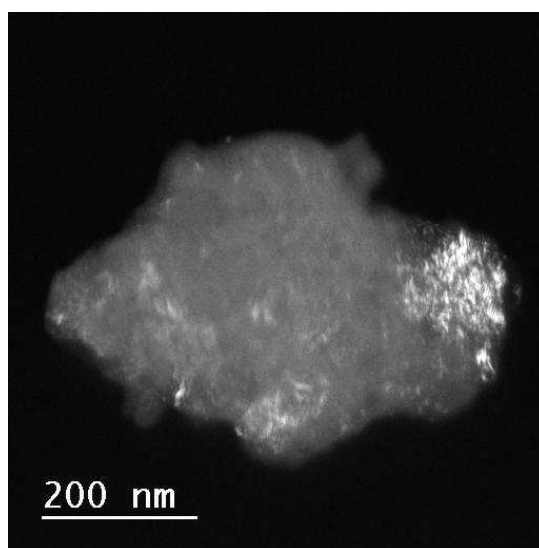
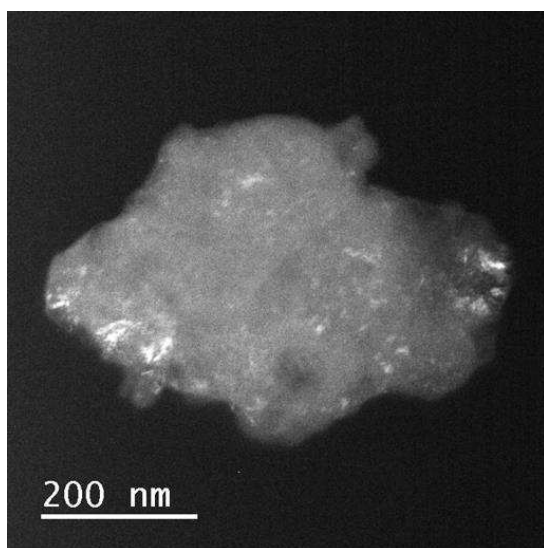
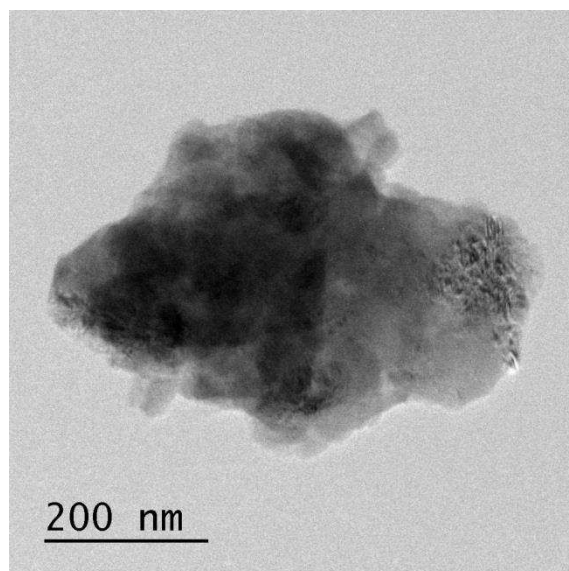


Figure 7-8. Transmission electron microscopy images of AA-H-1h. (Top) Original TEM image of agglomerate particle. (Bottom Left) TEM Darkfield view of the same particle with the beam at a random orientation. (Bottom Right) TEM Darkfield view of the same particle with the beam at a random 90° relative to the previous orientation highlighting the crystalline regions of the particle. The scale bar for the darkfield images is the same as for the normal view image. Note the crystalline regions that are on the order of 10–50 nm in length.

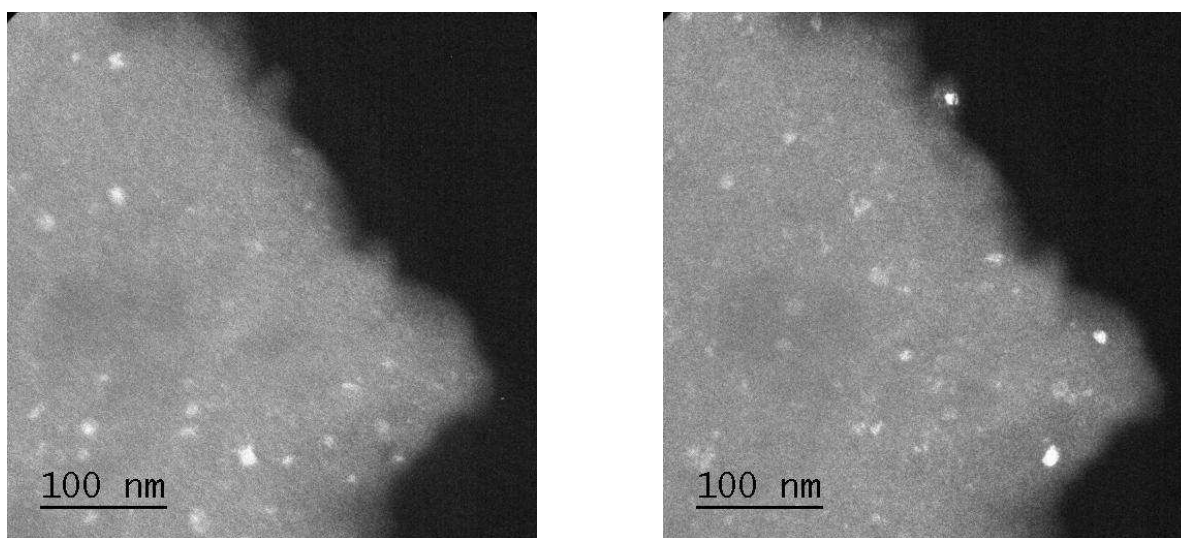


Figure 7-9. Transmission electron microscopy images of AA-H-5h. (Left) TEM Darkfield view of a particle showing the crystalline regions, and the size of the crystallites. (Right) TEM darkfield image of the same particle rotated 90° relative to the previous image highlighting the crystalline regions of the particle. Note the crystalline regions (some that only show up in the 0° orientation and some that only show up in the 90° orientation) are on the order of 5–12 nm in length.

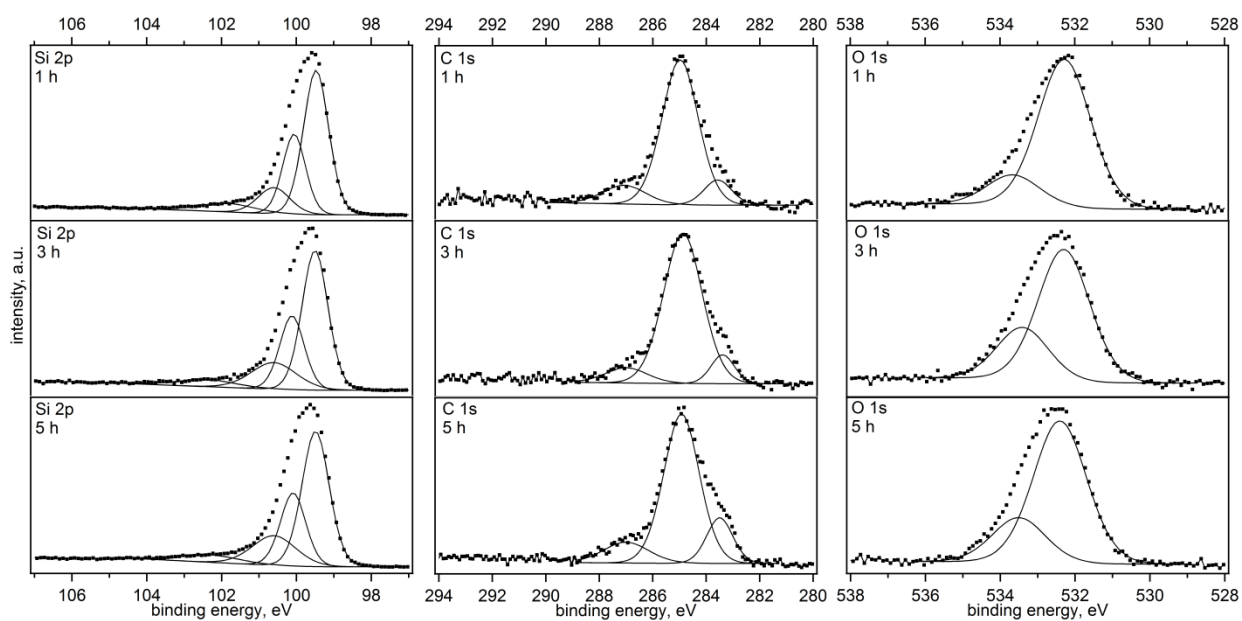


Figure 7-10. X-ray photoelectron spectroscopy of A-H-1h, top, A-H-3h, middle, and A-H-5h, bottom. Few changes are observed in the XPS spectra of samples milled anaerobically in heptane for varying amounts of time. This indicates that there is little change in the surface chemistry after the first hour of milling anaerobically in heptane.

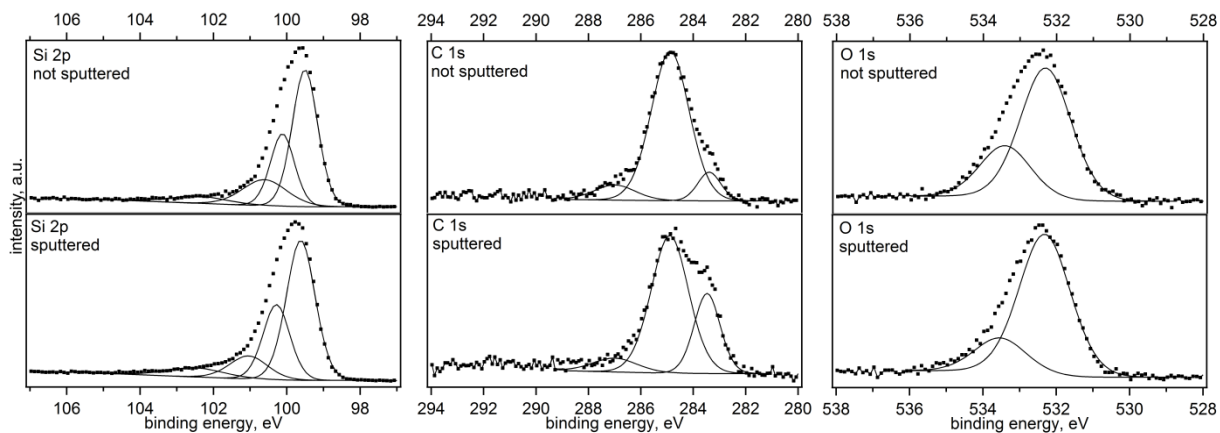


Figure 7-11. X-ray photoelectron spectroscopy of A-H-3h as made top, and sputtered, bottom. The Si-C peak is more pronounced in the C 1s spectrum after sputtering removed surface hydrocarbon contamination. Little change is observed in the other elements.

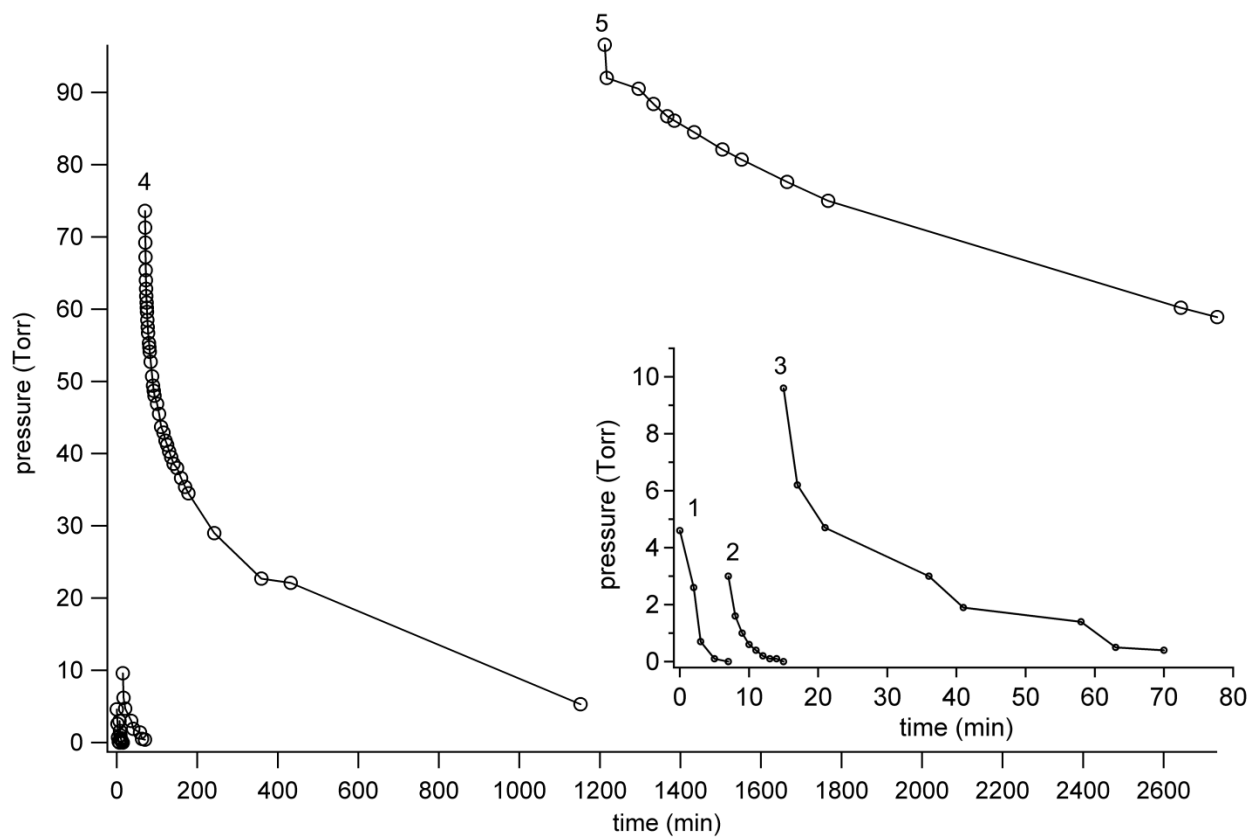


Figure 7-12. Post treatment of AA-H/M-5.5h with O₂. Rate of O₂(g) uptake of 5 doses of O₂(g) on a single sample (0.237 g) of AA-H/M-5.5h, order of doses indicated 1–5. The rate of uptake for each dose was graphed following one another. The expanded inset shows the first 3 doses and the rate of uptake over time for clarity.

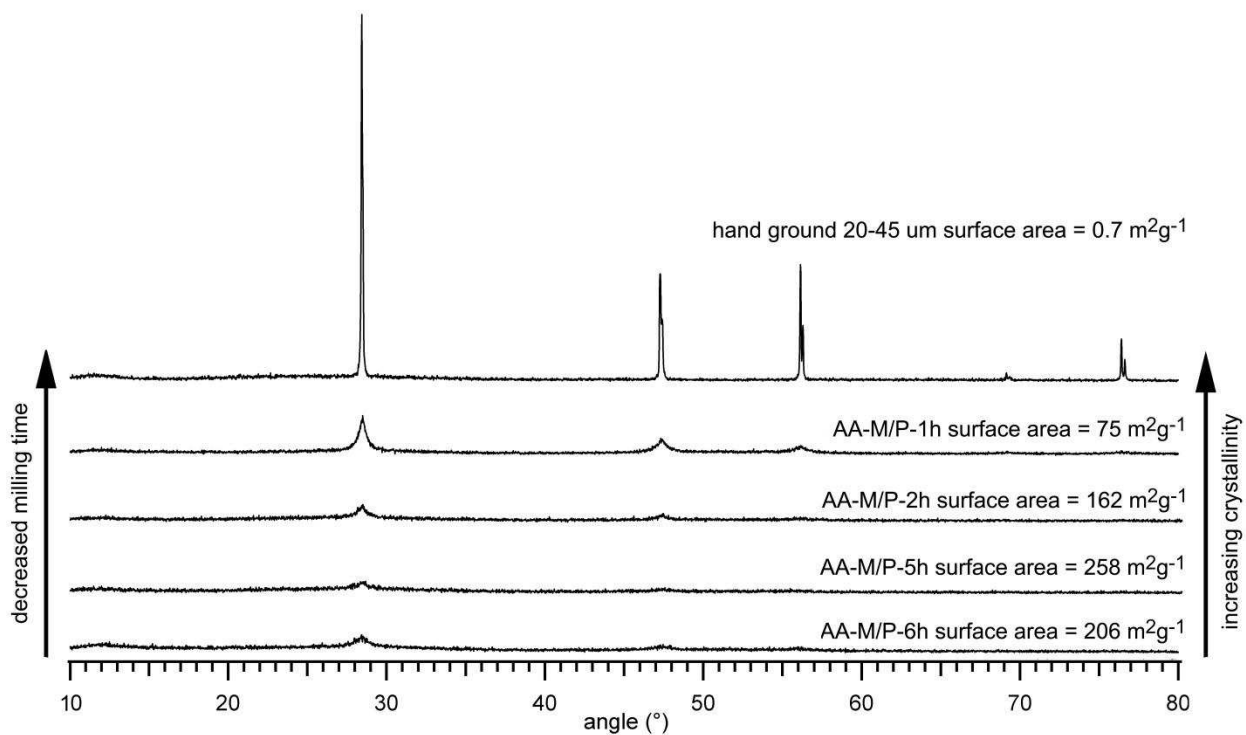


Figure 7-13. Anaerobic powder XRD of metallurgical silicon milled in dry, air-free mesitylene with pyrene additive for 1, 2, 5, and 6 h compared to hand ground silicon powder ranging in particle size from 20–45 μm . Note these XRD samples were prepared by dispersion on high-vacuum silicon grease on a glass slide under aerobic conditions. The samples did discolor upon exposure to air, but no change was observed in the XRD pattern.

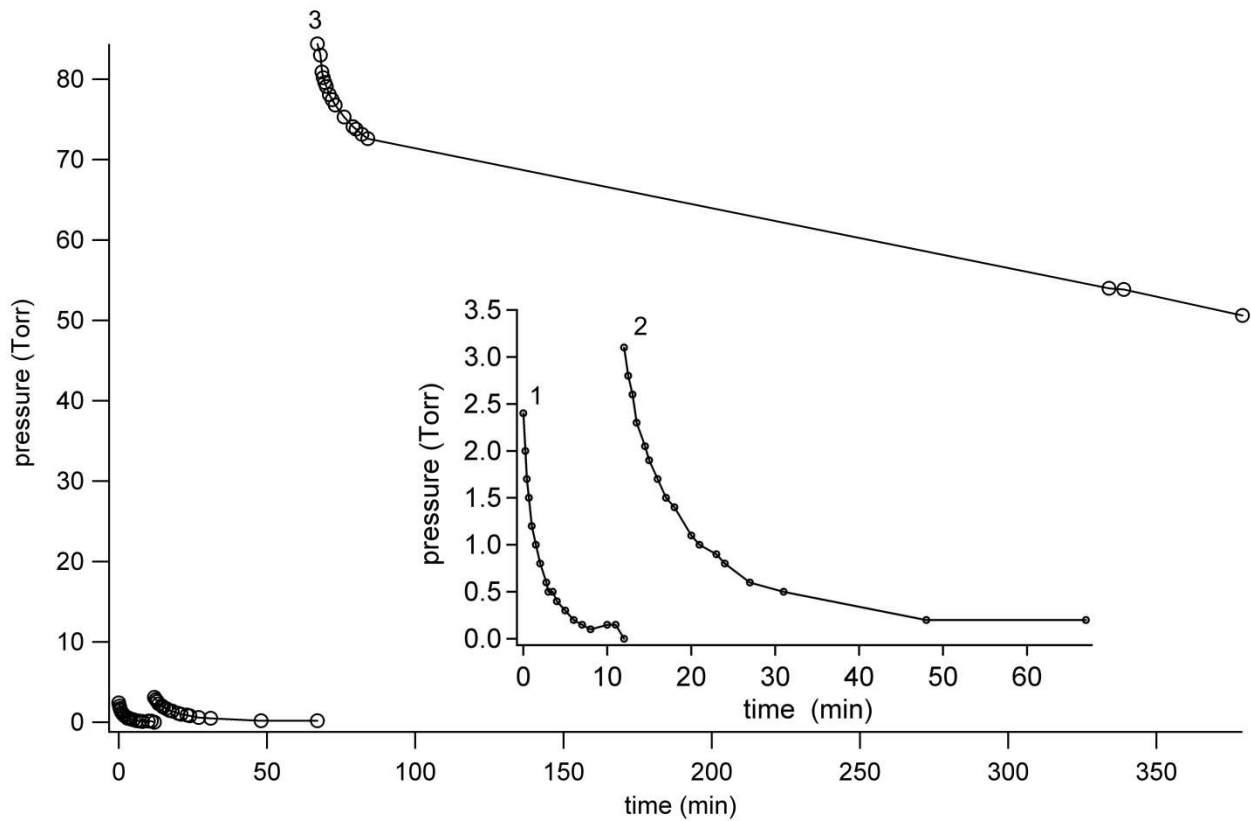


Figure 7-14. Post treatment of AA-M/P-5h with $O_2(g)$. Rate of $O_2(g)$ uptake of 3 doses of $O_2(g)$ on a single sample (0.235 g) of AA-M/P-5h, order of doses indicated 1–3. The rate of uptake for each dose was graphed following one another. The expanded inset shows the first 2 doses and the rate of uptake over time for clarity.

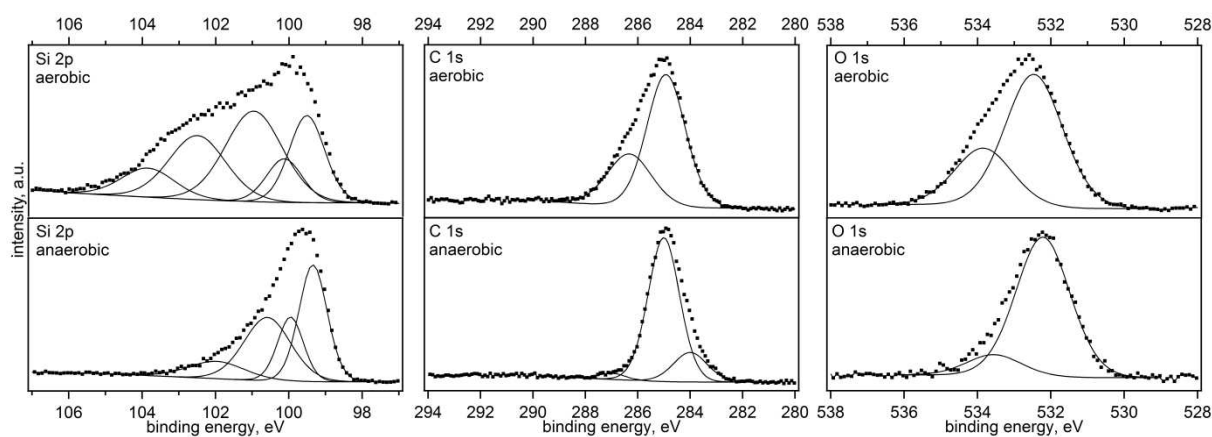


Figure 7-15. X-ray photoelectron spectroscopy of A-M/P-5h, top, and AA-M/P-5h, bottom. The aerobic sample contains SiO_2 (ca. 103.5 eV) that is not present in the anaerobic sample. The aerobic sample also had more silicon suboxide species (ca. 102 eV in Si 2p and ca. 533.5 eV in O 1s) than the anaerobic sample. For A-M/P-5h the Si-C peak in the C 1s spectrum is likely contained within the broader C-C/C-H peak.

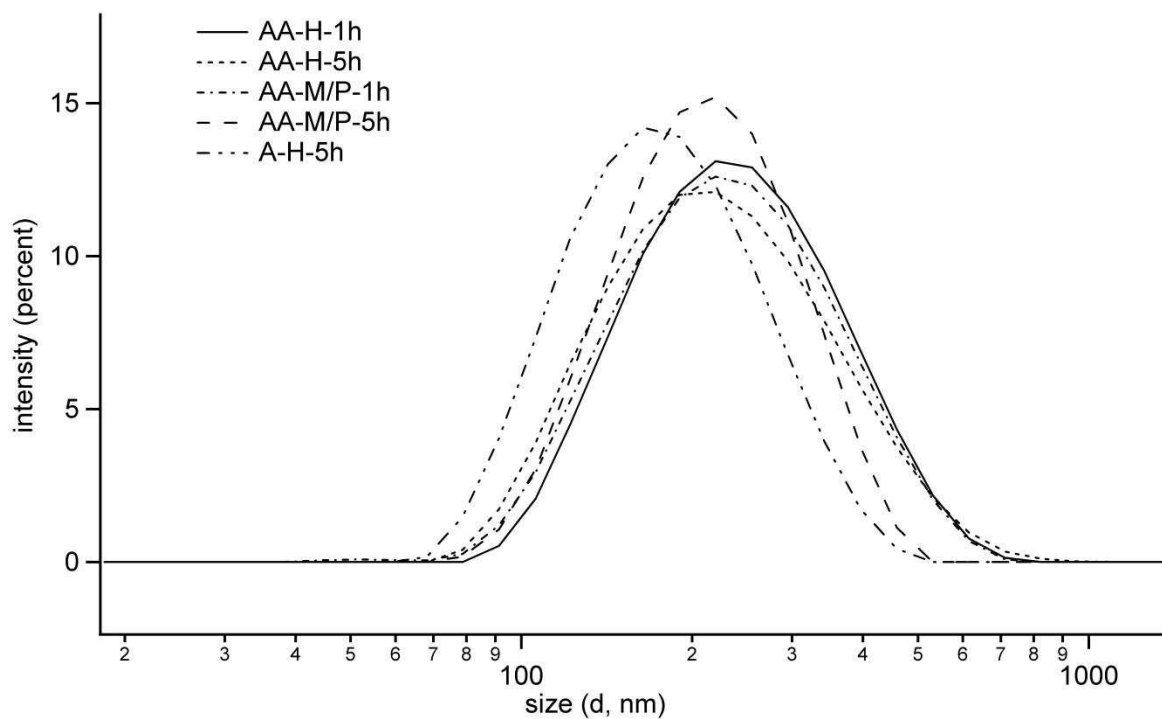


Figure 7-16. Dynamic light scattering analysis of 5 samples AA-H-1h, AA-H-5h, AA-M/P-1h, AA-M/P-5h, and A-H-5h dispersed in absolute ethanol. Displayed graphs are the average of 3 measurements where each measurement consists of 12–15 runs each. Samples were hand ground to break up clumps, and then dispersed in absolute ethanol with a bath sonicator for 10–15 min per sample. The DLS measurement was performed at 25 °C after 2 min equilibration at 25 °C for each sample. All samples had similar particle size and particle size distributions.

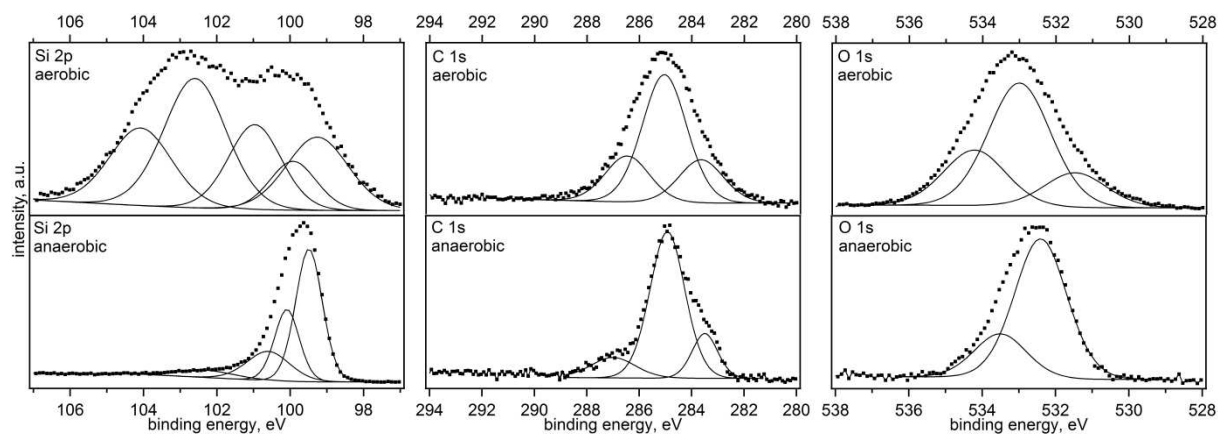


Figure 7-17. X-ray photoelectron spectroscopy of A-H-5h, top, and AA-H-5h, bottom. The aerobic sample contains SiO₂ (ca. 103.5 eV) which is not present in the anaerobic sample. The amounts of silicon suboxide species (ca. 102 eV) are also higher in the aerobic than the anaerobic. The Si–C shoulder (ca. 283.5 eV) is more evident in the anaerobic sample.

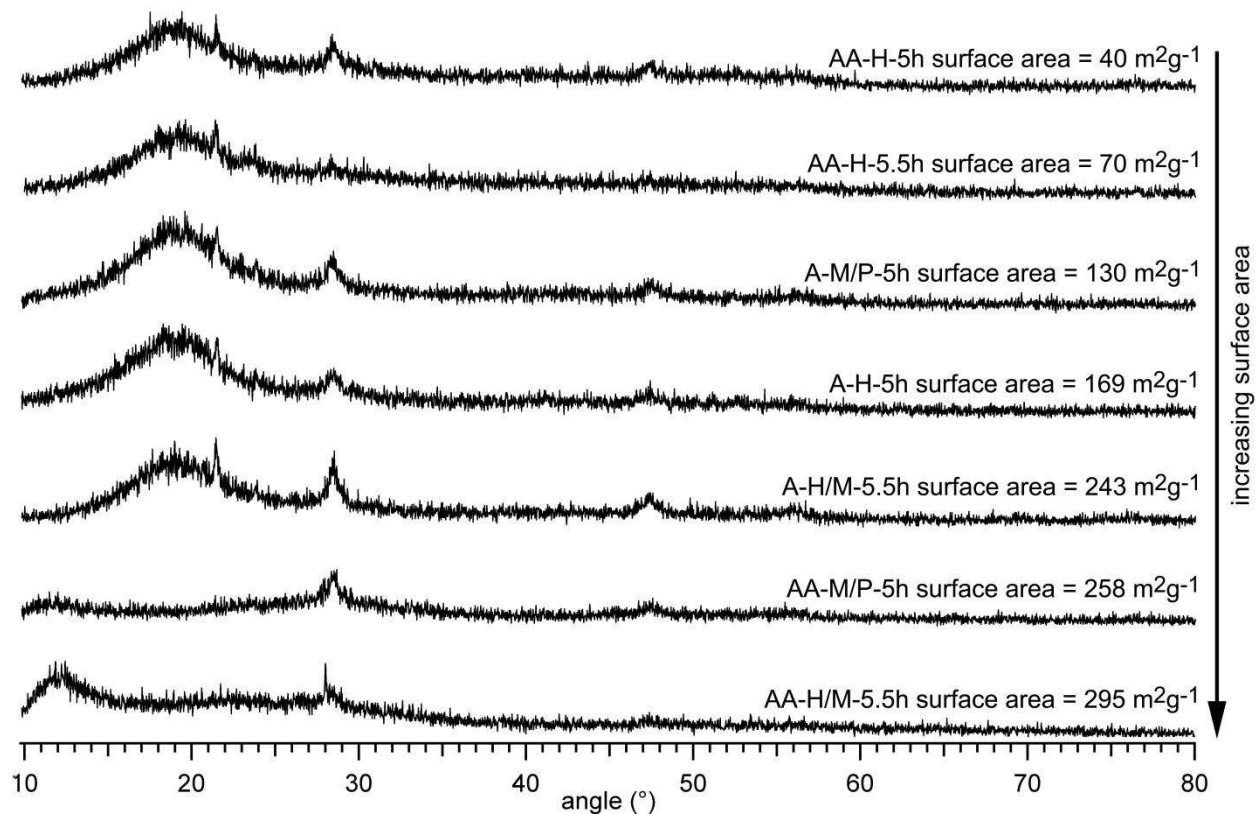
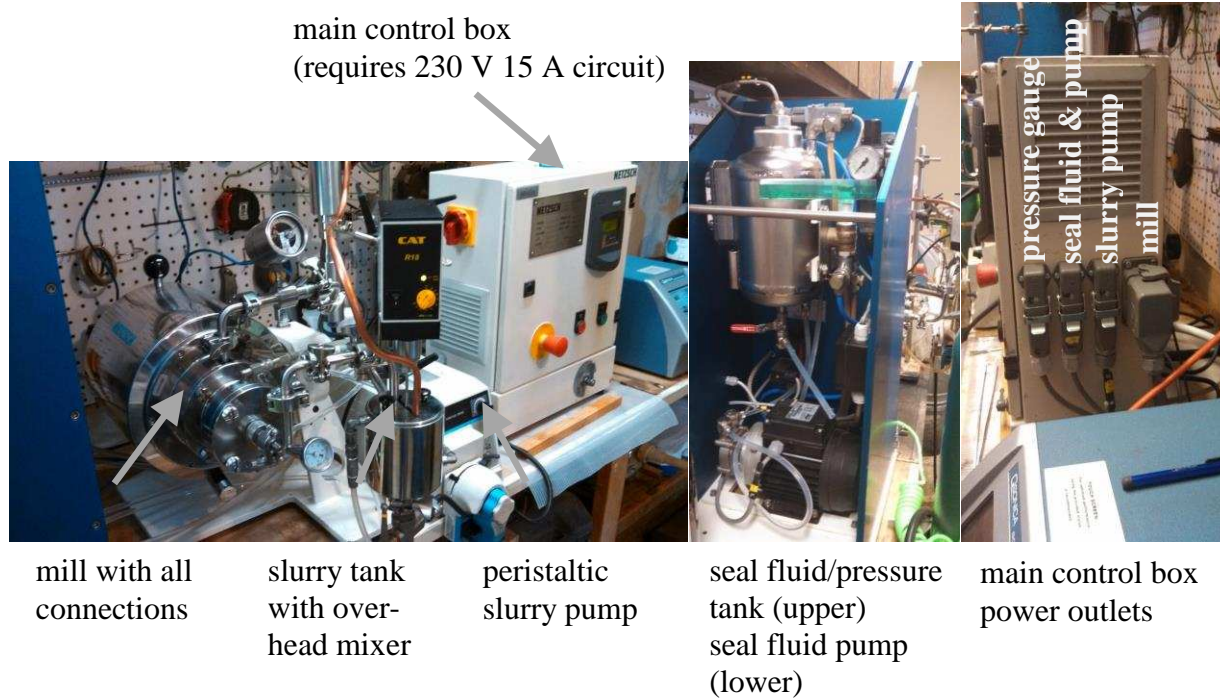


Figure 7-18. Anaerobic powder XRD of metallurgical silicon milled in dry, air-free heptane for 5–5.5 h. The AA-H/M-5.5h and AA-M/P-5h samples were exposed to air and spread on a thin film of high-vacuum grease; all other samples were mixed in Apiezon grease. Samples AA-H-5h, AA-H-5.5h, and A-M/P-5h were treated rigorously anaerobic.



Figure 7-19. The double-wide, double-deep Vacuum Atmospheres HE-453-4 glovebox housed in Prof. Strauss' lab before the modifications preparing it for the Netzsch mill.



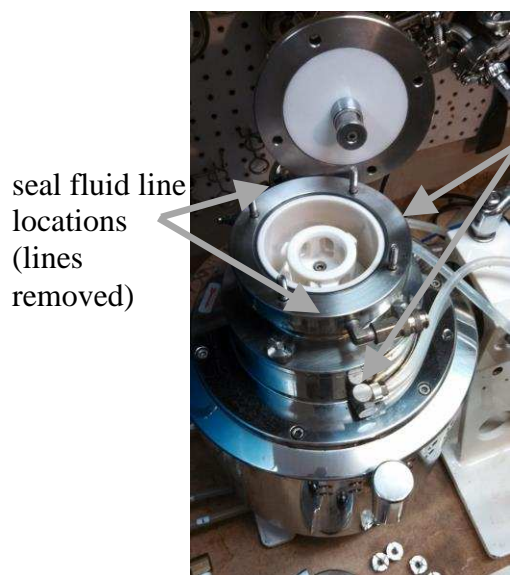
mill with all connections

slurry tank with overhead mixer

peristaltic slurry pump

seal fluid/pressure tank (upper)
seal fluid pump (lower)

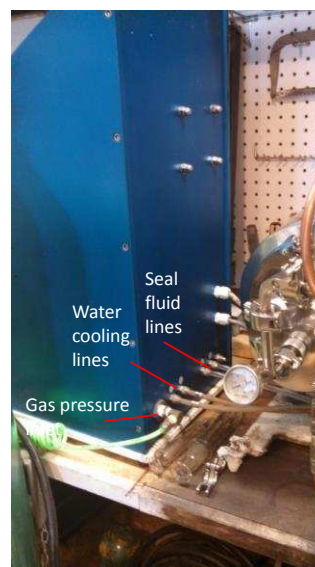
main control box power outlets



seal fluid line locations (lines removed)

cooling water lines

mill tipped up with face removed (how milling media is added to mill)



connection on back of seal fluid tank/pump unit

Figure 7-20. Components and required connections of the Netzsch Minicer mill.

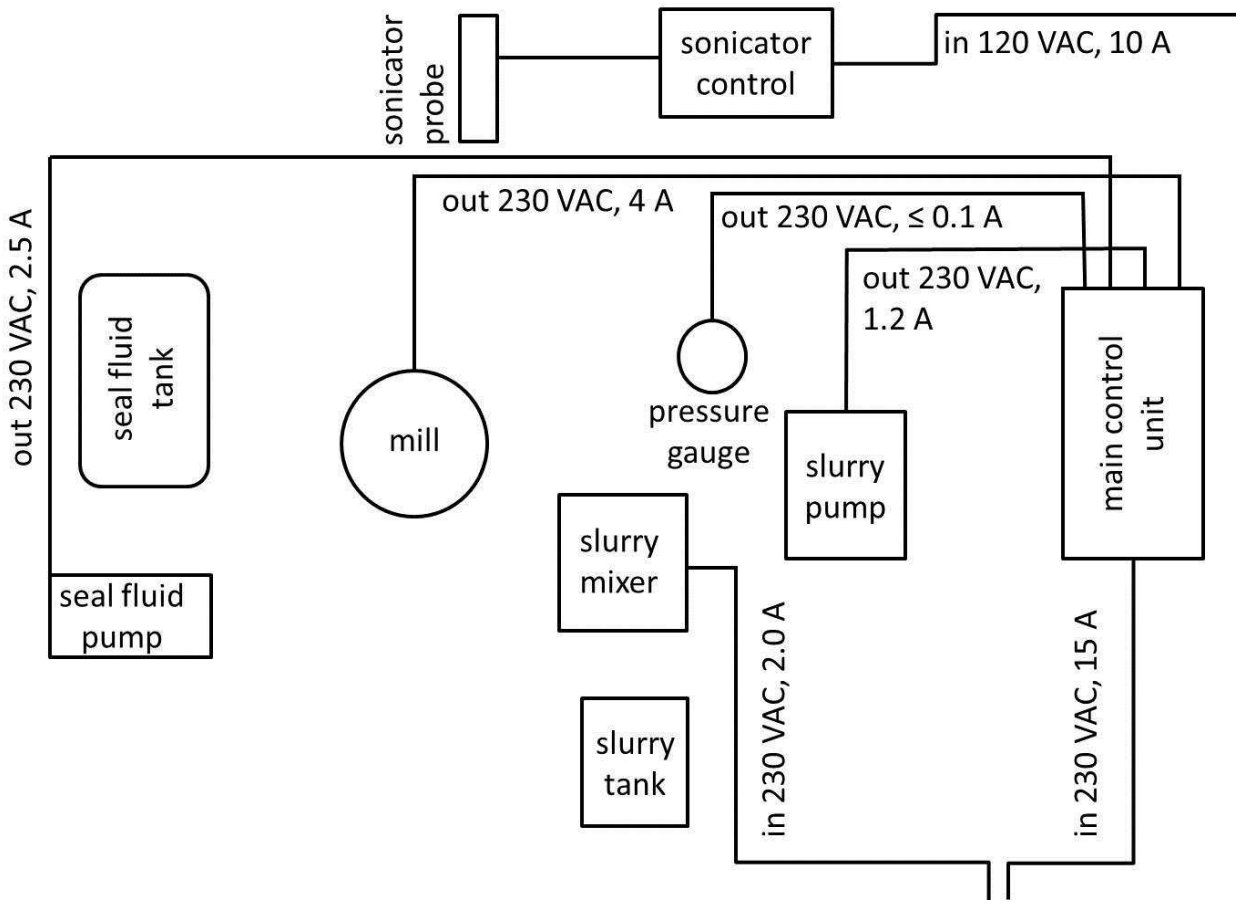


Figure 7-21. Original electrical connection diagram showing electrical connections between components of Netzsch Minicer mill.

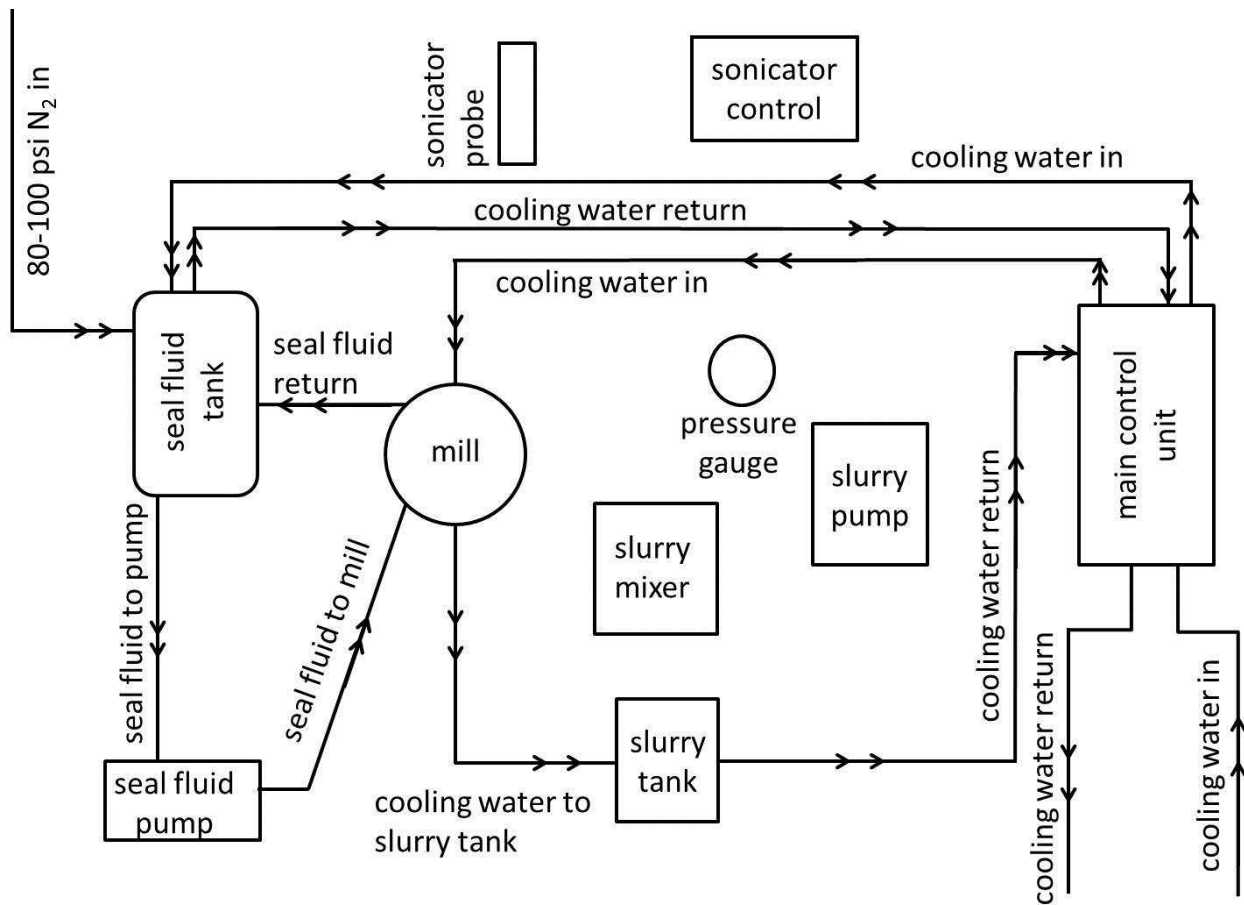


Figure 7-22. Original cooling water, seal fluid, and inert gas connection diagram showing requirements and connections between components of Netzsch Minicer mill.

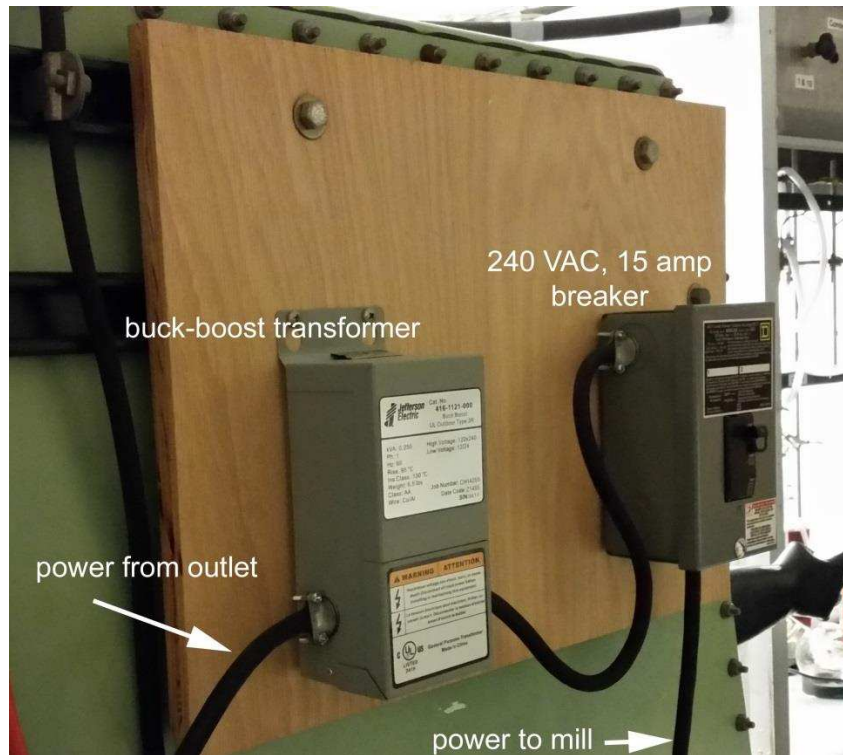
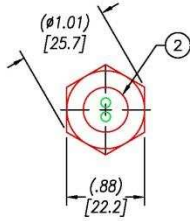


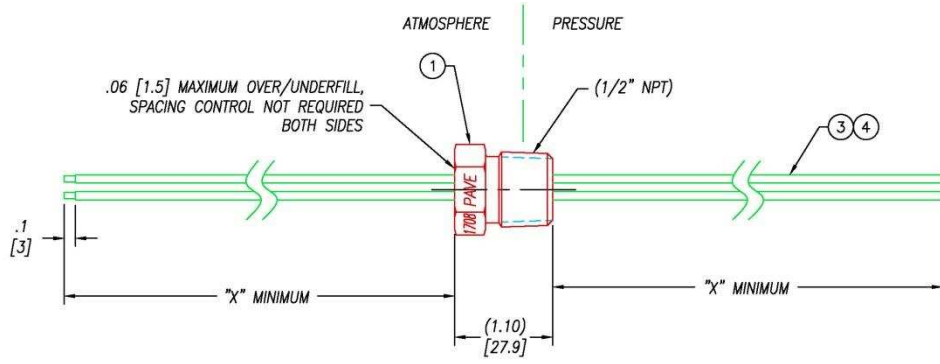
Figure 7-23. The Jefferson 0.25 kVA buck-boost transformer and the 15 A circuit breaker top, and a multimeter showing that the voltage by the transformer is ca. 230 V, bottom. The power cord exiting the circuit breaker (not shown) was wired into a junction box attached to the AI roof panel of the GB (Figure 7-25).

| PAVE# | "X" | "Y" |
|--------|----------|-----|
| 1708 | 10 [254] | 1 |
| 1708-1 | 24 [610] | 2 |



NOTES:

1. LEAK TEST: 80 PSI, NO BUBBLES "Y" MINUTES MINIMUM.
2. HYPOT 630 VDC 500 MD 0.01 SEC MINIMUM, WIRE TO WIRE & HOUSING.
3. ALL TESTS ARE PERFORMED AT ROOM TEMPERATURE.
4. ALL PARTS MUST PASS ALL TESTS.
5. WIRES ARE NOT REQUIRED TO BEND SHARPLY AT EPOXY SEAL SURFACE.
6. NO VOIDS LARGER THAN $\phi 0.035$ [0.89] ARE ACCEPTABLE.
7. REF-OPERATING TEMPERATURE RANGE -20°C TO 125°C .
8. DIMENSIONS ARE INCHES [millimeters].
9. PAVE-SEAL CAN BE A BI-DIRECTIONAL HERMETIC SEAL FOR VACUUM AND MOST PRESSURES. FOR PRESSURES ABOVE 150 PSI (10 BAR), CHECK WITH SALES ENGINEERING.



| 4 | 1 | EE14 YELLOW | WIRE 14EE MIL-W-16878/5 19/#27 .017 |
|------|-----|---------------|-------------------------------------|
| 3 | 1 | EE14 BLACK | WIRE 14EE MIL-W-16878/5 19/#27 .017 |
| 2 | A/R | PAVE-Seal 150 | EPOXY BLACK |
| 1 | 1 | 0346 | HOUSING PT8-SS |
| ITEM | QTY | PART# | DESCRIPTION |

ALL DIMENSIONS AND TOLERANCES APPLY TO FINISHED PART IN INCHES
 ALLOWABLE TOLERANCES UNLESS SPECIFIED OTHERWISE: NONE +/-0.5
 .X DECIMAL +/- 0.1 .XX DECIMAL +/- 0.02 .XXX DECIMAL +/-0.005
 ANGLES +/- 1 DEG SURFACE FINISH 128 microinch RMS

| | | |
|---|------------|---|
| | | 2701 Thunderbolt Court Dayton, Ohio 45414-3645 U.S.A. (937) 285-1100 Fax (937) 690-5185 www.pave-technology.com |
| DESCRIPTION PAVE-Seal® Cable Harnesses PT8-SS-150-2-TEE14-X-X | | |
| PART NUMBER | *SEE TABLE | REVISION |
| 1708* | | A |
| PROJECTION | | |

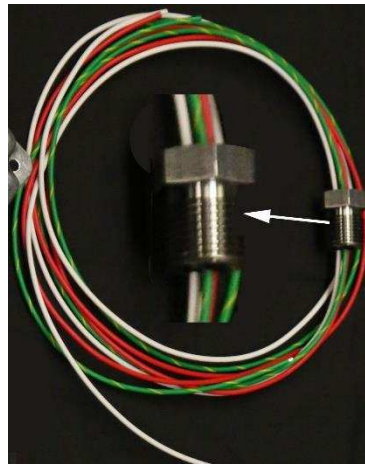


Figure 7-24. Specifications for the Pave Technology electrical bulkhead connector, top. Actual 3 wire bulkhead connector from Pave Technology, bottom.

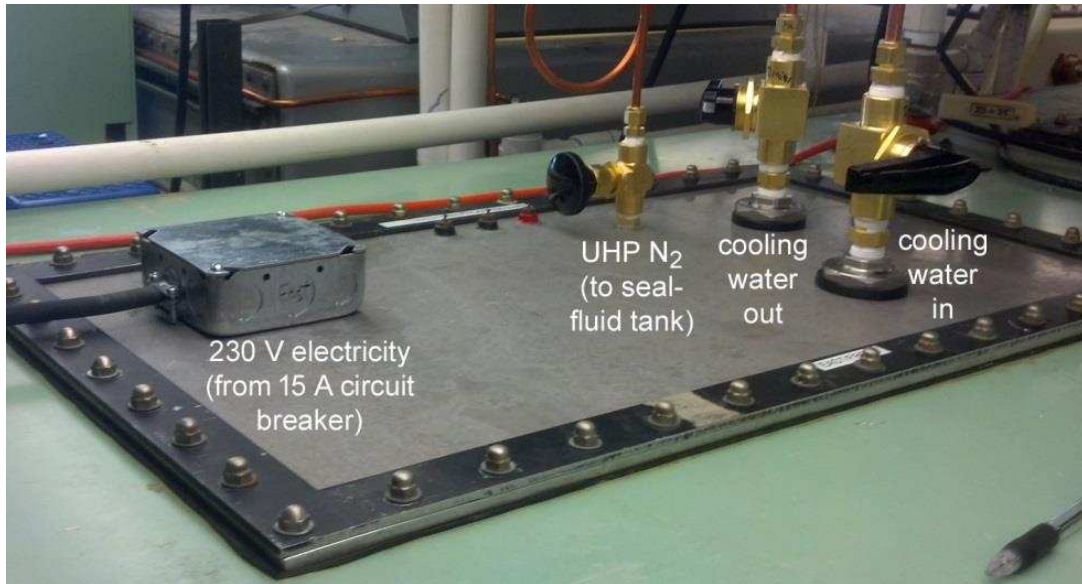


Figure 7-25. The final version of the Al roof panel for the GB. The electrical connector was wired directly inside the junction box on the roof panel. The power cord shown on the left side of the junction box was connected to the 15 A circuit breaker shown in Figure 7-23. Inside the GB was a similar metal box mounted to the Al panel but with a NEMA L6-20 receptacle shown in 7-26.

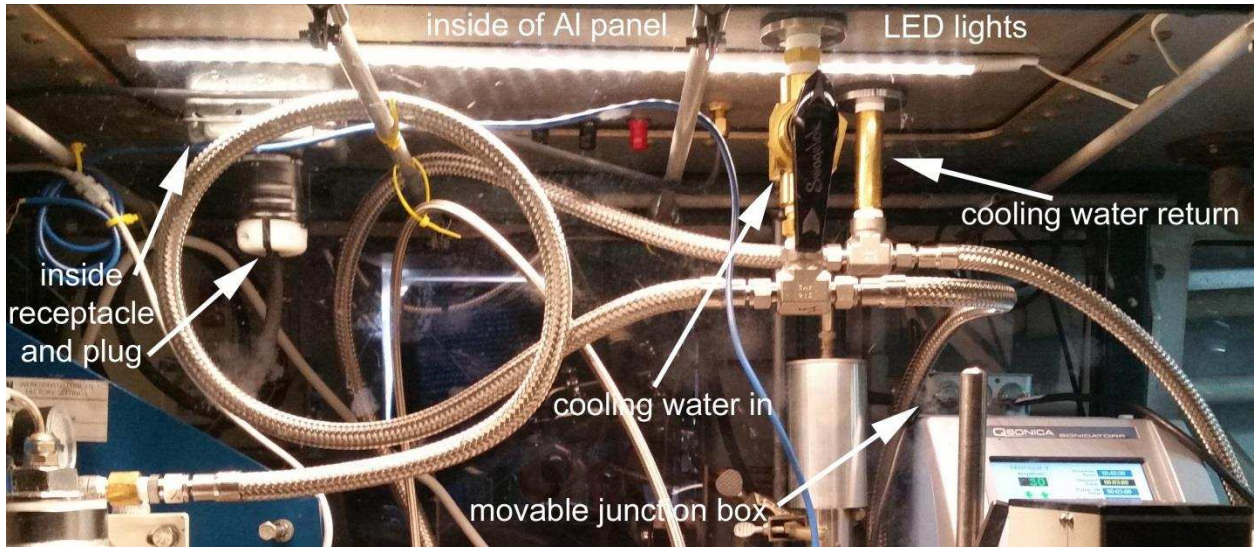


Figure 7-26. The receptacle and plug for the main power mounted inside of the Al roof panel.

remote on/off switch for
sonicator control box



Figure 7-27. The Netzsch main electronic control unit both outside, left, and inside, middle, and right. In the left photograph the four 230 V power cords exiting the unit can be seen.

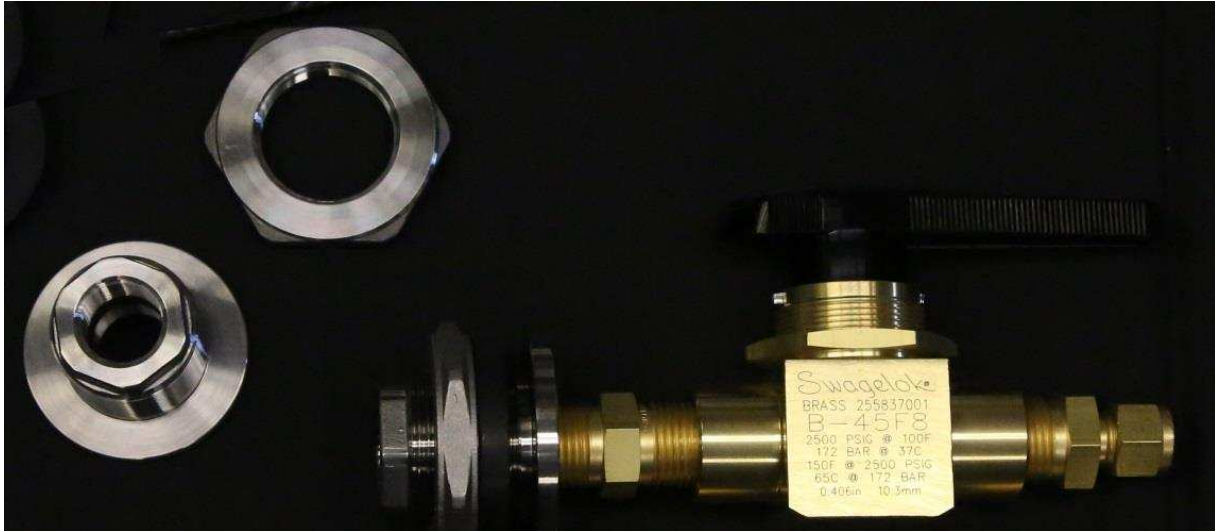


Figure 7-28. ALSCO ½" NPT stainless steel bulkhead connectors and a Swagelok brass B-45F8 ball valve shown with (i) a short ½" NPT brass nipple connecting the valve to an ALSCO bulkhead adaptor and (ii) a Swagelok ½" NPT-to-⅜" tube adaptor. The ¼" thick Teflon® gaskets used to seal the bulkhead connectors to both sides of the Al roof panel, and which were purchased from American Seal and Packing, are not shown.

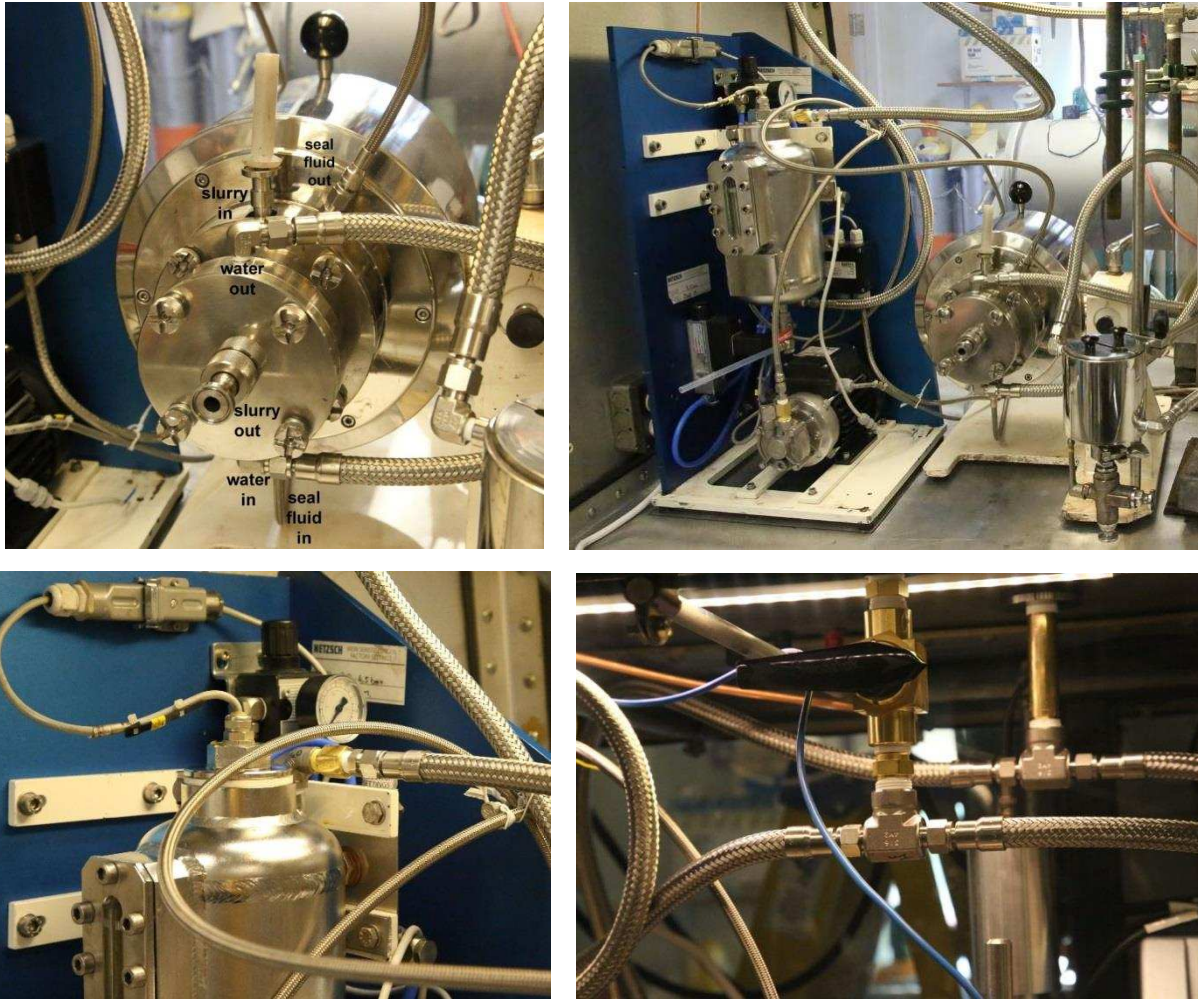


Figure 7-29. The Netzsch mill and seal-fluid unit with stainless steel braided flexible hose for cooling water and seal-fluid circulation installed.

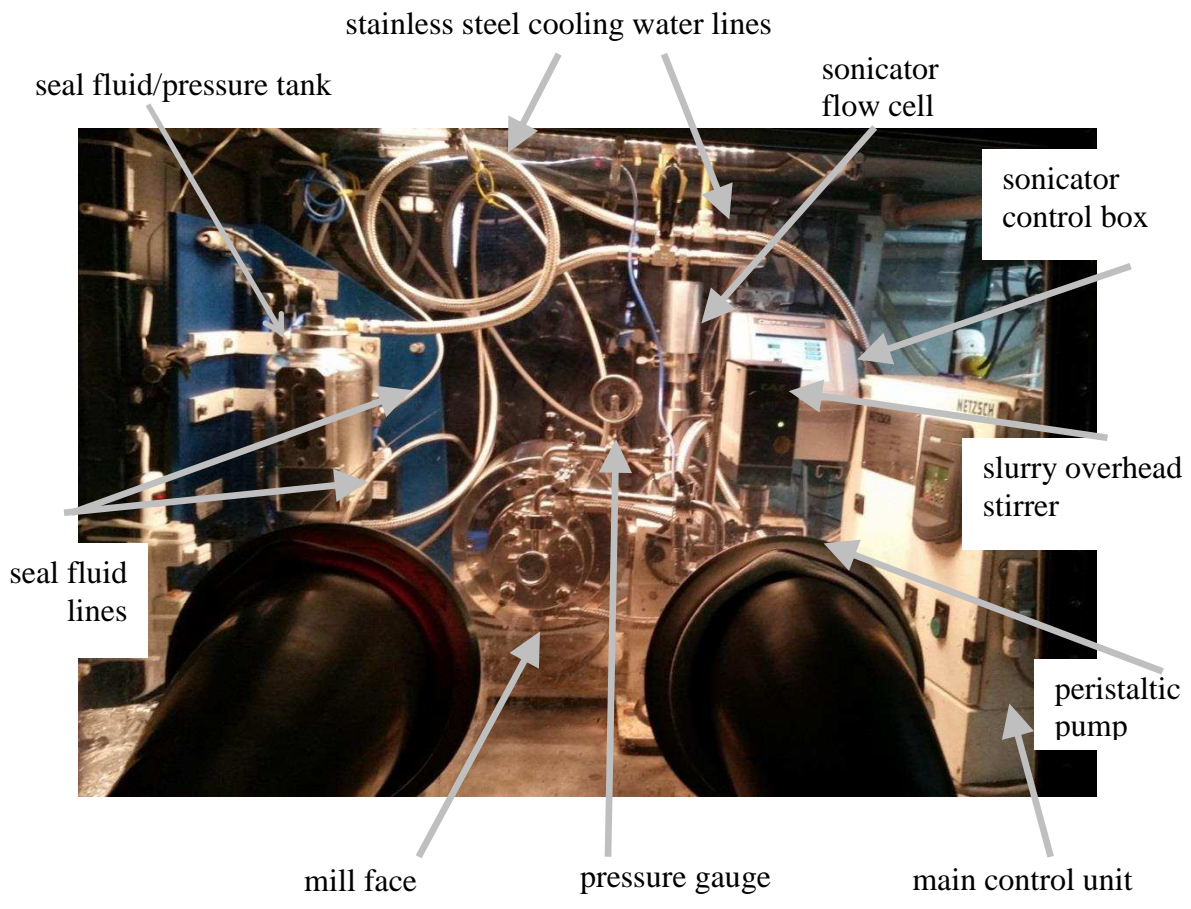


Figure 7-30. Final mill and axillary parts in glovebox with water cooling, seal fluid, and inert gas lines hooked up. Note, LED lighting had to be added inside the box to compensate for replacing the Lexan top panel with an aluminum panel that made the glovebox interior unacceptably dark.

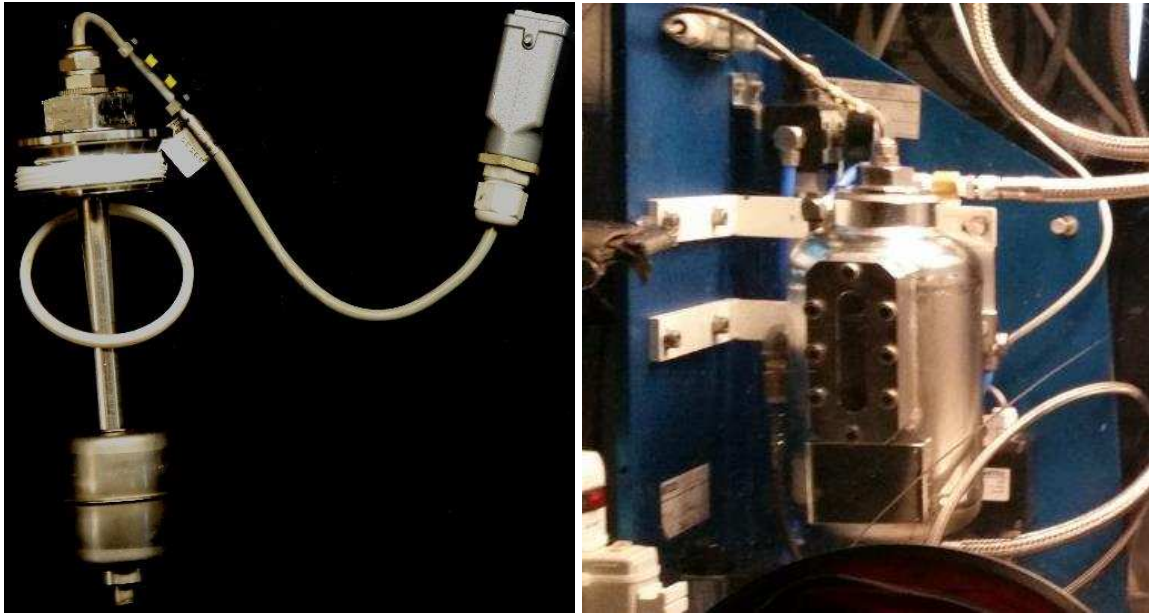


Figure 7-31. The threaded pressure sensor for the seal-fluid tank, left, and the threaded pressure sensor in place on the pressurized seal fluid tank, right.

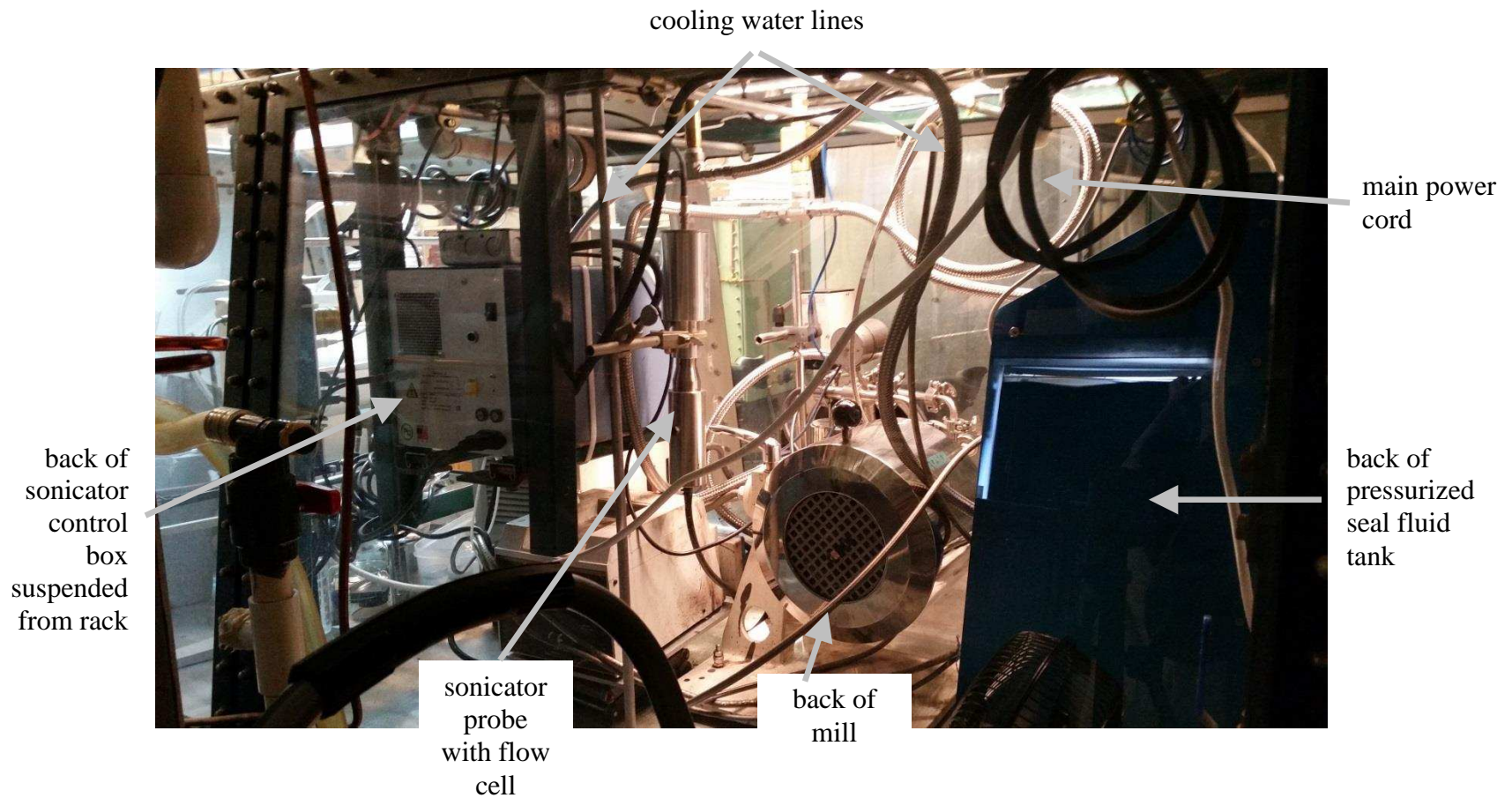


Figure 7-32. A Unistrut® rack was assembled inside the GB to suspend the flexible steel cooling water and seal-fluid lines, the flow cell sonicator and probe, electrical cords and even the sonicator control box.

7-8 Tables

Table 7-1. Summary of Milling Experimental Details.

| sample name | milled aerobic/anaerobic | seal-fluid | mill-fluid | additives (wt/wt% of MGS) | mill time (h) | BET surface area (m ² g ⁻¹) | Si-C (% by XPS) | Si-O (% by XPS) |
|-------------------------|-----------------------------|------------|------------|------------------------------|------------------|---|--------------------|--------------------|
| hand ground 20-45 μm | – | – | – | – | – | 0.7 | – | – |
| A-M/P-5h | aerobic | mesitylene | mesitylene | pyrene 9.0 | 5 | 130 | 34 | 35 |
| A-M/P-6h | aerobic | mesitylene | mesitylene | pyrene 9.0 | 6 | 140 | — | — |
| AA-M/P-1h | anaerobic | mesitylene | mesitylene | pyrene 9.0 | 1 | 75 | — | — |
| AA-M/P-2h | anaerobic | mesitylene | mesitylene | pyrene 9.0 | 2 | 162 | — | — |
| AA-M/P-5h | anaerobic | mesitylene | mesitylene | pyrene 9.0 | 5 | 258 | 33 | 11 |
| AA-M/P-6h | anaerobic | mesitylene | mesitylene | pyrene 9.0 | 6 | 206 | — | — |
| A-H/M-5.5h | aerobic | mesitylene | heptane | – | 5.5 | 243 | 13 | 41 |
| AA-H/M-5.5h | anaerobic | mesitylene | heptane | – | 5.5 | 295 | 38 | 9 |
| AA-H-5.5h | anaerobic | heptane | heptane | – | 5.5 | 70 | 23 | 5 |
| A-H-5h | aerobic | heptane | heptane | – | 5 | 169 | 19 | 53 |
| AA-H-1h | anaerobic | heptane | heptane | – | 1 | 44 | 12 | 7 |
| AA-H-2h | anaerobic | heptane | heptane | – | 2 | 45 | — | — |
| AA-H-3h | anaerobic | heptane | heptane | – | 3 | 33 | 17 | 6 |
| AA-H-4h | anaerobic | heptane | heptane | – | 4 | 36 | — | — |
| AA-H-5h | anaerobic | heptane | heptane | – | 5 | 40 | 18 | 6 |

Table 7-2. Amounts of Various Elements in All Samples Studied by XPS.

| sample | Si | C | O | F | N |
|-------------|--------|--------|--------|--------|--------|
| | atomic | atomic | atomic | atomic | atomic |
| | % | % | % | % | % |
| A-M/P-5h | 24 | 56 | 20 | — | — |
| AA-M/P-5h | 31 | 62 | 7 | — | — |
| A-H/M-5.5h | 33 | 35 | 32 | — | — |
| AA-H/M-5.5h | 38 | 55 | 6 | 1 | — |
| AA-H-5.5h | 53 | 38 | 8 | 2 | — |
| AA-H-1h | 67 | 22 | 11 | — | — |
| AA-H-1h | 70 | 16 | 8 | 3 | 3 |
| sputtered | | | | | |
| AA-H-3h | 62 | 23 | 11 | 3 | — |
| AA-H-3h | 66 | 18 | 10 | 5 | 1 |
| AA-H-5h | 59 | 26 | 12 | 4 | — |
| AA-H-5h | 65 | 19 | 8 | 3 | 4 |
| sputtered | | | | | |
| A-H-5h | 36 | 32 | 33 | — | — |

Table 7-3. Estimated Particle Size from BET surface Area Measurement Compared to DLS

| Particle Size sample | BET surface area ($\text{m}^2 \text{g}^{-1}$) | calculated particle size ^a (diameter nm) | DLS particle size ^b (mean, std dev nm) | estimated DLS particle ^c size range (nm) |
|-------------------------|--|--|--|--|
| AA-H-1h | 44 | 58.5 | 235, 0.92 | 80-850 |
| AA-H-5h | 40 | 64.3 | 208, 1.58 | 70-900 |
| AA-M/P-1h | 75 | 34.3 | 224, 0.79 | 70-850 |
| AA-M/P-5h | 258 | 9.98 | 235, 3.71 | 75-550 |
| A-H-5h | 169 | 15.2 | 167, 1.13 | 65-550 |

^a Particle size calculated assuming non-porous spheres with no size distribution. The particle size diameter was varied until the surface area was $\pm 0.1 \text{ m}^2 \text{g}^{-1}$ of the measured surface area.

^b DLS particle size mean was averaged from the three measurements using the Malvern software. The std. dev. is the standard deviation of the mean and was also calculated using the Malvern software.

^c The estimated DLS particle size range is taken from the graph (Figure 16).

Chapter 7 References

- (1) Balaz, P. In *Mechanochemistry in Nanoscience and Minerals Engineering*; Springer-Verlag Berlin Heidelberg: 2008, p 413.
- (2) Balaz, P.; Achimovicova, M.; Balaz, M.; Billik, P.; Cherkezova-Zheleva, Z.; Criado, J. M.; Delogu, F.; Dutkova, E.; Gaffet, E.; Gotor, F. J.; Kumar, R.; Mitov, I.; Rojac, T.; Senna, M.; Streletskii, A.; Wieczorek-Ciurowa, K. *Chemical Society reviews* **2013**, *42*, 7571.
- (3) Castro, C. L., Mitchell, B. S. In *Synthesis, Functionalization and Surface Treatment of Nanoparticles*; Baraton, M. I., Ed.; American Scientific Publishers: 2002, p 450.
- (4) McMahan, B. W.; Perez, J. P. L.; Yu, J.; Boatz, J. A.; Anderson, S. L. *ACS Applied Materials & Interfaces* **2014**, *6*, 19579.
- (5) Xing, T.; Sunarso, J.; Yang, W.; Yin, Y.; Glushenkov, A. M.; Li, L. H.; Howlett, P. C.; Chen, Y. *Nanoscale* **2013**, *5*, 7970.
- (6) Kim, H. S.; Hong, S. J. *Current Nanoscience* **2014**, *10*, 118.
- (7) Akdogan, N. G.; Hadjipanayis, G. C.; Sellmyer, D. J. *Journal of Applied Physics* **2009**, *105*, 07A710.
- (8) Monteiro, A.; Afolabi, A.; Bilgili, E. *Drug Development and Industrial Pharmacy* **2013**, *39*, 266.
- (9) Wang, W.; Datta, M. K.; Kumta, P. N. *J. Mater. Chem.* **2007**, *17*, 3229.
- (10) Wang, W.; Kumta, P. N. *J. Power Sources* **2007**, *172*, 650.
- (11) Kwon, S. G.; Hyeon, T. *Small* **2011**, *7*, 2685.
- (12) Ghorpade, U.; Suryawanshi, M.; Shin, S. W.; Gurav, K.; Patil, P.; Pawar, S.; Hong, C. W.; Kim, J. H.; Kolekar, S. *Chemical Communications* **2014**, *50*, 11258.
- (13) Williams, J. V.; Kotov, N. A.; Savage, P. E. *Industrial & Engineering Chemistry Research* **2009**, *48*, 4316.
- (14) Jankovic, A. *Minerals Engineering* **2003**, *16*, 337.
- (15) Stenger, F.; Mende, S.; Schwedes, J.; Peukert, W. *Chemical Engineering Science* **2005**, *60*, 4557.
- (16) Suryanarayana, C. *Progress in Materials Science* **2001**, *46*, 1.
- (17) Mende, S.; Stenger, F.; Peukert, W.; Schwedes, J. *Powder Technology* **2003**, *132*, 64.
- (18) Peukert, W.; Schwarzer, H.-C.; Stenger, F. *Chemical Engineering and Processing: Process Intensification* **2005**, *44*, 245.
- (19) Sommer, M.; Stenger, F.; Peukert, W.; Wagner, N. J. *Chemical Engineering Science* **2006**, *61*, 135.
- (20) Pourghahramani, P.; Altin, E.; Mallembakam, M. R.; Peukert, W.; Forssberg, E. *Powder Technology* **2008**, *186*, 9.
- (21) Knieke, C.; Sommer, M.; Peukert, W. *Powder Technology* **2009**, *195*, 25.
- (22) Knieke, C.; Berger, A.; Voigt, M.; Taylor, R. N. K.; Röhr, J.; Peukert, W. *Carbon* **2010**, *48*, 3196.
- (23) Knieke, C.; Steinborn, C.; Romeis, S.; Peukert, W.; Breitung-Faes, S.; Kwade, A. *Chemical Engineering & Technology* **2010**, *33*, 1401.
- (24) Knieke, C.; Romeis, S.; Peukert, W. *AIChE Journal* **2011**, *57*, 1751.
- (25) Pradeep, P. R.; Pitchumani, B. *Asia-Pacific Journal of Chemical Engineering* **2011**, *6*, 154.

- (26) Kirby, B. J. *Micro- and Nanoscale Fluid Mechanics. Transport in Microfluidic Devices*; First Edition ed.; Cambridge University Press, 2010.
- (27) Nic, M. J., J.; Kosata, B.; Updates by Jenkins, A. In *IUPAC. Compendium of Chemical Terminology, 2nd ed. (the "Gold Book")*, XML on-line corrected version: <http://goldbook.iupac.org> (2006-) McNaught, A. D. W., A., Ed.; Blackwell Scientific Publications, Oxford
- (28) Butyagin, P. Y.; Streletskii, A. N.; Berestetskaya, I. V.; Borunova, A. B. *Colloid Journal* **2001**, *63*, 639.
- (29) Van Devener, B.; Anderson, S. L. *Energy & Fuels* **2006**, *20*, 1886.
- (30) Van Devener, B.; Perez, J. P. L.; Jankovich, J.; Anderson, S. L. *Energy & Fuels* **2009**, *23*, 6111.
- (31) Gan, Y.; Qiao, L. *Combustion and Flame* **2011**, *158*, 354.
- (32) Tyagi, H.; Phelan, P. E.; Prasher, R.; Peck, R.; Lee, T.; Pacheco, J. R.; Arentzen, P. *Nano letters* **2008**, *8*, 1410.
- (33) Beloni, E.; Hoffmann, V. K.; Dreizin, E. L. *Journal of Propulsion and Power* **2008**, *24*, 1403.
- (34) Suryanarayana, C.; Ivanov, E.; Boldyrev, V. V. *Materials Science and Engineering: A* **2001**, *304–306*, 151.
- (35) Zhang, D. L. *Progress in Materials Science* **2004**, *49*, 537.
- (36) Heintz, A. S.; Fink, M. J.; Mitchell, B. S. *Advanced Materials* **2007**, *19*, 3984.
- (37) Heintz, A. S.; Fink, M. J.; Mitchell, B. S. *Applied Organometallic Chemistry* **2010**, *24*, 236.
- (38) Shen, T. D.; Shmagin, I.; Koch, C. C.; Kolbas, R. M.; Fahmy, Y.; Bergman, L.; Nemanich, R. J.; McClure, M. T.; Sitar, Z.; Quan, M. X. *Physical Review B* **1997**, *55*, 7615.
- (39) Shen, T. D.; Koch, C. C.; McCormick, T. L.; Nemanich, R. J.; Huang, J. Y.; Huang, J. G. *Journal of Materials Research* **1995**, *10*, 139.
- (40) Radvanyi, E.; De Vito, E.; Porcher, W.; Jouanneau Si Larbi, S. *J. Anal. Atomic Spec.* **2014**, *29*, 1120.
- (41) Nguyen, T.; Lefrant, S. *J. Phys.: Condens. Matter* **1989**, *1*, 5197.
- (42) Nie, M. Y.; Abraham, D. P.; Chen, Y. J.; Bose, A.; Lucht, B. L. *J. Phys. Chem. C* **2013**, *117*, 13403.
- (43) Philippe, B.; Dedryvere, R.; Gorgoi, M.; Rensmo, H.; Gonbeau, D.; Edstrom, K. *Chem. Mater.* **2013**, *25*, 394.
- (44) Shirahata, N.; Yonezawa, T.; Seo, W.-S.; Koumoto, K. *Langmuir* **2004**, *20*, 1517.
- (45) Miyoshi, K.; Buckley, D. H. *Appl. Surf. Sci.* **1982**, *10*, 357.
- (46) Wheeler, D.; Pepper, S. *Surface Interface Analy.* **1987**, *10*, 153.
- (47) Chockla, A. M.; Harris, J. T.; Akhavan, V. A.; Bogart, T. D.; Holmberg, V. C.; Steinhagen, C.; Mullins, C. B.; Stevenson, K. J.; Korgel, B. A. *J. Am. Chem. Soc.* **2011**, *133*, 20914.
- (48) Harikumar, K. R.; Polanyi, J. C.; Zabet-Khosousi, A. *Surface Science* **2012**, *606*, 1431.
- (49) Heintz, A. S., Tulane Univeristy, 2008.
- (50) Shaw, L. L.; Yang, Z.; Ren, R. *Journal of the American Ceramic Society* **1998**, *81*, 760.
- (51) Eubanks, I. D.; Abbott, F. J. *Analytical Chemistry* **1969**, *41*, 1708.
- (52) Shriver, D. F. *The manipulation of air-sensitive compounds*; Wiley: New York, 1986.
- (53) Brunauer, S.; Emmett, P. H.; Teller, E. *J Am Chem Soc* **1938**, *60*, 309.
- (54) Emmett, P. H.; Brunauer, S. *J Am Chem Soc* **1937**, *59*, 1553.

(55) Larryisgood; Wikimedia Commons: Online, 2015.

Chapter 8.

Summary and Future Work

8.1 General Conclusions

The major conclusions drawn from the work presented in this dissertation have been discussed in each chapter. A brief mention of those conclusions will be described here.

The crude $\text{K}_2\text{B}_{12}\text{F}_{12}$ produced in MeCN at 0 °C with $\text{F}_2(g)$ and excess KF produces a colored impurity that is difficult to remove, even with H_2O_2 as described in the published synthesis method. While the exact cause of the colored impurity could not be definitively determined, it is believed to originate by oxidation of MeCN during the fluorination reaction. A new liquid-liquid extraction method was developed to discontinue the use of H_2O_2 in the purification. From highly purified $\text{K}_2\text{B}_{12}\text{F}_{12}$, $\text{Li}_2\text{B}_{12}\text{F}_{12}$ and $\text{Na}_2\text{B}_{12}\text{F}_{12}$ can be made by cation-exchange with a strong-acid ion exchange column with the proper cation form. Both $\text{Li}_2\text{B}_{12}\text{F}_{12}$ and $\text{Na}_2\text{B}_{12}\text{F}_{12}$ can be thermally dried without decomposition.

A hydronium salt of $\text{B}_{12}\text{F}_{12}^{2-}$ can be made using the same cation-exchange with a strong-acid ion exchange column, with the column in the H^+ form. The salt $(\text{H}_3\text{O})_2\text{B}_{12}\text{F}_{12}\cdot 6\text{H}_2\text{O}$, can be thermally dried in stages, 2 H_2O molecules each, down to $(\text{H}_3\text{O})_2\text{B}_{12}\text{F}_{12}$ reversibly, however, attempts to remove the last 2 H_2O molecules at temperatures in excess of 300 °C causes the compound to decompose. A similar thermal loss of water in stages of 2 H_2O molecules each is observed in $(\text{NH}_4)\text{B}_{12}\text{F}_{12}\cdot 4\text{H}_2\text{O}$ and attempts to thermally remove the remaining 3 NH_3 molecules also results in decomposition at temperature in excess of 450 °C. Crystal structures of $(\text{H}_3\text{O})_2\text{B}_{12}\text{F}_{12}\cdot 6\text{H}_2\text{O}$ and $(\text{H}_3\text{O})_2\text{B}_{12}\text{F}_{12}\cdot 4\text{H}_2\text{O}$, exhibit two dimensional infinite hydrogen bonded

networks of H_3O^+ and H_2O , whereas the $(\text{NH}_4)_2\text{B}_{12}\text{F}_{12}\cdot 4\text{H}_2\text{O}$ only exhibits a one dimensional hydrogen bonded infinite network of NH_4^+ and H_2O .

Attempts to directly apply the Peryshkov fluorination method developed for $\text{K}_2\text{B}_{12}\text{H}_{12}$ (0°C MeCN, with $\text{F}_2(\text{g})$ and excess KF to absorb HF forming KHF_2) to the monoammonio anion $\text{KB}_{12}\text{H}_{11}\text{NH}_3$ results in significant decomposition before most of the target compound $\text{KB}_{12}\text{F}_{11}\text{NH}_3$ is formed. Without added KF, allowing HF to build-up during the reaction, the $\text{KB}_{12}\text{H}_{11}\text{NH}_3$ will completely fluorinate to $\text{KB}_{12}\text{F}_{11}\text{NH}_3$ with ca. 80% crude yield. Furthermore, contrary to the Peryshkov method where HF was reported to inhibit the fluorination of $\text{K}_2\text{B}_{12}\text{H}_{12}$, especially near the end of the reaction, the fluorination of $\text{KB}_{12}\text{H}_{11}\text{NH}_3$ appears to happen faster with added anhydrous HF. It should be noted, the Peryshkov method always had ca. 2% H_2O for the with and with added HF reactions when it was observed that HF slowed the fluorination rate. And the fluorination of $\text{KB}_{12}\text{H}_{11}\text{NH}_3$ takes place in anhydrous MeCN with anhydrous HF added due to the hygroscopic nature of the $\text{KB}_{12}\text{H}_{11}\text{NH}_3$. Additionally, the three diammono isomers of 1,2-, 1,7-, and 1,12- $\text{B}_{12}\text{H}_{10}(\text{NH}_3)_2$ have been synthesized, isolated and structurally characterized by single crystal X-ray diffraction. Furthermore, the 1,2-, 1,7-, and 1,12- $\text{B}_{12}\text{F}_{10}(\text{NH}_3)_2$ have been synthesized, isolated and the 1,7-, and 1,12- $\text{B}_{12}\text{F}_{10}(\text{NH}_3)_2$ have been structurally characterized by single crystal X-ray diffraction.

Three new isomers of $\text{C}_{60}(\text{CF}_3)_{10}$ have been structurally characterized by single crystal X-ray diffraction as well as a cyclo adduct, 1,9- $\text{C}_{60}(\text{cyclo-CF}_2(2\text{-C}_6\text{F}_4))$. Additionally, a previously reported isomer of $\text{C}_{60}(\text{CF}_3)_{10}$ has been structurally characterized confirming the addition pattern previously reported based on spectroscopic methods. The crystal structure packing, nearest neighbors and cage surface to cage surface distances of the $\text{C}_{60}(\text{CF}_3)_{10}$ isomers and 1,9- $\text{C}_{60}(\text{cyclo-CF}_2(2\text{-C}_6\text{F}_4))$ were compared to the industry-standard fullerene acceptor phenyl- C_{61} -butyric acid

methyl ester (PCBM) in organic photovoltaic devices and it was found that 1,9- $C_{60}(\text{cyclo-CF}_2(2-C_6F_4))$ had the experimentally calculated density and the largest number and shortest distance to nearest neighbor fullerenes. Based on the number and proximity of the closest fullerene cages in the crystal structure of 1,9- $C_{60}(\text{cyclo-CF}_2(2-C_6F_4))$, it is believed to have better electron conducting properties over the $C_{60}(\text{CF}_3)_{10}$ isomer and PCBM fullerenes.

A new metal reactor was developed and initially tested for the free radical substitution reaction of CF_3I with polycyclic aromatic hydrocarbons (PAH), and fullerenes. The metal reactor can operate at much higher pressures and slightly higher temperatures over the previously used sealed glass ampoules. The metal reactor produced both $\text{PAH}(\text{CF}_3)_n$ compounds, $C_{60}(\text{CF}_3)_n$ and $C_{70}(\text{CF}_3)_n$ compounds. The increased pressure in the metal reactor is thought to be part of the cause of an increase in the number of CF_3 additions to PAHs compared to the sealed glass ampoules.

Two compounds based on coronene isolated from a crude reaction mixture using the metal reactor (coronene, 34 equiv of CF_3I , excess copper powder at 450 °C for 4 h) were structurally characterized and found to both have adjacent sp^3 carbons with a CF_3 addition and hydrogen atom. Two other molecules presented also exhibited sp^3 carbons from two different reaction methods and starting materials. The four compounds with sp^3 carbons, from free radical addition starting from CF_3I and a PAH lead to the conclusion that the radical mechanism must form a $\text{CF}_3\text{-PAH}\cdot$ radical intermediate at some point in the reaction rather than a $\text{PAH}\cdot$ radical.

Finally, five $\text{PAH}(\text{CF}_3)_n$ structures were characterized by single crystal X-ray analysis to determine the number and proximity of nearest neighbors in a crystal lattice to qualitatively assess the electronic communication in each crystal structure. The $\text{PAH}(\text{CF}_3)_n$ structures examined were found to either be too far away or have poor aromatic overlap to be conducive to electronic

communication in the solid state. Conversely, it was determined that the TRPH(C₄F₄), with interplanar distances of 3.396 Å, approaching that of graphite, has three important physical characteristics that promote short interplanar distances. These three physical characteristics are (i) the C₄F₄ substitution does not greatly change the Z dimension of the triphenylene core, (ii) the C₄F₄ moiety makes the TRPH(C₄F₄) have a dipole causing the molecule to orient with a 180° rotation relative to molecules above and below (iii) the triphenylene core is still relatively open allowing for significant aromatic overlap.

Experiments involving the milling of metallurgical grade silicon (MGS) under aerobic and anerobic conditions yielded a surprising regarding the presence of O₂ and the ability to mill small particles. If milled anerobically, with no surface passivating additives, the MGS will reach mechanochemical equalibrium rapidly, and no more observable particle size derease will occur, only further amorphitization. As expected, anaerobically milled MGS, with no surface passivating additives is also quite reactive with oxygen. If surface passivating additives are used then smaller partical size can be realized due to less particle-particle interaction. One of the most unanticipated results from this research is that even when milling MGS aerobically, in only heptane a significant amout of Si-C bonds are formed as well as Si-O, indicating that all solvents, additives and even the atmosphere should be controled and condiseder when milling with a circulating stirred media mill.

8.2 Future Work

When performing research of a particular topic, the research is never fully "complete", there are always new directions, new experiments, and new control experiments that can be completed to more fully undersatand the particular system in which one is researching. Becasue of the unlimited possiblities of research the author has chosen to limit the "Future Work" section at the

end of each chapter and in the summary to the "next logical experiments" based on the conclusions drawn from the research presented.

Chapter 2. Improved Synthesis and Purification the of Superweak Anion Salts $\text{Li}_2\text{B}_{12}\text{F}_{12}$, $\text{Na}_2\text{B}_{12}\text{F}_{12}$, and $\text{K}_2\text{B}_{12}\text{F}_{12}$

Future experiments that could be performed regarding the purification of $\text{K}_2\text{B}_{12}\text{F}_{12}$, and the $(\text{H}_3\text{O})_3\text{B}_{12}\text{F}_{12}\cdot 6\text{H}_2\text{O}$, $\text{Li}_2\text{B}_{12}\text{F}_{12}$, and $\text{Na}_2\text{B}_{12}\text{F}_{12}$ salts are; (i) if decomposed MeCN is likely the colored impurities in the $\text{K}_2\text{B}_{12}\text{F}_{12}$ made in MeCN with $\text{F}_2(g)$, then try to come up with and test a new solvent (knowing the properties of $\text{F}_2(g)$, not an easy task), (ii) actually test the conductivity of $\text{Na}_2\text{B}_{12}\text{F}_{12}$ in electrolyte solvents ($\text{Li}_2\text{B}_{12}\text{F}_{12}$ conductivity known in literature) and test the proton conducting properties of solid, purified, $(\text{H}_3\text{O})_3\text{B}_{12}\text{F}_{12}\cdot 6\text{H}_2\text{O}$, and (iii) determine the Cl^- content (possibly using a titration method or ion chromatography analysis method) of the $(\text{H}_3\text{O})_3\text{B}_{12}\text{F}_{12}\cdot 6\text{H}_2\text{O}$, $\text{Li}_2\text{B}_{12}\text{F}_{12}$, and $\text{Na}_2\text{B}_{12}\text{F}_{12}$ made from strong acid ion exchange chromatography.

Chapter 3. Synthesis and Properties of Anhydrous and Hydrated Hydronium Salts of $\text{B}_{12}\text{F}_{12}^{2-} (\text{H}_3\text{O})_2\text{B}_{12}\text{F}_{12}\cdot n(\text{H}_2\text{O})$ ($n = 6, 4, 2, 0$): In Search of $\text{H}_2\text{B}_{12}\text{F}_{12}$

There are at least three experiments that would make the research of $(\text{H}_3\text{O})_2\text{B}_{12}\text{F}_{12}\cdot n\text{H}_2\text{O}$ and its hydrated phases more complete. First, measure the proton conduction of $(\text{H}_3\text{O})_2\text{B}_{12}\text{F}_{12}\cdot n\text{H}_2\text{O}$ hydrated salts in both solid and aqueous samples. This would allow direct comparison with other proton conducting salts, and determine the viability of $(\text{H}_3\text{O})_2\text{B}_{12}\text{F}_{12}\cdot n\text{H}_2\text{O}$ hydrated salts as proton conductors in commercial applications. Second, attempt to chemically desolvate $(\text{H}_3\text{O})_2\text{B}_{12}\text{F}_{12}\cdot n\text{H}_2\text{O}$ or $(\text{NH}_4)_2\text{B}_{12}\text{F}_{12}\cdot n\text{H}_2\text{O}$ as a novel method to form the putative superacid $\text{H}_2\text{B}_{12}\text{F}_{12}$. Chemical desolvation to form the superacid $\text{H}_2\text{B}_{12}\text{F}_{12}$ will be challenging because,

hypothetically, almost anything will react with $\text{H}_2\text{B}_{12}\text{F}_{12}$, making a salt, even benzene as described by Reed et al.¹ Rather than a direct chemical desolvation, the formation of $\text{H}_2\text{B}_{12}\text{F}_{12}$ might occur with a moderate temperature and a strong desiccant. For example, dried KOH(s) in an Abnerholden drying pistol with refluxing mesitylene to keep the sample around 165 °C. This could slowly drive off the water and trap it in a strong desiccant. Assuming there is a slight equilibrium to produce $\text{H}_2\text{O(g)}$ under such dry conditions, this method would constantly shift the equilibrium towards producing more $\text{H}_2\text{O(g)}$, eventually drying the sample without decomposition. Finally, the $\text{H}_2\text{B}_{12}\text{F}_{12}$ putative super acid should be synthesized using literature methods previously described (Section 3.2) in order to study and compare the properties and acidity of $\text{H}_2\text{B}_{12}\text{F}_{12}$ with other previously researched literature superacids.

Chapter 4. New or Improved Syntheses of the $\text{B}_{12}\text{H}_{11}(\text{NH}_3)^-$ and $\text{B}_{12}\text{F}_{11}(\text{NH}_3)^-$ Anions and the 1,2-, 1,7-, and 1,12- Isomers of $\text{B}_{12}\text{H}_{10}(\text{NH}_3)_2$ and $\text{B}_{12}\text{F}_{10}(\text{NH}_3)_2$ and Their Spectroscopic and Structural Characterization

Multiple experiments are necessary to elucidate the surprising phenomenon that $\text{KB}_{12}\text{H}_{11}\text{NH}_3$ will completely fluorinate forming $\text{KB}_{12}\text{F}_{11}\text{NH}_3$ in the presence of > 10 equiv of HF, a result exactly opposite to the complete fluorination of $\text{K}_2\text{B}_{12}\text{H}_{12}$ forming $\text{K}_2\text{B}_{12}\text{F}_{12}$. The first desired experiment is to take an equal molar mixture of $\text{KB}_{12}\text{H}_{11}\text{NH}_3$ and $\text{K}_2\text{B}_{12}\text{H}_{12}$ in anhydrous MeCN with 10-12 equiv of HF. The first problem with such an experiment is that $\text{K}_2\text{B}_{12}\text{H}_{12}$ has low solubility in anhydrous MeCN, which is why 2.4% H_2O is typically added during the first step of the fluorination of $\text{K}_2\text{B}_{12}\text{H}_{12}$. If necessary, a minimal amount of water could be added to the anhydrous MeCN to get $\text{K}_2\text{B}_{12}\text{H}_{12}$; however, it may also be the case that the added HF would raise the dielectric strength of the MeCN enough to dissolve the $\text{K}_2\text{B}_{12}\text{H}_{12}$. If in this experiment $\text{K}_2\text{B}_{12}\text{H}_{12}$ still completely fluorinates without a drastic decrease in the rate than other control

experiments are required. First, attempt to fluorinate $K_2B_{12}H_{12}$ in anhydrous MeCN with addition of anhydrous HF, since Peryshkov always used added H_2O in his fluorinations in MeCN, if he used aqueous HF instead of anhydrous HF, this could have a drastic effect on solvent properties. Next fluorinate a single isomer of $B_{12}H_{10}(NH_3)_2$, preferably 1,12- because then only one type of B–H is being fluorinated during the reaction. Finally, some DFT calculations such as which B_3 face would be the lowest energy for protonation of $B_{12}H_{11}NH_3^-$ and $B_{12}HF_{10}NH_3^-$, do those positions change in a higher dielectric medium, and does the $-NH_3$ electronic effects on the B_{12} cage change the way B–H bonds and B_3 faces interact with HF, or F_2 in MeCN would aid in determining the unanticipated, reproducible result that $B_{12}H_{11}NH_3^-$ fluorinates faster in the presence of HF.

Chapter 5. Single-Crystal X-ray Structural Characterization of C_{60} Derivatives with Perfluoroalkyl and Related Perfluorinated Substituents: Seven Isomers of $C_{60}(CF_3)_{10}$ and 1,9- $C_{60}(cyclo-CF_2(2-C_6F_4))$, a Faux Hawk Fullerene with PCBM-like Properties

The research into $C_{60}(CF_3)_2$ and other C_{60} electron acceptor fullerenes is very well established, but there are a few experiments regarding phase changes and thermal stability that could be tested. It is known that the industry-standard fullerene acceptor phenyl- C_{61} -butyric acid methyl ester (PCBM) decomposes upon heating to temperatures used for chemical vapor deposition of films. It has also been demonstrated that 1,9- $C_{60}(cyclo-CF_2(2-C_6F_4))$ is much more thermally stable to the same temperatures. What has not been established for any of these C_{60} electron acceptor fullerenes (to the best of this authors knowledge) is any crystal structure phase changes that can occur in anyone of the processing steps of using these C_{60} based fullerenes in OPV devices. The heating and cooling, the multiple materials and solvents, all could lead to quite different crystal packing of the C_{60} electron acceptor material when actually in the device.

While getting single crystal X-ray data from a full device, high resolution powder data might be more than enough to at least determine if different chemical vapor deposition temperature, drying, solution casting etc. have an effect on the phase (and commensurately) the packing in the crystal structure, that would affect electronic communication between fullerene molecules.

Chapter 6. Versatile Robust Metal Reactor for High Temperature Trifluoromethylation of PAHs and Fullerenes; X-ray Structural Characterization of PAH(CF₃)_n and Related Compounds and Insights into the Mechanism of Radical Substitution

Important future experiments regarding the metal reactor include using larger, more thermally stable PAHs to determine if the reactor works for other large PAHs that were unsuccessful in the sealed glass ampoules. Perform reactions with a mixture of CF₃I and N₂(g) (or other inert gas) to determine if the increased pressure is changing the reaction or just the concentration of CF₃I. Also test new I₂(g) scavengers that do not change the reaction by changing the thermal homolysis temperature of the C–I bond, CF₃I adsorption/desorption kinetics, I•/I₂ scavenging etc.) as much as copper powder. Determine if I• is important to eliminate HI and rearomatize the PAH core after the CF₃ addition, by a control experiment hexafluoroacetone as the F₃C• radical generator removing I• from the reaction. Finally, to determine if CF₃ can be removed from a F₃C–PAH during the reaction a second control experiment with only a single PAH(CF₃)_n heated to a temperature or many temperatures to see if it is thermally stable once produced. Furthermore, study phase changes of these materials for the same reasons described in the fullerene X-ray crystal structure chapter above.

Chapter 7. Preparation and Characterization of Silicon Nanoparticles by Anaerobic Wet Milling

While the Strauss-Boltalina group no longer has access to the Netzsch MiniCer Laboratory stirred media mill, there are some follow-on experiments that would be an interesting addition to this research. First, repeat the aerobic and anaerobic milling of the metallurgical grade silicon with even more reactive organic additives and solvents to try and more completely surface passivate the Si nanoparticles. Reactive additives can include aldehydes, amides, and alkenes, more reactive solvents could include cyclohexene, ethylene carbonate, or propylene glycol. With new additives, different chemistry could be occurring on the surface of the nanoparticles. Further attempts should be made to characterize what is on the surface of the nanoparticles by solid state NMR, or attenuated total reflectance FT-IR analysis of the surface. Depending on the residual surface chemistry, nano particles produced with this type of chemically modified surface could be further reacted to augment their surface chemistry for a particular application.

Since so many practical uses of nanoparticles have been optimized for regular-shaped nanoparticles, methods to make regular shaped and low size distribution nano-scale materials by top-down-milling would be advantageous over bottom-up-solution methods. Methods to polish the irregular shaped particles produced by this type of milling method, either during the milling process or in a secondary milling process would be of great interest for many applications requiring expensive bottom-up synthesized nanoparticles. This polishing can be accomplished by further wearing and fracture of the particles (similar to polishing a metal surface with finer and finer grit sand paper) or by a chemical polishing method.